frontiers | Research Topics

# Advances in ocean bottom seismology

**Edited by**
Francisco Javier Nuñez-Cornu, Susan Bilek, Nathaniel Lindsey,
Diana Núñez and Charlotte A. Rowe

**Published in**
Frontiers in Earth Science

ISSN 1664-8714
ISBN 978-2-88974-943-0
DOI 10.3389/978-2-88974-943-0

## About Frontiers

Frontiers is more than just an open access publisher of scholarly articles: it is a pioneering approach to the world of academia, radically improving the way scholarly research is managed. The grand vision of Frontiers is a world where all people have an equal opportunity to seek, share and generate knowledge. Frontiers provides immediate and permanent online open access to all its publications, but this alone is not enough to realize our grand goals.

## Frontiers journal series

The Frontiers journal series is a multi-tier and interdisciplinary set of open-access, online journals, promising a paradigm shift from the current review, selection and dissemination processes in academic publishing. All Frontiers journals are driven by researchers for researchers; therefore, they constitute a service to the scholarly community. At the same time, the *Frontiers journal series* operates on a revolutionary invention, the tiered publishing system, initially addressing specific communities of scholars, and gradually climbing up to broader public understanding, thus serving the interests of the lay society, too.

## Dedication to quality

Each Frontiers article is a landmark of the highest quality, thanks to genuinely collaborative interactions between authors and review editors, who include some of the world's best academicians. Research must be certified by peers before entering a stream of knowledge that may eventually reach the public - and shape society; therefore, Frontiers only applies the most rigorous and unbiased reviews. Frontiers revolutionizes research publishing by freely delivering the most outstanding research, evaluated with no bias from both the academic and social point of view. By applying the most advanced information technologies, Frontiers is catapulting scholarly publishing into a new generation.

## What are Frontiers Research Topics?

Frontiers Research Topics are very popular trademarks of the *Frontiers journals series*: they are collections of at least ten articles, all centered on a particular subject. With their unique mix of varied contributions from Original Research to Review Articles, Frontiers Research Topics unify the most influential researchers, the latest key findings and historical advances in a hot research area.

Find out more on how to host your own Frontiers Research Topic or contribute to one as an author by contacting the Frontiers editorial office: frontiersin.org/about/contact

# Advances in ocean bottom seismology

**Topic editors**

Francisco Javier Nuñez-Cornu — University of Guadalajara, Mexico
Susan Bilek — New Mexico Institute of Mining and Technology, United States
Nathaniel Lindsey — Stanford University, United States
Diana Núñez — Complutense University of Madrid, Spain
Charlotte A. Rowe — Los Alamos National Laboratory (DOE), United States

**Citation**

Nuñez-Cornu, F. J., Bilek, S., Lindsey, N., Núñez, D., Rowe, C. A., eds. (2023). *Advances in ocean bottom seismology*. Lausanne: Frontiers Media SA.
doi: 10.3389/978-2-88974-943-0

# Table of contents

frontiers in Earth Science

EDITORIAL
published: 25 March 2022
doi: 10.3389/feart.2022.852059

# Editorial: Advances in Ocean Bottom Seismology

*Charlotte A. Rowe*[1]*, *Francisco J. Núñez-Cornú*[2], *Diana Núñez*[2], *Susan Bilek*[3] and *Nathaniel Lindsey*[4]

[1]Los Alamos National Laboratory (DOE), Los Alamos, NM, United States, [2]Centro de Sismología y Vulcanología de Occidente, Universidad de Guadalajara, Puerto Vallarta, Mexico, [3]New Mexico Institute of Mining and Technology, Socorro, NM, United States, [4]Fibersense, Canton, MA, United States

**Keywords: marine, ocean, seismologic observatories, active source, passive**

## Editorial on the Research Topic

## Advances in Ocean Bottom Seismology

Among the physical sciences, seismology is relatively young; with the continued advances in instrumental technologies and computer capacity, ours has to be one of the most rapidly evolving subject areas within the Earth Sciences writ large. Exploration of the Earth by way of seismic observation and modeling is expanding not only in the range of capabilities - from reservoir scale to whole-Earth sensing - but in recent decades seismology has resolutely marched from the Earth's continents and sea shores into the oceans, which cover nearly 75% of the Earth and have until recently hindered our ability to more fully explore the planet.

The past few decades have brought about advances in design and deployment of ocean bottom seismic sensors and their data acquisition capacity, resulting in an exponential increase in seafloor seismic experiments driven by both pure scientific inquiry as well as economic development. With the increasing focus on what is arguably Earth's last frontier for seismology, it is timely that we present some of the latest new results, observations, modeling and technological advances in ocean bottom seismology.

Many traditional seismic techniques that have been used in special land-based deployments are also undertaken by marine seismologists. Their work is made more challenging by difficult deployment requirements and the long time gap between station installation and data retrieval. Hindering many fundamental analyses is the appreciable seismic noise environment on the ocean floor, inaccessibility of sensors for validation of precise location, attitude and orientation, coupling and response issues and possible errors or mishaps that cannot be addressed in near real time as they would on land. Nosov et al. present here an intriguing new approach to evaluate the impacts of these issues, however. Such difficulties have not daunted researchers, who have been able to gain unprecedented observations and new understanding of geodynamic processes in spreading centers, triple junctions and transform systems, such as Núñez-Cornú et al.'s TSUJAL passive experiment offshore Western Mexico and the active-source profiling near the Mexican Islas Marias combined with passive data (Madrigal et al.; Núñez et al.) to further explore tectonic structures and correlate the observations with detailed bathymmetry.

Evaluation of seismic hazard and improved location capability for near-shore offshore events - including potentially tsunamigenic earthquakes - are historically difficult when observations are restricted to onshore networks, but a better picture of offshore seismicity for assessing hazards is demonstrated for an OBS experiment in the Ionian Sea by Sgroi et al.

Innovative application, or adaptation, of new and specialized seismic methods are demonstrated with seafloor data, providing an exciting opportunity for insights and uses for these sometimes

OPEN ACCESS

***Edited and reviewed by:***
*Carolina Lithgow-Bertelloni, University of California, Los Angeles, United States*

***Correspondence:**
*Charlotte A. Rowe*
*char@lanl.gov*

***Specialty section:***
*This article was submitted to Solid Earth Geophysics, a section of the journal Frontiers in Earth Science*

***Received:*** *10 January 2022*
***Accepted:*** *27 January 2022*
***Published:*** *25 March 2022*

***Citation:***
*Rowe CA, Núñez-Cornú FJ, Núñez D, Bilek S and Lindsey N (2022) Editorial: Advances in Ocean Bottom Seismology. Front. Earth Sci. 10:852059. doi: 10.3389/feart.2022.852059*

challenging observations. Laske demonstrates robust observations of normal modes using broadband OBS data, making a convincing case that the best possible sensors should be deployed in marine experiments, allowing for exploitation of observations beyond those which may be initially targeted by a particular deployment. Along the same vein, Tonegawa et al. show that the often-problematic seafloor seismic noise can be exploited, as in on-land noise surveys, to derive structural information in the absence of earthquake or air gun sources in some circumstances.

Creative application of techniques not previously applied to seafloor data are demonstrated by González-Fernández, in his full-wave extension of the generalized reciprocal method on refraction data to image structure beneath the Gulf of California, while Bayrakci et al. apply seismic anistropy methods to seafloor data to illuminate fractures that may be associated with seafloor methane venting in the North Sea, a significant concern for climate change. Dhakal and Kunugi report on strong motion analyses using the cabled S-net and K-net OBS deployments offshore of Japan, and the implications for earthquake early warning.

Finally, looking ahead, we have promising efforts underway in instrumentation and analytical advances related to seafloor cables themselves. Howe et al. and Matias et al. bring reports on developments for new capacity on seafloor cables. The planned deployment of Science Monitoring And Reliable Telecommunications (SMART) cables in the north Atlantic, targeting the Azores and offshore seismic sources impacting Iberia will exploit not only the cables' repeater-housed sensors but also Digital Acoustic Sensing (DAS) and laser interferometry techniques to provide real-time high-resolution observations and analysis of this tectonically active and hazardous area. The overall motivation, current status and important contributions anticipated by the SMART Cables initiative and its worldwide impact on seafloor geophysics (and oceanography) for not only earthquake observations and both earthquake and tsunami early warning, but also critical climate change data, provide us with a vision for ubiquitous sensing and real-time data return that is moving closer to reality for our science.

Any volume of research and review papers can only provide a snapshot in time of the state of the science, but we hope the wide spectrum of projects and analyses presented here can motivate additional research, new ways to exploit data already acquired and new approaches to solving the perplexing problems associated with expanding our seismic view into the oceans.

## AUTHOR CONTRIBUTIONS

Editorial written by CR, edited, modified by all other guest editors.

## ACKNOWLEDGMENTS

This is Los Alamos publication LA-UR-22-20191.

**Conflict of Interest:** NL is employed by Fibersense.

The remaining authors declare that the research was conducted in the absence of any commercial or financial relationships that could be construed as a potential conflict of interest.

**Publisher's Note:** All claims expressed in this article are solely those of the authors and do not necessarily represent those of their affiliated organizations, or those of the publisher, the editors and the reviewers. Any product that may be evaluated in this article, or claim that may be made by its manufacturer, is not guaranteed or endorsed by the publisher.

frontiers in Earth Science

ORIGINAL RESEARCH
published: 21 January 2021
doi: 10.3389/feart.2020.610993

# Near-Field Body-Wave Extraction From Ambient Seafloor Noise in the Nankai Subduction Zone

*Takashi Tonegawa*, Toshinori Kimura and Eiichiro Araki*

*Research Institute for Marine Geodynamics, Japan Agency for Marine-Earth Science and Technology (JAMSTEC), Yokosuka, Japan*

Ambient noise correlation is capable of retrieving waves propagating between two receivers. Although waves retrieved using this technique are primarily surface waves, the retrieval of body waves, including direct, refracted, and reflected waves, has also been reported from land-based observations. The difficulty of body wave extraction may be caused by large amplitudes and little attenuation of surface waves excited by microseisms, indicating that body wave extraction using seafloor records is very challenging because microseisms are generated in ocean areas and large amplitudes of surface waves are presumably observed at the seafloor. In this study, we used a unique dataset acquired by dense arrays deployed in the Nankai subduction zone, including a permanent cabled-network of 49 stations, a borehole sensor, and 150 temporary stations, to attempt to extract near-field body waves from ambient seafloor noise observed by multivariate sensors of broadband and short-period seismometers, differential pressure gauges (DPGs), and hydrophones. Our results show that *P* waves are extracted only in the DPG-record correlations at a frequency of 0.2–0.5 Hz, which can be seen up to a separation distance of two stations of 17 km with an apparent velocity of 3.2 km/s. At 1–3 Hz, *P* waves are observed only in the vertical-record correlations up to a separation distance of 11 km with an apparent velocity of 2.0 km/s. These velocity differences reflect the vertical velocity gradient of the accretionary prism, because the *P* waves at low frequencies propagate at relatively long distances and therefore the turning depth is greater. Moreover, the long-period and short-period *P* waves are observed at the slope and flat regions on the accretionary prism, respectively. To investigate the retrieved wavefield characteristics, we conducted a two-dimensional numerical simulation for wave propagations, where we located single sources at the sea surface above the flat and slope bathymetry regions. Based on our observations and simulations, we suggest that the retrieval of near-field body waves from ambient seafloor noises depends on the relative amplitudes of *P* and other surface waves in the ambient noise wavefield, and those are controlled by the subseafloor velocity structure, seafloor topography, and water depth.

**Keywords: Ambient noise, seafloor observation, body wave, broadband, subduction zone (Min5-Max 8)**

OPEN ACCESS

***Edited by:***
*Susan Bilek, New Mexico Institute of Mining and Technology, United States*

***Reviewed by:***
*Feng Cheng, Rice University, United States*
*Emanuel David Kästle, Freie Universität Berlin, Germany*

****Correspondence:***
*Takashi Tonegawa*
*tonegawa@jamstec.go.jp*

***Specialty section:***
*This article was submitted to Solid Earth Geophysics, a section of the journal Frontiers in Earth Science*

***Received:*** *28 September 2020*
***Accepted:*** *15 December 2020*
***Published:*** *21 January 2021*

***Citation:***
*Tonegawa T, Kimura T and Araki E (2021) Near-Field Body-Wave Extraction From Ambient Seafloor Noise in the Nankai Subduction Zone. Front. Earth Sci. 8:610993. doi: 10.3389/feart.2020.610993*

## INTRODUCTION

Ambient noise analysis applied to land-based seismic records has retrieved various wavefields propagating between two receivers (Wapenaar, 2004). Retrieved waves are mainly surface waves (e.g., Sabra, 2005; Shapiro et al., 2005), but body wave retrievals by correlating ambient noises from land-based observations have also been reported (Roux et al., 2005; Draganov et al., 2007; Zhan et al., 2010; Poli et al., 2011; Ryberg, 2011; Takagi et al., 2014). In particular, reflections from the 410 and 660 km discontinuities in the upper mantle could be detected from ambient noise records observed in Finland (Poli et al., 2012). Body waves propagating through the deep interior of the Earth, including core phases, have been extracted using globally distributed broadband seismometers (Nishida, 2013). Near the coastline, direct and refracted *P* waves could be detected by a dense array of seismometers deployed at Long Beach, California, and those waves can be used to estimate the three-dimensional (3D) velocity structure at shallow depth (Nakata et al., 2015).

The difficulty of extracting body waves is primarily caused by large amplitudes of surface waves observed at land stations, which correspond to microseisms excited by ocean swells in the ocean areas (Longuet-Higgins, 1950; Hasselmann, 1963). Retrievals of body waves may be owing to either large amplitudes of body waves excited by ocean swells near the coastline (Nakata et al., 2015) or low amplitude of surface waves in quiet regions that are away from the coastlines. On the other hand, for seafloor observations, if wave-wave interactions of ocean swell persistently excites microseisms including body and surface waves, seafloor sensors may capture such signals because they are close to excitation regions of the microseisms. Waves extracted from seafloor observations are primarily surface waves, including Rayleigh waves, Love waves, their higher modes (e.g., Takeo et al., 2013; Lin et al., 2016; Isse et al., 2019; Kawano et al., 2020), Scholte waves (Mordret et al., 2014), and ocean acoustically-coupled Rayleigh (ACR) waves (Ewing et al., 1957; Sugioka et al., 2001; Butler and Lomnitz, 2002; Butler, 2006). Here, ACR waves (or seismoacoustic modes) can be observed at frequencies of 0.5–5.0 Hz, which include higher modes of Rayleigh waves whose energies are distributed in the ocean and marine sediment, and have a propagation velocity slightly less than 1.5 km/s (Tonegawa et al., 2015). However, teleseismic body waves excited in the ocean areas can be observed at land stations (Gerstoft et al., 2006; Koper et al., 2010; Landès et al., 2010; Gualtieri et al., 2014; Farra et al., 2016; Nishida and Takagi, 2016). Although this means that most of the body wave energy is transmitted to the interior of the Earth and can be observed at distant stations, near-field body waves are also possibly observed under the conditions of dense seismic sensors deployed at the seafloor.

In the Nankai subduction zone, south of Japan, the Philippine Sea Plate (PHS) subducts northwestwards from the Nankai Trough, historically leading to megathrust earthquakes along the plate boundary. To investigate the seismic structure of the subduction zone, seismic exploration surveys have been conducted with dense survey lines, in which temporary ocean bottom seismometers (OBSs), each equipped with a hydrophone, have been deployed for refraction surveys (e.g., Nakanishi et al., 2018). Moreover, to monitor seismic activity in this region, a permanent cabled-network of seismometers and pressure gauges (Dense Oceanfloor Network System for Earthquakes and Tsunamis: DONET) (Kaneda et al., 2015; Kawaguchi et al., 2015) has been installed on the accretionary prism where the bathymetry from the trough gradually becomes shallower landwards to a distance of 30–40 km, after which it is almost flat until 20–30 km before the coastline.

To explore the retrieval of body waves propagating between two seafloor receivers, we employed ambient noise records acquired by seismometers and pressure sensors of DONET and temporary OBSs. Such retrievals have potential for investigating the 3D seismic structure beneath the seafloor without natural and artificial seismic sources. In this study, we show near-field P-wave extractions at frequencies of 0.2–0.5 Hz from seafloor pressure gauges, mainly deployed at the slope bathymetry region, and those at frequencies of 1–3 Hz from seafloor seismometers, mainly deployed at the flat bathymetry region. Those extractions are further examined by 2D numerical simulations.

## MATERIALS AND METHODS

### Station Data

The continuous records used in this study consist of three-component seafloor motions and pressure fluctuation and were acquired by broadband seismometers and differential pressure gauges (DPGs) at each station of DONET and 4.5 Hz short-period sensors and hydrophones at each temporary station. The broadband seismometers (Guralp CMG-3T) of DONET were buried 1 m below the seafloor, and have a flat velocity response from 100 Hz to 360 s (e.g., Nakano et al., 2013). The response of the hydrophone decreases from 2 Hz to lower frequencies (e.g., Tonegawa et al., 2015). Also used were the three components of a broadband seismometer deployed in a borehole at a depth of 900 m from the seafloor (Kopf et al., 2011; 2016), at which lower noise levels than those at the seafloor are observed due to the amplitude decay of persistently propagating surface waves. The sampling rates of all sensors are decimated to 40 Hz. The stations in DONET are installed in the eastern (DONET1) and western (DONET2) part of the Nankai subduction zone with a station spacing of 15–20 km, whereas the temporary stations are distributed along five lines that cover the central to eastern part of the subduction zone with a station spacing of 5 km (**Figure 1**). The observation periods of DONET and temporary stations are 2011~present and September–December of 2011, respectively. We prepared two datasets of the continuous records to retrieve wavefields of lower (0.2–0.5 Hz) and higher frequency (1–3 Hz) components using an ambient noise analysis. Dataset 1 for the lower frequency range includes all four components of 49 stations of DONET and the three components of the borehole sensor, connected to the DONET cable, for February–March of 2016 (**Figure 1**). Dataset 2 for the higher frequency range includes all four components of 20 DONET stations and 150 temporary

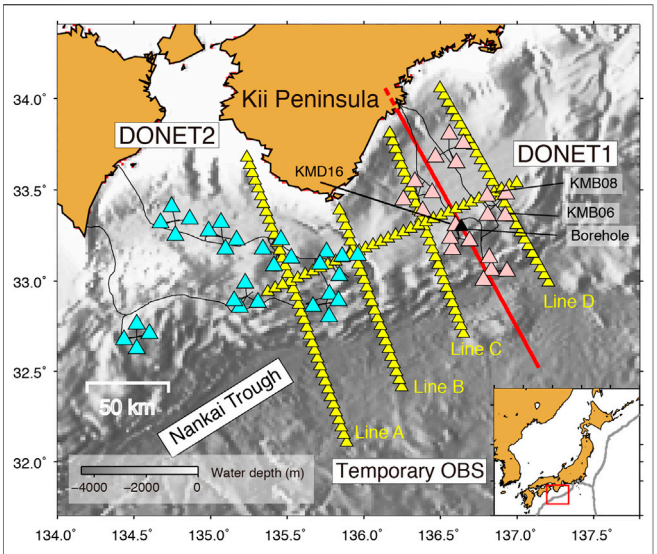


**FIGURE 1 |** Map showing the stations used in this study. Yellow, pink, and light-blue triangles represent temporary, DONET1, and DONET2 stations, respectively. The black triangle indicates the borehole location. The red line show the location of *Vp* structure (Nakanishi et al., 2008) used in the numerical simulation. The dashed red line represents the region where the one-dimensional profile at the northern edge of the *Vp* structure is extended.

stations for October–November of 2011 (**Figure 1**). Moreover, an additional dataset was prepared covering the middle frequency range (0.5–1.0 Hz) from DONET records for February–March of 2016. We did not use records of DONET2 in Dataset 2 because it had not yet been installed in 2011.

## Cross-Correlation Function Calculation

Cross-correlation functions (CCFs) were calculated with ambient noise records in which energetic signals including earthquakes were suppressed by the following log-normal shaped function.

$$F(t) = \frac{1}{\sqrt{2\pi\sigma\,(t/T)}} \exp\left\{ -\frac{\left(\log\left(\frac{t}{T}\right)\right)^2}{2\sigma^2} \right\} \quad (1)$$

where σ = 2 and the time length, T = 400 s. When σ > 1 in **Equation 1**, the peak of the function is located forward and its tail amplitude is still preserved at the end of the time length (**Supplementary Figure S1**). The time length, T, was determined from the durations of relatively large earthquake signals at 0.2–0.5 Hz observed by DONET. **Supplementary Figure S1A** shows a waveform example for a deep earthquake with a magnitude of 5.7, a depth of 410 km (earthquake catalog from United States Geological Survey), and an epicentral distance of 3.67°. The coda amplitudes can be observed for a duration of ~400 s. If the coda portions of earthquakes are longer than 400 s and still have large amplitudes (see **Equations 2, 3** for amplitude criteria), **Equation 1** is repetitively applied to the rest of the coda. A cosine taper with a time window of 20 s was also applied to both the edges of the function. The root-mean-squared ($RMS_{1hour}$) amplitudes were calculated with 1-h continuous records at a frequency of 0.2–0.5 Hz. When amplitudes in the 1-h record at 0.2–0.5 Hz, $A_{max}$, exceed five times the $RMS_{1hour}$, the raw records were divided by the following function with a time shift of 80 s from the time of $A_{max}$:

$$S(t) = C \cdot F(t) \quad (2)$$

where

$$C = 3A_{max}/RMS_{1hour} \quad (3)$$

The reason of the time shift is that the maximum amplitude of the log-normal shaped function (**Equation 1**) is approximately 80 s from the starting time. In addition, when moderate-sized earthquakes occur in Japan, the large and small amplitudes of the *S* and *P* waves within an *S*–*P* time of <80 s are observed, and the *S* wave amplitude often corresponds to $A_{max}$. **Equation 2** with a time shift of 80 s and **Equation 3** can effectively suppress the large amplitudes of such earthquake signals. An example of the suppression of the deep earthquake signals is shown in **Supplementary Figure S1D**. The CCFs were calculated using a time window of 200 s with spectral whitening (Brenguier et al., 2007). The CCFs were stacked over 2 months. When the RMS of one segment (200 s) in the processed records was less than 0.3 times the $RMS_{1hour}$, the CCFs of those segments were discarded.

Previous studies calculated CCFs using continuous records with one-bit normalization where amplitudes are equalized while preserving their polarities. Using the continuous records acquired by a borehole sensor and a nearby seafloor sensor (KMD16, **Figure 1**) with a horizontal separation distance of 3.7 km, we compared the resulting CCFs (**Figure 2**). Without one-bit normalization they show *P* waves and ACR waves at lag times of ±2 s and +4 s, respectively, while with one-bit normalization the CCFs do not show any clear signals. The reasons for the absence of clear signals remains elusive, but we suppose that larger and smaller amplitudes in the ambient seafloor noise are dominated by different wavefields, as will be discussed in *Discussion*. In this study, we preserved amplitude information in the continuous records with suppressing energetic signals when calculating CCFs. Because CCFs calculated with spectral whitening measure the phase difference between two time series (e.g., Prieto et al., 2009; Tonegawa et al., 2009), the phase difference obtained in the CCFs reflects portions of the time series with relatively large amplitudes.

## RESULTS

**Supplementary Figure S2** shows CCFs for 4 × 4 components at 0.2–0.5 Hz. Most of the component combinations only show ACR wave propagations with a propagation velocity of 1.5 km $s^{-1}$ or surface waves with slower velocities, whereas pressure-pressure (P-P) CCFs show body wave propagations. In **Figure 3**, the reference station is located at a lower latitude, so that signals in the positive lag time represent waves propagating northwards. *P* wave propagations are observed up to a separation distance of 17 km in the positive lag time along the travel time curve of the *P* waves estimated from the velocity structure (Tonegawa et al.,

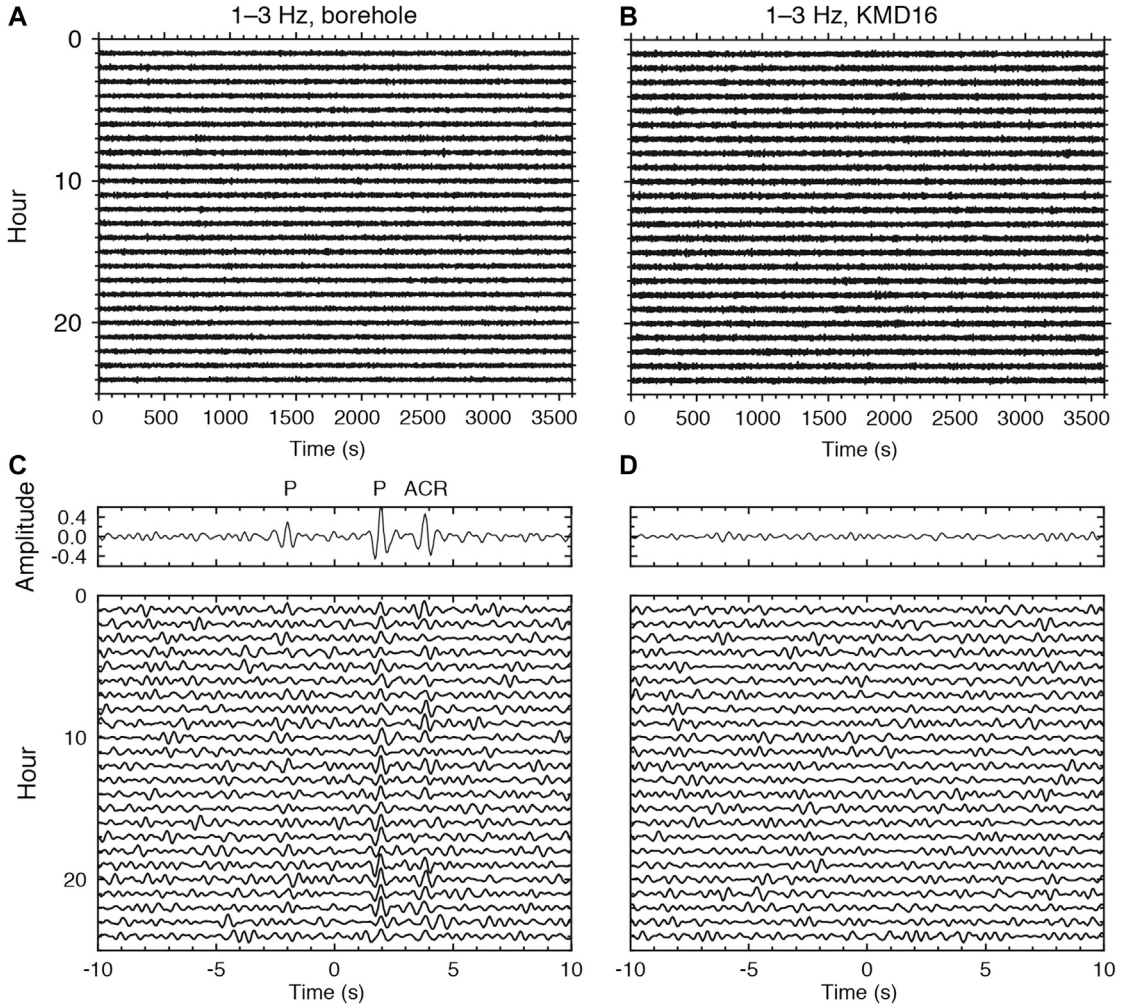


**FIGURE 2 |** Waveform examples recorded with borehole and seafloor sensors. **(A)** One-hour records of the vertical component at 1–3 Hz observed at the borehole sensor on February 9, 2016. **(B)** Same as **(A)**, but for KMD16. **(C)** One-hour CCFs using the waveforms in **(A,B)**, with the borehole as the reference site. The top panel represents the CCF stacked over the CCFs in the bottom panel. **(D)** Same as **(C)**, but for applying a one-bit normalization to the waveforms in **(A,B)**.

2017). Here, we constructed a one-dimensional (1D) velocity model averaged over all of the 1D velocity profiles obtained from the DONET stations below the seafloor (Tonegawa et al., 2017). The *P* wave can be observed in the positive lag time of the CCF for the station pair of KMB06 and KMB08 (**Figure 3D**). The turning depth of *P* waves reaches up to 6 km from the seafloor (**Figure 3**), which samples the plate boundary in the shallow subduction zone.

**Figure 4** shows P-P and vertical-vertical (Z-Z) CCFs at 1.0–3.0 Hz. Although *P* waves were observed in the P-P CCFs at 0.2–0.5 Hz, in the P-P CCFs at 1.0–3.0 Hz only ACR waves were observed. Instead, *P* waves were retrieved in the positive and negative lag times of the Z-Z CCFs at 1.0–3.0 Hz, and they reach up to 11 km in separation distance of two stations. At the middle frequency range of 0.5–1.0 Hz, we did not extract body waves (**Supplementary Figure S3**), and hence focus on body wave retrieval at the frequency bands of 0.2–0.5 Hz and 1.0–3.0 Hz in the subsequent sections.

To confirm the stability of the obtained CCFs, we compared them for stacking periods of 3 months, 1 month, and 2 weeks in the low frequency band (**Supplementary Figure S4**). Because the observation period of Dataset 2 was almost 2 months, we did not confirm the stability of Dataset 2. The CCFs were almost stable over all of the stacking periods; hence, we discuss the characteristics of the retrieved waves based on a 2 months stacking period.

# DISCUSSION

## P Wave Retrieval

We measured the apparent velocities of *P* waves in high and low frequency bands using a slant stack technique. Given apparent velocities, the theoretical travel times can be calculated using the distances between two stations. The apparent velocity was varied between 1 km/s and 5 km/s, with an increment of 0.1 km/s. We

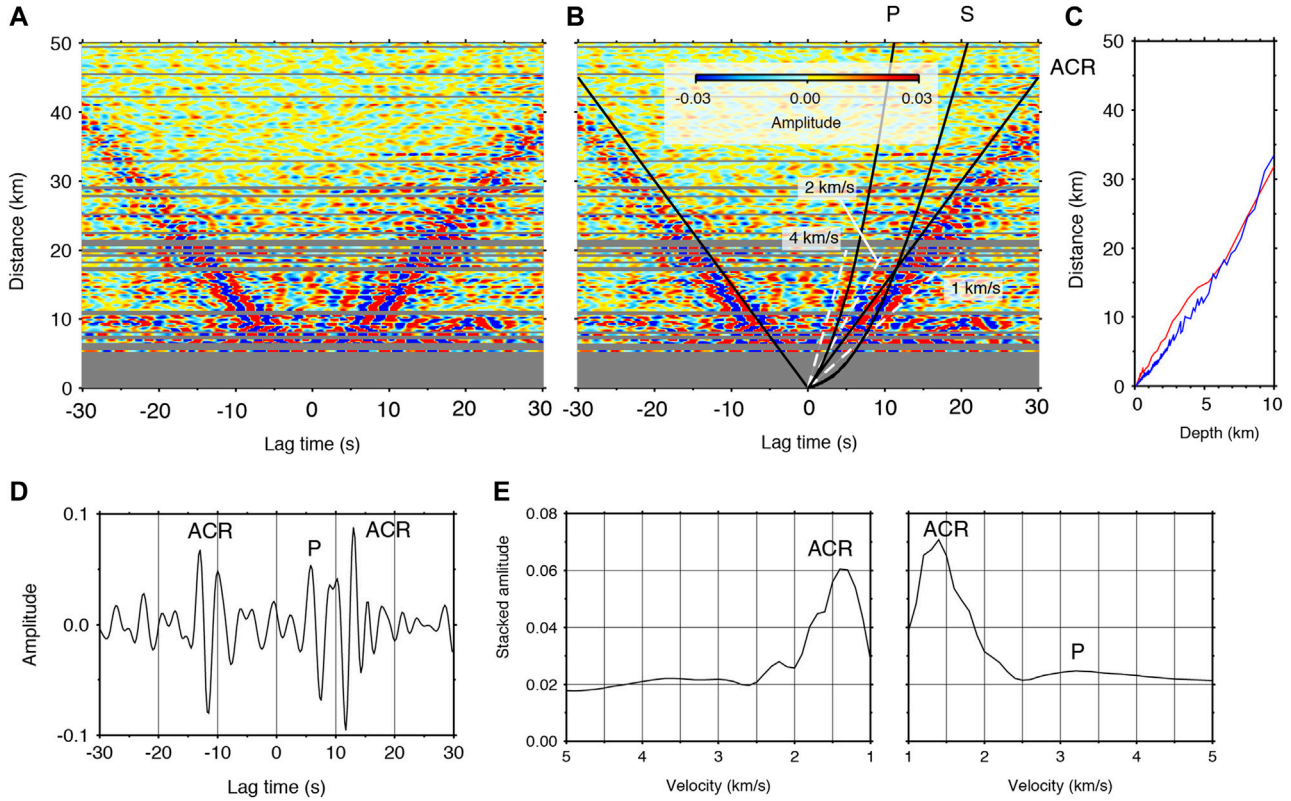


**FIGURE 3 |** CCFs aligned as a function of the separation distance of two stations. **(A)** P-P CCFs at 0.2–0.5 Hz using DPG records. **(B)** Same as **(A)**, but with travel time curves of *P* and *S* waves calculated with a velocity model (Tonegawa et al., 2017), and a solid line with a propagation velocity of 1.5 km/s. White dashed lines represent apparent velocities of 1, 2, and 4 km/s. **(C)** The bottoming depth of (red) *P* and (blue) *S* waves calculated using the velocity model (Tonegawa et al., 2017). **(D)** A stacked P-P CCF at 0.2–0.5 Hz for the KMB06–KMB08 station pair, with a separation distance of 14.0 km. **(E)** Slant stack results for **(left)** negative and **(right)** positive lag times of the CCFs in **(A)**.

averaged the absolute amplitudes of the CCFs within a 0.5 s time window from the theoretical travel time. The averaged values were stacked for the separation distances between two stations: less than 10 and 17 km for the high and low frequency bands, respectively, because large amplitudes were obtained in the distance ranges (**Figures 3**, **4**). This process was performed for positive and negative lag times.

We obtained velocities of 2.0 km/s in the high frequency band (**Figure 4**) and 3.2 km/s for positive lag times in the low frequency band (**Figure 3**). This velocity difference and the fact that *P* waves in the low frequency band propagate over relatively long distances indicate that the turning depths of these *P* waves were relatively shallow and deep, respectively, and the apparent velocities reflect the *P*-wave velocity structure (*Vp*) at these depths. Indeed, the travel time curve gradient of the *P* waves gradually increased as a function of distance (**Figure 3B**), which reflects the vertical velocity gradient of the accretionary prism. Seismic exploration surveys of the entire Nankai accretionary prism have also reported a *Vp* of 2.0–4.0 km/s in the marine sediments and a gradual increases with depth of the *Vp* structure at shallower depths in the accretionary prism (e.g., Kodaira et al., 2002; Takahashi et al., 2002; Nakanishi et al., 2008). In the higher frequency band, because the turning depth is relatively shallow, the turning *P* waves are simply observed at stations with separation distances less than 11 km. For the low frequency band, because the turning depth is close to the plate boundary, if seismic velocity discontinuities are present near the bottom of the prism, refracted and head waves can be generated. Indeed, the presence of a low velocity layer has been reported at the bottom of the accretionary prism in the southern DONET1 region (Park et al., 2010; Kamei et al., 2012; Akuhara et al., 2020). In this study, for the low frequency observations from DONET1, the retrieved P waves may contain such multiple *P* phases.

In order to investigate the region where *P* waves were retrieved at 0.2–0.5 Hz, we selected P-P CCFs that contain *P* waves by cross-correlating between the reference CCF and individual P-P CCFs, which is a similar approach to that of a previous study (Nakata et al., 2015). The reference CCF was calculated by stacking the P-P CCFs of all station pairs within separation distances of 10–17 km along the travel time curve of the *P* waves shown in **Figure 3B** (Tonegawa et al., 2017). We calculated the cross-correlation coefficients (CC) between the reference CCF and individual P-P CCFs with a time window of ±2 s from the travel time curve. If CC > 0.6, we consider that the CCF possibly contains *P* waves, and plot the pair in the map (red

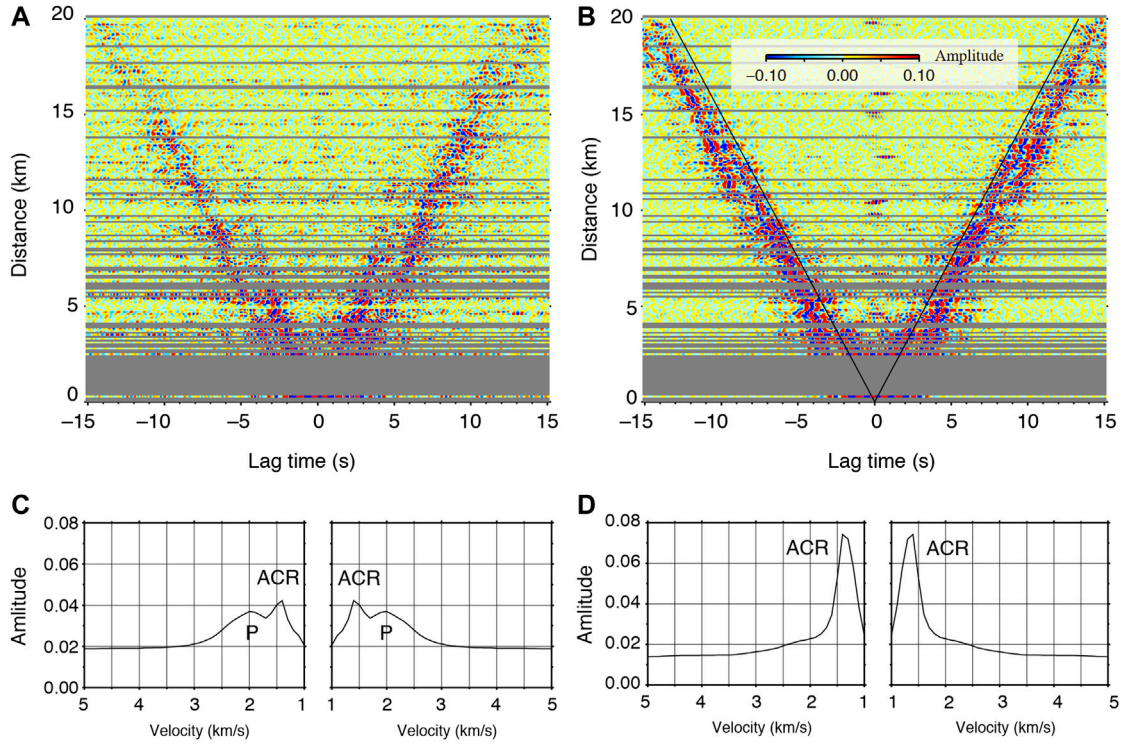


**FIGURE 4 |** CCFs aligned as a function of the separation distance of two stations. **(A)** Z-Z CCFs at 1–3 Hz using short-period sensor. **(B)** Same as **(A)**, but for P-P CCFs using hydrophone. Solid line indicates a wave propagation with a velocity of 1.5 km/s. **(C)** Slant stack results for **(left)** negative and **(right)** positive lag times of the CCFs in **(A)**. **(D)** Same as **(C)**, but for the CCFs in **(B)**.

lines in **Figure 5A**). As a result, pairs showing *P* waves are primarily concentrated at the southern part of DONET, where the seafloor slope to the trough is formed.

To explore the regions where *P* waves are observed at 1.0–3.0 Hz, we aligned Z-Z CCFs with the separation distance of two stations of 5 km along Lines A-D (**Figure 1**). Because the separation distances in the temporary OBS array were equal, aligning the CCFs with 5 km separation distances along lines allowed us to compare the retrieved waves with the geological setting. The result shows that *P* waves were primarily retrieved at the flat bathymetry region, while signals were weak at the slope bathymetry region (**Figure 6**). This contrasts with the retrieval of *P* wave at 0.2–0.5 Hz. Note that the retrieved *P* waves in the Z-Z CCFs are different from the ACR waves detected in the P-P CCFs using hydrophone records in a previous study (**Supplementary Figure S5**) (Tonegawa et al., 2015), in which the *P* waves in the Z-Z CCFs were faster.

Previous studies that retrieved body waves at land stations speculated that body waves are converted from the Rayleigh waves due to the heterogeneous structure of the Earth's upper crust (Roux et al., 2005), and that there are specific structures where body wave energy is trapped and scattered, such as low velocity layers, basins, topography, and heterogeneity (Zhan et al., 2010). Although the retrieved *P* waves retrieved in our observations may have included contributions from the correlation of *P* waves trapped and scattered by heterogeneities within the accretionary prism toe, in which the original *P* waves were generated by wave-wave interactions at the sea surface, the wavelength of the *P* wave at low frequency was 15 km, for a frequency of 0.2 Hz and a propagation velocity of 3.0 km/s. This wavelength appears to be long for sufficient seismic wave scattering. Therefore, we conducted numerical simulations to evaluate the contribution of the original P waves associated with wave-wave interactions to the P waves extracted from our observations.

## Wave Propagation From Numerical Simulation

In this section, we confirm whether the characteristics of the waves retrieved from ambient seafloor noises can be reproduced by a simple 2D numerical simulation for the ocean-solid Earth system. Since it appears that *P* retrieval is related to the slope and flat regions in the bathymetry, we compare wave propagations depending on frequency (0.2–0.5 Hz and 1–3 Hz), source locations (slope and flat), and component (vertical velocity and stress $\tau_{zz}$). We used a 2D finite difference method with a rotated-staggered grid for second order approximations in time and space (Saenger et al., 2000). The calculation has been performed in the displacement-stress scheme with an absorbing boundary condition (Clayton and Engquist, 1977), and converted the vertical displacement to vertical velocity seismograms to compare with the $\tau_{zz}$ component. We applied vertical single forces with Ricker wavelets for central (maximum)

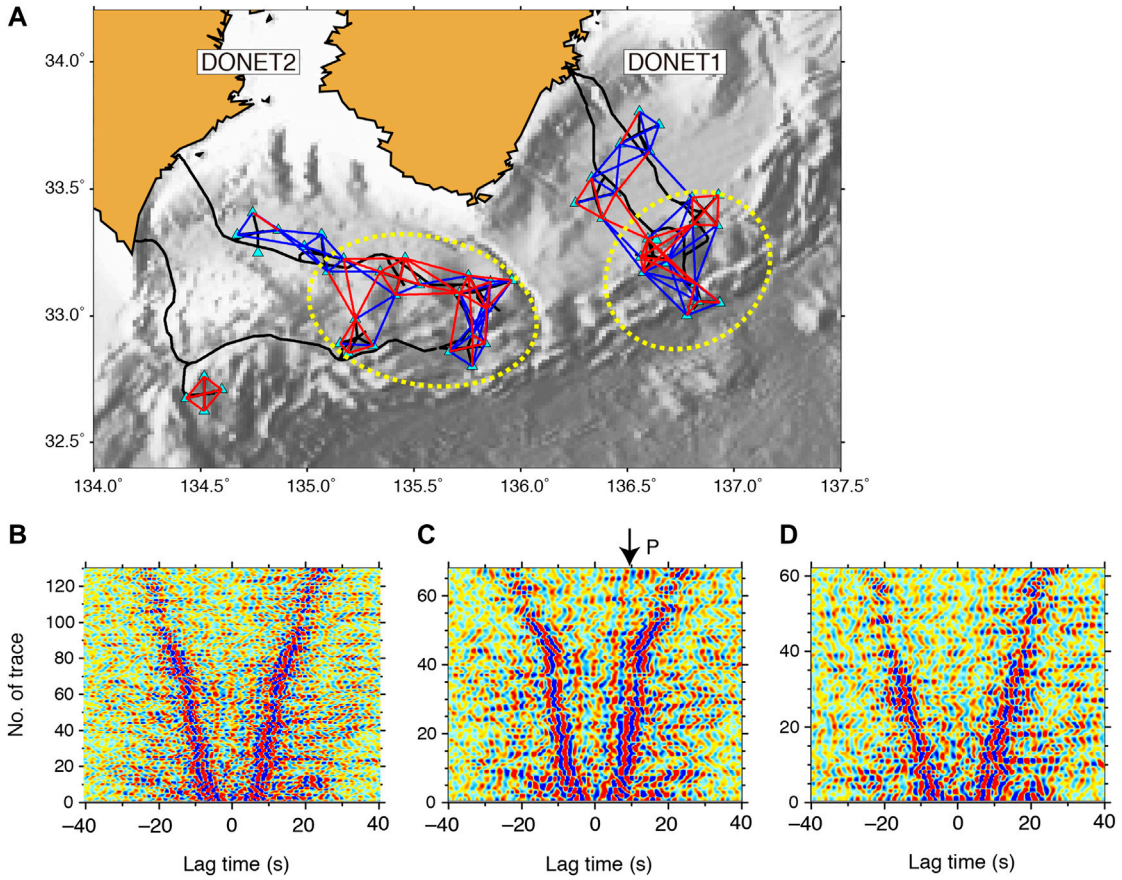


**FIGURE 5 |** Screening of CCFs that show *P* wave extractions. **(A)** Map showing pairs that (red line) shows *P* wave extractions and those that (blue line) do not show *P* extractions. Dotted yellow ellipses represent the regions where *P* waves are extracted. **(B)** P-P CCFs at 0.2–0.5 Hz ordered by separation distance of two stations **(C)** P-P CCFs that contain *P* waves are selected from CCFs in **(B)**. **(D)** P-P CCFs that do not contain *P* waves are selected from CCFs in **(B)**.

frequencies of 2.0 Hz (2.9 Hz) and 0.35 Hz (0.5 Hz), respectively, to produce wavefields at high and low frequencies. The grid size is 10 × 10 m and 20 × 20 m for high and low frequencies, respectively. Stations are set at the seafloor within a distance ranging between 0 and 200 km with an interval of 1 km.

The seismic velocity structure at the subseafloor is based on a *Vp* structure resulting from a seismic exploration survey (**Figures 1**, **7A**) (Nakanishi et al., 2008). The 1D *Vp* profile at the northern edge of the model is extended landward (**Figure 1**). The *Vs* and density were derived from *Vp* using empirical relations (Brocher, 2005). A 1D profile (depth dependent) of the *Vp* is applied to the sea water (Munk, 1974), while *Vs* and density are 0 and 1.02 g/cm$^3$, respectively. The calculation was unstable in the cases where *Vp*/*Vs* of the accretionary prism at shallow depths was large and the small horizontal-scale bathymetry was complex. To avoid these problems, we set *Vp*/*Vs* = 2.5 when *Vp*/*Vs* > 2.5 and applied a horizontal distance moving average of 10 km to the seafloor. The minimum *Vs* is 0.56 km/s because the minimum *Vp* in the sea water is approximately 1.4 km/s (Munk, 1974). The source locations were set to horizontal distances of 80 and 110 km at the sea surface, which correspond to the slope and flat bathymetry regions, respectively (**Figure 7A**).

The numerical simulation results at high frequency shows that direct and subsequent *P* waves are propagating within the subseafloor structure, and were produced by multiple reflections of *P* waves in the sea water (e.g., red arrow in **Figure 7B**). ACR waves can also be observed after the apparent velocity of 1.5 km/s (e.g., blue arrow in **Figure 7C**). At low frequency, in addition to *P* waves, subsequent *P* waves, and ACR waves, the propagation of Rayleigh waves with an apparent velocity of ~0.5 km/s was also extracted (e.g., orange arrow in **Figure 7D**). After the direct and subsequent *P* waves propagate to a horizontal distance of 30–40 km (**Figure 7B**), their amplitudes at both frequency bands are decayed at greater distances. Although our observations only show *P* wave propagations of 10–15 km in horizontal distance, such an amplitude decay as was obtained in the numerical simulation is one of the reasons for the absence of *P* wave propagations at farther distances.

We consider that the retrieved waves in our observation can be linked to the relative amplitudes of the waves that emerged in the numerical simulation. In our observation, *P* waves could be retrieved at a frequency of 1–3 Hz at the stations on the flat

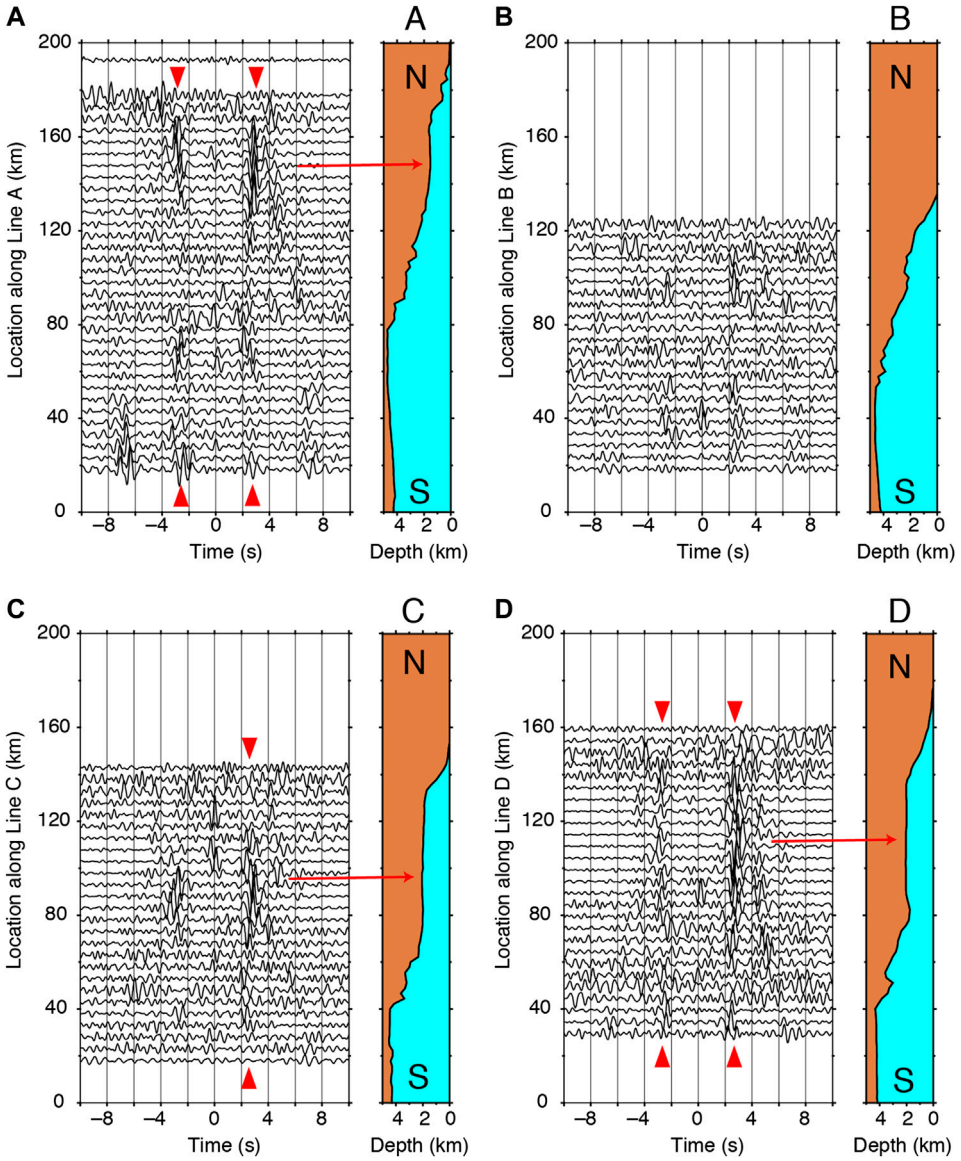


**FIGURE 6 |** *P* wave retrieval at 1–3 Hz. **(A)** Z-Z CCFs for pairs whose separation distance is 5 km are aligned along line A (**Figure 1**). Red triangles represent *P* wave retrievals, and red arrow indicates the location where the *P* wave is retrieved, which corresponds to the flat bathymetry region. Right panel shows the bathymetry along the line A. **(B)** Same as **(A)**, but for line B. **(C)** Same as **(A)**, but for line C. **(D)** Same as **(A)**, but for line D.

bathymetry. In the numerical simulation for the flat bathymetry, the amplitudes of direct and subsequent *P* waves in the vertical velocity component are larger than those in $\tau_{zz}$, and the amplitudes of the ACR waves are large in $\tau_{zz}$ (**Figure 7B**). Because we preserved the amplitude information when calculating CCFs, large amplitudes of those *P* and ACR waves may be correlated and emphasized in the Z-Z CCFs and P-P CCFs, respectively. Moreover, the amplitudes at the coda part of the ACR waves are large in the slope region (**Figures 7B,C**). This may hinder the retrieval of *P* wave at the slope region in our observation.

For the low frequency wavefields in our observation, *P* waves could be extracted at the slope region and mainly propagate northwards. In the numerical simulation for the bathymetric slope, direct and subsequent *P* waves propagating to shallow water depths have larger amplitudes than those propagating to deep water depths (arrow in **Figure 7E**), while the amplitudes to both directions are comparable in the flat bathymetry region (**Figure 7D**). This asymmetric radiation pattern of the *P* amplitudes may cause the azimuthally-asymmetric extraction of the retrieved *P* waves in our observation. Another important issue of the low-frequency *P* retrieval is that *P* waves could not be extracted in the observed Z-Z CCFs, although they have large amplitudes in the vertical velocity component in the numerical simulation (**Figure 7E**). This is because Rayleigh wave amplitudes significantly emerged in the vertical velocity component, compared with $\tau_{zz}$ (**Figure 7E**), and ACR and Rayleigh waves propagate long distance with relatively

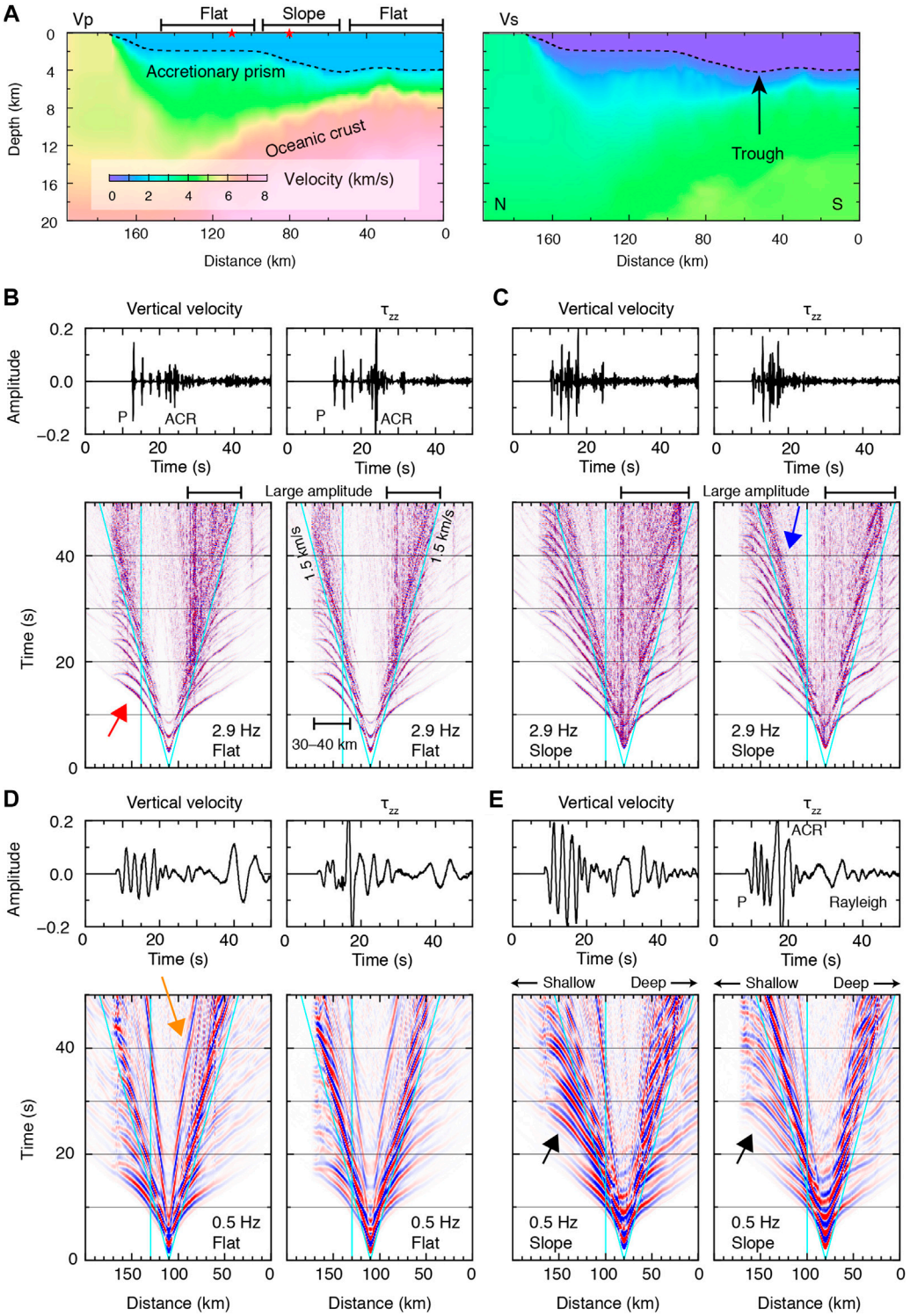


**FIGURE 7 |** Two-dimensional numerical simulation for wave propagation. **(A)** *Vp* model used in the numerical simulation. The dotted line shows the bathymetry. Red stars at 80 and 110 km in horizontal distance show the source locations at the sea surface. **(B)** Left panels show (top) a waveform example of the vertical velocity observed at 140 km in distance and (bottom) record section. The maximum frequency is 2.9 Hz. The source is located above the flat bathymetry region. Oblique and vertical light-blue lines represent 1.5 km/s and the waveform that corresponds to the top panel, respectively. The red arrow indicates direct and subsequent *P* waves. Right panels are the same as left panels, but for $\tau_{zz}$. The amplitudes of the record sections (bottom) are normalized by the maximum amplitude in each record section. **(C)** Same as **(B)**, but the source is located above the slope bathymetry region. The blue arrow indicates the ACR wave propagation. **(D)** Same as **(A)**, but the maximum frequency is 0.5 Hz. The orange arrow represents the Rayleigh wave propagation. **(E)** Same as **(C)**, but the maximum frequency is 0.5 Hz. The black arrows indicate the asymmetric radiation pattern of *P* wave amplitudes.

little attenuation, compared with *P* waves. Thus, it is considered that cross-correlating the vertical velocity components at the seafloor tends to result in the retrieval of Rayleigh and ACR waves. For the flat region in the simulation, because the Rayleigh waves have large amplitudes (**Figure 7D**) and propagate from the flat to slope regions, this effect also supports the idea that ACR and Rayleigh waves dominated the observed Z-Z CCFs at this frequency.

The ambient noise wavefield at the seafloor contains body waves and multiple modes of surface waves. Since their amplitudes vary with the geological setting, including subseafloor velocity structure, seafloor topography, and water depth, the summed amplitudes of the waves contribute to seafloor motions below the seafloor and pressure variations above the seafloor. This may result in wavefield differences across the seafloor in terms of amplitude and propagation velocity. We therefore considered that the wavefield differences in the solid Earth and ocean controls the extracted wavefield in the CCFs obtained from seismometers and pressure sensors in this study.

## Cross-Correlation Functions With and Without One-Bit Normalization

The one-bit normalization is capable of equalizing the energies of incoming waves from heterogeneously distributed sources, and useful for cross-correlating ambient noise records (Brenguier et al., 2007). We here compared the obtained CCFs with and without one-bit normalization at higher and lower frequencies in more details. **Supplementary Figure S6A** shows the P-P CCFs at 0.2–0.5 Hz with one-bit normalization. The propagations of the *P* and ACR waves are almost comparable to those in the P-P CCFs without one-bit normalization (**Figure 3**). On the other hand, the signal-to-noize ratios (S/Ns) of the *P* and ACR waves in the Z-Z CCFs at 1–3 Hz with one-bit normalization (**Supplementary Figure S6B**) are significantly lower than those without one-bit normalization (**Figure 4A**). This feature is consistent with the example shown in **Figure 2**, in which *P* and ACR waves can be constructed in 1-h CCFs without one-bit normalization.

Although the reason for such low S/Ns in the retrieved waves remains elusive, one possible reason may be related to the relative amplitudes between the wavefield right after excitation by wave-wave interaction and the wavefield where the excitation occurred some time ago. The wavefield associated with wave-wave interaction contains primary waves due to the wave-wave interaction with relatively large amplitudes and secondary waves that contain multiply scattered waves of the primary waves. For example, the primary waves include direct and subsequent *P* waves and ACR waves, and the secondary waves are dominated by ACR waves, particularly at higher frequencies, scattered by both small-scale heterogeneous structures below the seafloor and complicated seafloor topography. If we calculate CCFs without one-bit normalization, the CCFs possibly contain the effects of the primary waves. However, if we calculate CCFs with one-bit normalization, because the amplitudes of primary and secondary waves are equalized, correlating those waves presumably requires a larger amount of ambient noise records. This may also be related to the rapid convergence to a robust CCF when non one-bit normalization was applied (Seats et al., 2012), although the time window used for calculating the CCFs did not overlap in the present study, as in the case of Seats et al. (2012).

To evaluate this, CCF constructions from ambient noise in various marine geological settings are required. In particular, because the relative amplitudes of the ambient noise wavefields at the seafloor may be controlled by the subseafloor velocity structure, seafloor topography, and water depth, it is necessary that the retrieval of body waves and the convergence from multivariate components is analyzed with and without one-bit normalization in various marine settings. Such experiments may also be applicable to body-wave extractions from land-based three-component seismometer records.

## Acoustically-Coupled Rayleigh or S Wave?

At 0.2–0.5 Hz, clear signals can be traced in the positive and negative lag times along the travel time curve of the S wave up to a separation distance of two stations of 23 km (**Figure 3**). At separation distances greater than 23 km, the apparent velocity of the relatively weak signals is close to 1.5 km/s and slower than the travel time curve of the S wave, which corresponds to ACR waves. If the waves observed at distances up to 23 km corresponds to S waves, the pressure gauges observe the pressure response associated with the seafloor displacement corresponding to S waves from the subseafloor structure, including incident S, reflected P, and reflected S waves.

However, it appears that these waves also correspond to ACR waves. Our numerical simulation indicates that ACR waves have higher phase velocities than the group velocity of ~1.5 km/s (arrow in **Supplementary Figure S7**), which reflect the shear wave velocity at the deeper part of the accretionary prism. It is therefore considered that the observed waves corresponding to the S-wave travel time curve are the results of cross-correlating the ACR waves with high phase velocities. The reason for the apparent velocity change at a distance of 23 km may be that the wave propagations at distances greater than 23 km primarily reflect the seismic structure beneath the flat region because relatively longer separation distances of two stations can be used in this region.

# CONCLUSION

We present the retrieval of near-field *P* waves from ambient noise records observed at the seafloor, using data from a permanent cabled network (DONET) and temporary stations. The following are the major findings on the characteristics of *P* retrievals.

(1) P waves could be extracted in the P-P CCFs at 0.2–0.5 Hz in the slope bathymetry region, and they propagate to shallow water depths.
(2) P waves could be extracted in the Z-Z CCFs at 1–3 Hz in the flat bathymetry region.
(3) Our numerical simulations indicate that the relative amplitudes among the P, ACR, and Rayleigh waves and their attenuations are important for the extraction of the waves.
(4) The relative amplitudes of these waves are controlled by the marine geological setting, including the subseafloor seismic velocity structure, seafloor topography, and water depth.

The propagation distance of *P* wave is only up to 15–20 km, but their bottoming depth reaches up to 5–6 km below the seafloor. This indicates that the *P* wave can reach the plate boundary in the shallow Nankai subduction zone. If such retrievals can be realized in various shallow subduction zones, the retrieved *P* waves can be used to investigate seismic structures by, e.g., tomographic approaches. It is expected that more details on near-field body wave extractions from ambient seafloor records will be investigated under various conditions in seismic seafloor experiments.

## DATA AVAILABILITY STATEMENT

The data analyzed in this study is subject to the following licenses/restrictions: Seafloor seismometer data are available from JAMSTEC upon request. The data that support the findings of this study are available from the corresponding author upon reasonable request. Requests to access these datasets should be directed to Takashi TONEGAWA, tonegawa@jamstec.go.jp.

## AUTHOR CONTRIBUTIONS

TT processed the data, and drafted the manuscript. TK and EA acquired the data underlying this study. All authors contributed to interpretation and the final manuscript.

## FUNDING

This work was supported by JSPS KAKENHI Grant Number 19H04632 in Scientific Research on Innovative Areas "Science of Slow Earthquakes."

## ACKNOWLEDGMENTS

We thank A. Nakanishi for providing us the Vp model. This study used records obtained at an array deployed by Japan Agency for Marine-Earth Science and Technology (JAMSTEC) as a part of "Research concerning Interaction Between the Tokai, Tonankai and Nankai Earthquakes" funded by the MEXT of Japan, and also used the seismic data of Dense Oceanfloor Network system for Earthquakes and Tsunamis (DONET) from the National Research Institute for Earth Science and Disaster Resilience: https://doi.org/10.17598/NIED.0008. Earthquake catalog information was obtained from the U.S. Geological Survey.

## SUPPLEMENTARY MATERIAL

The Supplementary Material for this article can be found online at: https://www.frontiersin.org/articles/10.3389/feart.2020.610993/full#supplementary-material.

## REFERENCES

Akuhara, T., Tsuji, T., and Tonegawa, T. (2020). Overpressured underthrust sediment in the nankai trough forearc inferred from transdimensional inversion of high-frequency teleseismic waveforms. *Geophys. Res. Lett.* 47 (15), e2020GL088280. doi:10.1029/2020GL088280

Brenguier, F., Shapiro, N. M., Campillo, M., Nercessian, A., and Ferrazzini, V. (2007). 3-D surface wave tomography of the Piton de la Fournaise volcano using seismic noise correlations. *Geophys. Res. Lett.* 34, L02305. doi:10.1029/2006GL028586

Brocher, T. M. (2005). Empirical relations between elastic wavespeeds and density in the earth's crust. *Bull. Seismol. Soc. Am.* 95, 2081–2092. doi:10.1785/0120050077

Butler, R., and Lomnitz, C. (2002). Coupled seismoacoustic modes on the seafloor. *Geophys. Res. Lett.* 29, 57–61. doi:10.1029/2002GL014722

Butler, R. (2006). Observations of polarized seismoacoustic T waves at and beneath the seafloor in the abyssal Pacific ocean. *J. Acoust. Soc. Am.* 120, 3599–3606. doi:10.1121/1.2354066

Clayton, R., and Engquist, B. (1977). Absorbing boundary condition for acoustic and elastic wave equations. *Bull. Seismol. Soc. Am.* 67, 1529–1540

Draganov, D., Wapenaar, K., Mulder, W., Singer, J., and Verdel, A. (2007). Retrieval of reflections from seismic background-noise measurements. *Geophys. Res. Lett.* 34, 158–164. doi:10.1029/2006GL028735

Farra, V., Stutzmann, E., Gualtieri, L., Schimmel, M., and Ardhuin, F. (2016). Ray-theoretical modeling of secondary microseism Pwaves. *Geophys. J. Int.* 206, 1730–1739. doi:10.1093/gji/ggw242

Gerstoft, P., Fehler, M. C., and Sabra, K. G. (2006). When Katrina hit California. *Geophys. Res. Lett.* 33, 040099–Q4016. doi:10.1029/2006GL027270

Gualtieri, L., Stutzmann, E., Farra, V., Capdeville, Y., Schimmel, M., Ardhuin, F., et al. (2014). Modelling the ocean site effect on seismic noise body waves. *Geophys. J. Int.* 197, 1096–1106. doi:10.1093/gji/ggu042

Hasselmann, K. (1963). A statistical analysis of the generation of microseisms. *Rev. Geophys.* 1, 177–210

Isse, T., Kawakatsu, H., Yoshizawa, K., Takeo, A., Shiobara, H., Sugioka, H., et al. (2019). Surface wave tomography for the Pacific Ocean incorporating seafloor seismic observations and plate thermal evolution. *Earth Planet. Sci. Lett.* 510, 116–130. doi:10.1016/j.epsl.2018.12.033

Kamei, R., Pratt, R. G., and Tsuji, T. (2012). Waveform tomography imaging of a megasplay fault system in the seismogenic Nankai subduction zone. *Earth Planet. Sci. Lett.* 317-318, 343–353. doi:10.1016/j.epsl.2011.10.042

Kaneda, Y., Kawaguchi, K., Araki, E., Matsumoto, H., Nakamura, T., Kamiya, S., et al. (2015). "Development and application of an advanced ocean floor network system for megathrust earthquakes and tsunamis," in *Seafloor Observatories.* Editors P. Favali, L. Beranzoli, and A. De Santis (Berlin, Heidelberg: Springer Berlin Heidelberg), 643–662.

Kawaguchi, K., Kaneko, S., Nishida, T., and Komine, T. (2015). "Construction of the DONET real-time seafloor observatory for earthquakes and tsunami monitoring," in *Seafloor Observatories.* Editors P. Favali, L. Beranzoli, and A. De Santis (Berlin, Heidelberg: Springer Berlin Heidelberg), 211–228.

Kawano, Y., Isse, T., Takeo, A., Kawakatsu, H., Suetsugu, D., Shiobara, H., et al. (2020). Persistent long-period signals recorded by an OBS array in the western-central pacific: activity of ambrym volcano in vanuatu. *Geophys. Res. Lett.* 47, 1–8. doi:10.1029/2020GL089108

Kodaira, S., Kurashimo, E., Park, J.-O., Takahashi, N., Nakanishi, A., Miura, S., et al. (2002). Structural factors controlling the rupture process of a megathrust earthquake at the Nankai trough seismogenic zone. *Geophys. J. Int.* 149, 815–835. doi:10.1046/j.1365-246x.2002.01691.x

Koper, K. D., Seats, K., and Benz, H. (2010). On the composition of earth's short-period seismic noise field. *Bull. Seismol. Soc. Am.* 100, 606–617. doi:10.1785/0120090120

Kopf, A., Araki, E., and Toczko, S. (2011). Expedition 332 scientists integrated ocean drilling program. *Proc. IODP* [Epub ahead of print. doi:10.2204/iodp.proc.332.2011

Kopf, A., Saffer, D., and Toczko, S. (2016). Expedition 365 preliminary report: NanTroSEIZE stage 3: shallow megasplay long-term borehole monitoring system (LTBMS) (international ocean discovery program). *Int.Ocean Discovery Program* [Epub ahead of print]. doi:10.14379/iodp.pr.365.2016

Landès, M., Hubans, F., Shapiro, N. M., Paul, A., and Campillo, M. (2010). Origin of deep ocean microseisms by using teleseismic body waves. *J. Geophys. Res.* 115, 672–714. doi:10.1029/2009JB006918

Lin, P.-Y. P., Gaherty, J. B., Jin, G., Collins, J. A., Lizarralde, D., Evans, R. L., et al. (2016). High-resolution seismic constraints on flow dynamics in the oceanic asthenosphere. *Nature Publishing Group* 535, 538–541. doi:10.1038/nature18012

Longuet-Higgins, M. S. (1950). A theory OF the origin OF microseisms. *Phil. Trans. Roy. Soc. Lond. Math. Phys. Sci.* 243, 1–35. doi:10.1098/rsta.1950.0012

M. Ewing, W. S. Jardetzky, and F. Press (1957). *Elastic waves in layered media*. New York, NY: McGraw-Hill.

Mordret, A., Landès, M., Shapiro, N. M., Singh, S. C., and Roux, P. (2014). Ambient noise surface wave tomography to determine the shallow shear velocity structure at Valhall: depth inversion with a neighbourhood algorithm. *Geophys. J. Int.* 198, 1514–1525. doi:10.1093/gji/ggu217

Munk, W. H. (1974). Sound channel in an exponentially stratified ocean, with application to SOFAR. *J. Acoust. Soc. Am.* 55, 220–226. doi:10.1121/1.1914492#

Nakanishi, A., Kodaira, S., Miura, S., Ito, A., Sato, T., Park, J.-O., et al. (2008). Detailed structural image around splay-fault branching in the Nankai subduction seismogenic zone: results from a high-density ocean bottom seismic survey. *J. Geophys. Res.* 113, 119–214. doi:10.1029/2007JB004974

Nakanishi, A., Takahashi, N., Yamamoto, Y., Takahashi, T., Ozgur Citak, S., Nakamura, T., et al. (2018). "Three-dimensional plate geometry and P-wave velocity models of the subduction zone in SW Japan: implications for seismogenesis," in *Geology and Tectonics of subduction zones: a Tribute to gaku kimura*. Editors T. Byrne, M. B. Underwood, D. Fisher, L. McNeill, D. Saffer, K. Ujiie, et al. (Boulder, CO: Geological Society of America), 69–86.

Nakano, M., Nakamura, T., Kamiya, S., Ohori, M., and Kaneda, Y. (2013). Intensive seismic activity around the Nankai trough revealed by DONET ocean-floor seismic observations. *Earth Planets Space* 65, 5–15. doi:10.5047/eps.2012.05.013

Nakata, N., Chang, J. P., Lawrence, J. F., and Boué, P. (2015). Body wave extraction and tomography at Long Beach, California, with ambient-noise interferometry. *J. Geophys. Res. Solid Earth* 120, 1159–1173. doi:10.1002/2015JB011870

Nishida, K. (2013). Global propagation of body waves revealed by cross-correlation analysis of seismic hum. *Geophys. Res. Lett.* 40, 1691–1696. doi:10.1002/grl.50269

Nishida, K., and Takagi, R. (2016). Teleseismic S wave microseisms. *Science* 353, 919–921. doi:10.1038/nphys3711

Park, J.-O., Fujie, G., Wijerathne, L., Hori, T., Kodaira, S., Fukao, Y., et al. (2010). A low-velocity zone with weak reflectivity along the Nankai subduction zone. *Geology* 38, 283–286. doi:10.1130/G30205.1

Poli, P., Campillo, M., and Pedersen, H.LAPNET Working Group (2012). Body-wave imaging of earth's mantle discontinuities from ambient seismic noise. *Science* 338, 1063–1065. doi:10.1126/science.1228194

Poli, P., Pedersen, H. A., and Campillo, M. (2011). The POLENET/LAPNET Working GroupEmergence of body waves from cross-correlation of short period seismic noise. *Geophys. J. Int.* 188, 549–558. doi:10.1111/j.1365-246X.2011.05271.x

Prieto, G. A., Lawrence, J. F., and Beroza, G. C. (2009). Anelastic Earth structure from the coherency of the ambient seismic field. *J. Geophys. Res.* 114, B07303. doi:10.1029/2008JB006067

Roux, P., Sabra, K. G., Gerstoft, P., Kuperman, W. A., and Fehler, M. C. (2005). P-waves from cross-correlation of seismic noise. *Geophys. Res. Lett.* 32 , L19303. doi:10.1029/2005GL023803

Ryberg, T. (2011). Body wave observations from cross-correlations of ambient seismic noise: a case study from the Karoo. *RSA. Geophys. Res. Lett.* 38, L13311. doi:10.1029/2011GL047665

Sabra, K. G. (2005). Extracting time-domain Green's function estimates from ambient seismic noise. *Geophys. Res. Lett.* 32, 547–555. doi:10.1029/2004GL021862

Saenger, E. H., Gold, N., and Shapiro, S. A. (2000). Modeling the propagation of elastic waves using a modified finite-difference grid. *Wave Motion.* 31, 77–92. doi:10.1016/s0165-2125(99)00023-2

Seats, K. J., Lawrence, J. F., and Prieto, G. A. (2012). Improved ambient noise correlation functions using Welch's method. *Geophys. J. Int.* 188, 513–523. doi:10.1111/j.1365-246X.2011.05263.x

Shapiro, N. M., Campillo, M., Stehly, L., and Ritzwoller, M. H. (2005). High-Resolution surface-wave tomography from ambient seismic noise. *Science* 307, 1615–1618. doi:10.1126/science.1108339

Sugioka, H., Fukao, Y., Okamoto, T., and Kanjo, K. (2001). Detection of shallowest submarine seismicity by acoustic coupled shear waves. *J. Geophys. Res.* 106, 13485–13499. doi:10.1029/2000jb900476

Takagi, R., Nakahara, H., Kono, T., and Okada, T. (2014). Separating body and Rayleigh waves with cross terms of the cross-correlation tensor of ambient noise. *J. Geophys. Res. Solid Earth* 119, 2005–2018. doi:10.1002/2013JB010824

Takahashi, N., Kodaira, S., Nakanishi, A., Park, J.-O., Miura, S., Tsuru, T., et al. (2002). Seismic structure of western end of the Nankai trough seismogenic zone. *J. Geophys. Res. Solid Earth* 107, 2212. doi:10.1029/2000JB000121

Takeo, A., Nishida, K., Isse, T., Kawakatsu, H., Shiobara, H., Sugioka, H., et al. (2013). Radially anisotropic structure beneath the Shikoku Basin from broadband surface wave analysis of ocean bottom seismometer records. *J. Geophys. Res. Solid Earth* 118, 2878–2892. doi:10.1002/jgrb.50219

Tonegawa, T., Araki, E., Kimura, T., Nakamura, T., Nakano, M., and Suzuki, K. (2017). Sporadic low-velocity volumes spatially correlate with shallow very low frequency earthquake clusters. *Nat. Commun.* 8, 2048. doi:10.1038/s41467-017-02276-8

Tonegawa, T., Fukao, Y., Takahashi, T., Obana, K., Kodaira, S., and Kaneda, Y. (2015). Ambient seafloor noise excited by earthquakes in the Nankai subduction zone. *Nat. Commun.* 6, 6132. doi:10.1038/ncomms7132

Tonegawa, T., Nishida, K., Watanabe, T., and Shiomi, K. (2009). Seismic interferometry of teleseicmic S-wave coda for retrieval of body waves: an application to the Philippine Sea slab underneath the Japanese Islands. *Geophys. J. Int.* 178, 1574–1586. doi:10.1111/j.1365-246X.2009.04249.x

Wapenaar, K. (2004). Retrieving the elastodynamic green's function of an arbitrary inhomogeneous medium by cross correlation. *Phys. Rev. Lett.* 93, 254301. doi:10.1103/PhysRevLett.93.254301

Zhan, Z., Ni, S., Helmberger, D. V., and Clayton, R. W. (2010). Retrieval of Moho-reflected shear wave arrivals from ambient seismic noise. *Geophys. J. Int.* 169 408–420. doi:10.1111/j.1365-246X.2010.04625.x

**Conflict of Interest:** The authors declare that the research was conducted in the absence of any commercial or financial relationships that could be construed as a potential conflict of interest.

frontiers in Earth Science

BRIEF RESEARCH REPORT
published: 31 March 2021
doi: 10.3389/feart.2021.661337

# Approbation of the Method for Examining the Performance of Seafloor Observatory Sensors Using Distant Earthquakes Records

*Mikhail Nosov*[1,2], *Viacheslav Karpov*[1]*, *Kirill Sementsov*[1], *Sergey Kolesov*[1,2], *Hiroyuki Matsumoto*[3] *and Yoshiyuki Kaneda*[4]

[1] *Chair of Physics of Sea and Inland Water, Faculty of Physics, M.V.Lomonosov Moscow State University, Moscow, Russia,* [2] *Institute of Marine Geology and Geophysics, Far Eastern Branch of Russian Academy of Sciences, Yuzhno-Sakhalinsk, Russia,* [3] *Japan Agency for Marine-Earth Science and Technology, Yokosuka, Japan,* [4] *Institute of Education, Research and Regional Cooperation for Crisis Management Shikoku, Kagawa University, Takamatsu, Japan*

An algorithm is presented for testing the calibration accuracy of both z-accelerometers and pressure gauges (PG) installed in seafloor observatories. The test is based on the linear relationship between the vertical acceleration component of the seafloor movement and variations of the seafloor pressure, which is a direct consequence of Newton's 2-nd law and holds valid in the frequency range of "forced oscillations." The operability of the algorithm is demonstrated using signals registered by 28 observatories of the DONET-2 system during 4 earthquakes of magnitude $M_W \sim 8$ that took place in 2018-2019 at epicentral distances from 55° up to 140°.

**Keywords: seafloor observatory, ocean-bottom seismometer, z-accelerometer, pressure gauge, earthquake, sensor testing**

OPEN ACCESS

***Edited by:***
*Francisco Javier Nuñez-Cornu, University of Guadalajara, Mexico*

***Reviewed by:***
*Chao An, Shanghai Jiao Tong University, China*
*Masanori Kameyama, Ehime University, Japan*

***Correspondence:**
*Viacheslav Karpov*
*va.karpov@physics.msu.ru*

***Specialty section:***
*This article was submitted to Solid Earth Geophysics, a section of the journal Frontiers in Earth Science*

***Received:*** *30 January 2021*
***Accepted:*** *09 March 2021*
***Published:*** *31 March 2021*

***Citation:***
*Nosov M, Karpov V, Sementsov K, Kolesov S, Matsumoto H and Kaneda Y (2021) Approbation of the Method for Examining the Performance of Seafloor Observatory Sensors Using Distant Earthquakes Records. Front. Earth Sci. 9:661337. doi: 10.3389/feart.2021.661337*

## 1. INTRODUCTION

During the first decades of the twenty-first century at least several hundred seafloor observatories equipped with ocean bottom seismometers (OBS) and pressure guages (PG) were installed in the oceans all over the World. Without pretending to present the full list, we shall mention several such systems: DONET (Dense Ocean-floor Network system for Earthquakes and Tsunamis) (Kaneda et al., 2015; Kawaguchi et al., 2015), S-net (Seafloor Observation Network for Earthquakes and Tsunamis) (Kanazawa, 2013), NEMO-SN1 (NEutrino Mediterranean Observatory-Submarine Network 1) (Favali et al., 2013), NEPTUNE (North East Pacific Time-series Underwater Networked Experiments) (Barnes and Team, 2007), MACHO (MArine Cable Hosted Observatory) (Hsiao et al., 2014), and others. Seafloor observatories are made for resolving numerous scientific and practical problems (Favali et al., 2010), but one of their most important purposes consists in the early warning of earthquakes and tsunamis (Rabinovich and Eblé, 2015; Mulia and Satake, 2020).

Deep-water PG and OBS are intended for long-term operation in an active and aggressive sea-water medium at high pressures. In spite of the applied measuring systems being highly reliable, the precision of their calibration still needs to be checked periodically. Nowadays hundreds of pairs of PG&OBS are in operation. Thousands of similar measuring systems will be deployed in the near future (Tilmann et al., 2017; Ranasinghe et al., 2018). One should expect some human errors in calibration of ocean-bottom sensors. Recently we revealed such an error in calibration of z-accelerometer of E18/DONET observatory (Nosov et al., 2018; Karpov et al., 2020). Even if one

excludes human errors, the possibility cannot be excluded of the sensitivity of sensors changing with time or owing to external influences. Strong ground motion during nearby earthquake can affect the orientation of ocean-bottom sensors (Nakamura and Hayashimoto, 2019). It results in changing output both OBS (Graizer, 2010; Javelaud et al., 2011) and PG (Chadwick et al., 2006). Moreover, PG can be covered with a layer of sediments gradually year by year or suddenly due to a landslide or mud flow which can distort the frequency-response function of the sensor.

A method for examining the performance of seafloor observatory sensors was proposed and substantiated in our works (Nosov et al., 2018; Karpov et al., 2020). We considered mutual verification of the calibration of a PG and a z-accelerometer (OBS that measures the vertical component of the ocean bottom acceleration). The method does not require direct access to the sensors installed at large depths. A check of the calibration is implemented remotely by analysis of records that are obtained during the registration of an earthquake.

The method is based on variations of the bottom pressure $p$ and the vertical acceleration component $a_z$ of the ocean bottom motion being related linearly:

$$p = ma_z, \tag{1}$$

where $m$ is the mass of a water column of unit cross section. The existence of such a relationship was first mentioned in (Bradner, 1962; Filloux, 1982; Webb, 1998). Different approaches to theoretical justification of expression (1) are presented in (Levin and Nosov, 2016; An et al., 2017; Nosov et al., 2018; Iannaccone et al., 2021). Note, also, that relationship (1) permits, if necessary, to use a PG as a seismometer (Kubota et al., 2017; Iannaccone et al., 2021).

When applying formula (1) one must take into account that it does not always hold true, but only under certain conditions. The first condition was already mentioned in (Filloux, 1983): relationship (1) holds true, when the layer of water behaves like an incompressible medium, i.e., at frequencies lower than the minimum acoustic resonance (normal) frequency: $f_{ac}$. The frequency $f_{ac}$ is the lower limit of the frequency range of existing hydroacoustic waves, and it is determined by the following formula (Tolstoy and Clay, 1987):

$$f_{ac} = c/4H, \tag{2}$$

where $c$ is the speed of sound in water, $H$ is the ocean depth.

The second condition also concerns a frequency restriction, but imposed on low frequencies. In (Levin and Nosov, 2016; Nosov et al., 2018; Iannaccone et al., 2021) it was shown that oscillations of the ocean bottom with frequencies $f > f_g$ cannot excite gravity surface waves. The value of $f_g$ is estimated by the following formula

$$f_g = 0.366\sqrt{g/H}, \tag{3}$$

where $g$ is the gravity acceleration. The factor "0.366" in Equation (3) comes from solution of transcendent equation $1/\cosh(kH) = 0.01$, where $k$ is the wavenumber related to the cyclic frequency $\omega$ ($\omega = 2\pi f$) by the dispersion relation $\omega^2 = gk\tanh(kH)$. The spatial spectrum of gravity waves generated by ocean-bottom motions is always modulated by function $1/\cosh(kH)$. Physical meaning of the factor "0.366" is a 100-fold attenuation of the wave amplitude compared to the amplitude of bottom oscillations.

Thus, seismic movements of the ocean bottom in the range of $f_g < f < f_{ac}$ excite neither hydroacoustic nor gravity waves. Within this range there exists a form of movement of the water layer, termed "forced oscillations." Relationship (1), which is a direct consequence of Newton's 2-nd law, holds valid for forced oscillations.

A third important condition for relationship (1) to be valid consists in the arrangement of the measuring system on a flat horizontal ocean bottom, while the steep under-water slopes must be far from the measurement point, at least at a distance exceeding 2 ocean depths (Nosov et al., 2018).

A first attempt at testing relationship (1) in natural conditions was made using signals registered by the seafloor observatory Kushiro-Tokachi/JAMSTEC during the 2003 Tokachi-oki earthquake (Bolshakova et al., 2011). Although the PG and OBS were separated in space by several kilometers, the spectra of pressure variations and of the z-acceleration turned out to be quite close within the frequency range of forced oscillations.

In An et al. (2017) comparison was made of waveforms registered by the PG and OBS of the seafloor observatory Hatsushima/JAMSTEC during three earthquakes (2016-04-15, M7.0, Kumamoto; 2016-07-29, M7.7, Mariana Islands; 2016-03-02, M7.8, Sumatra). Unlike the Kushiro-Tokachi observatory, the PG and OBS of the Hatsushima observatory were situated close to each other. The pressure and acceleration variations in the frequency range of 0.02–0.2 Hz recalculated to pressure units by formula (1), demonstrated an impressive similarity. Note that the indicated frequency range is close to the range of forced oscillations (0.03–0.3 Hz), determined in accordance with formulas (2) and (3) by the depth at which the Hatsushima observatory is installed (1,176 m).

In Matsumoto et al. (2015, 2017) and Nosov et al. (2018) an analysis was performed of records obtained by ten DONET-1 observatories during the 2011 Great East Japan Earthquake. The spectra of pressure and z-acceleration variations within the range $f_g < f < f_{ac}$ turned out to be practically identical, and the cross-spectral analysis of these signals permitted to demonstrate that relationship (1) is satisfied exactly within the frequency range indicated.

Information on one more successful test of relationship (1)—this time by data from measuring devices installed at small depths (40–76 m) in the Gulf of Pozzuoli (Italy)—is presented in a most recently published work (Iannaccone et al., 2021).

The main point of the method for examining the performance of seafloor observatory sensors consists in finding the ratio of the power spectra of pressure and z-acceleration variations registered during an earthquake (Karpov et al., 2020). In the case of correct calibration of sensors in the frequency range $f_g < f < f_{ac}$ the ratio of the spectra should be a constant value equal to $m^2$. For approximate estimates, or when performing theoretical investigations under the assumption of an ocean of fixed density, the mass of a water column of unit cross section can be calculated

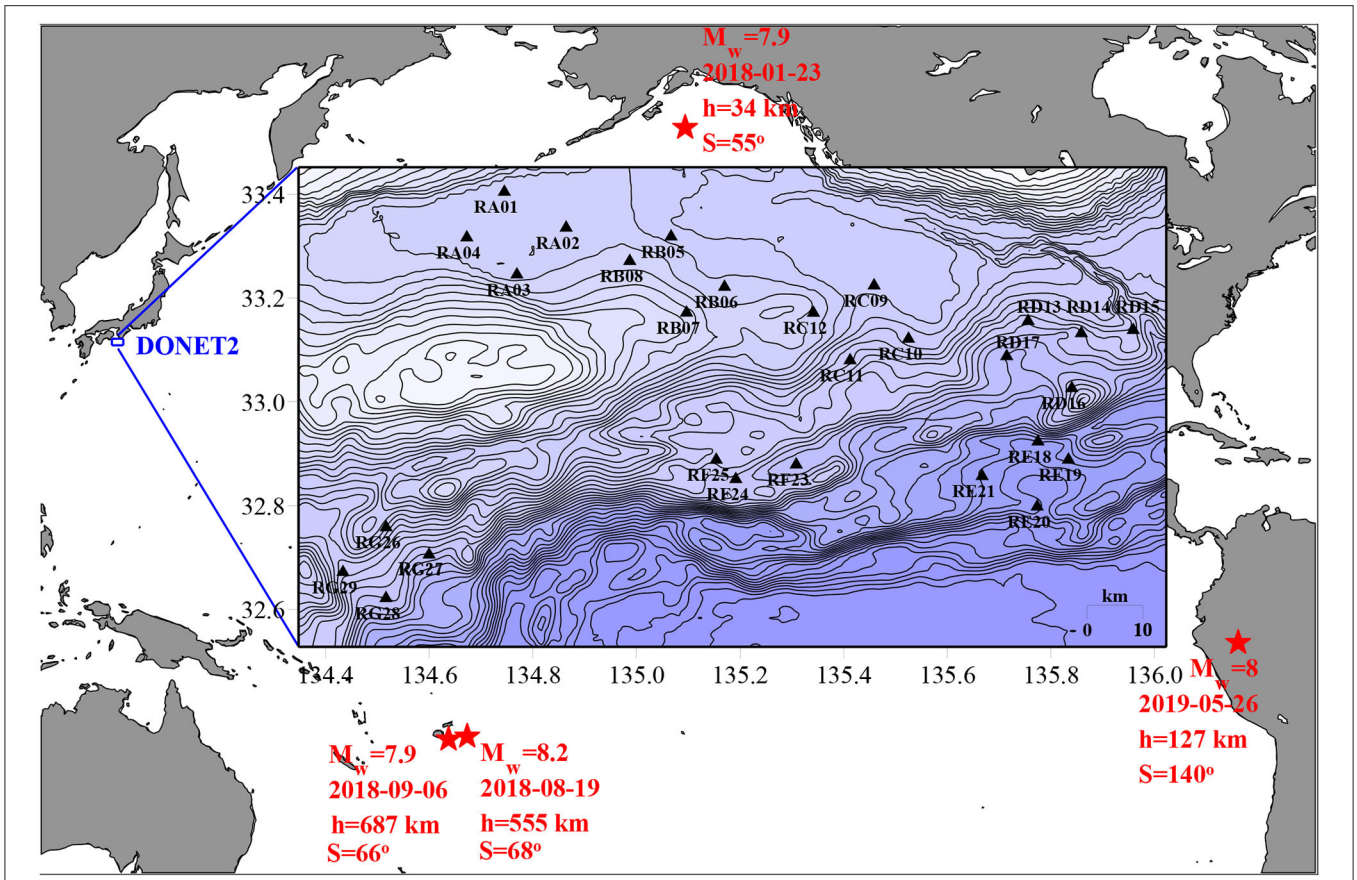


**FIGURE 1 |** Mutual arrangement of the DONET-2 system and the epicenters of four earthquakes, the signals of which are analyzed in this work. The following quantities associated with each seismic event are indicated in the figure: the moment magnitude $M_w$, the date, the epicenter depth $h$ and the epicentral distance in degrees of the great circle, $S$. The insert presents a map with the arrangement of 28 seafloor observatories of the DONET-2 system. The distribution of depths in the insert is shown by isobaths in steps of 100 m. The scale (10 km) is indicated in the lower right angle of the insert.

via the average density of water $\rho$ and the ocean depth: $\rho H$. This is precisely what most researchers do (Bradner, 1962; Filloux, 1982; Webb, 1998; An et al., 2017). In Nosov et al. (2018) and Karpov et al. (2020) we have shown it to be advisable to base accurate calculations on the value measured by PG, i.e., $\overline{P}$ – the total pressure averaged over time, and on the relationship of hydrostatics, $m = \overline{P}/g$.

The first successful application of the method described in Karpov et al. (2020) was based on data registered by the DONET-1 system during the 2011 Great East Japan Earthquake at a distance of about 800 km from the epicenter. Such strong and close seismic events are extremely rare, while calibration tests must be performed regularly. The main purpose of the present work consists in estimation of the operability of the method, when records are used of distant earthquakes of magnitude $M_w \sim 8$, that usually take place several times a year. The second goal of the work is to develop an algorithm for estimating the sensor calibration accuracy, which would permit to automatically provide a quantitative estimation of the calibration accuracy of sensors of seafloor observatories, or a conclusion asserting it to be impossible to perform a test for objective reasons.

## 2. METHOD

In this work records are considered of PGs and z-accelerometers (OBSs) of the DONET-2 system. Since 2015 the DONET data are held by the National Research Institute for Earth Science and Disaster Resilience (NIED), which has made these data accessible to the scientific community. We have considered more than a dozen strong earthquakes, that occurred in 2015-2019, and selected four events for a detailed analysis on the basis of the following arguments: the earthquake had to be registered by a maximum number of DONET-2 observatories and the seismic signal must be clearly distinguished from the background of noise.

The mutual arrangement of the DONET-2 system and the epicenters of the four earthquakes is shown in **Figure 1**. The earthquake parameters indicated in the figure were taken from the Global CMT Catalog (Ekström et al., 2010). During all the four seismic events 28 seafloor observatories of the DONET-2 system were functioning. The observatories were installed in the Nankai Trough area at depths from 1,077 down to 3,603 m. The arrangement of the DONET-2 seafloor

observatories and the ocean bottom relief are shown in the insert of **Figure 1**.

The OBSs of the DONET-2 system register signals with a frequency of 100 Hz, and the PGs with a frequency of 10 Hz. Before being processed seismic signals were downsampled to 10 Hz, in the case of the PG the original discreteness of the time series—10 Hz—was retained.

In **Figure 2** the example is presented of signals, registered by the PG and z-accelerometer of the Mra01 observatory during an earthquake of magnitude $M_w = 8.2$, which occurred on 2018-08-19 in the Fiji Islands region. The signals are shown together with the spectrograms, constructed with the aid of the Morlet wavelet transformation. Each spectrogram is normalized to its maximum value $S_0$ (the color scale is shown at the top of the figure). The white dotted lines in the spectrograms show the position of the critical frequencies $f_g$ and $f_{ac}$, determining the position of the frequency band of "forced oscillations."

From **Figure 2** it is seen that, the amplitude of vertical accelerations was at a level of 1 mm/s$^2$, the amplitude of pressure variations was at a level of 1 kPa (0.1 m of the water column). The seismic signal is certainly noticeable against the background of noise. But the noise background was actually significant. In particular, the noise in the spectrograms is well seen at a frequency of 0.2 Hz and is, apparently, microseisms. At any rate this noise remains unchanged in time and is manifest at all stations (**Supplementary Figures 1–112**).

From the spectrograms the conclusion can also be made that the seismic signal is distinguishable against the background during 1 hour. On the basis of this fact, for detailed analysis we choose segments of OBS and PG records one hour long from the onset moment of the seismic signal. The number of readouts in each of the series processes amounted to 36,000.

The method for testing the calibration of sensors is based on application of spectral and cross-spectral analysis (Nosov et al., 2018; Karpov et al., 2020). For calculation of the spectra and the cross-spectra we used Welch's averaging method (Bendat and Piersol, 2010). The time series was divided with the aid of the Hann window into 8 segments with a 50% overlap. The size of a segment amounted to 8,192 readouts. The resolution of spectra and cross-spectra in frequency was 0.0012 Hz. The confidence interval for the ratio of spectra was calculated by the technique described in Shin and Hammond (2008).

We shall further describe the calibration test algorithm, which consists of several stages. The first three stages represent a development of the technology proposed in (Karpov et al., 2020). The concluding stage of the algorithm is presented for the first time.

At the ***first stage***, the total mean pressure at the ocean bottom, $\overline{P}$, is determined as the simple arithmetic average of the $P$ values, measured by the PG. Then, the variations of the ocean bottom pressure is found in accordance with the formula

$$p = P - \overline{P}. \tag{4}$$

At the ***second stage***, the cross-spectrum is calculated of variations of the ocean bottom pressure $p$ and of the vertical acceleration $a_z$. Examples of the calculation of cross-spectra are presented in **Figure 3**. A complete set of plots for all the DONET-2 observatories and for all four earthquakes considered is presented in the (**Supplementary Figures 113–140**).

From **Figure 3** it is seen that for the series of harmonics within the range of "forced oscillations," the magnitude-squared coherence (MSC) turns out to be close to 1, while the Phase Lag (PL) – to 0. This means that at the given frequencies the values of $p$ and $a_z$ are proportional to each other, and, consequently it is possible to test the calibration of sensors. In other cases, the MSC differs noticeably from 1, which points to violation of the proportionality between $p$ and $a_z$. Independently of the reasons that caused violation of proportionality (Nosov et al., 2018), calibration testing by these harmonics is impossible.

To minimize the influence on the result of microseismic noise at the frequency $\sim$ 0.2 Hz (**Figure 2**) we exclude from consideration the frequency range $f > 0.1$ Hz. Note that in all cases considered, even for the most deep-water observatory (3,603 m), $f_{ac} > 0.1$ Hz. Therefore, the frequency range of "forced oscillations" is substituted by a somewhat more narrow range: $f_g < f < 0.1$ Hz. Within this range we single out a discrete set of harmonics $f_j$, for which the condition $MSC \geq 0.99$ is satisfied and, consequently, the signals p and $a_z$ must be proportional to each other. We shall further term the set of frequencies $f_j$ "good frequencies."

The amount of "good frequencies" should not be less than 25% of the total number of harmonics that happen to be within the frequency range $f_g < f < 0.1$ Hz. If the number of points in the array $f_j$ does not comply with the condition indicated, then the conclusion is made that a calibration test cannot be performed for this pair of PG and OBS records.

At the ***third stage*** the power spectra are calculated of signals $S_p$ and $S_{a_z}$, and the ratio is sought of the spectra: $S_p/S_{a_z}$. Examples of calculated ratios of spectra are presented in **Figure 3**. The complete set of plots for all the DONET-2 observatories and all the four earthquakes considered is presented in the Supplementary Material (**Supplementary Figures 141–168**). Theoretically, the calibration of sensors is correct, if the ratio of spectra is equal to the constant value $(\overline{P}/g)^2$ within the frequency range $f_g < f < f_{ac}$. In **Figure 3** this level is shown by the horizontal dotted line. From the figure it is seen that on the whole the ratios of spectra quite comply with the indicated level. This means no gross mistakes were made in calibrating the sensors. But careful examination of the ratios of spectra demonstrates that insignificant deviations are actually present. Our further goal is to provide a quantitative characteristic for the deviations.

At the ***fourth stage*** only those values are selected from the array, representing the ratio of spectra $S_p/S_{a_z}$, that correspond to "good frequencies" $f_j$. We assume the mean value of this sample to be the mean ratio of spectra, $\overline{S_p/S_{a_z}}$.

As a criterion indicating possible deviation of the calibration we assume the value

$$\Delta = \sqrt{\overline{S_p/S_{a_z}}}/(\overline{P}/g) - 1. \tag{5}$$

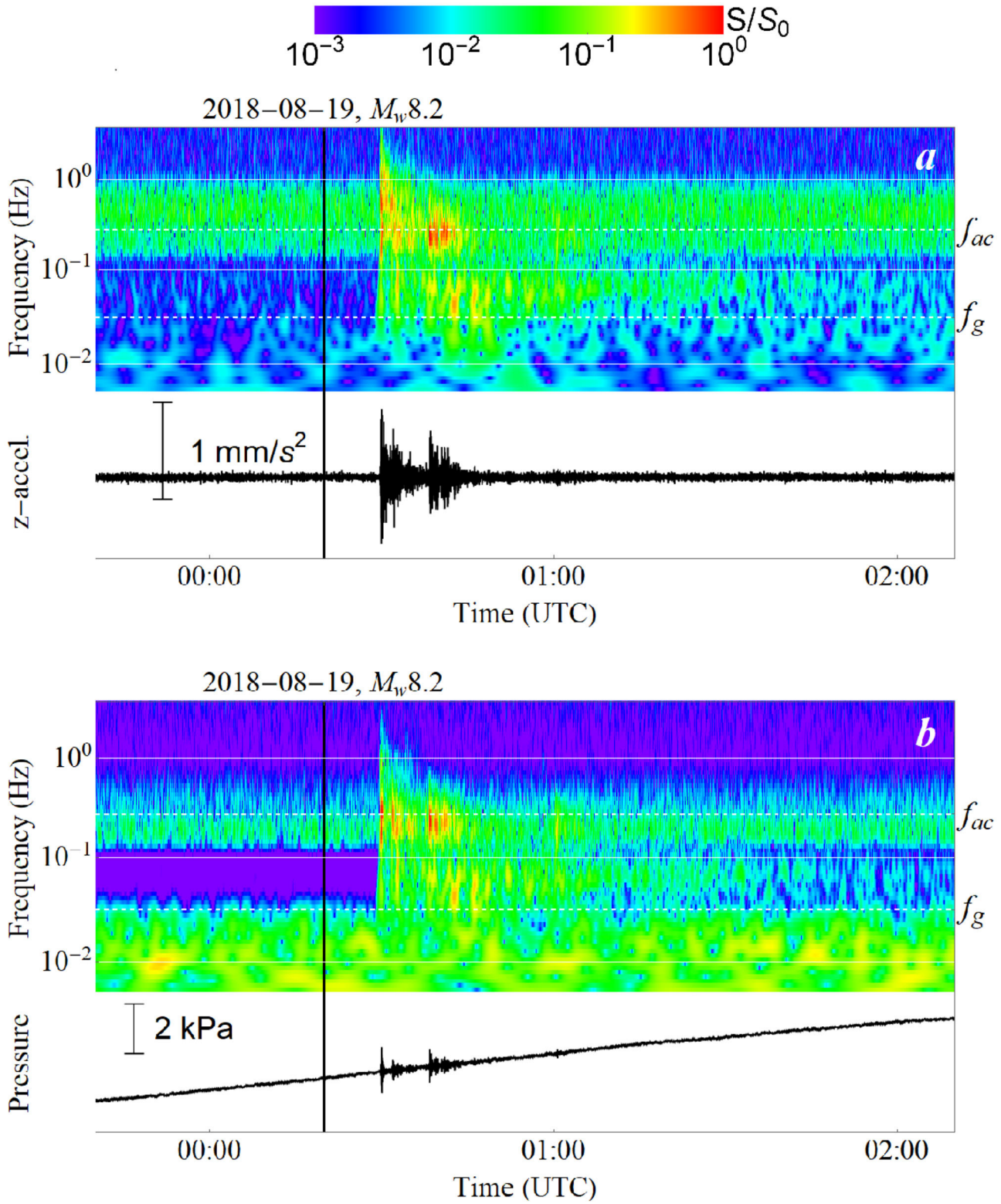


**FIGURE 2 |** The signals registered by the PG **(a)** and the z-accelerometer **(b)** of the Mra01 observatory during the earthquake, that occurred on 2018-08-19 in the region of the Fiji Islands ($M_w$ = 8.2). The spectrograms are constructed with the aid of the Morlet wavelet transformation. Each spectrogram is normalized to its maximum value $S_0$ (the color scale is shown at the top of the figure). The white dotted lines in the spectrograms show the positions of the critical frequencies $f_g$ and $f_{ac}$, determining the position of the frequency range of "forced oscillations." The time moment corresponding to the beginning of the earthquake is indicated by black line.

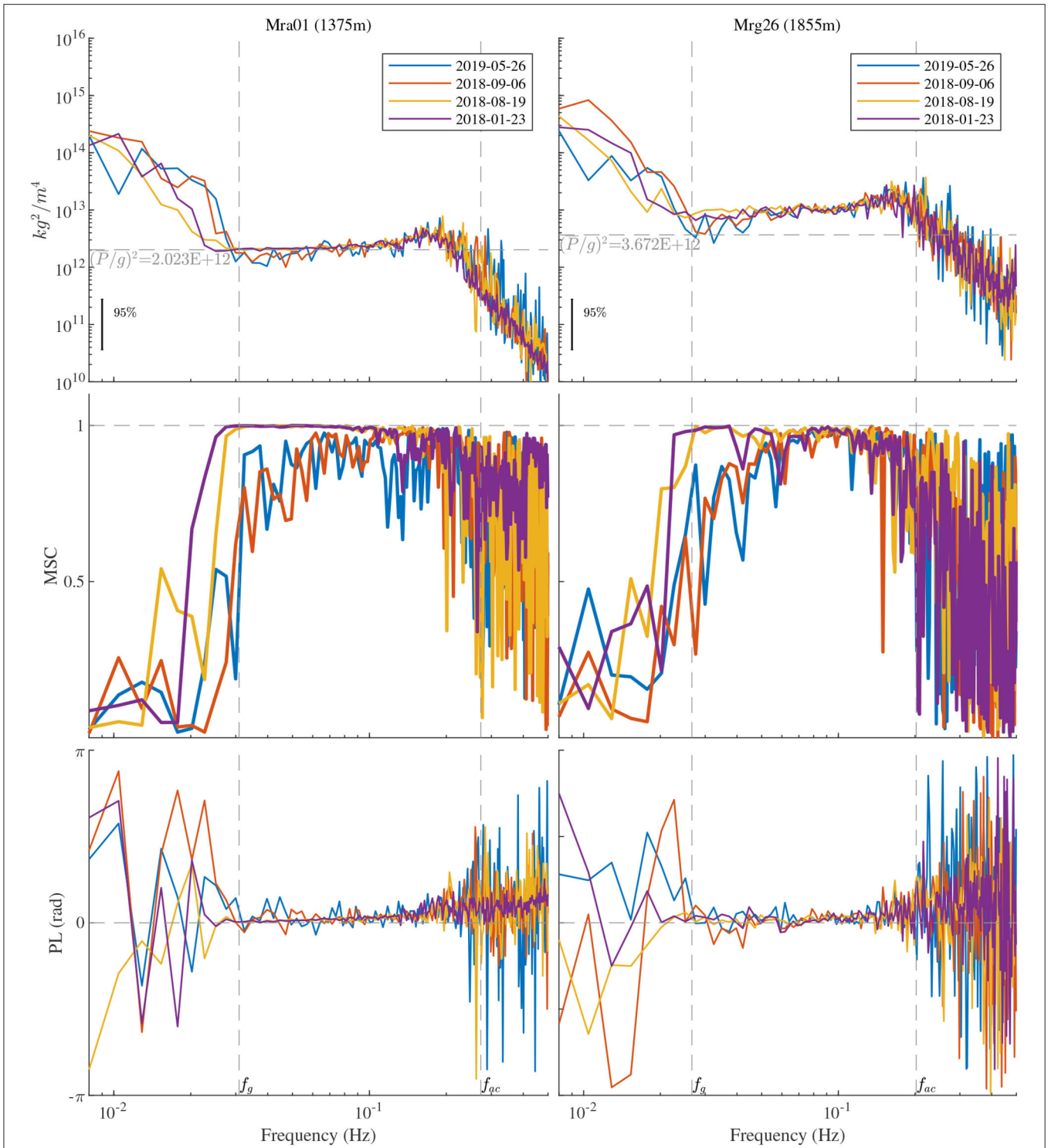


**FIGURE 3 |** Results of spectral processing of the signals registered by the PGs and z-accelerometers of the Mra01 (left column) and Mrg26 (right column) observatories. The colors of the curves correspond to the four seismic events dealt with (the dates are indicated in the legend). Fragments of the figure from top to bottom are: the ratio of power spectra of variations of the ocean bottom pressure ($p$) and the z-acceleration ($a_z$), the cross-spectrum of signals $p$ and $a_z$ (magnitude-squared coherence—MSC and Phase Lag—PL). The vertical dotted lines show the positions of frequencies $f_g$ and $f_{ac}$, that are limits imposed on the range of "forced oscillations." The horizontal dotted line in the upper row of fragments and the numbers under it show the value of $(\overline{P}/g)^2$.

**TABLE 1 |** Results of tests of the calibration accuracy—the value of Δ calculated by formula 5.

| | 2019-05-26 | 2018-09-06 | 2018-08-19 | 2018-01-23 | Trend |
|---|---|---|---|---|---|
| Mra01 | N/A | N/A | 0.05 | 0.04 | + |
| Mra02 | N/A | N/A | 0.05 | 0.04 | + |
| Mra03 | N/A | N/A | 0.05 | 0.04 | + |
| Mra04 | N/A | N/A | N/A | 0.28 | N/A |
| Mrb05 | N/A | N/A | 0.07 | 0.06 | + |
| Mrb06 | N/A | N/A | 0.04 | 0.04 | 0 |
| Mrb07 | 0.05 | 0.04 | 0.03 | 0.02 | + |
| Mrb08 | N/A | N/A | 0.05 | 0.04 | + |
| Mrc09 | N/A | 0.05 | 0.04 | 0.05 | 0 |
| Mrc10 | N/A | N/A | 0.06 | 0.05 | + |
| Mrc11 | N/A | N/A | 0.10 | 0.09 | + |
| Mrc12 | N/A | 0.07 | 0.05 | 0.04 | + |
| Mrd13 | N/A | N/A | 0.11 | 0.10 | + |
| Mrd14 | N/A | N/A | 0.08 | 0.06 | + |
| Mrd15 | N/A | N/A | 0.14 | 0.14 | 0 |
| Mrd16 | N/A | N/A | 0.16 | 0.13 | + |
| Mrd17 | N/A | N/A | 0.18 | 0.13 | + |
| Mre18 | N/A | N/A | 0.31 | 0.21 | + |
| Mre19 | N/A | N/A | 0.32 | 0.20 | + |
| Mre20 | N/A | N/A | 0.35 | 0.38 | – |
| Mre21 | N/A | N/A | 0.34 | 0.37 | – |
| Mrf23 | N/A | 0.29 | 0.19 | 0.17 | + |
| Mrf24 | N/A | N/A | 0.16 | 0.14 | + |
| Mrf25 | N/A | N/A | 0.15 | 0.13 | + |
| Mrg26 | N/A | N/A | 0.62 | 0.53 | + |
| Mrg27 | N/A | N/A | 0.23 | 0.11 | + |
| Mrg28 | N/A | N/A | 0.23 | 0.15 | + |
| Mrg29 | N/A | N/A | 0.14 | 0.08 | + |

*The left column contains the names of observatories, the earthquake date is shown in the upper row. The last column shows the trend in changes of the value of Δ.*

## 3. RESULTS

The results of application of the algorthim, described above, for testing the calibration are tabulated in **Table 1**. The numbers in **Table 1** represent a quantitative characteristic of the accuracy of calibration—the value of delta calculated by formula 5. The impossibility of testing the calibration is marked by "N/A."

From **Table 1** it is seen that in the case of most DONET-2 observatories, with a few exceptions, testing the calibration by the signals registered during the earthquakes 2018-09-06 and 2019-05-26 turned out to be impossible. The calibration being impossible is related to the low MSC level of the cross-spectra (see **Supplementary Figures 113–140**), which points to non-fulfillment of the condition necessary for calibration—the proportionality of pressure variations and the z-acceleration. Owing to a somewhat higher amplitude, the seismic signals of earthquakes 2018-01-23 and 2018-08-19, probably, turned out to be more suitable for testing the calibration.

From **Table 1** it is seen that $\Delta > 0$ in all cases. The value of Δ varies from 2 and 62%. It is remarkable that Δ is a more or less unchangeable for each observatory, while its variation in the case of transition from one seismic event to another is insignificant. A good example, here, is the Mrb07 observatory, the only station that could be tested in the case of all 4 events. Three observatories (Mrc09, Mrc12, Mrf23) were tested in the case of 3 events, the deviation for the first two was at a level of 7%, and it was more significant in the case of the last event (17–29%). The largest deviation (62 and 53%) was observed by station Mrg26. The manifestation of a possible calibration inaccuracy is seen clearly, here, and with respect to the spectra shown in **Figure 3**, also.

Together with the relative stability of the value of Δ attention must be drawn to the existing trends in the change of this value with time. The calibration accuracy of practically all observatories falls with time. Observatories Mre20 and Mre21, for which the accuracy increases, represent exceptions. Furthermore, the values of Δ turned out to be invariable for observatories Mrb06, Mrc09, Mrd15, while in the case of observatory Mra04, for which a test was implemented only for one earthquake, no trend can, evidently, be determined.

## 4. DISCUSSION

The method for testing the calibration accuracy, on the whole, demonstrated its reliability for distant earthquakes with a moment magnitude $M_w \sim 8$. Earthquakes 2018-08-19 ($M_w = 8.2, h = 555km, S = 68^\circ$) and 2018-01-23 ($M_w = 7.9, h = 34km, S = 55^\circ$) turned out to be suitable for testing practically all the DONET-2 observatories. An analysis of the records of these events revealed that the earthquake depth does not affect the test possibility. The calibration test by the data of another pair of seismic events with close magnitudes, 2019-05-26 ($M_w = 8.0, h = 127km, S = 140^\circ$) and 2018-09-06 ($M_w = 7.9, h = 687km, S = 66^\circ$), turned out to be difficult for most observatories, since application of the method was apparently at its limit, owing to the low signal-to-noise ratio. The reasons for the low signal-to-noise ratio are associated with the fact that the earthquake on 2019-05-26 occurred at the boundary of the shadow zone ($104^\circ - 140^\circ$), and because of the rather large focal depth, the formation of surface waves could not be effective. As for the earthquake on 2018-09-06, in contrast to the event with the same magnitude on 2018-01-23, it occurred further from DONET system and had much larger focal depth.

For the method to be reliable it is important for the seismic signal to be noticeably superior to the background noise in the frequency range of "forced oscillations," including the vicinity of its low-frequency limit $f_g$. The position of $f_g$ is determined by the ocean depth, and in the case of the deepest DONET-2 observatory (Mre20, 3,603 m) it is $f_g \approx 0.02$ Hz. The capability of an earthquake to create a low-frequency signal is

known to be related to the value of its moment magnitude (Denolle and Shearer, 2016). An earthquake with $M_w \sim 8$ can provide a seismic signal of the necessary level at a frequency of 0.02 Hz, but earthquakes with noticeably smaller magnitudes, most likely, cannot. Therefore, relatively weak seismic events of $M_w < 7$, even if they occur in close proximity to a seafloor observatory, may turn out to be useless for testing the calibration of sensors installed at depths of several kilometers. For observatories installed at small depths ($\sim$ 100 m) the frequency limit is shifted toward higher frequencies $f_g \approx 0.1$ Hz. In the case of such observatories, even an earthquake of $M_w \sim 7$ is suitable for calibration tests (Iannaccone et al., 2021).

An important feature of the method proposed for calibration tests consists in that possible inaccuracies in the PG calibration, under the condition of an absolutely flat amplitude-frequency characteristic (AFC) of the pressure gauge, should not manifest themselves in the value of $\Delta$. From the structure of formula (5) the calibration factor, to which both pressure variations and the total mean pressure value are proportional, is reduced. Consequently, a deviation of the value of $\Delta$ from 1 only reveals an inaccuracy in the z-accelerometer calibration, but not in the calibration of both gauges. As to testing the PG calibration, it can be done by comparison of the total mean pressure and the value prescribed by the law of hydrostatics, $\overline{P} = \rho g H$. As a rule, the depth, at which an observatory is installed, is well-known. Thus, the accuracy of a PG calibration test relies on the accuracy of the knowledge of the average sea water density.

## DATA AVAILABILITY STATEMENT

Publicly available datasets were analyzed in this study. This data can be found at: https://hinetwww11.bosai.go.jp/auth/download/cont/.

## AUTHOR CONTRIBUTIONS

MN played a leading role in this study, suggested the main idea, and provided interpretation of data processing results. VK carried out spectral and cross-spectral analysis, prepared **Figures 1**, **3** and **Table 1**, and all the related **Supplementary Material**. KS prepared **Figure 2** and all the related **Supplementary Material**. SK preprocessed the data and downsampled accelerograms. HM provided technical information on DONET system and some references. YK facilitated data transfer and communication between Russian and Japanese teams and suggested a number of important references. All authors read and approved the final manuscript.

## FUNDING

This work was supported by the Russian Foundation for Basic Research, projects 19-05-00351, 20-07-01098, 20-35-70038.

## ACKNOWLEDGMENTS

We are grateful for the data of Dense Oceanfloor Network system for Earthquakes and Tsunamis (DONET) from the National Research Institute for Earth Science and Disaster Resilience (NIED, 2019). We thank GEBCO Compilation Group (2020) GEBCO 2020 Grid (GEBCO, 2020) for bathemetry data. A special thanks goes to the editor and to the reviewers for their constructive comments that helped to improving this article.

## SUPPLEMENTARY MATERIAL

The Supplementary Material for this article can be found online at: https://www.frontiersin.org/articles/10.3389/feart.2021.661337/full#supplementary-material

## REFERENCES

An, C., Cai, C., Zheng, Y., Meng, L., and Liu, P. (2017). Theoretical solution and applications of ocean bottom pressure induced by seismic seafloor motion. *Geophys. Res. Lett.* 44, 10272–10281. doi: 10.1002/2017GL075137

Barnes, C. R., and Team, N. C. (2007). "Building the world's first regional cabled ocean observatory (neptune): realities, challenges and opportunities," in *OCEANS 2007* (Vancouver, BC), 1–8.

Bendat, J. S., and Piersol, A. G. (2010). *Random Data: Analysis and Measurement Procedures, 4th Edn*. Wiley series in probability and statistics. Hoboken, NJ: Wiley.

Bolshakova, A., Inoue, S., Kolesov, S., Matsumoto, H., Nosov, M., and Ohmachi, T. (2011). Hydroacoustic effects in the 2003 Tokachi-oki tsunami source. *Russ. J. Earth Sci.* 12, 1–14. doi: 10.2205/2011ES000509

Bradner, H. (1962). Pressure variations accompanying a plane wave propagated along the ocean bottom. *J. Geophys. Res.* 67, 3631–3633.

Chadwick, W. W., Nooner, S. L., Zumberge, M. A., Embley, R. W., and Fox, C. G. (2006). Vertical deformation monitoring at Axial Seamount since its 1998 eruption using deep-sea pressure sensors. *J. Volcanol. Geotherm. Res.* 150, 313–327. doi: 10.1016/j.jvolgeores.2005.07.006

Denolle, M. A., and Shearer, P. M. (2016). New perspectives on self-similarity for shallow thrust earthquakes: source properties of thrust earthquakes. *J. Geophys. Res. Solid Earth* 121, 6533–6565. doi: 10.1002/2016JB013105

Ekström, G., Nettles, M., and Dziewoński, A. (2010). The global CMT project 2004–2010: centroid-moment tensors for 13,017 earthquakes *Phys. Earth Planet. Interiors* 200–201, 1–9. doi: 10.1016/j.pepi.2012.04.002

Favali, P., Chierici, F., Marinaro, G., Giovanetti, G., Azzarone, A., Beranzoli, L., et al. (2013). Nemo-sn1 abyssal cabled observatory in the Western Ionian Sea. *IEEE J. Ocean. Eng.* 38, 358–374. doi: 10.1109/JOE.2012.2224536

Favali, P., Person, R., Barnes, C. R., Kaneda, Y., Delaney, J. R., and Hsu, S.-K. (2010). Seafloor observatory science. *Proc. OceanObs* 9, 21–25. doi: 10.5270/oceanobs09.cwp.28

Filloux, J. H. (1982). Tsunami recorded on the open ocean floor. *Geophys. Res. Lett.* 9, 25–28.

Filloux, J. H. (1983). Pressure fluctuations on the open-ocean floor off the gulf of California: tides, earthquakes, tsunamis. *J. Phys. Oceanogr.* 13, 783–796.

GEBCO (2020). *The GEBCO_2020 Grid - A Continuous Terrain Model of the Global Oceans and Land*. Medium: Network Common Data Form Version Number: 1 type: dataset.

Graizer, V. (2010). Strong motion recordings and residual displacements: what are we actually recording in strong motion seismology? *Seismol. Res. Lett.* 81, 635–639. doi: 10.1785/gssrl.81.4.635

Hsiao, N.-C., Lin, T.-W., Hsu, S.-K., Kuo, K.-W., Shin, T.-C., and Leu, P.-L. (2014). Improvement of earthquake locations with the Marine Cable Hosted Observatory (MACHO) offshore NE Taiwan. *Mar. Geophys. Res.* 35, 327–336. doi: 10.1007/s11001-013-9207-3

Iannaccone, G., Pucciarelli, G., Guardato, S., Donnarumma, G. P., Macedonio, G., and Beranzoli, L. (2021). When the hydrophone works as an accelerometer. *Seismol. Res. Lett.* 92, 365–377. doi: 10.1785/0220200129

Javelaud, E. H., Ohmachi, T., and Inoue, S. (2011). A quantitative approach for estimating coseismic displacements in the near field from strong-motion accelerographs. *Bull. Seismol. Soc. Am.* 101, 1182–1198. doi: 10.1785/0120100146

Kanazawa, T. (2013). "Japan Trench earthquake and tsunami monitoring network of cable-linked 150 ocean bottom observatories and its impact to earth disaster science," in *2013 IEEE International Underwater Technology Symposium (UT)* (IEEE: Tokyo), 1–5.

Kaneda, Y., Kawaguchi, K., Araki, E., Matsumoto, H., Nakamura, T., Kamiya, S., et al. (2015). "Development and application of an advanced ocean floor network system for megathrust earthquakes and tsunamis," in *Seafloor Observatories* (Berlin; Heidelberg: Springer), 643–662.

Karpov, V. A., Sementsov, K. A., Nosov, M. A., Kolesov, S. V., Matsumoto, H., and Kaneda, Y. (2020). Method for examining the performance of seafloor observatory Sensors. *Moscow Univ. Phys. Bull.* 75, 371–377. doi: 10.3103/S0027134920040086

Kawaguchi, K., Kaneko, S., Nishida, T., and Komine, T. (2015). "Construction of the DONET real-time seafloor observatory for earthquakes and tsunami monitoring," in *Seafloor Observatories* (Berlin; Heidelberg: Springer), 211–228.

Kubota, T., Saito, T., Suzuki, W., and Hino, R. (2017). Estimation of seismic centroid moment tensor using ocean bottom pressure gauges as seismometers. *Geophys. Res. Lett.* 44, 10907–10915. doi: 10.1002/2017GL075386

Levin, B. W. and Nosov, M. A. (2016). *Physics of Tsunamis, 2nd Edn*. Cham: Springer International Publishing, 388.

Matsumoto, H., Nosov, M. A., Kaneda, Y., and Kolesov, S. V. (2015). "Ocean-bottom pressure and seismic signals at tsunamigenic earthquake," in *2015 IEEE Underwater Technology (UT)* (Chennai: IEEE), 1–5.

Matsumoto, H., Nosov, M. A., Kolesov, S. V., and Kaneda, Y. (2017). Analysis of pressure and acceleration signals from the 2011 tohoku earthquake observed by the donet seafloor network. *J. Disaster Res.* 12, 163–175. doi: 10.20965/jdr.2017.p0163

Mulia, I. E., and Satake, K. (2020). Developments of Tsunami observing systems in Japan. *Front. Earth Sci.* 8:145. doi: 10.3389/feart.2020.00145

Nakamura, T., and Hayashimoto, N. (2019). Rotation motions of cabled ocean-bottom seismic stations during the 2011 Tohoku earthquake and their effects on magnitude estimation for early warnings. *Geophys. J. Int.* 216, 1413–1427. doi: 10.1093/gji/ggy502

NIED (2019). *NIED DONET*. National Research Institute for Earth Science and Disaster Resilience.

Nosov, M., Karpov, V., Kolesov, S., Sementsov, K., Matsumoto, H., and Kaneda, Y. (2018). Relationship between pressure variations at the ocean bottom and the acceleration of its motion during a submarine earthquake. *Earth Planets Space* 70:100. doi: 10.1186/s40623-018-0874-9

Rabinovich, A. B., and Eblé, M. C. (2015). Deep-ocean measurements of Tsunami waves. *Pure Appl. Geophys.* 172, 3281–3312. doi: 10.1007/s00024-015-1058-1

Ranasinghe, N., Rowe, C., Syracuse, E., Larmat, C., and Begnaud, M. (2018). Enhanced global seismic resolution using transoceanic SMART cables. *Seismol. Res. Lett.* 89, 77–85. doi: 10.1785/0220170068

Shin, K., and Hammond, J. K. (2008). *Fundamentals of Signal Processing for Sound and Vibration Engineers*. Chichester; Hoboken, NJ: John Wiley & Sons.

Tilmann, F., Howe, B., and Butler, R. (2017). Commercial Underwater Cable Systems Could Reduce Disaster Impact. *Eos*. 98. doi: 10.1029/2017EO069575

Tolstoy, I., and Clay, C. S. (1987). *Ocean Acoustics: Theory and Experiment in Underwater Sound*. New York, NY: Published for the Acoustical Society of America by the American Institute of Physics.

Webb, S. C. (1998). Broadband seismology and noise under the ocean. *Rev. Geophys.* 36, 105–142.

**Conflict of Interest:** The authors declare that the research was conducted in the absence of any commercial or financial relationships that could be construed as a potential conflict of interest.

frontiers in Earth Science

ORIGINAL RESEARCH
published: 27 May 2021
doi: 10.3389/feart.2021.626416

# Seismic Anisotropy Within an Active Fluid Flow Structure: Scanner Pockmark, North Sea

*G. Bayrakci[1,2]*, B. Callow[2], J. M. Bull[2], T. A. Minshull[2], G. Provenzano[2,3], L. J. North[1], C. Macdonald[4], A. H. Robinson[2], T. Henstock[2] and M. Chapman[4]*

*[1]Ocean Bio-Geoscience, Department of Science and Technology, National Oceanography Centre, Southampton, United Kingdom, [2]School of Ocean and Earth Science, University of Southampton, National Oceanography Centre Southampton, Southampton, United Kingdom, [3]University of Grenoble Alpes, ISTerre, F-38058 Grenoble, France, [4]School of Geosciences, Grant Institute, University of Edinburgh, Edinburgh, United Kingdom*

OPEN ACCESS

**Edited by:**
*Francisco Javier Nuñez-Cornu, University of Guadalajara, Mexico*

**Reviewed by:**
*Maureen Long, Yale University, United States*
*David Iacopini, University of Naples Federico II, Italy*

***Correspondence:**
*G. Bayrakci*
*G.Bayrakci@noc.ac.uk*

**Specialty section:**
*This article was submitted to Solid Earth Geophysics, a section of the journal Frontiers in Earth Science*

**Received:** *05 November 2020*
**Accepted:** *04 May 2021*
**Published:** *27 May 2021*

**Citation:**
*Bayrakci G, Callow B, Bull J M, Minshull TA, Provenzano G, North LJ, Macdonald C, Robinson AH, Henstock T and Chapman M (2021) Seismic Anisotropy Within an Active Fluid Flow Structure: Scanner Pockmark, North Sea. Front. Earth Sci. 9:626416. doi: 10.3389/feart.2021.626416*

Understanding sub-seabed fluid flow mechanisms is important for determining their significance for ocean chemistry and to define fluid pathways above sub-seafloor $CO_2$ storage reservoirs. Many active seabed fluid flow structures are associated with seismic chimneys or pipes, but the processes linking structures at depth with the seabed are poorly understood. We use seismic anisotropy techniques applied to ocean bottom seismometer (OBS) data, together with seismic reflection profiles and core data, to determine the nature of fluid pathways in the top tens of meters of marine sediments beneath the Scanner pockmark in the North Sea. The Scanner pockmark is 22 m deep, 900 m × 450 m wide and is actively venting methane. It lies above a chimney imaged on seismic reflection data down to ~1 km depth. We investigate azimuthal anisotropy within the Scanner pockmark and at a nearby reference site in relatively undisturbed sediments, using the PS converted (C-) waves from a GI gun source, recorded by the OBS network. Shear-wave splitting is observed on an OBS located within the pockmark, and on another OBS nearby, whereas no such splitting is observed on 23 other instruments, positioned both around the pockmark, and at an undisturbed reference site. The OBSs that show anisotropy have radial and transverse components imaging a shallow phase (55–65 ms TWT after the seabed) consistent with PS conversion at 4–5 m depth. Azimuth stacks of the transverse component show amplitude nulls at 70° and 160°N, marking the symmetry axes of anisotropy and indicating potential fracture orientations. Hydraulic connection with underlying, over pressured gas charged sediment has caused gas conduits to open, either perpendicular to the regional minimum horizontal stress at 150–160 N or aligned with a local stress gradient at 50–60 N. This study reports the first observation of very shallow anisotropy associated with active methane venting.

**Keywords: azimuthal anisotropy, S-wave splitting, ocean bottom seismometer, wide-angle seismic, scanner pockmark**

# INTRODUCTION

## Overview

Subsurface heterogeneities play a major role in controlling fluid flow phenomena and behavior in sedimentary basins. Fluid conduits, such as connected fracture networks, may create focused flow in sedimentary systems by enhancing porosity and permeability, or, conversely, may cause reservoir compartmentalization. Therefore, an assessment of fracture azimuth, aperture, spatial density and connectivity can improve understanding of subsurface fluid flow. Larger fractures can ordinarily be detected and quantified using traditional seismic reflection imaging techniques, which may include attribute analysis (e.g., Bahorich and Farmer, 1995). In order to constrain and resolve fractures at sub-seismic scale, seismic anisotropy analysis can be employed, which uses directional variations of seismic velocities and amplitudes.

The most common form of anisotropy within sediments is vertical transverse isotropy (VTI), where the symmetry plane is parallel to the sedimentary layering. The presence of aligned micro-cracks and vertical fractures is known to produce horizontal transverse isotropy (HTI), where the symmetry plane is perpendicular to the sedimentary layering (Wild, 2011). More broadly, HTI can be produced by any aligned vertical features, which may include geological structures originating from glaciological processes, such as tunnel valleys, striations, and iceberg scour marks, known as ice ploughmarks.

Shear-wave splitting (SWS) is a recognized method which can be used to constrain the orientation and spatial density of aligned vertical structures within a HTI medium (e.g.,Crampin, 1985). SWS analysis within shallow sediments normally uses P-to-S converted waves (C-waves), created using an active seismic source near the sea surface. When a shear wave (S-wave) enters a HTI medium (e.g., vertically fractured sediment), S-waves split into two components (**Figure 1**). The split S-waves propagate through the anisotropic medium, and are subsequently polarized along (fast, S1) and across (slow, S2) the vertical features, resulting in a difference between the detected arrival times and signal amplitudes (Lynn and Thomsen, 1990; Thomsen, 1999; Tsvankin et al., 2010). The time delay between S1 and S2 observed on the radial component (**Figure 1B**), and the amplitude nulls observed on the transverse component (**Figure 1C**), can be used respectively to constrain the percentage of anisotropy and therefore the spatial density, and the orientation of aligned vertical fractures exhibiting HTI anisotropy (e.g., Crampin, 1985; Bale et al., 2009). SWS analysis of active source data recorded on ocean bottom seismometers (OBSs) has been successfully applied for marine slope stability assessment on the west Svalbard continental slope (Haacke and Westbrook, 2006) and for the identification of vertical fluid migration pathways within hydrate-bearing sediments in the Storrega slide offshore Norway (Exley et al., 2010). Here we apply this method for the first time at a site of active natural venting of methane, the Scanner Pockmark Complex (SPC) with the objective of identifying fracture alignment and intensity, a proxy for the permeability, to characterize vertical fluid migration pathways within the shallow sediment.

Pockmarks occur when fluid flow is focused and escapes from shallow, low-permeability, fine-grained surficial sediments (Hovland et al., 2002). The Scanner pockmark is a seafloor depression located in the northern North Sea (UK License Block 15/25), within the Witch Ground Basin. Large pockmarks, including Scanner, are continuously active in this area, with vigorous venting of methane (Böttner et al., 2019). At the Scanner pockmark complex, the seafloor and shallow sediments are also heavily disturbed by smaller pockmarks and palaeo-pockmarks (>1500 across 225 $km^2$), with a principal NNE/SSW orientation, that are interpreted as dewatering features due to localized pressure changes (Gafeira and Long, 2015; Böttner et al., 2019).

On seismic reflection profiles, the large active pockmarks are commonly associated with bright spots at shallow depth, interpreted as gas-charged sediments, and are underlain by seismic chimneys or pipes, referred herein as chimneys. At the Scanner pockmark complex, the chimneys are imaged as sub-vertical columns of acoustic blanking reaching depths of several hundred meters. Chimneys have been interpreted as focused fluid migration pathways, hydraulically connecting deeper stratigraphic layers to the shallow sediment overburden (Berndt, 2005; Karstens and Berndt, 2015). Chimney-like features may also be generated as seismic artifacts due to scattering by near-surface features (e.g. Dean et al., 2015). Improved understanding of these shallow fluid flow systems is critical for assessing the integrity of future sub-seafloor Carbon Capture and Storage (CCS) sites.

## Aims and Objectives

Here, we analyze data from a unique active-source seismic anisotropy experiment conducted using OBSs at the Scanner Pockmark Complex, an active methane venting seafloor depression. We investigate the presence of azimuthal anisotropy from beneath the Scanner pockmark, using SWS, and compare with results from a nearby reference site where there is no evidence for presence of gas such as seafloor gas emission, chimney structures or gas-bearing sediment. We conduct a multi-frequency seismic reflection analysis of the shallow sub-surface to constrain the geometry and azimuth of the observed geological features at the depth range resolved by the SWS analysis. We compare the seismic images with the results of SWS analysis to provide a complete characterization of the shallow subsurface structure directly beneath the Scanner pockmark. The SWS analysis is complemented by laboratory measurements of S-wave velocities which, in conjunction with seismic stratigraphy, enable the depth of the anisotropic layers in conjunction with seismic stratigraphy to be determined. The key aim of this study is to develop a further understanding of the structural control on fluid-escape at the Scanner Pockmark Complex by resolving the orientation and network geometry of the subsurface heterogeneities. In this paper we focus on observations of SWS from very shallow interfaces (< 10 m); future studies will investigate SWS over a greater depth range.

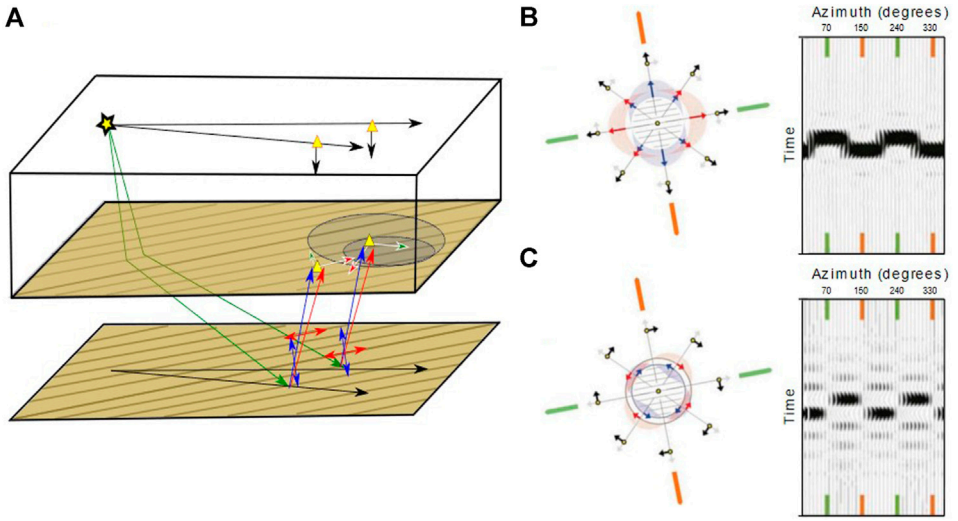


**FIGURE 1 |** Diagram illustrating shear wave splitting (modified after Bale et al., 2009) at two ocean bottom seismometers located in, or close to a pockmark, sitting within seabed sediments containing vertical parallel fractures (HTI). **(A)** The pockmarks are shown as concentric circles on the seabed. Direction of shading indicates orientation of the vertical fractures. The lower surface (reflector) is the base of the anisotropic layer, across which S-wave conversion occurs. Yellow star shows location of an airgun shot near the sea surface. Yellow triangles are ocean bottom seismometers: black outline = on seafloor, red outline = projected to sea surface, to indicate the sagittal (shot – receiver) azimuth. Radial and transverse directions are indicated by black arrows. The white arrows represent the horizontal geophone orientations: green = X; red = Y component. The green arrow is the down-going P-wave phase. Fast (S1) and slow (S2) S-waves are represented with red and blue arrows respectively and their particle motions are indicated by double-ended red and blue arrows. **(B)** Aligned vertical fractures with 70°N azimuth viewed from the top indicating the amplitudes of fast (red arrows) and slow (blue arrows) S-waves in radial direction (black arrows) and corresponding radial seismogram. Green and orange arrows lines indicate the fracture parallel and fracture perpendicular directions. **(C)** same as b, transverse component. The presence of HTI is easily identifiable from the azimuthal variation seen on the radial and transverse components.

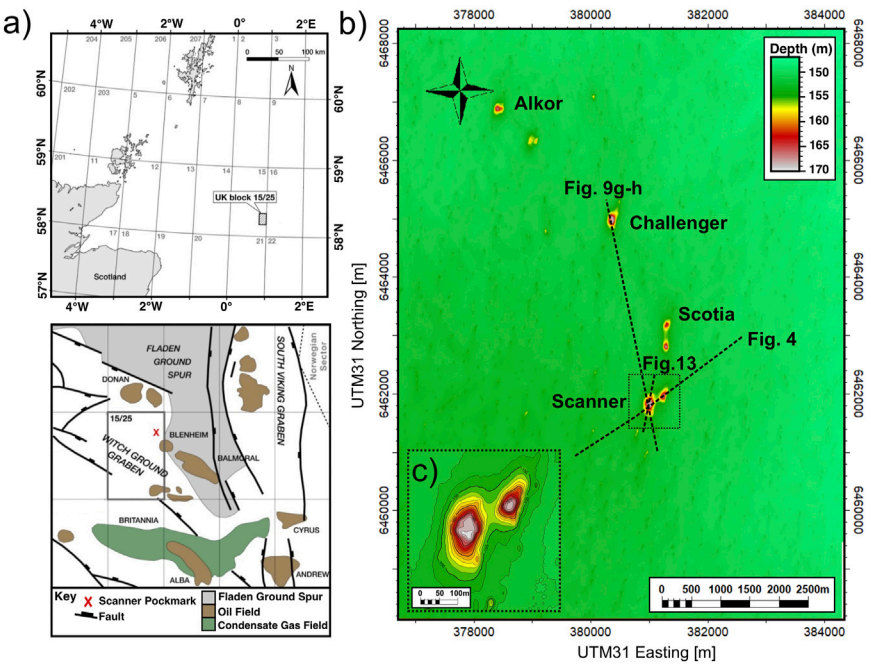


**FIGURE 2 | (A)** Position of the Scanner Pockmark within the UK Sector of the North Sea. **(B)** Bathymetric map of the Scanner Pockmark Complex. Dashed lines highlight seismic lines used in **Figures 4**, **9G,H**. Dotted square box shows inset **(C)**. **(C)** Scanner pockmark, displaying East and West Scanner.

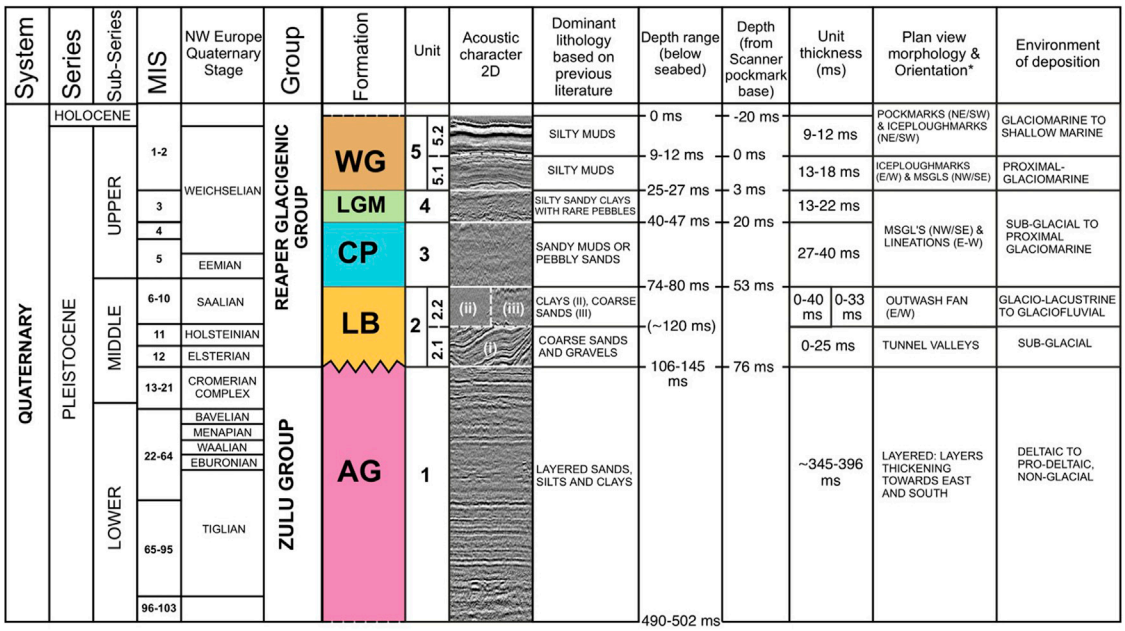


**FIGURE 3 |** Stratigraphy of the Scanner Pockmark Complex. The chronostratigraphy, seismostratigraphy and lithostratigraphy of the Scanner Pockmark Complex is described. AG - Aberdeen Ground (purple), LB - Ling Bank (orange), CP - Coal Pit (blue), LGM - Last Glacial Maximum Deposits (green) and WG - Witch Ground (brown). The table has been created from a synthesis of Böttner et al. (2019), Ottesen et al. (2014), Stewart and Lonergan (2011), Stoker et al. (2011), Judd et al. (1994) and Andrews et al. (1990).

## STRATIGRAPHY AND SEISMOSTRATIGRAPHIC FRAMEWORK

The Scanner pockmark is a composite feature comprising two overlapping seabed pockmarks (East and West Scanner), with a combined size of ~900 m × 450 m wide and depth of 22 m, lying in ~155 m water depth. Direct evidence for methane venting is provided by the water column imaging of Li et al. (2020), who calculate a gas flux of 1.6 and 2.7 × $10^6$ kg/year (272–456 l/min), as well as the presence of methane-derived authigenic carbonate (MDAC) recovered from within the pockmarks, which formed due to anaerobic oxidation of escaping methane (Judd and Hovland, 2009).

The seismostratigraphy and lithostratigraphy hosting the Scanner pockmark complex comprises a ~600 m-thick Quaternary sediment succession that has been described previously (Stoker et al., 2011; Böttner et al., 2019; Robinson et al., 2020), where it is sub-divided into five units, S1 to S5 (**Figures 2**, **3**). Deposited within the Witch Ground basin, this stratigraphic complex is underlain by the Hordland and Nordland Groups, of Palaeogene and Neogene age respectively, which are composed of low-permeability claystone (Judd et al., 1994). The Scanner pockmark depression erodes down to the base of the shallowest unit, S5 (the Witch Ground Formation).

The Witch Ground Basin was the locus of rapid fine-grained sediment deposition between Marine Isotope Stages (MIS) 1–2, around 15–13 ka, after the end of the last glacial period (Stoker et al., 2011). Following the stabilization of sea level after the last glaciation, sedimentation into the Witch Ground Basin has become negligible, and hence the pockmarks at the current seabed demonstrate the effects of active fluid escape over at least the last 8 ka (Böttner et al., 2019).

## EXPERIMENT AND DATASETS

In September 2017, we carried out the CHIMNEY seismic experiment around the Scanner Pockmark in the North Sea using RRS James Cook (cruise JC152) (Bull, 2018; Bull et al., 2018; Robinson et al., 2020), acquiring wide-angle and multi-channel seismic and high-frequency acoustic recordings.

### Ocean Bottom Seismometer Data

A total of 25 four-component OBSs were deployed during the survey. These instruments were equipped with three orthogonal 4.5 Hz geophones fixed rigidly to the instrument frame, and a hydrophone. The OBS sampling rate was 4 kHz. Eighteen OBSs were deployed around the Scanner pockmark, with two instruments located within the pockmark (**Figure 4**). The OBS spacing was generally 200 m, with closer spacing within the pockmark. Seven OBSs were also deployed with 200 m spacing at a reference site, that displayed no evidence for water column venting, or subsurface fluid migration.

All 25 OBSs recorded shot profiles acquired using five different seismic sources: Bolt and GI airguns, Squid and Duraspark surface sparkers and a deep-towed sparker. For the SWS study we used the shots acquired with the GI-gun source (2 × 210 $in^3$),

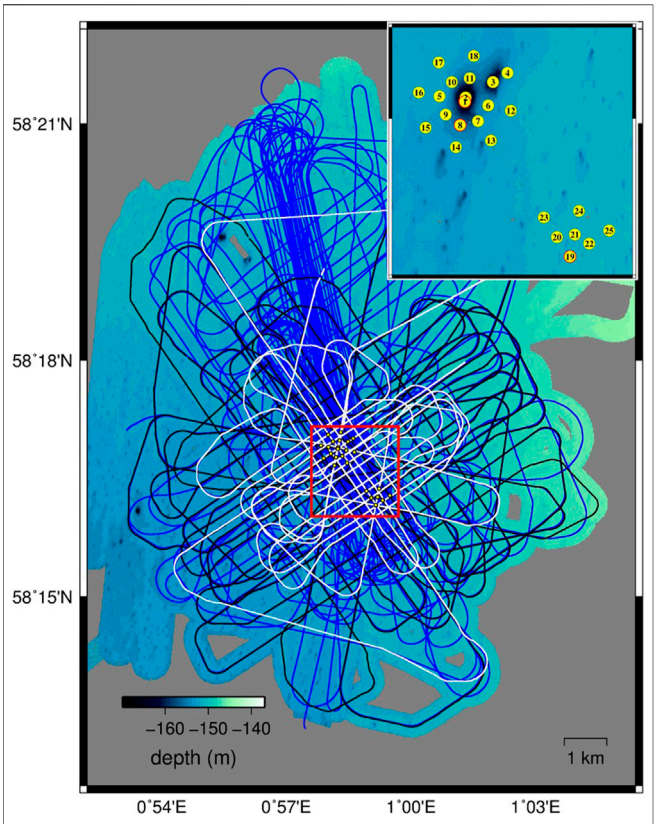


**FIGURE 4 |** Map of the CHIMNEY seismic experiment. Black, white and blue profiles represent GI-gun, Squid 2000 sparker and sub-bottom profiler shots respectively. The 3D seismic volume extends over the entire area displayed. Yellow dots are the OBSs. Red square shows the location of the inset. Inset shows the location of the OBSs around the Scanner pockmark and at the reference site. OBSs 1, 8 and 19 shown in **Figures 6–8** are surrounded in red.

which generated frequencies of 3–300 Hz. The geometry of the GI-gun profiles (**Figure 4**) was chosen to be an asterisk to ensure even azimuthal coverage at all offsets and simplify the processing. Four profiles were centered on the Scanner pockmark at an azimuth interval of 45° and with lengths greater than 10 km (**Figure 4**). A grid of profiles of 326° and 146° azimuth was also acquired to obtain full azimuthal coverage for the SWS study and a well-sampled shot coverage for seismic tomography. The shooting interval was 8 s, equivalent to 18.5 m at the mean vessel speed of 4.5 kn.

The shot positions were calculated initially by backprojecting the ship's GPS position to the airgun position, 84.1 m behind the ship. OBSs were deployed by free fall. Although the shallow water environment (~150 m) reduced the difference between drop and seabed positions, the small scale of our target requires that the positions of instruments and shots are defined precisely. Therefore, we used a grid search algorithm to find the optimal average water velocity (1490 m/s), receiver locations and delay time (which accounts for airgun depth variations and for feathering), by minimizing the sum of the squared residuals between observed and predicted direct arrival times at every point of the grid. Receiver depths were not included in the inversion as the seafloor dips are small and depth differences between deployment locations and relocated positions were already within the 0.5 m uncertainty expected from the fitting algorithm.

The SEG convention for four-component seismic records (Brown et al., 2000) is used for display of the geophone and hydrophone polarities. Accordingly, the direct wave has positive polarity on the vertical geophone and negative polarity on the

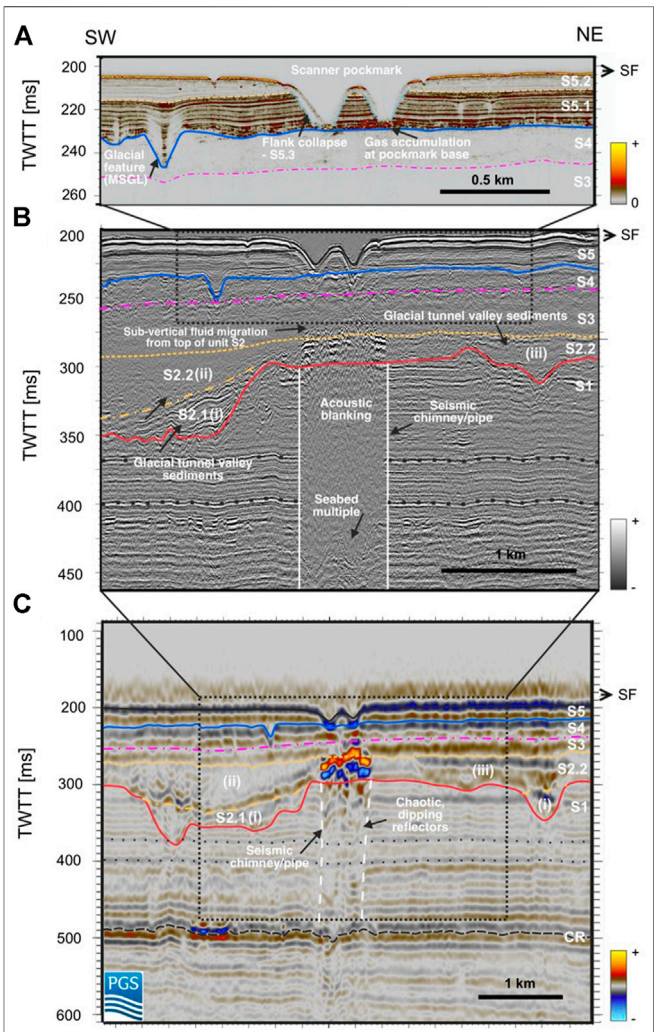


**FIGURE 5 |** Seismostratigraphy of the Scanner Pockmark region. The seismic profiles extend from southwest to northeast across the Scanner Pockmark Complex. **(A)** Sub-bottom profiler seismic reflection data. **(B)** 2D seismic reflection data acquired using Sparker source. **(C)** 3D seismic reflection data. Interpreted seismic units CR and S1 to S5 are shown. CR - Crenulate Reflector (top of Nordland Group), S1 – Aberdeen Ground Fm., S2 – Ling Bank Fm., S3-4 – Coal Pit Fm [S3 – Coal Pit and S4 – Last Glacial Maximum deposits (LGM)], S5 – Witch Ground Fm (S5.1 – Fladen Member, S5.2 – Witch Member, S5.3 - Glen Member). Black dashed line = CR; red line = top S1; orange dot-dashed line = top S2.1; orange dashed line = top S2.2; pink dot-dashed line = top S3; blue line = top S4; pale brown dashed line = top S5.1 and black line = top S5.2/SF = Seafloor. Outline of a chimney is displayed with sub-vertical white dashed line. TWT values here are milliseconds below the sea surface.

hydrophone. The up-going P-waves reflected from positive impedance contrasts are recorded with negative polarities on the vertical geophones. This is also the case on the hydrophones, which measure the pressure rather than a vector quantity. The x-geophone is considered to be positive when the distance vector from the shot to receiver is positive in Cartesian coordinates and the y-geophone is positive 90° clockwise from the positive $x$ direction (Brown et al., 2000).

## Seismic Reflection Data

Four different seismic sources (GI guns, Applied Acoustic Engineering Squid 2000 and Duraspark surface sparkers and a deep-towed sparker) were recorded by two different streamers (60-channel, University of Southampton, 120-channel, GeoEEL, TTS), operated at times separately and at times simultaneously (Robinson et al., 2021). In addition, a chirp source was used to acquire single-channel seismic data in sub-bottom profiler (SBP) mode. The experiment produced a broad-band seismic dataset, with frequencies from 3 to 6000 Hz.

In this study we use the SBP and Squid 2000 sparker data to generate 2D seismic reflection images around the Scanner pockmark. The SBP data were acquired using a chirp sweep lasting 0.035 s, with a bandwidth of 2.8–6 kHz, and a central frequency of 4.4 kHz. Over 100 SBP profiles were recorded (**Figure 4**). These profiles have a trace spacing of 2.5 m and a very high vertical resolution of <15 cm. The Squid 2000 surface sparker data were acquired at an energy of 2000 J giving a 80–1800 Hz source bandwidth and 2 s shot interval (~4.6 m at 4.5 kn), recorded by the two streamers (**Figure 4**). Thirteen Squid profiles were acquired across the Scanner pockmark and processed using a time-domain workflow outlined in Provenzano et al., (2020). These profiles have a cdp-trace spacing of 2 m and a vertical tuning thickness resolution <0.45 m.

3D time-migrated seismic data were also provided by PGS (CNS MegaSurveyPlus) for the purposes of this study (**Figure 5C**). The 3D seismic survey used in this study covers an area >500 km$^2$ and a depth of 1.5 s two-way travel time (TWT). The full-stack data has a trace spacing of 12.5 m and a vertical resolution of approximately 5–10 m.

# METHODS

## Ocean Bottom Seismometer Data

P- to S- converted (C-) waves were studied using GI-gun shots on all 25 OBSs of the CHIMNEY survey network. We rotated the horizontal seismograms into radial and transverse directions, by trace by trace minimizing the power ratio of the amplitude of radial and transverse components (Haacke and Westbrook, 2006). We first flattened the direct water wave by applying a static time shift as a function of the shot-receiver offset (i.e. linear move out). Only shots up to 300 m offsets were used because at greater offsets it was difficult to distinguish the direct wave from other arrivals. The power ratios of the amplitudes were calculated on a window of 3 ms half-length centered on the direct wave arrival flattened to 0 s. The trace-by-trace minimization was done by stepwise incrementing the optimum orientation angle for x

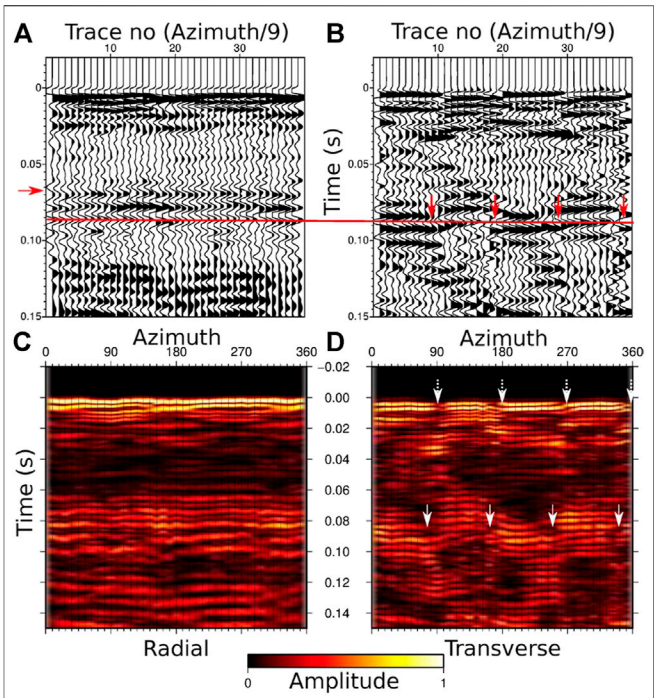


**FIGURE 6 |** 9° azimuth stacks recorded on OBS1 located within the pockmark. Left and right panels show radial and transverse components respectively. **(A)** Radial wiggle plot. The red arrow shows the arrival time (~65 ms TWT) of the C-wave phase on the radial seismogram. Red line shows the time at which the event is observed with highest amplitude due to ringing (see text). **(B)** Transverse wiggle plot. Red arrows show the polarity changes at 90° interval. **(C)** Radial envelope plot of the amplitudes (root of squared amplitudes). **(D)** Transverse envelope plot. White arrows show the amplitude nulls at ~90° intervals, corresponding to the orientation of the anisotropy axes (70 and 150°). Dashed white arrows at t = 0 indicate the geophone orientations.

geophone using the Seismic Unix (Stockwell, 1997) compatible surttmp software of Haacke and Westbrook (2006). We searched for the optimum rotation angle between 0° and 180° to cover the whole range of possible azimuths. Instead of using a single rotation angle for all shots, with the trace-by-trace estimation of the optimum rotation angle we obtained a rotation angle for each shot. This approach accounts for possible residual uncertainties in shot and OBS locations (< 0.5 m) and the potential effects of OBS tilt.

The resulting radial and transverse components were visualized in a composite plot (**Supplementary Figure S1**) to check the efficiency of the rotation. A difference of two orders of magnitude is observed in the amplitude of the direct water wave observed on the radial and transverse components of all studied OBSs indicating a successful rotation. The P-wave energy is visible on the radial component but diminished on the transverse component. Radial and transverse components of the OBSs were then stacked in 9° bins of sagittal (shot-receiver) azimuth. No filtering was applied during processing because filters modify the arrival times of short offsets used in this study and C-waves are easily identified without filtering (**Figures 4**, **6**).

## Seismic Reflection Data

The reflection data were interpreted using Schlumberger's Petrel software. Over 5400 breaks in the lateral continuity of seismic reflectors were observed on a total of 104 SBP lines (**Supplementary Figure S2**). Such discontinuities can be created by faults, fractures, and other geological features, such as ice ploughmarks. The dense spacing of the 2D data (**Figure 5**) allowed the discontinuities, which crosscut the seismic profile directions, to be mapped with confidence from profile to profile. The length and net azimuth of the discontinuities (within the range of 0° - north to 180° - south) were then derived. Due to the uneven spatial distribution of the 2D profiles (**Figure 4**), the approach taken was to produce RMS amplitude maps over a time window of ±2.5 ms TWT around the picked horizon (top S4). This approach also had the advantage that no errors would be introduced in any depth conversion due to uncertainties in sub-surface velocities.

Macro-scale geological features and discontinuities (> 12.5 m) were also observed on time surfaces of the 3D seismic data. Where horizons were laterally continuous within the 3D data across the full study area (e.g. top of the unit S4), a surface map was produced. Where deeper horizons were laterally discontinuous, a time slice map approach was used in a similar manner to the near-surface SBP data.

## Laboratory S-Wave Measurements

Knowledge of the S-wave velocities within the shallow sediments (<10 m depth) was needed to estimate the conversion depth of C-waves and thus the depth of the anisotropic layer. S wave velocities were determined from analysis of sediments cores collected during. RV Maria S Merian cruise MSM78 (Karstens et al., 2018). Sediment cores were collected from beneath the Scanner pockmark and a site 6 km northeast of the Scanner pockmark complex using a gravity corer and rock drill (RD2; British Geological Survey). A maximum penetration depth of ~6 and ~33 mbsf (meters below seafloor) was reached beneath the Scanner pockmark and the NE site, respectively. S-wave velocity measurements were taken in the Rock Physics laboratory of the National Oceanography center. S-wave velocity measurements were carried out on samples from four cores. The measurements were of the transmission type between two bimorph transducers inserted in to split core with their motion transverse to core major axis. Separation between transducers centers was ~80 mm. The excitation signal consisted of a two cycle cosine wave with a center frequency of 1 kHz multiplied by a Blackman-Harris window to limit high frequency content, thus reducing and supressing the production of P-wave precursors higher in the frequency spectrum (**Supplementary Figure S4**). Both, the input and transmitted signal were recorded using an oscilloscope. Processing was performed in two separate ways to reduce measurement uncertainty and cross-validate results (**Supplementary Figure S4**). The first method was a time-of-flight approach performed in the time domain. The first major peak of the input and transmitted signals were picked. The time difference between the two picks and the distance between transducers was used calculate shear wave sound speed. The first major peak, rather than first break, was chosen because this was less affected by any residual P-wave precursor signals. The second processing method was performed in the frequency domain and is based upon the rate of change of phase with respect to frequency. The input and transmitted time domain signals were windowed using a Tuckey window to remove the P-wave precursor, multiple reflections and multi-path signals after the direct wave. The windowed signals were de-convolved in the frequency domain and a least squares linear fit to the slope of the phase with respect to frequency was calculated. The gradient of the linear fit, which is proportional to the reciprocal of sound speed, was then used to calculate sound velocity. Sources of error for these measurements include multiple reflections, propagation modes other than pure shear wave modes and *p* wave precursors. System time delays, the acoustic center of the transducers and measurement accuracy were estimated by making multiple measurements over distances of 0.05–0.2 m acoustic path length on a 0.5 by 0.3 by 0.3 m slab of homogeneous Potter's clay. These reference measurements were then compared to measurements of the same Potter's clay in split core liner over a 0.1 m acoustic path similar to that used in the experiment. From comparison to these calibration data a typically 2σ measurement accuracy of 10% is expected.

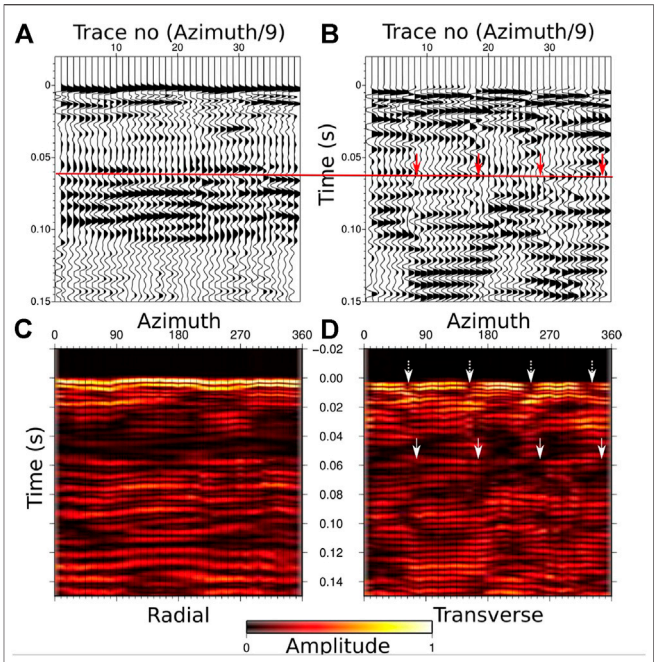


**FIGURE 7 |** 9° azimuth stacks recorded on OBS8 located on the southwestern rim of the Scanner Pockmark. Left and right panels show radial and transverse components respectively. **(A)** Radial wiggle plot. The red line shows the arrival time (~55 ms TWT) of the C-wave phase on the radial seismogram. **(B)** Transverse wiggle plot. Red arrows show the polarity reversals. **(C)** Radial envelope plot of the amplitudes (root of squared amplitudes). **(D)** Transverse envelope plot. White arrows show the amplitude nulls of ~90° degree interval, corresponding to the orientation of the anisotropy axes (70 and 150°). Dashed white arrows at t = 0 indicate the geophone orientations.

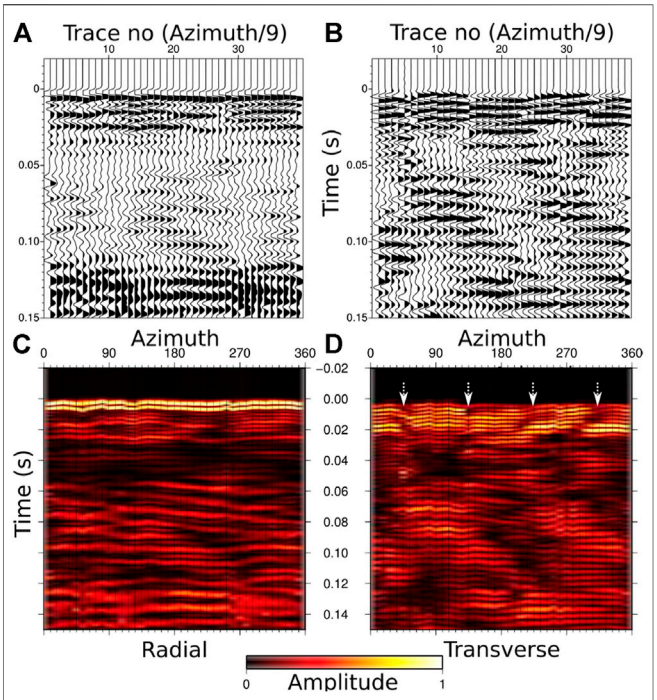


**FIGURE 8 |** 9° azimuth stacks recorded on OBS19 located in the reference site. Left and right panels show radial and transverse components respectively. **(A)** Radial wiggle plot. **(B)** Transverse wiggle plot. No C-wave event is observed on the records of this OBS. **(C)** Radial envelope plot of the amplitudes (root of squared amplitudes). **(D)**Transverse envelope plot. Dashed white arrows (at t = 0) show the geophone orientations.

# RESULTS

## Seismic Anisotropy

In this paper, two-way travel-time (TWT) values are given as milliseconds below the seafloor, unless stated otherwise. Two potential C-wave reflectors are observed at 45 and 65 ms TWT on the radial component of OBS1, located within the Scanner pockmark (**Figure 6**). Both reflections have apparent velocities of ~1500 m/s, as expected for signals that have most of their raypath in the water column.

On all OBSs, the direct water wave arrival is affected by instrument ringing, most likely due to seabed coupling issues, which lasts for 25 ms. The ringing is observed on all components in different ways (**Figures 6–8**). A potential C-wave arrival (45 ms TWT) is visible on the radial component of OBS one as a phase clearly separated from the instrument ringing, but with a lower amplitude than the later arrival (65 ms). However, this phase is not observed on other OBSs (**Figures 7**, **8**) as a clear arrival and is also not present on the transverse component of OBS1, suggesting that it represents either a P-wave reflection or a C-wave propagating within an isotropic medium. We interpret this early phase as a P-wave reflection from the base of seismic unit S3 (bottom of the Coal Pit Formation), since seismic units S5.1–5.2 are not present within the Scanner Pockmark, and the base of seismic unit S4 would be too shallow (20 ms TWT) to produce an arrival at this time.

The second reflection is observed at 65 ms TWT on the stacked radial component of OBS1, and it spans on a time interval between 65 and 90 ms. The extended duration of this arrival may be due either to some instrument ringing (most likely), or the dynamic response of a localized shallow heterogeneity (Rubin et al., 2014). Polarity changes (**Figure 6B**) and energy nulls at ~90° azimuthal intervals (**Figures 6B–D**) are observed on the transverse component, as expected for C-waves travelling within an anisotropic HTI medium. The energy nulls observed on the transverse component lie at 70° and 160° azimuths suggesting that the anisotropy symmetry axes follow these orientations. The polarity changes and the amplitude nulls are best observed at 80 ms TWT instead of 65 ms TWT, possibly because the amplitude of this event is too low to be observed at the onset of the phase, but then is amplified later due to constructive interference from the ringing. If this observed event was a residual direct water wave due to the unsuccessful rotation to radial and transverse components, the observed energy nulls would follow the geophone orientations. However, the X-geophone component of OBS1 is oriented to the north (0°), with the energy nulls at 90° intervals (**Figure 6D**; at 90°, 180°, 270° and 360°). There is a difference of ~20° between the energy nulls observed on the direct wave and those observed for the C-wave event (70°–160°), and therefore we are confident of our C-wave identification. The early arrival time of the phase indicates that the S-wave conversion occurs at a very shallow reflector and the short travel time of the phase prevents the development of an observable delay between the fast and slow S-waves propagating parallel and perpendicular to the orientation of vertical fractures respectively.

A C-wave phase at 55 ms TWT (**Figure 7**) is observed on the radial component of OBS8. Ringing affects both the direct wave and the C-wave phase. Simultaneously, on the transverse component of OBS8, clear polarity changes are again observed, with the same azimuths as observed on OBS1 (70°–160°). Once again, there is a clear mismatch between the geophone orientations and the orientations of the anisotropy axes of the C-wave event which rules out the instrument ringing effect being misinterpreted as S-wave splitting within shallow sediments.

No potential early C-wave phase is observed on the records of the OBSs deployed at the reference site. For example, **Figure 7** shows the records of OBS19. The only potential C-wave event is observed at ~120 ms TWT with an incoherent, undulating nature on the radial component, and no polarity changes are observed on the transverse component. However, since here we focus on the SWS within the shallowest sediments, we cannot rule out the presence of deeper S-wave anisotropy around the Scanner pockmark and at our background site.

## Seismic Reflection

SBP, sparker seismic reflection, and conventional 3D seismic reflection data (**Figure 5**) image zones with high amplitudes, characteristic of free gas within the near-surface: at 1–2 m (3 ms TWT) depth beneath the base of the Scanner pockmark complex

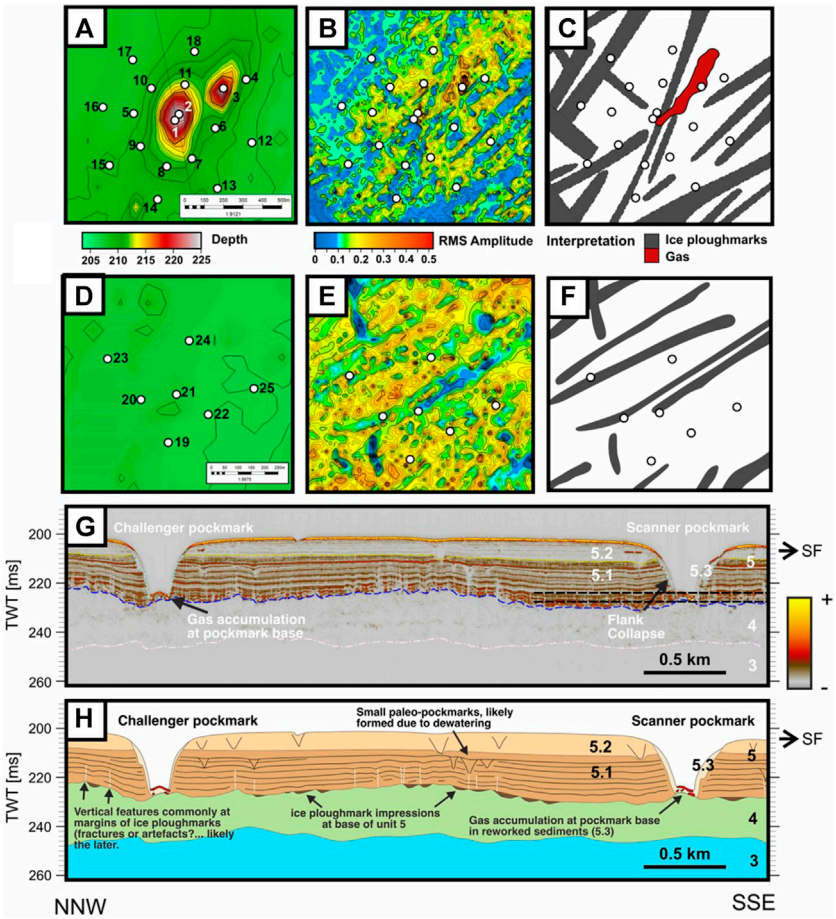


**FIGURE 9 |** Attribute analysis and interpretation of the Scanner pockmark and reference site. Sub-bottom profiler 2D seismic reflection data is used to generate time slice attribute maps of seismic unit top S4 of **(A–C)** the Scanner Pockmark and **(D–F)** the reference site. **(A, D)** Bathymetry maps of seabed with OBS locations and numbers displayed. **(B, E)** RMS amplitude maps acquired over a time window of ±2.5 ms around the picked horizon (225–227.5 ms TWT from the sea surface); the blue areas highlight the spatial extent and orientation of ice ploughmarks. **(C, F)** Geological interpretation of the surface amplitude maps, highlighting gas-charged sediment (red – high amplitude) and ice ploughmarks (blue – low amplitude). **(G–H)** Seismic profile extending from north to south highlighting the key geological features of interest.

(**Figure 5A**), and at 48 m (55 ms TWT) depth within the Upper Ling Bank Formation (unit S2.2; **Figure 5C**). Seismic chimneys are characterized on seismic images by a combination of seismic blanking and discontinuous or chaotic reflections (e.g., Løseth et al., 2011). Where free gas is present, high amplitudes are also observed at discrete intervals. The observed seismic characteristics support the interpretation that a chimney structure is present beneath Scanner pockmark (**Figures 5B,C**). The seismostratigraphy and observations of gas in the seismic reflection data are described in more detail by Böttner et al. (2019), Robinson et al. (2020).

Two potential causes of shallow HTI anisotropy are observed below the Scanner Pockmark (**Figure 9**). RMS amplitude maps derived from SBP profiles display seismic unit top S4, the uppermost sedimentary structure below the Scanner pockmark (**Figures 9B,E**). The presence of gas will result in a higher RMS amplitude. A prominent peak in RMS amplitude is observed at the Scanner Pockmark site, oriented at approximately 40°, and is located beneath OBS 3 (**Figure 9C**). The amplitude peak below OBS 3 extends towards the south west, with a small change in orientation to 50–60° azimuth below OBS1 (**Figure 9C**). No prominent amplitude peaks are observed at the reference site (**Figures 9E,F**). From a cross-sectional view, the amplitude peaks beneath the Scanner pockmark can be interpreted as due to gas-charged sediment (**Figures 9G,H**). The presence of gas also indicates a higher connected porosity which can be the origin of the observed S-wave splitting. In addition, the RMS amplitude maps also display areas of lower amplitude that are oriented at 50–60°, and are observed underlying several OBSs, including OBSs 1, 6, 8, 9, 14, 16, 17, and 21 (**Figures 9B–E**). In cross-sectional view, they are less than 80 m in width and U-shaped, with raised lateral berms, which are characteristic features of ice ploughmarks (e.g., Graham et al., 2007). Ice ploughmarks form as a result of iceberg keels coming into contact with the seafloor after calving from the marine termini of glaciers and ice sheets (Dowdeswell and Bamber, 2007). Ice-ploughmarks are

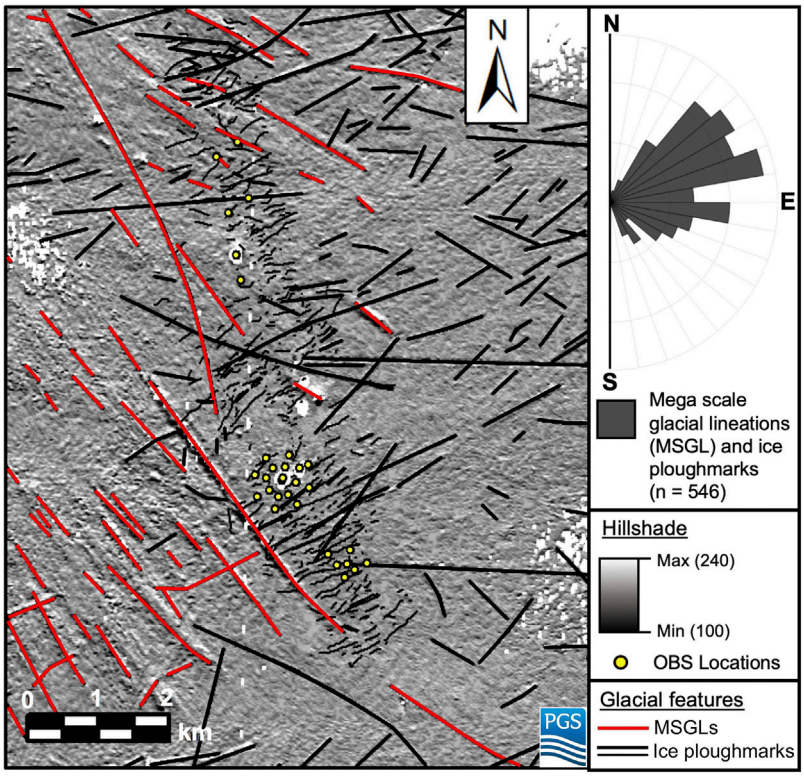


**FIGURE 10 |** Plan view of glacial features mapped onto seismic unit top S4 (see also **Supplementary Figures S2, S3**). The map shows a seismic amplitude contrast (hillshade) image of unit top S4 (base of the Witch Ground Formation). Black lines display mapped ice ploughmarks and red lines display mega-scale glacial lineations (MSGLs), interpreted using the 2D and 3D seismic reflection data. A length-weighted histogram displays the most common orientation of the glacial features across the Scanner Pockmark region, binned into 10° intervals.

common structures in the North Sea and their small dimension, and shape makes them another potential cause of S-wave splitting. In addition, sub-vertical discontinuity features can be observed on the sub-bottom profiler data within the seismic unit S5.1 (**Figures 9G,H**). The break in lateral continuity of the layers and minor resolvable vertical displacement may indicate the presence of fractures. These features are not visible in the sparker seismic profiles (**Figure 5B**) possibly because they are below the resolution of the sparker data.

At a larger scale (> 12.5 m resolution) features present at the top S4 surface were also mapped using the 3D seismic data (**Figure 10**). We observe a clear trend of interpreted ice ploughmarks, oriented at 50–80° (**Figure 10**). While less evident on the length-weighted histogram (**Figure 10**), there is also a series of larger, more linear features oriented at 150–160° to the south west of the Scanner pockmark and reference sites. The linear features are interpreted as mega-scale glacial lineations (MSGLs), in agreement with previous interpretations of the area (e.g. Graham et al., 2007). Ice ploughmarks and MSGL trends of 50–80° and 150–160°, respectively, correlate with the azimuth of energy nulls observed on OBS1 and OBS8.

Between 40 and 55 ms TWT, glacial meltwater channels extend from the east across the Scanner Pockmark region (**Figures 11A,B**). A relatively thin channel extends into the north east of the OBS configuration with an orientation of 50–60°, underlying OBSs 1–4, (**Figure 11B**). The channel may be interpreted as a source for the gas-charged sediment that has been observed directly beneath Scanner Pockmark, which follows the same orientation (**Figure 9C**). At greater depths (60–80 ms TWT; **Figure 11C**), the glacial channels (corresponding to seismic unit S2.2, iii) extend further to the west, terminating at the less permeable sediments of an older glacial channel (seismic unit S2.2, ii). Gas-charged sediments are present at the stratigraphic boundary of the two sub-units (**Figure 11D**). Beneath Scanner pockmark, there is a clear orientation of gas-charged sediments at 50–60°, as well as an orientation of 140–150° associated with gas accumulation along the margin of the subunits (seismic units S2.2 ii and iii; **Figures 10C,D**). The gas accumulation appears to underlie OBSs 1–5, 9, and 11 (**Figures 11C,D**). The gas-charged sediment trends of 50–60° and 140–150°, also appear to correlate with the azimuth of energy nulls observed on OBS 1.

## Core Shear-Wave Measurements

S-wave velocity measurements made of the sediment cores beneath the pockmark and at the site to the northeast are consistent and range in value between 57 and 115 m/s over a depth range of 2–22 m. There is a broad increase in velocity with depth (**Figure 12**) which is consistent with S-wave velocities of water-saturated clay, silty-, sandy-clay sediments (Hamilton, 1976;Hamilton, 1979).

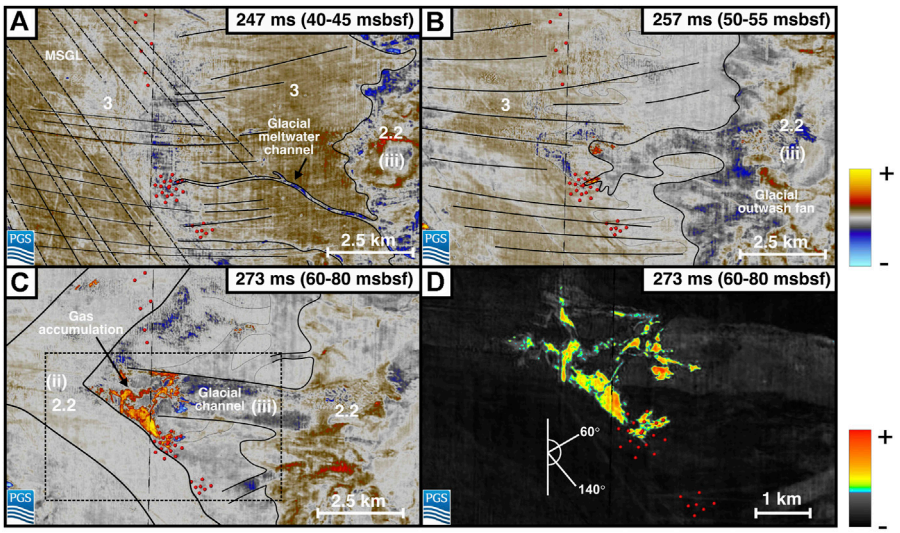


**FIGURE 11 |** Time slice amplitude maps that provide a regional context for the presence and orientation of the shallow gas. 3D seismic reflection data is used to generate surface amplitude maps at three time intervals: **(A)** 40–45 ms **(B)** 50–55 ms and **(C, D)** 60–80 ms two way travel time below seafloor. Black solid lines display boundaries between seismic units or highlight key geological features. **(D)** RMS amplitude map, acquired over a time window of ±2.5 ms TWT, highlighting the presence and orientation of gas charged sediments; two dominant orientations of 60° and 140° are observed, which correspond to the orientation of glacial channels and the stratigraphic juxtaposition of seismic units S2.2 ii and S2.2 iii, respectively.

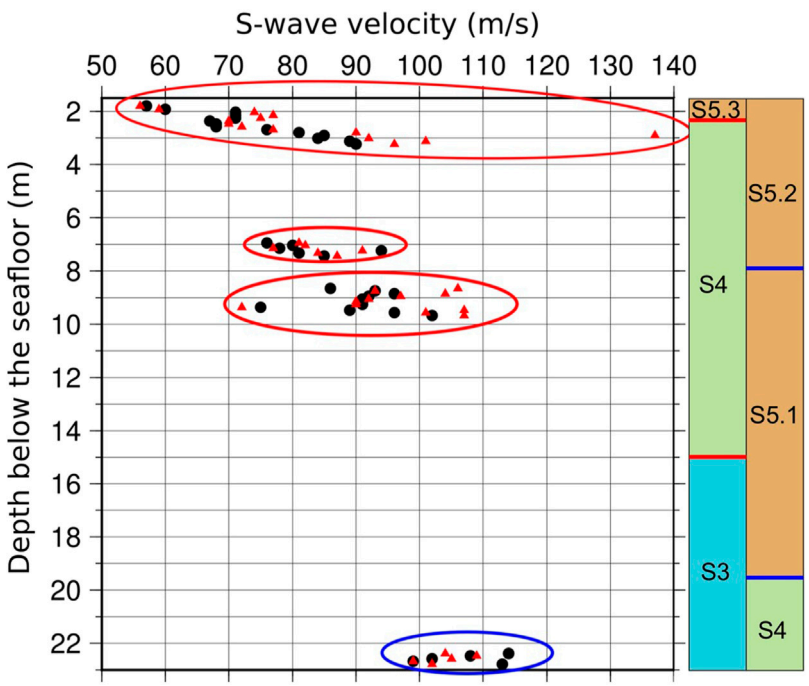


**FIGURE 12 |** Laboratory S-wave velocity measurements. Samples surrounded by red ellipses are acquired from the pockmark and blue surrounded ones are from the reference site. Black circles are the velocities derived in time domain. Red triangles are those derived in frequency domain. Two columns represent the stratigraphy within the pockmark (left) and at the reference site (right).

# DISCUSSION

## Fast S-Wave Orientation

On both OBS1 and OBS8, we observed clear SWS with consistent symmetry axes with azimuths of 70° and 160°. The delay between fast and slow S-wave arrivals observed on the radial component of the stacked azimuth *versus* time sections are usually used to infer the fast S-wave direction, which is commonly parallel to the fracture orientations. We do not observe significant time variations between fast and slow S-wave arrivals on the radial components of OBS1 (**Figures 6**, **7**), likely because their travel-time as S waves is insufficient to allow the development of an observable delay and the percentage of anisotropy is low. Therefore, we cannot uniquely define the fast S-wave orientation from the analysis of the seismograms. Hence, we first analyze potential features observed on seismic profiles that may cause anisotropy and shear wave splitting. Due to the difference between the P- and S-wave velocities, especially close to the seabed where Vp/Vs is typically high (Hamilton, 1979), the up-going S-wave ray path is close to vertical (Gaiser, 2016). Therefore, any near-vertical features causing the HTI anisotropy that generates the observed SWS will be located directly below the corresponding OBSs. First, we consider the potential sources of anisotropy based on their fit to the orientation of the observed SWS. We then consider the observed arrival times of the C-wave events relative to these different potential sources of SWS, in order to attribute the observations to valid causal mechanisms.

## Possible Causes of Seismic Anisotropy Within Scanner Pockmark

### Regional Horizontal Stress

The regional maximum horizontal stress (σ1) is oriented NW/SE, and the average in-situ minimum horizontal stress of the region (σ3) is 54°N ± 11° (Evans and Brereton, 1990). In the region, horizontal stress exceeds the vertical stress (σ2) (Evans and Brereton, 1990). Therefore extension (tension) fractures, if present, may be expected to form perpendicular to the minimum horizontal stress (σ3), i.e. at 150–160°.

We do not observe shallow SWS on every OBSs. Only OBS 1 located within the pockmark and OBS eight located at the southwestern rim of the pockmark exhibit shallow S-wave splitting. Both OBSs are located closer to the active methane venting zone within the pockmark. The observed SWS may result from the connected porosity within the sediments that is used as migration pathways for the vertical fluid flow, aligned in the direction of the maximum regional horizontal stress. OBS 2 which is also located within the pockmark does not show any SWS suggesting that the HTI structure directly underlies the OBSs where the SWS is observed.

### Local Stress

Below OBS 1, at the top S4 interface (3 ms TWT), gas-charged sediment is observed, oriented at 50–60° (**Figure 9C**). Gas-charged sediment is not clearly observed directly beneath OBS 8 but may be present at a scale below the horizontal resolution of the surface attribute map of 17.5 m × 17.5 m (**Figures 9B,C**). Where gas-charged sediment is present, gas-filled fracture corridors may form in the direction parallel to the localized overpressure gradient (e.g. Moss et al., 2003). In this case, extension (tension) fractures may form, with an orientation of 50–60°. The interpretation of gas-filled fractured sediment could explain the S-wave anisotropy directly beneath OBS 1.

Gas-charged sediment is also observed between 50–55 ms TWT with an orientation of 50–60° below OBSs 1–4 (**Figure 11B**), and between 60–80 ms TWT with an orientation of 140° below OBSs 1–5, 9, and 11 (**Figures 11C,D**). We do not observe shallow SWS on all these OBSs. However, further processing of the OBS data, including applying different normal move-out corrections to account for the increasing depth of P-S wave conversion and increase in shear-wave velocity with depth, in addition to layer stripping, to progressively correct for and remove the effects of anisotropy in shallower layers, may allow deeper SWS observations, caused by gas-filled fractures within deeper gas-bearing sediment, to be identified.

### Ice Ploughmarks

Ice ploughmarks are observed at the top of unit S4. They directly underlie both OBS1 and 8 and have an azimuth of 50–70° (**Figure 10**). Ice ploughmarks represent an erosional surface, where icebergs have scoured the former seabed surface within a shallow glacio-marine environment. The U-shaped impressions are later filled with younger sediment, and so these could, in theory, also create anisotropy. Ice ploughmarks can act as both lateral traps and channels for fluid, creating areas of focused fluid flow (Haavik and Landrø, 2014; Chand et al., 2016). However, ice ploughmarks also directly underlie other OBSs around the pockmark and the reference site (e.g., OBSs 16, 17, 20, and 21). Therefore, despite their comparable azimuth to the observed SWS, ice ploughmarks are unlikely to be the primary cause of SWS at the Scanner Pockmark site.

### Mega-Scale Glacial Lineations

MSGLs are also observed at the top S4 horizon, oriented at 150–160° (**Figures 5**, **10**). However, the MSGL features, which represent past grounded ice in a sub-glacial environment, are not observed directly beneath the Scanner pockmark site, so we rule them out as a cause of the anisotropy observed there. It is curious that the glacial features share a similar orientation to the regional stress field of the area, posing the question of whether the two are intrinsically linked. A link may have arisen because the stress regime guides the geometry of the Witch Ground Basin and the icebergs that generated the ploughmarks were driven by contour currents along the edge of the basin.

## Depth of S-Wave Conversion

Within the shallowmost water-saturated silty-clay sediments (S5, ~18 m thick), core-logging observations indicate that the P-wave velocity is similar to the water velocity (~1500 m/s). The corresponding S-wave velocities in shallow sediments are expected to be low and to increase with depth with a high

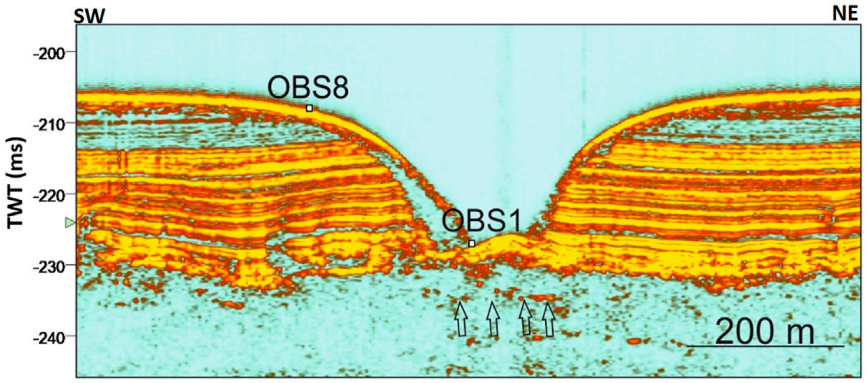


**FIGURE 13 |** SBP data sampling the locations of the OBS1 and 8. The white squares are OBS 1 and 8. The low amplitude reflector is shown in black arrows. TWT values here are milliseconds below the sea surface.

velocity gradient (Hamilton, 1976; Hamilton, 1979). The top S4 horizon, separating units S5 and S4, is the first sedimentary boundary observed as a high-amplitude reflector on the seismic profiles. At the depth of this reflector, there are three potential features (gas-charged sediments, ice-ploughmarks and MSGLs) with similar orientations to the anisotropic symmetry axes observed on OBS1 and OBS8. Therefore, we first considered this reflector, which has an average depth of 18 m, as the interface at which the conversion occurs. With a P-wave velocity of 1500 m/s, an S-wave velocity of ~419 m/s would be required to in order to match the arrival time of 0.055 s of the C-wave event observed on OBS 8. The Vp/Vs ratio of water-saturated silty-clay sediment varies between 13 and 7.35 in the first 20 m depth (Hamilton, 1979). In contrast, however, a Vp/Vs ratio of 3.6 is required here to match the arrival time of the C-wave event, which would be very low for these shallow sediments. We therefore ruled out the top S4 interface as the depth where the specific conversion occurs for the event observed on OBS 8.

At the NE drill site where we collected core samples and below OBS8, unit S5 exists with its full thickness. At ~23 m depth, near the top S4 reflector, the laboratory measured S-wave velocities vary from 99 to 114 m/s (**Figure 12**). Considering an S-wave velocity of 100 m/s (Vp/Vs = 15), the conversion depth for the

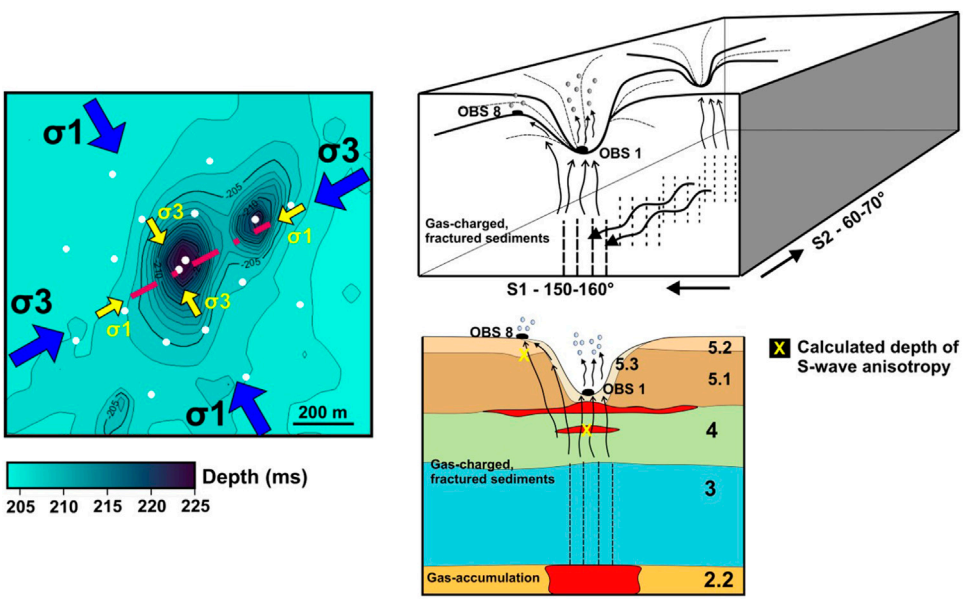


**FIGURE 14 |** Schematic diagram illustrating open gas migration pathways beneath Scanner pockmark that generate the shear-wave splitting observed on OBS1 and 8. Bottom right: Gas accumulations are present in S2.2, S4, and at the S4/S5.1 interface, indicated in red. Reference to color of seismic units S1-S5 found in **Figure 3**. Left: Blue arrows show regional maximum (σ1) and minimum (σ3) horizontal stress. Yellow arrows show local stress conditions caused by high pore fluid pressure. Red dashed line shows orientation of gas observed in **Figures 11C,D**. OBS locations shown in white. Top right image: S1 and S2 are the fast and slow S-wave directions, respectively.

C-waves events observed on the OBS1 and OBS8 are 6.1 and 5.15 m respectively, suggesting that the conversion occurs at the top S5.1 horizon below OBS 8 (**Figures 3**, **9G**,H). Below OBS 8, the top S5.1 horizon is observed as a bright reflector on the subbottom profiler data at 4.9 ms TWT (**Figures 9**, **13G**,H). Below OBS1 within the Scanner Pockmark, unit S5 has a reduced thickness of 3 ms TWT (**Figures 9**, **13G**,H) and it is reworked as it is exposed in the seafloor (unit S5.3 on **Figures 9G,H**). Here, unit S5.3 is underlain directly by unit S4. Within the S4 sediments, a low amplitude reflector is present on the SBP data at 7.2 ms TWT (**Figure 13**), which is likely to be the interface where the conversion occurs.

Considering a P-wave velocity of 1500 m/s, the depth to the reflectors observed on the SBP data below the OBS1 and OBS8 are 5.4 and 3.7 m respectively. If the observed C-wave events are converted from the reflectors identified on the subbottom profiler data, then average S-wave velocities of 88 and 69 m/s are required to match the arrival times of 65 and 55 ms arrival times observed on OBS1 and 8 respectively. S-wave velocity measurements on samples from corresponding depths vary between 56 and 137 m/s with an average of 83 m/s. There is a good match between calculated and measured S-wave velocities, although the laboratory measurements could be affected by sampling and measurement effects (Batzle et al., 2006).

Gas-filled fractures are observed within the Coal Pit Fm (unit S3). Gravity core observations of sediment fluidization features and disseminated iron sulphide, indicates active fluid flow directly beneath the pockmark. Evidence of methane-derived authigenic carbonates and gas ebullition at this site further demonstrates that active methane venting has persisted since 27 (Böttner et al., 2019; Li et al., 2020). As shown by controlled gas release experiments in weakly consolidated sediment (e.g., Roche et al., 2020), mature gas migration from an active, focused source may take place through stable open conduits. These conduits represent channels of enhanced permeability relative to background matrix permeability (Roche et al., 2020). The very shallow conversion depth of P-S waves, together with the evidence of active gas venting within the Scanner pockmark, suggest that the SWS occurs along vertically oriented gas conduits (**Figure 14**). Therefore, two potential causes of anisotropy remain valid from the evidence presented: 1) aligned gas conduits, in the form of fractures, opening perpendicular to the regional minimum horizontal stress at 150–160°, or 2) gas conduits aligned with a local stress gradient (50–60° azimuth) (**Figures 5**, **14**)., caused by a hydraulic connection with underlying, overpressured gas charged sediment within units S2.2-S3 (**Figures 5**, **14**).

## CONCLUSIONS

We observe evidence of shear wave splitting on two ocean bottom seismometers, located within and adjacent to a pockmark which is actively venting methane. Both instruments show symmetry axes consistent with a vertically aligned fractures (HTI anisotropic system), with fracture azimuths of 70° and 160°. Based on the arrival times of the SWS events, and shallow sediment core measurements of shear-wave velocity, P- to S-wave conversions occur at 4–5 m depth beneath the seabed. Comparing these orientations and depths to potential sources for SWS, we interpret these observations as being related to vertically aligned gas conduits, which facilitate the ebullition of methane at the seafloor. These gas conduits may either result from the opening of fractures perpendicular to the regional minimum horizontal stress, or they may be aligned with the local stress gradient driven by overpressure resulting from a gas accumulation at ~50 m depth beneath the pockmark. This study reports the first observation of very shallow anisotropy associated with active methane venting at the seabed.

## DATA AVAILABILITY STATEMENT

The raw data supporting the conclusions of this article will be made available by the authors, without undue reservation, to any qualified researcher.

## AUTHOR CONTRIBUTIONS

GB contributed to survey design, carried out the SWS analysis and led the manuscript writing. BC interpreted the seismic reflection data and contributed to manuscript writing. JB led the CHIMNEY survey at sea and contributed to the interpretation of the results. TM contributed to survey design, SWS analysis and the interpretation of the results. GP processed the seismic reflection data. LN carried out the S-wave velocity measurements on cores. CM calculated positions for the ocean bottom instruments and shots and contributed to the SWS analysis. AR contributed to the SWS analysis and to manuscript writing. TH led the acquisition of seismic reflection data and MC contributed to interpretation of the results from a rock physics perspective.

## FUNDING

This work received funding from the European Union's Horizon 2020 research and innovation programme under grant agreement No.654462 (STEMM-CCS) and the Natural Environment Research Council (CHIMNEY project: grants NE/N016130/1, NE/N016041/2 and NE/N015762/1).

## ACKNOWLEDGMENTS

We would like to thank all those involved in the planning and acquisition of data during research cruise JC152, including the officers, engineers and crews, the scientific parties, and all seagoing technicians and engineers. The NERC Ocean-Bottom Instrumentation Facility (Minshull et al., 2005) provided the

OBSs and their technical support at sea during JC152. We are also grateful for the support of Applied Acoustics Ltd. during Sparker data acquisition. We acknowledge PGS for the use of their dataset. We are grateful to Schlumberger Ltd. for the donation of Petrel software to the University of Southampton.

## SUPPLEMENTARY MATERIAL

The Supplementary Material for this article can be found online at: https://www.frontiersin.org/articles/10.3389/feart.2021.626416/full#supplementary-material

**Figure S1** | The composite plot of radial and transverse components along an inline profile recorded by 600 the OBS1. Even traces are the radial component and odd traces are the transverse component.

**Figure S2** | 2D seismic vertical seismic feature picking method. Individual sub-vertical discontinuities were picked along 104 profile lines (black dots in map view – top left; and light blue in seismic cross-section view - below). Discontinuities that extended laterally across multiple 2D profiles were interpreted (black and red lines in map view – top middle and right). The discontinuities correspond to ice ploughmarks (black lines) and Mega-scale glacial lineations (red lines), respectively (Fig. 5.9).

**Figure S3** | 3D seismic surface of unit top S4, uninterpreted. A seismic amplitude horizon surface (left) and hillshade map (right) is displayed.

**Figure S4** | Laboratory S-wave measurements. Top: Input signal. Middle: output signal. Bottom: Frequency domain estimation of the S-wave velocity.

## REFERENCES


Andrews, I. J., Long, D., Richards, P. C., Thomson, A. R., Brown, S., Chesher, J. A., et al. (1990). *The Geology of the Moray Firth*. London: HMSO Vol. 3

Bahorich, M., and Farmer, S. (1995). 3-D Seismic Discontinuity for Faults and Stratigraphic Features: The Coherence Cube. *The leading edge* 14 (10), 1053–1058. doi:10.1190/1.1437077

Bale, R., Gratacos, B., Mattocks, B., Roche, S., Poplavskii, K., and Li, X. (2009). Shear Wave Splitting Applications for Fracture Analysis and Improved Imaging: Some Onshore Examples. *First Break*. 27 (9). doi:10.3997/1365-2397.27.1304.32448

Batzle, M. L., Han, D.-H., and Hofmann, R. (2006). Fluid Mobility and Frequency-dependent Seismic Velocity - Direct Measurements. *Geophysics*. 71 (1), N1–N9. doi:10.1190/1.2159053

Berndt, C. (2005). Focused Fluid Flow in Passive Continental Margins. *Phil. Trans. R. Soc. A.* 363 (1837), 2855–2871. doi:10.1098/rsta.2005.1666

Böttner, C., Berndt, C., Reinardy, B. T. I., Geersen, J., Karstens, J., Bull, J. M., et al. (2019). Pockmarks in the Witch Ground Basin, Central North Sea. *Geochem. Geophys. Geosyst.* 20 (4), 1698–1719. doi:10.1029/2018gc008068

Brown, R. J., Stewart, R. R., Gaiser, J. E., and Lawton, D. C. (2000). *An Acquisition Polarity Standard for Multicomponent Seismic Data*. CREWES Research Report. doi:10.1190/1.1815611

Bull, J. M., Berndt, C. B., Minshull, T. M., Henstock, T., Bayrakci, G., Gehrmann, R., et al. (2018). Constraining Leakage Pathways through the Overburden above Sub-seafloor $CO_2$ Storage Reservoirs. in 14th Greenhouse Gas Control Technologies Conference, Melbourne, 21-26 October 2018 (GHGT-14)

Bull, J. M. (2018). Cruise Report – RRS James Cook JC152: CHIMNEY - Characterisation of Major Overburden Pathways above Sub-seafloor $CO_2$ Storage Reservoirs in the North Sea Scanner and Challenger Pockmark Complexes, University of Southampton. , 55 pp. Available at: https://eprints.soton.ac.uk/420257/

Chand, S., Thorsnes, T., Rise, L., Brunstad, H., and Stoddart, D. (2016). Pockmarks in the SW Barents Sea and Their Links with Iceberg Ploughmarks. *Geol. Soc. Lond. Mem.* 46 (1), 295–296. doi:10.1144/M46.23

Crampin, S. (1985). Evaluation of Anisotropy by Shear-wave Splitting. *Geophysics*. 50 (1), 142–152. doi:10.1190/1.1441824

Dean, M., Tucker, O. D., Strijbos, F. P. L., de Jong, R. A. M., Marshall, J., and Goswami Bv, R. (2015). *Characterisation and Monitoring of the Goldeneye CO2 Storage Site*. Madrid: 77th EAGE Conf. Exhibition. doi:10.3997/2214-4609.201412719

Dowdeswell, J. A., and Bamber, J. L. (2007). Keel depths of modern Antarctic icebergs and implications for sea-floor scouring in the geological record. *Mar. Geol.* 243, 120–131.

Evans, C. J., and Brereton, N. R. (1990). *In situ* crustal Stress in the United Kingdom from Borehole Breakouts. *Geol. Soc. Lond. Spec. Publications*. 48 (1), 327–338. doi:10.1144/gsl.Sp.1990.048.01.27

Exley, R. J. K., Westbrook, G. K., Haacke, R. R., and Peacock, S. (2010). Detection of Seismic Anisotropy Using Ocean Bottom Seismometers: a Case Study from the Northern Headwall of the Storegga Slide. *Geophys. J. Int.* 183 (1), 188–210. doi:10.1111/j.1365-246x.2010.04730.x

Gafeira, J., and Long, D. (2015). Geological Investigation of Pockmarks in the Scanner Pockmark SCI Area. JNCC Report No 570. JNCC Peterborough. Available at: http://data.jncc.gov.uk/data/290b95b7-fcfc-4c76-8780-8714329dcf0c/JNCC-Report-570-FINAL-WEB.pdf

Gaiser, J. (2016). "Chapter 7. Inversion Applications," in *3C Seismic and VSP: Converted Waves and Vector Wavefield Applications*. Editor J. Gaiser (Society of Exploration Geophysicists), 341–418. doi:10.1190/1.9781560803362.ch7

Graham, A., Lonergan, L., and Stoker, M. (2007). Evidence for Late Pleistocene Ice Stream Activity in the Witch Ground Basin, Central North Sea, from 3D Seismic Reflection Data. *Quat. Sci. Rev.* 26 (5-6), 627–643. doi:10.1016/j.quascirev.2006.11.004

Haacke, R. R., and Westbrook, G. K. (2006). A Fast, Robust Method for Detecting and Characterizing Azimuthal Anisotropy with marinePSconverted Waves, and its Application to the West Svalbard Continental Slope. *Geophys. J. Int.* 167 (3), 1402–1412. doi:10.1111/j.1365-246x.2006.03186.x

Haavik, K. E., and Landrø, M. (2014). Iceberg Ploughmarks Illuminated by Shallow Gas in the Central North Sea. *Quat. Sci. Rev.* 103, 34–50. doi:10.1016/j.quascirev.2014.09.002

Hamilton, E. L. (1976). Shear-wave Velocity versus Depth in Marine Sediments: a Review. *Geophysics*. 41 (5), 985–996. doi:10.1190/1.1440676

Hamilton, E. L. (1979). Vp/Vs and Poisson's Ratios in Marine Sediments and Rocks. *The J. Acoust. Soc. America* 66 (4), 1093–1101. doi:10.1121/1.383344

Hovland, M., Gardner, J. V., and Judd, A. G. (2002). The Significance of Pockmarks to Understanding Fluid Flow Processes and Geohazards. *Geofluids*. 2 (2), 127–136. doi:10.1046/j.1468-8123.2002.00028.x

Judd, A., and Hovland, M. (2009). *Seabed Fluid Flow: The Impact on Geology, Biology and the Marine Environment*. Cambridge University Press. doi:10.1017/CBO9780511535918

Judd, A., Long, D., and Sankey, M. (1994). Pockmark Formation and Activity, UK Block 15/25, North Sea. *Bull. Geol. Soc. Denmark* 41, 34–49.

Karstens, J., and Berndt, C. (2015). Seismic Chimneys in the Southern Viking Graben - Implications for Palaeo Fluid Migration and Overpressure Evolution. *Earth Planet. Sci. Lett.* 412, 88–100. doi:10.1016/j.epsl.2014.12.017

Karstens, J., Böttner, C., Edwards, M., Falcon-Suarez, I., Flohr, A., James, R., et al. (2018). RV MARIA S. MERIAN Fahrtbericht/Cruise Report MSM78-PERMO 2, Edinburgh, UK: Edinburgh.

Li, J., Roche, B., Bull, J. M., White, P. R., Leighton, T. G., Provenzano, G., et al. (2020). Broadband Acoustic Inversion for Gas Flux Quantification—Application to a Methane Plume at Scanner Pockmark, Central North Sea. *J. Geophys. Res. Oceans* 125 (9), e2020JC016360. doi:10.1029/2020jc016360

Løseth, H., Wensaas, L., Arntsen, B., Hanken, N.-M., Basire, C., and Graue, K. (2011). 1000 M Long Gas Blow-Out Pipes. *Mar. Pet. Geology.* 28 (5), 1047–1060. doi:10.1016/j.marpetgeo.2010.10.001

Lynn, H. B., and Thomsen, L. A. (1990). Reflection Shear-wave Data Collected Near the Principal Axes of Azimuthal Anisotropy. *Geophysics* 55 (2), 147–156. doi:10.1190/1.1442821

Minshull, T. A., Sinha, M. C., and Peirce, C. (2005). Multi-disciplinary, Sub-seabed Geophysical Imaging. *Sea Technology* 46 (10), 27–31. Available at: http://eprints.soton.ac.uk/id/eprint/18172.

Moss, B., Barson, D., Rakhit, K., Dennis, H., Swarbrick, R., Evans, D., et al. (2003). "Formation Pore Pressures and Formation Waters," in *The Millennium Atlas:*

*Petroleum Geology of the Central and Northern North Sea*. Editor D. Evans (Geological Society of London), 317–329.

Ottesen, D., Dowdeswell, J. A., and Bugge, T. (2014). Morphology, Sedimentary Infill and Depositional Environments of the Early Quaternary North Sea Basin (56°-62°N). *Mar. Pet. Geology.* 56, 123–146. doi:10.1016/j.marpetgeo.2014.04.007

Provenzano, G., Henstock, T. J., Bull, J. M., and Bayrakci, G. (2020). Attenuation of Receiver Ghosts in Variable-Depth Streamer High-Resolution Seismic Reflection Data. *Mar. Geophys. Res.* 41, 1–15. doi:10.1007/s11001-020-09407-9

Robinson, A. H., Callow, B., Böttner, C., Yilo, N., Provenzano, G., Falcon-Suarez, I. H., et al. (2020). Multiscale Characterisation of Chimneys/pipes: Fluid Escape Structures within Sedimentary Basins. *Int. J. Greenhouse Gas Control.* doi:10.5194/gmd-2019-304-rc2

Roche, B., Bull, J. M., Marin-Moreno, H., Leighton, T., Falcon-Suarez, I. H., White, P. R., et al. (2020). Time-lapse Imaging of $CO_2$ Migration within Near-Surface Sediments during a Controlled Sub-seabed Release Experiment. *Int. J. Greenh. Gas Control.* In press.

Rubin, S., Shtivelman, V., Keydar, S., and Lev, A. (2014). Seismic Ringing Effect in the Shallow Subsurface. *Near Surf. Geophys.* 12 (6), 687–696. doi:10.3997/1873-0604.2014030

Stewart, M. A., and Lonergan, L. (2011). Seven Glacial Cycles in the Middle-Late Pleistocene of Northwest Europe: Geomorphic Evidence from Buried Tunnel Valleys. *Geology.* 39 (3), 283–286. doi:10.1130/g31631.1

Stockwell, J. W., Jr (1997). Free Software in Education: A Case Study of CWP/SU: Seismic Un*x. *The Leading Edge* 16 (7), 1045–1050. doi:10.1190/1.1437723

Stoker, M. S., Balson, P. S., Long, D., and Tappin, D. R. (2011). *An Overview of the Lithostratigraphical Framework for the Quaternary Deposits on the United Kingdom Continental Shelf*. Nottingham, UK: British Geological Survey. doi:10.21236/ada557589Available at: http://nora.nerc.ac.uk/id/eprint/15939

Thomsen, L. (1999). Converted-wave Reflection Seismology over Inhomogeneous, Anisotropic Media. *Geophysics* 64 (3), 678–690. doi:10.1190/1.1444577

Tsvankin, I., Gaiser, J., Grechka, V., Van Der Baan, M., and Thomsen, L. (2010). Seismic Anisotropy in Exploration and Reservoir Characterization: An Overview. *Geophysics*. 75 (5), 75A15–75A29. doi:10.1190/1.3481775

Wild, P. (2011). Practical Applications of Seismic Anisotropy. *First Break* 29 (5).

**Conflict of Interest:** The authors declare that the research was conducted in the absence of any commercial or financial relationships that could be construed as a potential conflict of interest.

frontiers in Earth Science

ORIGINAL RESEARCH
published: 11 June 2021
doi: 10.3389/feart.2021.682206

# Crustal Structure Across the Northern Region of the Islas Marías Archipelago

*Luis Alfredo Madrigal[1†], Diana Núñez[1*†], Felipe de Jesús Escalona-Alcázar[1,2†] and Francisco Javier Núñez-Cornú[1†]*

[1]Centro de Sismología y Volcanología de Occidente (SisVOc), CUCosta, Universidad de Guadalajara, Puerto Vallarta, Mexico, [2]Unidad Académica de Ciencias de la Tierra, Universidad Autónoma de Zacatecas, Zacatecas, Mexico

The tectonic interaction between the Rivera and North American plates north of the Bahía de Banderas is poorly understood. The nature of the crust and where the subduction ends in the western part of the Islas Marias Archipelago are still controversial. Based on new geophysical data provided by the TsuJal project, we present the shallow and deep crustal structure of the Rivera–North American plate contact zone along two seismic transects, TS09b and RTSIM01b, and the bathymetry obtained across the northern region of María Madre Island. Detailed bathymetric analysis allowed mapping of a series of lineaments along the study region, with two main preferred tendencies (020–050° and 290–320°) associated with the evolution of the Pacific-Rivera rise and the transform faults of the Gulf of California, respectively. The shallow structure is characterized by five sedimentary basins without deformation, whose horizons are subparallel, suggesting that the sediment deposition occurred after the extension process ended. The deep structure corresponds to a transition between oceanic crust (Rivera Plate), with an average thickness of ~10 km to the Islas Marías Escarpment, and a thinned continental crust, whose thickness increases toward the continent until it reaches 28 km, with a dip angle of 7–10°. The absence of an accretionary prism suggests that the subduction process of the Rivera Plate beneath the North American Plate to the north of Islas Marías has ceased. In this study, we determined that the morphological expression of the northern limit of the Rivera Plate corresponds to the Islas Marías Escarpment.

**Keywords: Rivera Plate, crustal structure, amphibious network, horst and graben array, Islas Marías Archipelago**

OPEN ACCESS

***Edited by:***
*Lara S. Wagner, Carnegie Institution for Science (CIS), United States*

***Reviewed by:***
*Laura Gómez de la Peña, GEOMAR Helmholtz Center for Ocean Research Kiel, Germany*
*Justin Estep, Northern Arizona University, United States*

***Correspondence:**
*Diana Núñez*
*diana@sisvoc.mx*

**†ORCID:**
*Luis Alfredo Madrigal*
*orcid.org/0000-0001-5309-0706*
*Diana Núñez*
*orcid.org/0000-0003-0572-3905*
*Felipe de Jesús Escalona-Alcázar*
*orcid.org/0000-0002-4066-6160*
*Francisco Javier Núñez-Cornú*
*orcid.org/0000-0003-1515-1349*

***Specialty section:***
*This article was submitted to Solid Earth Geophysics, a section of the journal Frontiers in Earth Science*

***Received:*** *18 March 2021*
***Accepted:*** *20 May 2021*
***Published:*** *11 June 2021*

***Citation:***
*Madrigal LA, Núñez D, Escalona-Alcázar FdeJ and Núñez-Cornú FJ (2021) Crustal Structure Across the Northern Region of the Islas Marías Archipelago. Front. Earth Sci. 9:682206. doi: 10.3389/feart.2021.682206*

## INTRODUCTION

During most of the Cenozoic, the tectonic setting of Western Mexico has been a complex system of convergent, divergent, and transform boundaries between the various active tectonic units. The oblique subduction of the Farallon Plate beneath the North American Plate (NAP) progressively ceased since the Oligocene time as the Pacific-Farallon ridge approached North America and the triple junction moved southward. Along the Baja California Peninsula, from Miocene to recent, the movement of the triple junction produced the fragmentation of the Farallon Plate and formation of short-lived oceanic microplates, as well as the capture of the Baja California Peninsula by the Pacific Plate. All these processes, together with ridge rotation and the cessation of ridge activity along some segments west of the Baja California Peninsula, promoted plate reorganization (e.g., Mammerickx and Klitgord, 1982; Lonsdale, 1991; Bohannon and Parsons, 1995; Ferrari, 1995; Fletcher et al., 2007; Sutherland et al., 2012). After 12 Ma, the Pacific-Guadalupe ridge in the southern Baja California Peninsula broke up and rotated clockwise and oriented the rise to the NE (Mammerickx and

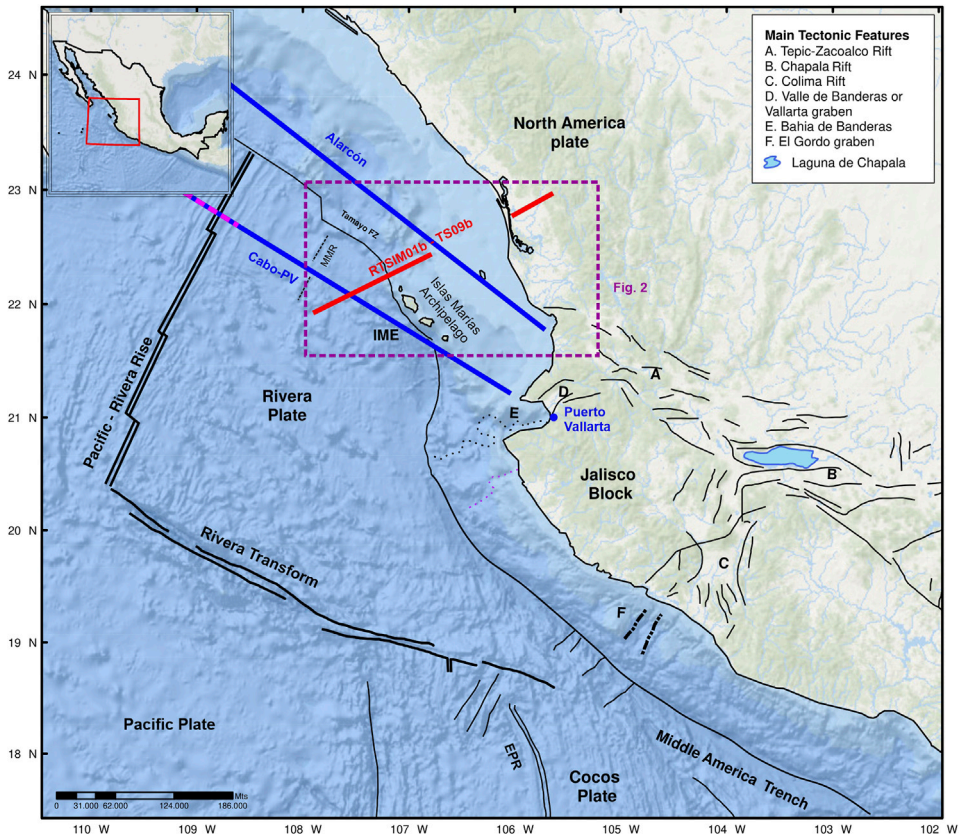


**FIGURE 1 |** Location of the investigated area in its tectonic context. *Abbreviations*: *EPR*, East Pacific Rise; *IME*, Islas Marías Escarpment; *MMR*, María Magdalena Rise. (*Inset*) Location map of the study area within the North American continent. In this scheme the Alarcón and Cabo-Puerto Vallarta segments (blue lines) analyzed by Lizarralde et al. (2007) are depicted, together with the TsuJal TS09b/RTSIM01b seismic profiles (red lines). Páramo et al. (2008) (magenta dash line) do not reach the study area. The purple rectangle shows the location of **Figure 2**. The position of the María Magdalena Rise is vague (Lonsdale, 1989), mainly in its southern part since it is poorly defined, causing its location to be unclear (dash line).

Klitgord, 1982; Stock and Hodges, 1989). In this new plate configuration, the Pacific-Rivera and Pacific-Cocos ridges were formed (Mammerickx and Klitgord, 1982; Stock and Hodges, 1989; Lonsdale, 1991; Nicholson et al., 1994; Stock and Lee, 1994). The northern boundary of the Rivera Plate is defined by the Tamayo fracture zone (**Figure 1**), but the boundary extending from the Islas Marías Archipelago throughout Puerto Vallarta is less clear. Along this region, a lack of lithological and structural data, sedimentary cover, scarce outcrops on the islands, and issues with accessibility make it a challenge to get the necessary data to define this boundary precisely. Although several tectonic, structural, and marine geophysical studies were carried out, the continental crustal architecture and oceanic crust transition are not yet fully understood. Most of the geological and geophysical surveys are only in a few, limited places on islands, along seismic profiles, in mainland Mexico and the Baja California Peninsula (Fletcher et al., 2007; Housh et al., 2010; Sutherland et al., 2012; Ferrari et al., 2013; Pompa-Mera et al., 2013; Balestrieri et al., 2017). No study on the scale required to precisely define the plate boundary had yet been undertaken.

The Rivera Plate (RP), in terms of tectonic boundaries and motion, is problematic; it is an independent oceanic microplate (Atwater, 1970) of ~100,000 km$^2$ (DeMets and Stein, 1990) with distinct kinematics with respect to the NAP and Cocos Plate (Eissler and McNally, 1984; Bandy and Yan, 1989; DeMets and Stein, 1990). The RP is located to the west of Mexico; the northern limit is the Tamayo fracture zone. The eastern limit is the Middle America Trench subduction zone which truncates at the Tamayo fracture zone (e.g., Stoiber and Carr, 1973; Dean and Drake, 1978; Nixon, 1982; Bevis and Isacks, 1984; Ponce et al., 1992). The western limit of the RP is the Pacific-Rivera Rise, as part of the East Pacific Rise. The junction between the Pacific-Rivera Rise and the Rivera Transform is located 165 km west of the Middle America Trench (Bourgois and Michaud, 1991). The Rivera–Cocos Plate boundary runs from El Gordo graben and is continuous at depth along a line located east of the Colima Rift (Bandy et al., 1995). The crustal between RP and NAP at the northern part of the Islas Marías Archipelago is not clearly defined due to the low rate of recorded earthquake activity and the absence of bathymetric features of subduction in the zone (**Figure 1**).

To increase the structural understanding of the Islas Marías Archipelago and surroundings, a marine geophysical survey of the TsuJal project was performed (Núñez-Cornú et al., 2016).

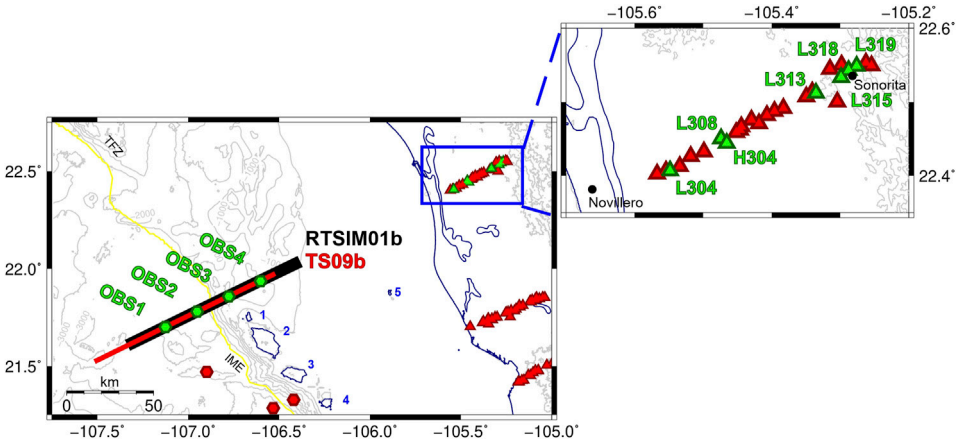


**FIGURE 2 |** Deployment map in the study area with seismic stations (green symbols) used to generate the P-wave velocity model of RTSIM02 seismic transect (black line) and multichannel seismic profile TS09b (red line). Red symbols depict those stations not used in this study. *Abbreviations*: *IME*, Islas Marías Escarpment; *TFZ*, Tamayo fault zone; *1*, San Juanito Island; *2*, María Madre Island; *3*, María Magdalena Island; *4*, María Cleofas Island; *5*, Isabel Island; *OBS*, Ocean-bottom seismometer.

**TABLE 1 |** Seismic source parameters used during the RTSIM01b wide-angle (WAS) and the TS09b multichannel seismic (MCS) data acquisition.

| Seismic source parameters | WAS | MCS |
|---|---|---|
| Source controller | Big Shot® | Big Shot® |
| Source type | Bolt® G.Guns 1500LL | Bolt® G.Guns 1500LL |
| Air pressure | 2000 psi | 2000 psi |
| Volume | 6,800 $in^3$ | 3,540 $in^3$ |
| Compressors | 4 x Hamworthy® $4^{TH}$ 565 W100 | 4 x Hamworthy® $4^{TH}$ 565 W100 |
| Number of air guns and strings | 11 air guns in 5 strings | 12 air guns in 4 strings (3 air gun/string) |
| Synchronization | ±0.1 ms | ±0.1 ms |
| Deployment depth | 15 m | 8 m |
| Trigger interval | 120 s | 50 m |

During the TsuJal project, several geophysical surveys were carried out combining sea–land studies with investigations involving the application of various geophysical techniques to characterize the surficial and crustal structure in the contact zone between RP and NAP. This article analyzes the results obtained from two seismic profiles, the RTSIM01b wide-angle seismic transect of 240 km and the lengthy TS09b multichannel seismic profile of 115 km, along with bathymetric data for this region. Both seismic lines are located in the north of the Islas Marías with SW–NE orientation (**Figure 2**) and are perpendicular to the contact between RP and NAP.

## DATA AND METHODOLOGIES

During the active part of the TsuJal project, the British research vessel *RRS James Cook* collaborated in acquiring multidisciplinary data (multichannel, wide-angle seismic, multibeam bathymetry and gravity and magnetism) in the western coast of Jalisco and Nayarit states. Moreover, this vessel deployed and collected the ocean-bottom seismometers (OBSs) and provided the seismic sources for the seismic experiment (**Table 1**).

### Bathymetric Data

The JC098 cruise provided the bathymetric and multichannel seismic data (MCS) analyzed in this work measured in the northern region of the María Madre Island, perpendicular to the coastline (**Figure 2**). Two multibeam echosounder systems (Kongsberg EM120 and EM710) acquired the bathymetric data used in this study. We also included the bathythermograph (XBT) probes and sound velocity profiles in the water column obtained daily during the data processing stage.

The bathymetric data recovered in the northern area of the TsuJal project across the RTSIM01b and TS09b seismic profiles were processed using CARIS HIPS and SIPS (Teledyne) software. We used sound speed and tide corrections provided by the Centro de Investigación Científica y de Educación Superior de Ensenada (CICESE) to produce vertical and horizontal data and georeferenced data, including calculating the total propagated uncertainty for each sounding. Finally, we obtained regular grid and variable resolution surfaces by applying various filters and editors to generate the final bathymetric surface with an 80 × 80 m resolution grid. This surface was interpolated and depicted using System for Automated Geoscientific Analyses (SAGA) and Geographic Information Systems (GIS) (Conrad et al., 2015).

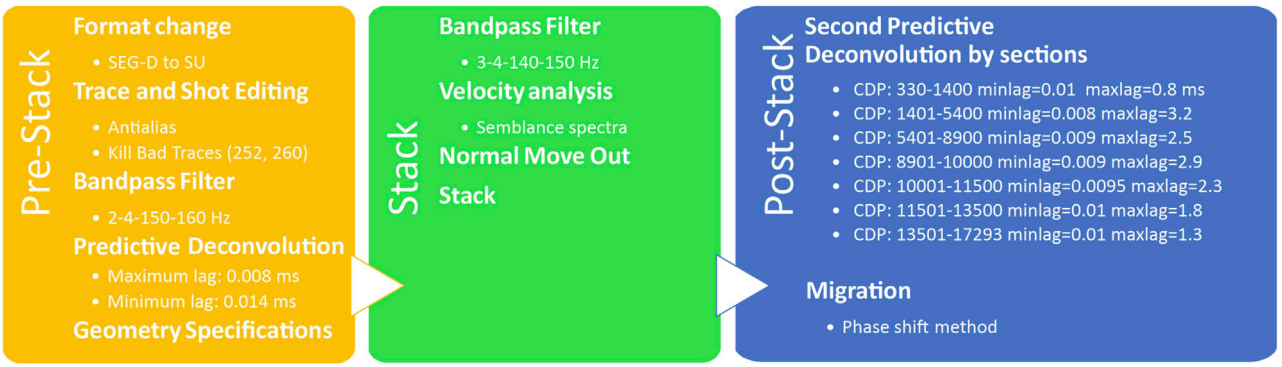


**FIGURE 3 |** Processing flow applied to the TS09b multichannel seismic profile using Seismic Unix.

## Multichannel Seismic Data

The MCS data were acquired by using a SASS Multichannel Sentinel Sercel® streamer of 5.85 km length (468 active channels, separated 12.5 m) deployed at 10 m depth. The common depth point (CDP) distance is 6.25 m, providing a CDP nominal fold of 58–59 traces. These data were recorded initially in SEG-D format and sampled at 1 ms. The technical parameters of the seismic source used in this study are shown in **Table 1**. The TS09b seismic line consisted of 2,305 shots with a total length of 115 km approximately.

**Figure 3** shows the main steps of the processing stage, which was carried out by Seismic Unix software (Cohen and Stockwell, 2013). We carried out a traditional processing methodology to increase the horizontal and vertical resolution to obtain the best possible seismic image of the TS09b seismic profile. The sequence shown in **Figure 3** includes the following steps:

1. Pre-stacked signal calculations (eliminate aliasing, eliminate incorrect traces, and filtering)
2. Spherical corrections and predictive deconvolution for improving the resolution in time
3. Velocity analysis by semblance method every 100 CDP
4. Correction of normal move out
5. Stack to increase the signal-to-noise ratio
6. Phase shift migration with turning rays for increasing horizontal resolution and collapse diffractions, which relocate the reflectors in time.

## Wide-angle Seismic Data Acquisition and Seismic Phases

The wide-angle seismic data correspond to a SW–NE trending line (RTSIM01b) along the north of the María Madre Island, perpendicular to the coastline (**Figure 2**). The length of the shooting line was 110 km approximately. These shots were recorded on land 240 km from the first shot of the transect. The seismic source consisted of two air gun subarrays with a total capacity of 6,800 $in^3$, shooting every 120 s, and with a cruise velocity of five knots (**Table 1**). In addition, these shots were registered by an amphibious seismic network composed of four OBSs and 27 temporary seismic stations deployed from Novillero to Sonorita (Nayarit) (**Figure 2**). The OBSs were short-period model LC2000SP with L-28 three-component geophone sensors (4.5 Hz) and one HiTech HYI-90-U hydrophone (OBS1, OBS2, OBS3, and OBS4). The instruments used for the terrestrial network were single, vertical component TEXAN 125A (Reftek, Trimble), a TAURUS Digital Seismograph (Nanometrics), and WorldSensing Spidernano data loggers both with a short-period sensor 1-Hz LE-3D/lite (Lennartz) and a CMG-6TD (Güralp Systems). Of the 27 seismic stations deployed along this line, we have selected those whose signal-to-noise ratio was low, resulting in seven high-quality stations (L304, L308, H305, L313, L315, L318, and L319) (**Figure 2**).

The data processing included band-pass filtering and navigation data. Instrumental drift corrections, zero-phase band-pass filter (4–10 Hz), and travel time corrections were also applied (Núñez et al., 2016). Furthermore, topography and bathymetric data were included for P-wave phase determination (**Figures 4**, **5**), which consisted of correlating reflected and refracted phases observed at the different crust and uppermost mantle discontinuities. We calculated the apparent velocities from P-wave refracted phases used for initial velocity and depth modeling. We identified five refracted phases [three within the sediments ($P_{S1}$, $P_{S2}$, and $P_{S3}$), one within the crust ($P_I$), and one within the uppermost mantle ($P_n$)] and four reflected phases [one intermediate-lower crust discontinuity ($P_{LC}P$), one crust-mantle boundary reflection ($P_MP$), and two reflections in the first layers of the upper mantle ($P_{M1}$ and $P_{M2}$)].

The sedimentary cover across the RTSIM01b transect was sampled by the refracted phases mainly observed in OBS seismic record sections (**Figure 4**). The $P_{S1}$, $P_{S2}$, and $P_{S3}$ phases were identified from 3 to 15 km of the source–receiver offset distance for the shallowest refracted phases, while between 6 and 30 km for the third one, in most OBS sections. The average apparent velocities calculated were 2.8, 4.1, and 5.1 km/s, respectively. The next phase, $P_I$, is observed in the offset interval 10–30 km for the marine record sections, and it was identified from 96 to 111 km in the station closest to the coast (L304) with 5.8 km/s. The $P_{LC}P$ seismic phase is correlated between 10 and 46 km offset distance for OBS1 and 30–45 km for OBS2 and OBS3 (**Figure 4**). All of the seismic sections exhibit a secondary arrival, $P_MP$, indicating an abrupt discontinuity between the crust and the

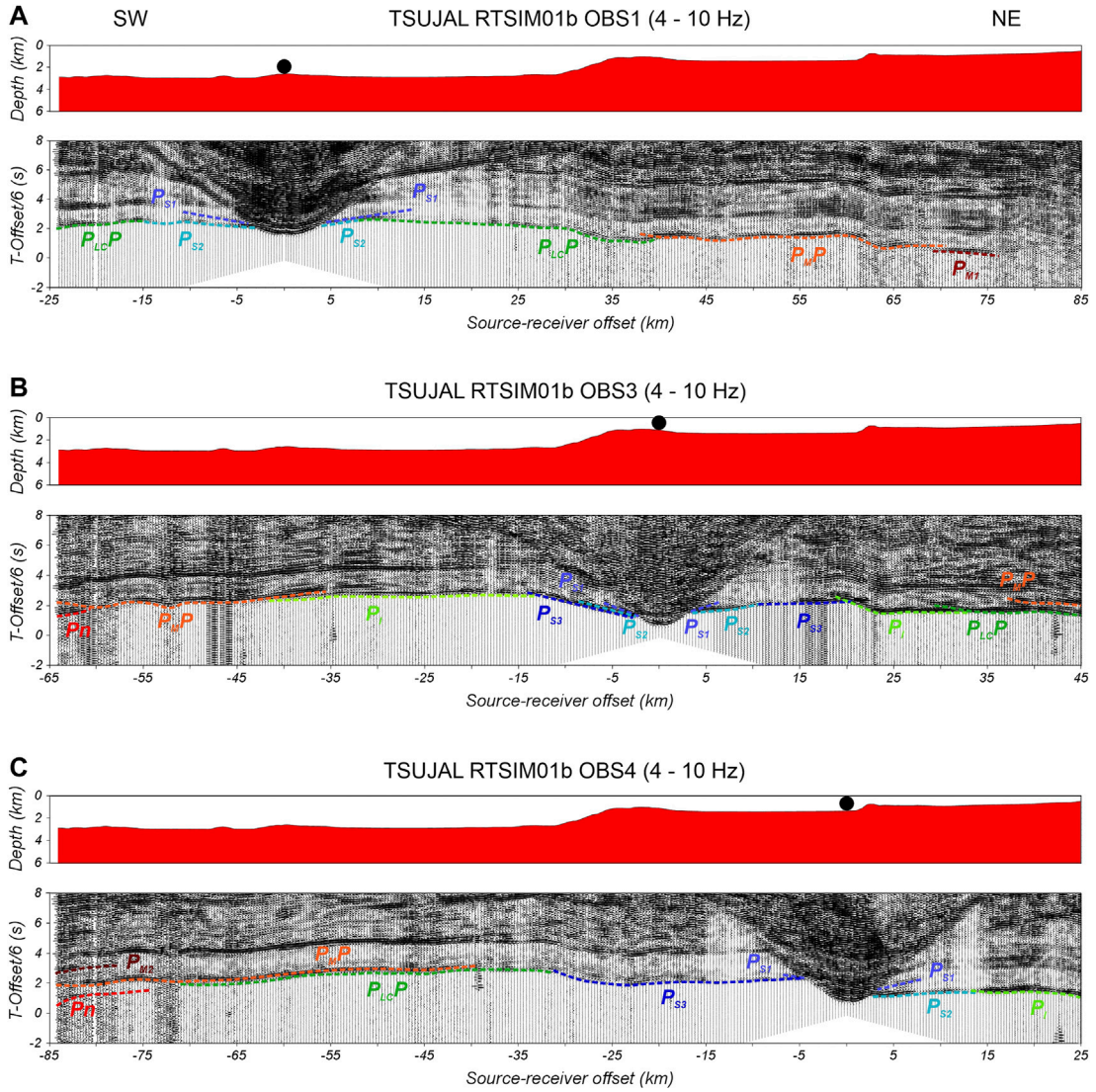


**FIGURE 4 |** Record sections of the marine seismic stations recording the RTSIM01b seismic transect. All of them have the bathymetry along with the RTSIM01b seismic profile in the upper panel. The lower panel shows the vertical component of the corresponding station with a reduced velocity of 6 km/s, 4–10 Hz band-pass filter applied, trace-normalized amplitudes, and interpreted reflected and refracted P-wave horizons indicated by different color dashed lines as marked. **(A)** OBS1. **(B)** OBS3. **(C)** OBS4.

upper mantle. In both sections recorded by marine and land stations, we identified the Pn phase with an average apparent velocity of 8.1 km/s offshore and 8.5 km/s for the onshore region. The uppermost mantle discontinuities are primarily identified in the temporary land stations in the offset interval 135–170 km for $P_{M1}$ and 170–220 km of source–receiver offset distance for $P_{M2}$ (**Figure 5**).

A total of 1,617 arrivals were manually picked, defining the seismic phases identified throughout changes in amplitude or frequency content with an average estimated picking error of 108 ms. The best 2D velocity and interface structure model that fits the previous WAS data was obtained using the Zelt and Smith (1992) software package, applying forward modeling, travel time inversion, and synthetic seismograms.

# RESULTS

## Multichannel Seismic and Bathymetric Data

Along the JC098 cruise track, we obtained the bathymetric data around the Islas Marías Archipelago (**Figure 6**). The detailed bathymetry is shown in **Figure 6A**, whereas a 3D perspective is shown in **Figure 6B**. Based on the alignment of the submarine relief, we interpreted 88 structural lineaments and calculated a rose diagram from their azimuths. The detected lineaments could be either faults or fractures, with the former no longer being active, and provide the preferred structural trends of the region (**Figure 6C**). Two main tendencies were obtained: 1) between 020 and 050° and 2) between 290 and 320°. Both tendencies are spatially well defined. The first one is located west and northwest

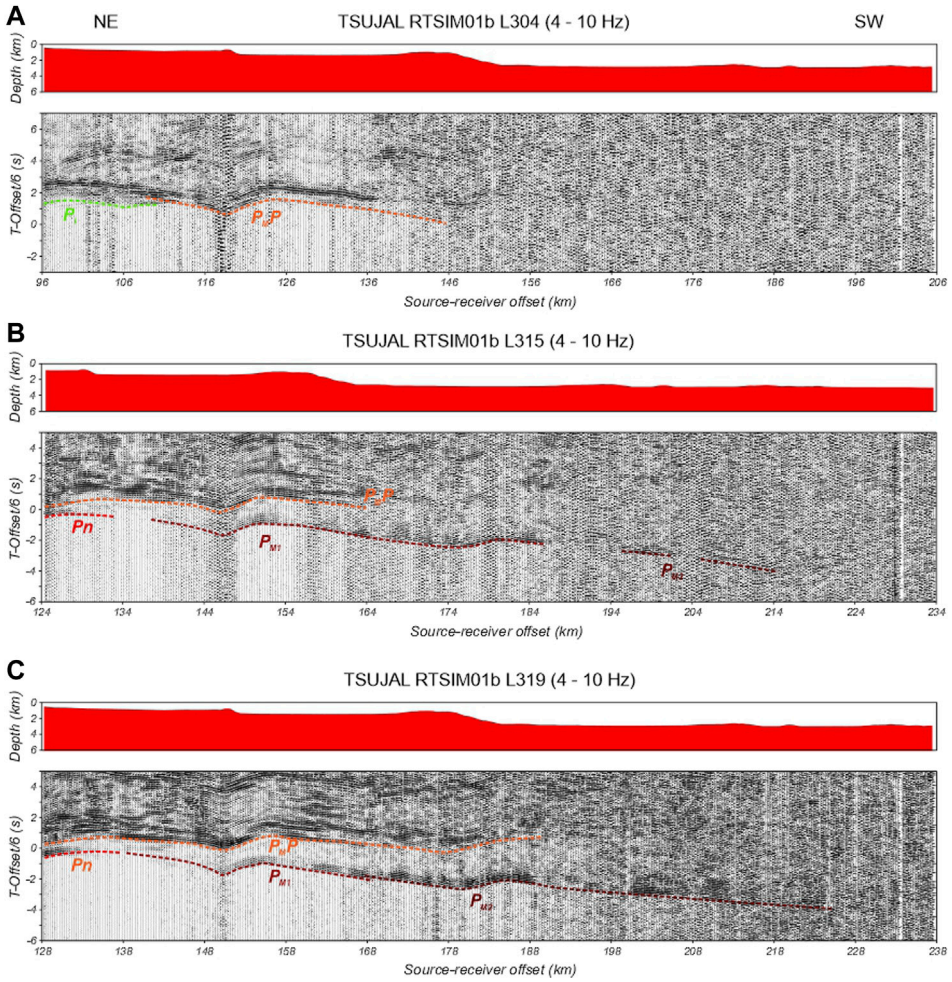


**FIGURE 5 |** Record sections of the terrestrial seismic stations recording the RTSIM01b seismic transect. Each panel shows the vertical component of the corresponding station with a reduced velocity of 8 km/s, 4–10 Hz band-pass filter applied, trace-normalized amplitudes, and interpreted reflected and refracted P-wave horizons indicated by different color dashed lines as marked. **(A)** L305. **(B)** L315. **(C)** L319.

of the archipelago, probably related to the RP oceanic crust. The second trend is placed at the southwestern and west sides of the islands within the transitional or continental crust of the NAP. In the west area of María Madre and María Magdalena islands, the structural lineaments have an ENE–WSW trend, which is oblique to the main trend from the adjacent areas.

The study of shallow structures to the north of Islas Marías Archipelago included the seismic transect TS09b (**Figure 7**), where we were able to identify two main seismic facies: the acoustic basement and different sedimentary packages distributed in five basins. Three of them are on the RP (Rivera, North Rivera, and Islas Marías basins) and two on the NAP (East Nayarit and San Blas troughs). From SW to NE, we found part of the Rivera Basin located between marks 0 and 15 km. It is infilled by up to 0.3 s of two-way travel time (twtt) of sediments. Toward the northeast, the North Rivera Basin is observed between 27 and 40 km with a thickness of 0.6 s approximately (**Figure 7**). In this basin, a structure rises from the acoustic reflector, which could be a volcano, as Dañobeitia et al. (2016) suggested, or a horst since it is fault-bounded. Moreover, the sedimentary horizons are subhorizontal on both sides of the horst.

The Islas Marías Basin corresponds to the largest basin identified along our MCS profile, extending between 45 and 77 km infilled by up to 1 s (twtt) of sediments. This basin is limited to the SW by the María Range and to the NE by the Islas Marías Escarpment (**Figures 6**, **7**). The sedimentary horizons are subparallel, and we identified a fault, not reported in previous studies, located to the SE of the Tres Marías Fault, crosscutting the lower part of the sedimentary infill. Located to the northeast side of the Islas Marías Escarpment, in the southernmost part of the East Nayarit Trough, we find the deepest basin between 95 and 110 km (15 km) infilled by up to 1.5 s sediments, bounded by the Oriental Nayarit Fault on the eastern edge of the trough. The sedimentary horizons have a splay array toward the Oriental Nayarit Fault. This feature is not observed in any other basins, suggesting that the Oriental Nayarit Fault could be active. The northeasternmost basin corresponds to the San Blas Trough with

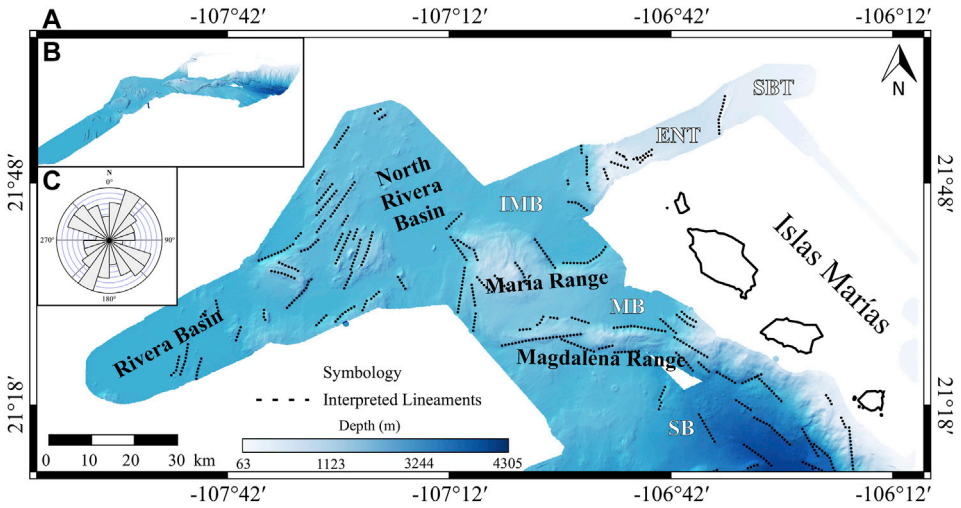


**FIGURE 6 |** Bathymetric map of the northern Islas Marías Archipelago. **(A)** Hypsometric map with interpreted surface lineaments. **(B)** 3D view of the hypsometric map. **(C)** Rose diagram showing two preferential tendencies. Black dotted lines represent the interpreted lineaments observed. Data obtained with an EM120 multibeam echosounder and processed with CARIS Hips and Sips (v.10.4). *Abbreviations*: *ENT*, East Nayarit Trough; *IMB*, Islas Marías Basin; *MB*, Magdalena Basin; *SB*, Sisvoc Basin; *SBT*, San Blas Trough.

a 3-km width and 0.5 s (twtt) of thickness whose sedimentary horizons are subhorizontal.

The basement and the acoustic basement along the profile showed extensional deformation, indicating a horst and graben array (**Figure 7**). In general, the sediment horizons are not deformed within the basins, suggesting that the extension finished before the sedimentation started. However, the splay array adjacent to the Oriental Nayarit Fault could be related to some activity along this fault. Along this transect, neither have we detected the presence of an accretion prism.

## WAS Data

The final P-wave velocity model corresponding to the wide-angle seismic profile RTSIM01b is an offshore–onshore transect of 240 km length, which characterizes the northern region of the Islas Marías Archipelago tectonically (**Figure 8**). The profile's origin was located at 24 km between the OBS1 and the shot situated farther to the southwest. We divide our model according to P-wave velocities in the upper crust and sedimentary cover, the crust (middle and lower), and the upper mantle.

The sedimentary cover along the RTSIM01b profile is characterized by three basins with different depths and velocities. From SW to NE, we found the North Rivera Basin is located from 25 to 53 km from the model origin with an average thickness of 1 km with a maximum value of ~2 km around OBS2 and a velocity range of 2.5–4.2 km/s. From 65 to 85 km of model distance (**Figure 8**), the Islas Marías Basin corresponds to the deepest basin across the transect with ~3 km of thickness, and for the upper crust or sediment layer, the average velocity is 3.6 km/s, and velocities from top to bottom vary between 2.5 and 4.6 km/s. The northeasternmost basin, the East Nayarit Trough, has a P-wave velocity interval of 2.8–3.8 km/s and 1.3 km thick. The middle crust below the sedimentary cover has a vertical velocity gradient of 5.3–5.8 km/s, with thickness increasing to the northeast direction, reaching 10 km depth in the continental region. Two layers comprise the lower crust, where the thickness of the oceanic crust is ~6 km, increasing toward the northeast up to 10 km thick, and P-wave velocity changes for the upper and lower layers are 6.3–6.5 km/s and 6.7–6.9 km/s, respectively. The Moho depth reaches 10 km depth in the Rivera Plate region, thickening up to 28 km in the continental part of the model with a velocity contrast of 6.9 km/s to 7.9 km/s (**Figure 8**). In the upper mantle, we characterized two seismic layers with increasing velocity at a depth from 8.1–8.4 km/s down to 40 km.

After adjusting travel times, we controlled by amplitudes using synthetic seismograms to get our final P-wave velocity model. This model reproduces 1,592 of 1,617 (98%) of observed travel times throughout the entire length of the profile (240 km). We determined the arrival-time fit quality ($\chi^2_N$) for each interpreted phase with the following values for $P_{S1}$ (0.4), $P_{S2}$ (0.3), $P_{S3}$ (1.2), $P_I$ (1.3), $P_{LC}P$ (0.7), $P_{LC}$ (0.9), $P_MP$ (2.4), and $P_n$ (0.9), and reflected P-phases observed in the mantle $P_{M1}$ (1.1) and $P_{M2}$ (0.8). Our final model is not far from the ideal case ($\chi^2_N = 1$), producing a $\chi^2_N$ of 1.6.

## DISCUSSION

The complex architecture of Rivera and North American plate interaction has been studied in the northern region of Islas Marías Archipelago. Previous bathymetric studies have been reported in this area, but few have been analyzed together with multichannel seismic profiles (Lizarralde et al., 2007 (**Figure 1**); Sutherland et al., 2012; Dañobeitia et al., 2016; Carrillo-de la Cruz et al., 2019). Most of the studies tried to establish the nature of the crust of the Islas Marías, which is still under debate. Lonsdale (1989) considered the Islas Marias to be a block of continental crust,

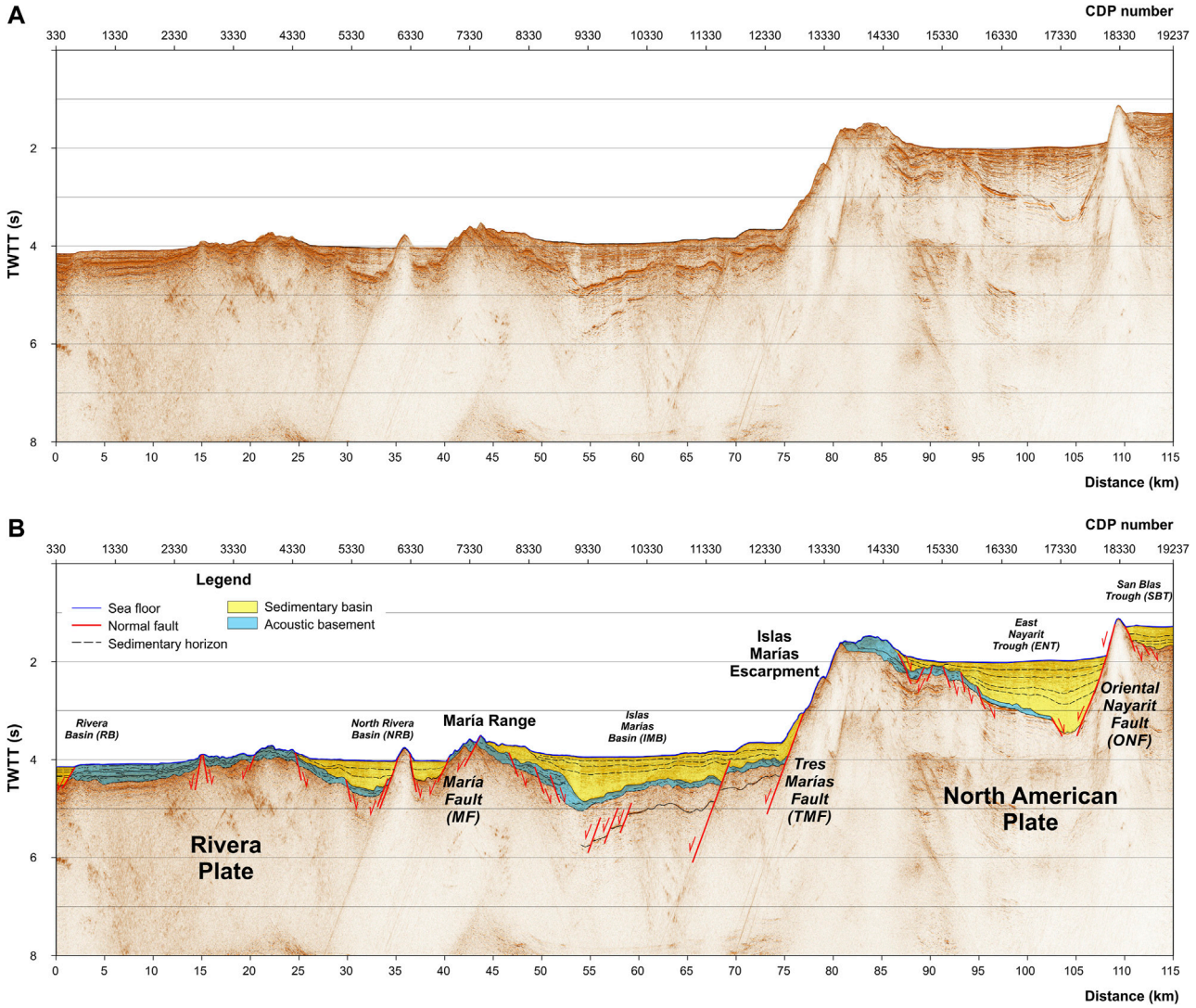


**FIGURE 7 |** TS09b Multichannel seismic profile, original **(A)** and interpreted **(B)**. *Abbreviations*: *CDP*, common depth point; *TWTT*, two-way travel time.

while Schaaf et al. (2015a, 2015b) suggested that in María Magdalena Island, the lithologic assemblage includes oceanic crust. Additionally, Lizarralde et al. (2007) suggested a transitional crust, while Carrillo-de la Cruz et al. (2019) suggested a thinned continental crust. Our structural interpretation of the bathymetric features (**Figure 6**) indicates two preferred orthogonal tendencies, whose location and orientation indicate deformation in the oceanic and thinned continental crust. The structural trend in the thinned continental crust (**Figure 6C**) ranges from 290 to 320°, which is subparallel to the 305° azimuth of the transform faults within the Gulf of California (Lonsdale, 1989). The orthogonal structures are associated with the Pacific-Rivera rise evolution (Lonsdale, 1989).

The seismic profiles (**Figure 2**) show a P-wave velocity distribution of< 6 km/s that corresponds to the continental crust that thins (**Figure 8A**) and extends west and NW of the Islas Marías Archipelago (Acosta-Hernández, 2017; Dañobeitia et al., 2016; Carrillo-de la Cruz, 2017; Madrigal-Ávalos, 2018; Carrillo-de la Cruz et al., 2019). The subduction of the RP beneath of NAP at the southern contact is clearly defined with a dip angle of 12–14° (Núñez et al., 2019), with the Middle America Trench acting as the morphological expression of the contact between them. To the NW of the Middle America trench, the only bathymetric expression of the contact between RP and NAP is the Islas Marías Escarpment. The Islas Marías Escarpment is a normal fault reported in its southern part by Carrillo-de la Cruz et al. (2019). Some authors establish the location of the active subduction west of our profile at ca. 15 Ma (Lonsdale, 1989) and ca. 12 Ma (Fletcher et al., 2007; Sutherland et al., 2012; Ferrari et al., 2013; Duque-Trujillo et al., 2014). The dip angle obtained from our P-wave velocity model is 7–10° (**Figure 8**), according to the values reported by Dañobeitia et al. (1997).

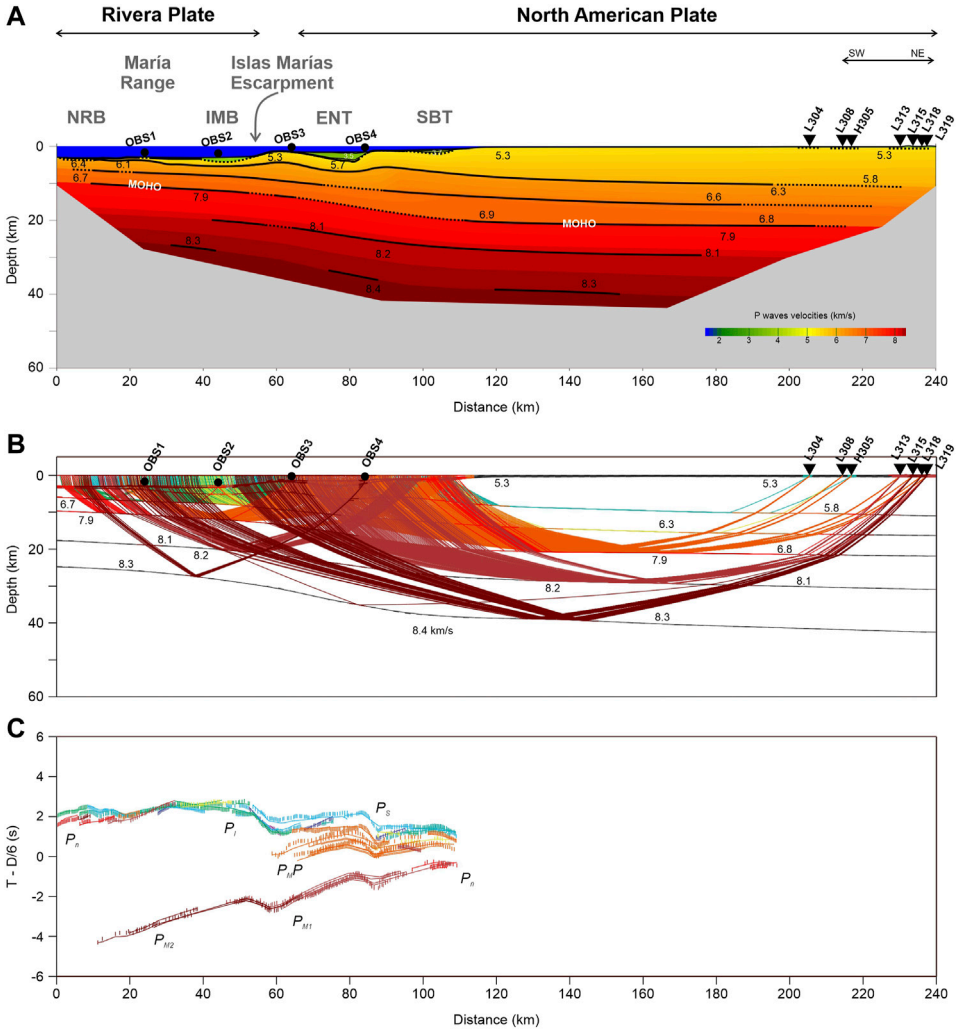


**FIGURE 8 | (A)** Final RTSIM01b P-wave velocity model across the septentrional region of Islas Marías Archipelago (Mexico). Black inverted triangles depict land stations and black circles the ocean-bottom seismometers (OBSs) of the TsuJal RTSIM01b seismic profile. Vertical and horizontal axes show depth below sea level and model position, respectively. The colored area is the region where ray tracing provides the velocity values. Layer boundaries are described by black lines, and the thick ones mark positions where rays are reflected, showing the well-defined areas. The gray zone represents the area not crossed by rays. **(B)** Ray tracing and velocity model with average velocities in km/s. **(C)** Comparison between observed (vertical bars) and calculated (lines) travel times. In all panels, distances refer to the velocity model origin. *Abbreviations*: *ENT*, East Nayarit Trough; *IMB*, Islas Marías Basin; *NRB*, North Rivera Basin; *SBT*, San Blas Trough.

Along the TS09b profile (**Figure 7**), the identified structures are normal faults in a horst and graben array. Most of these faults are currently inactive, as suggested by the subhorizontal sedimentary horizons within the basins and troughs, and the lack of seismicity. Moreover, the normal faults truncate at the surface of the acoustic basement and do not extend into the sedimentary deposits of the basins (**Figure 7B**). The only structure that could have some extant seismic activity is the Oriental Nayarit Fault since the sediments have a splay array that becomes horizontal at the top. No other fault seems to be active along the TS09b profile.

Furthermore, our study clarifies the nature of two structures previously not adequately located in the study region. One is the fault-bounded María Range (Escalona-Alcázar et al. submitted), which was previously mistakenly reported as the María Magdalena Rise (Dañobeitia et al., 2016). However, according to Lonsdale (1989), the María Magdalena Rise is situated to the west of the TS09b profile (**Figure 1**). The southern segment of the María Magdalena Rise (**Figure 1**) is not well defined in extension and length (Lonsdale, 1989), so this segment would intersect the TS09b/RTSIM01b profiles at ~15 km from its beginning. At this length, there is a tiny horst-like structure (~0.5 km wide) (**Figure 7B**), and, 7.5 km to the NE, another horst of ~ 4 km wide is located. It is not clear if one of them could be related to the southern segment of the María Magdalena Rise. The first ~ 30 km of the TS09b/RTSIM01b profiles have a pop-up–like shape, with a horst and graben array with no sediments in

between (**Figures 7**, **8**). The bathymetric heights at 15 and 35 km from the profile starting point were interpreted as a volcano (Dañobeitia et al., 2016). Nonetheless, they could be horst since the normal faults go from the surface to below the acoustic basement (**Figure 7A**); additionally, the P-wave velocities shown in **Figure 8A** are of < 6 km/s, typical of the continental crust.

Between Los Cabos and Puerto Vallarta, the faults were mainly oriented NE–SW due to extension at the mouth of the Gulf of California after ca. 6 Ma (Lonsdale, 1989; Stock and Hodges, 1989; Sutherland et al., 2012; Abera et al., 2016). At the same time, the extension expanded to the east, thinning the continental crust. In this scenario, the role of the María Magdalena Rise is unclear, but its orientation (azimuth 025°; Lonsdale, 1989) parallel to the Tamayo and Nayarit troughs, both adjacent to the mainland Mexico, as well as the structural trend of the María Madre Island (Escalona-Alcázar et al., 2014), suggests a wide area of extension. Around the TS09b profile, this extension could have ceased at ca. 3.5 Ma, when the María Magdalena Rise ended its activity (Lonsdale, 1989); then the sedimentary fill started.

## CONCLUSION

The analysis and interpretation of the study carried out in the northern region of the Islas Marías Archipelago provide new information about the structure and tectonics of the region, where it is possible to establish that Rivera Plate subduction under the North American Plate has likely ceased or never took place at this location. Nevertheless, we determined that the morphological expression of the northern limit of the Rivera Plate is the Islas Marías Escarpment.

The average crustal thickness for the Rivera Plate is ~10 km up to the Islas Marías Escarpment, estimating a depth of Moho deeper than 13 km in the collision zone between both tectonic plates. The crust of the North American Plate thickens from the Islas Marías Escarpment to the NE, up to reach 28 km.

From the MCS seismic image, it has been possible to characterize five sedimentary basins without deformation associated with compressional movements, where the absence of an accretionary prism is also relevant, demonstrating there is no active subduction process in this region. Sedimentary horizons in all basins are subhorizontal, suggesting that they were deposited after extension in the area ended during the late Pliocene. Only the Oriental Nayarit Fault could possibly support some seismic activity.

## DATA AVAILABILITY STATEMENT

The raw data supporting the conclusion of this article will be made available by the authors, without undue reservation.

## AUTHOR CONTRIBUTIONS

LM: data processing, investigation, and original draft writing. DN: conceptualization, methodology, investigation, data processing, data analysis, conclusions, and original draft writing. FE-A: data analysis, methodology, investigation, original draft writing, and conclusions. FN-C: conceptualization, funding acquisition, methodology, investigation, review, and editing.

## FUNDING

This research was mainly funded by Consejo Nacional de Ciencia y Tecnología (CONACYT)—FOMIXJal (2012-08-189963) (Mexico) and CGL (2011–29,474-C02–01) DGI Plan Nacional I + D + i (Spain) (TsuJal Project). LM was financially supported by a master fellowship from CONACyT with code 422412 and CVU704296.

## ACKNOWLEDGMENTS

We gratefully thank Wendy McCausland for her valuable comments and observations, including the English grammar revision, Juan Luis Carrillo-de la Cruz for his help with bathymetric figure and the suggestions of two reviewers that help to improve this article. The authors also truly appreciate the colaboration during the TsuJal project of NOC Cruise JC098, RRS James Cook (United Kingdom); COIP/COPO/UNAM J-GAP2013 Cruise (BO El Puma); Unidad de Tecnología Marina (Spain); Secretaría de Marina (Mexico) ARM Holzinger; Secretaría de Defensa Nacional (Mexico); Unidad Municipal de Protección Civil y Bomberos (Jalisco State, Mexico); Unidad Municipal de Protección Civil y Bomberos (Puerto Vallarta, Mexico); Unidad Estatal de Protección Civil y Bomberos (Nayarit State, Mexico); Reserva de la Biosfera (Islas Marías) CONANP-SEMARNAT; Secretaría de Relaciones Exteriores (Mexico); and Órgano Desconcentrado de Prevención y Readaptación Social de la SEGOP. Some figures were generated using the Generic Mapping Tools (GMT-6; Wessel et al., 2019).

## REFERENCES

Abera, R., van Wijk, J., and Axen, G. (2016). Formation of continental Fragments: The Tamayo Bank, Gulf of California, Mexico. *Geology* 44, 595–598. doi:10.1130/g38123.1

Acosta-Hernández, J. A. (2017). Estudio de la corteza en la zona Occidental de las islas Marías mediante métodos sísmicos. Master in Sciences Thesis. Puerto Vallarta, México: Universidad de Guadalajara, 113 (In Spanish).

Atwater, T. (1970). Implications of Plate Tectonics for the Cenozoic Tectonic Evolution of Western North America. *Geol. Soc. America Bull.* 81, 3513–3536. doi:10.1130/0016-7606(1970)81[3513:ioptft]2.0.co;2

Balestrieri, M. L., Ferrari, L., Bonini, M., Duque-Trujillo, J., Cerca, M., Moratti, G., et al. (2017). Onshore and Offshore Apatite Fission-Track Dating from the Southern Gulf of California: Insights into the Time-Space Evolution of the Rifting. *Tectonophysics* 719-720, 148–161. doi:10.1016/j.tecto.2017.05.012

Bandy, W. L., and Yan, C. Y. (1989). Present-day Rivera-Pacific and Rivera-Cocos Relative Plate Motions (Abstract). *EOS Trans AGU* 70, 1342.

Bandy, W., Mortera-Gutiérrez, C., Urrutia-Fucugauchi, J., and Hilde, T. W. C. (1995). The Subducted Rivera-Cocos Plate Boundary: Where Is it, what Is it, and what Is its Relationship to the Colima Rift? *Geophys. Res. Lett.* 22, 3075–3078. doi:10.1029/95gl03055

Bevis, M., and Isacks, B. L. (1984). Hypocentral Trend Surface Analysis: Probing the Geometry of Benioff Zones. *J. Geophys. Res.* 89, 6153–6170. doi:10.1029/jb089ib07p06153

Bohannon, R. G., and Parsons, T. (1995). Tectonic Implications of post-30 Ma Pacific and North American Relative Plate Motions. *Geol. Soc. Am. Bull.* 107, 937–0959. doi:10.1130/0016-7606(1995)107<0937:tiopmp>2.3.co;2

Bourgois, J., and Michaud, F. (1991). Active Fragmentation of the North America Plate at the Mexican Triple junction Area off Manzanillo. *Geo-Marine Lett.* 11, 59–65. doi:10.1007/bf02431030

Carrillo-de la Cruz, J. L., Núñez, D., Escalona-Alcázar, F. J., Núñez-Cornú, F. J., González-Fernández, A., Córdoba, D., et al. (2019). Tectonic Analysis of the Southern of María Cleofas Island from Bathymetric and Seismic Data. *Seismol. Res. Lett.* 90, 1748–1755.

Carrillo-de la Cruz, J. L. (2017). Análisis estructural de la zona adyacente y meridional de las islas Marías. Master Thesis in Sciences. Puerto Vallarta, México: Universidad de Guadalajara, 68 (In Spanish).

Cohen, J. K., and Stockwell, J. W., Jr. (2013). *CWP/SU: Seismic Un*x Release No. 43R4: An Open Source Software Package for Seismic Research and Processing*. Golden, CO: Center for Wave Phenomena, Colorado School of Mines.

Conrad, O., Bechtel, B., Bock, M., Dietrich, H., Fischer, E., Gerlitz, L., et al. (2015). System for Automated Geoscientific Analyses (SAGA) V. 2.1.4. *Geosci. Model. Dev.* 8, 1991–2007. doi:10.5194/gmd-8-1991-2015

Dañobeitia, J., Bartolomé, R., Prada, M., Nuñez-Cornú, F., Córdoba, D., Bandy, W. L., et al. (2016). Crustal Architecture at the Collision Zone between Rivera and North American Plates at the Jalisco Block: Tsujal projectGeodynamics of the Latin American Pacific Margin. *Pure Appl. Geophys.* 173, 3553–3573. doi:10.1007/978-3-319-51529-8_18

Dañobeitia, J. J., Cordoba, D., Delgado-Argote, L. A., Michaud, F., Bartolomé, R., Farran, M., et al. (1997). Expedition Gathers New Data on Crust beneath Mexican West Coast. *Eos Trans. AGU* 78, 565–572. doi:10.1029/97eo00338

Dean, B. W., and Drake, C. L. (1978). Focal Mechanism Solutions and Tectonics of the Middle America Arc. *J. Geology.* 86, 111–128. doi:10.1086/649659

DeMets, C., and Stein, S. (1990). Present-day Kinematics of the Rivera Plate and Implications for Tectonics in Southwestern Mexico. *J. Geophys. Res.* 95 (21), 21931–21948. doi:10.1029/jb095ib13p21931

Duque-Trujillo, J., Ferrari, L., Orozco-Esquivel, T., López-Martínez, M., Lonsdale, P., Bryan, S. E, et al. (2014). Timing of Rifting in the Southern Gulf of California and Its Conjugate Margins: Insight from the Plutonic Record. *Geol. Soc. Am. Bull.*127, 702–736. doi:10.1130/B31008.1

Eissler, H. K., and McNally, K. C. (1984). Seismicity and Tectonics of the Rivera Plate and Implications for the 1932 Jalisco, Mexico, Earthquake. *J. Geophys. Res.* 89, 4520–4530. doi:10.1029/jb089ib06p04520

Escalona-Alcázar, F. J., Núñez-Cornú, F. J., Córdoba-Barba, D., Ruiz-Martínez, V. C., and Escudero-Ayala, C. R. (2014). "El estilo de deformación de la isla María Madre: resultados preliminares," Unión Geofísica Mexicana Annual Meeting, 2014, Puerto Vallarta, Jalisco, November 2–7, 2014 (GEOS) 34, 104.

Escalona-Alcázar, J. F., Núñez-Cornú, J. F., Núñez, D., and Córdoba-Barba, D. A Bathymetric and Structural Analysis of the Islas Marías Archipelago, Mexico, and Surroundings. Submitted. *J. Struct. Geology.*

Ferrari, L., López-Martínez, M., Orozco-Esquivel, T., Bryan, S., Duque-Trujillo, J., Lonsdale, P., et al. (2013). Late Oligocene to Middle Miocene Rifting and Synextensional Magmatism in the Southwestern Sierra Madre Occidental, Mexico: The Beginning of the Gulf of California Rift. *Geosphere* 9, 1161–1200. doi:10.1130/GES00925.1

Ferrari, L. (1995). Miocene Shearing along the Northern Boundary of the Jalisco Block and the Opening of the Southern Gulf of California. *Geology* 23, 751–754. doi:10.1130/0091-7613(1995)023<0751:msatnb>2.3.co;2

Fletcher, J. M., Grove, M., Kimbrough, D., Lovera, O., and Gehrels, G. E. (2007). Ridge-trench Interactions and the Neogene Tectonic Evolution of the Magdalena Shelf and Southern Gulf of California: Insights from Detrital Zircon U-Pb Ages from the Magdalena Fan and Adjacent Areas. *Geol. Soc. America Bull.* 119, 1313–1336. doi:10.1130/b26067.1

Housh, T. B., Aranda-Gómez, J. J., and Luhr, J. F. (2010). Isla Isabel (Nayarit, México): Quaternary Alkalic Basalts with Mantle Xenoliths Erupted in the Mouth of the Gulf of California. *J. Volcanology Geothermal Res.* 197, 85–107. doi:10.1016/j.jvolgeores.2009.06.011

Lizarralde, D., Axen, G. J., Brown, H. E., Fletcher, J. M., González-Fernández, A., Harding, A. J., et al. (2007). Variation in Styles of Rifting in the Gulf of California. *Nature* 448, 466–469. doi:10.1038/nature06035

Lonsdale, P. (1989). "Geology and Tectonic History of the Gulf of California," in *The Eastern Pacific Ocean and Hawaii*. Editors E. L. Winterer, D. M. Hussong, and R. W. Decker (Boulder, CO: The Geology of North America), 499–521.

Lonsdale, P. (1991). "Structural Patterns of the Pacific Floor Offshore Peninsular California," in *The Gulf and Peninsular Provinces of the Californias*. Editors J. P. Dauphin and B. R. T. Simmoneit (Memoir: Am. Assoc. Petr. Geol.), 47, 87–125.

Madrigal, L. A. (2018). Estructura litosférica en la región septentrional de las islas Marías. Master in Sciences Thesis. Puerto Vallarta, México: Universidad de Guadalajara, 79 (In Spanish).

Mammerickx, J., and Klitgord, K. D. (1982). Northern East Pacific Rise: Evolution from 25 m.Y. B.P. To the Present. *J. Geophys. Res.* 87, 6751–6759. doi:10.1029/jb087ib08p06751

Nicholson, C., Sorlien, C. C., Atwater, T., Crowell, J. C., and Luyendyk, B. P. (1994). Microplate Capture, Rotation of the Western Transverse Ranges, and Initiation of the San Andreas Transform as a Low-Angle Fault System. *Geology* 22, 491–495. doi:10.1130/0091-7613(1994)022<0491:mcrotw>2.3.co;2

Nixon, G. T. (1982). The Relationship between Quaternary Volcanism in central Mexico and the Seismicity and Structure of Subducted Ocean Lithosphere. *Geol. Soc. America Bull.* 93, 514–523. doi:10.1130/0016-7606(1982)93<514:trbqvi>2.0.co;2

Núñez, D., Córdoba, D., Cotilla, M. O., and Pazos, A. (2016). Modeling the Crust and Upper Mantle in Northern Beata ridge (CARIBE NORTE Project). *Pure Appl. Geophys.* 173, 1639–1661. doi:10.1007/s00024-015-1180-0

Núñez, D., Núñez-Cornú, F. J., Escalona-Alcázar, F. J., Córdoba, D., López-Ortiz, J. Y., Carrillo-de la Cruz, J. L., et al. (2019). Seismic Structure of the Southern Rivera Plate and Jalisco Block Subduction Zone. *Seismol. Res. Lett.* 90, 1756–1766. doi:10.1785/0220180399

Núñez-Cornú, F. J., Córdoba, D., Dañobeitia, J. J., Bandy, W. L., Ortiz-Figueroa, M., Bartolomé, R., et al. (2016). Geophysical Studies across Rivera Plate and Jalisco Block, Mexico: TsuJal Project. *Seismol. Res. Lett.* 87, 59–72. doi:10.1785/0220150144

Páramo, P., Holbrook, W. S., Brown, H. E., Lizarralde, D., Fletcher, J., Umhoefer, P., et al. (2008). Seismic Structure of the Southern Gulf of California from Los Cabos Block to the East Pacific Rise. *J. Geophys. Res.* 113, B03307. doi:10.1029/2007JB005113

Pompa-Mera, V., Schaaf, P., Hernández-Treviño, T., Weber, B., Solís-Pichardo, G., Villanueva-Lascuraín, D., et al. (2013). Geology, Geochronology, and Geochemistry of Isla María Madre, Nayarit, Mexico. *Rev. Mex. Cienc. Geol.* 30, 1–23.

Ponce, L., Gaulon, R., Suárez, G., and Lomas, E. (1992). Geometry and State of Stress of the Downgoing Cocos Plate in the Isthmus of Tehuantepec, Mexico. *Geophys. Res. Lett.* 19, 773–776. doi:10.1029/92gl00437

Schaaf, P., Böhnel, H., Weber, B., Hernández-Treviño, T., Solís-Pichardo, G., Pompa-Mera, V., et al. (2015b). "Magmatic Activity at Islas Marías Archipelago: Key Events for Understanding Gulf of California Tectonics," in 26th IUGG General Assembly, Pague, Czech Republic, June 22–July 2, 2015. (. IAVCEI, 2015b ) VS-24, IUGG-5302.

Schaaf, P., Villanueva, D., Hernández, T., Böhnel, H., Solís-Pichardo, G., and Weber, B. (2015a). Actividades magmáticas en el archipiélago de las islas Marías: litósfera oceánica versus componentes de un arco magmático Cretácico-Jurásico. *GEOS* 35, 209.

Stock, J. M., and Hodges, K. V. (1989). Pre-Pliocene Extension Around the Gulf of California and the Transfer of Baja California to the Pacific Plate. *Tectonics* 8, 99–115. doi:10.1029/tc008i001p00099

Stock, J. M., and Lee, J. (1994). Do microplates in Subduction Zones Leave a Geological Record? *Tectonics* 13, 1472–1487. doi:10.1029/94tc01808

Stoiber, R. E., and Carr, M. J. (1973). Quaternary Volcanic and Tectonic Segmentation of Central America. *Bull. Volcanol.* 37, 304–325. doi:10.1007/bf02597631

Sutherland, F. H., Kent, G. M., Harding, A. J., Umhoefer, P. J., Driscoll, N. W., Lizarralde, D., et al. (2012). Middle Miocene to Early Pliocene Oblique Extension in the Southern Gulf of California. *Geosphere* 8, 752–770. doi:10.1130/ges00770.1

Wessel, P., Luis, J. F., Uieda, L., Scharroo, R., Wobbe, F., Smith, W. H. F., et al. (2019). The Generic Mapping Tools Version 6. *Geochem. Geophys. Geosyst.* 20, 5556–5564. doi:10.1029/2019GC008515

Zelt, C. A., and Smith, R. B. (1992). Seismic Traveltime Inversion for 2-D Crustal Velocity Structure. *Geophys. J. Int.* 108, 16–34. doi:10.1111/j.1365-246x.1992.tb00836.x

**Conflict of Interest:** The authors declare that the research was conducted in the absence of any commercial or financial relationships that could be construed as a potential conflict of interest.

frontiers in Earth Science

ORIGINAL RESEARCH
published: 21 June 2021
doi: 10.3389/feart.2021.679958

# Observations of Earth's Normal Modes on Broadband Ocean Bottom Seismometers

*Gabi Laske* *

*Cecil H. and Ida M. Green Institute of Geophysics and Planetary Physics, Scripps Institution of Oceanography, UC San Diego, La Jolla, CA, United States*

It is generally thought that high noise levels in the oceans inhibit the observation of long-period earthquake signals such as Earth's normal modes on ocean bottom seismometers (OBSs). Here, we document the observation of Earth's gravest modes at periods longer than 500 s (or frequencies below 2 mHz). We start with our own 2005–2007 Plume-Lithosphere-Undersea-Mantle Experiment (PLUME) near Hawaii that deployed a large number of broadband OBSs for the first time. We collected high-quality normal mode spectra for the great November 15, 2006 Kuril Islands earthquake on multiple OBSs. The random deployment of instruments from different OBS groups allows a direct comparison between different broadband seismometers. For this event, mode ${}_0S_6$ (1.038 mHz) consistently rises above the background noise at all OBSs that had a Nanometrics Trillium T-240 broadband seismometer. We also report observations of other deployments in the Pacific ocean that involved instruments of the U.S. OBS Instrument Pool (OBSIP) where we observe even mode ${}_0S_4$ (0.647 mHz). Earth's normal modes were never the initial target of any OBS deployment, nor was any other ultra-low-frequency signal. However, given the high costs of an OBS campaign, the fact that data are openly available to future investigators not involved in the campaign, and the fact that seismology is evolving to investigate ever-new signals, this paper makes the case that the investment in a high-quality seismic sensor may be a wise one, even for a free-fall OBS.

**Keywords: seismology, instrumentation, ocean bottom seismometers, broadband seismology, earth's normal modes, earth structure**

OPEN ACCESS

***Edited by:***
*Charlotte A. Rowe, Los Alamos National Laboratory (DOE), United States*

***Reviewed by:***
*Arwen Deuss, Utrecht University, Netherlands*
*Lapo Boschi, University of Padua, Italy*

***Correspondence:**
*Gabi Laske*
*glaske@ucsd.edu*

***Specialty section:***
*This article was submitted to Solid Earth Geophysics, a section of the journal Frontiers in Earth Science*

***Received:*** *12 March 2021*
***Accepted:*** *07 June 2021*
***Published:*** *21 June 2021*

***Citation:***
*Laske G (2021) Observations of Earth's Normal Modes on Broadband Ocean Bottom Seismometers. Front. Earth Sci. 9:679958. doi: 10.3389/feart.2021.679958*

## 1 INTRODUCTION

Ocean bottom seismometers (OBSs) that record seismic signals on the ocean floor after a free-fall deployment are subject to tilt noise from deep-ocean currents, and there is ample evidence that burial can alleviate the noise problem (e.g. Collins et al., 2001). However, burial of an OBS is time consuming and usually requires remotely operated vehicles (e.g. Dziewonski et al., 1991; Montagner et al., 1994; Romanowicz et al., 2006). Burial is therefore cost-prohibitive when conducting campaign-style deployments of multiple OBSs, as opposed to installing a single permanent ocean floor observatory. Instrument tilt affects the horizontal seismometer components particularly strongly. This study therefore concentrates on observations on the less-affected vertical components.

It is generally thought that the noise from ocean infragravity waves inhibits meaningful observations of seismic signal at periods longer than 80 s or so. Yet, some island stations of the

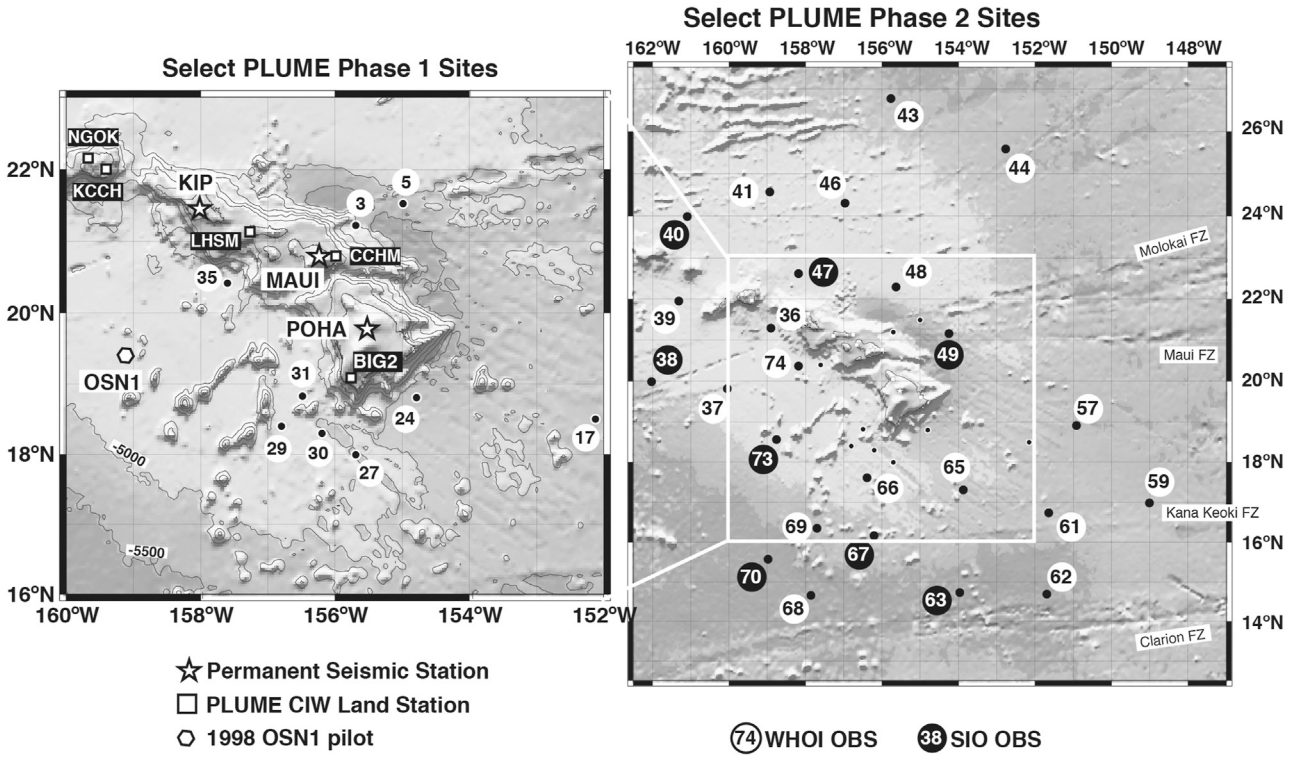


**FIGURE 1 |** Site locations of the two deployment phases of the Hawaiian PLUME project. Phase 1 operated from January 2005 through January 2006 and phase 2 from April 2006 through June 2007. Only the sites discussed in this paper are shown. See Laske et al. (2009) for complete station and deployment history. The OSN1 label marks the location of the 1998 OSN pilot deployment (Dziewonski et al., 1991). Also shown are GSN observatory stations: KIP (Kipapa, Oahu) is jointly operated by GEOSCOPE and the U.S. Geological Survey (USGS). The primary instrument is a Wielandt-Streckeisen STS-1. The primary sensor at POHA (Pohakuloa, Hawaii), operated by the USGS, is a Teledyne-Geotech KS54000 borehole seismometer. MAUI was operated by GEOFON and featured a Wielandt-Streckeisen STS-2. The primary sensor at USGS-run MIDW (Midway Island, 28.22°N, 177.37°W, not shown), is a STS-2.

Global Seismographic Network (GSN) in the open ocean, including station KIP, Kipapa in Hawaii (operated jointly by the US Geological Survey and the French GEOSCOPE), exhibit perhaps surprisingly high signal levels, even at extremely low frequencies. The question then becomes whether at least some deep-ocean environments far away from long coastlines allow the observation of ultra-low frequency seismic signal as well.

The deployment of broadband ocean bottom seismometers (OBSs) for the Hawaiian Plume Lithosphere Undersea Mantle Experiment (PLUME) in 2005–2007 (**Figure 1**) provided one of the first opportunities to observe Earth's normal modes on OBSs to unprecedented signal levels (Laske et al., 2007), to frequencies below 1 mHz. The collocation of temporary and permanent seismic stations on the Hawaiian Islands provides a unique opportunity to assess and quantify the quality of these observations. Subsequent analyses of other OBS deployments in the Pacific ocean involving instruments of the U.S. OBS Instrument Pool (OBSIP) provide additional high-quality normal-mode spectra.

Such spectra are typically observed on broadband seismometers that have a corner period of 120 s or longer. But some spectra recorded on a Nanometrics Trillium T-40 (corner period 40 s) for the NoMelt experiment to the far south of Hawaii (Lin et al., 2016) and the ALBACORE experiment off-shore southern California (Reeves et al., 2015) also are of astonishing quality. Earth's normal modes were never the initial target of any OBS deployment, nor was any other ultra-low-frequency signal. However, given the high costs of an OBS campaign, the fact that data are openly available to future investigators not involved in the campaign, and the fact that seismology is evolving to investigate ever-new signals, this paper makes the case that the investment in a high-quality seismic sensor may be a wise one, even for a free-fall OBS.

In the following sections, we first introduce general instrumentation requirements for observing Earth's normal modes. We then elaborate on our PLUME deployments near Hawaii and place it in context with the previous OSN pilot experiment (Dziewonski et al., 1991). A detailed comparison between our OBS observations on one hand but also in the context of land installations on the other documents the consistently high quality of ultra-low frequency normal mode spectra, particularly those on Nanometrics Trillium T-240 seismometers. A note of caution hereby addresses the contamination by low-frequency transients during earlier deployments of Scripps Institution of Oceanography (SIO) instruments. We also discuss spectra collected on more recent

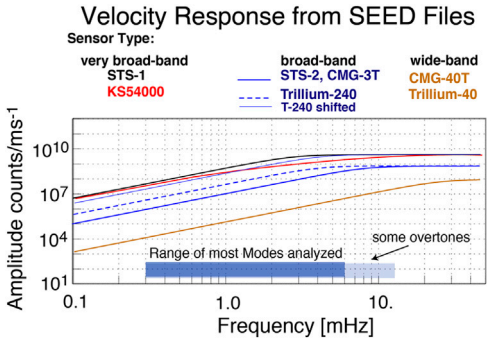


**FIGURE 2 |** Long-period protion of the velocity response of sensors used in broadband seismology. The Wielandt Streckeisen STS-1 vault seismometer (corner period 360 s) and the Teledyne-Geotech KS54000 borehole seismometer are considered very broadband sensors, while the STS-2 and the Güralp CMG-3T (corner period 120 s) are broadband sensors. The Nanometrics Trillium T-240 (corner period 240 s) falls in between. Sensors with a corner period of 40 s (e.g. the Trillium T-40 or the CMG-40T) are wideband sensors (often mislabelled as broadband). For better comparison of the low-frequency roll-off of the Trillium 240 with that of the STS-1, it is also plotted with a thin blue line and shifted to match the STS-1 response at 10 mHz.

deployments such as the NoMelt experiment (Lin et al., 2016), the ALBACORE deployment (Reeves et al., 2015) and a short test deployment off-shore southern California (Berger et al., 2016). All of these used SIO instruments but do not have the 'transients problem'.

# 2 REQUIREMENTS TO OBSERVE EARTH'S NORMAL MODES: INSTRUMENTATION AND INSTALLATION

## 2.1 Instrumentation

Of all seismic data, Earth's free oscillations (normal modes) probably pose the highest demands on seismometry. To be recorded with high fidelity, noise levels in a seismic record have to stay consistently low for several days, sometimes weeks, without interruption or the interference from other seismic events. Normal mode seismometry therefore relies on the records of observatory instruments such as those of the GSN, GEOSCOPE (the French global network) or GEOFON (the German global network). The instruments of these permanent installations are typically located in a sheltered environment such as a vault, an abandoned mine or a borehole. A very-broadband sensor, such as a Wielandt-Streckeisen STS-1 vault seismometer or a Teledyne-Geotech KS54000 borehole seismometer, is needed to record Earth's normal modes at frequencies below 1 mHz with high fidelity (**Figure 2**). The broadband Wielandt-Streckeisen STS-2 and the Güralp CMT-3T seismometers that are often used in temporary deployments or regional seismic networks are typically not considered to be in this category. However, the GEOFON and German Regional Seismic Network (GRSN) network operators achieved a remarkable noise reduction on their STS-2 installations by thermally insulating the sensor with a thermal blanket inside an aluminum bell jar (Hanka, 2000). This noise reduction consistently allows the observation of low-frequency normal modes after large earthquakes down to mode ${}_0S_4$ (0.647 mHz).

Ocean islands are usually thought of as being noisy sites for the GSN. In the microseism band between 15 and 5 s, noise levels can easily be 10–20 dB higher than at stations in the interiors of continents. On the other hand, and somewhat curiously, several Pacific island sites are some of the world's quietest to record vertical ground motion in the free oscillation band at periods longer than 200 s (frequencies below 5 mHz). This includes station KIP (Kipapa, on Oahu; Hawaii) but also GEOSCOPE stationPPT (Pamatai, Papete; Tahiti). **Supplementary Figure S1** shows some examples of noise curves published in the Federation of Digital Seismic Network (FDSN) station book. Station KIP compares favorably to remote installations in the interiors of continents even for the horizontal components. In this paper, we concentrate our discussion on vertical components, for two reasons. The vertical components are usually the quieter components in general. Secondly, the normal mode spectra of vertical components are easier to assess because of the general absence of toroidal modes as they have only horizontal motion, and so spectral peaks are farther apart on the vertical component than on the horizontal components that record both spheroidal and toroidal modes.

## 2.2 Benchmark Earthquake–The 1998 Balleny Island Earthquake at Ocean Seismic Network1

On the ocean floor, long-period noise levels are reported to be considerably higher than on land as a consequence of exposure to wind-generated infragravity waves (Webb, 1998). It has therefore been expected that free oscillations can only be observed on buried sensors. Even then, burial does not guarantee success. For example, the buried and cabled ocean bottom station H2O, halfway between Hawaii and the coast of Oregon was operational between 1999 and 2003 and was witness to several large earthquakes. But we did not obtain any convincing and consistent normal mode spectrum. The exact sensor type was a subject of long debate but may not have been a broadband sensor after all.

Just before H2O went online, the Ocean Seismic Network (OSN) initiative deployed a KS54000 very-broadband borehole sensor at ODP site 843B south of Oahu, Hawaii, about 250 m below the seafloor (Dziewonski et al., 1991; Vernon et al., 1998). During this roughly 4-months long pilot deployment, OSN1, the great $M_S$ = 8.0; $M_0 = 17.0 \times 10^{20}$ Nm Balleny Island earthquake occurred on March 25, 1998. This event was perhaps the first great earthquake for which free oscillations were observed on the ocean floor (**Figure 3**), and we use it as benchmark for normal mode observations during the later PLUME deployments.

To keep the data processing consistent between deployments and between earthquakes, we perform minimal data editing which may include the interactive removal of single-point spikes or similar. We apply bandpass convolution filters with a

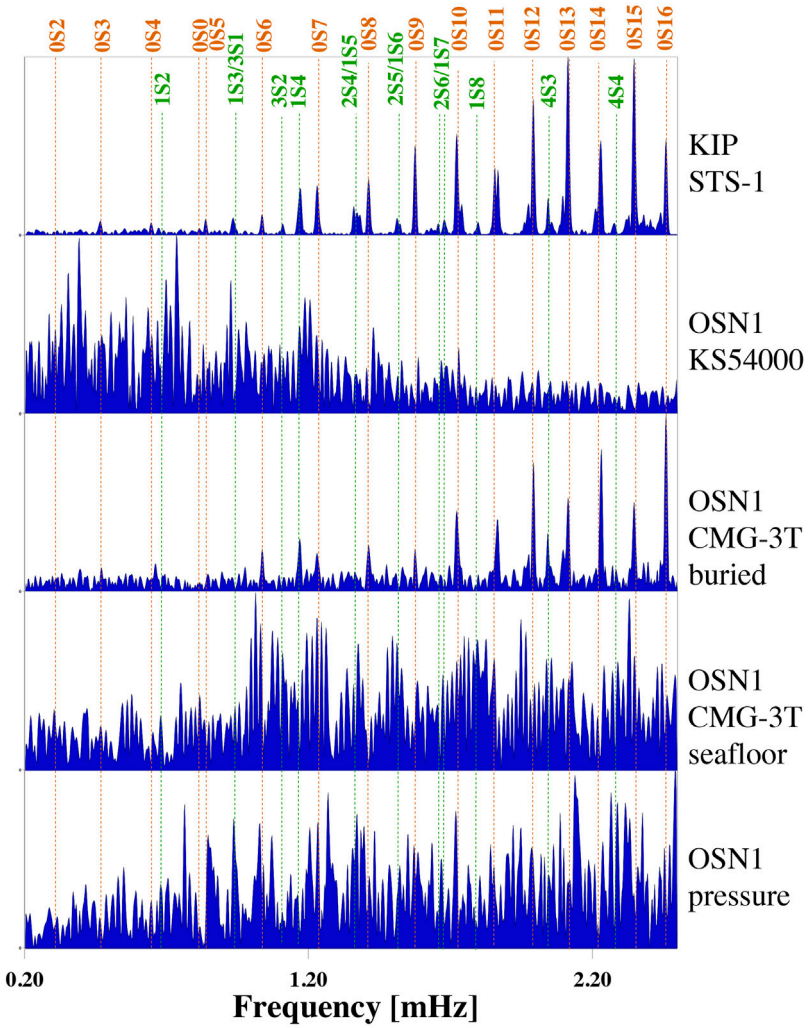


**FIGURE 3 |** Raw vertical-component spectra for the March 25, 1998 Balleny Island earthquake of 50-hour long segments, starting 1.5 h after the source time. Hanning tapers are applied. Shown are spectra for GSN station KIP and the ocean bottom sensors deployed at OSN1(**Figure 1**). Comments below the station name denote the seismic sensor. At OSN1, pressure was recorded on a Cox-Webb differential pressure gauge (DPG Cox et al., 1984). In the frequency range shown here, corrections for respective instrument responses (**Figure 2**) change the relative shape of the spectra only marginally, but modes and background noise at frequencies below 1 mHz would be enhanced. The spectra are self-normalized for optimal display. Orange lines mark fundamental mode frequencies for model PREM(Dziewonski and Anderson, 1981), while green lines mark overtones.

40-dB lowpass roll-off between 40 and 50 mHz and a gently decaying highpass with a roll-off of 20 dB between 0 and 0.5 mHz to suppress tidal signals. A Hanning taper is applied before computing the spectra. But we do not correct for the instrument response, nor do we perform any noise-optimization measures such as the correction for tilt and/or pressure (Webb and Crawford, 1999; Crawford and Webb, 2000; Bell et al., 2015).

At stations on land, normal modes can be observed very clearly down to mode ${}_0S_3$ (0.469 mHz) at the quietest GSN stations, including KIP (**Figure 3**). No other station nearby was available or recorded this event with high fidelity. Not shown, Rayleigh wave train $R_1$ is discernible in the STS-2 record at XMAS (Kiritimati Island, Kiribati), about 2,600 km from Hawaii, but significant long-period noise does not allow us to identify any modes. Station JOHN (Johnston Atoll, operated by the USGS) started operation not until July 1998 and other stations started even later: MAUI in June 1999, POHA (Pohakuloa, Hawaii) in November 1999 and MIDW (Midway Island) in June 2002.

At OSN1, the spectrum for the KS54000 fails to show Earth's normal modes. Unfortunately, long-period convection of fluids in

the borehole caused long-period noise (Vernon et al., 1998) to levels too high for standard normal-mode observations that involve time series lengths of several days. For extremely short windows (e.g. 20 h), some isolated modes such as ${}_0S_{30}$ at 3.815 mHz appear to emerge barely above the background noise, but frequency measurements are not very robust, and the fact that neighboring modes do not appear makes these observations suspect. OSN1 also operated two broadband OBSs (BBOBSs). One was placed on the seafloor, while the other one was buried about half a meter using a remotely operated vehicle (ROV) (Collins et al., 2001). The buried CMG-3T had noise levels low enough for clear normal mode observations down to mode ${}_0S_6$ (1.038 mHz) (**Figure 3**). However, the overall noise level was significantly higher than at KIP which hampers the identification of some overtones between the fundamental modes at frequencies near or below 2 mHz, such as modes ${}_4S_4$ and ${}_1S_8$. Neither the seafloor BBOBS nor its pressure sensor (a Cox-Webb differential pressure gauge, DPG; Cox et al., 1984) produced a consistent normal-mode spectrum. While some spectral lines for both may coincide with mode identifiers (e.g. $\frac{{}_1S_3}{S_1}$, ${}_0S_{10}$ for pressure), we very much doubt that these are actual normal mode peaks.

Events of the size of the Balleny Island earthquake occur perhaps every other year. The last previous event with a similar moment was the February 17, 1996 Irian Jaya earthquake ($M_0 = 24.1 \times 10^{20}$ Nm). The Balleny Island event was surpassed in moment not until the June 23, 2001 Arequipa, Peru earthquake ($M_0 = 46.7 \times 10^{20}$ Nm) though a smaller, tsunami-genic earthquake ($M_0 = 12.4 \times 10^{20}$ Nm) occurred in New Ireland on November 16, 2000. The main point here is that a year-long temporary deployment may or may not capture such a large earthquake, perhaps more often than not missing it. Smaller events occur more frequently. However, since the Balleny Island earthquake produced observable low-frequency normal modes only on the buried OBS, perhaps expectations were justifiably low for Earth's normal modes to be observed on free-fall OBSs. This has proven too pessimistic, as the following examples will show.

# 3 THE HAWAIIAN PLUME-LITHOSPHERE-UNDERSEA-MANTLE EXPERIMENT PROJECT

In 2005, we launched a large broadband OBS network to investigate the fine-scale seismic structure of the crust and mantle beneath Hawaii (**Figure 1**). The PLUME OBS network included 73 sites that were occupied in two phases by 74 instruments (Laske et al., 2009). These instruments were provided by the two OBSIP institutional operators at the time: SIO and Woods Hole Oceanographic Institution (WHOI). The Carnegie Institution of Washington (CIW) operated ten temporary land stations for the entire duration of the field campaign. An inner OBS network of 35 sites recorded continuously from January 2005 through January 2006 (phase 1). An outer OBS network of 38 sites recorded from April 2006 through June 2007 (phase 2). During both deployment phases, the WHOI instruments were equipped with Güralp CMG-3T sensors. PLUME was the first experiment to deploy these OBSs in large numbers. The SIO instruments featured a Nanometrics Trillium T-40 wideband sensor during phase 1 and a Trillium T-240 broadband sensor during phase 2. All instruments included a Cox-Webb DPG (Cox et al., 1984). Several instruments were lost, some instruments did not record useful seismic signal, and some sites were excluded for other reasons (e.g., some phase 1 SIO OBSs recorded only on horizontal components). **Figure 1** shows only the sites discussed in this paper.

During the two PLUME OBS deployments, 11 great earthquakes with scalar seismic moments $M_0 = 2.0 \times 10^{20}$ Nm or larger occurred (**Supplementary Table S1**) each of which excited Earth's free oscillations. Five of these events had a scalar seismic moment similar or larger than the 1998 Balleny Island event, with one of them during phase 1. With a scalar seismic moment $M_0 = 111 \times 10^{20}$ Nm, the great March 28, 2005 Sumatra-Andaman earthquake, was by far the largest earthquake. Accordingly, normal modes can be observed to frequencies far below 1 mHz, even on the OBSs (**Figure 4**). But our collection also includes spectra for a much smaller event. The June 13, 2005 Tarapaqa, Chile earthquake had a scalar seismic moment $M_0 = 5.14 \times 10^{20}$ Nm and was more than three times smaller than the 1998 Balleny Island event.

During the phase 2 deployment, four of the recorded events were very large, with scalar seismic moments greater than $10 \times 10^{20}$ Nm. The largest was the tsunami-genic Kuril Islands earthquake on November 15, 2006. On the vertical components, the signal-to-noise ratio (SNR) observed in the normal mode band below 10 mHz is surprisingly high on the PLUME OBSs (Laske et al., 2007). In fact, for the 2006 Kuril Islands event, it is clearly higher than on those of the PLUME land stations though not as high as on those of observatory stations KIP, POHA and MIDW.

## 3.1 The March 28, 2005 Sumatra Earthquake

The March 28, 2005 Sumatra earthquake was an aftershock of the devastating, tsunami-genic December 26, 2004 Sumatra-Andaman earthquake. With a scalar seismic moment $M_0 = 111 \times 10^{20}$ Nm, this event was 6.5 times larger than the 1998 Balleny Island event. We therefore hoped that SNRs may be high enough to observe normal modes on unburied seismometers. At land station KIP, the free oscillation spectrum is of extremely high quality (**Figure 4A**). Mode ${}_0S_3$ (0.469 mHz) that is observed only for the largest earthquakes can be identify clearly (in the STS-1 record) and several other very quiet GSN stations. AT KIP, even the STS-2 record has SNRs high enough to observe mode ${}_0S_4$ (0.647 mHz). The KS5400 at POHA did not record any seismic signals at the time, so no modes can be seen in the spectrum. At frequencies below 2 mHz, the STS-2 record at this location is significantly noisier than that at KIP but mode pair $\frac{{}_1S_3}{S_1}$ at 0.94 mHz may rise above the noise. At station MIDW, the first four surface wave trains can be observed during the first 6 h after the event before the records are severely contaminated by secondary signals. This is too short to make any meaningful mode measurements.

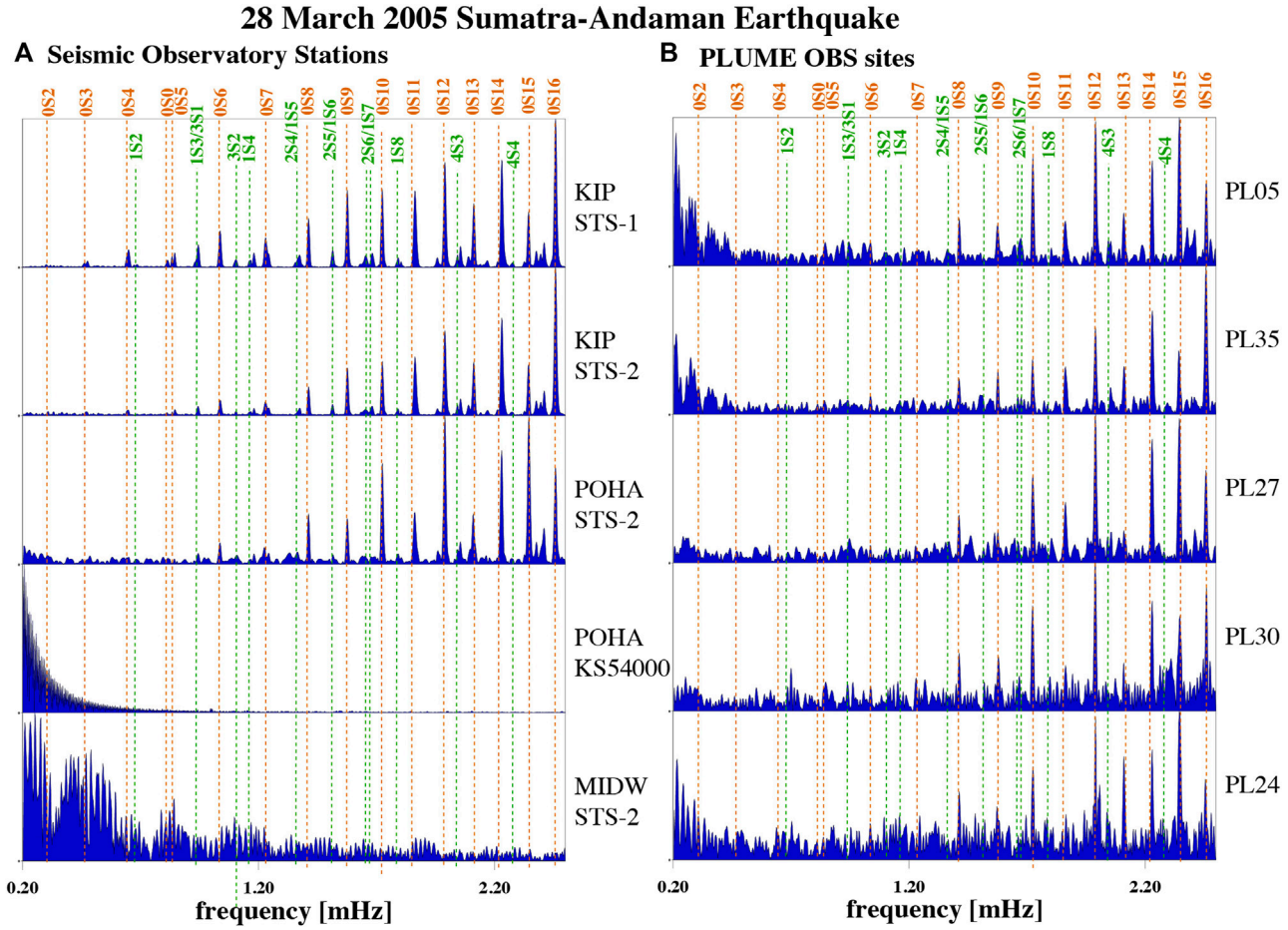


**FIGURE 4 |** Normalized raw vertical-component spectra for the March 28, 2005 Sumatra-Andaman earthquake of 50-hour long segments, starting 1.5 h after the event time. **(A)** Spectra at stations of permanent observatory stations KIP, POHA and MIDW. The sensor type is listed below the stations name. Stations KIP and POHA featured two sensors, where the secondary sensor (location code 10) was a STS-2 broadband sensor. **(B)** Spectra at five OBS sites with the best signal-to-noise ratio. The sensor was a Güralp CMG-3T sensor. See **Supplementary Table S1** in the supplement for earthquake parameters.

The quality of spectra recorded on the PLUME OBSs varies greatly, but mode ${}_0S_8$ (1.412 mHz) clearly stands out against the background noise, and at some sites we may even observe mode ${}_0S_6$ (1.038 mHz) (e.g. PL35 in **Figure 4B**). The figure shows the best five spectra but there are several others of nearly the same quality. Noise levels in these spectra are higher than those of the STS-2 at land station POHA. However, compared to the 1998 Balleny Islands spectrum of the unburied BBOBS at OSN1, we are not only able to identify normal modes in the PLUME OBS spectra, but also to very low frequencies below 1.5 mHz. To our knowledge, these are the first ever mode observations on OBSs at such low frequencies. Inspection of the DPG records is discouraging as we cannot consistently identify large groups of modes in any of the spectra.

## 3.2 The June 13, 2005 Tarapaca, Northern Chile Earthquake

Events as large as the March 28, 2005 Sumatra event occur perhaps less than once a decade. High-quality spectra for this event therefore should be expected, and a favorable comparison with the 1998 Balleny Island may not be representative of the high quality of spectra collected for the PLUME project. We therefore also inspect smaller events. **Figure 5** shows the spectra of the $M_S = 7.9; M_0 = 5.14 \times 10^{20}$ Nm June 13, 2005 Tarapaca, Northern Chile earthquake that was more than 3 times smaller than the 1998 Balleny Island event. This earthquake was followed about 28 h later by a $M_S = 7.0$ event in the Gorda Plate off the coast of California. Even though the scalar seismic moment was less that $1 \times 10^{20}$ Nm, this event produced waveforms at Hawaiian stations so that spectra for the Tarapaca event have to be calculated for shorter time windows, and we would normally not include this event in our normal mode analyses. But to prove the point of observability, the STS-1 spectrum at KIP clearly shows mode ${}_0S_5$ (0.840 mHz) against the background noise. Robust measurements may also be possible for mode ${}_0S_4$ (0.649 mHz). The STS-2 spectrum as well as the spectra at POHA show modes down to ${}_0S_6$ (1.038 mHz), while modes down to ${}_0S_8$ (1.413 mHz) can be discerned at station MIDW. The spectra at the PLUME OBSs are considerably noisier but some instruments clearly show mode ${}_0S_{13}$ (2.112 mHz) consistently

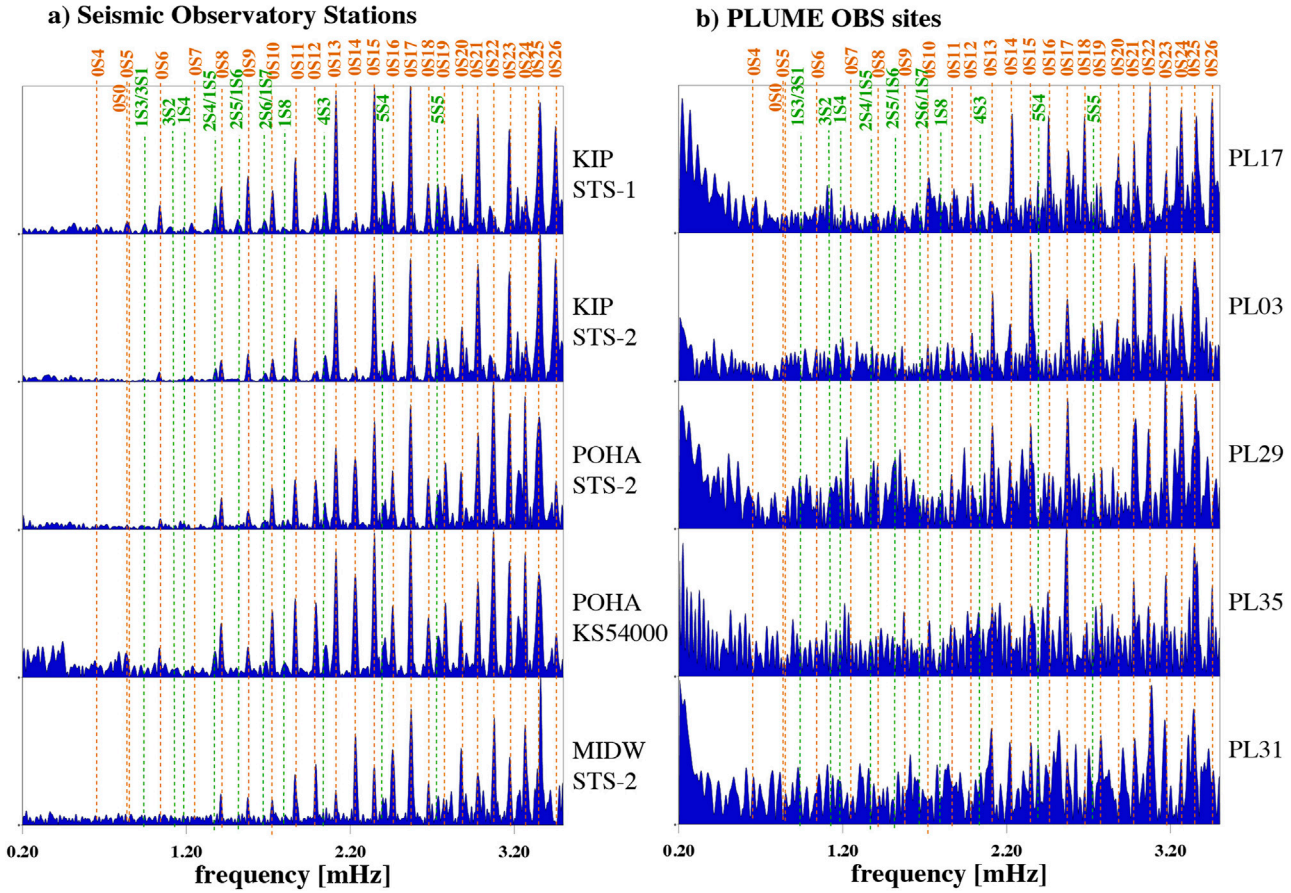


**FIGURE 5 |** Normalized raw vertical-component spectra for the June 13, 2005 Tarapaqa, Northern Chile earthquake of 25-hour long segments, starting 1.5 h after the event time. **(A)** Spectra at stations of the GSN; **(B)** Spectra at five OBS sites with the best signal-to-noise ratio. See **Supplementary Table S1** in the supplement for earthquake parameters. This event was more than three times smaller than the 1998 Balleny Island earthquake (see **Figure 3**). Yet, we are able to observe normal modes on unburied OBSs.

against the background noise. This is in stark contrast to the surface BBOBS of OSN1.

## 3.3 The November 15, 2006 Kuril Islands Earthquake

During PLUME phase 2, we captured four very large earthquakes with scalar seismic moment $M_0 = 10 \times 10^{20}$ Nm or larger. The events occurred in different source regions so were not associated with the great December 26, 2004 Sumatra-Andaman earthquake.

With a scalar seismic moment $M_0 = 35 \times 10^{20}$ Nm, the November 15, 2006 Kuril Islands event was the largest of the phase 2 events. **Figure 6** shows the spectra at the GSN and PLUME land stations. For this event, the record at KIP is somewhat noisier than that at the other GSN stations. At POHA and perhaps at MIDW, mode ${}_0S_5$ (0.840 mHz) rises above the background noise, while the first robust observation at KIP is probably that of mode ${}_0S_6$ (1.038 mHz). For such a large earthquake, and to analyze the lowest-frequency modes, we would choose a longer time window. For example, the time in which the amplitude of mode ${}_0S_4$ decays to $1/e$ is 98 h, so we would choose 98 h for this particular mode. In this case, only the very best GSN stations would be included in an analysis as the spectra at many stations degrade due to increasing noise contamination. However, for a consistent comparison for this paper, we keep the 50-hour windows fixed for all earthquakes shown here.

Except for station KCCH, the noise level at the PLUME land stations is considerably higher though robust observations for mode ${}_0S_7$ (1.231 mHZ) are possible. Station KCCH may even show mode ${}_0S_5$. Among the PLUME land stations, KCCH has a vastly better spectrum than BIG2. Through a grading scheme we make a first attempt to quantify the quality of these spectra. When initially inspecting very low-frequency free oscillation spectra, we assess the overall signal-to-noise ratio over a frequency band that

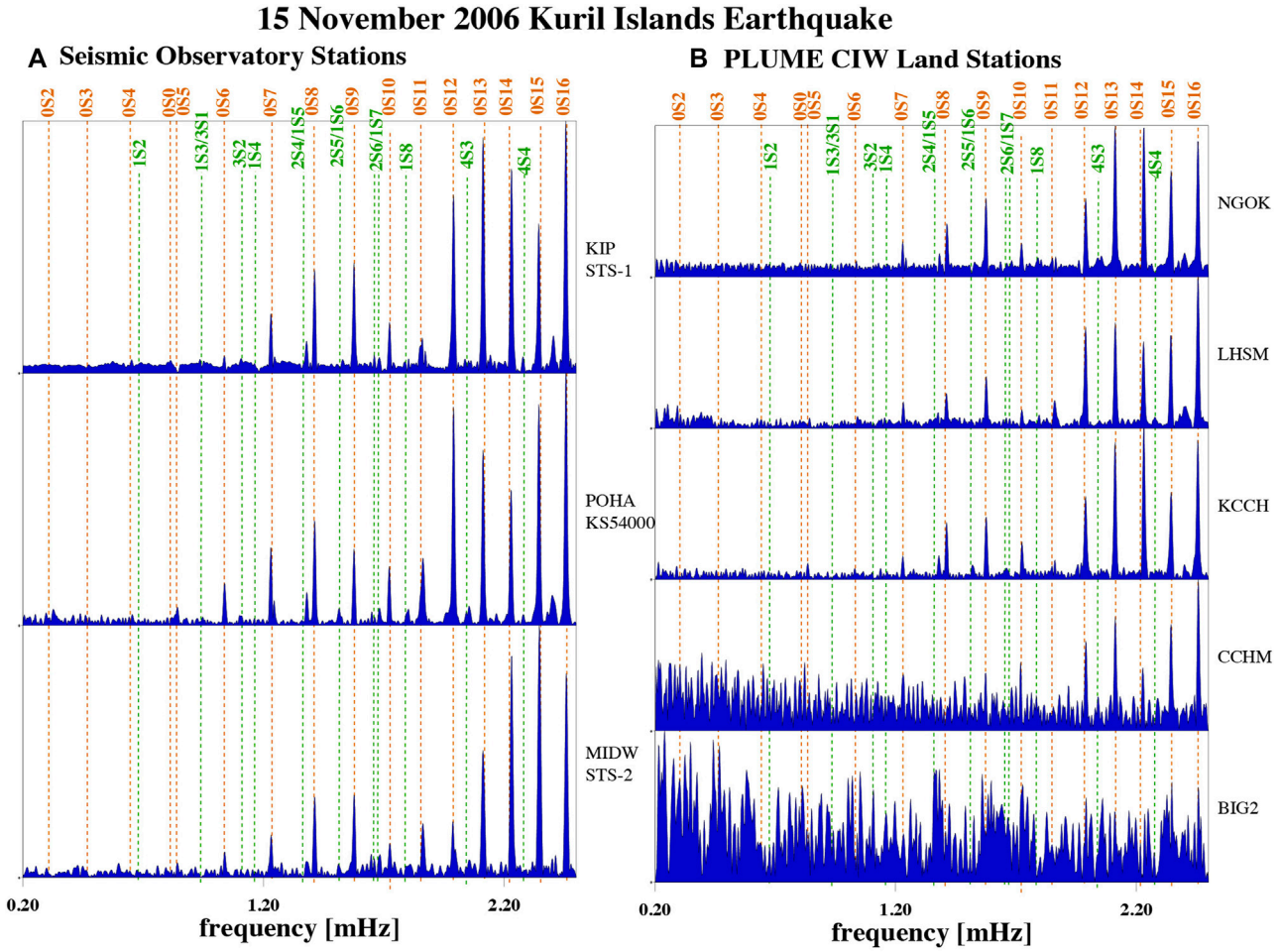


**FIGURE 6 |** Normalized raw vertical-component spectra for the November 15, 2006 Kuril Islands earthquake of 50-hour long segments, starting 1.5 h after the event time. **(A)** Spectra at stations of the GSN. See **Supplementary Table S1** in the supplement for earthquake parameters. **(B)** Spectra at the five CIW land stations still operating at the time. All CIW stations were equipped with a Wielandt-Streckeisen STS-2 seismometer.

includes all modes up the 2 mHz, and assign grades. This will help later when zooming in on individual modes to decide whether a spectral peak is really a mode or likely noise that happens to have a frequency close to a mode frequency. Grade "A" is assigned for the best spectra for a particular earthquake. Greater earthquakes are expected to reach higher overall SNRs than smaller earthquakes, so exactly what constitutes grade "A" may vary by earthquake. For the Kuril Islands event, modes ${}_0S_6$ through ${}_0S_8$ should very clearly rise above the background noise. Grade "B" is assigned if some noise is obvious, grade "C" when modes at slightly higher frequencies (such as ${}_0S_{10}$ at 1.725 mHz) are questionable. For grade "D" modes below 2 mHz are usually not visible and grade "E" is assigned if no mode is visible in the current window but in significantly shorter ones, or if Rayleigh waves are clearly visible in the time series. Grade "F" is assigned if no seismic signal is discernible. The spectra at POHA, MIDW and KCCH are grade "A" (see also **Supplementary Table S2**), while that of KIP and LHSM are borderline "A" or "B", CCHM is a "C", while BIG2 needs extremely short windows for modes to rise above the noise (grade "E").

Taking these spectra as benchmark, we also grade the OBS spectra (**Supplementary Table S2**). Spectra at some of the WHOI OBSs compare quite favorably (**Figure 7**). At stations PL44 and PL69 (grade "A" though PL69 experienced minor data dropouts), mode ${}_0S_6$ (1.038 mHz) rises above the noise. Regarding SNR, these spectra may be superior to the OBS spectra collected for the March 2005 Sumatra event (**Figure 4**) which was 3.5 times larger. The other shown WHOI spectra are grade "B", with ${}_0S_8$ (1.413 mHz) clearly visible in most of them. The spectra at all but the prematurely failing SIO OBS site PL38 are of exceptionally high quality, with low noise levels between modes, and ${}_0S_6$ (1.038 mHz) rising above the noise very clearly in most of the spectra. All of them are grade "A" and compare favorably with the spectrum at WHOI site PL44. In fact, these spectra appear to be superior to the spectra at all PLUME land stations as **Supplementary Table S2** documents.

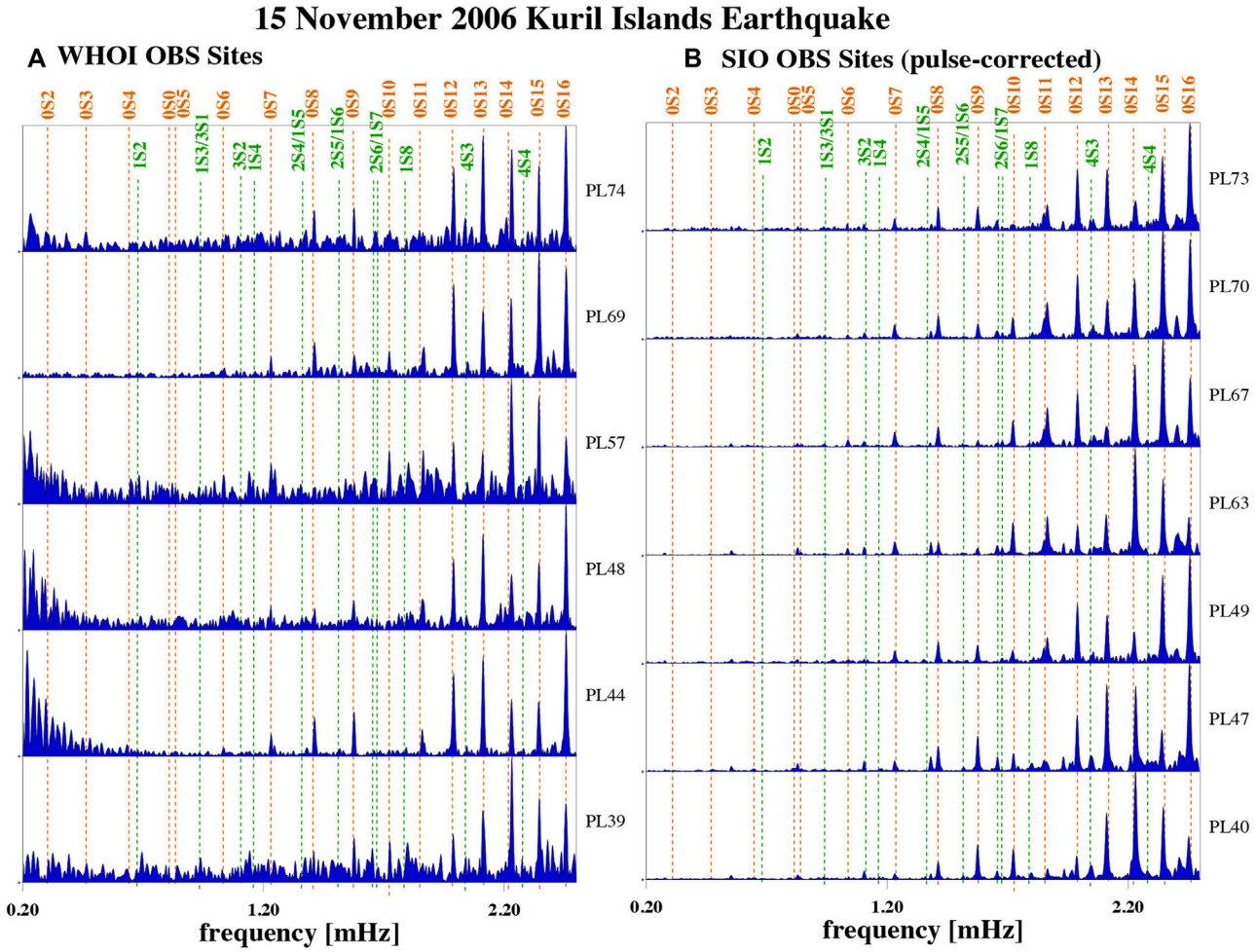


**FIGURE 7 |** Normalized raw vertical-component spectra for the November 15, 2006 Kuril Islands earthquake of 50-hour long segments, starting 1.5 h after the event time. **(A)** Spectra at the six best WHOI OBS sites. The recording sensor was a CMG-3T. **(B)** Spectra at seven of the eight SIO OBS sites. The 8th instrument failed earlier and did not record seismic data at the time. The recording sensor was a T-240. For event details see **Figure 6**. The SIO spectra have been corrected for instrument-generated harmonic signals (see text for detail).

The process of assigning grades is somewhat subjective so we conduct a more quantitative assessment where we measure the peak amplitudes of the five fundamental modes ${}_0S_6$ through ${}_0S_{10}$ against the background noise using our interactive screen tool. To assess overall performance of each instrument type (SIO/WHOI OBS, CIW-land), we determine the average SNR and the standard deviation thereof for each mode (**Figure 8**). Analysis for several modes is necessary for a better overall assessment as small changes in location may significantly lower the SNR for a certain mode while others are not affected. The set of SNRs for the SIO instruments compare favorably with those of the PLUME land instruments (CIW), particularly for mode ${}_0S_6$. However, on average and individually, the quality does not quite reach that of station POHA (note that GSN stations KIP and MIDW also do not quite reach POHA, as discussed above). The set of WHOI OBSs fare significantly worse, with lower SNRs for all modes. The systematically smaller SNRs may be a result of the significantly larger set of stations including noisier ones. We therefore redo an analysis using only the seven best instruments. But even then, the average SNRs do not reach that of the SIO instruments nor the PLUME land stations. Together with visual inspection of the spectra, we conclude that the SIO OBSs systematically deliver higher-quality spectra for modes at the lowest frequencies.

Drawing from longtime experience with analyzing GSN data, we are aware that Güralp CMG-3T spectra can be of high quality. But the variance in the quality of CMG-3T spectra is much greater than in those for Nanometrics Trillium T-240 sensors that consistently deliver high SNR spectra. Another factor that distinguishes the two types of OBSs is the installation of the sensor: the WHOI sensor ball in which the seismometer is housed is dropped directly into the seafloor mud, while the SIO sensor

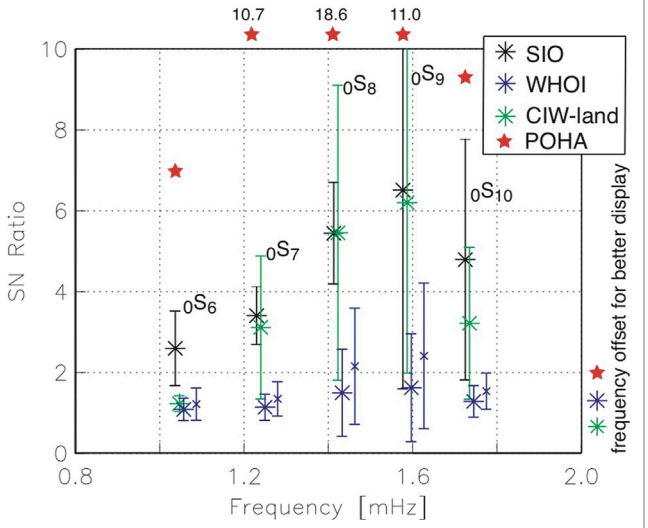


**FIGURE 8 |** Average of signal-to-noise ratios for different instrument types and five low-frequency normal modes. Averages were determined over 7 SIO, 5 CIW-land and 17 WHOI instruments. The results are slightly offset in frequency between instrument types for better display. For reference, red stars mark the SNR measured at GSN station POHA. Blue 'x' mark a reanalysis of the seven best WHOI instruments.

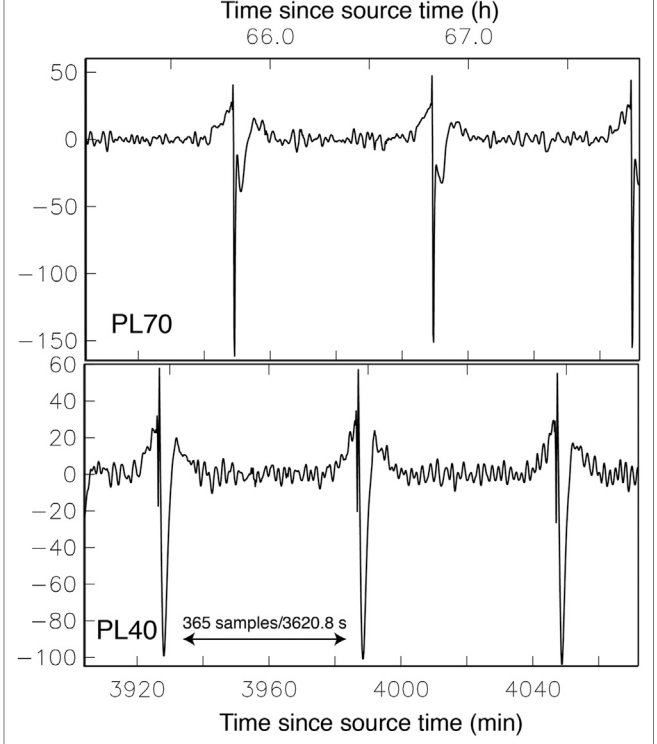


**FIGURE 9 |** A sequence of three low-frequency transients in the bandpass filtered time series of the vertical component of SIO OBSs PL40 and PL70 many hours after the November 15, 2006 Kuril Islands earthquake. Spectral analysis indicates that the distance between pulses is 3,620.56 s, which is about 365 samples (a sample is 9.92 s, so 365 samples would be 3,620.8 s; see text for details).

ball stands on a small tripod whose footprint reaches just beyond that of the sensor ball. It has been argued that such an installation increases turbulences and may induce high-frequency noise but *in-situ* test deployments have so far been inconclusive (Jeff Babcock, 2016, personal communication). The tripod may well provide a more stable coupling to the ground though at this point this is highly speculative.

Unfortunately, the SIO spectra are fraught with instrument-generated low-frequency harmonic noise that remains visible even after a correction for it (see also Ringler et al., 2021). The transients were generated by the gimbal electronics in the sensor ball that awaken to check whether the seismometer needs to be relevelled. This process is a low-frequency process and is not visible in the raw data. But in lowpass filtered data, long-duration transients (up to 20 min long) become visible that have been described as 'glitches' (Deen et al., 2017). In the early deployments of SIO OBSs, the relevel checks were performed nearly every hour (every 3,620.56 s to be more precise) which causes the harmonics in the spectrum. Why the relevel check occurs every 3,620.56 s and not every 3,600 s is unclear. The lowest-frequency harmonic related to these checks is at 0.2762 mHz (hence the derived repeat time just mentioned). Unfortunately, higher harmonics overlap in frequency with some of Earth's normal modes, including $_0S_5$ and $_3S_2$, which renders the spectra questionable for a mode analysis. Even at higher frequencies beyond 2 mHz, the spectral amplitude of the harmonics is quite high. Since the number of Earth's normal modes in any given frequency interval increases with frequency, the chances increase that a higher harmonic will overlaps with a normal mode.

The transients are different in shape between different instruments (**Figure 9**) but are rather reproducible on the same instrument, at least within a five-day period. The temporal distance between transients also is the same between instruments. Our somewhat ad-hoc approach to remove the transients is as follows: we determine the average 'transient' starting 10 h into a 110-hour long time series after the earthquake. A step in the data preprocessing is a downsampling from an original sampling rate of 31.25 Hz to a sampling interval of 9.92 s. Hence our repeat transient segment is 365 samples long (3,620.8 s). We then subtract a reconstructed time series consisting of repeats of the 365-sample transient from the entire time series. Spectra before and after the correction are juxtaposed in **Supplementary Figure S2**. The choice to start the averaging 10 h into the time series is the results of visually optimizing the removal of the offending harmonics at ultra-low frequencies. Starting later provides a smoother average transient in the time domain and removes more of the higher harmonics beyond 5 mHz. But this leaves more harmonics at frequencies below 2 mHz. An earlier start brings no improvement. This optimal start time of 10 h after the source time may depend on the earthquake analyzed. A mismatch

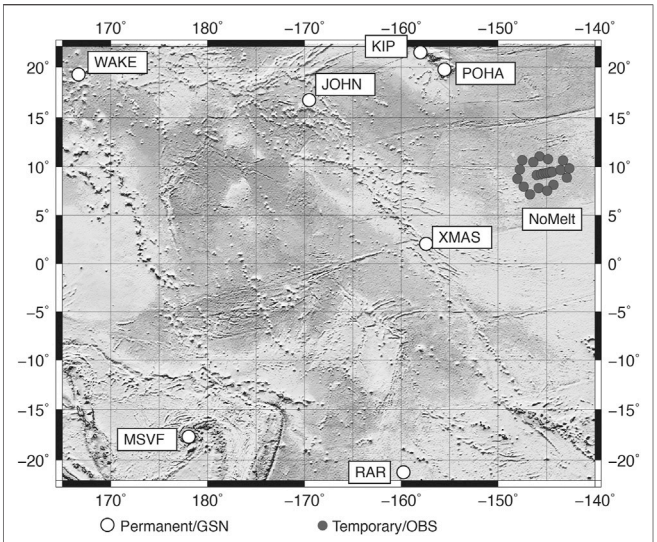


**FIGURE 10 |** Site locations of the broadband NoMelt OBS network (Dec 2011–Jan 2013). Also shown are sites of permanent observatory stations of the GSN: KIP (Kipapa, Oahu; primary sensor: STS-1), POHA (Pohakuloa, Hawaii; KS54000), JOHN (Johnston Island; KS54000), WAKE (Wake Island; KS54000), XMAS (Kiritimati Island, Kiribati; STS-2); RAR (Rarotonga, Cook Islands (KS54000); MSVF (Monasavu, Fiji; KS54000).

between the 365-sample repeat (as constrained by the 9.92 s sampling interval) and the inferred 3,620.56 s repeat from the lowest-frequency harmonic produces a one-sample (12 s) mismatch 50 h into the time series. However, a correction in a 0.992 s downsampled time series yields no noticeably improvement. Since the correction for the transients still leaves considerable signal in the spectra, we would rather not include such spectra in a normal-mode analysis, for affected modes. After providing feedback to the SIO OBS operator, the schedule for the relevel checks was changed to occur less frequently, most recently to once a week (Martin Rapa, personal communication). The examples shown in the rest of this paper are from a time after this change in protocol occurred.

# 4 OTHER OCEAN BOTTOM SEISMOMETER INSTRUMENT POOL DEPLOYMENTS IN THE PACIFIC OCEAN

## 4.1 NoMelt

The NoMelt experiment (Lin et al., 2016; Russell et al., 2019) combined passive broadband and active-source seismic refraction/reflection surveys with the deployment of marine magnetotelluric instruments to explore 70-million year old oceanic lithosphere about 1700 km southeast of Hawaii (**Figure 10**). The broadband passive deployment recorded data between December 2011 and January 2013 and encompassed 20 broadband sensors as well as two additional T-40 wideband sensors. During the deployment time, six earthquakes occurred with a scalar seismic moment $M_0 \geq 2.0 \times 10^{20}$ Nm (**Supplementary Table S1**). A seventh very large event occurred about an hour after the 11 April main shock in the Indian ocean. With $M_0 \geq 29 \times 10^{20}$ Nm, this aftershock alone would probably qualify as a once-every-few-years event. The main shock was just above three times larger which makes a standard single-spectrum analysis of this event difficult unless we apply a technique such as our autoregressive splitting matrix analysis (Masters et al., 2000) that does not depend on details of the seismic source. One difficulty of analyzing spectra of such 'double-events' is that spectral peaks may split, thereby falsely suggesting that normal-modes splitting due to Earth structure is observed. However, for the sake of this paper, we can still explore the quality of the spectra. Of the 22 stations, seven produced grade E or F spectra and so are excluded. The remaining 15 spectra are shown in **Figure 11**. Because of the aftershock, we start the time window for the spectra 2 h after the source time. Since this event was so large, we increase the time window length to 60 h.

A direct quantitative comparison with land installations is somewhat hampered as the closest GSN station, XMAS (Kirimati Island, Kiribati), is about 1,500 km away. At such distances, spectral amplitudes for a mode can be vastly different between stations while that of other modes are not affected as much. In a somewhat extreme case, for a station about 90° away from the source, every other fundamental mode may experience a greatly reduced amplitude (Laske and Widmer-Schnidrig, 2015). Bearing this in mind, **Figure 12** displays seven representative spectra in the southwestern Pacific ocean. For all but one station (MSVF) we consider both the primary and the secondary sensors (location codes 00 and 10) and make a decision which sensor in the better one to include in this study. For stations WAKE, RAR and XMAS, we choose the secondary sensor, a Wielandt-Streckeisen STS-2. At XMAS, the record of the primary sensor was a grade F, at WAKE we see a Rayleigh wave on the primary sensor but normal mode peaks appear only at frequencies above 2 mHz and only if we take shorter records (grade E). At station RAR, the quality of the spectrum for the primary sensor was of marginally less quality than that of the secondary sensor though it would hamper analysis of mode ${}_0S_3$ (0.469 mHz).

The spectra for this event are remarkable, for a number of reasons. Firstly, mode ${}_0S_3$ clearly appears above the background noise at a number of GSN stations and may be observed at even the one or other NoMelt OBS (e.g., B26). Together with mode ${}_0S_2$ (0.309 mHz), this mode is rather rarely observed, and only on records of the highest GSN quality. Secondly, mode ${}_0S_4$ (0.647 mHz) appears clearly against the background noise at about half of the NoMelt OBS sites, a document of perhaps the best-quality OBS normal mode spectra on OBSIP OBSs collected so far. Thirdly, one of these spectra is that of station B17. According to the meta data, this site was equipped with a wideband sensor (T-40). There always is a possibility of an error in the meta database. However, inspection of the spectra confirms that this was a T-40. Evaluating the instrument responses in **Figure 2**, a raw signal at 1 mHz is likely reduced by a factor of about 20 when compared to a signal at 40 mHz. In our raw spectra, the low-frequency roll-off is much steeper at this site than at the other sites (**Supplementary Figure S3**). Arguably, the B17

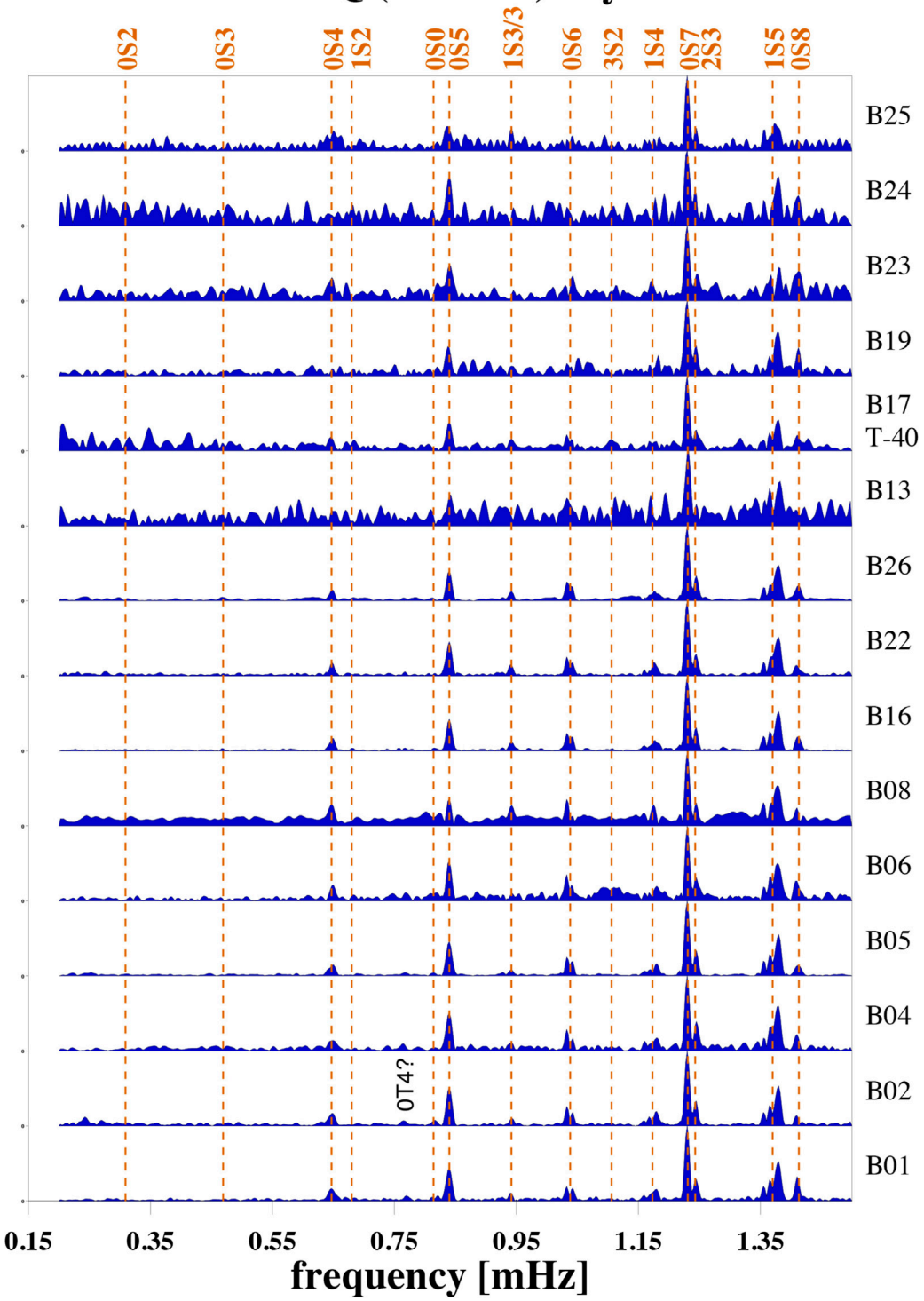


**FIGURE 11 |** Normalized raw vertical-component spectra for the April 11, 2012 Indian Ocean earthquake of 60-hour long segments, starting 2 h after the event time. See **Supplementary Table S1** in the supplement for earthquake parameters. Site B17 featured a Nanometrics Trillium T-40 wideband sensor.

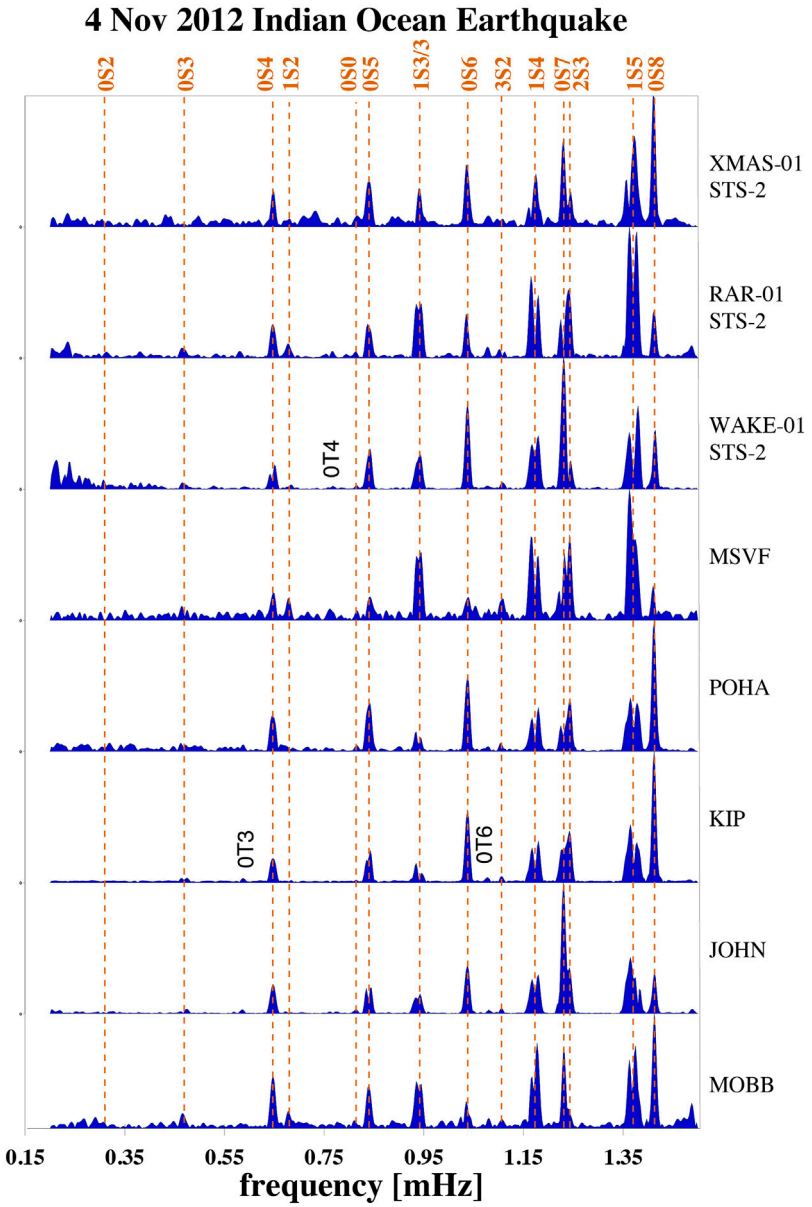


**FIGURE 12 |** Normalized raw vertical-component spectra at GSN stations for the April 11, 2012 Indian Ocean earthquake of 60-hour long segments, starting 2 h after the event time. A code 01 after the station code means that we use the secondary sensor for analysis (sensor type below the station name). Also shown is the spectrum of seafloor observatory MOBB off-shore California (see **Figure 13**).

spectrum in **Figure 11** is the noisiest of the 'good' spectra but the fact that this instrument recorded low frequency modes at such high quality, let alone having mode ${}_0S_5$ stand out clearly above the background noise is a manifest for exceptional low-frequency performance of this particular sensor. Unfortunately, we are unable to backtrack the physical specifications (i.e. serial numbers) of the OBS hardware, including the sensor as the packages are routinely taken apart and reassembled for future deployments. But we note that the ALBACORE deployment in the California Borderland (see next section) also had such an exceptional T-40 performance.

To complement the comparison, seafloor observatory MOBB off-shore California (Romanowicz et al., 2006) (**Figure 13**) also recorded this event with high fidelity. This site has a broadband Güralp CMG-1T seismometer that is buried beneath at least 10 cm of sediments and is located at a water depth of 1,000 m. At this water depth, we normally expect high noise levels in the infragravity band at frequencies below about 10 mHz. Yet, the spectrum at MOBB is also of extremely high quality where mode ${}_0S_4$ easily stands out against the background noise, and even mode ${}_0S_3$ is clearly discernible. A SNR analysis similar to that in **Figure 8** can be found in the online supplement (**Supplementary**

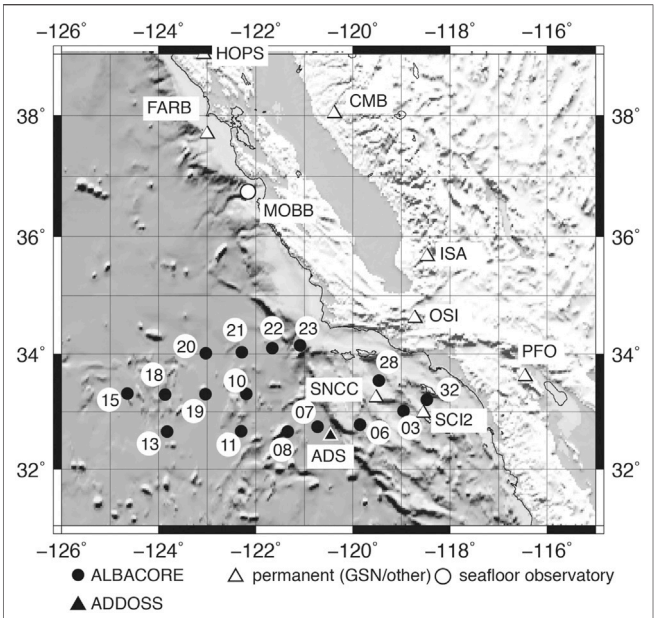


**FIGURE 13 |** Site locations of the 16 broadband stations of the ALBACORE network (Aug 2010–Sep 2011) used in this study. Also shown are sites of permanent observatory stations of the GSN: PFO (Piñon Flat Observatory; primary sensor: STS-1), stations of the CI network (OSI, Osito Adit, STS-1; ISA, Isabella; ,STS-1; SNCC, San Nicolas Island, STS-1; SCI2, San Clemente Island, STS-2), stations of the BK network (HOPS, Hopland Field station, STS-1; CMB, Columbia College, STS-1; BKS, Berkeley, Byerly Vault, STS-1; FARB, Farallon Islands, STS-2) and seafloor observatory MOBB (Monterey Bay Broadband Ocean Botton Seismic Observatory, CMG-1T). The ADDOSS OBS as site ADS operated Dec 2013 through Mar 2014 (Berger et al., 2016). A student-led repeat deployment followed in summer 2015.

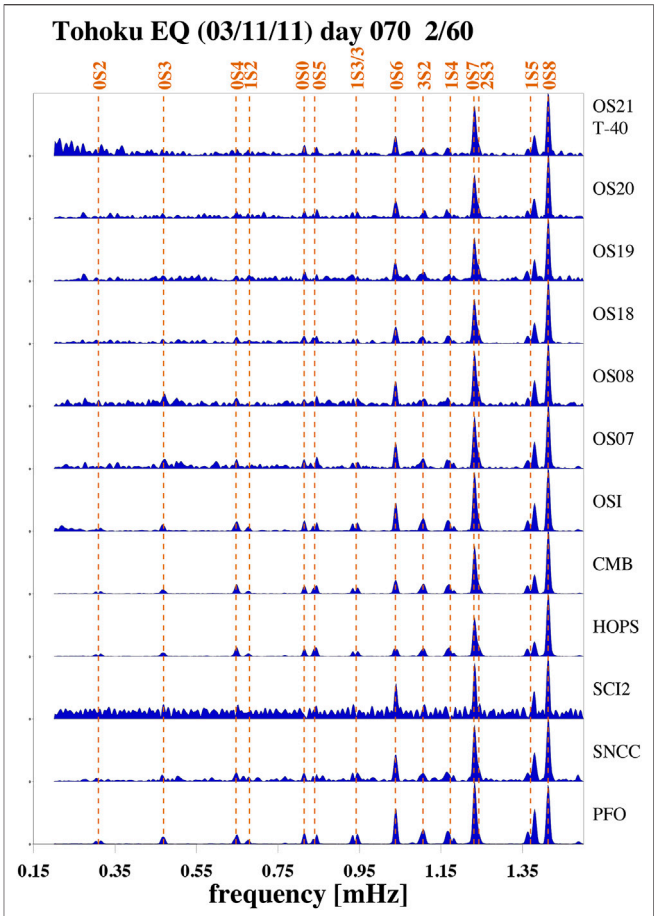


**FIGURE 14 |** Normalized raw vertical-component spectra for the March 11, 2011 Tohoku, Japan earthquake of 60-hour long segments, starting 2 h after the event time. The bottom six spectra are from permanent land stations (see 15), while the top six spectra are for ALBACORE OBS sites. Site OS21 featured a Nanometrics Trillium T-40 wideband sensor. See online supplement for the spectra of all broadband OBSs.

**Figure S4**). Mode ${}_0S_6$ has a relatively low SNR because the spectral amplitude of that mode is relatively low at this station. But the other modes compare favorably. In fact, mode ${}_0S_4$ has a higher SNR than the average of the GSN records considered here.

Noteworthy, a number of GSN stations but also NoMelt OBSs exhibit spectral peaks at the frequencies for toroidal modes ${}_0T_6$ (1.079 mHz), ${}_0T_4$ (0.767 mHz), and in some cases even ${}_0T_3$ (0.588 mHz). Toroidal modes have exclusively horizontal shear motion and so should show only on horizontal seismometer components. However, mode coupling between spheroidal and toroidal modes caused by the Coriolis force can cause toroidal-mode energy to appear on the vertical seismometer component. This effect is particularly strong when the frequencies of a ${}_0S_l$ mode is close to that of a ${}_0T_{l+1}$ mode (e.g. Masters et al., 1983) and is well-observed for normal modes at frequencies above 1.8 mHz. In rare cases, for very large earthquakes and exceptionally high SNR-stations, toroidal modes can be observed on vertical components in the ultra-low frequency band below 1 mHz as well (Zürn et al., 2000) as a result of Coriolis coupling and, to a lesser extent, mode coupling caused by Earth's ellipticity and 3-dimensional structure, and even though normal mode frequencies are not as close.

We also inspect all of the NoMelt DPG spectra. While it is tempting to associate individual peaks across all stations with a normal mode, none of the 22 DPG exhibits a consistent spectrum that displays at least three adjacent fundamental modes with clear SNRs, regardless of the time series length. On the other hand, such sensors allow the analysis of semi-diurnal tidal peaks (e.g. Doran et al., 2019). Since the tidal signal is much larger than that of earthquakes, we infer that noise levels in the free oscillation band are too high to observe even very large earthquakes.

## 4.2 ALBACORE

The passive broadband OBS deployment for the ALBACORE experiment in the California Borderland (Reeves et al., 2015) occurred from August 2010 through September 2011 and so immediately preceded the NoMelt experiment. The metadata at the IRIS DMC includes station information for 36 OBS sites. Twelve of these were equipped with short-period instruments. Three of the remaining sites were equipped with a T-40 wideband sensor, while the rest had a T-240 broadband sensor. We obtained data for 21 stations. Five of these are grade F, exhibiting only bit

noise (i.e. signals of a few counts), one T-40 record was suspicious (counts were primarily single-sided). This leaves us with usable records at 16 OBS sites (see **Figure 13**), one of which featured a T-40. In the following, we use four letters to name the stations though the original station names consist of five (OBS?? where '?' is a number). During this deployment, four large distinct earthquakes occurred. By far the largest was the March 11, 2011 Tohoku, Japan earthquake (scalar seismic moment $M_0 = 531.2 \times 10^{20}$ Nm). Two large aftershocks to this earthquake occurred within 30 min which we do not consider separate free-oscillation earthquakes, and our analysis starts 2 h after the main shock. For an earthquake this large, expectations are high that even the noisiest station should produce a good SNR free oscillation spectrum.

Accordingly, spectra collected on land stations are of the highest quality and set a rather high bar for any OBS recording (**Figure 14**). The spectra of the best stations clearly show the gravest mode ${}_0S_2$ (0.309 mHz) rising above the noise (**Supplementary Figure S6** in the supplement provides a zoom-in). These include stations PFO, CMB and HOPS, and perhaps OSI and even SNCC. On the other hand, stations SCI2 and ISA (not shown) have rather noisy spectra where mode ${}_0S_6$ is probably the lowest-frequency mode above the noise. Also shown in the figure are spectra at six of the ALBACORE sites. At least five more OBS spectra have this kind of quality (**Supplementary Figure S5**). While we should not hope to observe the gravest modes at frequencies below 0.5 mHz (many GSN stations do not rise to this bar), modes ${}_0S_5$ (0.840 mHz), ${}_0S_0$ (0.814 mHz) and ${}_0S_4$ (0.647 mHz) clearly rises above the noise, and maybe even ${}_0S_3$ (0.469 mHz). These observations should make the ALBACORE and the NoMelt experiments the first broadband OBS experiments that allowed free oscillation observations to such low frequencies.

Most remarkably, the sensor at site OS21 is the wideband T-40. A double-check of the raw spectra confirms a similar finding as that of site B17 for NoMelt and confirms that we are dealing with a T-40 and not a typo in the metadata. At this point, we doubt that all T-40s perform this well but as described above, the other two T-40s in this experiments did not provide usable data. One must wonder whether this was the same sensor as that at NoMelt site B17. Unfortunately, this sensor is likely no longer in the fleet as the SIO OBS group subsequently exchanged T-40 sensors for T-240s. While T-240s are expected to perform better in the free oscillation band, the loss of this particular T-40 is arguable a great loss for ocean bottom normal-mode seismology and engineering alike. It would have been nice to explore in more detail exactly what made this particular sensor so unique in its performance.

The deployment of ALBACORE OBSs in a wide range of water depths allows us to explore the influence of water depth on the quality of the free-oscillation SNR. While most of the OBSs were deployed in the deeper ocean at depths greater than 3,500 m, even the spectrum for OS23 at a water depth near 2000 m is acceptable (see **Supplementary Figure S5**). But a deployment at shallower depths clearly increases noise levels. To quantify this further, we measure the SNR for six modes at the six shallowest sites and compare that against the SNR at the other ten sites. A split into four shallow vs twelve deeper sites would follow the narrative

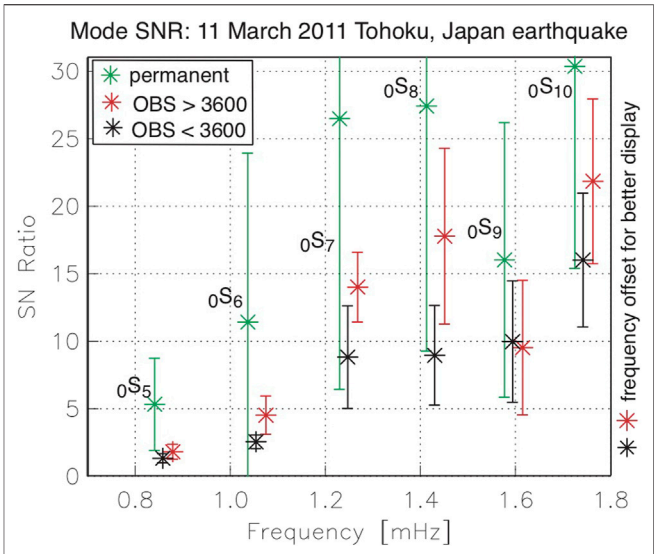


**FIGURE 15 |** Average of signal-to-noise ratios for the 16 ALBACORE stations that had useful seismic data (15 broadband, 1 wideband). The results are slightly offset in frequency between instrument types for better display. Six grade-E or F stations were discarded and not included (5 broadband, 1 wideband). Black: 10 OBSs in deeper water (> 3,600 m). Red: 6 OBSs in shallower water (< 3,600 m). Green: Average over 10 records at nine permanent land stations (shown in **Figure 13**).

above better, but we feel that the subsequently smaller standard deviations for smaller samples would not be representative. **Figure 15** confirms that the shallower sites have lower SNRs for all modes than the deeper sites. The relatively low SNR for mode ${}_0S_9$ is a result of relatively low spectral amplitudes at some OBSs, compared to neighboring modes, or even neighboring OBSs. For comparison, we also determine the SNR for a set of ten spectra at nine land stations: SNCC, SCI2, PFO, OSI, ISA, BKS, CMB, FARB and HOPS. As expected, SNRs at permanent observatory seismic stations are consistently higher than those at the OBS sites. Spectral amplitudes for mode ${}_0S_9$ are relatively low at northern California stations, which results in lower SNRs at the land stations as well.

We briefly also discuss the other large earthquakes observed at the ALBACORE deployment. With a scalar seismic moment $M_0 = 2.99 \times 10^{20}$ Nm, the July 6, 2011 Kermadec earthquake is one of the smaller ones in our list. The spectra for 40-h time series exhibit normal modes with good SNR at OBSs OS13, OS11 and OS07, while spectra at OS15, OS19 and OS22 exhibit more noise though modes are still clearly visible down to mode ${}_0S_{10}$ (1.725 mHz). The seafloor depths overlap so we find no obvious relationship. The quality of spectra at the island and land stations in southern and northern California also varies. Station SNCC has an excellent spectrum that compares well with that of the best land stations, while SCI2 has a rather noisy spectrum. Station SNCC has higher SNR down to mode ${}_0S_8$ (1.413 mHz) than at the primary sensor at PFO. Mode ${}_0S_4$ (0.647 mHz) still rises above the noise. This earthquake has a record at seafloor observatory MOBB but its spectrum does not show any modes, nor do those at stations OSI and ISA that usually produce high-quality spectra.

With a scalar seismic moment $M_0 = 6.77 \times 10^{20}$ Nm, the October 25, 2011 Mentawai, Sumatra earthquake was more that twice as large but the spectra in California are noisier than those of the Kermadec earthquake. Station MOBB has no record for this time. On the best land station in southern California, mode ${}_0S_8$ (1.413 mHz) rises above the noise for the secondary sensor at station PFO, while stations OSI and ISA are much noisier. In northern California, mode ${}_0S_5$ (0.840 mHz) rises above the noise at stations HOPS and CMB. The best stations of the ALBACORE deployment show modes consistently above the noise down to mode ${}_0S_{15}$ (2.345 mHz), at sites OS07, OS08 and OS13 (water depths ranging from 3,769 to 4,281 m). Individual spectral peaks may align with single modes at lower frequencies though this alignment may be coincidence rather than a high-SNR mode observation.

The December 21, 2010 Izu Bonin was an earthquake with a scalar seismic moment less than $M_0 = 2 \times 10^{20}$ Nm. Nevertheless spectra for 40-h time series are of high quality at stations HOPS, FARB, CMB and BKS, with mode ${}_0S_7$ clearly rising above the noise (HOPS even shows ${}_0S_6$). On the other hand, spectra at other stations are rather noisy (SCI2, ISA), and the lowest-frequency mode observed at PFO is ${}_0S_{13}$ (2.112 mHz). Against this backdrop, it is perhaps remarkable, that some OBSs (OS18, OS13, OS11) exhibit normal mode spectra of better quality than at PFO, with ${}_0S_{12}$ (1.989 mHz) and all modes at higher frequencies consistently above the noise, whereby OS11 includes lower-frequency modes to maybe even ${}_0S_6$. A forth OBS (OS08) is slightly noisier. All four OBS were located at water depth greater than 3,800 m. Unfortunately, the lack of a record at seafloor observatory MOBB does not allow a comparison.

### 4.3 ADDOSS

Another deployment of broadband OBSs in the California Borderland was the ADDOSS (Autonomously Deployable Deep-Ocean Seismic System) experiment (Berger et al., 2016). The final of several deployments occurred from December 2013 through March 2014 on the deep-ocean side of the Patton Escarpment (site ADS3 in **Figure 13**) where two broadband OBSs were deployed within 1 km of each other. The primary goal of this deployment was a proof-of-concept study that a wave glider can hold station around the OBS drop location and serve as acoustic-satellite relay to transmit data from the ocean floor to a desktop computer on land in near-real time. During the three months, we recorded numerous teleseismic, regional and local earthquakes, but the scalar seismic moment of the largest earthquake remained below $M_0 = 0.4 \times 10^{20}$ Nm. Hence the deployment was no witness to a free oscillation earthquake.

We were luckier when one of the ADDOSS instruments was redeployed 18 months later as a piggy-back to a short student-led experiment near the ADS3 site. With a scalar seismic moment $M_0 = 32.3 \times 10^{20}$ Nm, the September 16, 2015 Chile earthquake was the largest earthquake for the year. This earthquake produced free oscillation spectra of the highest quality at GSN station PFO, and CI stations OSI and ISA. While the primary sensor at PFO exhibited some noise, Earth's gravest mode ${}_0S_2$ (0.309 mHz) rises clearly above the noise floor in the spectrum of the secondary sensor (T-240) and at station OSI. On the other hand, the spectrum at island station SCI2 is extremely noise, where mode ${}_0S_9$ (1.577 mHz) barely rises above the noise, while station SNCC did not record that day. Since the spectrum at ADS3 in only marginally better than that at SCI2, we do not show a figure for this event. The stations to the north fared only marginally better. While ${}_0S_2$ also shows up in the spectra at stations BKS, CMB and HOPS, island station FARB is noisy, with perhaps ${}_0S_7$ (1.231 mHz) rising above the noise. MOBB recorded this event as well. Its background noise in much less, allowing the observation of ${}_0S_7$, and perhaps even ${}_0S_6$ (1.038 mHz). But given the discussion of previous events, the data quality on OBSs for this event is somewhat disappointing. We cannot easily explain why noise levels were so high. There was no storm activity in the area. The earthquake produced a tsunami that was still measurable at local tide gauge stations (on the order of less than 10 cm). Tsunami are recorded quite well on the horizontal OBS components (e.g., Nov 2006 Kuril Islands earthquake during PLUME), but not on the vertical. So this should not explain increased noise levels.

## 5 SUMMARY AND DISCUSSION

We showed vertical-component free oscillation spectra for data collected during a number of ocean bottom seismometer (OBS) deployments in the Pacific Ocean that occurred over the last 20 years. Broadband seismology on the ocean floor using free-fall OBSs is expected to be hampered at long periods as a result of noise contamination by ocean infragravity waves. Yet, our examples showed that some spectra collected on broadband seismic sensors in the free oscillation band can reach the quality a data analyst is used from land observatory stations such as those of the Global Seismographic Network (GSN). This includes mode observations at frequencies below 1.5 mHz which require low-noise records several days long.

The SIO OBSs that are equipped with a Nanometrics Trillium T-240 sensor were found to produce consistently high-quality spectra to very low frequencies. Records include even diurnal and semi-diurnal tidal modes (e.g. Doran et al., 2019) which helps recalibrate nominal instrument responses for the pressure sensors, typically a broadband Cox-Webb differential pressure gauge (Cox et al., 1984) where sensor sensitivities can effectively vary by a factor of two. Earlier SIO OBS records are contaminated by approximately hourly transients that hamper a normal modes analysis, at least for certain modes. A removal of these signals in post-processing is moderately successful, as we and others showed (Deen et al., 2017). The low-frequency transients are generated in the electronics to check whether the seismometer needs to be relevelled even though the sensor is not mechanically relevelled. For the SIO OBSs that were part of the national OBS Instrument Pool (OBSIP), the relevel schedule was changed shortly after our Hawaiian PLUME deployment to have less frequent relevel checks. However, the approximately hourly schedule may still be set on instruments sold by the SIO OBS group to others (e.g. Deen et al., 2017).

The T-240s have also been deployed in the Atlantic, where a recent study reported earthquake-generated free oscillation observations (Bécel et al., 2011). Our study concentrated on

normal modes at ultra-low frequencies that are excited by large earthquakes. At higher frequencies, Earth's 'hum' that consists primarily of fundamental modes and that is thought to be excited by ocean infragravity waves interacting on shelves (Webb, 2007) was recently observed on free-fall OBSs in the Indian ocean Deen et al. (2017).

We performed minimal data processing, and so did not correct the vertical seismometer components for pressure nor tilt noise (e.g. Webb and Crawford, 1999; Crawford and Webb, 2000; Bell et al., 2015). A correction may improve the signal-to-noise ratio, even in the normal mode band below 5 mHz. We also did not correct the records of the 1998 ocean seismic network (OSN) pilot experiment that was located within our PLUME network. Crawford et al. (2006) describe a procedure to remove much of the noise for this specific deployment. Using a barometer, noise corrections on vertical components can also be performed for land observatory stations (e.g. Zürn and Widmer, 1995), and many, if not most GSN stations are now equipped with such a sensor.

The ALBACORE deployment off-shore southern California (Reeves et al., 2015) allowed us to investigate long-period background noise as function of water depth. We found a clear separation in quality between mode spectra for deep deployments (3,600 m or deeper) and shallower deployments. A spectrum collected at 2000 m also was of acceptable quality, while spectra at shallower sites contained more low-frequency noise but still revealed modes at frequencies down to 1 mHz. The best OBS spectra for the ALBACORE and NoMelt (Lin et al., 2016) deployments contained modes down to ${}_0S_4$ (0.647 mHz), maybe even ${}_0S_3$ (0.469 mHz). Some spectra were of such high quality that several of the gravest, Coriolis-coupled toroidal modes appeared in vertical-component spectra.

Our study focused on the vertical seismometer components. The horizontal seismometer components are noisier in general, and much more so in the oceans. Here, tilt noise contaminates the seismic record in a wide range of frequencies. At PLUME, we noted a semidiurnal cycle that suggests that tidal currents trigger the noise. Yet, it is possible to observe useful signals such as Love waves or shear-wave splitting observations during relatively low-noise times. Finally, while ground motion spectra are of high quality, we have yet to find a convincing pressure spectrum in which Earth's normal modes rise above the background noise. There have been debates whether the money spent on an expensive broadband seismometer for an OBS is a wise investment since it is often contested that observations at low and ultra-low frequencies are possible. This paper documents that, given the high costs of an OBS in general, the investment in a high-quality broadband seismic sensor is well justified.

## DATA AVAILABILITY STATEMENT

The original contributions presented in the study are included in the article/**Supplementary Material**, further inquiries can be directed to the corresponding author.

## AUTHOR CONTRIBUTIONS

The author confirms being the sole contributor of this work and has approved it for publication.

## FUNDING

National Science Foundation grants EAR11-13075 and OCE18-30959.

## ACKNOWLEDGMENTS

The author would like to thank the teams and operators of the OSN1 pilot experiment, the NoMelt team and the ALBACORE team for their efforts to conduct their experiments and ultimately deliver and share high-quality broadband seismic data. Instruments for the latter two as well as the Hawaiian PLUME experiment were provided by the NSF OBS Instrument Pool. The OBS instruments were prepared, deployed and recovered by the OBS teams at WHOI and at SIO. Network operators of land seismic observatories include the IRIS-IDA (network code II) and IRIS-USGS (network code IU) operators of the GSN, and the operators of GEOSCOPE (network code G) and GEOFON (network code GE). Stations in California are operated by the University of California Berkeley Digital Seismograph Network team (network code BK) and the Caltech/USGS Southern California Seismic Network team (network code CI). Station characteristics in the supplement were taken from the Federation of Digital Seismograph Networks (FDSN) station book. All data are available for download at the IRIS data management center (DMC). The author is indebted to SIO OBS team member Martin Rapa for many fruitful discussions. The ADDOSS follow-up cruise was funded through UC Shipfunds and led by graduate student Adrian Doran. The maps were drawn using the Generic Mapping Tools (GMT Wessel et al., 2013).

## SUPPLEMENTARY MATERIAL

The Supplementary Material for this article can be found online at: https://www.frontiersin.org/articles/10.3389/feart.2021.679958/full#supplementary-material

## REFERENCES

Bécel, A., Laigle, M., Diaz, J., Montagner, J. -P., and Hirn, A. (2011). Earth's Free Oscillations Recorded by Free-Fall OBS Ocean–Bottom Seismometers at the Lesser Antilles Subduction Zone. *Geophys. Res. Lett.* 38, L24305. doi:10.1029/2011GL049533

Bell, S. W., Forsyth, D. W., and Ruan, Y. (2015). Removing Noise from the Vertical Component Records of Ocean-Bottom Seismometers: Results from Year One of the Cascadia Initiative. *Bull. Seismological Soc. America* 105 (1), 300–313. doi:10.1785/0120140054

Berger, J., Laske, G., Babcock, J., and Orcutt, J. (2016). An Ocean Bottom Seismic Observatory with Near Real-time Telemetry. *Earth Space Sci.* 3, 68–77. doi:10.1002/2015EA000137

Collins, J. A., Vernon, F. L., Orcutt, J. A., Stephen, R. A., Peal, K. R., Wooding, F. B., et al. (2001). Broadband Seismology in the Oceans: Lessons from the Ocean Seismic Network Pilot Experiment. *Geophys. Res. Lett.* 28, 49–52. doi:10.1029/2000gl011638

Cox, C., Deaton, T., and Webb, S. (1984). A Deep-Sea Differential Pressure Gauge. *J. Atmos. Oceanic Technol.* 1, 237–246. doi:10.1175/1520-0426(1984)001<0237:adsdpg>2.0.co;2

Crawford, W. C., Stephen, R. A., and Bolmer, S. T. (2006). A Second Look at Low-Frequency marine Vertical Seismometer Data Quality at the OSN-1 Site off Hawaii for Seafloor, Buried, and Borehole Emplacements. *Bull. Seismological Soc. America* 96 (5), 1952–1960. doi:10.1785/0120050234

Crawford, W. C., and Webb, S. (2000). Identifying and Removing Tilt Noise from Low-Frequency. *Bull. Seismological Soc. America* 90 (4), 952–963. doi:10.1785/0119990121

Deen, M., Wielandt, E., Stutzmann, E., Crawford, W., Barruol, G., and Sigloch, K. (2017). First Observation of the Earth's Permanent Free Oscillations on Ocean Bottom Seismometers. *Geophys. Res. Lett.* 44 (), 10,988–10,996. doi:10.1002/2017GL074892

Doran, A. K., Rapa, M., Laske, G., Babcock, J., and McPeak, S. (2019). Calibration of Differential Pressure Gauges through *In Situ* Testing. *Earth Space Sci.* 6, 2663–2670. doi:10.1029/2019EA000783

Dziewonski, A. M., and Anderson, D. L. (1981). Preliminary Reference Earth Model. *Phys. Earth Planet. Interiors* 25, 297–356. doi:10.1016/0031-9201(81)90046-7

Dziewonski, A., Wilkens, R. H., Firth, J. V., and Science Party, Shipboard. (1991). Background and Objectives of the Ocean Seismographic Network, and Leg 136 Drilling Results. *Proc. Ocean Drilling Program* 136/137, 3–8.

Hanka, W. (2000). *Comparison of GEOFON and GRSN Shielding. http://geofon.gfz-potsdam.de/geofon/manual/gfz-grsn-shield.html.*

Laske, G., Collins, J. A., Wolfe, C. J., Solomon, S. C., Detrick, R. S., Orcutt, J. A., et al. (2009). Probing the Hawaiian Hot Spot with New Broadband Ocean Bottom Instruments. *Eos Trans. AGU* 90 (41), 362–363. doi:10.1029/2009eo410002

Laske, G., Orcutt, J. A., Collins, J. A., Detrick, R. S., Wolfe, C. J., Solomon, S. C., et al. (2007). Broadband Ocean Bottom Instruments Record Earth's Free Oscillations during the Hawaiian PLUME experiment. *Eos Trans. AGU* 88 (52), 1, 2007 . Fall Meeting suppl., abstract S23A-1107.

Laske, G., and Widmer-Schnidrig, R. (2015). "Theory and Observations: Normal Mode and Surface Wave Observations,"in. *Treatise on Geophysics*. Editor G. Schubert. Second Edition (Elsevier), 1, 117–167. doi:10.1016/b978-0-444-53802-4.00003-8

Lin, P.-Y. P., Gaherty, J. B., JinCollins, G. J. A., Collins, J. A., Lizarralde, D., Evans, R. L., et al. (2016). High-resolution Seismic Constraints on Flow Dynamics in the Oceanic Asthenosphere. *Nature* 535 (52), 538–541. doi:10.1038/nature18012

Masters, G., Laske, G., and Gilbert, F. (2000). Autoregressive Estimation of the Splitting Matrix of Free-Oscillation Multiplets. *Geophys. J. Int.* 141, 25–42. doi:10.1046/j.1365-246x.2000.00058.x

Masters, G., Park, J., and Gilbert, F. (1983). Observations of Coupled Spheroidal and Toroidal Modes. *J. Geophys. Res.* 88, 10,285–10,298. doi:10.1029/jb088ib12p10285

Montagner, J.-P., Karczewski, J.-F. o., Romanowicz, B., Bouaricha, S., Lognonne´, P., Roult, G. v., et al. (1994). The French Pilot Experiment OFM-SISMOBS: First Scientific Results on Noise Level and Event Detection. *Phys. Earth Planet. Interiors* 84, 321–336. doi:10.1016/0031-9201(94)90050-7

Reeves, Z., Lekić, V., Schmerr, N., Kohler, M., and Weeraratne, D. (2015). Lithospheric Structure across the California Continental Borderland from Receiver Functions. *Geochem. Geophys. Geosyst.* 16, 246–266. doi:10.1002/2014GC005617

Ringler, A. T., Mason, D., Storm, T., Laske, G., Templeton, M., and Anthony, R. E. (2021). Why Do My Squiggles Look Funny? A Gallery of Instrumentation Failure Modes. *Seismol. Res. Lett.* in review.

Romanowicz, B., Stakes, D., Dolenc, D., Neuhauser, D., McGill, P., Uhrhammer, R., et al. (2006). The Monterey Bay Broadband Ocean Bottom Seismic Observatory. *Ann. Geophys.* 49, 607–623. doi:10.4401/ag-3132

Russell, J. B., Gaherty, J. B., Lin, P. Y. P., Lizarralde, D., Collins, J. A., Hirth, G., et al. (2019). High-Resolution Constraints on Pacific Upper Mantle Petrofabric Inferred from Surface-Wave Anisotropy. *J. Geophys. Res. Solid Earth* 124, 631–657. doi:10.1029/2018JB016598

Vernon, F. L., Collins, J. A., Orcutt, J. A., Stephen, R. A., Peal, K., Wolfe, C. J., et al. (1998). Evaluation of Teleseismic Waveforms and Detection Thresholds from the OSN Pilot Experiment. *EOS Trans. AGU* 79, F650. doi:10.1121/1.425544

Webb, S. C. (1998). Broadband Seismology and Noise under the Ocean. *Rev. Geophys.* 36 (1), 105–142. doi:10.1029/97rg02287

Webb, S. C., and Crawford, W. C. (1999). Long Period Seafloor Seismology and Deformation under Ocean Waves. *Bull. Seismol. Soc. Am.* 89, 1535–1542.

Webb, S. C. (2007). The Earth's 'hum' Is Driven by Ocean Waves over the continental Shelves. *Nature* 445, 754–756. doi:10.1038/nature05536

Wessel, P., Smith, W. H. F., Scharroo, R., Luis, J., and Wobbe, F. (2013). Generic Mapping Tools: Improved Version Released. *EOS Trans. AGU* 94, 409–410. doi:10.1002/2013EO450001

Zürn, W., Laske, G., Widmer-Schnidrig, R., and Gilbert, F. (2000). Observation of Coriolis Coupled Modes below 1 mHz. *Geophys. J. Int.* 143, 113–118. doi:10.1046/j.1365-246x.2000.00220.x

Zürn, W., and Widmer, R. (1995). On Noise Reduction in Vertical Seismic Records below 2 mHz Using Local Barometric Pressure. *Geophys. Res. Lett.* 22, 3537–3540. doi:10.1029/95gl03369

**Conflict of Interest:** The author declares that the research was conducted in the absence of any commercial or financial relationships that could be construed as a potential conflict of interest.

frontiers in Earth Science

ORIGINAL RESEARCH
published: 20 July 2021
doi: 10.3389/feart.2021.686296

# The Contribution of Submarine Optical Fiber Telecom Cables to the Monitoring of Earthquakes and Tsunamis in the NE Atlantic

*Luis Matias[1]*, Fernando Carrilho[2], Vasco Sá[3], Rachid Omira[1], Manfred Niehus[3,4], Carlos Corela[1], José Barros[5] and Yasser Omar[6]*

*[1]Instituto Dom Luiz, Faculdade de Ciências, Universidade de Lisboa, Lisbon, Portugal, [2]Instituto Português do Mar e da Atmosfera, Lisbon, Portugal, [3]Instituto de Telecomunicações, Physics of Informations and Quantum Technologies Group, Lisbon, Portugal, [4]Instituto Superior de Engenharia de Lisboa, Lisbon, Portugal, [5]Autoridade Nacional de Comunicações, Lisbon, Portugal, [6]Instituto Superior Técnico, Universidade de Lisboa, Lisbon, Portugal*

Recent developments in optical fiber cable technology allows the use of existing and future submarine telecommunication cables to provide seismic and sea-level information. In this work we study the impact of three different technologies, 1) SMART, Science Monitoring and Reliable Telecommunications; 2) DAS, Distributed Acoustic Sensing, and; 3) LI, Laser Interferometry, for effective earthquake and tsunami monitoring capabilities on the NE Atlantic. The SW Iberia is the source area of the largest destructive earthquake that struck Europe since the year 1000, the November 1, 1755 event. This earthquake generated also a destructive tsunami affecting the whole basin. This tectonically active area is crossed by the CAM (Continent-Azores-Madeira) submarine cable on a ring configuration. Due to the end of cable lifetime the current cables need to be replaced by 2024 and the technical requirements must be defined in mid-2021. The Azores archipelago is the focus of frequent seismic crizes and occasionally destructive earthquakes. A common feature of these seismic events is that they take place offshore, an area that is difficult to monitor from land-based instruments. In this work we evaluate the contribution of SMART cables to the earthquake monitoring and tsunami early warning system in SW Iberia and show how DAS and LI can improve earthquake monitoring on two active domains of the Azores. For tsunami early warning, we show how the offshore sea-level measurements provide clean offshore tsunami records when compared to coastal observations by tide gauges, which greatly improves the efficiency of the system. For earthquake monitoring, the data processing operational routine is examined using Monte-Carlo simulations. These take into consideration the errors in phase picking and the uncertainty on the 1D velocity model used for earthquake location. Quality of earthquake location is examined using the difference between the true location and the centroid of the computed epicenters and by the overall ellipse of uncertainty obtained from 100 runs. The added value provided by instrumented submarine telecommunication cables to mitigate earthquake and tsunami risk demonstrated in this work will help authorities and the society in general to take the political decisions required for its full implementation worldwide.

**Keywords: earthquakes, tsunamis, early warning, submarine optical fiber cables, DAS**

OPEN ACCESS

***Edited by:***
*Charlotte A. Rowe, Los Alamos National Laboratory (DOE), United States*

***Reviewed by:***
*Francesca Di Luccio, Istituto Nazionale di Geofisica e Vulcanologia (INGV), Italy*
*Jie Deng, University of California, Los Angeles, United States*

****Correspondence:***
*Luis Matias*
*lmatias@fc.ul.pt*

***Specialty section:***
*This article was submitted to Solid Earth Geophysics, a section of the journal Frontiers in Earth Science*

***Received:*** *26 March 2021*
***Accepted:*** *06 July 2021*
***Published:*** *20 July 2021*

***Citation:***
*Matias L, Carrilho F, Sá V, Omira R, Niehus M, Corela C, Barros J and Omar Y (2021) The Contribution of Submarine Optical Fiber Telecom Cables to the Monitoring of Earthquakes and Tsunamis in the NE Atlantic. Front. Earth Sci. 9:686296. doi: 10.3389/feart.2021.686296*

## INTRODUCTION

The high capacity telecommunications between Portugal mainland, archipelagos of Madeira and Azores are sustained by three submarine cables laid as a ring, as sketched in **Figure 1**. Such a geometry allows for redundancy in the case of any incident occurring in one of the branches. In the Azores, the 9 Islands are also connected by unrepeatered submarine telecommunication cables, as illustrated in **Figure 2**. The first set of cables is known as CAM from C (Continental mainland), A (Azores) and M (Madeira).

Mainland, Madeira and the Azores comprise one tectonic domain influenced by the interplay between three major tectonic plates, which is generally designated as the Azores-Gibraltar fracture zone (AGFZ). Eurasia and Nubia are colliding at a slow speed (~4–5 mm/year, e.g., Fernandes et al., 2007) S and SW Portugal mainland and slide along the Gloria Transform Fault North of Madeira. In the Azores we have a diffuse oblique spreading regime East of 30°W and a triple junction between Nubia, Eurasia and the North-American plates (**Figure 1**).

Earthquake and tsunami catalogues document several large events on the AGFZ, marking the western plate boundary between the Eurasian and Nubian plates. In the SW Iberia Margin (SWIM), eastern domain of the AGFZ, the largest destructive earthquake in Europe history since the year 1000, took place on November 1st, 1755 (e.g., Gutenberg and Richter, 1949; Johnston, 1996; Martinez-Solares and Lopez-Arroyo, 2004; Stucchi et al., 2013). This earthquake caused a destructive tsunami that hit the coasts of Portugal, Spain and Morocco, and reached France, England, the Caribbean and Brazil (Baptista and Miranda, 2009). The SWIM was also responsible for the most important earthquake of the 20th century that occurred on February 28th, 1969 and triggered a small tsunami that was recorded by the tide gauge networks of Portugal, Spain and Morocco (Baptista and Miranda, 2009). The central domain of the AGFZ, the Gloria Fault, although exhibiting a low seismic activity, was the place of the November 25th, 1941, largest strike-slip event ever recorded (Bird and Kagan, 2004) until the April 11, 2012 Mw 8.6 Sumatra earthquake. A small tsunami followed the 1941 earthquake with a maximum wave height of ~0.45 m recorded at Casablanca (Morocco) tide gauge station (Baptista et al., 2016). In the Azores, western domain of the AGFZ, seismic crizes are frequent and destructive earthquakes occasionally occur. The January 1st, 1980 and the July 9th, 1998 are recent examples of large earthquakes that struck the Azores (Hirn et al., 1980; Matias et al., 2007). Another major event that affected the Madeira archipelago, was the May 26th, 1975, magnitude 8.1 Ms (Kanamori and Abe, 1979), originated north of Madeira archipelago and located south of the Gloria Fault. This event generated a tsunami well recorded in Azores (~35 cm) and mainland harbors (~30 cm) (Baptista and Miranda, 2009).

A common feature of most past large earthquakes is that they occurred offshore, in areas not covered by any type of detection instruments. Furthermore, the tsunami waves took only few tens of minutes to reach the closest coasts. IPMA (Instituto Português do Mar e da Atmosfera), as the Portuguese Agency responsible for seismic and tsunami monitoring, faces the challenge of using land-based seismometers providing less coverage of offshore

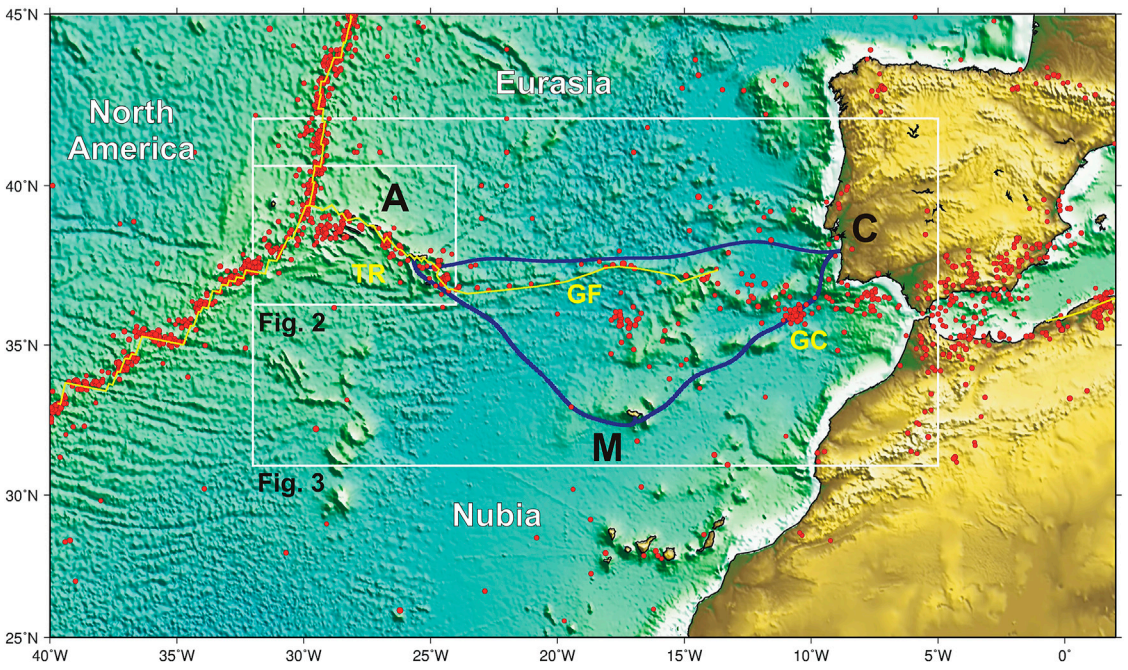


**FIGURE 1 |** Shaded bathymetry map of Iberia, northwest Africa and Central Atlantic (Smith and Sandwell, 1997). Solid yellow line: plate boundaries from Bird (2003). White boxes, location for **Figures 2**, **3**. Small red circles: epicenters, from ISC, M > 4, 1964–2018, http://www.ISC.ac.uk. GC: Gulf of Cadiz; GF: Gloria Fault; TR: Terceira Ridge; C: Mainland Portugal; A: Azores archipelago; M: Madeira archipelago. Thick blue lines show the CAM submarine cables to be replaced by 2024.

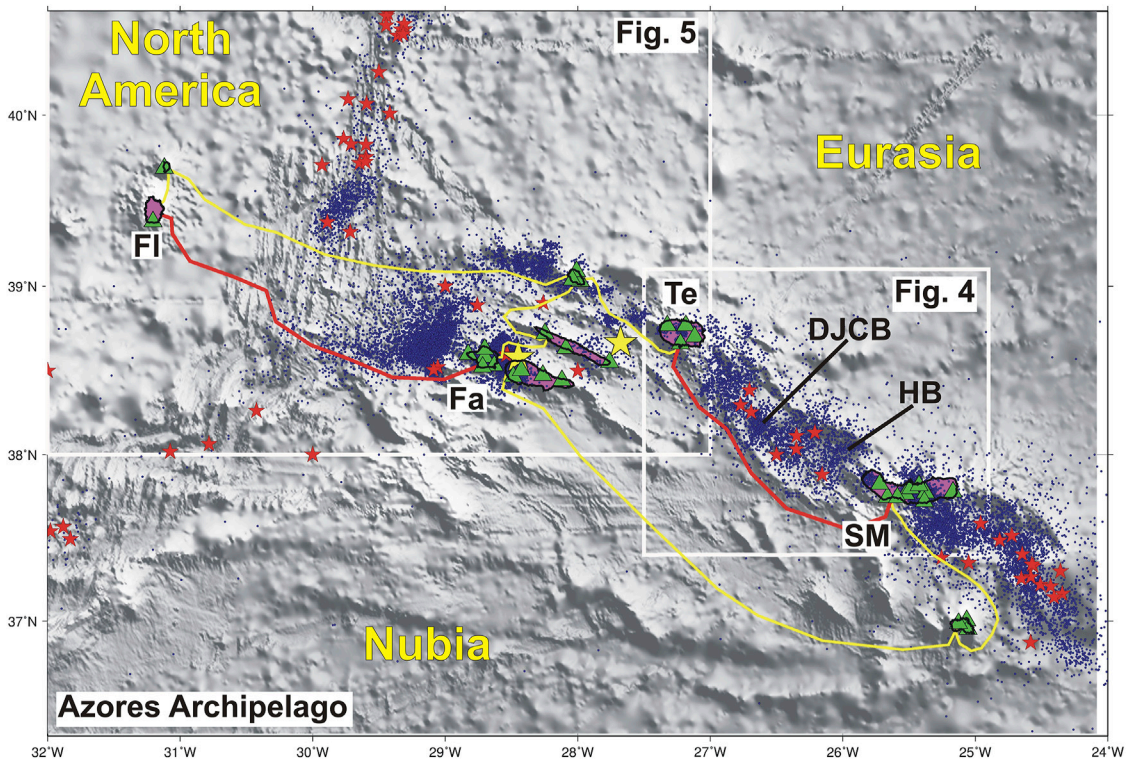


**FIGURE 2 |** Sketch location of the submarine telecom cables in operation at the Azores archipelago (yellow and red lines) overlaying the shaded bathymetry map (Smith and Sandwell, 1997). Frame location provided on figure 1. The cables in red will be discussed in detail later in the text. White boxes for **Figures 4**, **5**. Green triangles show the location of the land seismic stations used by IPMA for earthquake monitoring. Small blue dots: epicenters from ISC, 1960–2019, http://www.ISC.ac.uk. Red starts show the epicenters for M > 5 from ISC, 1920–2019. The large yellow stars show the location of the two most recent destructive earthquakes, the January 1, 1980 and July 9, 1998. Islands mentioned in the text, Fl – Flores, Fa – Faial, Te – Terceira, SM – S. Miguel. DJCB – D. João de Castro Bank, HB – Hirondelle Basin.

earthquakes and tide gauges allowing to detect the tsunami only when they reach the coast. Yet, a unique opportunity is emerging to improve the earthquake and tsunami forecast capabilities in the NE Atlantic using the submarine cables that cross the main active tectonic areas and join Portugal mainland, Madeira and Azores archipelagos on a ring configuration. The current cables will cease their operation by 2024, 2025 and 2028 (due to the end of cable lifetime), and the process of their replacement by a new set of cables is now under consideration by the Portuguese authorities with the technical requirements to be defined in mid-2021. New developments in optical fiber cable technology allowing the use of existing telecommunication cables to provide seismic and tsunami information would be also beneficial to enhance the IPMA's monitoring network capabilities in the Atlantic Ocean.

The mitigation of the hazards posed by offshore earthquakes and tsunamis requires that the monitoring networks provide a timely and precise evaluation of the tectonic sources. There are considerable constraints and limitations when only land stations and coastal tide-gauges are used for the monitoring effort. In this work we show how submarine telecommunication cables can be used to improve the reliability of earthquake and tsunami monitoring. In *Earthquake and Tsunami Monitoring* we describe the current status of the seismic and tide-gauge monitoring networks and the procedures for issuing the first information message for the Civil Protection Agency. In *Optical Fiber Telecommunication Cable Technologies Available* we present briefly three available technologies to provide offshore monitoring services. In *Testing Scenarios* we define the testing scenarios and methodology to be used for each of the three cable technologies. In *Methods and Results* we present the simulation results and make a discussion and conclusions in *Discussion and Conclusions*.

## EARTHQUAKE AND TSUNAMI MONITORING

IPMA (Instituto Português do Mar e da Atmosfera) is the Portuguese Agency responsible for earthquake and tsunami monitoring and it has the responsibility to inform authorities as fast as possible on occurring earthquakes and possible tsunamis. For this purpose, IPMA is collecting seismic data from a dense network, exclusively based on land stations, many of them available through international cooperation (**Figure 3**) (Carrilho et al., 2021). **Figure 3** also shows the

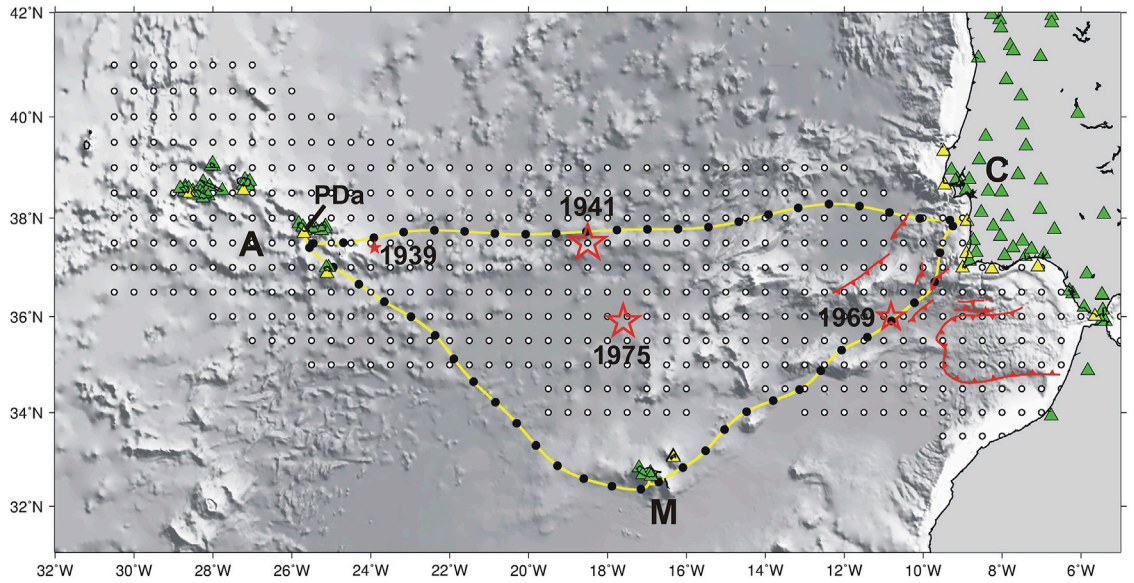


**FIGURE 3 |** Hypothesized location of the submarine telecom cables that are expected to begin operation in 2024 in yellow. The black dots mark the presumed location of telecom repeaters, every 70 km spaced offshore, with the first repeater 40 km from the shoreline. The red stars show the epicenter location of the largest earthquakes that occurred in the area since 1940, 1941, 1975, and 1969. Several tectonic structures (in red) have been proposed SW Iberia as the source of the large earthquake and tsunami the November 1st, 1755. The smallest red star shows the location of the May 8th 1939 (Ms7.1) earthquake that caused a small tsunami recorded in several tide gauges in the Azores. Green triangles show the location of the land seismic stations used by IPMA for earthquake monitoring. PDa – Ponta Delgada tide gauge. Yellow triangles show the location of the coastal tide gauges that are monitored by IPMA for tsunami early warning. The white dots show the location of the tsunami sources in the IPMA scenario database, spaced every half a degree (Annunziato et al., 2009).

location of the largest magnitude earthquakes that occurred in the offshore domain between Portugal mainland and the Azores, all of them having generated tsunamis. Given that there is no consensus on the source area for the Mw ~ 8.5 November 1st, 1755 earthquake and tsunami (Stucchi et al., 2013) we show on **Figure 3** a series of tectonic structures that have been suggested by several authors as its possible source. Another earthquake that occurred close to the Azores, generating a small tsunami, is also mentioned (the Ms7.1 May 8th 1939, Reis et al., 2017).

IPMA is collecting data continuously and seismic events are first detected and evaluated automatically and later on confirmed by an on-duty analyst covering 24/7. The analyst starts validating the phase picks and earthquake parameters as soon as 10 clear waveforms are received recording P-wave arrivals. The detection, classification and location of all offshore earthquakes is a continuous observation as the earthquakes evolves so that the source parameters can be updated in order to inform the local authorities no later than 5 min after the event onset. This first information may be refined and updated afterwards when more data is analyzed by the analyst, but in this work, we focus on the quality of the earthquake parameters presented on this first message.

In parallel IPMA runs the Portuguese National Tsunami Warning Centre (PT.NTWC) which is in charge to issue to Civil Protection and authorities messages reporting the tsunami threat when a large offshore, or close to the shore, earthquake occurs. IPMA is also now recognized by the ICG-NEAMTWS (Intergovernmental Coordination Group for the Tsunami Early Warning and Mitigation System in the North-eastern Atlantic, the Mediterranean and connected seas) as an accredited International Tsunami Service Provider (TSP) responsible for tsunami information to the subscribing countries in the NE Atlantic. Both National and International systems operate under the same rules. As soon as the preliminary earthquake parameters are obtained in the 24/7 operational room, a decision matrix is applied to define the level of tsunami threat and the areas where such a level is applicable. The earthquake parameters required to apply the decision matrix are the epicenter location, magnitude and focal depth. The decision matrix was agreed by the ICG-NEAMTWS based on the best knowledge of past tsunamis in the NE Atlantic. It is a conservative rule that was established with the aim to avoid missing any possible tsunami. Considering this, linked to the uncertainty on the fast earthquake parameters, it is likely that the first message issued by this PT.NTWC/TSP (and others operating under the same rules) will give an alert level often exceeding the final observed tsunami waves. To better evaluate the tsunami threat sea-level observations are required. When these are made available, additional messages are sent updating the threat level and/or cancelling the tsunami alert. With only coastal tide-gauges available (**Figure 3**), considering also that some minutes are needed to measure the initial tsunami wave height (typically a quarter of a period), it is clear that large stretches of the coastline (those where the tsunami arrives first) will not benefit from the more reliable threat level evaluation given by these secondary messages (Omira et al., 2009).

Given that the most credible sources for large tsunamis lie offshore SW Iberia, Omira et al. (2009) showed, using tsunami

simulations, that most on the southern coasts of Portugal do not benefit from enough warning time when the confirmation message is sent. These authors also showed the need to include offshore sea-level real-time measurements in the PT.NTWC/TSP to ensure that all Portugal would benefit from 10 min lead time before the first tsunami wave hits the shore.

The effectiveness and reliability of the earthquake and tsunami monitoring system, that must respond only a few minutes after the event onset, relies heavily on the geometry of the first seismic stations that are used for earthquake location, namely its geographical spreading and distance to the source. We show here two examples of location uncertainties and bias that result from a less than optimal station distribution. These examples reinforce the need for offshore sensors as the ones that can be provided by the fiber optic cable technologies discussed in this work.

From August 2007 to July 2008 a set of 24 broadband Ocean Bottom Seismometers (OBS) were deployed in the Gulf of Cadiz, SW Iberia, within the EU-funded NEAREST project (Integrated observations from NEARshore sourcES of Tsunamis: towards an early warning system) (Geissler et al., 2010). The OBS network revealed many earthquakes that were not previously recorded by the land network and its tectonic interpretation is provided in Silva et al. (2017). Geissler et al. (2010) used the 37 largest earthquakes recorded by the land network and relocated them with the OBS data. Using the information provided by Geissler et al. (2010) we make a graphical comparison between the epicenters and focal depths computed by the two networks, land and OBS. This comparison is shown in **Supplementary Figure S1**. The epicenters located with the land network are several km displaced to land, showing a systematic bias (bias = 17.5 ± 8.9 km). The largest difference between the two networks is found on the focal depth. OBS have shown that most local earthquakes are sourced in the upper mantle, tens of km deeper than the depth obtained from the land network (bias = 32 ± 11 km).

The July 9$^{th}$, 1998 a strong earthquake (ML5.8, Mw6.1) struck the island of Faial causing 9 casualties, more than 150 people injured and the damaging of over 1,500 houses (Matias et al., 2007). This event was recorded by the Azores seismic network and also worldwide with several agencies providing estimates for epicenter, magnitude and focal mechanism in the few hours following the earthquake origin. Matias et al. (2007) show in their **Figure 4** a compilation of published parameter events and those from real-time services available on the Internet. This figure shows a very wide dispersion in the epicenter location that was interpreted as being a consequence of the absence of near-source seismic data. The closest station with data available by international agencies lied in S. Miguel Island, ~300 km away from the source.

## OPTICAL FIBER TELECOMMUNICATION CABLE TECHNOLOGIES AVAILABLE

Recent developments in optical fiber technology allows the use of existing and new submarine telecommunication cables to provide seismic and sea-level information crucial to monitor both earthquakes and tsunamis. In this work we study the potential impact of three different technologies, 1) SMART, Science Monitoring and Reliable Telecommunications; 2) DAS, Distributed Acoustic Sensing, and; 3) LI, Laser Interferometry, on the NE Atlantic earthquake and tsunami monitoring capabilities. From these technologies, only SMART can provide sea-level data to support the Tsunami Early Warning Systems.

### Smart

SMART cables (Howe et al., 2019) are not yet implemented in any place on the world. There are already several dedicated submarine cables with geophysical sensors delivering essential data in real-time to the shore for early warning purposes in Japan (e.g., Okada et al., 2004), United States and Canada (e.g., Barnes et al., 2015; Trowbridge et al., 2019). However, this existing technology is not yet deployed on telecom submarine cables, as proposed by Howe et al. (2019). SMART sensors can only be installed on new submarine cables or reusing decommissioned telecom cables. The basic sensor package that is being proposed comprises ground motion sensors (seismometers, accelerometers or both), absolute pressure gauges for tsunami early warning and environmental monitoring, and one thermometer.

### Das

DAS typically uses a single dedicated (dark) fiber on an installed submarine cable, with a length about ~70 km (although ranges up to 180 km have been mentioned). DAS technology uses optical time domain reflectometry based in Rayleigh or other backscattering effect to detect and localize discontinuities of optical fiber parameters along its length. Due to the backscattering along the fiber, the energy of a particular pulse of time duration T sent to the fiber is detected in the same sending side, as a received signal with time duration of the double of the travel time of the pulse along the fiber. Analyzing the received signal, associated with each sent pulse, with Digital Signal Processing it is possible to measure and define for each specific portion of the fiber (Gauge Length) the respective changes of the fiber strain, from sending pulse to sending pulse. The gauge Length is associated with the time interval T of the pulse sent. A DAS system can be modelled as a one dimensionally distributed fiber strain sensor, with localization ability (Gauge Length) down to some meters. DAS is nowadays a common tool on seismic exploration in the Oil and Gas industry and heavy civil construction infrastructures, being demonstrated its ability to record earthquakes with a resolution similar to broadband seismic sensors.

### Li

In the seminal proof of concept of the method (Marra et al., 2018) the authors use a metrology grade frequency stabilized laser. The laser light is injected into the line as unmodulated sinusoidal carrier wave, with a carrier optical frequency stabilized to optical bandwidth of order 1 Hz. For telecom standards, this is an exceptional low value, albeit standard in time and frequency metrology instrumentation. It is more than a thousand times

below state of the art telecom industry standards, including submarine links. The demonstration (Marra et al., 2018) used an optical back loop at the far side, where a radio-frequency modulation of an acoustic modulator was used to shift the optical carrier frequency. At the receptor side, the two light wave branches were interferometrically combined and detected and analyzed with RF techniques, and the optical phase shift monitored. The LI signal tracks the temporal changes of phase integrated over the whole link range. In bi-directional mode the arrival point of the first seismic waves can be determined and hence the system can be modeled as a distributed sensor. The traces of monitored optical phase shifts can then be compared with typical seismic traces. The proof of concept demonstration showed similarity when compared to seismic traces. LI may use a dedicated so-called dark fiber, or a single wavelength ITU (International Telecommunication Union) channel in an optical fiber with commercial traffic co-existing on adjacent channels. The detection capability of LI probably will extend over the full range of the cable without length limitations.

# TESTING SCENARIOS

## The Background Scenario

The monitoring of earthquakes and tsunamis done in real-time 24/7 by IPMA is exclusively based on land seismic stations and coastal tide-gauges (**Figure 3**). The contribution of submarine cables to this monitoring effort depends on the location of the seismic sources. We then investigate the added value of the three fiber optic technologies considering a regular set of tectonic sources encompassing the main seismically active domains along the Portugal mainland, Madeira and Azores regions.

At the largest scale we used the IPMA tsunami scenario database described in Annunziato et al. (2009). This database comprises a regular set of epicenters (considered as the center of the surface projection of the fault trace) that span the tectonically active areas and cover the main tsunamigenic sources identified (**Figure 3**) with 0.5° interval. At each epicenter the tsunami source considered is the worst case possible (pure dip slip events) with fault parameters as

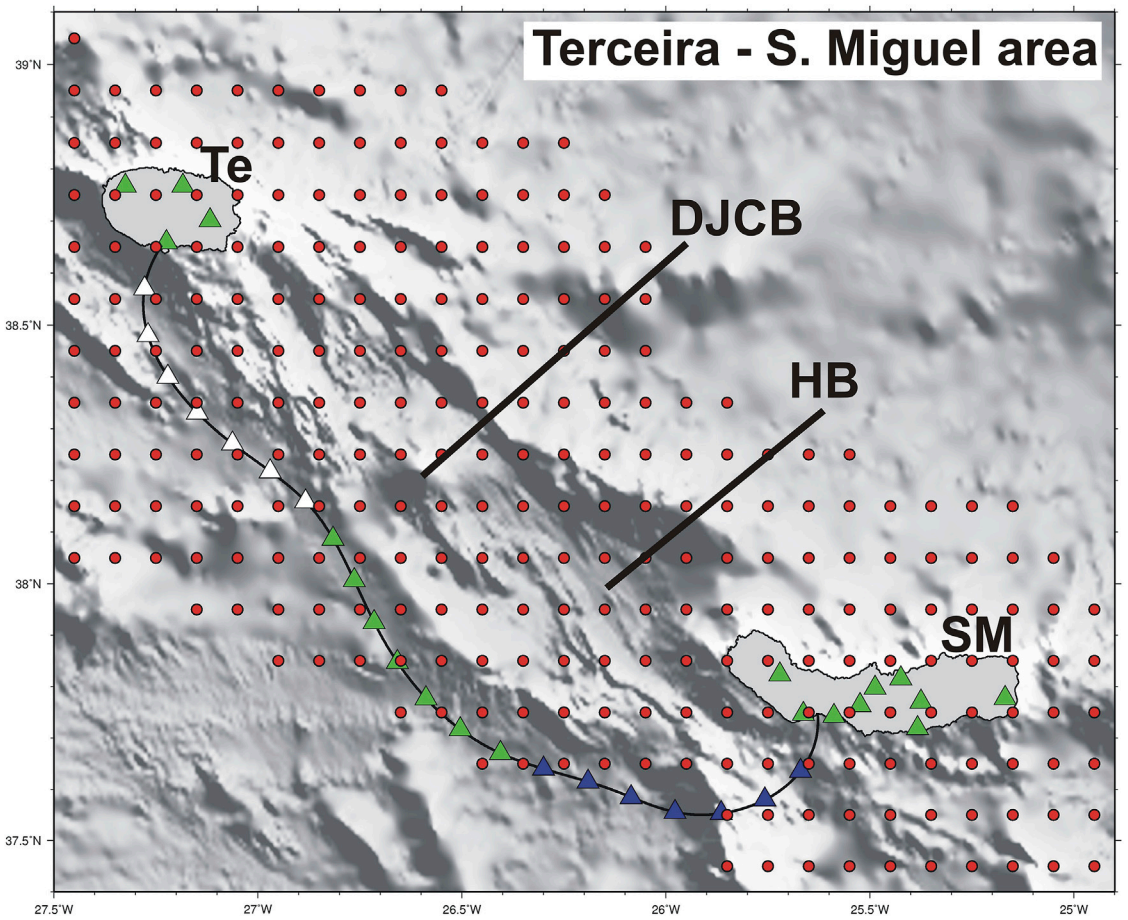


**FIGURE 4 |** Layout of sensors and sources for the investigation of the DAS contribution to the monitoring of earthquakes in the Azores. Red dots show the epicenter synthetic locations, a regular grid with 0.1° interval. The green triangles on land show the existing seismic stations operated by IPMA. Black line is the presumed location of the Terceira-S. Miguel submarine cable, along which the colored triangles show the virtual seismic stations spaced every 10 km. The location strategy adopted considers the cable split into 3 segments that are identified with different colors. Te – Terceira Island, SM – S. Miguel Island, DJCB – D. João de Castro Bank, HB – Hirondelle Basin.

defined in Matias et al. (2013). The depth of the top of the fault is fixed to 5 km (worst case scenario) and magnitudes range from 6.5 to 8.75, spaced every 0.25. A total of ~7,000 scenarios was defined accordingly (~500 locations) and for each scenario the tsunami arrival time and tsunami amplitude at the coast (50 m depth) was numerically computed. The tsunami waveform at each coastal location can be obtained in real time by interpolation of the computed tsunami grids available every minute. The purpose of such tsunami scenario database was to help the tsunami warning system operator to define the threat level to be communicated to Civil Protection and authorities. The database is still used in training but not in the operational procedures, where the decision matrix is applied.

In the Azores this epicenter grid is too sparse, and we used another regular set of synthetic epicenters with a finer grid, appropriate to the known seismicity.

## The Submarine Cable Scenarios

We consider that, whatever the fiber optic cable technology used, the cable can be represented by an additional set of seismic stations and sea-level sensors, contributing to the earthquake and tsunami monitoring like its land and coastal based counterparts, helping to constrain the offshore sources given their closer proximity.

### SMART

In order to meet the low data latency, instrument location and spacing for an effective earthquake and tsunami early warning system we consider that the seismic and absolute pressure gauge sensors are positioned at the presumed locations of the cable repeaters. The closest repeaters to the shore are placed 40 km along the cable while the other sensors are regularly spaced with ~70 km interval. These locations are shown in **Figure 3** for a presumed trajectory of the new CAM ring cables, to be operational in 2024.

### DAS

We consider here that the maximum range of useful information by DAS is 100 km from the land station. This limits the usefulness of DAS in SW Portugal where the most credible sources for large earthquakes and tsunamis are offshore and most of them too distant from the presumed track of the new CAM ring cables (**Figure 3**). However, this technology may prove to be very useful in the Azores archipelago where most of the strongest earthquakes occur offshore, not very far from the Islands, and the seismic stations are concentrated on the Islands forming patches of sensors.

For this reason, we selected one of the most active areas in offshore Azores, the D. João de Castro Bank and Hirondelle Basin, one domain bordered by a submarine telecommunication cable between Terceira and S. Miguel Islands (**Figure 2**).

DAS can provide information on the strain rate along the cable with a gauge length as small as 10 m. For one monitoring length of 100 km, DAS provides information on 10,000 sensors, which is clearly in excess to what can be processed in the earthquake monitoring center. For this evaluation exercise we consider that DAS data is decimated in order to provide strain rate data on virtual sensors spaced 10 km along the cable (**Figure 4**). The cable layout shown is an estimate of the true cable positioning. The synthetic earthquake scenario comprises a regular grid of epicenters with 0.1° interval, spanning the recognized active area (**Figure 4**). As before, focal depth is fixed to 5 km.

### LI

The laser interferometry technology as described in this work allows one to obtain the location of the point in the cable that the seismic waves hit first and the azimuth to the source waves, that must be orthogonal to the cable, with an ±180° ambiguity. This ambiguity can be easily solved in the operational room when more recordings from the land stations are available, or if another LI cable is operating nearby (e.g., Marra et al., 2018). The LI instrumented cable operates as one seismic station where the P-wave arrival time can be measured and where the cable to source azimuth can be also evaluated. However, this seismic station can be anywhere along the cable, depending on the relationship between the cable and the earthquake epicenter.

To evaluate the contribution of LI technology to the monitoring of earthquakes we consider that it can be replaced by a regular set of seismic stations (able to compute also the azimuth to the source) with a regular spacing of 8 km along the cable. This value exceeds the probable location uncertainty of the impact point on the cable, but it was found adequate for the following analysis. The longer the cable, the more advantageous will be the LI technology. Since the Azores – Madeira – Mainland is investigated using the SMART technology, we choose the Azores as the most interesting area to demonstrate the added value of LI. In the Azores, one of the longest cables is the one joining Faial and Flores Islands (**Figure 2**) 260 km long. It crosses the Mid-Atlantic Ridge plate boundary and borders by the south a very seismically active area, west of Faial, where several felt earthquakes have been generated in the past causing concern among the population and authorities. The total number of virtual seismic stations along the cable is 32. The experiment layout for LI is shown in **Figure 5**. The focal depth of the synthetic epicenter grid is fixed to 5 km.

# METHODS AND RESULTS

## Tsunami Monitoring

Out of the three fiber optic technologies investigated in this work, only SMART sensors, measuring the absolute pressure with high resolution (by an APG), can provide offshore real-time data as required for an effective PT.NTWC/TSP. In Howe et al.[1] (submitted) we find the gain in warning time that a set of sensors deployed along the cables Mainland-Madeira and Mainland-Azores can provide. This is a simple consequence of

[1]Howe, B., Angove, M., Arcas, D., Aucan, J., Barnes, C. R.,Barros, J., et al. (2020). SMART Subsea Cables for Observing the Earth and Ocean: Update. Front. Mar. Sci.

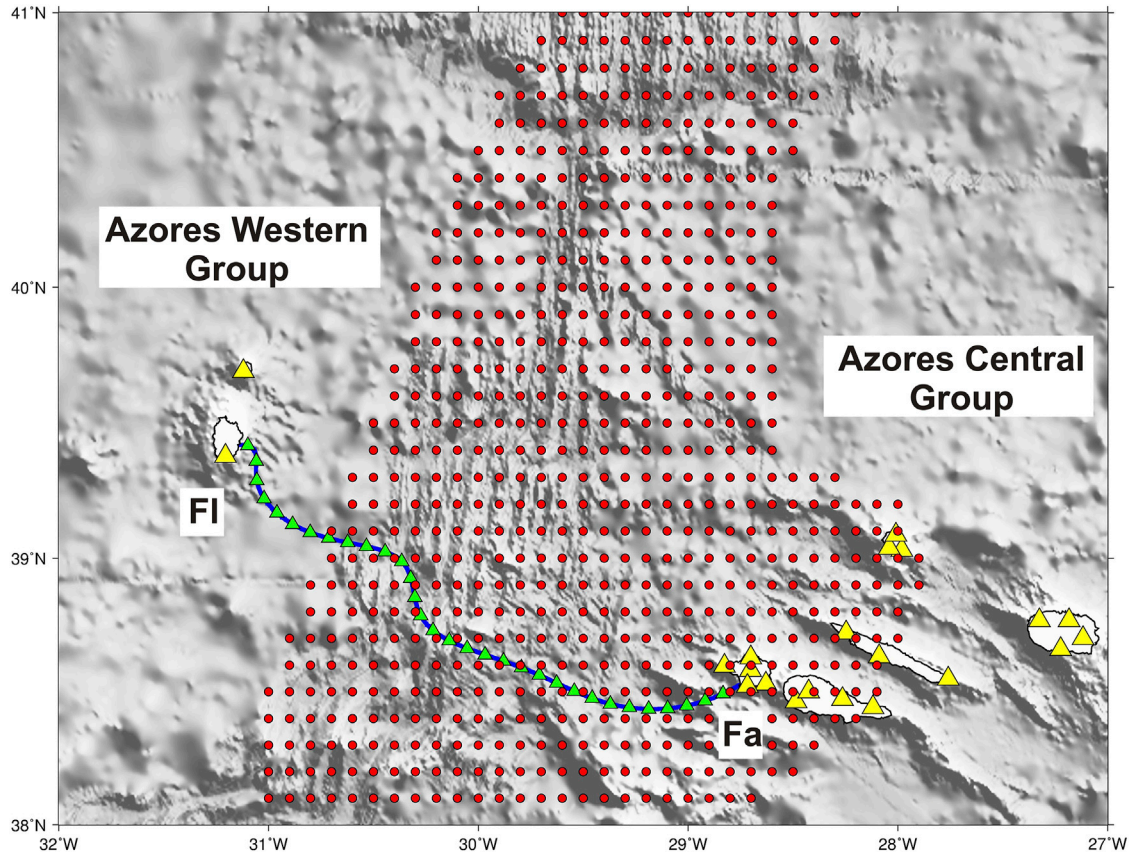


**FIGURE 5 |** Layout of sensors and sources for the investigation of the LI contribution to the monitoring of earthquakes in the Azores. Red dots show the epicenter synthetic locations, a regular grid with 0.1° interval. The yellow triangles on land show the existing seismic stations operated by IPMA. Blue line is the presumed location of the Faial-Flores submarine cable, along which the green triangles show the virtual seismic stations spaced every 8 km. FI – Flores Island, Fa – Faial Island.

the geometry of the offshore APGs and required only the computation of the minimum tsunami travel time to the land based, or cable based, sensor networks.

In addition to the gain on the minimum-tsunami detection time, we believe that the proposed cabled sensors will allow improving the performance of the PT.NTWC through recording tsunami signals of better quality than the ones typically recorded by the coastal tide gauge (CTG) network. The preparation of the tsunami confirmation messages by the PT.NTWC operator requires the identification and measurement of tsunami wave characteristics (arrival time, wave height, and period). Sometimes, this task is hard to perform due to the quality of the sea-level signal at CTG that usually includes the tidal variation and is contaminated by coastal effects, involving noise able to mask the tsunami signal. Any additional treatment of the sea-level record to isolate the tsunami signal (quality control, de-tiding and noise removing) before measuring the waves characteristics may consume critical operator time. The presence of cabled sensors will allow overcoming this limitation as they will offer the possibility to record the tsunami in the open ocean without the coastal effects. To explore such a benefit, we present a numerical tsunami propagation scenario involving a Mw8.3 earthquake similar to the 1941 strike-slip event that took place on the Gloria Fault (Omira et al., 2019). The tsunami numerical simulation is performed using a validated non-linear shallow water code in the presence of both offshore geophysical repeaters (cabled sensors) and coastal tide gauges (**Figure 6A**). Synthetic sea-level records at both the costal tide gauge of Ponta Delgada (**Figure 6B**) and the cabled sensor GR-8 (**Figure 6C**) are then compared. The comparison clearly shows that the cabled sensor allows a fast confirmation of tsunami occurrence and an easy measurement of the wave characteristics (wave arrival, height and period) required to update the tsunami alert messages.

It is also worth mentioning that the installation of sensors in the submarine cable can significantly boost the development of the next-generation TWS in the NE Atlantic. Integrating rapid offshore tsunami observations and advanced tsunami numerical models is crucial to develop real-time and reliable tsunami forecasting (Titov et al., 2005). The Pacific TWS inverses the offshore tsunami signals (from oceanic buoys) to determine the earthquake-induced initial sea surface perturbation. This latter is

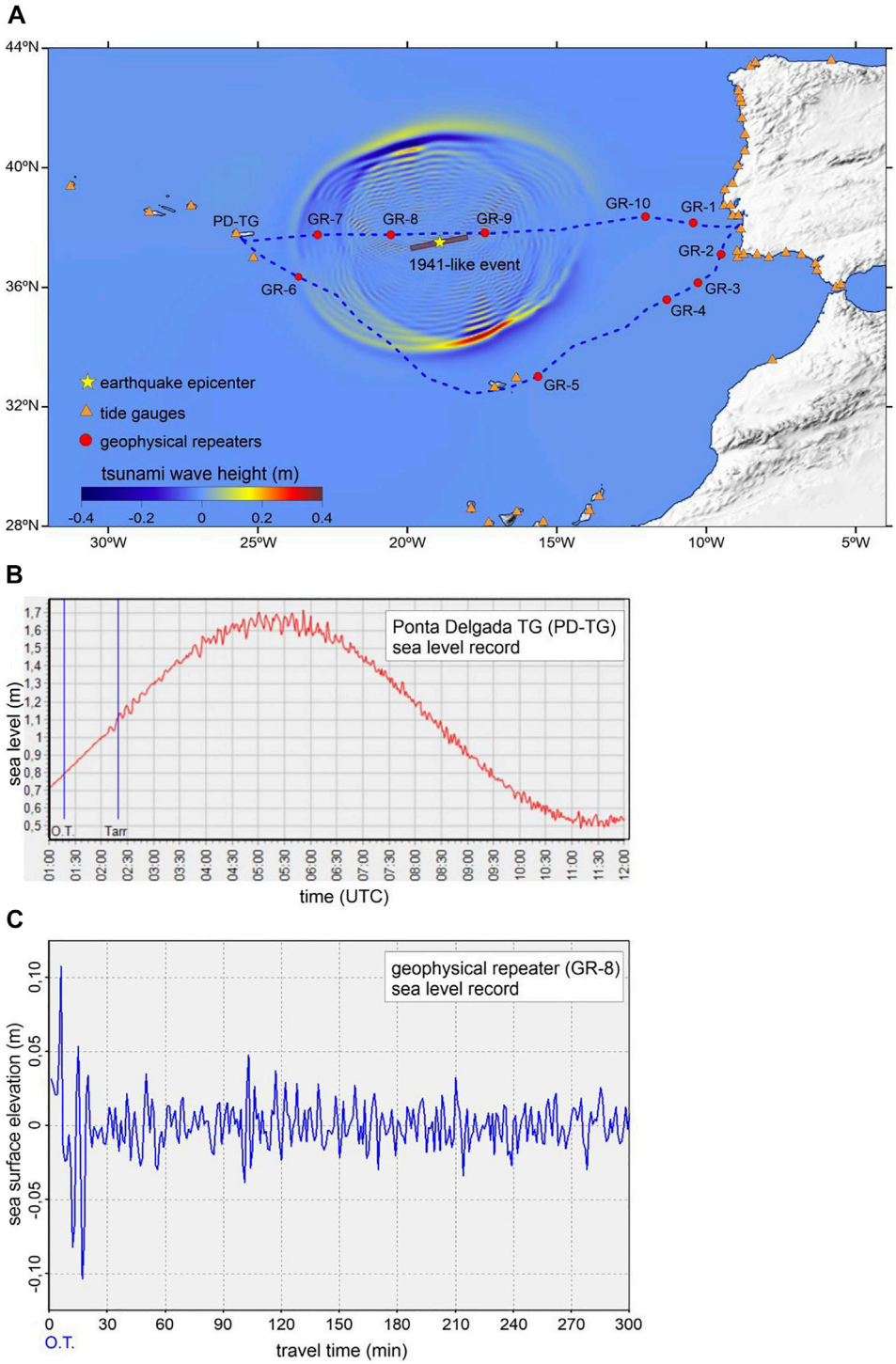


**FIGURE 6 |** Sea-level signal quality comparison. **(A)** tsunami numerical propagation for a 1941-like earthquake in the presence of cabled sensors and tide gauge stations **(B)** signal recorded at the Ponta Delgada tide gauge; **(C)** signal recorded by a cabled sensor (GR-8 in a). OT = earthquake origin time.

then used as initial condition for "faster-than-real-time" numerical code enabling to predict the tsunami threat on the coast. The implementation of such a methodology in the NE Atlantic TWS would be possible with the presence of cabled sensors allowing early and high-quality tsunami observations. Offshore real-time sea level measurements may also provide early warning for non-tectonic tsunami sources like submarine landslides.

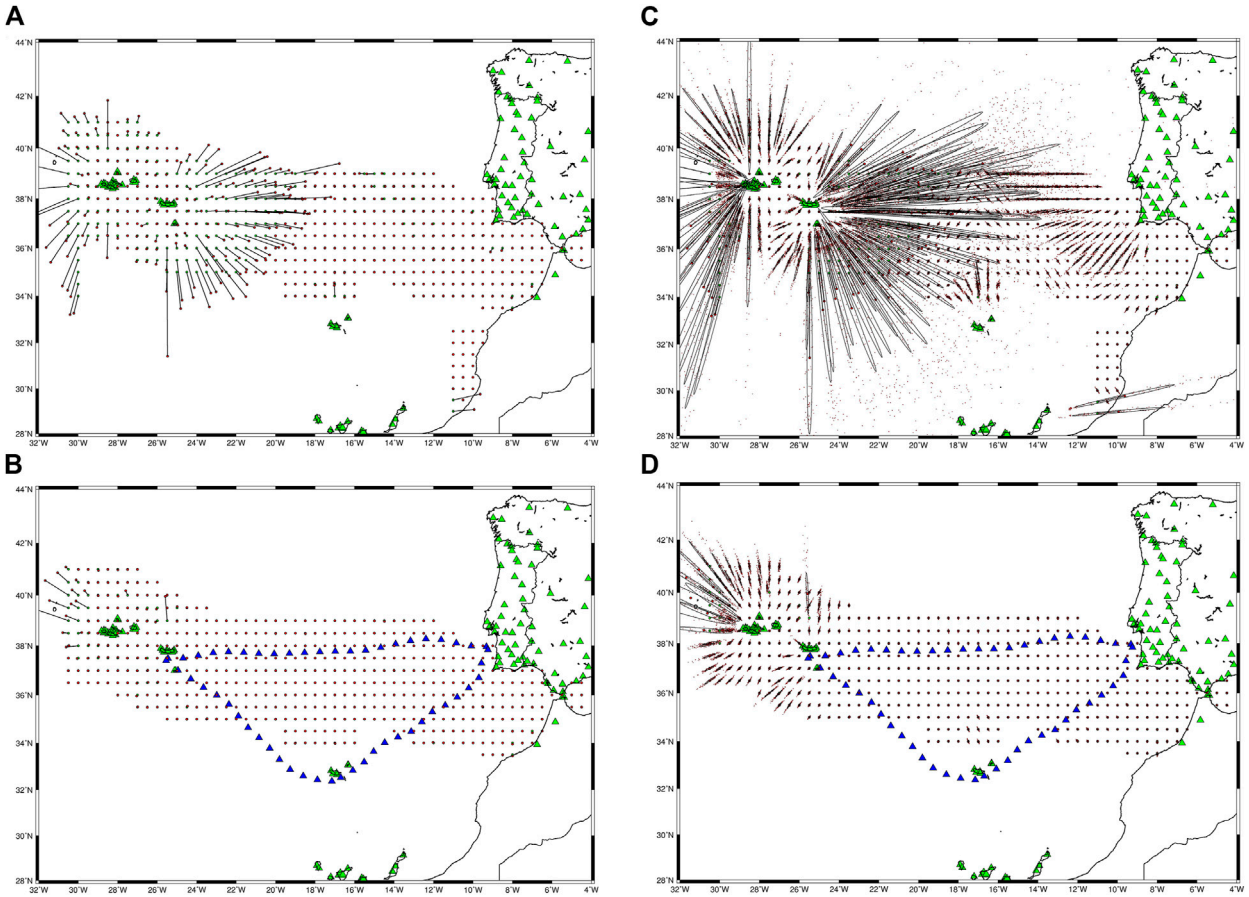


**FIGURE 7 |** Visual comparison of Monte-Carlo quality earthquake location parameters when the synthetic catalogue is analyzed by the land only seismic station network (LAND, green triangles) or analyzed by the land and cabled (CABLE, blue triangles). **(A)** Distance between the MC centroid (in red) and the true location (in green) for LAND. **(B)** Distance between the MC centroid (in red) and the true location (in green) for CABLE. **(C)** All MC epicenters computed, and the uncertainty ellipse computed from the covariance of the horizontal coordinates for LAND. **(D)** All MC epicenters computed, and the uncertainty ellipse computed from the covariance of the horizontal coordinates for CABLE.

## Earthquake Monitoring

The quality of the fast-computed earthquake parameters that are used for alerting Civil Protection is critically dependent on the geometry of the seismic network and its relationship with the source location. In Howe et al. (submitted) we examined the added value of cabled sensors using the SMART technology on 2 geometric parameters: 1) the maximum azimuthal gap between epicenter and recording stations; 2) the geometrical quality defined by Bondár and McLaughlin (2009) that takes also into consideration the regularity of the azimuth distribution. We also computed the gain in earthquake warning time which is a parameter that only depends on the network geometry (Howe et al., submitted). This parameter is most relevant for the performance of an Earthquake Early Warning System (EEWS) which is planned but not yet operational in Portugal. The great improvement on the performance of one EEWS in Portugal demonstrated in Howe et al. (submitted) will not be further discussed in the present work.

These geometrical parameters, though relevant, cannot make a realistic assessment of the uncertainty that arises while determining earthquake parameters from a limited set of P-wave readings poorly located, either for the stations being far from the source or for them being too close together. In this work we present and apply Monte-Carlo simulations that take into consideration the errors in phase picking and the level of uncertainty on the velocity model used to compute the theoretical phase arrival times for a more representative evaluation of earthquake parameter uncertainties.

### The Monte-Carlo Approach

We use 100 simulations of a synthetic set of phase readings computed with a velocity model that is altered from the used after for earthquake location. The location code is Hypocenter (Lienert et al., 1986), included in the seismic analysis tool SEISAN (Havskov et al., 2020). This is the same routine that IPMA uses in the seismic operational room. It uses a 1D velocity model that is changed according to the domain where the

epicenter is found. These 1D models were obtained from published geophysical studies and they should represent an average of the velocity structure in each domain. However, the earth structure is not 1D.

To make a 1st order account for the 3D nature of the Earth in the AZGFZ area, IPMA uses in earthquake location different 1D models according to the earthquake epicenter (see Custódio et al., 2015, **Figure 3**). The models that apply to Portugal margins and the Gulf of Cadiz, to the oceanic domain to the West up to the Azores Archipelago, and to the Azores platform are shown in **Supplementary Figure S2**. The IPMA models are compared to two local models derived for detailed studies, Geissler et al. (2010) in the Gulf of Cadiz et al. (2007) in the Central Group of the Azores, showing the heterogeneity of the area at different scales. It was not the purpose of the present investigation to check if a 3D velocity model was more appropriate than 1D models for earthquake location. Instead, we wanted to explore the performance of cabled and not cabled seismic networks when a change in the "true" 1D velocity is considered. For this purpose, we used the IPMA "Margin" model to investigate the CAM geometry and used the IPMA "Azores" model to investigate the contributions of DAS and LI to earthquake location.

Starting with the "true" location on the synthetic catalogue, each Monte-Carlo (MC) simulation begins by defining one set of phase arrivals considering two types of random fluctuations: 1) P-wave phase picks are changed by a Gaussian random error with SD 0.2 s; 2) the velocity model is also modified by a Gaussian random perturbation. The velocity values are modified with 10% SD and the layer depths are changed by 1 km SD. These may be considered conservative values since we expect larger differences on the average velocity model the further away the station is from the epicenter.

Each MC simulation results into a set of earthquake location parameters computed with slightly different input parameters. Taken together, the 100 simulations can be used to assess the earthquake parameter uncertainty for a given network geometry, land stations only or land plus cabled sensors, for a set of synthetic locations regularly spaced. We translate this variability in a geographical grid using two quality parameters: 1) DD – the distance between the MC epicenter centroid and its true location; b) SS one length parameter equal to the square root of the area of the uncertainty ellipse defined by the covariance of the 100 simulations, $SS = \sqrt{s_1 s_2}$ where $s_1$, $s_2$ are the eigen values of the covariance matrix on the epicenter latitude and longitude measured in km. SS represents the radius of the circle that has the same area as the epicenter uncertainty ellipse. This is easier to interpret than using $s_1$ or $s_2$ since the ellipses are usually very elongated on one direction due to the geometrical constrains of the observation networks.

## SMART

The added value of the SMART cable to earthquake monitoring is presented here considering the domain between Portugal mainland and the Azores, as displayed in **Figure 3**. This figure also shows the synthetic epicenter grid that will be used in the evaluation. The background scenario was computed considering that the fast earthquake parameters are obtained with the first 10 P-wave arrivals recorded on the land stations that were presented in **Figure 3**.

**Figure 7A** shows the comparison of the centroid location from the 100 MC simulations and the true synthetic catalogue. From the 100 locations on each synthetic epicenter we compute the covariance matrix of the epicenter coordinates to define an uncertainty ellipse. This ellipse and all epicenters are displayed in **Figure 7C**. These two plots show sharp transitions on these two quality parameters that are related to the geographical distribution of stations that are used for each location. The wider this distribution, the better constrained is the MC epicenter.

The contribution of the SMART cable to earthquake monitoring is evaluated using the cabled sensors presented in **Figure 3** on all 3 branches. The same operational procedure is used here, the epicenters are computed using the first 10 stations (on land or on the cable) to record the P-wave arrival. When we began evaluating the results, we noted that quite a few of the offshore events were very poorly located by the "land pluscabled" network when only cabled sensors were used for the 10 first recordings. This is easy to explain since the cabled sensors are deployed along the linear cable which is a very poor distribution for stations to compute earthquake parameters. This is a problem, poor azimuthal coverage of the first 10 stations, that is already found by IPMA in the Azores, where the stations are concentrated on the Islands forming an E-W elongated archipelago. When a poorly constrained geometry is identified by the operator, it is decided to force the analysis to use data from close by Islands. A similar procedure was used here to mitigate the problem of having a large number of stations located along a line.

We split the cable into its 3 branches, CM, CA and MA, and forced the location algorithm to use at least one station from 4 groups of stations, 3 cabled plus the land network. **Figures 7B and 7D** display for the MC simulation of "land plus cabled" network locations respectively the comparison between centroid and true location (used to define the DD quality parameter) and the uncertainty location ellipses (used to compute the SS quality parameter). When compared to the land only results, a general improvement on the earthquake locations is observed when using the cabled sensors. There remain a few outliers, most of them at the border of the area investigated by the synthetic catalogue hinting that additional operational rules might need to be considered to address these particular events.

To quantify the added value of the SMART cable we built geographical grids with the DD and SS quality parameters previously defined. The gain in DD and SS obtained by the SMART cable is shown in **Figure 8**. The largest improvement on DD, the distance between the true epicenter location and the MC centroid is observed East of the Azores Archipelago, up to 21°W. East of 21°W the gain in DD is smaller, with some patches showing no improvement and others showing an improvement up to 40 km.

The added value of the SMART cable is more evident when we consider the reduction in the length parameter SS shown in **Figure 8B**. All domain between the Azores and 8°W is benefited with a gain in SS that attains 100% or more. There is a triangular shape north of Madeira where the reduction in SS is smaller but still very significant, larger than 40%. The Azores Archipelago is not covered by cabled sensors and consequently there is no gain

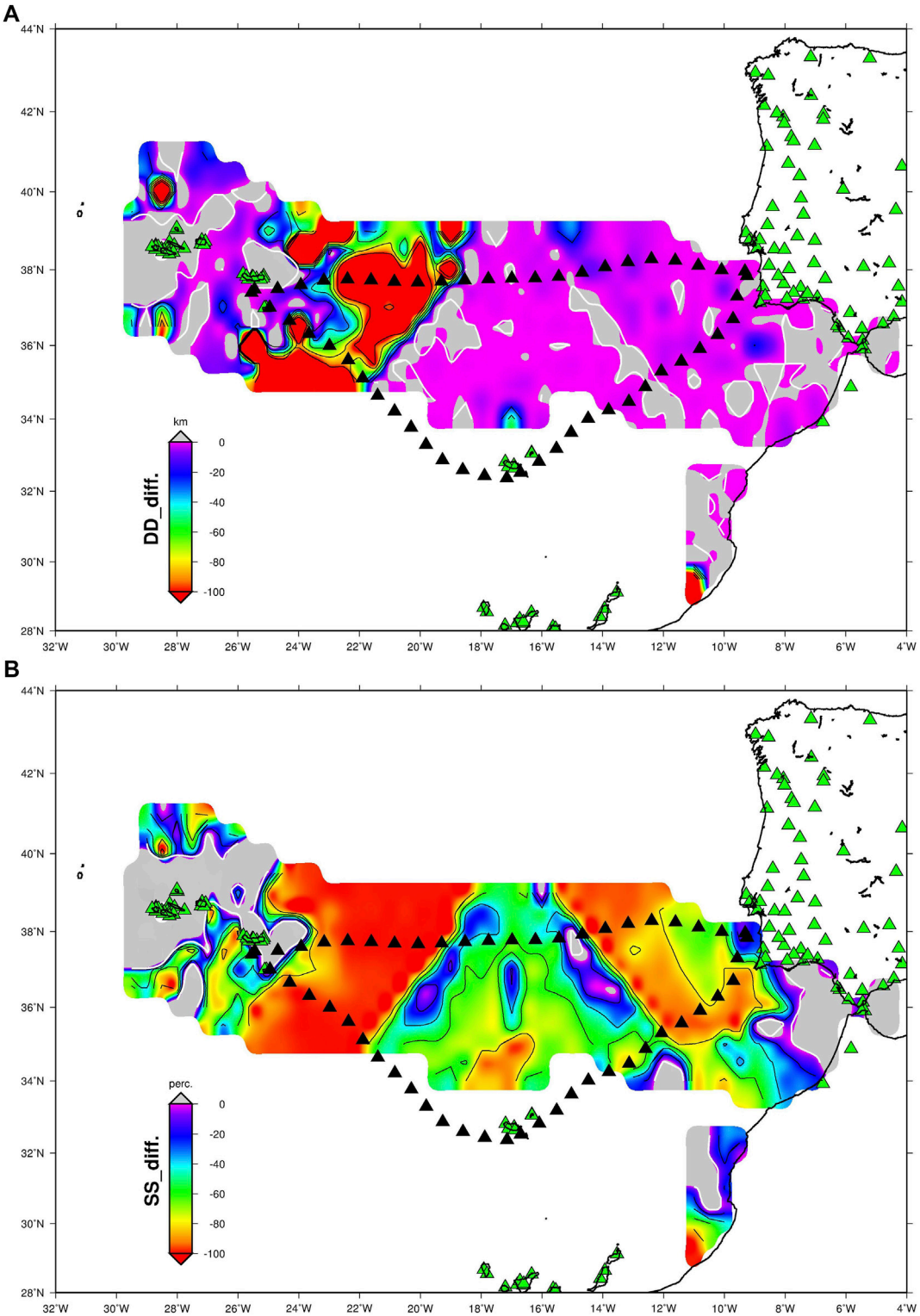


**FIGURE 8 |** Measure of the added value of the SMART cables to the earthquake fast parameter determination using Monte-Carlo simulations. Green triangles show the land seismic stations while the cabled stations are shown as blue triangles. **(A)** Difference between "land plus cabled" and land only networks for the DD quality parameter. **(B)** Difference between "land plus cabled" and land only networks for the SS quality parameter, in %. On both images red areas show the domains were the difference is less than the maximum value, light grey areas show the domains were no improvement was observed.

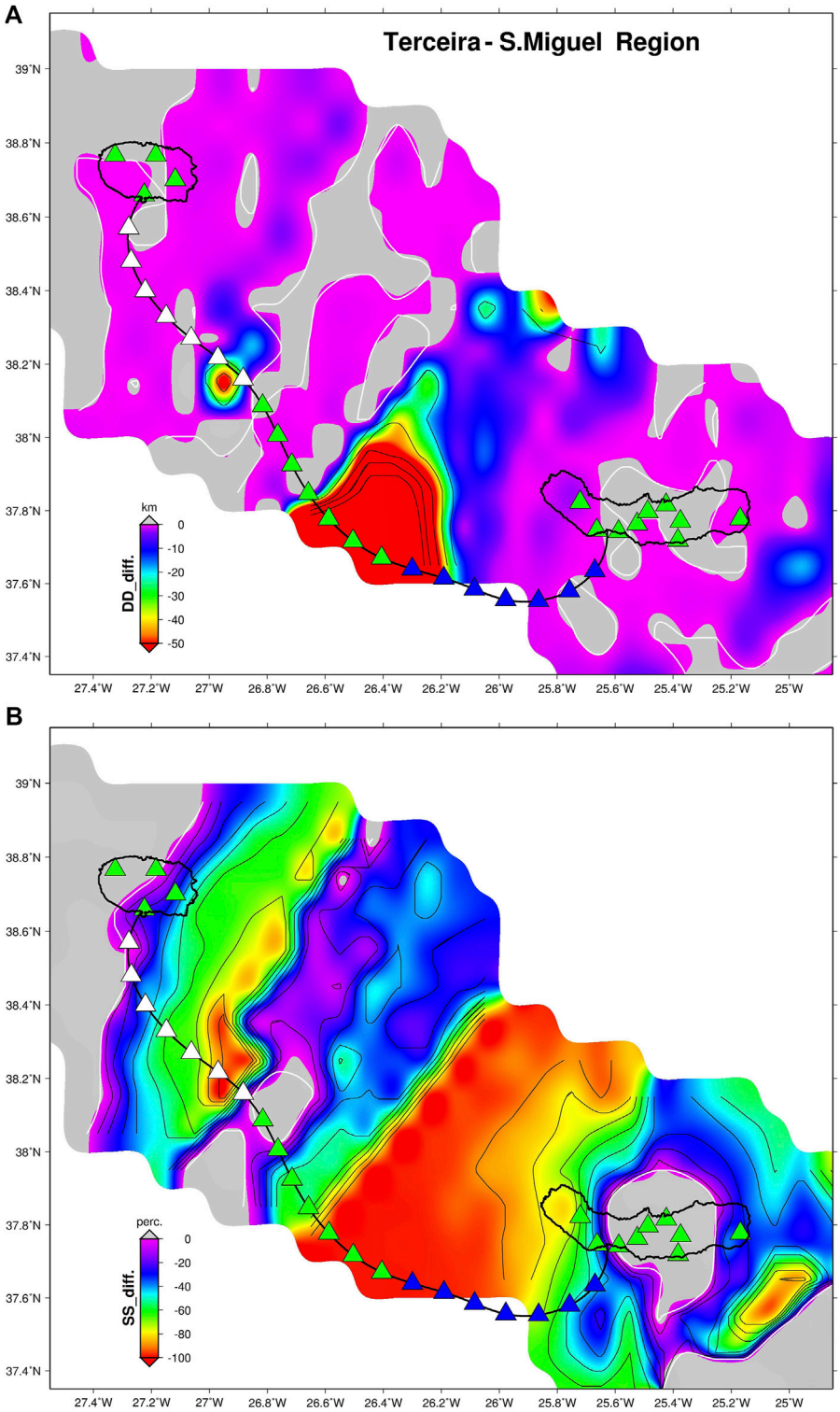


**FIGURE 9 |** Measure of the added value of the DAS to the earthquake fast parameter determination using Monte-Carlo simulations. Green triangles show the land seismic stations while the cabled stations are shown as blue triangles. **(A)** Difference between "land plus cabled" and land only networks for the DD quality parameter. **(B)** Difference between "land plus cabled" and land only networks for the SS quality parameter, in %. On both images red areas show the domains were the difference is less than the maximum value, light grey areas show the domains were no improvement was observed.

in most of the region. There is no gain also east of 8°W because the contribution of the cabled sensors is done by stations that are very far away.

### DAS

The layout of the experiment designed to evaluate the added value of DAS to earthquake monitoring was explained in *Testing Scenarios*. Station distribution and synthetic epicentres are shown in **Figure 4**. We consider that one event is ready for location as soon as the P-wave reaches the 10 closest stations. For offshore events this may result in poor locations when all these stations are the cable sensors that are located along a line with bad azimuthal coverage. For this reason, we split the full set of sensors into 5 groups, one for each island and the cable split into 3 additional groups (**Figure 4**). The location is done only when at least one station from each group is included in the first 10 stations. Later P-wave arrivals are discarded until this condition is met. The background scenario comprises the land stations only.

**Supplementary Figures S3A** shows the comparison of the centroid location from the 100 MC simulations and the true synthetic catalogue for the background scenario. For this scenario, the uncertainty ellipse computed from the covariance matrix of the epicenter coordinates is displayed in **Supplementary Figure S3C**. The same parameters for the "land plus cabled" scenario are shown in **Supplementary Figures S3B,D**.

The added value of the DAS is better expressed by comparing the geographical grids built with the DD and SS quality parameters, as shown in **Figure 9**. The gain in DD (**Figure 9A**) is small in most of the domain investigated, less than 10 km or absent. The larger difference (greater than 10 km) is obtained West and NW of S. Miguel Island, with maximum decreases in DD larger than 50 km.

The gain in SS (measuring the MC uncertainty ellipse area) is more widespread over the whole offshore domain investigated between S. Miguel and Terceira Islands (**Figure 9B**). The % decrease in SS in larger than 50% in most areas, except for one transversal domain, closer to Terceira Island. The sharp transition in SS values observed is a natural consequence of the geometry of the network and the resulting choice of the 10 best stations to use for the fast earthquake parameter determination.

### LI

The LI experiment was presented in *Testing Scenarios* and the layout of seismic stations and synthetic epicenters was shown in **Figure 5**. As before, we consider that the first earthquake location is obtained when 10 P-wave arrivals are recorded. The cable LI counts as a unique station that has two properties, it can be anywhere in the cable (split into 8 km sections) and that station, besides the phase arrival time, can provide the station to azimuth angle. The 180° ambiguity can be easily sorted out on the operation room. In the process of selecting the 10 stations used for computation we discard the LI stations that are closest to the shore. We consider that, for those locations, the azimuth is unreliable because the seismic waves can be originated from any location to the East or West of the cable. It is clear that the LI cable will improve the fast earthquake location if and only if one of the virtual cable locations is used.

**Supplementary Figure S4A** shows the comparison of the centroid location from the 100 MC simulations and the true synthetic catalogue for the background scenario. For this scenario, the uncertainty ellipse computed from the covariance matrix of the epicenter coordinates is displayed in **Supplementary Figure S4C**. The same parameters for the "land plus cabled" scenario are shown in **Supplementary Figures S4B,D**.

By gridding DD and SS for the two scenarios, we can measure the gain provided by LI on a geographical grid. The gains obtained are shown in **Figures 10A,B** for DD and SS respectively. The comparison between MC centroids and the true synthetic location shows that LI improves significantly on a small domain in the middle of the LI cable. The remaining area investigated shows only a small improvement (less than 10 km) or no gain at all. The patchy pattern observed is a consequence of the MC simulations with random stochastic variations. Two runs of 100 simulations will not be identical even if using the same set of stations.

On the other hand, the comparison of the uncertainty ellipse area, SS shown in **Figure 10B**, displays a considerable gain obtained by the LI cable on a large triangular domain with one vertex to the NE of the cable. This triangular shape illustrated the source domain where one LI cable station contributes to the earthquake location. When that happens, the knowledge of one additional P-wave arrival and the azimuth from station to event improves significantly the fast determination of earthquake parameters, essential for Civil Protection authorities. One single station could make a huge difference.

## DISCUSSION AND CONCLUSIONS

Fiber optic submarine cables that are used for telecommunications provide nowadays two technologies that can be used for the improvement of offshore earthquake and tsunami monitoring: 1) SMART – the deployment of geophysical sensors on new cables (Howe et al., 2019); 2) DAS – recording fiber strain rate on existing (or new) dark fibers (e.g., Fernández-Ruiz et al., 2020). One emerging technology, LI, is based on ultra-stable laser interferometry, it can be used on existing cables, doesn't need a dark fiber to be applied, and shows high potential for real-time measurements of strain rate along the fiber (Marra et al., 2018). In this work we explored and quantified the contributions that each of the three technologies could bring to the earthquake monitoring effort along the Azores-Gibraltar plate boundary, a very active domain responsible for the largest earthquake in Europe since year 1000 (Stucchi et al., 2013). As regards tsunami observation, only SMART cables can provide sea-level observations on the open ocean, as required by a fast and reliable evaluation of the tsunami threat level.

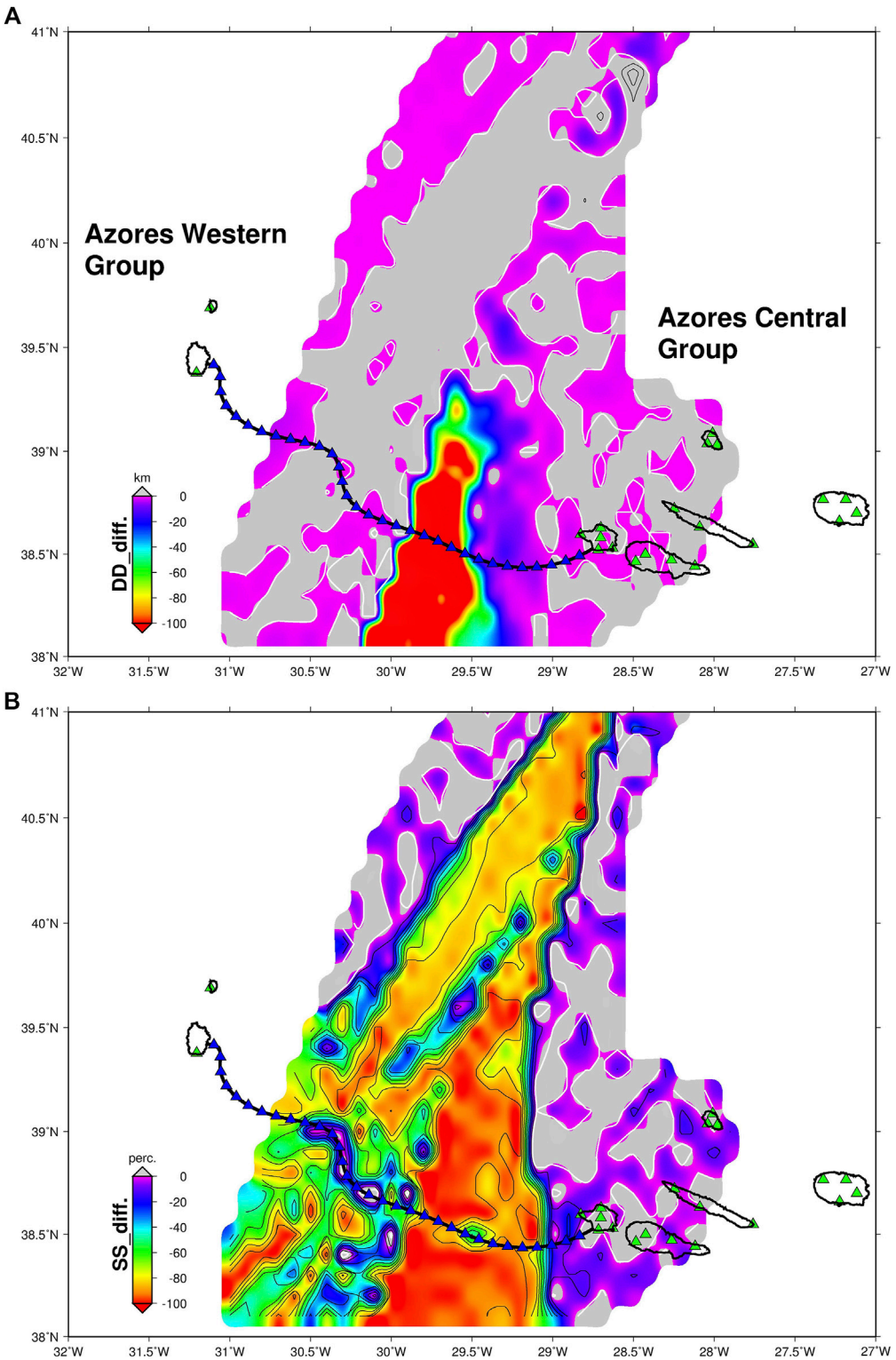


**FIGURE 10 |** Measure of the added value of the LI cable to the earthquake fast parameter determination using Monte-Carlo simulations. Green triangles show the land seismic stations while the cabled stations are shown as blue triangles. **(A)** Difference between "land plus cabled" and land only networks for the DD quality parameter. **(B)** Difference between "land plus cabled" and land only networks for the SS quality parameter, in %. On both images red areas show the domains were the difference is less than the maximum value, light grey areas show the domains were no improvement was observed.

Our exercise was based on the standard operation routines at IPMA, the Portuguese agency responsible for the earthquake monitoring in this domain, namely that the first message to be issued to authorities has to be delivered in less than 5 min after the event onset. The operator starts the validation of the automatic picking and earthquake parameter computation as soon as 10 P-wave arrivals are received. The quality of these first parameters is strongly dependent on the geometry of the 10 stations that are used for the location. Tsunami waves can only be currently observed by coastal tide gauges and the update of tsunami information will not benefit the coasts that are hit first.

The changes in parameters that depend exclusively on the geometry of the network, maximum azimuthal gap between recording stations, the U parameter defined by Bondár and McLaughlin (2009), the time needed to reach the minimum number of seismic stations for Earthquake Early Warning, the time needed to reach the first sea-level sensor used for Tsunami Early Warning, are presented in Howe et al. (submitted). In this work we proposed to go one step further from simple geometrical considerations.

Considering tsunamis, we showed how the detection of changed sea-level is much faster and simpler in offshore sensors than in coastal tide-gauges, opening the opportunity for assessing the tsunami threat by numerical modeling, before the waves arrive to the coast.

As regards earthquake monitoring, we concentrated our efforts on the gain that cable sensors can provide to the very first information that is communicated to the authorities based on the first 10 P-wave readings that are recorded by the seismic network. The earthquake location is then derived using an appropriate 1D velocity model. Two sources of errors contribute to the uncertainty on the epicenter location, an ambiguity in the P-wave reading and the inadequacy of the velocity model to simulate the wave propagation on a 3D Earth structure. We used 100 Monte-Carlo simulations to assess the variability on the epicenter computation that results from these two sources of uncertainty. Two MC quality parameters were considered: DD – the distance between the MC centroid of epicenters and the true location defined on a synthetic catalogue; SS – the square root of the area of the uncertainty ellipse as defined by the covariance matrix of the epicenter coordinates. Since the cabled sensors are aligned along the linear submarine cable, they are not very helpful, due to its poor azimuthal coverage, if they are the only sensors used for earthquake location. For this reason, we devised a strategy for the choice of the 10 stations to be used for the fast earthquake parameter determination, that can be easily implemented in the operational room taking the IPMA practice in the Azores as an example.

When comparing the background scenario (land stations only) with the improved scenario (land plus cabled network) we observed that the comparison of MC centroid locations was not very helpful to bring out the added value of the cable technologies. The centroid is an average and it seems that, with the simulation parameters used, in many domains, the land only network is able to recover the true epicenter on average. However, in real life we don't have 100 repetitions of each event. We showed that, despite DD being small, the uncertainty on epicenter determination as measured by SS is large or very large when land stations only are used. All 3 technologies investigated, SMART, DAS and LI showed very significant reduction on the epicenter uncertainty in the offshore domains that are known to be able to generate strong earthquakes and tsunamis.

The added value provided by instrumented submarine telecommunication cables to mitigate earthquake and tsunami risk that is demonstrated in this work may help authorities and the society in general to take the political decisions required for its full implementation.

## DATA AVAILABILITY STATEMENT

The original contributions presented in the study are included in the article/**Supplementary Material**, further inquiries can be directed to the corresponding author.

## AUTHOR CONTRIBUTIONS

LM wrote the 1st version of the manuscript with input from all authors. All authors made substantial contributions to the overall science case and manuscript and approved it for publication. RO and FC drafted the tsunami monitoring case. LM, FC, and CC drafted the earthquake monitoring case. VS, MN, and YO drafted the DAS and LI cases. JB contributed the manuscript ideas and for the references calling the attention for the need of having political decisions.

## FUNDING

The authors thank the support from Fundação para a Ciência e a Tecnologia (FCT, Portugal), namely through projects UIDB/50019/2020 and UIDB/50008/2020.

## ACKNOWLEDGMENTS

The investigation presented in this work is one of the activities that have been conducted by LEA, Listening to the Earth under the Atlantic partnership which resulted from an agreement established between IT, IPMA and IDL. One of the main objectives of LEA is to promote research, development, training and outreach on the observation and recording of geophysical and oceanographic phenomena using submarine cables, fostering its applications to Science and Civil protection. LM acknowledges the fruitful discussions with Bruce Howe, Bill Fry and Amir Salaree.

## SUPPLEMENTARY MATERIAL

The Supplementary Material for this article can be found online at: https://www.frontiersin.org/articles/10.3389/feart.2021.686296/full#supplementary-material

## REFERENCES


Annunziato, A., Carrilho, F., Matias, L., Baptista, M. A., and Omira, R. (2009). Progresses in the Establishment of the Portuguese Tsunami Warning System. *EMSC Newsletter*, 10–12. April.

Baptista, M. A., Miranda, J. M., Batlló, J., Lisboa, F., Luis, J., and Maciá, R. (2016). New Study on the 1941 Gloria Fault Earthquake and Tsunami. *Nat. Hazards Earth Syst. Sci.* 16, 1967–1977. doi:10.5194/nhess-16-1967-2016

Baptista, M. A., and Miranda, J. M. (2009). Revision of the Portuguese Catalog of Tsunamis. *Nat. Hazards Earth Syst. Sci.* 9, 25–42. doi:10.5194/nhess-9-25-2009

Barnes, C. R., Best, M. M. R., Johnson, F. R., and Pirenne, B. (2015). "NEPTUNE Canada: Installation and Initial Operation of the World's First Regional Cabled Ocean Observatory," in *In Seafloor Observatories: A New Vision of Earth from the Abyss*. Editors A. De Santis, P. Favali, and L. Beranzoli (Berlin: Springer-Verlag Berlin Heidelberg), 415–438. doi:10.1007/978-3-642-11374-1_16

Bird, P. (2003). An Updated Digital Model of Plate Boundaries. *Geochem. Geophys. Geosyst.* 4, 1027. doi:10.1029/2001gc000252

Bird, P., and Kagan, Y. Y. (2004). Plate-tectonic Analysis of Shallow Seismicity: Apparent Boundary Width, Beta, Corner Magnitude, Coupled Lithosphere Thickness, and Coupling in Seven Tectonic Settings. *Bull. Seismological Soc. America* 94, 2380–2399. doi:10.1785/0120030107

Bondár, I., and McLaughlin, K. L. (2009). A New Ground Truth Data Set for Seismic Studies. *Seismological Res. Lett.* 80, 465–472. doi:10.1785/gssrl.80.3.465

Carrilho, F., Custódio, S., Bezzeghoud, M., Oliveira, C. S., Marreiros, C., Vales, D., et al. (2021). The Portuguese National Seismic Network-Products and Services. *Seismological Res. Lett.* 92, 1541–1570. doi:10.1785/0220200407

Custódio, S., Dias, N. A., Carrilho, F., Góngora, E., Rio, I., Marreiros, C., et al. (2015). Earthquakes in Western Iberia: Improving the Understanding of Lithospheric Deformation in a Slowly Deforming Region. *Geophys. J. Int.* 203 (1), 127–145. doi:10.1093/gji/ggv285

Fernandes, R. M. S., Miranda, J. M., Meijninger, B. M. L., Bos, M. S., Noomen, R., Bastos, L., et al. (2007). Surface Velocity Field of the Ibero-Maghrebian Segment of the Eurasia-Nubia Plate Boundary. *Geophys. J. Int.* 169, 315–324. doi:10.1111/j.1365-246x.2006.03252.x

Fernández-Ruiz, M. R., Soto, M. A., Williams, E. F., Martin-Lopez, S., Zhan, Z., Gonzalez-Herraez, M., et al. (2020). Distributed Acoustic Sensing for Seismic Activity Monitoring. *APL Photon.* 5, 030901. doi:10.1063/1.5139602

Geissler, W. H., Matias, L., Stich, D., Carrilho, F., Jokat, W., Monna, S., et al. (2010). Focal Mechanisms for Sub-crustal Earthquakes in the Gulf of Cadiz from a Dense OBS Deployment. *Geophys. Res. Lett.* 37, n/a. doi:10.1029/2010GL044289

Gutenberg, B., and Richter, C. F. (1949). *Seismicity of the Earth and Associated Phenomena*. Princeton, New Jersey: Princeton University Press, 273.

Havskov, J., Voss, P. H., and Ottemöller, L. (2020). Seismological Observatory Software: 30 Yr of SEISAN. *Seismological Res. Lett.* 91, 1846–1852. doi:10.1785/0220190313

Hirn, A., Haessler, H., Trong, P. H., Wittlinger, G., and Victor, L. A. M. (1980). Aftershock Sequence of the January 1st, 1980, Earthquake and Present-Day Tectonics in the Azores. *Geophys. Res. Lett.* 7, 501–504. doi:10.1029/gl007i007p00501

Howe, B. M., Arbic, B. K., Aucan, J., Barnes, C. R., Bayliff, N., Becker, N., et al.on behalf of the Joint Task Force for SMART Cables (2019). SMART Cables for Observing the Global Ocean: Science and Implementation. *Front. Mar. Sci.* 6, 424. doi:10.3389/fmars.2019.00424

Johnston, A. C. (1996). Seismic Moment Assessment of Earthquakes in Stable continental Regions-III. New Madrid 1811-1812, Charleston 1886 and Lisbon 1755. *Geophys. J. Int.* 126, 314–344. doi:10.1111/j.1365-246x.1996.tb05294.x

Kanamori, H., and Abe, K. (1979). Reevaluation of the Turn-Of-The-Century Seismicity Peak. *J. Geophys. Res.* 84 (B11), 6131. doi:10.1029/JB084iB11p06131

Lienert, B. R., Berg, E., and Frazer, L. N. (1986). HYPOCENTER: An Earthquake Location Method Using Centered, Scaled, and Adaptively Damped Least Squares. *Bull. Seismological Soc. Am.* 76, 771–783. doi:10.1785/bssa0760030771

Marra, G., Clivati, C., Luckett, R., Tampellini, A., Kronjäger, J., Wright, L., et al. (2018). Ultrastable Laser Interferometry for Earthquake Detection with Terrestrial and Submarine Cables, 361, 486–490. doi:10.1126/science.aat4458

Martinez-Solares, J. M., and Lopez-Arroyo, A. (2004). The Great Historical 1755 Earthquake. Effects and Damage in Spain. *J. Seismology* 8, 275–294. doi:10.1785/bssa0760030771

Matias, L., Dias, N. A., Morais, I., Vales, D., Carrilho, F., Madeira, J. L., et al. (2007). The 9th of July 1998 Faial Island (Azores, North Atlantic) Seismic Sequence. *J. Seismol* 11, 275–298. doi:10.1007/s10950-007-9052-4

Matias, L. M., Cunha, T., Annunziato, A., Baptista, M. A., and Carrilho, F. (2013). Tsunamigenic Earthquakes in the Gulf of Cadiz: Fault Model and Recurrence. *Nat. Hazards Earth Syst. Sci.* 13, 1–13. doi:10.5194/nhess-13-1-2013

Okada, Y., Kasahara, K., Hori, S., Obara, K., Sekiguchi, S., Fujiwara, H., et al. (2004). Recent Progress of Seismic Observation Networks in Japan -Hi-Net, F-Net, K-NET and KiK-Net-. *Earth Planet. Sp* 56, xv–xxviii. doi:10.1186/bf03353076

Omira, R., Baptista, M. A., Matias, L., Miranda, J. M., Catita, C., Carrilho, F., et al. (2009). Design of a Sea-Level Tsunami Detection Network for the Gulf of Cadiz. *Nat. Hazards Earth Syst. Sci.* 9, 1327–1338. doi:10.5194/nhess-9-1327-2009

Omira, R., Neres, M., and Batista, L. (2019). The Gloria Transform Fault-NE Atlantic: Seismogenic and Tsunamigenic Potential. *Transform Plate Boundaries and Fracture Zones*, Elsevier, chap. 8, 157–167. doi:10.1016/b978-0-12-812064-4.00008-6

Reis, C., Omira, R., Matias, L., and Baptista, M. A. (2017). On the Source of the 8 May 1939 Azores Earthquake–Tsunami Observations and Numerical Modelling. *Geomatics Nat. Haz. Risk,* 8 (2), 328–347. doi:10.1080/19475705.2016.1218944

Silva, S., Terrinha, P., Matias, L., Duarte, J. C., Roque, C., Ranero, C. R., et al. (2017). On the Source of the 8 May 1939 Azores Earthquake - Tsunami Observations and Numerical Modelling. *Geomatics, Nat. Hazards Risk* 8, 226–241. doi:10.1080/19475705.2016.1218944

Smith, W. H. F., and Sandwell, D. T. (1997). Global Sea Floor Topography from Satellite Altimetry and Ship Depth Soundings. *Science* 277, 1956–1962. doi:10.1126/science.277.5334.1956

Stucchi, M., Rovida, A., Gomez Capera, A. A., Alexandre, P., Camelbeeck, T., Demircioglu, M. B., et al. (2013). The SHARE European Earthquake Catalogue (SHEEC) 1000-1899. *J. Seismol.* 17, 523–544. doi:10.1007/s10950-012-9335-2

Titov, V. V., Gonzalez, F. I., Bernard, E. N., Eble, M. C., Mofjeld, H. O., Newman, J. C., et al. (2005). Real-time Tsunami Forecasting: Challenges and Solutions. *Nat. Hazards* 35, 35–41. doi:10.1007/s11069-004-2403-3

Trowbridge, J., Weller, R., Kelley, D., Dever, E., Plueddemann, A., Barth, J. A., et al. (2019). The Ocean Observatories Initiative. *Front. Mar. Sci.* 6. doi:10.3389/fmars.2019.00074


**Conflict of Interest:** The authors declare that the research was conducted in the absence of any commercial or financial relationships that could be construed as a potential conflict of interest.

frontiers in Earth Science

ORIGINAL RESEARCH
published: 21 July 2021
doi: 10.3389/feart.2021.699439

# An Evaluation of Strong-Motion Parameters at the S-net Ocean-Bottom Seismograph Sites Near the Kanto Basin for Earthquake Early Warning

*Yadab P. Dhakal* and Takashi Kunugi*

*National Research Institute for Earth Science and Disaster Resilience, Tsukuba, Japan*

We analyzed strong-motion records at the ground and borehole in and around the Kanto Basin and the seafloor in the Japan Trench area from three nearby offshore earthquakes of similar magnitudes (Mw 5.8–5.9). The seafloor strong-motion records were obtained from S-net, which was established to enhance tsunami and earthquake early warnings after the 2011 great Tohoku-oki earthquake disaster. The borehole records were obtained from MeSO-net, a dense network of seismometers installed at a depth of 20 m in the Tokyo metropolitan area. The ground records were obtained from the K-NET and KiK-net networks, established after the 1995 great Hanshin-Awaji earthquake disaster. The MeSO-net and S-net stations record the shakings continuously, while the K-NET and KiK-net records are based on triggering thresholds. It is crucial to evaluate the properties of strong motions recorded by the S-net for earthquake early warning (EEW). This paper compared the peak ground accelerations (PGAs) and peak ground velocities (PGVs) between the S-net and K-NET/KiK-net stations. Because the MeSO-net records were from the borehole, we compared the PGAs and significant durations of the low-frequency motions (0.1–0.5 Hz) between the S-net and MeSO-net stations from identical record lengths. We found that the horizontal PGAs and PGVs at the S-net sites were similar to or larger than the K-NET/KiK-net sites for the S wave. In contrast, the vertical PGAs and PGVs at the S-net sites were similar to or smaller than those at the K-NET/KiK-net sites for the S wave. Particularly, the PGAs and PGVs for the P-wave parts on the vertical-component records of S-net were, on average, much smaller than those of K-NET/KiK-net records. The difference was more evident in the PGAs. The average ratios of S-wave horizontal to vertical PGAs were about 2.5 and 5 for the land and S-net sites, respectively. The low-frequency PGAs at the S-net sites were similar to or larger than those of the MeSO-net borehole records. The significant durations between the two-networks low-frequency records were generally comparable. Quantification of the results from a larger dataset may contribute to ground-motion prediction for EEW and the design of the offshore facilities.

**Keywords: S-net, ocean-bottom seismograph network, Japan Trench, MeSO-net, Kanto Basin, earthquake early warning, peak ground acceleration, strong-motion duration**

OPEN ACCESS

***Edited by:***
*Francisco Javier Nuñez-Cornu, University of Guadalajara, Mexico*

***Reviewed by:***
*Thorne Lay, University of California, Santa Cruz, United States*
*Ryota Takagi, Tohoku University, Japan*

****Correspondence:***
*Yadab P. Dhakal*
*ydhakal@bosai.go.jp*

***Specialty section:***
*This article was submitted to Solid Earth Geophysics, a section of the journal Frontiers in Earth Science*

***Received:*** *23 April 2021*
***Accepted:*** *05 July 2021*
***Published:*** *21 July 2021*

***Citation:***
*Dhakal YP and Kunugi T (2021) An Evaluation of Strong-Motion Parameters at the S-net Ocean-Bottom Seismograph Sites Near the Kanto Basin for Earthquake Early Warning. Front. Earth Sci. 9:699439. doi: 10.3389/feart.2021.699439*

## INTRODUCTION

A large-scale seafloor observation network for earthquake and tsunami, known as S-net, consisting of 150 observatories, has been established in the Japan Trench area after the 2011 Tohoku-oki earthquake disaster and has been operated by National Research Institute for Earth Science and Disaster Resilience (NIED) since 2016 (NIED 2019a; Aoi et al., 2020). This is an in-line-type cabled network, with seismometers housed in cylindrical pressure vessels, most of which, including the cables, were buried to a depth of about 1 m in the shallow water regions (water depth <1,500 m). In the deeper water regions, the cylindrical vessels were freely sited on the seafloors. The interstation distance is about 30 and 50 km in perpendicular and parallel to the trench axis, respectively. The network records and transmits waveform data to the data center of NIED continuously. It is expected that the S-net data contribute to earthquake and tsunami early warning. A detailed description of the S-net can be found in Aoi et al. (2020). To improve earthquake early warning (EEW) for offshore earthquakes, it is important to understand the characteristics of strong motions in the offshore area. It is also crucial to examine the properties of the recorded motions at the ocean-bottom sites for various seismological and engineering applications by comparing with the data recorded by seismometers installed firmly on the ground or borehole because the waveforms at the ocean-bottom sites are likely to be contaminated by various factors such as tilting of the sensors due to strong motions and poor coupling between the sensor houses and the seabed sediments (e.g., Nakamura and Hayashimoto 2019; Takagi et al., 2019).

There is a paucity of literature regarding the strong-motion observation in the offshore areas. The study by Boore and Smith (1999) showed that the offshore motions are low in vertical accelerations at short periods, and shear-wave velocities beneath a site are more important than the water layer in determining the property of ground motions at lower frequencies. Hu et al. (2020) also reported that the spectral accelerations of vertical component records were slightly smaller than those of the records on land at short periods, while the long-period ground motions were noticeably larger at the offshore sites. Previous studies (e.g., Nakamura et al., 2015; Noguchi et al., 2016; Todoriki et al., 2017; Kubo et al., 2019) had commonly shown that the amplitudes of long-period (> 2 s) ground motions were substantially larger at the ocean bottom sites than the land sites. One of the reasons for the large long-period ground motions was attributed to the thick unconsolidated sediments in the offshore region. Dhakal et al. (2021) compared horizontal peak ground accelerations (PGAs), peak ground velocities (PGVs), and acceleration response spectra at selected periods between the land and S-net sites for nine selected earthquakes. They reported that the ground motions at periods longer than about 0.5 s were more prominent at the S-net sites. Dhakal et al. (2021) also showed the example accelerograms recorded at the land and S-net sites and noted that the vertical component PGAs at the S-net sites were almost half the values at the land sites at similar distances. However, they focused on the horizontal components of motions and discussed little the vertical component of motions.

In this study, the peak amplitude and duration features of S-net records are evaluated with reference to the records from the other three networks, namely, K-NET, KiK-net, and MeSO-net for both horizontal and vertical components of motions. The K-NET and KiK-net are countrywide networks with an average spacing of about 20 km established after the 1995 great Hanshin-Awaji earthquake disaster (e.g., Okada et al., 2004; NIED 2019b; Aoi et al., 2020). The MeSO-net, abbreviated for the Metropolitan Seismic Observation network, is a dense network of about 300 seismometers installed at the borehole depth of 20 m in the Tokyo Metropolitan area (e.g., Sakai and Hirata 2009; NIED 2019c). The average interstation distance of MeSO-net is about 3 km. One of the primary objectives of the MeSO-net was to contribute to a better understanding of seismic hazards in the Tokyo metropolitan area, such as by detailed imaging of the possible large-scale faults beneath the urban areas. The MeSO-net stations record the waveform data continuously. This means that the long-duration records can be obtained from the S-net and MeSO-net. However, it isn't easy to compare the high-frequency ground motions recorded at the MeSO-net sites with those at the S-net sites because the MeSO-net seismometers are installed at the borehole, as mentioned above. On the other hand, the K-NET seismometers are installed at the ground surface, while the KiK-net consists of a pair of seismometers installed at the ground surface and the borehole. The K-NET and KiK-net stations get triggered after some threshold ground accelerations, and the records get terminated when the threshold motions are not exceeded for a certain duration. As a result, the record lengths are not uniform from the K-NET and KiK-net. Therefore, the S-net records may be compared with the K-NET and KiK-net surface records for the high-frequency motions while taking advantage of the MeSO-net records for the long-period ground motions, which persist for longer durations in the sedimentary basin areas.

In the paper, a general comparison of the peak ground accelerations (PGAs) and peak ground velocities (PGVs) for the P-wave and S-wave parts is made between the S-net ocean-bottom and K-NET/KiK-net sites from three earthquakes of Mw 5.8–5.9, which occurred nearby the Kanto Basin. Similarly, the PGAs and significant durations of relatively low-frequency motions (0.1–0.5 Hz) at the S-net sites are compared with those from the MeSO-net sites from long-duration records. One of the primary objectives of this paper is to understand the peak amplitude and duration features of the S-net strong-motion recordings for the development of ground-motion prediction models for EEW. In the current system of EEW by the Japan Meteorological Agency (JMA), vertical component displacement amplitude has been employed to reduce the effect of site amplification and rotational motions on the recorded motions at the S-net sites, while three-component records have been used for the station on land (e.g., Hayashimoto et al., 2019; JMA 2019). The present study may be considered a foundational work for future more detailed analyses for quantifying the variation of P- and S-wave amplitudes at different frequencies in the offshore stations for possible application to EEW. Furthermore, the study of low-frequency peak motions and ground-motion durations may help to understand the effect of deeper suboceanic and water layers on

**TABLE 1 |** Source parameters of earthquakes used in the study.

| Event code | Date and time (JST) | Japan meteorological agency (JMA) | | | | F-net moment tensor | |
|---|---|---|---|---|---|---|---|
| | | Longitude | Latitude | Focal depth | Mj | Mw | Depth |
| 2018 | 2018/07/07, 20:23 | 140.5920 | 35.1653 | 56 | 6.0 | 5.9 | 56 |
| 2020a | 2020/01/03, 03:23 | 141.1150 | 35.8100 | 34 | 5.8 | 5.8 | 38 |
| 2020b | 2020/06/25, 04:47 | 141.1117 | 35.5533 | 36 | 6.1 | 5.9 | 29 |

the recorded motions. Many ocean-bottom seismograph networks of different scales are in operation for EEW and many other geophysical studies in the world (e.g., Romanowicz et al., 2009; Hsiao et al., 2014; Barnes et al., 2015). Thus, the results presented in this paper also contribute to the engineering and seismological community literature for a comparative study about offshore strong motions around the globe. First, we explain the earthquake data and their processing in the next section. Then, we present and discuss the results.

## DATA AND PROCESSING

In this article, the expressions such as the ocean-bottom (OB) stations or ocean-bottom seismographs (OBS) refer to the S-net stations unless explicitly mentioned. We selected records on the land and OB stations from three earthquakes of Mw values equal to 5.8 (one event) and 5.9 (two events). The source parameters of the earthquakes are given in **Table 1**. The epicenters of the earthquakes are shown in **Figure 1**. The order of earthquakes in **Table 1** follows the occurrence date of the earthquakes. The first earthquake occurred on July 7, 2018, which had Mw value of 5.9. The second earthquake occurred on January 3, 2020, which had Mw value of 5.8. The third earthquake occurred on June 25, 2020, which had Mw value of 5.9. The Mw values were taken from the F-net moment-tensor catalog by NIED. Hereafter, the above-mentioned earthquakes are called the 2018, 2020a, and 2020b events, respectively, in the paper. The JMA magnitudes of the earthquakes were 6.0, 5.8, and 6.1, respectively. Similarly, the JMA focal depths of the events were 56, 34, and 36 km, respectively. The 2018, 2020a, and 2020b events are classified as intraslab, interplate, and crustal earthquake types based on focal depths estimated by JMA and focal mechanisms and depths estimated by F-net (NIED) moment-tensor solution.

We retrieved 10 min of continuous acceleration waveform data at S-net and MeSO-net stations, beginning from one minute before the earthquake origin time. We could not control the record length of the K-NET/KiK-net because the recording system was based on a "trigger algorithm" as mentioned previously. The MeSO-net and K-NET/KiK-net sensors were aligned in horizontal and vertical directions, but the azimuths of the horizontal sensors were not aligned in the north-south and east-west directions for the MeSO-net. We used the azimuths of the MeSO-net sensors from Kano et al. (2015) to compare the MeSO-net records with other networks. On the other hand, the three-component sensors at

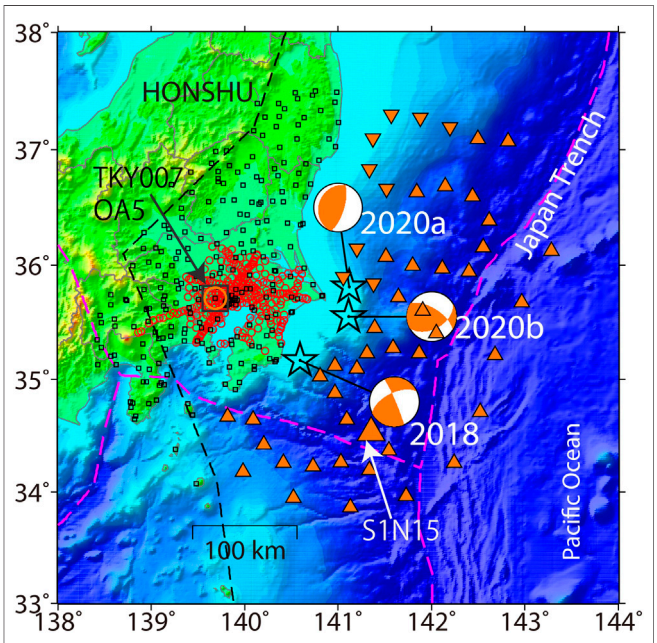


**FIGURE 1 |** Index map showing location of strong-motion stations and epicenters of earthquakes used in this study. The triangles denote the S-net ocean-bottom stations (inverted triangles denote the buried stations). The squares and circles denote the K-NET/KiK-net and MeSO-net stations, respectively. The stars denote epicenters of the earthquakes. The focal mechanism plots of the earthquakes are connected to the corresponding epicenters by straight lines and are annotated by event codes (see **Table 1** for the event information). The large square, circle, and triangle, pointed by arrows, denote the locations of the sites, namely TKY007 (K-NET), OA5 (MeSO-net), and S1N15 (S-net), respectively; example waveforms are shown in the later figures recorded at the sites. The dashed black line denotes the volcanic front, and the purple lines tectonic boundaries.

the S-net stations were not necessarily aligned in the horizontal and vertical directions. Therefore, the original S-net records were rotated to obtain the horizontal and vertical component motions by applying the matrix operations given in Takagi et al. (2019). The azimuths of the cable axes, also determined by Takagi et al. (2019), were employed to rotate the seismograms in the preferred directions for comparison with other network recordings.

Example records and their Fourier spectra at the MeSO-net OA5 and K-NET TKY007 sites for the 2018 event are shown in **Figure 2** (see **Figure 1** for the location of the sites and epicenter of the event). These sites are in the Shinjuku area of Tokyo, in the neighborhood of which many high-rise

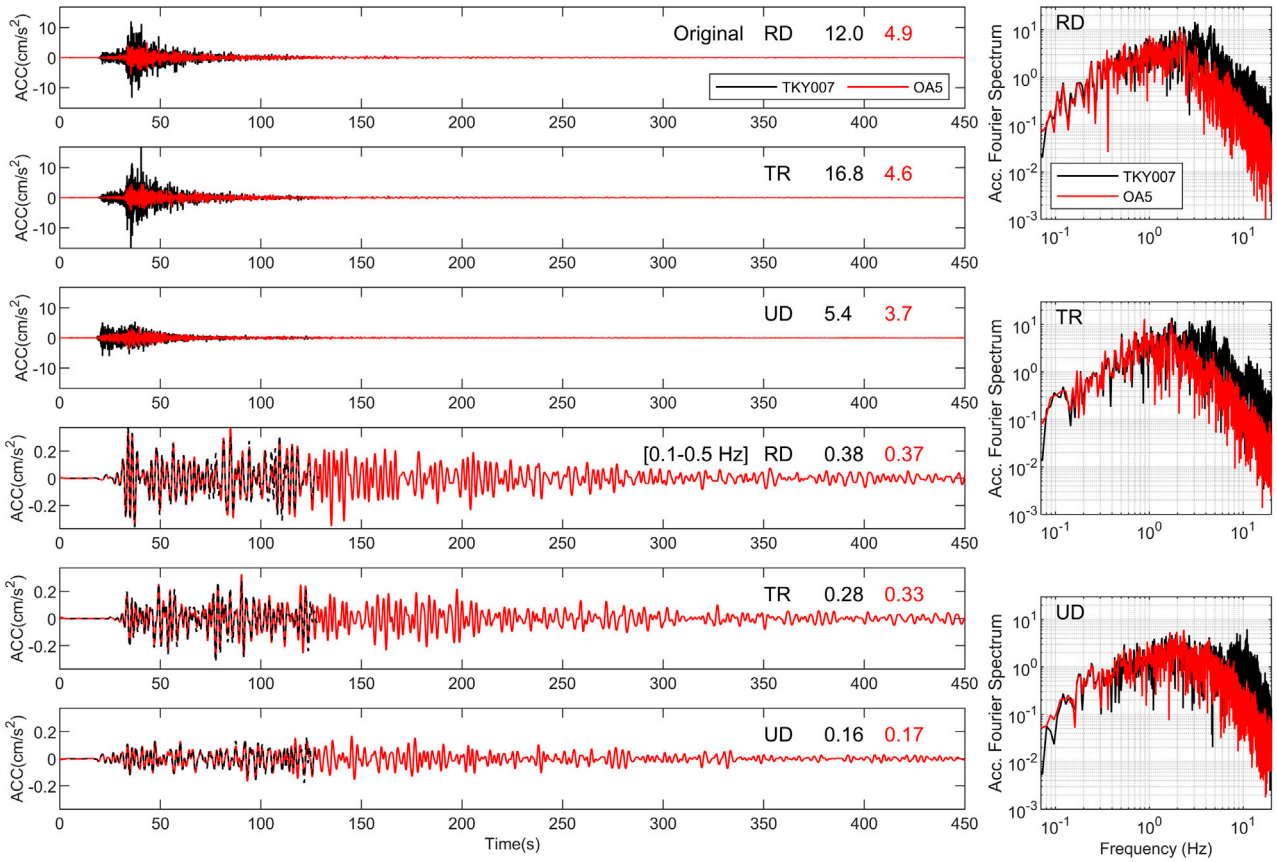


**FIGURE 2 |** Example acceleration waveforms for the radial (RD), transverse (TR), and vertical (UD) components recorded at the K-NET TKY007 site (black) and MeSO-net OA5 site (red) during the 2018 event (see **Figure 1** for the location of the sites and the event. See **Table 1** for the event information). The upper-three left panels show the as-recorded accelerograms rotated to radial, transverse, and vertical components, while the lower-three left panels show the 0.1–0.5 Hz bandpass-filtered waveforms. Note that the record length for the K-NET TKY007 site is shorter than that for the MeSO-net OA5 site and is about 130 s. The peak values of the waveforms are indicated above the traces with the same color of the corresponding waveforms. The right panels show the Fourier spectra for the RD, TR, and UD components, respectively, computed for the identical record length of about 130 s.

buildings are built. The inter-station distance between the two sites was about 350 m, and the epicentral distance to OA5 was about 102 km. The Fourier spectra plots in **Figure 2** show that the Fourier amplitudes computed from equal time windows are noticeably larger at the K-NET TKY007 site than the MeSO-net OA5 site at frequencies over 2 Hz. In contrast, the Fourier amplitudes are similar at lower frequencies. In **Figure 2**, it can also be seen that the 0.1–0.5 Hz bandpass-filtered records are very similar between the two sites. However, the K-NET TKY007 site records were terminated before the long-period ground motions die out, as depicted on the records of the OA5 site of MeSO-net. Similarly, an example plots of accelerograms recorded at the S-net S1N15 site located at an epicentral distance of about 99 km, is shown in **Figure 3** for the 2018 event. The epicentral distances to the OA5 and S1N15 sites were comparable (102 km vs. 99 km). Accelerograms are shown without filtering and with bandpass filtering (0.1–0.5 Hz) to see the high- and low-frequency waveforms. Generally, the long-period waves continue for longer durations, similar to those shown in **Figure 2** for the MeSO-net site. Thus, these plots illustrated that the long-duration records are preferable to compare the long-period ground motions in the seafloor and sedimentary areas in and around the Kanto Basin. In the right panels of **Figure 3**, the Fourier spectral amplitudes at the S-net S1N15 site are compared with those from the MeSO-net OA5 site. The Fourier spectral amplitudes shown in **Figure 2** were computed from time windows of about 130 s. On the other hand, the Fourier spectral amplitudes shown in **Figure 3** were computed from time windows of 450 s after the earthquake origin time. The spectral amplitudes at the MeSO-net site are smaller than those at the S-net site at frequencies higher than about 3 Hz for the horizontal components and about 5 Hz for the vertical component. These results are nearly similar to those discussed previously between the MeSO-net and K-NET sites. At lower frequencies, the spectral amplitudes at the S-net site are approximately similar to or larger than those at the MeSO-net site.

The PGAs, PGVs, and significant durations were computed for each record after processing uniformly. In the present

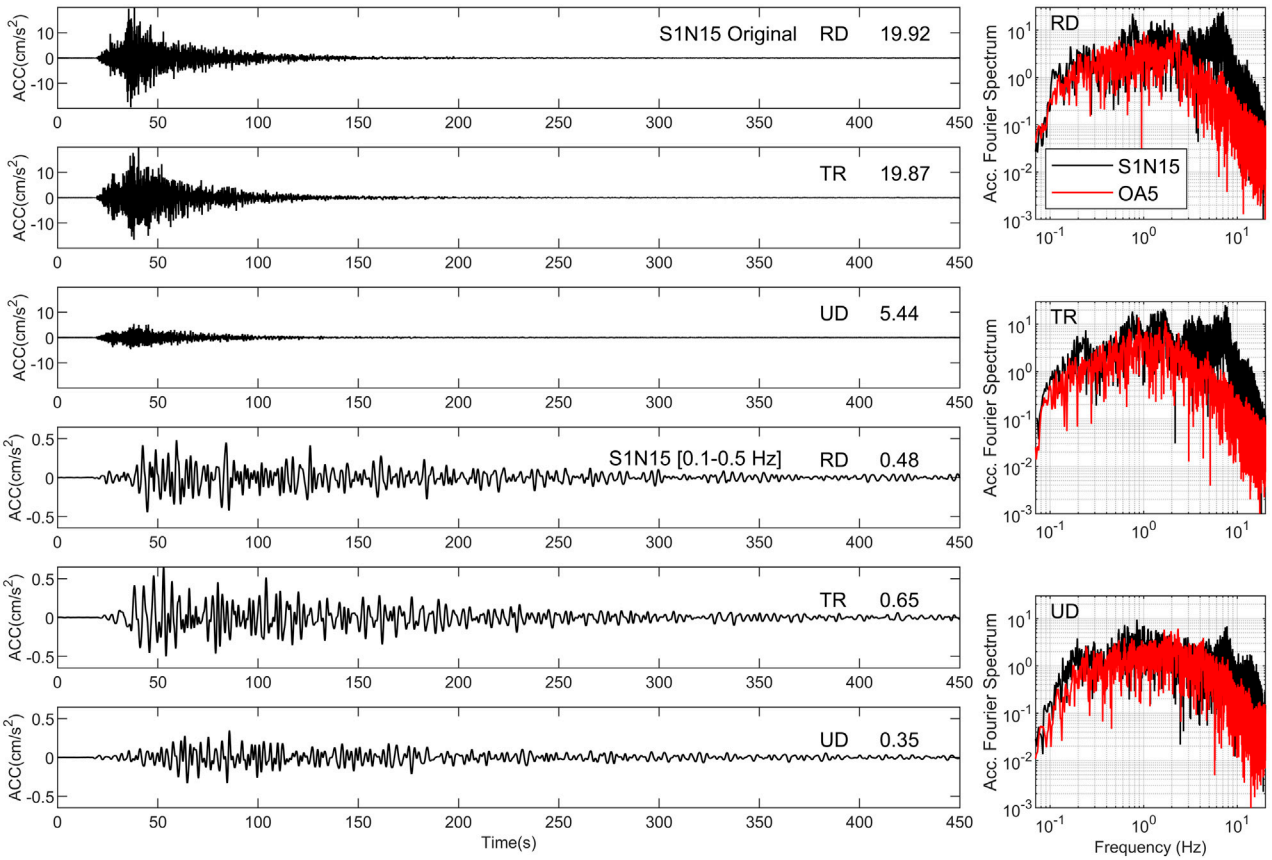


**FIGURE 3 |** Example acceleration waveforms for the radial (RD), transverse (TR), and vertical (UD) components recorded at the S-net S1N15 site during the 2018 event (see **Figure 1** for the location of the site and the event and **Table 1** for the event information). The upper three left panels show the waveforms without filtering, while the lower three left panels show the 0.1–0.5 Hz bandpass-filtered waveforms. The peak accelerations of the waveforms are indicated above the corresponding traces. The right panels show a comparison of the acceleration Fourier spectra for the RD, TR, and UD components, respectively, between the S-net S1N15 and MeSO-net OA5 sites computed from the record lengths of 450 s. See **Figure 2** for the records at the OA5 site.

study, the mean of a 1 min pre-event noise window was subtracted at each time step for the S-net and MeSO-net records. For the K-NET/KiK-net records, the mean of 10 s pre-event noise window was subtracted if the noise window was available; otherwise, the mean of the whole record was subtracted. Then, fourth-order high-pass Butterworth filtering was applied to suppress low-frequency noises at 0.1 Hz to compare the peak parameters between the S-net and K-NET/KiK-net sites. The peak parameters of the long-duration records of MeSO-net and S-net were obtained for 0.1–0.5 Hz bandpass-filtered records. The PGVs were obtained from velocity seismograms obtained by integration of the filtered acceleration records. The accelerograms were not used if the records within the selected time windows were noticeably contaminated by later events; this is especially the case for the analysis of significant duration. All the acceleration records were visually examined to exclude the records with spikes, offsets, and trends before and after the filtering. The velocity seismograms were also visually examined to confirm that the integration operation did not produce any trend in the seismograms. The onsets of P- and S-waves were identified manually required for the comparison of PGAs and PGVs for the P-wave and S-wave portions of the records.

## COMPARISON OF THE PEAK GROUND ACCELERATIONS AND PEAK GROUND VELOCITIES BETWEEN THE S-NET AND K-NET/KIK-NET SITES

Here we present the comparison of the PGAs and PGVs between the S-net and K-NET/KiK-net sites for the three events listed in **Table 1**. In this comparison, we used the data recorded within the 200 km of hypocentral distance. As the S-waves do not propagate through the liquid medium, the S-wave part of the seafloor records for the horizontal components may be considered to be equivalent to those recorded on the ground surface. In this paper, the S-wave part or S-wave window means the 20 s time window starting from the S-onset. Perhaps, the source duration was not so long for these Mw 5.9 earthquakes, but a wider window ensures that

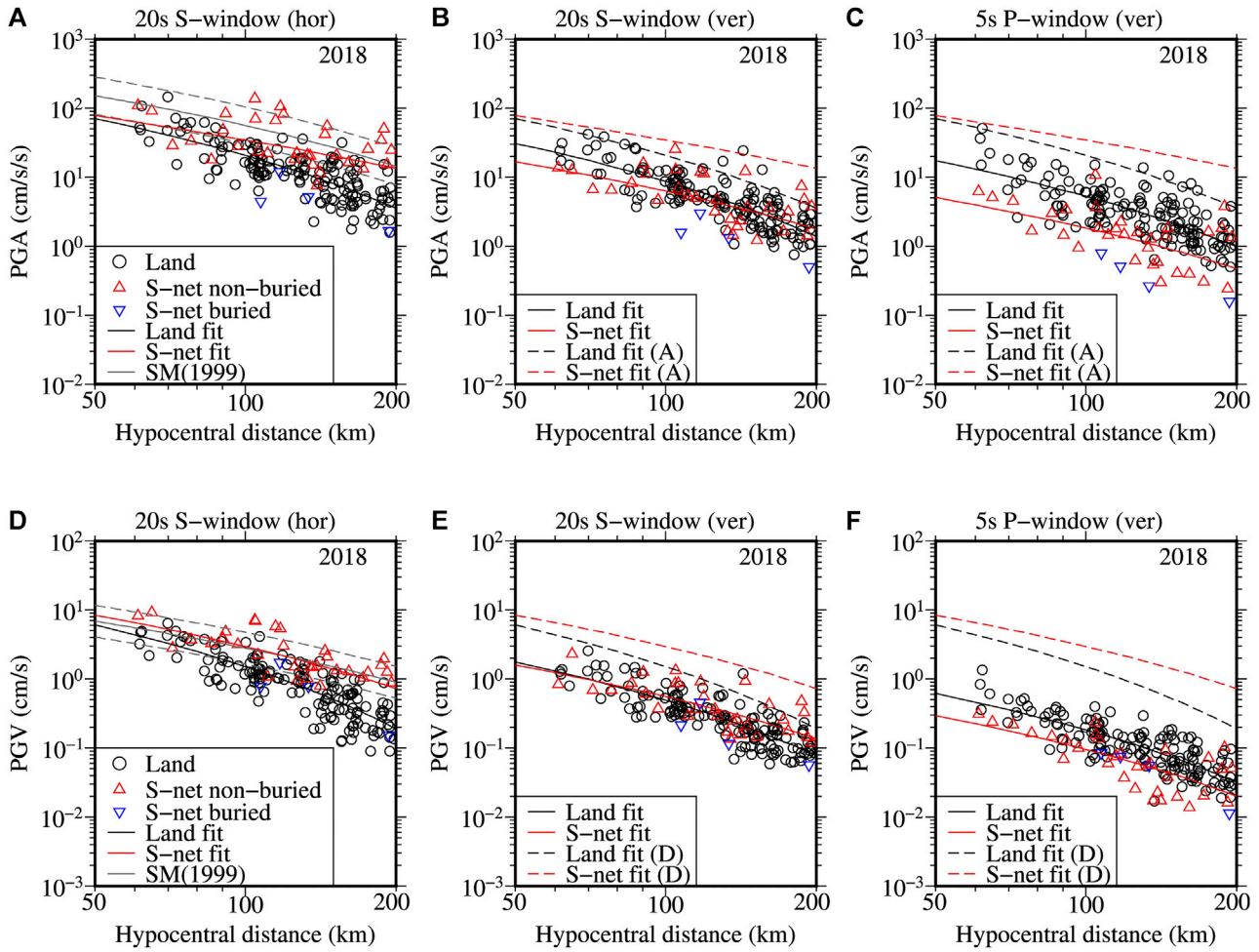


**FIGURE 4 |** Plots of PGAs **(A, B, C)** and PGVs **(D, E, F)** as a function of hypocentral distance for the 2018 event (see **Table 1** for the event information). The left and middle panels show the peak values of the 20 s time windows starting from the S-onset for the horizontal (hor) and vertical (ver) components, respectively. The right panels show the peak values of the 5 s time windows starting from the P-onset for the vertical components. The plotted values for the horizontal components are the larger ones of the peak values of the two horizontal components. The circles denote the K-NET/KiK-net stations, simply written as Land in the legends, and the triangles S-net stations of which the inverse triangles (blue colored) denote the buried S-net stations. The black and red solid lines represent the fitted lines between the observed values and hypocentral distances for the K-NET/KiK-net and S-net stations in each panel. The solid and dashed grey lines denote the median prediction curves and range of one standard deviation for soil site condition in **(A)** and Vs30 = 300 m/s in **(D)** using the GMPEs in Si and Midorikawa (1999), written as SM (1999) in the legend, for an intraslab-type earthquake. The dashed black and red lines in **(B, C)** and **(E, F)** denote the fitted black and red solid lines in **(A)** and **(C)**, respectively, for comparison.

the uncertainty in the source duration and effects of multiple reflections by the sedimentary layers are well-considered. In this paper, the horizontal PGA means the larger one of the PGA values of the two horizontal components. The horizontal PGAs of the S-wave parts, the vertical PGAs of the S-wave parts, and the vertical PGAs of the P-wave parts are plotted as a function of hypocentral distance in **Figure 4A,B,C** respectively, for the 2018 event. Similarly, the PGVs for the corresponding time windows are plotted in **Figure 4D,E,F** respectively, for the 2018 event. The peak values for the P-wave parts, plotted in **Figure 4C,F** were computed from the shorter time window of 5 s as the S-P time is short near the epicenters. The values for the S-net sites are denoted by triangles, while the values for the K-NET/KiK-net sites are indicated by circles. We also show the median prediction curves for the horizontal PGAs and PGVs using the ground motion prediction equations (GMPEs) in Si and Midorikawa (1999, 2000) in **Figure 4A,D**. The GMPEs for the PGVs in Si and Midorikawa (1999) have been used in Japan to estimate ground motion intensities for EEW and seismic hazard analysis (e.g., Hoshiba et al., 2008; HERP (Headquarters for Earthquake Research Promotion), 2018). The values at the K-NET/KiK-Net sites are somewhat overestimated by the GMPEs, while the S-net data are explained generally well.

**Figure 4** also includes the fitted lines between the peak values and hypocentral distances for the present dataset. If we assume that the average source effect was similar to the land and S-net sites because the land and S-net sites are almost

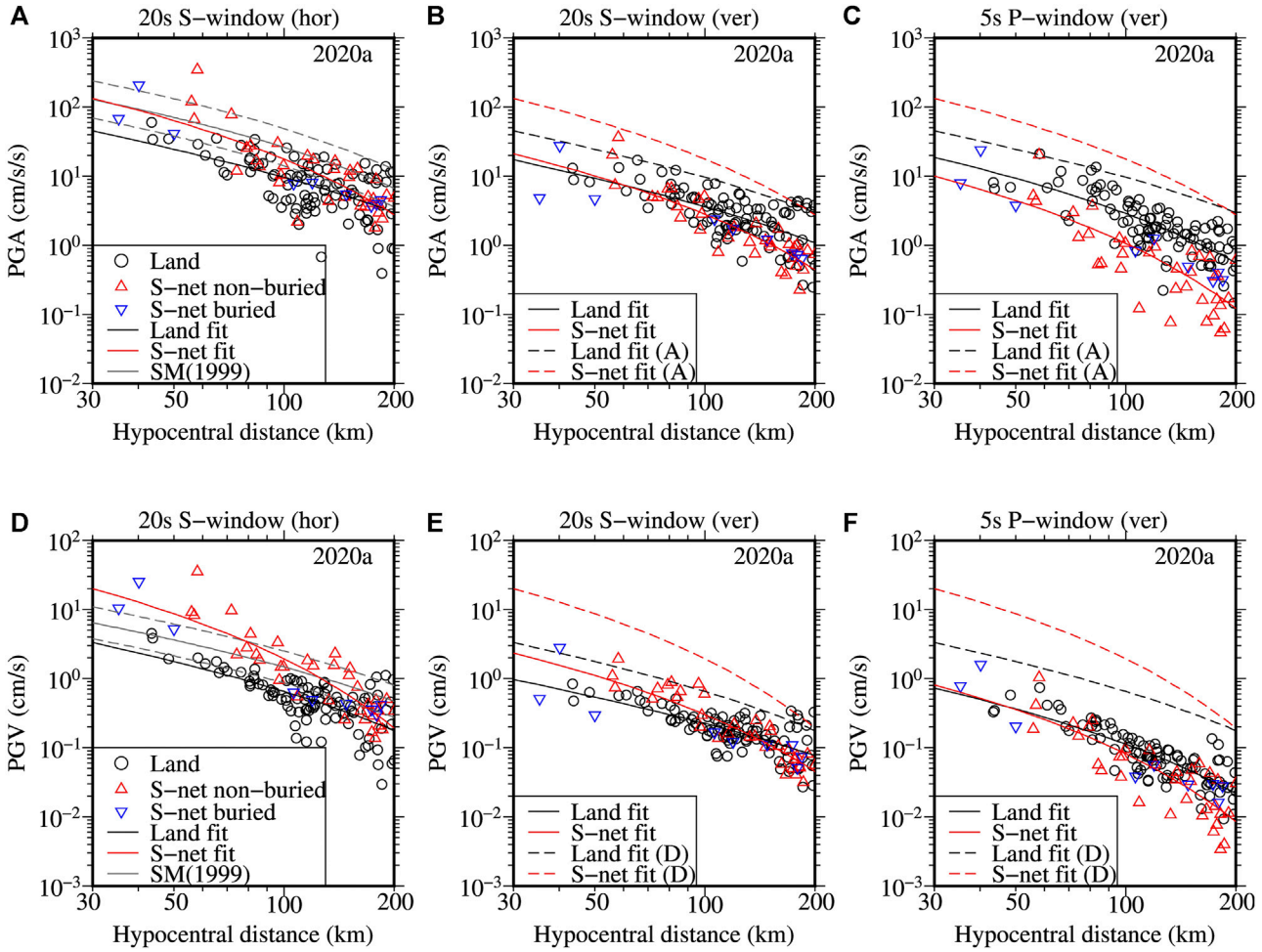


**FIGURE 5 |** Same as **Figure 4**, but for the 2020a interplate event (see **Table 1** of the original article for the event information). The GMPEs for an interplate-type earthquake are used in the panels **(A)** and **(D)**.

similarly distributed in the western and eastern sides of the epicenter, the difference between the land and S-net data may be attributed to the difference in the average site and path conditions. The difference between the two fitted lines increases with the distance for the S-wave parts of the horizontal components, as shown in **Figure 4A,D**. The vertical component PGAs and PGVs for the S-wave parts show a relatively smaller difference between the K-NET/KiK-net and S-net sites (**Figure 4B,E**). In contrast, the PGAs for the P-wave parts of the vertical components are, on average, larger, at the K-NET/KiK-net sites than the S-net sites by a factor of about 2.5 (averaged over the distance) (**Figure 4C**). The PGVs for the P-wave parts also show similar results between the land and ocean-bottom sites, but the difference is smaller (**Figure 4F**). The fitted lines for the horizontal PGAs and PGVs of S-wave parts are also shown in the plots of the vertical PGAs and PGVs of S-wave parts in **Figure 4B,E**. The fitted lines indicate that the horizontal PGAs and PGVs on land are about 2.5 times the corresponding values for the S-wave parts on the vertical components, while the corresponding ratios are about 5 for the S-net sites. The ratios of the average peak values (fitted lines) between the 5 s P-window (vertical component) and the 20 s S-window (horizontal component) are much larger for the S-net sites, as shown in **Figure 4C,F**.

In the plots for the PGAs (**Figure 4A–C**), the values at the buried sites are generally smaller than those for the non-buried sites at equal distances. However, the difference between the buried and non-buried sites is smaller for the PGVs as shown in **Figure 4D–F**. This difference was not so conspicuous for the 2020a and 2020b events, but the tendency that the buried sites had smaller PGAs and PGVs was present for the S-wave parts (**Figure 5A,B,D,E**, and **Figure 6A,B,D,E**). These results are generally similar to those reported in Dhakal et al. (2021), where the residual values at short periods were biased between the buried and non-buried sites for the horizontal components. The larger PGAs at the S-net sites compared to the values at the land sites at longer distances generally

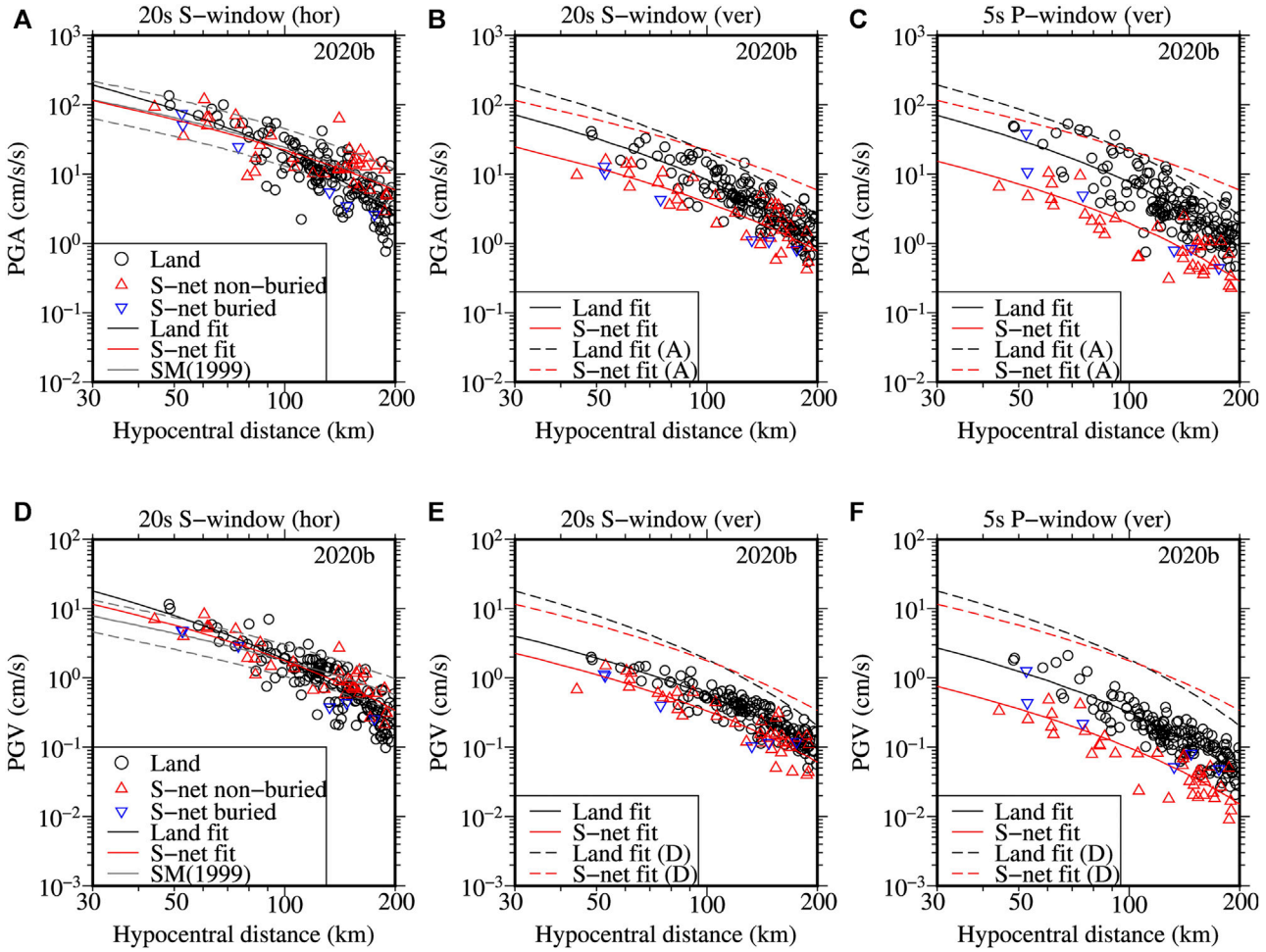


**FIGURE 6 |** Same as **Figure 4**, but for the 2020b crustal event (see **Table 1** of the original article for the event information). The GMPEs for a crustal-type earthquake are used in the panels **(A)** and **(D)**.

commensurate with the high Q values in the oceanic plates (e.g., Umino and Hasegawa 1984). However, an objective evaluation of the difference between the S-net and land sites and within the S-net sites is not easy as the shallow site profiles such as the Vs30 values (average S-wave velocity in the top 30 m soil column) are not measured or estimated at the S-net sites.

The plots of the PGAs and PGVs as a function of hypocentral distance for the 2020a event are shown in **Figure 5**. The PGAs for the three different segments of the records (S-wave part of horizontal, S-wave part of vertical, and P-wave part of vertical records) are depicted in **Figure 5A–C**, respectively. Similarly, the PGVs for the corresponding segments are plotted in **Figure 5D–F**, respectively. Similar to the results shown in **Figure 4A,D** for the 2018 event, the horizontal PGAs and PGVs for the S-wave parts are generally larger at the S-net sites than the K-NET/KiK-net sites, but the fitted lines indicate that the difference decreases with the distance in contrast to that for the 2018 event. The difference between the two events may be attributed to the different ray paths; a significant fraction of the ray paths lies within the high Q slab for the 2018 intraslab event, while the ray paths are shorter in the high Q zone for the 2020 interplate event. The PGA data are generally explained well by the GMPEs in Si and Midorikawa (1999) at the S-net sites at smaller distances while the difference grows at larger distances. The GMPEs overestimate the PGAs on land. The fitted lines suggest that the average difference of the PGVs between the land and S-net sites (**Figure 5D**) is larger than the average difference of the PGAs between the two groups of data (**Figure 5A**). The difference between the two groups of data for the vertical PGAs and PGVs for the S-wave parts is smaller than those for the horizontal components. The mean ratio of the horizontal PGAs to the vertical PGAs of the S-wave parts obtained from the fitted lines is about 2.5 for the sites on land, while the ratio is about 6 for the sites at the seafloor; the corresponding ratios for the PGVs were similar to those of the PGAs. In contrast, the PGAs for the P-wave parts of the vertical

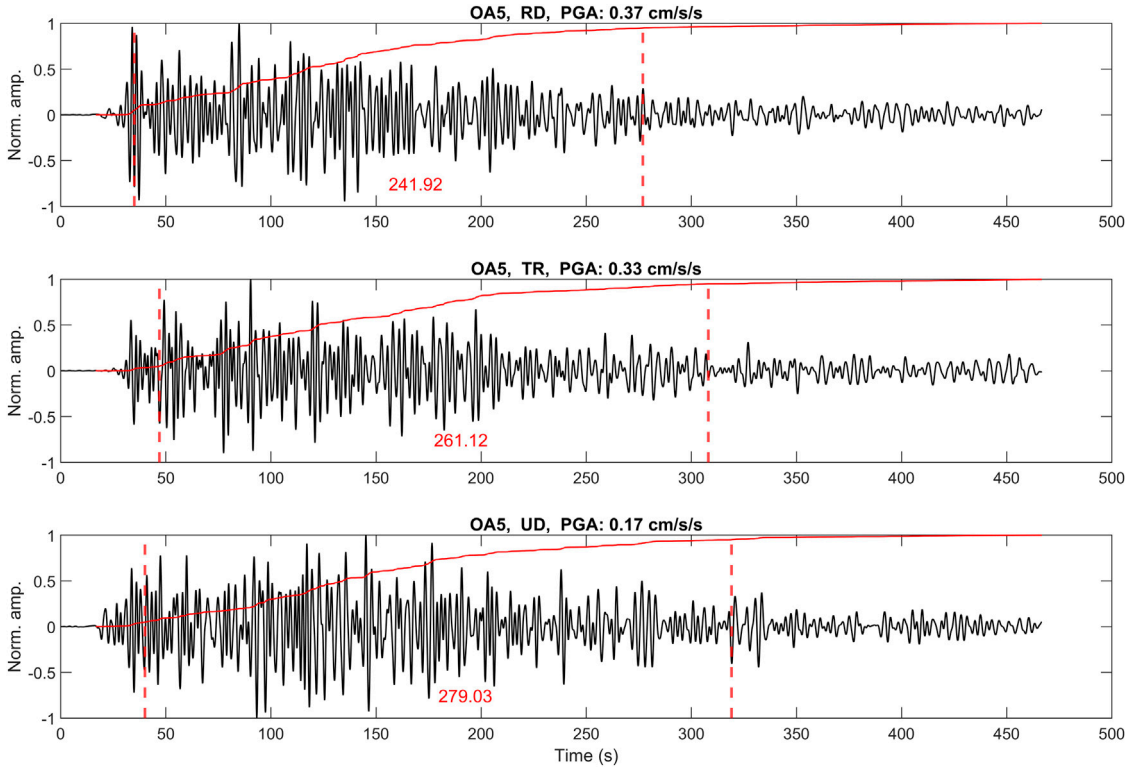


**FIGURE 7 |** Example Husid plots (red curves) for significant durations. The dashed vertical lines indicate 5 and 95% of the Husid plots in each panel, and the time lengths between the vertical lines give the values of significant durations as defined in the paper. The traces denote the 0.1–0.5 Hz bandpass-filtered waveforms recorded at the MeSO-net OA5 station during the 2018, Mw 5.9 event (see **Figure 1** for the location of event-site pair and **Figure 2** for the unfiltered waveforms). Note that the vertical scale gives the normalized amplitudes of the waveforms and Husid plots by the corresponding maximum values in each panel.

components are, on average, larger, at the K-NET/KiK-net sites than the S-net sites by a factor of about 3 (**Figure 5C**). While the vertical PGVs for the P-wave parts are nearly similar at small distances between the land and S-net sites, the mean ratio is about 1.5 at longer distances (**Figure 5F**).

The plots of the PGAs and PGVs as a function of hypocentral distance for the 2020b event are shown in **Figure 6**. The PGAs for three different segments of the records are depicted in **Figure 6A–C**, respectively. Similarly, the PGVs for the corresponding segments are depicted in **Figure 6D–F**, respectively. For this event, the horizontal PGAs and PGVs for the S-wave parts are nearly similar. The PGAs and PGVs of the S-wave parts of the vertical components at the land sites are, on average, about 2 and 1.5 times the values at the S-net sites for the 2020b event. The ratios of the values between the horizontal and vertical component PGAs and PGVs for the S-wave parts are about 2.5 and 3 for the land sites, while the corresponding ratios are about 6 and 5 for the S-net sites. The PGAs and PGVs for the P-wave parts of the vertical components on land are about 4 and 3 times the corresponding values at the seafloor sites.

The smaller values of the PGAs and PGVs, discussed above for the P-wave and S-wave parts on the vertical component records at the S-net sites, were most probably due to the presence of the water layer above the seabed as reported in several previous studies (e.g., Crouse and Quilter 1991; Boore and Smith 1999; Hongqi et al., 2014). For example, Crouse and Quilter (1991) formulated transfer function ratios with and without water layer for vertical P-wave and showed that the vertical peak accelerations as much as 50% were reduced due to the presence of water layer at short periods. Boore and Smith, (1999) showed by theoretical calculations that the water layer had little effect on the horizontal components of motion but that it produced a strong spectral null on the vertical component at the resonant frequency of P waves in the water layer.

Our main objective in this paper is to examine the properties of the S-net ocean-bottom records in relation to the records from the Kanto Basin area from the selected earthquakes. However, it is of interest to compare the peak values for the land-only or offshore-only sites between the used events as the magnitudes of the events were similar. A comparison of the horizontal and vertical component PGAs and PGVs between the three events for the same group of stations are provided in a supplementary file. It was found that the PGAs and PGVs from the S-wave parts between the 2018 and 2020b events were, on average, similar at equal distances for the land sites; both events had Mw value of 5.9. The 2020a event had smaller PGAs and PGVs compared to those for the 2018 and 2020b events. The 2020a event had a smaller magnitude by 0.1 unit than the other events. The 2020a event was an interplate event, which may have lower source spectral values than the other events

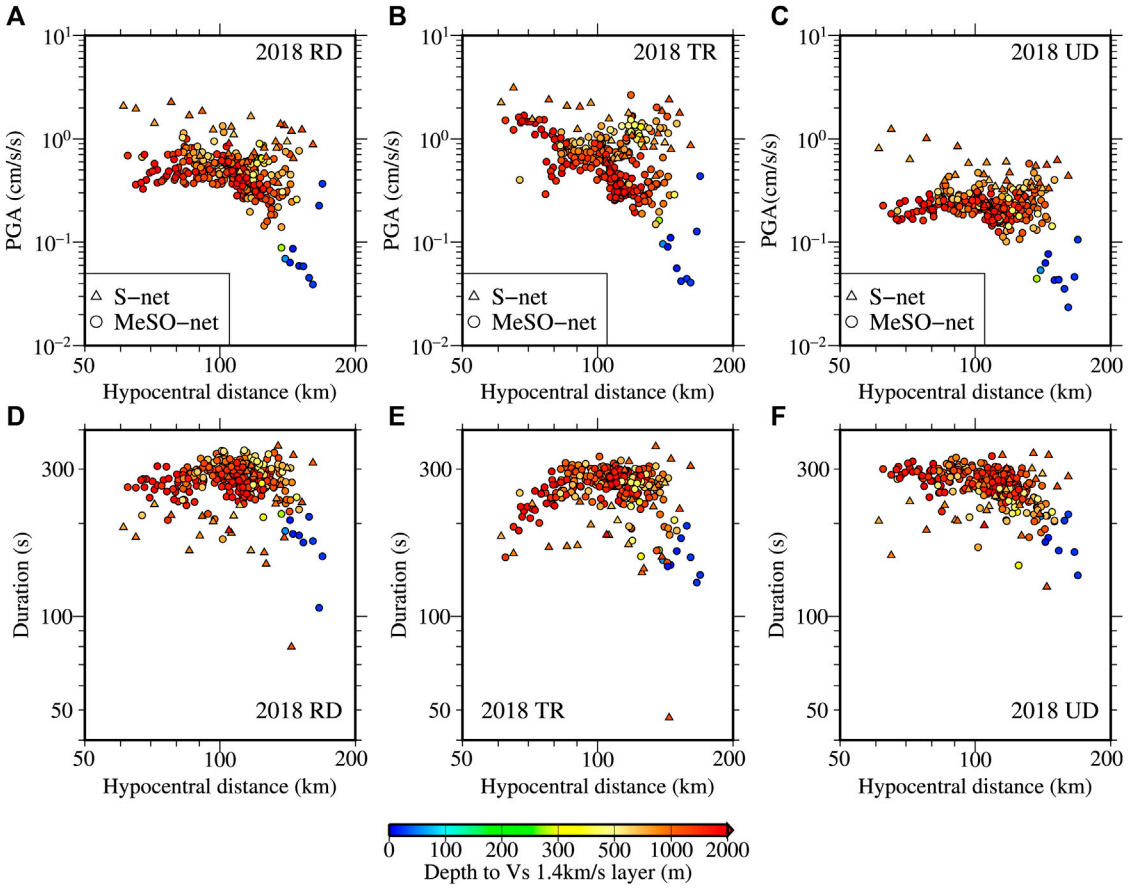


**FIGURE 8 |** Upper three panels: comparison of the PGAs computed from the 0.1–0.5 Hz bandpass-filtered records at the S-net (triangles) and MeSO-net (circles) sites for the radial (RD) **(A)**, transverse (TR) **(B)**, and vertical (UD) **(C)** components, respectively, as a function of hypocentral distance for the 2018 event (see **Table 1** for the event information). Lower three panels: comparison of the significant durations computed from the 0.1–0.5 Hz bandpass-filtered records at the S-net (triangles) and MeSO-net (circles) sites for the radial (RD) **(D)**, transverse (TR) **(E)**, and vertical (UD) **(F)** components for the same dataset used in **(A)**, **(B)**, and **(C)**, respectively. The values are colored by the depth to Vs 1.4 km/s layer in all panels.

(e.g., Allmann and Shearer 2009). The difference in source amplitude spectra may have also resulted in the smaller PGAs and PGVs for the 2020a event. The comparison for the S-net sites showed that the peak values for the 2018 event (having greater focal depth) were, on average, larger, than those for the other two events. However, the PGAs and PGVs for the P-wave parts were not the largest in amplitude for the 2018 event at the both land and S-net sites. Further analysis is necessary to understand the reason for these differences.

## COMPARISON OF THE LOW-FREQUENCY MOTIONS BETWEEN THE S-NET AND MESO-NET SITES

By comparing the bandpass-filtered waveforms at the nearby K-NET/KiK-net and MeSO-net sites discussed in the data section, we found that the MeSO-net records and K-NET/KiK-net records were similar at frequencies lower than about 0.5 Hz. This means that the top 20 m soil column has little effect on the ground motions lower than 0.5 Hz. This enables us to compare the peak values and other properties of the S-net longer duration records with the MeSO-net borehole records of identical time lengths at lower frequencies. In this section, we compare the PGAs and significant durations between the S-net ocean-bottom records and MeSO-net borehole records, which were bandpass-filtered between 0.1 and 0.5 Hz. The significant duration for each component was determined as the time interval between the 5 and 95% of the Husid plot (Husid 1969) for Arias intensity (Arias 1970). The Arias intensity is defined in **Equation 1**.

$$\mathrm{AI} = \frac{\pi}{2g}\int_0^{t_r} a^2(t)dt \tag{1}$$

where $a(t)$ is the acceleration time history, $t_r$ is the total duration of the time history, and $g$ is an acceleration due to gravity. Interested readers can find a comprehensive review and discussion of the duration of strong motions in Bommer and Martínez-Pereira (1999) and the references therein. One of the objectives of comparing the significant durations

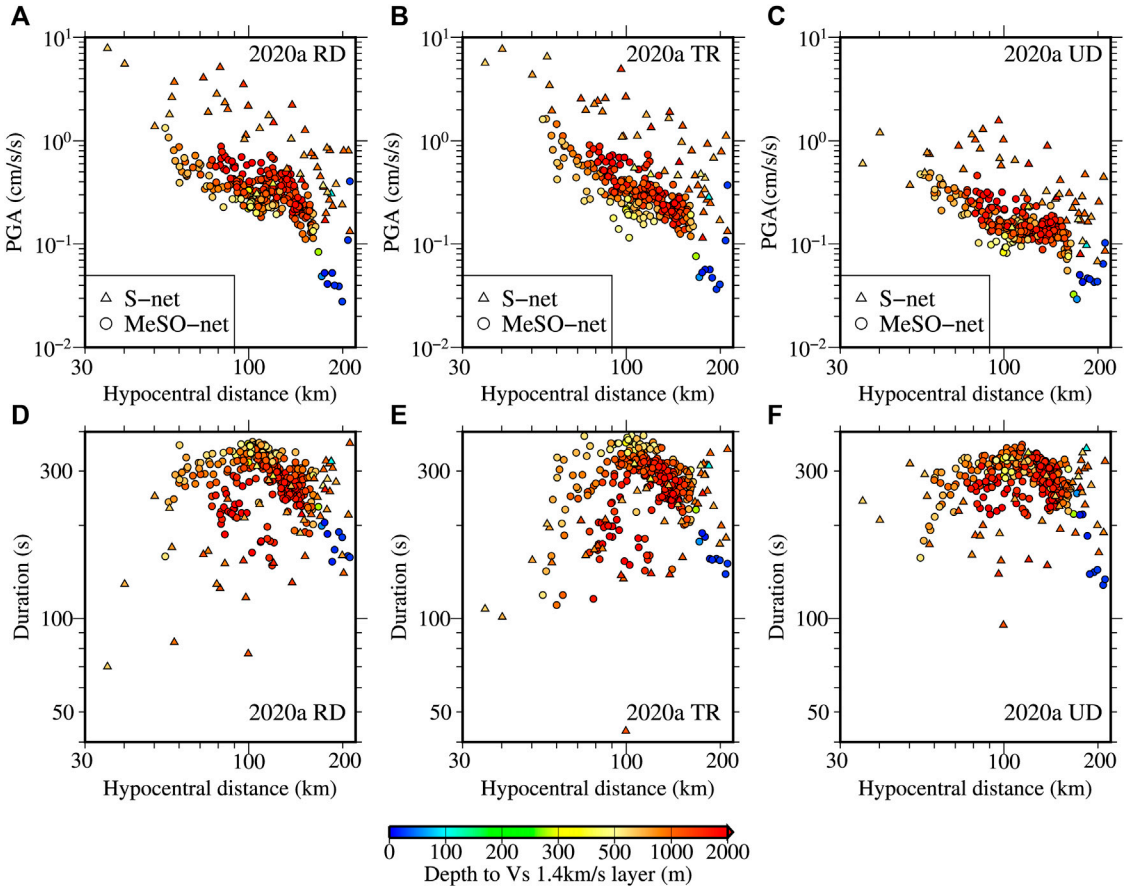


**FIGURE 9 |** Same as **Figure 8**, but for the 2020a interplate event (see **Table 1** for the event information).

between the two sets of data (land vs. seafloor) is to qualitatively grasp the influence of site conditions at the S-net sites because the local geological profiles at the offshore sites are either poorly resolved or unknown. In the present paper, the Husid plot is constructed for the time window of 450 s after the onset of P wave. An example Husid plots for the 0.1–0.5 Hz bandpass-filtered accelerograms recorded at the MeSO-net OA5 site for the 2018 event is shown in **Figure 7**. The significant durations for the radial, transverse, and vertical component records at the OA5 site are approximately 242, 261, and 279 s, respectively. The records at the TKY007 site (the nearest K-NET site from the MeSO-net OA5 site, see **Figure 1** for the site locations and **Figure 2** for the waveform comparisons between the TKY007 and OA5 sites) account for only about 60% of the significant duration of the records at the MeSO-net OA5 site due to the limited record length at the K-NET station.

The PGAs and significant durations between the S-net and MeSO-net sites are shown in **Figures 8–10** for the 2018, 2020a, and 2020b, respectively. As the deep sediments significantly influence the low-frequency motions, the values plotted in the figures are colored by the corresponding depths to the layer having Vs value of 1.4 km/s (hereafter abbreviated as D14). The D14 values were taken from the subsurface velocity model available at Japan Seismic Hazard Information Station (J-SHIS) (Fujiwara et al., 2012). The D14 was the suitable parameter to reduce the errors of the GMPEs for long periods (1–10 s) in Morikawa and Fujiwara (2013) and Dhakal et al. (2015). The D14 values are distributed over a relatively narrow depth range for the S-net sites compared to those for the MeSO-net sites. **Figures 8–10** demonstrate that the PGAs and significant durations were noticeably smaller at sites having D14 values smaller than about 100 m at the MeSO-net sites. The PGAs obtained from the bandpass-filtered accelerograms were generally larger at the S-net sites than the MeSO-net sites at equal distances. The PGAs for both S-net and MeSO-net sites showed a general decreasing trend with distance for all the events, but it was less conspicuous for the radial and vertical components at the MeSO-net sites for the 2018 event. It may be due to the different basin effects for the 2018 event. It was also due to an

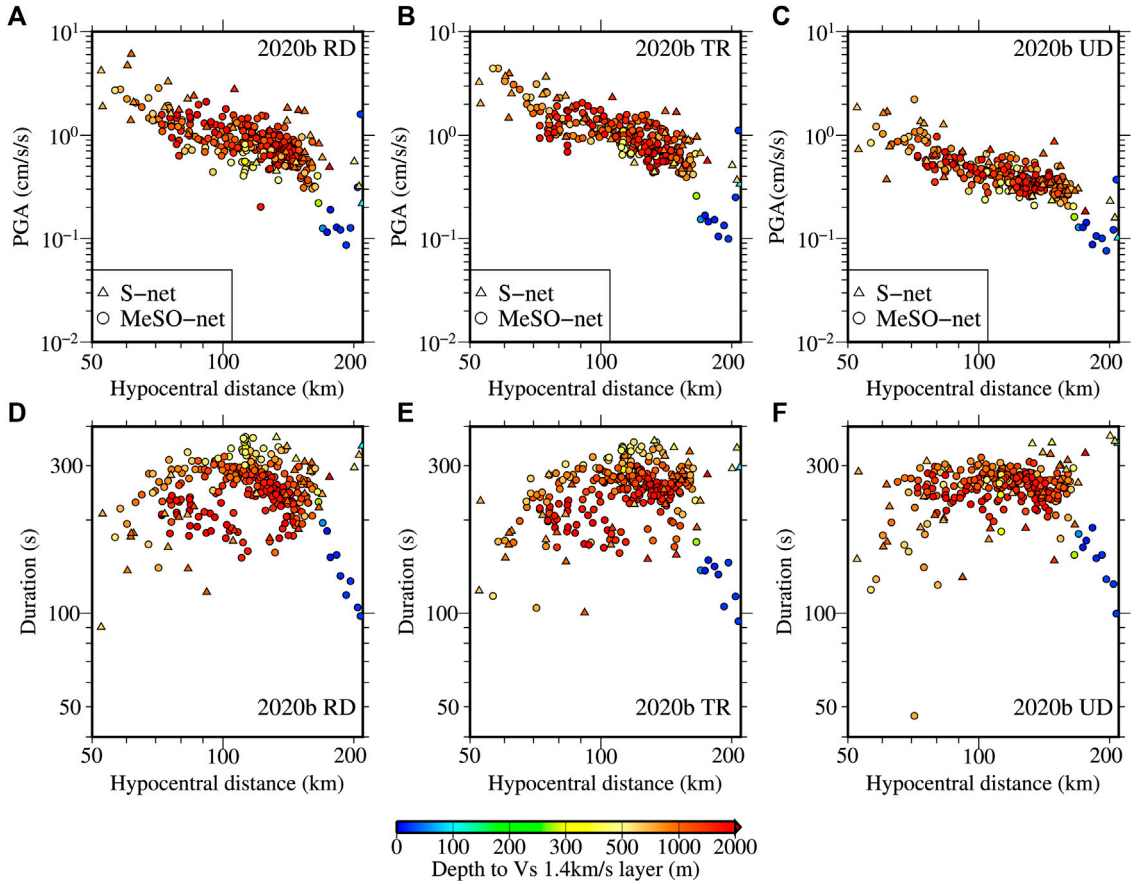


**FIGURE 10 |** Same as **Figure 8**, but for the 2020b crustal event (see **Table 1** for the event information).

apparent effect because the MeSO-net sites for the 2018 event cover a smaller distance range compared to the other events. The maximum hypocentral distance among the MeSO-net sites for the 2018 event was about 170 km, while it was about 210 km for the 2020 events. Also, the difference between the maximum and minimum hypocentral distances was smaller for the 2018 event due to the deeper focal depth compared to the 2020 events. Except for the MeSO-net sites having D14 values smaller than about 100 m, the significant durations generally rise with distance for the MeSO-net and S-net records. The difference of the significant durations between the S-net and MeSO-net sites was not so obvious at deep sedimentary sites. At smaller distances, the durations tended to be shorter at the S-net sites than the MeSO-net sites, while the durations tended to be longer at the larger distances at the S-net sites. At intermediate distances around 100 km, the durations at the MeSO-net sites appear to be longer. This latter result can be seen well for the 2020a event in **Figure 9D–F**.

We show a comparison of the PGAs and significant durations between the three events at the MeSO-net and S-net sites in a supplementary file. It was found that the low-frequency PGAs for the shallow event were generally larger at the MeSO-net sites in the Kanto Basin compared to the values from the deeper event (identical magnitude), while the values at the seafloor sites were generally similar between the events. These results may suggest that the focal depth is an important factor to predict ground motions in the Kanto Basin.

Finally, we compare the significant durations between the radial and transverse and radial and vertical components for the MeSO-net and S-net sites in **Figure 11**. We also compare the PGAs between the radial and transverse components at the MeSO-net and S-net sites in **Figure 12**. All these comparisons are from the 0.1–0.5 Hz bandpass-filtered accelerograms as introduced at the beginning of this section. **Figure 11** shows that the significant durations between the radial and transverse components are more similar than those between the radial and vertical components at both land and ocean-bottom sites. Although it is not discernible at the MeSO-net sites, the significant durations for the vertical components are, on average, larger at the S-net sites for all the events. This latter result may suggest that the vertical component long-period (low-frequency) records are influenced by the water

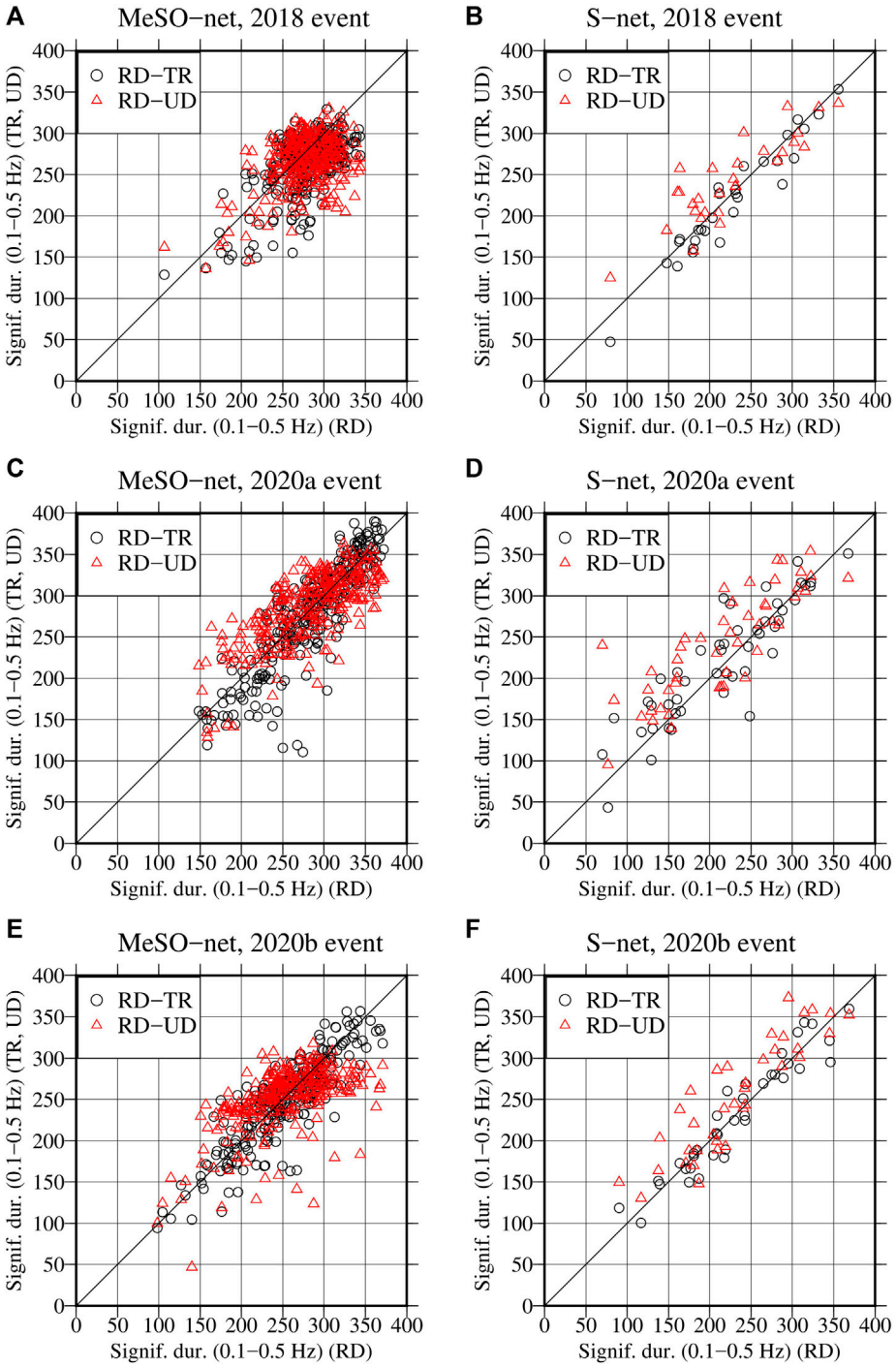


**FIGURE 11 |** Comparison of the significant durations computed from the 0.1–0.5 Hz bandpass-filtered records for the 2018 event between the radial and transverse (RD-TR) components and radial and vertical (RD-UD) components at the MeSO-net sites **(A)** and S-net sites **(B)**, respectively. The plots **(C)** and **(D)** are similar to the plots **(A)** and **(B)**, respectively, but for the 2020a event. Similarly, the plots **(E)** and **(F)** are for the 2020b event. See **Table 1** for the events information.

layer and are generally in agreement with the previous simulation studies (e.g., Todoriki et al., 2017). Todoriki et al. (2017) showed by numerical simulations that the long-period radial and vertical component records persisted for longer durations at the seafloors because of the water layer compared to the transverse components. In **Figure 12**, it can be seen that the PGAs of the radial and transverse components are generally similar except for the 2018 event. For the 2018 event, many sites recorded larger PGAs on the transverse components. The larger PGAs are more evident in the plots

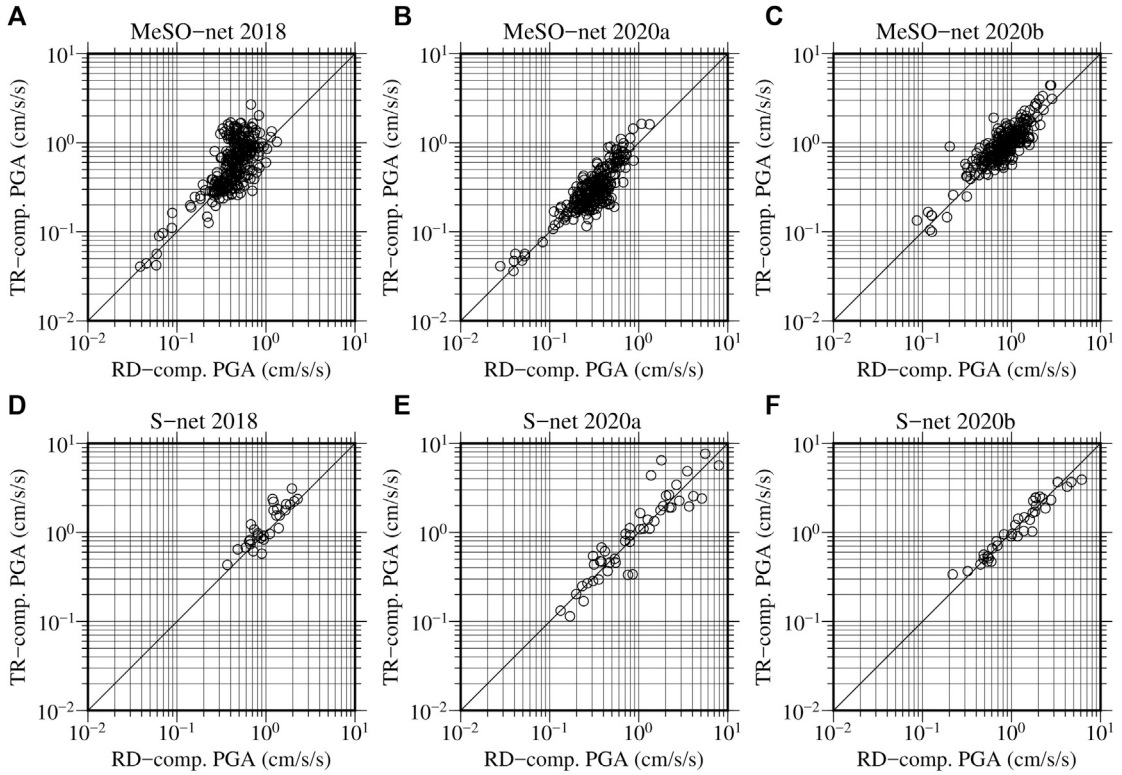


**FIGURE 12 |** Comparison of the PGAs between the radial (RD) and transverse (TR) components of motions between 0.1 and 0.5 Hz. Panels **(A)**, **(B)** and **(C)** show the plots for the 2018, 2020a, and 2020b events, respectively, for the MeSO-net sites. **(D)**, **(E)**, and **(F)** are similar to the panels **(A)**, **(B)**, and **(C)**, but for the S-net sites. See **Table 1** for the events information.

for the MeSO-net sites. The similarities of the significant durations and PGAs between the radial and transverse components at the S-net sites may suggest the presence of considerably thick sediments in the wider oceanic area because the transverse components mostly comprise the S-waves and love waves, which do not propagate through the liquid medium. The D14 values in the J-SHIS model also suggest considerably thick sedimentary layers distributed in the wider offshore area. The S-net records provide an excellent opportunity to reconstruct the velocity models of the offshore area to understand the source process of the earthquakes better (e.g., Okamoto et al., 2018; Hua et al., 2020), and we expect many results in the future.

## CONCLUSION

Strong-motion records were analyzed at the S-net ocean-bottom seismograph sites located close to the Kanto Basin and at the K-NET/KiK-net surface sites and MeSO-net borehole sites located in and around the Kanto Basin for three nearby earthquakes of comparable magnitudes (Mw 5.8–5.9) but differing in tectonic types and focal depths. The horizontal component PGAs and PGVs for the two events (intraslab and interplate events) were, on average, larger at the S-net ocean bottom sites than those at the K-NET/KiK-net land sites. The results are generally expected considering the lower Vs values for the subsea sediments and higher Q value in the Pacific Plate. In contrast, the vertical component PGAs and PGVs from P-wave portions were generally smaller at the S-net sites than those at the K-NET/KiK-net sites for all the events, even though the difference was less conspicuous for the PGVs. These results are also expected as the water layer makes the ocean bottom sites equivalent to the borehole sites on the land for the P-waves, causing a reduction of high-frequency amplitudes due to transmission and reflection of P-waves at the sediment-water interface. For S-wave parts on the vertical components, the PGAs and PGVs from the crustal event were smaller at the S-net sites than those at the K-NET/KiK-net sites, while they were either comparable or did not show the consistent difference for the other events. The PGAs computed from the 0.1–0.5 Hz bandpass-filtered records at the S-net sites were either comparable or larger than those at the MeSO-net sites. On the other hand, the significant durations computed from the 0.1–0.5 Hz bandpass-filtered records at the S-net and MeSO-net sites were generally comparable, given that the sediment thicknesses were also similar. The significant durations between the radial and transverse components were more similar than those between the radial and vertical

components both at the land and ocean-bottom sites. At the S-net sites, the significant durations of the vertical component records were, on average, larger than those of the radial components, while it was not so evident for the MeSO-net sites. This latter result at the S-net sites may suggest that the water layer also contributed to the duration elongation for the vertical component records. The results presented in this paper hinted that it is important to consider the effects of the water layer on the recorded motions at the S-net sites for seismological and engineering applications such as EEW and the design of offshore facilities. We have planned to analyze a more extensive data set at the S-net sites for the source, path, and site characterization for EEW and report the detailed results in a future paper.

## DATA AVAILABILITY STATEMENT

The K-NET and KiK-net strong-motion records were obtained from the website http://www.kyoshin.bosai.go.jp/. The MeSO-net and S-net records were obtained from the website https://hinetwww11.bosai.go.jp/auth/download/cont/?LANG=en. The hypocenter information of the events were taken from https://www.data.jma.go.jp/svd/eqev/data/bulletin/hypo_e.html. The moment magnitude for the events were taken from http://www.fnet.bosai.go.jp/event/joho.php?LANG=en. The J-SHIS deep subsurface model was obtained from http://www.j-shis.bosai.go.jp/map/JSHIS2/download.html?lang=en. The original contributions presented in the study are included in the article/**Supplementary Material**, further inquiries can be directed to the corresponding author.

## AUTHOR CONTRIBUTIONS

YD designed the study, analyzed the data, and drafted the manuscript. TK provided guidance in the data processing and interpretation. Both authors approved the manuscript for publication.

## FUNDING

This study was supported by "Advanced Earthquake and Tsunami Forecasting Technologies Project" of NIED and JSPS KAKENHI Grant Number JP20K05055.

## ACKNOWLEDGMENTS

We would like to thank the Japan Meteorological Agency for providing us with hypocenter information for the earthquakes used in this study. We would also like to thank Wessel and Smith (1998) for providing us with Generic Mapping Tools, which were used to make some figures in the manuscript. I would like to thank the Editor Francisco Javier Nuñez-Cornu for arranging review of this manuscript and two reviewers for their constructive and helpful comments.

## SUPPLEMENTARY MATERIAL

The Supplementary Material for this article can be found online at: https://www.frontiersin.org/articles/10.3389/feart.2021.699439/full#supplementary-material

## REFERENCES

Allmann, B. P., and Shearer, P. M. (2009). Global Variations of Stress Drop for Moderate to Large Earthquakes. *J. Geophys. Res.* 114, B01310. doi:10.1029/2008JB005821

Aoi, S., Asano, Y., Kunugi, T., Kimura, T., Uehira, K., Takahashi, N., et al. (2020). MOWLAS: NIED Observation Network for Earthquake, Tsunami and Volcano. *Earth Planets Space* 72, 126. doi:10.1186/s40623-020-01250-x

Arias, A. (1970). "A Measure of Earthquake Intensity," in *Seinnic Design for Nuclear Power Plants*. Editor R. Hansen (Cambridge, Massachusetts: MIT Press), 438–483.

Barnes, C. R., Best, M. M. R., Johnson, F. R., and Pirenne, B. (2015). "NEPTUNE Canada: Installation and Initial Operation of the World's First Regional Cabled Ocean Observatory," in *SEAFLOOR OBSERVATORIES* (Berlin, Heidelberg: Springer Praxis BooksSpringer), 415–438. doi:10.1007/978-3-642-11374-1_16

Bommer, J. J., and Martínez-pereira, A. (1999). The Effective Duration of Earthquake strong Motion. *J. Earthquake Eng.* 3 (2), 127–172. doi:10.1080/13632469909350343

Boore, D. M., and Smith, C. E. (1999). Analysis of Earthquake Recordings Obtained from the Seafloor Earthquake Measurement System (SEMS) Instruments Deployed off the Coast of Southern California. *Bull. Seism. Soc. Am.* 89 (1), 260–274. doi:10.1785/bssa0890010260

Crouse, C. B., and Quilter, J. (1991). "Seismic hazard Analysis and Development of Design Spectra for Maul A Platform," in Proc. Pacific Conf. on Earthquake Engineering, New Zealand, 20-23 Nov, 3. 137–148.

Dhakal, Y. P., Kunugi, T., Suzuki, W., Kimura, T., Morikawa, N., and Aoi, S. (2021). Strong Motions on Land and Ocean Bottom: Comparison of Horizontal PGA, PGV, and 5% Damped Acceleration Response Spectra in Northeast Japan and the Japan Trench Area. *Bull. Seism. Soc. Am.* doi:10.1785/0120200368

Dhakal, Y. P., Suzuki, W., Kunugi, T., and Aoi, S. (2015). Ground Motion Prediction Equations for Absolute Velocity Response Spectra (1-10 S) in Japan for Earthquake Early Warning. *J. JAEE* 15, 91–96. doi:10.5610/jaee.15.6_91

Hayashimoto, N., Nakamura, T., and Hoshiba, M. (2019). A Technique for Estimating the UD-Component Displacement Magnitude for Earthquake Early Warnings that Can Be Applied to Various Seismic Networks Including Ocean Bottom Seismographs. *Q. J. Seismol.* 83, 1–10. (in Japanese with English abstract).

HERP (Headquarters for Earthquake Research Promotion) (2018). *Report: National Seismic hazard Maps for Japan*. (in Japanese). Retrieved from https://www.jishin.go.jp/main/index-e.html.(Accessed September 5, 2020)

Hongqi, D., Hu, J., and Lili, X. (2014). Effect of Seawater on Incident Plane P and SV Waves at Ocean Bottom and Engineering Characteristics of Offshore Ground Motion Records off the Coast of Southern California, USA. *Earthq. Eng. Eng. Vib.* 13, 181–194. doi:10.1007/s11803-014-0222-4

Hoshiba, M., Kamigaichi, O., Saito, M., Tsukada, S. y., and Hamada, N. (2008). Earthquake Early Warning Starts Nationwide in Japan. *Eos Trans. AGU* 89, 73–74. doi:10.1029/2008eo080001

Hsiao, N.-C., Lin, T.-W., Hsu, S.-K., Kuo, K.-W., Shin, T.-C., and Leu, P.-L. (2014). Improvement of Earthquake Locations with the Marine Cable Hosted Observatory (MACHO) Offshore NE Taiwan. *Mar. Geophys. Res.* 35, 327–336. doi:10.1007/s11001-013-9207-3

Hu, J., Tan, J., and Zhao, J. X. (2020). New GMPEs for the Sagami Bay Region in Japan for Moderate Magnitude Events with Emphasis on Differences on Site Amplifications at the Seafloor and Land Seismic Stations of K-NET. *Bull. Seism. Soc. Am.* 110, 2577–2597. doi:10.1785/0120190305

Hua, Y., Zhao, D., Toyokuni, G., and Xu, Y. (2020). Tomography of the Source Zone of the Great 2011 Tohoku Earthquake. *Nat. Commun.* 11, 1163. doi:10.1038/s41467-020-14745-8

Husid, L. R. (1969). 8. Santiago de Chile: Revista del IDIEM, 21–42.Caracteristicas de terremotos. Analisis general

JMA (Japan Meteorological Agency) (2019). *Utilization of Seafloor Earthquake Observation Data for Earthquake Early Warning*. (in Japanese). Retrieved from https://www.jma.go.jp/jma/press/1906/21a/eewkatsuyou20190621.html (Accessed 6 16, 2021).

Kano, M., Nagao, H., Sakai, S. i., Nakagawa, S., Mizusako, S., Hori, M., et al. (2015). Azimuth Verification of the MeSO-Net Seismographs. *Jssj* 68 (2), 31–44. (in Japanese with English abstract). doi:10.4294/zisin.68.31

Kubo, H., Nakamura, T., Suzuki, W., Dhakal, Y. P., Kimura, T., Kunugi, T., et al. (2019). Ground-Motion Characteristics and Nonlinear Soil Response Observed by DONET1 Seafloor Observation Network during the 2016 Southeast Off-Mie, Japan, Earthquake. *Bull. Seism. Soc. Am.* 109, 976–986. doi:10.1785/0120170296

Morikawa, N., Fujiwara, H., and Fujiwara, H. (2013). A New Ground Motion Prediction Equation for Japan Applicable up to M9 Mega-Earthquake. *J. Disaster Res.* 8, 878–888. doi:10.20965/jdr.2013.p0878

Nakamura, T., and Hayashimoto, N. (2019). Rotation Motions of Cabled Ocean-Bottom Seismic Stations during the 2011 Tohoku Earthquake and Their Effects on Magnitude Estimation for Early Warnings. *Geophys. J. Int.* 216, 1413–1427. doi:10.1093/gji/ggy502

Nakamura, T., Takenaka, H., Okamoto, T., Ohori, M., and Tsuboi, S. (2015). Long-period Ocean-Bottom Motions in the Source Areas of Large Subduction Earthquakes. *Sci. Rep.* 5, 16648. doi:10.1038/srep16648

NIED (2019a). *NIED S-Net*. Tsukuba, Japan: National Research Institute for Earth Science and Disaster Resilience. doi:10.17598/NIED.0007

NIED (2019b). *NIED K-NET, KiK-Net*. Tsukuba, Japan: National Research Institute for Earth Science and Disaster Resilience. doi:10.17598/NIED.0004

NIED (2019c). *NIED MeSO-Net*. Tsukuba, Japan: National Research Institute for Earth Science and Disaster Resilience. doi:10.17598/NIED.0023

Noguchi, S., Maeda, T., and Furumura, T. (2016). Ocean-influenced Rayleigh Waves from Outer-Rise Earthquakes and Their Effects on Durations of Long-Period Ground Motion. *Geophys. J. Int.* 205, 1099–1107. doi:10.1093/gji/ggw074

Okada, Y., Kasahara, K., Hori, S., Obara, K., Sekiguchi, S., Fujiwara, H., et al. (2004). Recent Progress of Seismic Observation Networks in Japan -Hi-Net, F-Net, K-NET and KiK-Net-. *Earth Planet. Sp* 56, xv–xxviii. doi:10.1186/bf03353076

Okamoto, T., Takenaka, H., and Nakamura, T. (2018). Evaluation of Accuracy of Synthetic Waveforms for Subduction-Zone Earthquakes by Using a Land-Ocean Unified 3D Structure Model. *Earth Planets Space* 70, 98. doi:10.1186/s40623-018-0871-z

Romanowicz, B., McGill, P., Neuhauser, D., and Dolenc, D. (2009). Acquiring Real Time Data from the Broadband Ocean Bottom Seismic Observatory at Monterey Bay (MOBB). *Seismological Res. Lett.* 80 (2), 197–202. doi:10.1785/gssrl.80.2.197

Sakai, S., and Hirata, N. (2009). Distribution of the Metropolitan Seismic Observation Network. *Bull. Earthq. Res. Inst. Univ. Tokyo* v84, 57–69. (in Japanese with English abstract).

Si, H., and Midorikawa, S. (1999). New Attenuation Relationships for Peak Ground Acceleration and Velocity Considering Effects of Fault Type and Site Condition. *Nihon Kenchiku Gakkai Kozokei Ronbunshu* 64, 63–70. (in Japanese with English abstract). doi:10.3130/aijs.64.63_2

Si, H., and Midorikawa, S. (2000). "New Attenuation Relations for Peak Ground Acceleration and Velocity Considering Effects of Fault Type and Site Condition," in Proceedings of the 12th World Conference on Earthquake Engineering, Auckland, New Zealand, January 30 - February 4 2000. paper no. 0532.

Takagi, R., Uchida, N., Nakayama, T., Azuma, R., Ishigami, A., Okada, T., et al. (2019). Estimation of the Orientations of the S-net Cabled Ocean-Bottom Sensors. *Seismol. Res. Lett.* 90, 2175–2187. doi:10.1785/0220190093

Todoriki, M., Furumura, T., and Maeda, T. (2017). Effects of Sea Water on Elongated Duration of Ground Motion as Well as Variation in its Amplitude for Offshore Earthquakes. *Geophys. J. Int.* 208, 226–233. doi:10.1093/gji/ggw388

Umino, N., and Hasegawa, A. (1984). Three-Dimensional Qs Structure in the Northeastern Japan Arc. *Jssj* 37 (2), 217–228. (in Japanese with English abstract). doi:10.4294/zisin1948.37.2_217

Wessel, P., and Smith, W. H. F. (1998). New, Improved Version of Generic Mapping Tools Released. *Eos Trans. AGU* 79, 579. doi:10.1029/98EO00426

Fujiwara, H., Kawai, S., Aoi, S., Morikawa, N., Senna, S., Azuma, H., Ooi, M., Hao, K.X., Hasegawa, N., Maeda, T., Iwaki, A., Wakamatsu, K., Imoto, M., Okumura, T., Matsuyama, H., and Narita, A. (2012). Some improvements of seismic hazard assessment based on the 2011 Tohoku earthquake. *Technical Note of the National Research Institute for Earth Science and Disaster Prevention* 379, 1–349. (in Japanese)

**Conflict of Interest:** The authors declare that the research was conducted in the absence of any commercial or financial relationships that could be construed as a potential conflict of interest.

frontiers in Earth Science

CORRECTION
published: 27 September 2021
doi: 10.3389/feart.2021.765487

# Corrigendum: An Evaluation of Strong-Motion Parameters at the S-Net Ocean-Bottom Seismograph Sites Near the Kanto Basin for Earthquake Early Warning

*Yadab P. Dhakal* and Takashi Kunugi*

*National Research Institute for Earth Science and Disaster Resilience, Tsukuba, Japan*

**Keywords: S-net, ocean-bottom seismograph network, Japan Trench, MeSO-net, Kanto Basin, earthquake early warning, peak ground acceleration, strong-motion duration**

OPEN ACCESS

***Edited and reviewed by:***
*Francisco Javier Nuñez-Cornu, University of Guadalajara, Mexico*

****Correspondence:***
*Yadab P. Dhakal*
*ydhakal@bosai.go.jp*

***Specialty section:***
*This article was submitted to Solid Earth Geophysics, a section of the journal Frontiers in Earth Science*

***Received:*** *27 August 2021*
***Accepted:*** *31 August 2021*
***Published:*** *27 September 2021*

***Citation:***
*Dhakal YP and Kunugi T (2021) Corrigendum: An Evaluation of Strong-Motion Parameters at the S-Net Ocean-Bottom Seismograph Sites Near the Kanto Basin for Earthquake Early Warning. Front. Earth Sci. 9:765487. doi: 10.3389/feart.2021.765487*

## A Corrigendum on

**An Evaluation of Strong-Motion Parameters at the S-Net Ocean-Bottom Seismograph Sites near the Kanto Basin for Earthquake Early Warning**
*by Yadab P. Dhakal and Takashi Kunugi Front. Earth Sci. 9:699439. doi: 10.3389/feart.2021.699439*

In the original article, there was a mistake in the legend for S-net buried and S-net non-buried stations in **Figures 4**, **5**, and **6**. The symbols for the S-net buried and S-net non-buried stations were mistaken for each other. The correct legend appears below.

The authors apologize for this error and state that this does not change the scientific conclusions of the article in any way. The original article has been updated.

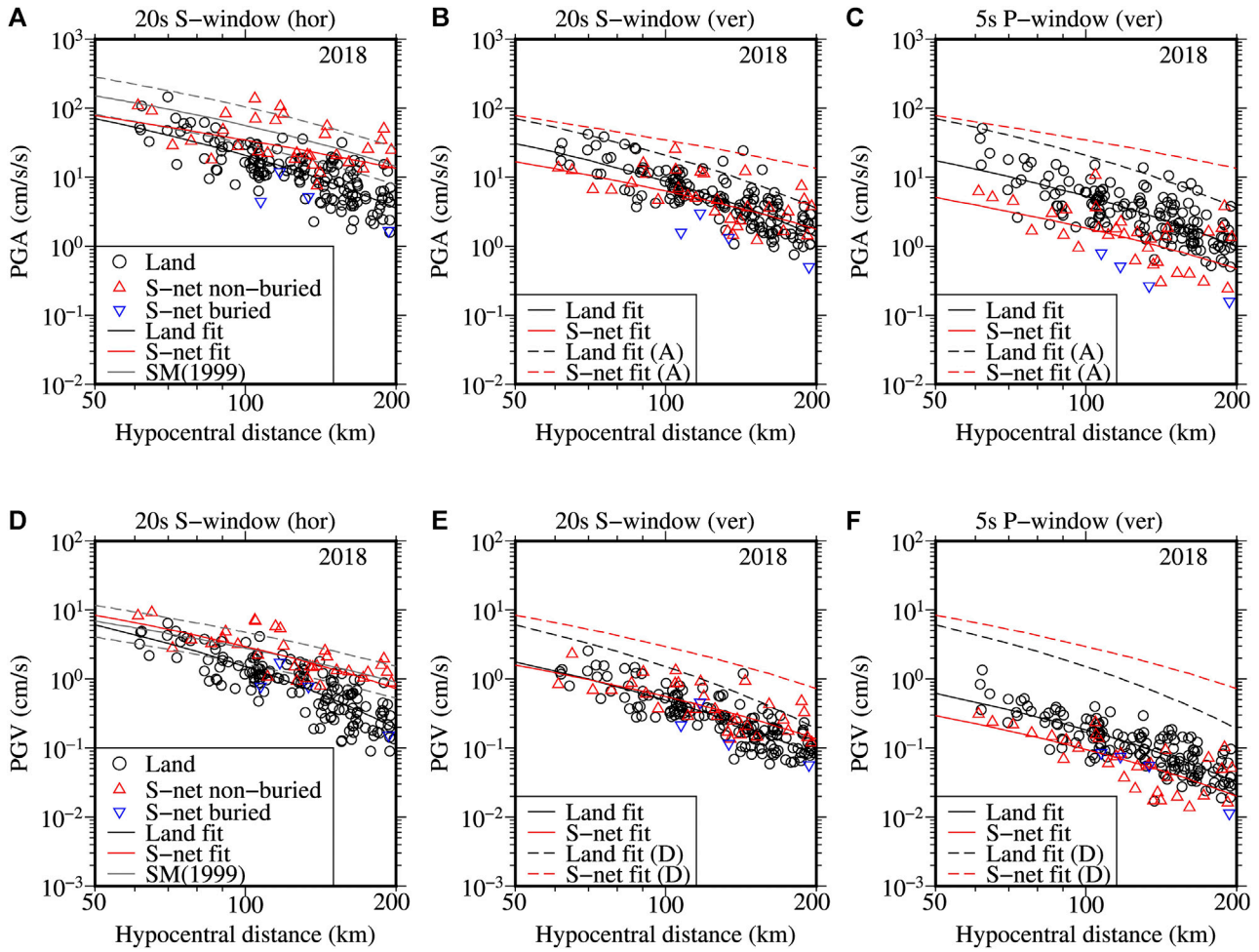


**FIGURE 4 |** Plots of PGAs **(A, B, C)** and PGVs **(D, E, F)** as a function of hypocentral distance for the 2018 event (see **Table 1** for the event information). The **left and middle panels** show the peak values of the 20 s time windows starting from the S-onset for the horizontal (hor) and vertical (ver) components, respectively. The **right panels** show the peak values of the 5 s time windows starting from the P-onset for the vertical components. The plotted values for the horizontal components are the larger ones of the peak values of the two horizontal components. The circles denote the K-NET/KiK-net stations, simply written as Land in the legends, and the triangles S-net stations of which the inverse triangles (blue colored) denote the buried S-net stations. The black and red solid lines represent the fitted lines between the observed values and hypocentral distances for the K-NET/KiK-net and S-net stations in each panel. The solid and dashed grey lines denote the median prediction curves and range of one standard deviation for soil site condition in **(A)** and Vs30 = 300 m/s in **(D)** using the GMPEs in Si and Midorikawa (1999), written as SM (1999) in the legend, for an intraslab-type earthquake. The dashed black and red lines in **(B, C)** and **(E, F)** denote the fitted black and red solid lines in **(A)** and **(C)**, respectively, for comparison.

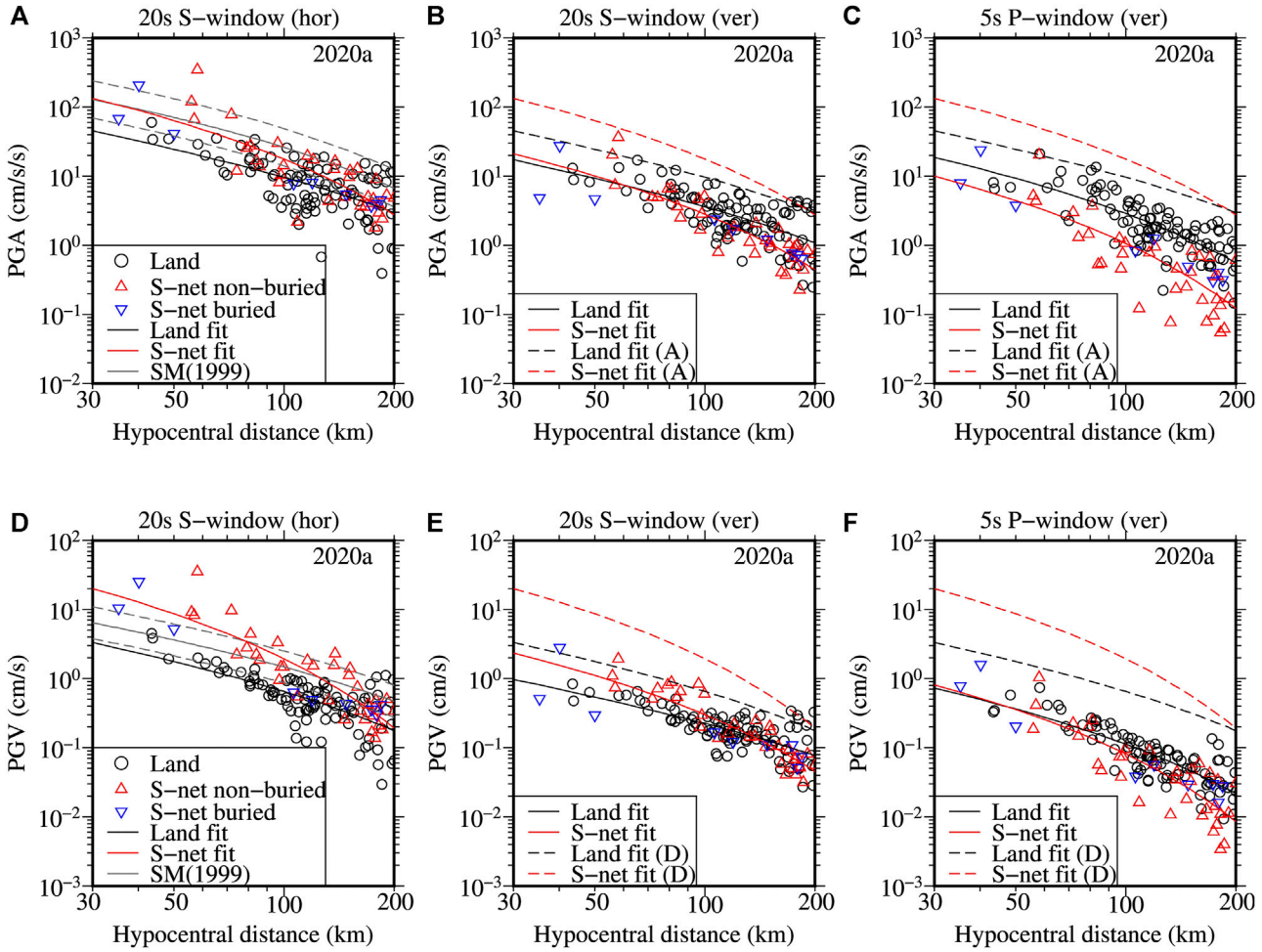


**FIGURE 5 |** Same as **Figure 4**, but for the 2020a interplate event (see **Table 1** of the original article for the event information). The GMPEs for an interplate-type earthquake are used in the panels **(A)** and **(D)**.

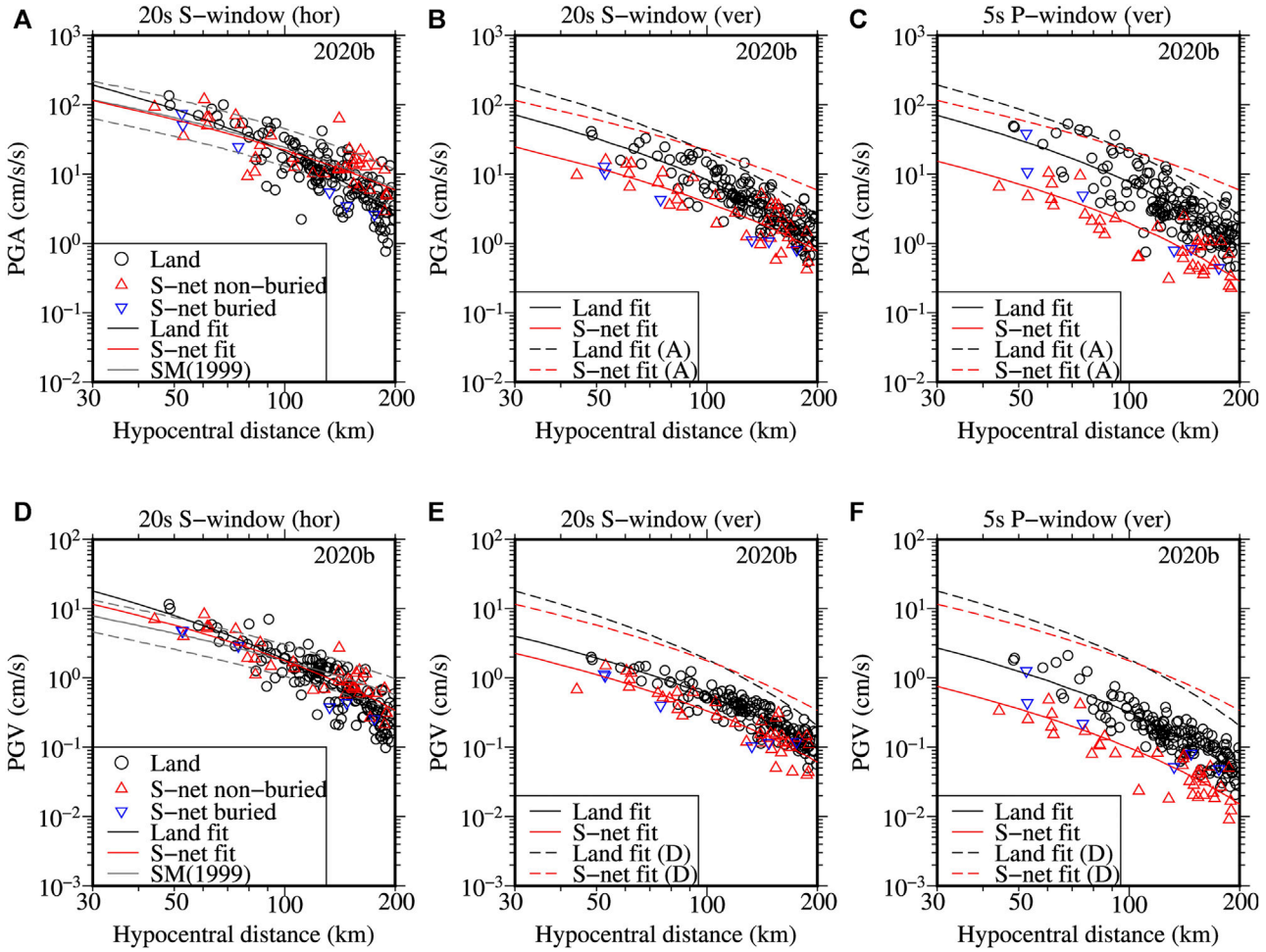


**FIGURE 6 |** Same as **Figure 4**, but for the 2020b crustal event (see Table 1 of the original article for the event information). The GMPEs for a crustal-type earthquake are used in the panels **(A)** and **(D)**.

frontiers in Earth Science

ORIGINAL RESEARCH
published: 29 July 2021
doi: 10.3389/feart.2021.661311

# One Year of Seismicity Recorded Through Ocean Bottom Seismometers Illuminates Active Tectonic Structures in the Ionian Sea (Central Mediterranean)

*Tiziana Sgroi[1], Alina Polonia[2], Laura Beranzoli[1], Andrea Billi[3]*, Alessandro Bosman[3], Antonio Costanza[4], Marco Cuffaro[3], Giuseppe D'Anna[4], Mariagrazia De Caro[1], Maria Di Nezza[1], Gioacchino Fertitta[4], Francesco Frugoni[1], Luca Gasperini[2], Stephen Monna[1], Caterina Montuori[1], Lorenzo Petracchini[3], Patrizio Petricca[5], Stefania Pinzi[6], Andrea Ursino[4] and Carlo Doglioni[5,7]*

[1]*Istituto Nazionale di Geofisica e Vulcanologia, Sezione Roma 2, Roma, Italy,* [2]*Istituto di Scienze Marine, CNR, Bologna, Italy,* [3]*Istituto di Geologia Ambientale e Geoingegneria, CNR, Roma, Italy,* [4]*Istituto Nazionale di Geofisica e Vulcanologia, Osservatorio Etneo, Sezione di Catania, Catania, Italy,* [5]*Dipartimento di Scienze della Terra, Sapienza Università di Roma, Roma, Italy,* [6]*Istituto Nazionale di Geofisica e Vulcanologia, Sezione Roma 1, Roma, Italy,* [7]*Istituto Nazionale di Geofisica e Vulcanologia, Roma, Italy*

OPEN ACCESS

**Edited by:**
*Susan Bilek,*
*New Mexico Institute of Mining and Technology, United States*

**Reviewed by:**
*Piero Poli,*
*Université Grenoble Alpes, France*
*Francisco Javier Nuñez-Cornu,*
*University of Guadalajara, Mexico*

***Correspondence:**
*Andrea Billi*
*andrea.billi@cnr.it*

**Specialty section:**
*This article was submitted to Solid Earth Geophysics, a section of the journal Frontiers in Earth Science*

**Received:** *30 January 2021*
**Accepted:** *14 July 2021*
**Published:** *29 July 2021*

**Citation:**
*Sgroi T, Polonia A, Beranzoli L, Billi A, Bosman A, Costanza A, Cuffaro M, D'Anna G, De Caro M, Di Nezza M, Fertitta G, Frugoni F, Gasperini L, Monna S, Montuori C, Petracchini L, Petricca P, Pinzi S, Ursino A and Doglioni C (2021) One Year of Seismicity Recorded Through Ocean Bottom Seismometers Illuminates Active Tectonic Structures in the Ionian Sea (Central Mediterranean). Front. Earth Sci. 9:661311. doi: 10.3389/feart.2021.661311*

Seismological data recorded in the Ionian Sea by a network of seven Ocean Bottom Seismometers (OBSs) during the 2017–2018 SEISMOFAULTS experiment provides a close-up view of seismogenic structures that are potential sources of medium-high magnitude earthquakes. The high-quality signal-to-noise ratio waveforms are observed for earthquakes at different scales: teleseismic, regional, and local earthquakes as well as single station earthquakes and small crack events. In this work, we focus on two different types of recording: 1) local earthquakes and 2) Short Duration Events (SDE) associated to micro-fracturing processes. During the SEISMOFAULTS experiment, 133 local earthquakes were recorded by both OBSs and land stations (local magnitude ranging between 0.9 and 3.8), while a group of local earthquakes (76), due to their low magnitude, were recorded only by the OBS network. We relocated 133 earthquakes by integrating onshore and offshore travel times and obtaining a significant improvement in accuracy, particularly for the offshore events. Moreover, the higher signal-to-noise ratio of the OBS network revealed a significant seismicity not detected onshore, which shed new light on the location and kinematics of seismogenic structures in the Calabrian Arc accretionary prism and associated to the subduction of the Ionian lithosphere beneath the Apennines. Other signals recorded only by the OBS network include a high number of Short Duration Events (SDE). The different waveforms of SDEs at two groups of OBSs and the close correlation between the occurrence of events recorded at single stations and SDEs suggest an endogenous fluid venting from mud volcanoes and active fault traces. Results from the analysis of seismological data collected during the SEISMOFAULTS experiment confirm the necessity and potential of marine studies with OBSs, particularly in those geologically active areas of the Mediterranean Sea prone to high seismic risk.

**Keywords: ocean bottom seismometer (OBS), local earthquakes, short duration events (SDE), Ionian Sea (Italy), Calabrian Arc, marine network, SEISMOFAULTS, active faults**

## INTRODUCTION

The lithosphere beneath the Ionian Sea is an oceanic embayment (Catalano et al., 2001), which is subducting contemporaneously beneath the Apennines and the Hellenides (Carminati et al., 2012; Carminati et al., 2020). The related accretionary prisms form two major salients within the depressed basin. The Ionian basin and its margins are among the most seismically active areas in the Mediterranean region. Here, some of the strongest earthquakes took place during historical and recent times, including the largest events ever recorded in Italy (e.g., 1169, Mw 6.6; 1693, Mw 7.4; 1908, Mw 7.2; 1990, Mw 5.7; Boschi et al., 1997). Despite many studies and large sets of data collected during marine geological campaigns (Bianca et al., 1999; Argnani and Bonazzi, 2005; Polonia et al., 2011; Gutscher et al., 2016), the offshore location of seismogenic sources and causative faults of large magnitude historical earthquakes are still debated. Part of the problem is the inadequacy of the onshore seismic network in locating medium-low-magnitude earthquakes occurring offshore. In fact, the location of these events based solely on land station recordings appears affected by considerable errors (Sgroi et al., 2006; Sgroi et al., 2021).

For the offshore records, land seismic observations suffer particularly from insufficient azimuthal coverage, which results in misdetection (or non-detection) of small-to-moderate magnitude earthquakes. These limits can be overcome by implementing networks of Ocean Bottom Seismometers (OBSs), designed as self-contained data acquisition systems deployed at the seafloor, where they are able to self-install and record ground motion data with high signal-to-noise ratio. The OBSs constitute the bulk modules or multi-sensor seafloor observatories, a new class of instruments, which are changing our knowledge of geologic processes in seas and oceans, gathering useful data for a variety of scientific investigations ranging from the deep Earth's structure to surface processes (e.g., Favali and Beranzoli, 2006; Billi et al., 2020).

Since the '80s, thanks to the technological development, OBSs and seafloor observatories have been deployed in different regions of the world, mainly to improve location of earthquakes occurring offshore and in coastal areas, complementing data from land based networks (e.g., Lawton et al., 1982; Hino et al., 1996; Hsiao et al., 2014), and to perform 1D and 3D seismic velocity crustal studies in the offshore (e.g., Husen et al., 2000; Montuori et al., 2007; Chang et al., 2008; Monna et al., 2013; Sgroi et al., 2021).

In recent years, several seismological experiments have been carried out in the Tyrrhenian and Ionian seas, with the deployment of OBSs and seafloor observatories (Dahm et al., 2002; Favali et al., 2015; Coltelli et al., 2016). In the southern Tyrrhenian Sea, an OBS network surrounding the Aeolian Islands operated for six months during the TYDE experiment (Dahm et al., 2002), detecting an intense seismicity of tectonic and volcanic origins (Sgroi et al., 2006; Sgroi et al., 2009). In the Ionian Sea, the deployment of the NEMO-SN1 seafloor observatory (Favali and Beranzoli, 2006) allowed for synchronous recordings of time-series for multidisciplinary studies and provided useful information on oceanic areas and, in particular, on volcanic and tectonic structures (Sgroi et al., 2007; Sgroi et al., 2014; Sgroi et al., 2019; Sgroi et al., 2021).

The SEISMOFAULTS project (www.seismofaults.it) has been the first experiment designed to illuminate geological active features offshore Sicily and south Calabria through the deployment of an OBS network (Billi et al., 2020). The SEISMOFAULTS main purpose was to explore seismicity of the submerged portion of the Calabrian Arc subduction complex, starting from observations carried out during marine geophysical/geological expeditions in the Ionian Sea (Polonia et al., 2016).

To gather information on the location of active tectonic features, we analysed data from a broad-band array of seven OBSs deployed in the Ionian Sea from May 2017 to May 2018, which recorded several thousands of distinct events including teleseismic, regional, and local earthquakes. Below, the character of seismic events is defined in terms of their spatial and temporal distribution, and in relation with the knowledge of the present tectonic setting (**Figure 1**). We acknowledge that the OBS network has significantly improved the determination of seismic events in the offshore and along the coasts. It has also allowed investigating the nature of seismogenic structures in the Ionian Sea through analysis of the microseismicity consisting of several thousands of low-magnitude earthquakes and short duration events (SDE), the latter suggesting microfracturing processes, endogenous venting from presumably active faults, and active geofluid venting from mud volcanoes.

## TECTONIC SETTING

The Ionian Sea is located within the deformed Africa-Eurasia plate boundary in the Mediterranean region, where slab retreat occurs along the Calabrian Arc subduction (Doglioni, 1991; Devoti et al., 2008), i.e., the subduction hinge diverges relative to the upper Eurasian plate (**Figure 1**). The Calabrian Arc evolved on top of a NW-dipping subduction system where the subducting Ionian lithosphere sinks into the mantle forming subduction zone with a wide accretionary complex in the Calabrian Arc (Doglioni et al., 1999; Polonia et al., 2011; Maesano et al., 2017) and intense back-arc volcanism along the Aeolian Arc in Tyrrhenian Sea (Peccerillo, 2005). Present-day plate motion occurs in this region at slow velocities, in the order of a few mm/yr, as determined by space geodesy measurements (Devoti et al., 2008; Palano et al., 2015), accommodating mostly shortening inside the accretionary wedge and along the outer deformation front of the subduction arc (Doglioni et al., 1999; Polonia et al., 2011; Gallais et al., 2012, and references therein). In the Ionian Sea, the Calabrian accretionary prism is bounded towards the SW by the Malta Escarpment (**Figure 1**), where the Ionian salient along its western

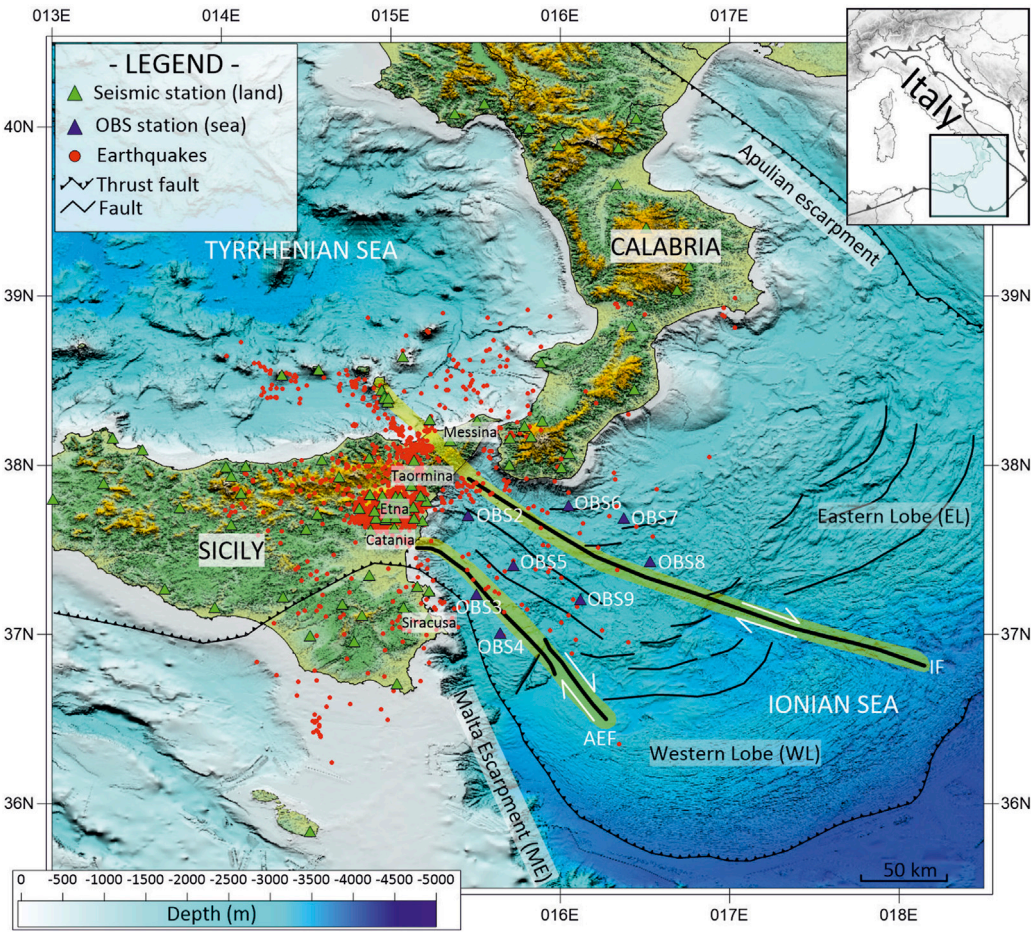


**FIGURE 1 |** Morphological map of the Western Ionian Sea and surroundings, indicating: main geological features, including Alfeo-Etna Fault (AEF) and Ionian Fault (IF) systems (Polonia et al., 2016), and Malta escarpment (ME); seismic stations used in this work (filled green triangles are land stations; filled blue triangles represent the OBSs); red dots indicate the locations of earthquakes from the land seismic bulletin of INGV and occurring during the SEISMOFAULTS experiment. About 2,400 events were located by INGV seismological network. Bathymetric data were obtained from high resolution multibeam soundings during the SEISMOFAULTS first cruise (Cuffaro et al., 2019; Billi et al., 2020) and merged with DEMs from https://portal.emodnet-bathymetry.eu/.

right-lateral transpressive segment merges into the Hyblean recess inland Sicily, cross-cutting the underlying Malta escarpment (Mariotti and Doglioni, 2000; Doglioni et al., 2001).

The Calabrian wedge in the Ionian Sea is characterized by sectors with different rheology and tectonic architectures: 1) the post-Messinian accretionary wedge; 2) the pre-Messinian accretionary wedge; and 3) the inner plateau, as described by Polonia et al. (2011). Generally, the post-Messinian and the pre-Messinian accretionary wedges include thick layers of evaporites and Tertiary/Mesozoic sediments, respectively. Fault zones are detected in the area between the pre-Messinian accretionary prism and the flat inner plateau, with a diffuse presence of mud volcanism (Loher et al., 2018; Cuffaro et al., 2019, and references therein).

Long fault lineaments and NW-SE transverse deformation zones cut through the NE-SW-trending Calabrian accretionary prism (**Figure 1**). Most of such structures are active and characterized by right-lateral to transtensional kinematics (Polonia et al., 2011, 2016, 2017a; Gallais et al., 2012, Gallais et al., 2013; Gutscher et al., 2016; Bortoluzzi et al., 2017). Some of them represent the surface expression of deep geodynamic processes, as suggested by mantle diapirs detected along the faults (Polonia et al., 2017).

Two major fault systems with opposite dip are identified in the region, i.e., the Ionian Fault (IF) and the Alfeo-Etna Fault (AEF) systems (**Figure 1**). The IF separates two distinct sectors of the Calabrian accretionary prism, the western and the eastern lobes (WL, offshore Sicily; EL, offshore Calabria), which show important structural differences, such as average topographic heights, more elevated in the EL, or variable slope angles and deformation rates, both higher in the EL. Using seismological data, Sgroi et al. (2021) observed spatial changes in depth distribution of earthquakes recorded in the Ionian Sea, implying that the IF system constitutes a structural boundary between the two lobes, with changes in thickness of the seismogenic layer.

The AEF represents the main tectonic lineament of a set of NNW-SSE striking faults affecting the WL. The IF and AEF

**TABLE 1 |** Coordinates of OBSs deployed during the SEISMOFAULTS survey and computed time drift at each instrument. Unfortunately, the OBS4 was not recovered at the end of the experiment.

| Instrument ID | OBSH2 | OBSH3 | OBSH4 | OBSH5 | OBSH6 | OBSH7 | OBSH8 | OBSH9 |
|---|---|---|---|---|---|---|---|---|
| Latitude | 37°42.22′ | 37°14.28′ | 37°00.47′ | 37°24.55′ | 37°45.77′ | 37°41.37′ | 37°25.91′ | 37°12.37′ |
| Longitude | 15°27.33′ | 15°30.35′ | 15°38.79′ | 15°43.39′ | 16°02.83′ | 16°22.49′ | 16°31.78′ | 16°07.10′ |
| Depth [m] | 1767 | 2,256 | 2,330 | 2,242 | 1,583 | 2065 | 2,671 | 2,752 |
| Measured drift [ms] | −86.9 | 479.0 | LOST | 172.5 | −215.0 | −438.4 | −363.5 | 447.8 |
| Mission length [days] | 371 | 371 | | 371 | 371 | 371 | 371 | 402 |

systems are the most seismically active tectonic features in the region (Totaro et al., 2013; Polonia et al., 2016; Presti, 2020) and the main targets of the SEISMOFAULTS project (Billi et al., 2020).

# THE OCEAN BOTTOM SEISMOMETER/ HYDROPHONE (OBS/H) NETWORK

## Instrumental Features

An OBS/H network including eight stations was deployed in May 2017 and seven of them were recovered in May 2018 (**Figure 1**; **Table 1**; Billi et al., 2020). Unfortunately, the OBS4 could not be recovered at the end of the experiment. All instruments were designed, assembled and tested at the INGV OBS Lab in Gibilmanna (Sicily). The OBS/H model B used in the SEISMOFAULTS experiment is equipped with a Trillium Compact OBS sensor and a 120-s broadband seismometer with 750 V s/m sensitivity. When the OBS reaches the seafloor, the sensor is dropped from a short height onto the sediments, establishing in this way a good mechanical coupling with the seafloor. The OBS includes a telescopic shield that isolates the sensor from bottom currents. In addition to the seismometer, the OBS includes a hydrophone with a 0.001–5 kHz bandwidth. A Guralp CD24 recorder digitizes and acquires data from both sensors, and stores them in local flash memory along with status information. Sampling frequency was set to 100 Hz during the experiment. The digitizer includes a precision clock, based on a Temperature Compensated Crystal Oscillator (TCXO), synchronized to UTC with a GPS receiver just before the deployment. After recovery, the GPS receiver was connected to the digitizer once again, to measure the clock drift accumulated during the mission. Estimated time drifts were $< 0.5$ s for all OBS/Hs (detailed time drift for each OBS are reported in **Table 1**), and this linear correction of the time drift was applied to the dataset.

Each OBS/H station was equipped with auxiliary systems operating during deployment and recovery, such as the acoustic release, i.e. an acoustic transponder combined with an actuator, which has the following function. During normal operations, a ballast anchors the instrument to the seafloor. Upon reception of a command through an acoustic link, the acoustic release detaches the ballast and the OBS/H leaves the seafloor reaching the sea surface, where it can be recovered. Some features, such as a flashing light and a radio and satellite beacons, help locating the instruments once at the surface. A cylindrical vessel, rated for 6,000 m depth, houses all the electronics and batteries. A titanium frame supports the vessel holding the instrumentation, the release, the beacons, and some buoys required to control the OBS velocity during descent and ascent.

Before data analysis, a quality check of the collected data showed very few gaps in the data stream, with over 99.9% of valid recordings detected. From March 2nd, 2018, to the end of the experiment, OBS7 showed strong disturbances on Z, N and E channels, not detected by the hydrophone, making the identification of seismic signals very difficult. About 549 Gb of data in GCF (Güralp Compressed Format) were converted in SAC (Seismic Analysis Code) format, organized and stored in a simple filesystem archive.

## Deployment Sites

The choice of the OBSs deployment sites (**Figure 1**) was guided by the strategy of monitoring those fault/fault systems considered seismically active or potentially active on the basis of previous geological/geophysical studies (Polonia et al., 2011, Polonia et al., 2016, Polonia et al., 2017a; Gutscher et al., 2016). The choice was also tested against available information on seismic records obtained by the INGV network (CSI catalogue, Castello et al., 2006; the ISB catalogue, Italian Seismic Bulletin, ISIDe Working Group, 2007). Final adjustments in the station's positioning were performed analysing marine geophysical data, such as high resolution multibeam bathymetry and single-channel seismic profiles collected during the oceanographic cruises (e.g., Bortoluzzi et al., 2017). Seafloor structures such as scars and/or submarine landslide deposits, as well as canyon drainages and rocky outcrops were carefully avoided. Areas potentially affected by active gravitative and high-energy sedimentary processes were also excluded. Submarine flat surfaces with fine-grained sediments were preferentially chosen, for an optimal coupling of the stations with the seafloor.

The external boundaries of the OBS network were selected to include major lithospheric faults according to available large-scale structural models of the Calabrian Arc (Minelli and Faccenna, 2010; Polonia et al., 2011, Polonia et al., 2016, Polonia et al., 2017a; Gutscher et al., 2016). Our interest was particularly focused on major out-of-sequence thrust faults (splay faults of Polonia et al., 2011) and on lithospheric discontinuities orthogonally segmenting the accretionary wedge, i.e., the Alfeo-Etna and Ionian fault systems (Polonia et al., 2016; Sgroi et al., 2021). The stations were deployed over an area of about 150 × 100 km with a spacing of ~30 km between stations.

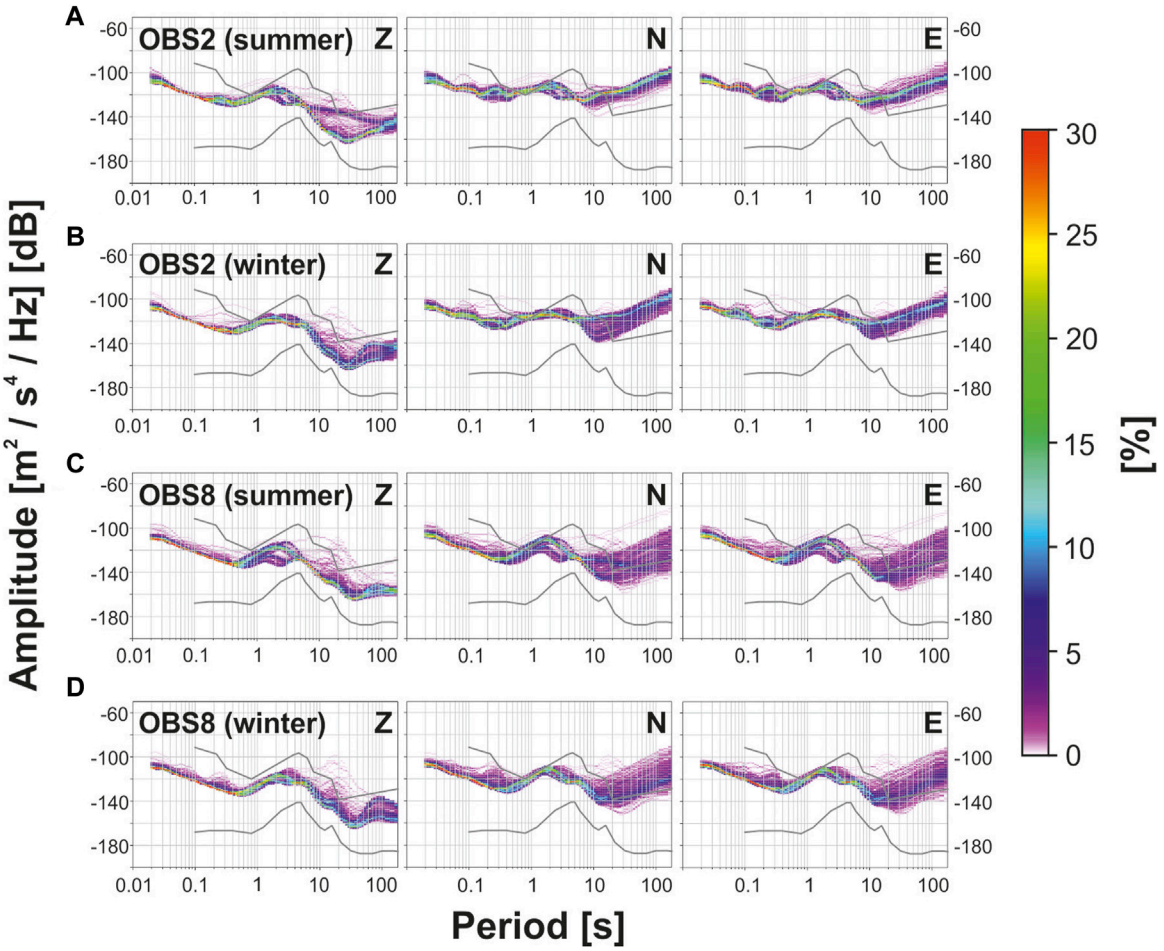


**FIGURE 2 |** Probability density function (PDF) for the three seismic components (Z, N, E), built during six days in two periods of the year **(A)** OBS2 during 2017, 11–16 July (summer) and **(B)** 2018, 25–30 January (winter) **(C)** OBS8 during the summer and **(D)** winter seasons. The amplitude is given in units of decibels with respect to acceleration ($m^2/s^4$/Hz). The colour bar represents the probability of occurrence of each PSD normalized from 0 to 30%.

## DATA QUALITY

The probability density functions were constructed for the recorded seismic data considering six days in different seasons (**Figure 2**). We used a routine tool for assessing the seismic data quality, using the statistical calculation of the Probability Density Function (PDF). The PDF analysis was performed with the algorithm proposed by McNamara and Buland (2004) and McNamara et al. (2009). Following McNamara and Buland (2004), we constructed the Power Spectral Density (PSD) for data recorded by the sensors during the experiment. Using this technique, the noise-spectra levels are compared with the reference Low Noise Model (LNM) and High Noise Model (HNM) curves obtained by Peterson (1993). The efficient detection of seismic waves and the accurate recognition of seismic phases from all distances are limited by the levels of background noise in different frequency bands of the signal.

**Figure 2** shows an example of PDFs calculated on the three seismic components of the OBS2 (**Figures 2A,B**) and OBS8 (**Figures 2C,D**) during six days in two different seasonal times: summer (July 11–16, 2017; **Figures 2A,C**) and winter (January 25–30, 2018; **Figures 2B,D**). The comparison of our results with the LNM and HNM reference curves shows that the noise spectra levels are generally contained within the Peterson (1993) model limits, except for the high noise on horizontal components at low frequency (long period), both in summer and winter times. The fairly high noise levels in the long-period band (>10 s) observed on the horizontal components are due to the sea currents that are an important noise source at the seafloor sites (which tilt the sensor; Webb and Crawford, 2010). The typical microseismic peaks are recognizable: Single Frequency peak (SF), at 10–20 s and the much stronger Double Frequency peak (DF), at about 5 s (Webb, 1998). The SF is generated by non-linear coupling of sea waves and bathymetry, while DF is produced by the interaction of sea gravity waves with the seafloor (Webb, 1998; Webb, 2002). Sometimes the DF peak can split into two peaks: the first at ~5–12 s (LPDF, Long Period Double Frequency) generated in open sea during favourable weather condition and the second peak, of a shorter period ~2–5 s (SPDF, Short Period

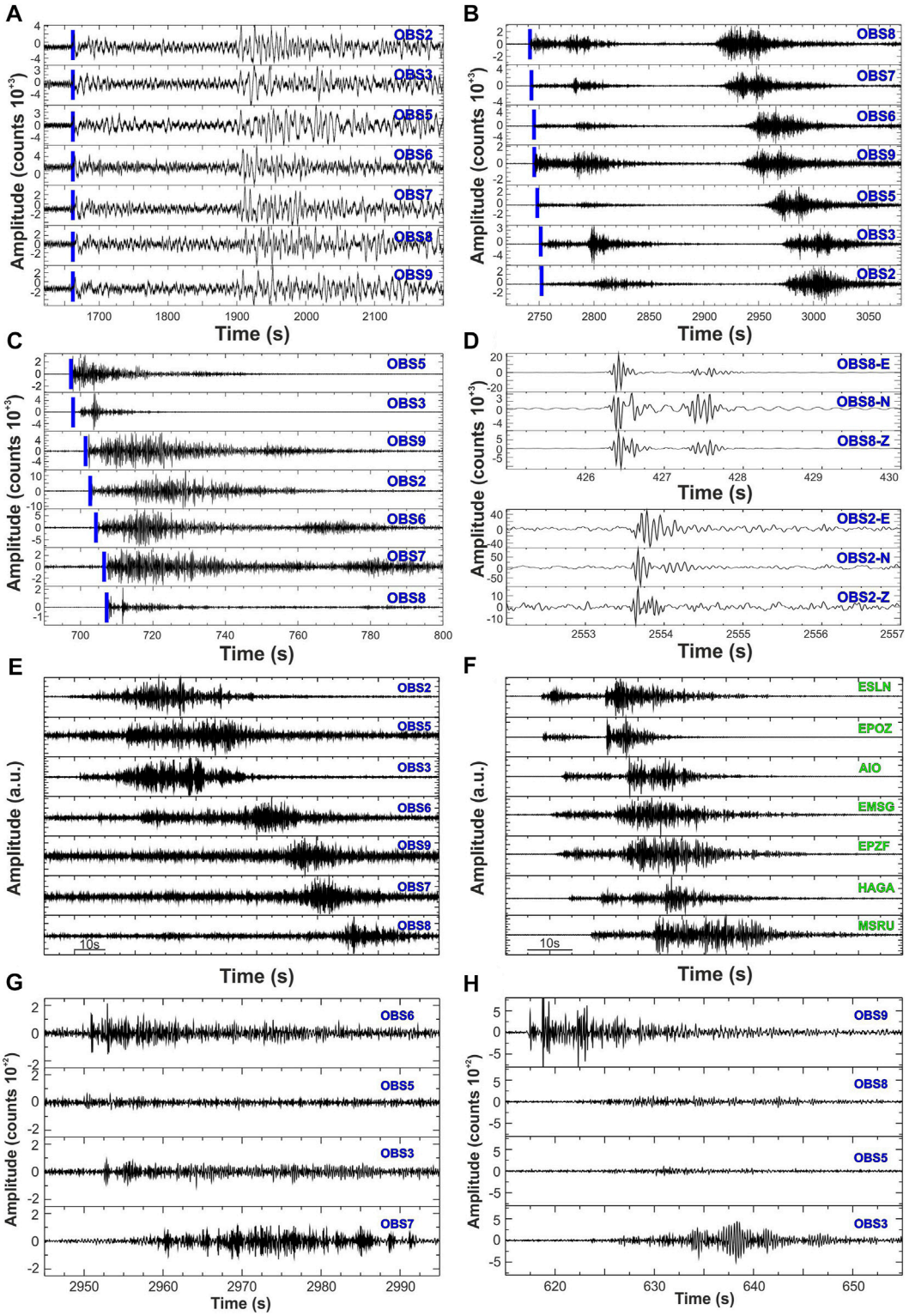


**FIGURE 3 |** Example of seismic waveforms recorded by the OBS network **(A)** teleseismic event (vertical component, unfiltered; 2018, January 14 h 09:18 UTC M = 7.1 38 km SSW Acari, Perù) **(B)** regional earthquake from Greece (vertical component, 2–12 Hz filtered; 2018, February 21 h 23:44 UTC, $M_L$ = 4.8) **(C)** local earthquake (vertical component, 2–12 Hz filtered; 2017, October 23 h 19:11 UTC, $M_L$ = 3.0); the blue vertical bars on earthquake signals indicate the P-wave arrivals **(D)** Examples of short duration events (three-components, 2–12 Hz filtered) recorded by OBS8 **(up)** and OBS2 **(bottom)**, respectively **(E–F)** Waveforms (vertical components, 2–12 Hz filtered) of an earthquake occurring in the Etna area (2017, June 23 h 20:32 UTC, $M_L$ = 2.2) located by land network (an example of waveforms

(*Continued*)

**FIGURE 3** | recorded by land seismic station is shown on right; stations on https://www.fdsn.org/networks/detail/IV/) and that was well-recorded also by most distant OBS (waveforms of marine stations are shown on left) **(G, H)** Examples of waveforms of two earthquakes (vertical component, 2–12 Hz filtered) recorded only by the marine network.

Double Frequency), associated with local windy conditions (e.g. Bromirski et al., 2005).

On the Ionian seafloor, it is possible to observe the splitting of the DF especially during the summer period (e.g., De Caro et al., 2014). In **Figures 2A–C** low noise level during some days around the period range of the SPDF peak is evident. This peak, clearly observed in the summer season, increases in winter time due to a high probability of having frequent windy meteorological conditions. Thanks to the OBS deposition depth, both in summer and winter times, a low anthropogenic noise (short period band <0.2 s) is verified.

The good data quality, also derived from the relatively high recording rate, was checked through comparison with earthquake waveforms recorded by land stations. We found that the OBS stations recorded data from different epicentral distance ranges, i.e., teleseismic, regional, local, and very local events (**Figures 3A–D**), the last ones being recorded solely by the OBS network and not by land stations. **Figures 3E,F** show seismic waveforms (vertical component) of an earthquake located in the Mt. Etna area, associated to the seismic activity of the volcano (2017, June 23 h 20:32 UTC, $M_L$ = 2.2). The location of this earthquake was processed by standard methods in the frame of the monitoring activity by the land network of the Istituto Nazionale di Geofisica e Vulcanologia (INGV). Despite uncertainties in P-and S-phases determination, this event was clearly recorded by the OBS network, also by the most distant stations. Another example concerns an earthquake that occurred in the Ionian Sea (2017, October 23 $M_L$ = 2.8). **Figure 4** shows the picking of P- and S-phases performed on waveforms of land stations and OBSs. The comparison of parameters for the location performed with and without OBSs for this event is reported in **Supplementary Tables 1,2**. Finally, **Figures 3G,H** shows two examples of low-magnitude earthquakes recorded only by the OBS network.

## LOCAL EARTHQUAKES

Data collected by OBSs allow us to locate seismic events in the Ionian Sea more accurately, particularly for what concerns hypocentre depth estimates generally affected by large errors due to the lack of an adequate seismic station coverage. Moreover, an intense low-magnitude seismicity often undetected by land stations was recorded (e.g. Sgroi et al., 2007).

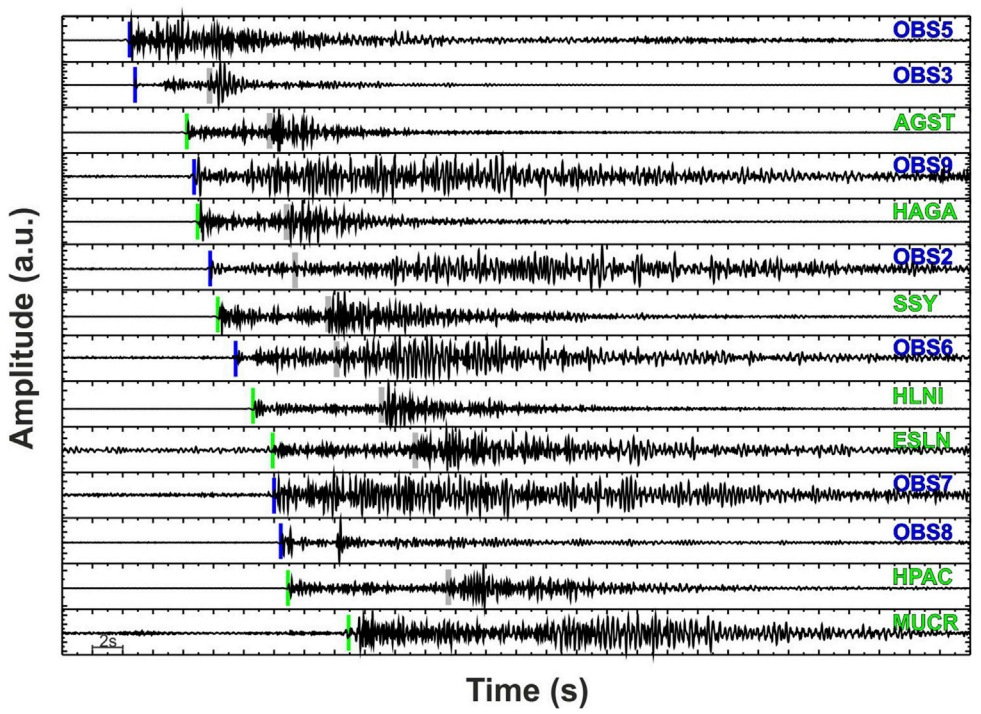


**FIGURE 4 |** Example of seismic waveform (vertical component) for the local events occurring on October 23, 2017 h 19:11 UTC ($M_L$ = 2.8) and recorded by both land network (a sample of travel times from land stations is represented) and OBS network. The blue and green bars represent the P-phase picked on OBSs and land stations, respectively; grey bars represent the S-phases, picked on horizontal components for both OBSs and land stations. Parameters of location performed with and without the use of OBSs for this event are listed in **Supplementary Tables 1–2**.

The eastern Sicily area is continuously monitored from the seismological and volcanological points of view, due to the presence of active tectonic structures, mostly located offshore, that were the likely sources of large magnitude events in the recent past, and an active volcano, Mt. Etna, which also triggers an intense seismicity. An example of waveforms of a volcano-tectonic earthquake occurring on Mt. Etna and well-recorded by all OBSs is shown in **Figure 3E**, whereas **Figure 3F** shows waveforms of the same event recorded by land stations. However, detailed information regarding tectonic and volcanic structures in the offshore result incomplete when only analysing data derived from the onshore networks, i.e., the National Seismic Network (RSN) and the Etna Regional Network (ERN), both managed by the INGV (INGV Seismological Data Centre, 2006). Currently, the land network (RSN together with ERN) consists of about 90 broadband three-component stations (Trillium 40 s sensors) deployed in Sicily, the Aeolian Islands, and southern Calabria. This network can optimally locate earthquakes occurring on land, but the location of events occurring offshore remains inaccurate. The SEISMOFAULTS OBS network was deployed to mitigate this problem. Here we demonstrate how the network permitted us to find more stable solutions in the earthquake location process for earthquakes occurring offshore.

## Local Earthquakes: Integrated Locations

As a first step, we collected available information on earthquake locations, by analysing the seismicity recorded by the land network as reported in the CSI catalogue (Castello et al., 2006), the Italian Seismic Bulletin (Bollettino Sismico Italiano, BSI; ISIDe Working Group, 2007), in the time period covered by the OBSs monitoring.

During the experiment (from May 2017 to May 2018) about 2,400 crustal and sub-crustal earthquakes ($0.4 \leq ML \leq 3.9$) were recorded by the RSN and ERN and located, as reported by the seismic bulletin of the INGV (**Figure 1**). Distribution of these events is non-homogeneous, with the largest clusters clearly linked to the volcanic activity of Mt. Etna. A smaller but relevant cluster of earthquakes is related to seismicity occurring in the southern Tyrrhenian Sea, whereas a smaller number of dispersed seismicity occurred in correspondence of the onshore/offshore transition of the Hyblean plateau and in the external part of the Calabrian Arc in the Ionian Sea. Since our objective was to improve the offshore earthquake location, we concentrated our work on the seismicity that occurred in the Ionian Sea and in the coastal area of eastern Sicily and southern Calabria, by selecting from the land bulletin 133 crustal and sub-crustal events.

After the selection of the events, we looked for them on the OBS seismograms. Then the P- and S-wave arrivals on OBSs were manually picked for these earthquakes (P-phases were determined on the vertical component, while S-phases were picked on the horizontal components). The obtained travel times were added to those from land stations (**Figure 4**) to perform integrated locations. The locations were processed with the tomoDDPS algorithm (Zhang et al., 2009) and a 3D velocity model recently computed for the Ionian Sea (Sgroi et al., 2021). This 3D velocity model derives from a detailed 3D image of the Calabro-Ionian subduction system. The model was obtained by seismic tomography, and shows a Moho depth of about 20 km in correspondence of the OBSs deployment sites. The tomoDDPS software has the advantage of using a combination of both absolute and differential arrival time readings, so that for earthquakes with foci lying close to each other, travel time errors due to incorrect velocity models in the volume outside the cluster will essentially be cancelled. Furthermore, the algorithm can produce a better clustering of earthquakes and, after a few interactions of inversion, a notable residuals reduction of about 43% (from 0.74 to 0.42 s) and 33% (from 0.85 to 0.56 s) is observed for both locations without and with OBS, respectively.

We located the 133 crustal and sub-crustal events with and without the travel times from OBS, and compared the results of the two locations. **Figure 5** shows maps and E-W and N-S sections related to the locations without (**Figure 5A**) and with (**Figure 5B**) data from the OBSs. Although, at first glance, the comparison between relocation with and without OBSs travel times does not show visible differences in the map and on the E-W and N-S sections, they are perceptible in terms of location parameters.

The use of the combined network of land stations and OBSs has improved the earthquake location in terms of horizontal and vertical errors but the most impressive result is the strong decrease of azimuthal GAP. The presence of the marine network allowed us to significantly decrease the Mean (M) and Standard Deviation (SD) values computed on GAP, horizontal (ErrX and ErrY) and vertical (ErrZ) errors (**Figure 6**). As expected, a rough increase of Mean and Standard Deviation (SD) of rms (root mean squares travel-time residual in s) values is observed. As a matter of fact, average rms for all events span from M = 0.24 s (SD = 0.13) of locations without OBSs to 0.36 s (M) of locations with OBSs (SD = 0.17). On the other hand, the consistent decreases in azimuthal gap and on horizontal and vertical errors demonstrate the major stability of the integrated location solutions. Average GAP for the 133 events decreases from M = 207° (SD = 54) of locations without OBSs to M = 131° (SD = 63) of locations with OBSs. Most of the events have consistent decreases of GAP up to 251°. One significant example is the earthquake that occurred on 2017, December 26 ($M_L = 2.3$) and located with OBSs at 37.8805 latitude and 15.44433 longitude (30.91 km depth). The horizontal (ErrX, ErrY) errors of locations without OBSs are characterized by M = 0.44 km (SD = 0.30; ErrX), M = 0.46 km (SD = 0.29; ErrY), while vertical error (ErrZ) shows M = 0.76 km (SD = 0.58). The horizontal errors of the location with OBSs are lower: namely, ErrX is characterized by M = 0.40 km (SD = 0.22) and ErrY has M = 0.34 km (SD = 0.22), while ErrZ is significantly lower and it is characterized by M = 0.46 km (SD = 0.32). In general, differences in the azimuthal GAP can exceed about 76°, while notable reductions of horizontal and vertical errors (up to 1.00 and 1.05 km for the two horizontal errors and 3.26 km for vertical errors) are also observed. A comparison of the parameters obtained in the two cases for an earthquake in the Ionian Sea is reported in **Supplementary Tables 1–2**, which report the results of the 133 locations performed without and with OBSs travel times, respectively.

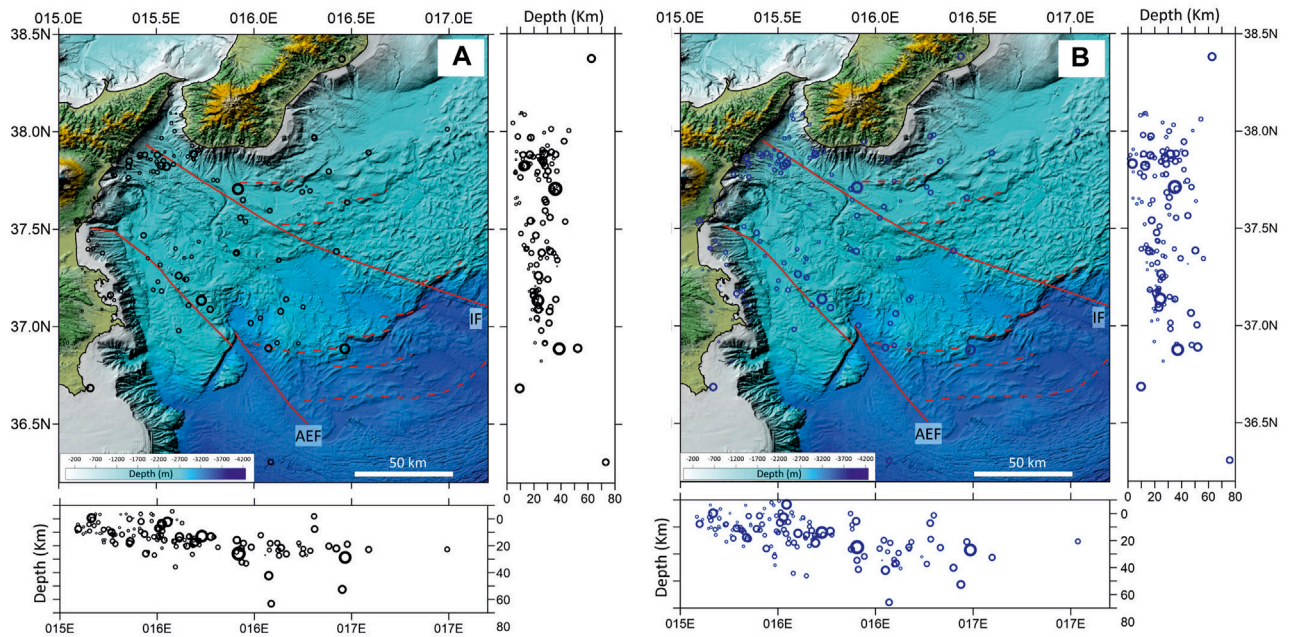


**FIGURE 5 |** Maps and E-W and N-S sections of 133 earthquake relocations based on a previous 3D velocity model (Sgroi et al., 2021) and computed **(A)** without OBSs travel-times (black circles) and **(B)** with OBSs travel-times (blue circles). The circle sizes are proportional to the $M_L$ as reported on land seismic bulletin. Parameters of location performed with and without the use of OBSs are listed in **Supplementary Tables 1–2**. Red lines indicate the position of Alfeo-Etna fault (AEF), Ionian fault (IF) and splay faults (**Supplementary Tables 1,2,3**). Bathymetric map was obtained from high resolution multibeam collected during the oceanographic cruise of SEISMOFAULTS project (Cuffaro et al., 2019; Billi et al., 2020) and merged with DEMs from https://portal.emodnet-bathymetry.eu/.

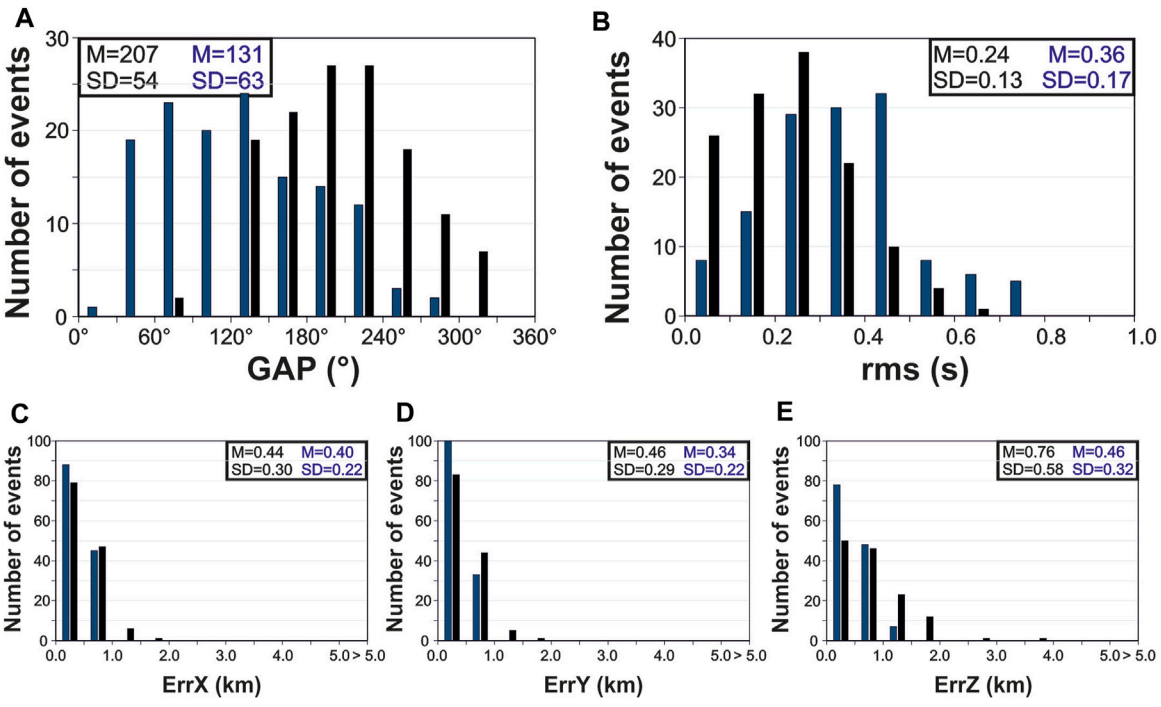


**FIGURE 6 |** Statistical analysis in terms of Mean (M) and Standard Deviation (SD) values computed on GAP **(A)**, rms **(B)**, and **(C, D, E)** horizontals (ErrX, ErrY), and vertical (ErrZ) errors for location with OBS travel times (blue histograms) and without OBS travel times (black histograms). The presence of an offshore network contributed to an improved relocation quality.

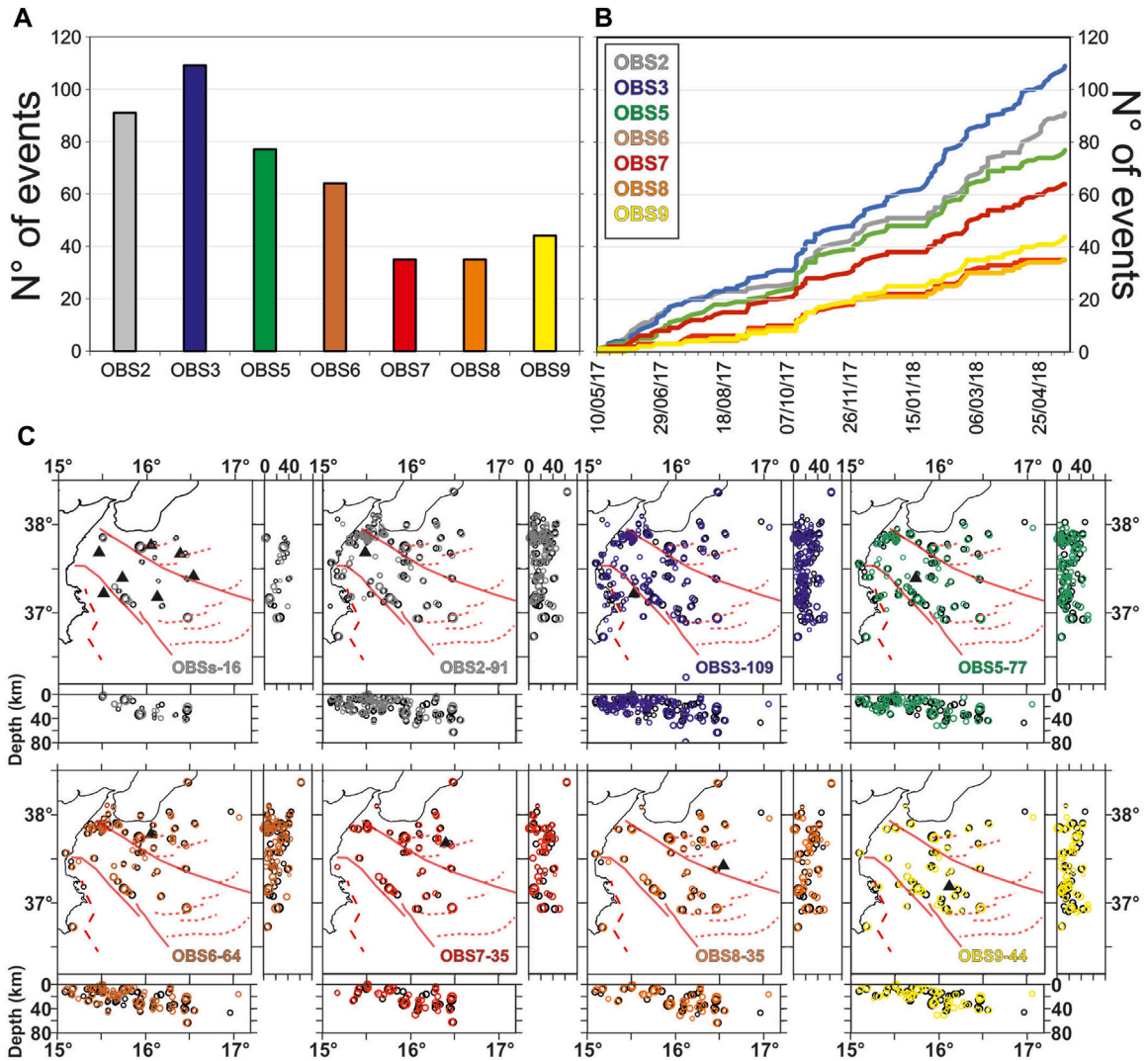


**FIGURE 7 |** Detection efficiency of the OBS network for 133 local earthquakes located through the integration of travel times by marine and land stations **(A)** Histograms and **(B)** occurrence in time of the number of earthquakes recorded at each OBS **(C)** Maps and E-W and N-S sections of earthquakes recorded by each OBS. Main geological features including the Alfeo-Etna Fault and Ionian Fault (Polonia et al., 2016) and the Malta Escarpment are sketched in red.

**TABLE 2 |** Number of integrated locations (on 133) of earthquakes recorded both by land and OBS stations, locations (on 76) of low-magnitude earthquakes recorded only by the OBS network, earthquakes and SDE recorded at the single OBS station. The asterisk in OBS7 indicates that this computation is up to 2018 February 28.

| | OBS2 | OBS3 | OBS5 | OBS6 | OBS7 | OBS8 | OBS9 |
|---|---|---|---|---|---|---|---|
| Local earthquakes | 91 | 109 | 77 | 64 | 35 | 35 | 43 |
| Low-magnitude earthquakes | 50 | 65 | 61 | 63 | 49 | 42 | 51 |
| Single OBS earthquakes | 46 | 486 | 148 | 23 | 72* | 579 | 110 |
| SDE | 614 | 3,136 | 1,246 | 339 | 1,022* | 2,681 | 904 |

We now consider the detection capability of the OBS network. A group of 16 earthquakes (on a total 133 integrated locations) were recorded at all OBS stations (1.9 $\leq M_L \leq 3.8$). Since most of the earthquakes are near the eastern Sicily coast, OBS3 recorded the largest number of events (**Figures 7A,B**; **Table 2**). Histograms detailing the number

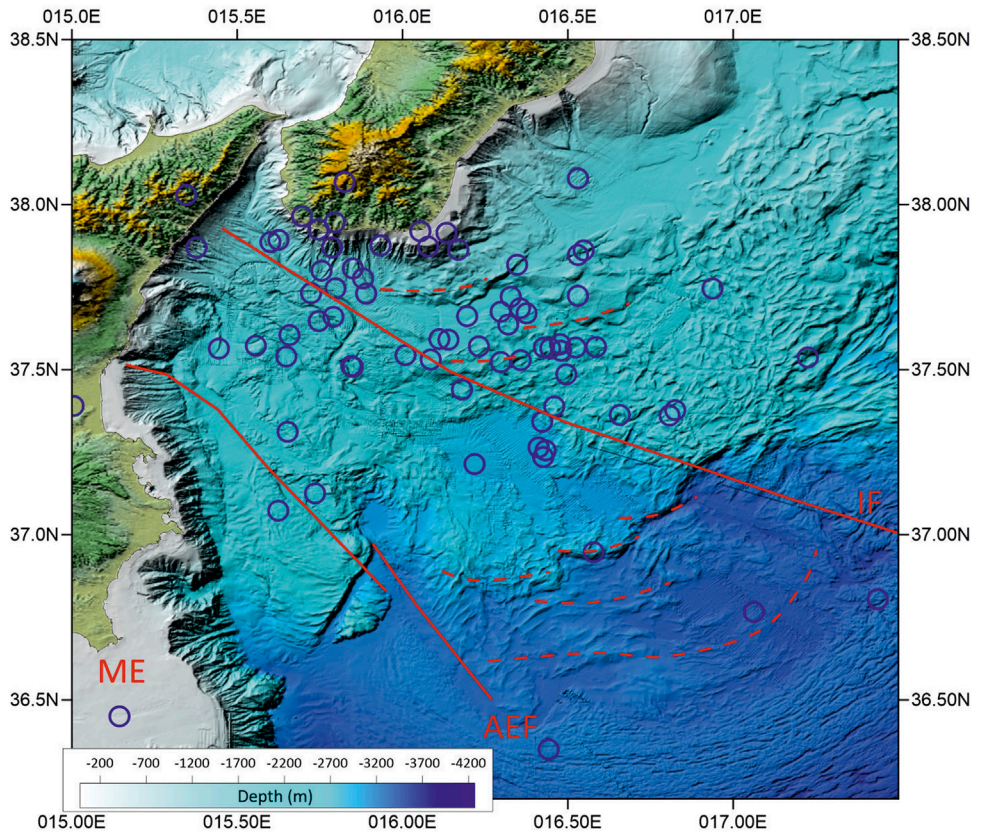


**FIGURE 8 |** Distribution of epicentres of the 76 earthquakes recorded only by the OBS network. Parameters of location for these events are listed in **Supplementary Table 3**. The main tectonic structures including the Alfeo-Etna Fault and Ionian Fault (Polonia et al., 2016) are sketched in red. Bathymetric map was obtained from high resolution multibeam collected during the oceanographic cruise of SEISMOFAULTS project (Cuffaro et al., 2019; Billi et al., 2020) and merged with DEMs from https://portal.emodnet-bathymetry.eu/.

of located earthquakes (on 133) for each OBS as well as maps and E-W and N-S sections of locations (with and without travel times from OBSs) are shown in **Figures 7A–C**. In **Figure 7C** the shift between the two locations (with and without OBS) can be observed. Major differences are evident for the most external areas of the Ionian basin where the gap of seismicity exists. This gap is due to the fact that the land network alone is not able to cover the hypocentres well. On the other hand, differences are visible also in certain onshore and coastal areas that are characterized by high values of shift, as for example in correspondence of the Hyblean Plateau, Etna offshore and the Messina Strait.

## Local Earthquakes: Low-Magnitude Event Locations and Single Station Events

The Ionian Sea tectonic structures are a source of significant microseismicity, mostly undetected by the land network. As an example, the NEMO-SN1 seafloor observatory deployed about 25 km offshore Catania, recorded more than 400 earthquakes not present in the bulletins of land stations during the 2002–2003 Etna eruption (Sgroi et al., 2007). This occurrence was considered an additional opportunity for the SEISMOFAULTS experiment to contribute with new microseismicity records to the long-lasting discussion about seismic hazards in the area.

An in-house STA/LTA algorithm, applied to the OBS vertical component, was tuned to automatically detect local seismic events not identified by land stations. As a few thousands of triggers were revealed, a software code was compiled aiming to select records probably including events detected by two or more OBSH, and to organize relative waveforms in individual directories. Finally, waveforms in each directory were manually picked by analysts to identify body-wave arrivals associated to the same earthquake and used for event location.

From the total list of triggers, we removed the travel times related to the earthquakes reported on the local and regional seismic catalogues, obtaining more than 1,600 events not detected by land stations (**Table 2**). About 1,400 events were recorded only at the single OBS while more than 230 earthquakes were contemporaneously recorded by at least three OBSs. For 236 earthquakes recorded by at least three OBS, we attempted a location, using the tomoDDPS algorithm (Zhang et al., 2009) and a recent 3D velocity model computed in the western Ionian area (Sgroi et al., 2021) that well represent the pattern of the tectonic structures in terms of velocity and depth layers.

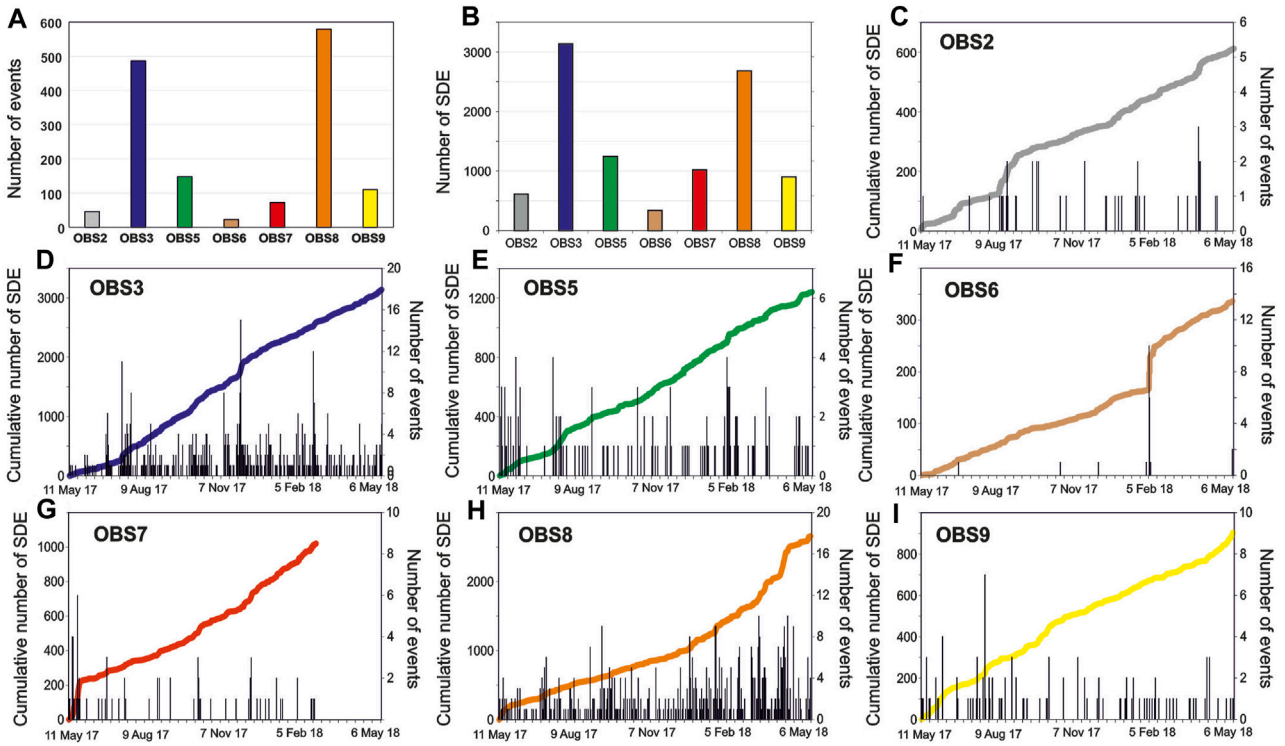


**FIGURE 9 | (A)** Histograms of the number of single station earthquakes recorded only by the single OBS **(B)** Histograms of the number of SDE recorded by the single OBS **(C–I)** Comparison between the number of SDE and the number of single station events recorded at each OBS.

We manually picked P- and S- phases (as described above) and a location was attempted for events recorded at least at three OBSs and having a minimum of 6 phases. Identifying seismic phases is somewhat more difficult for OBSs (**Figures 3G,H**). This is partially due to the relatively weak coupling of the instrument with the poorly consolidated, water-saturated sediment environment, and above all it is due to the low-magnitude of events. Non-ideal coupling leads to damping of the seismic signals, which strongly attenuate the amplitudes at higher frequencies. As an example, **Figures 3G,H** show the waveforms of two events recorded and located only by the OBS network. Few events were recorded at several OBSs (as for the example shown in **Figures 3G,H**), but in most cases the earthquakes were recorded by at most three or four OBSs. These low-magnitude local events, having low energy, generate waves that attenuate within a few tens of kilometres, as testified by the recorded amplitude of waveforms. As reading the S-phases was very difficult, the depth of events is not reliable in most cases. Moreover, since the seismicity recorded by OBSs only was of low magnitude, also the spacing of the OBS network, preclude an accurate location of the events. In spite of these problems, we were able to locate 76 "new" earthquakes. The distribution of locations by OBS is shown in **Figure 8** (location parameters are reported in **Supplementary Table 3**). The distribution of seismicity is well related with the pattern of tectonic structures that exist in the Ionian Sea. Small clusters are identified, and, in particular, three south of Calabria are well correlated with the tectonic structures proposed by Polonia et al. (2016), whose state of activity was evidenced by Sgroi et al. (2021).

A high number of events was recorded only at the single OBS. Histograms of **Figure 9A** show the number of single station events. The seafloor stations that recorded the highest number of events were the OBS3 (486 earthquakes) and the OBS8 (579 earthquakes), whereas the minimum number of events were recorded by the OBS6 (23 events only). As these low-magnitude events are recorded at the single station, it is reasonable that their sources are within the semi-interspacing between two adjacent OBS (about 15 km). Due to the large multitude of single station earthquakes, it is our intention to implement an automatic system of detection and classification of seismic signals of various kinds recorded only by the OBS stations and to better identify the seismogenic source, as proposed by Sánchez-Reyes et al. (2021) for the Balsorano seismic sequence. Although we do not perform an extensive data analysis in this work, the distribution of number of events on each OBS is indicative of the state of seismic activity associated to the tectonic structures.

## Short Duration Events

Our dataset includes a large number of short, impulsive signals which, in the literature are defined as Short Duration Events (SDE; **Figure 4**). These kinds of signals are currently detected at the seafloor in different parts of the world, and they have been associated with several possible sources, including fluid-filled cracks in sedimentary basins (Diaz et al., 2007), gas seepages along active faults (Tary et al., 2012; Embriaco et al., 2014), or even due to biological activity (Buskirk et al., 1981;

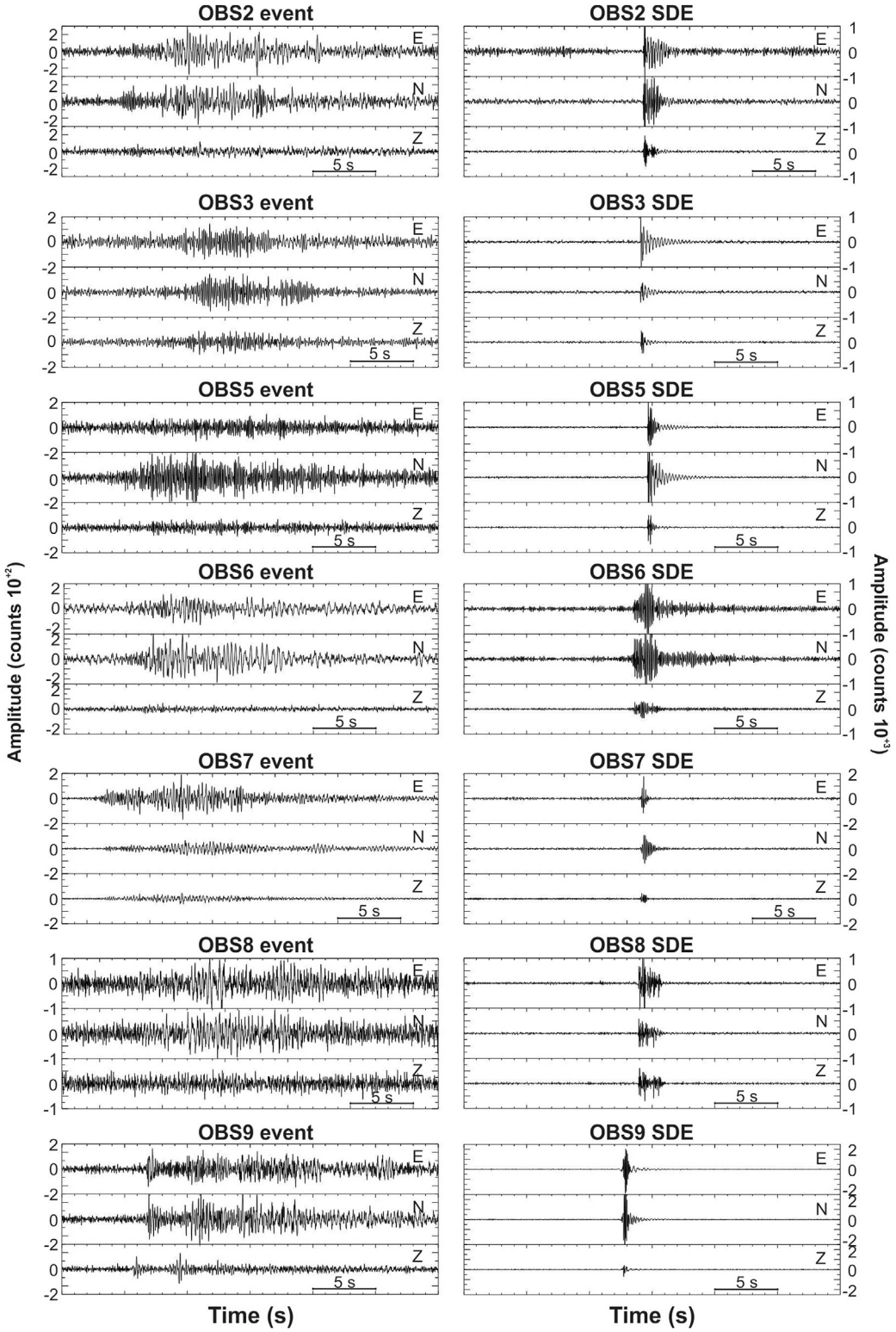


**FIGURE 10 |** Comparison between waveforms (three components) of earthquakes **(left)** and SDEs **(right)** recorded at the single OBS. Time window is 30 s long for both signals and all records were filtered with band-pass Butterworth filter in the same frequency range 2–25 Hz.

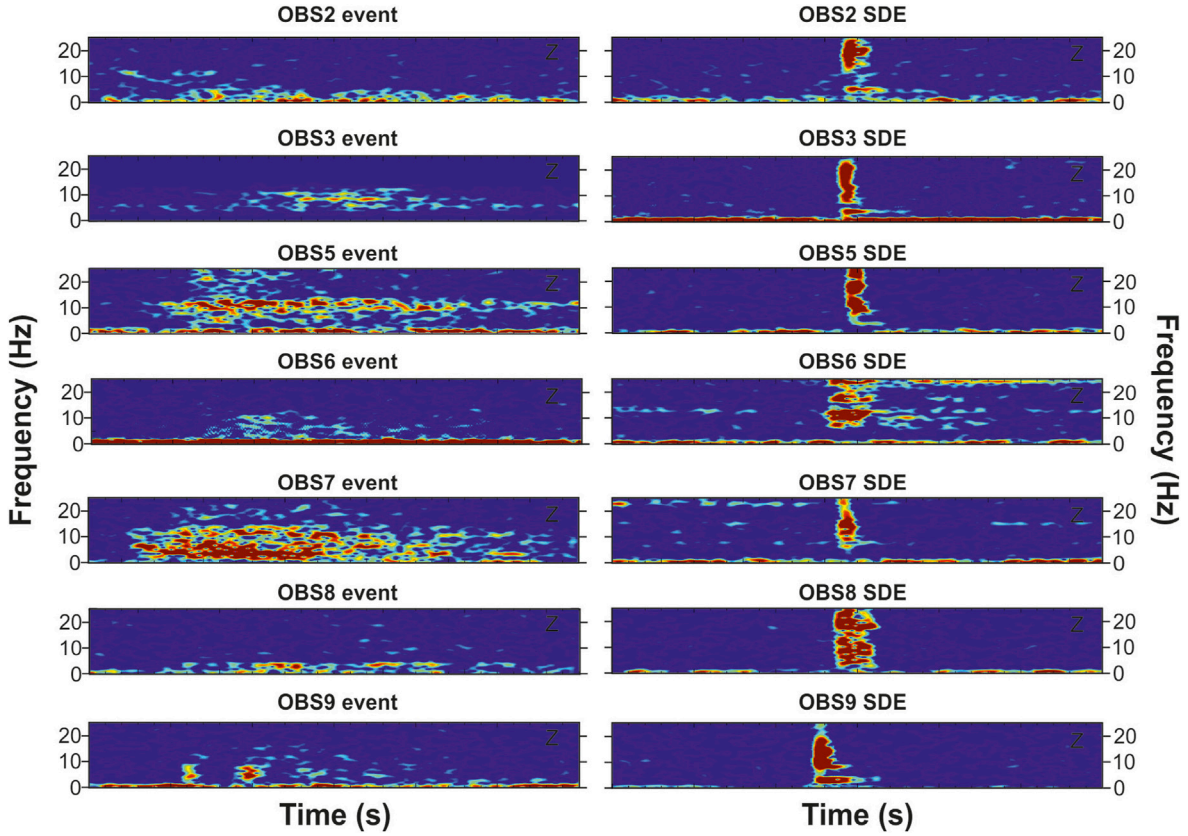


**FIGURE 11 |** Spectrograms computed on vertical component of earthquakes **(left)** and SDEs **(right)** recorded at the single OBS. Records were filtered with band-pass Butterworth filter in the frequency range 2–25 Hz. Colours of spectrograms are in log(counts $^2$/Hz) units and represent distribution of energy of the recorded signals as a function of time (*x* axis) and frequency (*y* axis). Warm colours (red, yellow and green) define the dominant spectral amplitudes; cooler colours (light to dark blue) define lower spectral amplitudes and background.

Bowman and Wilcock, 2014). In general, SDEs are ascribable to hydraulic micro-fracturing processes, such as pressure transients generated by fluid-filled cracks (Diaz et al., 2007), and they have been best described in hydrothermal and volcanic (e.g., Sohn et al., 1995), as well as tectonic (e.g., Embriaco et al., 2014) systems. Moreover, such a small seismicity shows similarity with slow-slip events associated to a shear zone with low-friction (e.g., Matsuzawa et al., 2010) that occur in the deeper extents of areas where large earthquakes are expected in subduction zones. In the Ionian Sea, Sgroi et al. (2014) showed that SDE signals recorded by the NEMO-SN1 seafloor observatory could result from hydrofracturing induced by magmatic activity around Mt. Etna.

During the one-year-long SEISMOFAULTS experiment, about ten thousand of SDEs (**Table 2**) were recorded by the OBS network, whose detection in correspondence of the single OBS is reported in **Figure 9B**. As the number of SDEs and their waveforms varied on each OBS (**Figure 10** shows examples of SDE waveforms recorded at the single OBS), it is reasonable to think that their origin process may be different, depending on the position of the seafloor station. In general, SDEs (**Figures 4**, **10**) are characterized by sharp waveforms, high-frequency content (from about 1 Hz up to 50 Hz; **Figure 11**), and very short duration (about 2 s). Moreover, this signal rapidly attenuates as the wave travels, and this points to the small scale of the SDE generation process and to a nearby source.

As for the single station events, the OBSs that recorded the highest number of SDEs were OBS3 (3,136) and OBS8 (2,681), while the lowest number is observed on OBS6 (339). The detection of SDEs by the OBSs varies in time and occurs in clusters in time. A direct proportionality between the occurrence of SDE and single station events is observed on all OBSs (**Figure 9**). The most impressive relation between SDE and low-magnitude events is visible on the OBS6 (due to its lower number of these events) that shows a time distribution of SDE characterised by the occurrence of a small swarm of 69 SDE in the period 2018, February 4–7 (**Figure 9F**). Moreover, the waveforms of SDE signal recorded at the OBS3-OBS5-OBS7-OBS9 (**Figure 10**) show similitude with signals conducible to microfracturing processes, while SDEs recorded at the OBS2-OBS6- OBS8 are almost different from the same signal recorded by the former OBS stations, showing typical features of cracks associated to gas seepage variations (Franek et al., 2017). The same groupings are well defined when comparing spectrograms computed on both events and SDE recorded at the single station (**Figure 11**).

We cannot accurately locate the SDE source since we only have data from one seismic station: as demonstrated in previous studies performed in other areas, the SDE source distance from the sensor is estimated in the order of hundreds of meters (Sultan et al., 2011), or even tens of meters (Tary et al., 2012), whereas their amplitude is roughly higher than the one of single station earthquakes (see amplitude values in **Figure 10** for single station events and SDE) and their distribution is indicative of the state of activity of structures placed in the Ionian Sea. As differences in the waveforms and spectrograms of SDE are also observed at each OBS (**Figures 10**, **11**), we can argue that different processes generate these signals.

The distribution of SDEs recorded during the SEISMOFAULTS experiment could be associated with active tectonic and volcanic processes, also demonstrated by the good correlation between the occurrence of events and the occurrence of SDEs, both recorded by the single OBS (**Figures 9C–I**). This comparison shows that the increase in the number of SDEs coincides with the occurrence of a higher number of earthquakes in the same time period recorded at the single OBS.

## DISCUSSION AND CONCLUSIONS

Prior to the SEISMOFAULTS experiment, available seismological data, collected both by onshore seismic station and by the NEMO-SN1 seafloor observatory (Sgroi et al., 2021), have shown that the submarine Calabrian Arc is characterized by a pattern of small magnitude, scattered earthquakes, mainly due to slow rates of NW-directed Ionian subduction. The new data acquired during the SEISMOFAULTS project show a significant number of seismic events not detected by the land stations (**Figure 8**) that could provide a more complete picture of the active seismicity in the region. Integrated analyses of OBSs and land stations data show that seismicity is mostly located off southern Calabria and Taormina, in southeastern Sicily, where a dense cluster of events was recorded, as well as south of Catania. A diffuse seismicity pattern characterizes the central Ionian Sea, the alleged site where most active tectonic features of the submerged part of the Calabrian Arc are located.

The OBSs that have recorded the largest number of events are those located close to Mt. Etna (OBS2), where seismic activity is mostly related to fluids associated to volcanism and across the AEF (OBS3 and OBS5 in **Figure 1**). Together with OBS3 and OBS5, also OBS8 shows a larger number of SDE events, which are possibly related to fracturing triggered by fluid flows (Franek et al., 2017). This occurrence suggests a likely relationship between fluid flow and tectonics since these OBSs are close to the AEF and IF systems that were described, based on independent geophysical data, as seismogenic structures (Polonia et al., 2011). We cannot exclude that the increased number of events recorded by these OBSs might be related to their deployment sites characterized by flat regions surrounded by relatively wide sedimentary basins, favouring an optimal coupling between instrument and seafloor, and decreasing their detection thresholds. This observation confirms the need for a careful site selection for the OBS deployment, avoiding actively deforming areas, canyons, and submarine landslides, which can be achieved thanks to a close cooperation between seismologists and geologists.

**Figure 9A** shows the number of low-magnitude earthquakes recorded by the OBSs. The distribution of these events roughly mimics the IF trend, which marks the SW boundary of a crustal block in the Calabrian Arc (EL), where earthquakes are more clustered (**Figures 5**, **8**). This agrees with a more intense deformation offshore southern Calabria, as also shown by analysis of multichannel seismic reflection profiles (Polonia et al., 2011) and by seismological observations (Sgroi et al., 2021). South of 37.4° latitude, the low-magnitude earthquakes detected by the OBS network are located to the SW of the Ionian Fault and might correlate with tectonic activity along the out-of-sequence thrust faults (**Supplementary Tables 1,2,3**) bounding the landward limit of the external accretionary wedge, which is made primarily of evaporites (Polonia et al., 2011). At the contact between the salt-bearing wedge and the inner clastic wedge, splay faults develop and accommodate such rheological change.

The distribution of cumulative recorded events (**Figures 5**, **8**) allows us to unravel the connection between seismicity and active tectonics. Moving from W to E along the accretionary wedge of the Calabrian Arc, we recognize different clusters of earthquakes with different characters.

The seismic events observed close to the Eastern Sicily coast are shallow, occurring within a depth interval <20–22 km, which correspond to crustal levels of the upper plate, in agreement with a Moho depth of about 20 km in this area (Sgroi et al., 2021). Some of these events might be correlated with the Mt. Etna activity, while those to the south might correlate with the Malta Escarpment, which appears tectonically active north of Siracusa (**Figure 1**).

The largest magnitude events (**Figure 5**) appear to correlate with the major fault systems, i.e., the AEF, the out-of-sequence splays **Supplementary Tables 1,2,3**, and the IF. These structures were described as source regions for major historical earthquakes based on structural maps and paleoseismological data (Polonia et al., 2012; Polonia et al., 2017b). A number of seismic events are concentrated along the AEF and occur at greater depth >30 km implying a seismogenic thickness larger than those close to the ME. The greater hypocentral depth is reached by earthquakes along the IF and splay faults where the seismogenic layer appear to be from 30 to 60 km thick. The earthquakes located in the more external region, in particular, have depths of 40–60 km, suggesting that they might be related to the lower underplating African plate. Most epicentres fall within the deformation band associated to the Ionian Fault that seems to be the most seismically active feature in the studied area together with a parallel fault a few kilometers to the south of the Ionian Fault. It is remarkable that the Ionian Fault is particularly active (seismically) at its northwestern tip that is only a few kilometers to the south of the Messina Straits. This tip activity is interesting as it could potentially activate, in the future, extensional earthquakes in the Messina Straits according to the wing fracturing process proposed by Sgroi et al. (2021). The Messina Straits, in fact, occupies the extensional quadrant at the northwestern tip of the right-lateral transtensional IF (Polonia et al., 2016) in the region characterized by differential rollback of the Ionian subduction (Doglioni et al., 2001).

We observe widespread seismicity to the north of the Ionian Fault near the southern coast of Calabria. We cannot ascribe this seismicity to a tectonic domain with certainty; however, the presence in that region of seismically active shortening (Sgroi et al., 2021) allows us to hypothesize that this seismicity may be linked to the compressive structures described through geophysical data (Polonia et al., 2011).

The occurrence of SDE events and their close correlation with the occurrence of microseismicity could indicate significant contamination of the bottom waters from saline (evaporate-type) CH4-dominated crustal-derived fluids. These were observed in the Ionian Sea, in correspondence of a mud volcano (the Bortoluzzi Mud Volcano; BMV) discovered during the SEISMOFAULTS cruise in May 2017 (Cuffaro et al., 2019). The BMV is one of many mud volcanoes offshore Calabria. It is therefore reasonable to suppose that the origin of SDE recorded by OBS6 and OBS8 may be associated to active geofluid venting. For the OBS2 the association of SDE source mechanisms to fluids linked to Mt. Etna volcanism is also conceivable. On the other hand, OBS3-OBS5-OBS7-OBS9 show similarities with signals conducible to microfracturing processes.

In synthesis, one year of recording by a network of seven OBS in the Ionian Sea shows the seismic activity of the most important tectonic features of the study area, including the Ionian Fault and other transverse faults across the Calabrian Arc such as the Alfeo-Etna Fault and the Malta Escarpement. Active thrusting may also occur off southern coast of Calabria pointing for active subduction processes along the Ionian slow convergent system.

## DATA AVAILABILITY STATEMENT

The original contributions presented in the study are included in the article/**Supplementary Material**, further inquiries can be directed to the corresponding author.

Waveform data of earthquakes recorded by the INGV stations (land stations) are available online from the European Integrated Data Archive (EIDA) at http://eida.rm.ingv.it.

P- and S-phase arrival times associated to earthquakes occurred in the Ionian basin and analysed in this study are available online in the database ISIDe (Italian Seismological Instrumental and parametric Data-base; http://cnt.rm.ingv.it/iside). The catalogues of all located earthquakes published in this study are available in the **Supplementary Material**.

## AUTHOR CONTRIBUTIONS

TS conceived and designed the original idea of the study. TS, AP, and ABo wrote the manuscript and prepared figures. AC, GD'A, GF designed, assembled, and tested the OBS stations. TS, MCa, MN, FF, SM, CM, LP, PP, SP, AU analysed the data. LB, ABi, MCu, LG, CM, SM, AU, and CD contributed in the revision of the manuscript and the figures.

ABi, AP, MCu, TS, LB, GD'A, LG, and CD conceived and coordinated the SEISMOFAULTS experiment, from which this study derives.

## FUNDING

The OBS experiment complements the characterisation of a key area hosting the Western Ionian Sea Facility of EMSO research Infrastructure (www.emso.eu) of which NEMO-SN1 is one of the observation components. The SEISMOFAULTS experiment was partially supported by the Italian Ministry of University and Research in the framework of Italian participation to EMSO.

## ACKNOWLEDGMENTS

Thanks to Stephen Conway for revising the English form of the manuscript. We also wish to acknowledge the Guest Associated Editor Susan Bilek and the insightful and constructive reviews of two reviewers.

## SUPPLEMENTARY MATERIAL

The Supplementary Material for this article can be found online at: https://www.frontiersin.org/articles/10.3389/feart.2021.661311/full#supplementary-material

## REFERENCES

Argnani, A., and Bonazzi, C. (2005). Malta Escarpment Fault Zone Offshore Eastern Sicily: Pliocene-Quaternary Tectonic Evolution Based on New Multichannel Seismic Data. *Tectonics* 24, TC4009. doi:10.1029/2004TC001656

Bianca, M., Monaco, C., Tortorici, L., and Cernobori, L. (1999). Quaternary normal Faulting in southeastern Sicily (Italy): a Seismic Source for the 1693 Large Earthquake. *Geophys. J. Int.* 139, 370–394. doi:10.1046/j.1365-246x.1999.00942.x

Billi, A., Cuffaro, M., Beranzoli, L., Bigi, S., Bosman, A., Caruso, C., et al. (2020). The SEISMOFAULTS Project: First Surveys and Preliminary Results for the Ionian Sea Area, Southern Italy. *Ann. Geophys.* 63. doi:10.4401/ag-8171

Bortoluzzi, G., Polonia, A., Torelli, L., Arton, A., Carlini, M., Carone, S., et al. (2017). Styles and Rates of Deformation in the Frontal Accretionary Wedge of the Calabrian Arc (Ionian Sea): Controls Exerted by the Structure of the Lower African Plate. *Ital. J. Geosci.* 136, 347–364. doi:10.3301/ijg.2016.11

Boschi, E., Guidoboni, E., Ferrari, G., Valensise, G., and Gasperini, P. (1997). *Catalogue of the strong Earthquakes in Italy from 461 BC to 1990.* Bologna: ING. & SGA, 973.

Bowman, D. C., and Wilcock, W. S. D. (2014). Unusual Signals Recorded by Ocean Bottom Seismometers in the Flooded Caldera of Deception Island Volcano: Volcanic Gases or Biological Activity? *Antartic Sci.* 26, 267–275. doi:10.1017/S0954102013000758

Bromirski, P. D., Duennebier, F. K., and Stephen, R. A. (2005). Mid-ocean Microseisms. *Geochem. Geophys. Geosyst.* 6, Q04009. doi:10.1029/2004GC000768

Buskirk, R. E., Frohlich, C., Latham, G. V., Chen, A. T., and Lawton, J. (1981). Evidence that Biological Activity Affects Ocean Bottom Seismograph Recordings. *Mar. Geophys. Res.* 5, 189–205.

Carminati, E., Lustrino, M., and Doglioni, C. (2012). Geodynamic Evolution of the central and Western Mediterranean: Tectonics vs. Igneous Petrology Constraints. *Tectonophysics* 579, 173–192. doi:10.1016/j.tecto.2012.01.026

Carminati, E., Petricca, P., and Doglioni, C. (2020). "Mediterranean Tectonics," in *Encyclopedia of Geology* (Amsterdam: Elsevier).

Castello, B., Selvaggi, G., Chiarabba, C., and Amato, A. (2006). *CSI Catalogo Della Sismicità Italiana 1981–2002*. Versione 1.1. Roma: INGV-CNT.

Catalano, R., Doglioni, C., and Merlini, S. (2001). On the Mesozoic Ionian basin. *Geophys. J. Int.* 144, 49–64. doi:10.1046/j.0956-540x.2000.01287.x

Chang, E. T. Y., Hsu, S. K., and Lee, C. S. (2008). Earthquake Swarm Recorded by an Ocean Bottom Seismic Array in Southwest Offshore of Taiwan in October, 2005. *Terr. Atmos. Ocean. Sci.* 19 (No. 6), 717–728. doi:10.3319/tao.2008.19.6.717(pt)

Coltelli, M., Cavallaro, D., Firetto Carlino, M., Cocchi, L., Muccini, F., D'Alessandro, A., et al. (2016). The marine Activities Performed within the TOMO-ETNA experiment. *Ann. Geophys.* 59 (4), S0428. doi:10.4401/ag-7081

Cuffaro, M., Billi, A., Bigi, S., Bosman, A., Caruso, C. G., Conti, A., et al. (2019). The Bortoluzzi Mud Volcano (Ionian Sea, Italy) and its Potential for Tracking the Seismic Cycle of Active Faults. *Solid Earth* 10, 741–763. doi:10.5194/se-10-741-2019

Dahm, T., Thorwart, M., Flueh, E. R., Braun, T., Herber, R., Favali, P., et al. (2002). Ocean Bottom Seismometers Deployed in Tyrrhenian Sea. *Eos Trans. AGU* 83 (29), 309–315. doi:10.1029/2002eo000221

De Caro, M., Monna, S., Frugoni, F., Beranzoli, L., and Favali, P. (2014). Seafloor Seismic Noise at Central Eastern Mediterranean Sites. *Seismological Res. Lett.* 85, 1019–1033. doi:10.1785/0220130203

Devoti, R., Riguzzi, F., Cuffaro, M., and Doglioni, C. (2008). New GPS Constraints on the Kinematics of the Apennines Subduction. *Earth Planet. Sci. Lett.* 273, 163–174. doi:10.1016/j.epsl.2008.06.031

Díaz, J., Gallart, J., and Gaspà, O. (2007). Atypical Seismic Signals at the Galicia Margin, North Atlantic Ocean, Related to the Resonance of Subsurface Fluid-Filled Cracks. *Tectonophysics* 433, 1–13. doi:10.1016/j.tecto.2007.01.004

Doglioni, C. (1991). A Proposal for the Kinematic Modelling of W-Dipping Subductions - Possible Applications to the Tyrrhenian-Apennines System. *Terra Nova* 3 (4), 423–434. doi:10.1111/j.1365-3121.1991.tb00172.x

Doglioni, C., Innocenti, F., and Mariotti, G. (2001). Why Mt Etna? *Terra Nova* 13 (1), 25–31. doi:10.1046/j.1365-3121.2001.00301.x

Doglioni, C., Merlini, S., and Cantarella, G. (1999). Foredeep Geometries at the Front of the Apennines in the Ionian Sea (central Mediterranean). *Earth Planet. Sci. Lett.* 168 (3-4), 243–254. doi:10.1016/s0012-821x(99)00059-x

Embriaco, D., Marinaro, G., Frugoni, F., Monna, S., Etiope, G., Gasperini, L., et al. (2014). Monitoring of Gas and Seismic Energy Release by Multiparametric Benthic Observatory along the North Anatolian Fault in the Sea of Marmara (NW Turkey). *Geophys. J. Int.* 196, 850–866. doi:10.1093/gji/ggt436

Favali, P., Beranzoli, L., and De Santis, A. (2015). *Seafloor Observatories: A New Vision of the Earth from the Abyss*. Berlin, Germany; Heidelberg, Germany: Springer-Verlag. doi:10.1007/978-3-642-11374-1

Favali, P., and Beranzoli, L. (2006). Seafloor Observatory Science: a Review. *Ann. Geophys.* 49 (2/3), 515–567. doi:10.4401/ag-3125

Franek, P., Plaza-Faverola, A., Mienert, J., Buenz, S., Ferré, B., and Hubbard, A. (2017). Microseismicity Linked to Gas Migration and Leakage on the Western Svalbard Shelf. *Geochem. Geophys. Geosyst.* 18, 4623–4645. doi:10.1002/2017GC007107

Gallais, F., Graindorge, D., Gutscher, M.-A., and Klaeschen, D. (2013). Propagation of a Lithospheric Tear Fault (STEP) through the Western Boundary of the Calabrian Accretionary Wedge Offshore Eastern Sicily (Southern Italy). *Tectonophysics* 602, 141–152. doi:10.1016/j.tecto.2012.12.026

Gallais, F., Gutscher, M.-A., Klaeschen, D., and Graindorge, D. (2012). Two-stage Growth of the Calabrian Accretionary Wedge in the Ionian Sea (Central Mediterranean): Constraints from Depth-migrated Multichannel Seismic Data. *Mar. Geol.* 326-328, 28–45. doi:10.1016/j.margeo.2012.08.006

Gutscher, M.-A., Dominguez, S., de Lepinay, B. M., Pinheiro, L., Gallais, F., Babonneau, N., et al. (2016). Tectonic Expression of an Active Slab Tear from High-Resolution Seismic and Bathymetric Data Offshore Sicily (Ionian Sea). *Tectonics* 35, 39–54. doi:10.1002/2015tc003898

Hino, R., Kanazawa, T., and Hasegawa, A. (1996). Interplate Seismic Activity Near the Northern Japan Trench Deduced from Ocean Bottom and Land-Based Seismic Observations. *Phys. Earth Planet. Interiors* 93, 37–52. doi:10.1016/0031-9201(95)03087-5

Hsiao, N.-C., Lin, T.-W., Hsu, S.-K., Kuo, K.-W., Shin, T.-C., and Leu, P.-L. (2014). Improvement of Earthquake Locations with the Marine Cable Hosted Observatory (MACHO) Offshore NE Taiwan. *Mar. Geophys. Res.* 35, 327–336. doi:10.1007/s11001-013-9207-3

Husen, S., Kissling, E., and Flueh, E. R. (2000). Local Earthquake Tomography of Shallow Subduction in north Chile: A Combined Onshore and Offshore Study. *J. Geophys. Res.* 105 (B12), 28183–28198. doi:10.1029/2000jb900229

INGV Seismological Data Centre (2006). *Rete Sismica Nazionale (RSN)*. Italy: Istituto Nazionale di Geofisica e Vulcanologia (INGV). doi:10.13127/SD/X0FXNH7QFY

ISIDe Working Group (2007). *Italian Seismological Instrumental and Parametric Database (ISIDe)*. Rome: Istituto Nazionale di Geofisica e Vulcanologia (INGV). doi:10.13127/ISIDE

Lawton, J., Frohlich, C., Pulpan, H., and Latham, G. V. (1982). Earthquake Activity at the Kodiak continental Shelf, Alaska, Determined by Land and Ocean Bottom Seismograph Networks. *Bull. Seismol. Soc. Am.* 72, 207–220. doi:10.1785/bssa0720010207

Loher, M., Ceramicola, S., Wintersteller, P., Meinecke, G., Sahling, H., and Bohrmann, G. (2018). Mud Volcanism in a Canyon: Morphodynamic Evolution of the Active Venere Mud Volcano and its Interplay with Squillace Canyon, Central Mediterranean. *Geochem. Geophys. Geosyst.* 19, 356–378. doi:10.1002/2017GC007166

Maesano, F. E., Tiberti, M. M., and Basili, R. (2017). The Calabrian Arc: Three-Dimensional Modelling of the Subduction Interface. *Sci. Rep.* 7, 8887. doi:10.1038/s41598-017-09074-8

Mariotti, G., and Doglioni, C. (2000). The Dip of the Foreland Monocline in the Alps and Apennines. *Earth Planet. Sci. Lett.* 181, 191–202. doi:10.1016/s0012-821x(00)00192-8

Matsuzawa, T., Hirose, H., Shibazaki, B., and Obara, K. (2010). Modeling Short- and Long-term Slow Slip Events in the Seismic Cycles of Large Subduction Earthquakes. *J. Geophys. Res. Solid Earth* 115 (B12), B12301. doi:10.1029/2010jb007566

McNamara, D. E., and Buland, R. P. (2004). Ambient Noise Levels in the continental United States. *Bull. Seismol. Soc. Am.* 94 (4), 517–527. doi:10.1785/012003001

McNamara, D. E., Hutt, C. R., Gee, L. S., Benz, H. M., and Buland, R. P. (2009). A Method to Establish Seismic Noise Baselines for Automated Station Assessment. *Seismological Res. Lett.* 80 (4), 628–637. doi:10.1785/gssrl.80.4.628

Minelli, L., and Faccenna, C. (2010). Evolution of the Calabrian Accretionary Wedge (central Mediterranean). *Tectonics* 29, TC4004. doi:10.1029/2009tc002562

Monna, S., Sgroi, T., and Dahm, T. (2013). New Insights on Volcanic and Tectonic Structures of the Southern Tyrrhenian (Italy) from marine and Land Seismic Data. *Geochem. Geophys. Geosyst.* 14 (9), 3703–3719. doi:10.1002/ggge.20227

Montuori, C., Cimini, G. B., and Favali, P. (2007). Teleseismic Tomography of the Southern Tyrrhenian Subduction Zone: New Results from Seafloor and Land Recordings. *J. Geophys. Res.* 112 (B3), B03311. doi:10.1029/2005JB004114

Palano, M., Schiavone, D., Loddo, M., Neri, M., Presti, D., Quarto, R., et al. (2015). Active Upper Crust Deformation Pattern along the Southern Edge of the Tyrrhenian Subduction Zone (NE Sicily): Insights from a Multidisciplinary Approach. *Tectonophysics* 657, 205–218. doi:10.1016/j.tecto.2015.07.005

Peccerillo, A. (2005). *Plio-quaternary Volcanism in Italy*, 365. New York: Springer-Verlag Berlin Heidelberg.

Peterson, J. (1993). Observation and Modeling of Seismic Background Noise. US Geological Survey Open File Report. Albuquerque, NM, USA: US Geological Survey, 93–322.

Polonia, A., Nelson, C. H., Romano, S., Vaiani, S. C., Colizza, E., Gasparotto, G., et al. (2017b). A Depositional Model for Seismo-Turbidites in Confined Basins Based on Ionian Sea Deposits. *Mar. Geol.* 384, 177–198. doi:10.1016/j.margeo.2016.05.010

Polonia, A., Torelli, L., Artoni, A., Carlini, M., Faccenna, C., Ferranti, L., et al. (2016). The Ionian and Alfeo-Etna Fault Zones: New Segments of an Evolving Plate Boundary in the central Mediterranean Sea? *Tectonophysics* 675, 69–90. doi:10.1016/j.tecto.2016.03.016

Polonia, A., Torelli, L., Gasperini, L., Cocchi, L., Muccini, F., Bonatti, E., et al. (2017a). Lower Plate Serpentinite Diapirism in the Calabrian Arc Subduction Complex. *Nat. Commun.* 8, 2172. doi:10.1038/s41467-017-02273-x

Polonia, A., Torelli, L., Gasperini, L., and Mussoni, P. (2012). Active Faults and Historical Earthquakes in the Messina Straits Area (Ionian Sea). *Nat. Hazards Earth Syst. Sci.* 12, 2311–2328. doi:10.5194/nhess-12-2311-2012

Polonia, A., Torelli, L., Mussoni, P., Gasperini, L., Artoni, A., and Klaeschen, D. (2011). The Calabrian Arc Subduction Complex in the Ionian Sea: Regional Architecture, Active Deformation, and Seismic hazard. *Tectonics* 30, TC5018. doi:10.1029/2010TC002821

Presti, D. (2019). Seismicity Supports the Theory of Incipient Rifting in the Western Ionian Sea, central Mediterranean. *Ann. Geopysics* 62 (2), SE225. doi:10.4401/ag-8360

Sánchez-Reyes, H., Essing, D., Beaucé, E., and Poli, P. (2021). The Imbricated Foreshock and Aftershock Activities of the Balsorano (Italy) 4.4 normal Fault Earthquake and Implications for Earthquake Initiation. *Seismol. Res. Lett.* 92, 1926–1936. doi:10.1785/0220200253

Sgroi, T., Beranzoli, L., Di Grazia, G., Ursino, A., and Favali, P. (2007). New Observations of Local Seismicity by the SN-1 Seafloor Observatory in the Ionian Sea, Off-Shore Eastern Sicily (Italy). *Geophys. J. Int.* 169 (2), 490–501. doi:10.1111/j.1365-246X.2007.03348.x

Sgroi, T., Braun, T., Dahm, T., and Frugoni, F. (2006). An Improved Seismicity Picture of the Southern Tyrrhenian Area by the Use of OBS and Land-Based Network: the TYDE experiment. *Ann. Geophys.* 49 (2-3), 801–817. doi:10.4401/ag-3130

Sgroi, T., De Nardis, R., and Lavecchia, G. (2012). Crustal Structure and Seismotectonics of central Sicily (Southern Italy): New Constraints from Instrumental Seismicity. *Geophys. J. Int.* 189 (3), 1237–1252. doi:10.1111/j.1365-246X.2012.05392.x

Sgroi, T., Di Grazia, G., and Favali, P. (2019). Volcanic Tremor of Mt. Etna (Italy) Recorded by NEMO-SN1 Seafloor Observatory: a New Perspective on Volcanic Eruptions Monitoring. *Geosciences* 9 (3), 115. doi:10.3390/geosciences9030115

Sgroi, T., Monna, S., Embriaco, D., Giovanetti, G., Marinaro, G., and Favali, P. (2014). Geohazards in the Western Ionian Sea: Insights from Non-earthquake Signals Recorded by the NEMO-SN1 Seafloor Observatory. *Oceanography* 27 (2), 154–166. doi:10.5670/oceanog.2014.51

Sgroi, T., Montuori, C., Agrusta, R., and Favali, P. (2009). Low-frequency Seismic Signals Recorded by OBS at Stromboli Volcano (Southern Tyrrhenian Sea). *Geophys. Res. Lett.* 36 (4), L04305. doi:10.1029/2008GL036477

Sgroi, T., Polonia, A., Barberi, G., Billi, A., and Gasperini, L. (2021). New Seismological Data from the Calabrian Arc Reveal Arc-Orthogonal Extension across the Subduction Zone. *Sci. Rep.* 11, 473. doi:10.1038/s41598-020-79719-8

Sohn, R. A., Hildebrand, J. A., Webb, S. C., and Fox, C. G. (1995). Hydrothermal microseismicity at the Megaplume site on the southern Juan de Fuca Ridge. *Bull. Seismol. Soc. America* 85, 775–778.

Sultan, N., Riboulot, V., Ker, S., Marsset, B., Géli, L., Tary, J. B., et al. (2011). Dynamics of Fault-Fluid-Hydrate System Around a Shale-Cored Anticline in deepwater Nigeria. *J. Geophys. Res.* 116, B12110. doi:10.1029/2011JB008218

Tary, J. B., Géli, L., Guennou, C., Henry, P., Sultan, N., Çağatay, N., et al. (2012). Microevents Produced by Gas Migration and Expulsion at the Seabed: A Study Based on Sea Bottom Recordings from the Sea of Marmara. *Geophys. J. Int.* 190, 993–1007. doi:10.1111/j.1365-246X.2012.05533.x

Totaro, C., Presti, D., Billi, A., Gervasi, A., Orecchio, B., Guerra, I., et al. (2013). The Ongoing Seismic Sequence at the Pollino Mountains, Italy. *Seismol. Res. Lett.* 84, 955–962. doi:10.1785/0220120194

Webb, S. C. (2002). "19 Seismic Noise on Land and on the Sea Floor," in *International Handbook of Earthquake and Engineering Seismology*. Editors W. H. K Lee, H. Kanamori, P. C. Jennings, and C. Kisslinger (Amsterdam, Netherlands: Academic Press), 81, 305–318. doi:10.1016/s0074-6142(02)80222-4

Webb, S. C. (1998). Broadband Seismology and Noise under the Ocean. *Rev. Geophys.* 36, 105–142. doi:10.1029/97rg02287

Webb, S. C., and Crawford, W. C. (2010). Shallow-water Broadband OBS Seismology. *Bull. Seismol. Soc. America* 100 (4), 1770–1778. doi:10.1785/0120090203

Zhang, H., Thurber, C., and Bedrosian, P. (2009). Joint Inversion for Vp, vs, and Vp/Vs at SAFOD, Parkfield, California. *Geochem. Geophys. Geosyst.* 10 (11), Q11002. doi:10.1029/2009GC002709

**Conflict of Interest:** The authors declare that the research was conducted in the absence of any commercial or financial relationships that could be construed as a potential conflict of interest.

**Publisher's Note:** All claims expressed in this article are solely those of the authors and do not necessarily represent those of their affiliated organizations, or those of the publisher, the editors and the reviewers. Any product that may be evaluated in this article, or claim that may be made by its manufacturer, is not guaranteed or endorsed by the publisher.

frontiers in Earth Science

METHODS
published: 06 August 2021
doi: 10.3389/feart.2021.660970

# Application of the Stacked Refraction Convolution Section to 2D Ocean Bottom Seismometer Wide-angle Seismic Data Along the Tamayo Through Basin, Gulf of California

*Antonio González-Fernández* *

*Departamento de Geología, División de Ciencias de la Tierra, Centro de Investigación Científica y de Educación Superior de Ensenada (CICESE), Ensenada, Mexico*

OPEN ACCESS

**Edited by:**
*Charlotte A. Rowe, Los Alamos National Laboratory (DOE), United States*

**Reviewed by:**
*Ryota Hino, Tohoku University, Japan*
*Roberto de Franco, Instituto di Geologia Ambientale e Geoingegneria (IGAG), Italy*
*Afonso Loureiro, FCiências.ID, Portugal*

***Correspondence:**
*Antonio González-Fernández*
*mindundi@cicese.mx*

**Specialty section:**
*This article was submitted to Solid Earth Geophysics, a section of the journal Frontiers in Earth Science*

**Received:** *30 January 2021*
**Accepted:** *27 July 2021*
**Published:** *06 August 2021*

**Citation:**
*González-Fernández A (2021) Application of the Stacked Refraction Convolution Section to 2D Ocean Bottom Seismometer Wide-angle Seismic Data Along the Tamayo Through Basin, Gulf of California. Front. Earth Sci. 9:660970. doi: 10.3389/feart.2021.660970*

The stacked refraction convolution section can be used as an interpretation tool in wide-angle refraction seismic data generated by air gun shooting and recorded by Ocean Bottom Seismometers (OBS). The refraction convolution section is a full-wave extension of the Generalized Reciprocal Method (GRM), a method frequently used in shallow refraction seismic interpretation, but not applied to deep crustal-scale studies. The sum of the travel times of the waves refracted in the same interface and recorded in a pair of forward and reverse profiles, time-corrected by the reciprocal time, is an estimation close to the two-way travel times of the multichannel seismic reflection sections, but with seismic rays illuminating the interfaces upwards. The sum of seismic traces is obtained with the convolution section. Furthermore, several pairs of convolved forward-reverse refraction recordings of the same area can be stacked together to improve the signal to noise ratio. To show the applicability of the refraction convolution section in OBS deep data, we interpreted the basement structure of the Tamayo Through Basin in the southern Gulf of California, offshore Mexico. We compared the results with both, a multichannel seismic section recorded in the same profile, and the previous interpretations of the same wide-angle seismic data modeled with ray tracing and tomography methods. The basement imaged by the stacked refraction convolution section is similar in geometry to that obtained by seismic reflection processing. The stacked refraction convolution section identifies the full extent of the basement and confirms the location of a nearly constant thickness volcanic layer in the northwestern half of the basin. However, only a small area of volcanic deposits is found in the shallower parts of the southwestern margin. We also show that the convolution process can be used to estimate the occurrence of lateral variations of seismic velocities in the basement, as a further application of the GRM to deep refraction data.

**Keywords: refraction convolution section, ocean bottom seismometer, wide-angle seismic data, refraction seismology, sedimentary basin, generalized reciprocal method, Gulf of California**

## INTRODUCTION

There are different methods of interpretation of 2D wide-angle refraction/reflection seismic data. The simplest ones are based on the transmission equations in stratified media. However, these methods are only useful in very simple geological structures. For complex subsurface structures, other methodologies are used. In crustal-scale, both on land and at sea, the traditional methods are, on the one hand, those based on ray tracing and synthetic seismogram calculation (e.g., Červený and Pšenčík, 1984; Zelt and Smith, 1992) and on the other hand, the tomography methods (e.g., Hole, 1992; Zelt and Barton, 1998; Zhang et al., 1998; Hobro, 1999; Korenaga et al., 2000; Hobro et al., 2003; Meléndez et al., 2015). Several scalar approaches have been used to reconstruct 2D complex crustal seismic structures, in order to generate robust initial models for direct or inverse interpretation. The final goal of all these techniques is parametric reconstruction, i.e., to obtain information about the seismic velocity structure. Recent developments make use of the full-wave refraction seismic recordings through interferometric imaging and reverse time migration, specifically for marine data (Verpahovskaya et al., 2017; Yang and Zhang, 2019).

In shallow refraction seismic interpretation, apart from tomography, delay time methods are frequently used, based on the sum of direct and inverse arrival times of refracted waves, to estimate the depth of interfaces, and subtraction of the same times to calculate propagation velocities in the different media. The use of direct and inverse travel times allows solving the ambiguity between seismic velocity and dip.

Among the delay time methods, the Generalized Reciprocal Method (GRM, Palmer, 1980; Palmer, 1981) allows the reconstruction of 2D complex seismic structures characterized by high velocity contrasts. It is mostly assumed that the delay time methods are exclusive to shallow seismic exploration and have not been applied to deep problems.

The reason for this difference in methodology according to the scale is not completely clear. The main issue of the application of delay time methods in crustal studies is that the interfaces are often transitional, so the basic hypothesis of sharp contrasts is not satisfied. However, in some instances, such as a basement with a high velocity contrast, the application is possible. Even in shallow seismic exploration, care should be taken to avoid the pitfall of trying to interpret diving waves as head waves. Another possible justification for the scale disparities in interpretation methods is the different wavelengths. This paper intends to show that the GRM is applicable for marine sedimentary basins of several km of depth and that the methodology does not exclude its use in deep environments.

The refraction convolution section or convolutional seismic section (Matsuoka et al., 2000; Palmer, 2001a, 2001b, 2001c) is an imaging extension of the scalar delay time methods, in particular the GRM, that uses the entire seismic trace, instead of just the travel times. Besides, when redundant data is available, it is possible to apply stacking to the convolutional seismic section (de Franco, 2005; Palmer and Jones, 2005) and improve the signal-to-noise ratio. Another advantage of the convolutional seismic section over traditional methods of delay time, tomography, and ray tracing is that it is unnecessary to measure travel times for all records, reducing data processing times. Furthermore, it is a simple methodology that involves a smaller computational cost than migration.

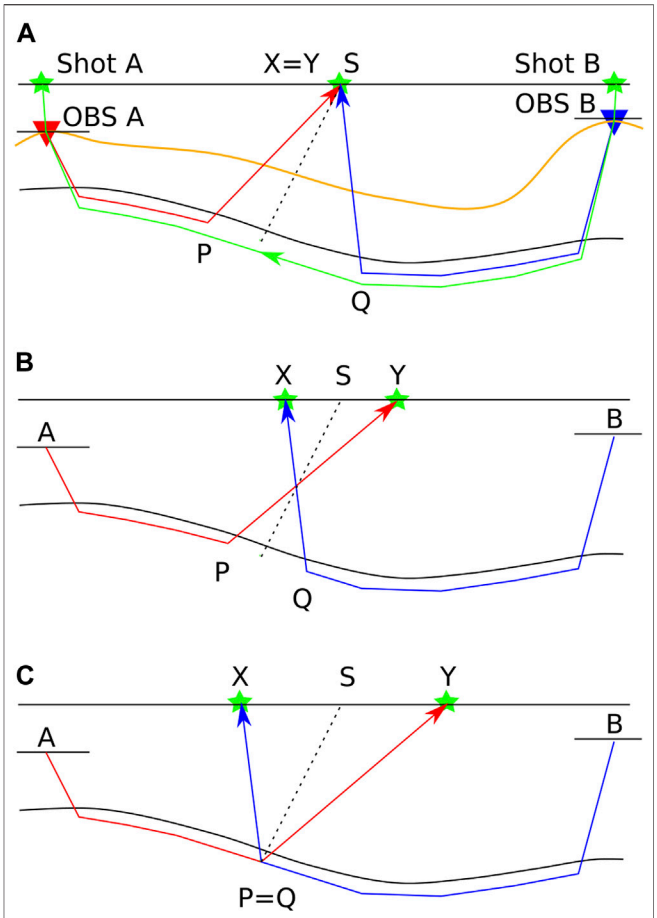


**FIGURE 1 |** Illustration of the Generalized Reciprocal Method (GRM) seismic rays. For Ocean Bottom Seismometer (OBS) recording and air-gun sources, XY is the distance between shots, $t_{AY}$ is the time corresponding to the direct direction recording OBS A-P-Y in red, and $t_{BX}$ is the time for the inverse direction recording OBS B-Q-X in blue. S is the sea surface location of the seismic trace that results from adding the direct and inverse traces. **(A)** distance XY = 0, **(B)** XY less than optimum, **(C)** XY optimum value. $t_{AB}$ is the reciprocal time, from Shot-A to Shot-B or reverse in green, the total travel time between the ends of the seismic profile, independent of the value of XY. Sea bottom in orange.

To demonstrate that the refraction convolution section methodology can be applied to real OBS data, we show an application in the Tamayo Through Basin, located in the southern part of the Gulf of California, offshore Mexico. Previous investigations of the basin, based on multichannel seismic data (Sutherland et al., 2012), could not image the basement properly due to insufficient signal penetration. OBS ray tracing and tomography models (Sutherland, 2006; Lizarralde et al., 2007) provided a low-resolution outline.

## MATERIALS AND METHODS

### GRM and Refraction Convolution Section

To obtain a section in time from seismic refraction data, the GRM (Palmer, 1980, Palmer, 1981) combines the travel times of the

refracted waves in the same discontinuity, for two shots, with direct and inverse recording. The travel times corresponding to the same recording point, or recording points separated by a constant distance, are added, and then the reciprocal time is subtracted. The reciprocal time is the time used for the wave to travel through the corresponding refractor between the two sources. The result is equivalent to two times the average of the direct and inverse delay times. This calculation is called the generalized time-depth function:

$$t_g(x) = t_{AY}\left(x + \frac{XY}{2}\right) + t_{BX}\left(x - \frac{XY}{2}\right) - \left[t_{AB} + \frac{XY}{v_n}\right], \quad (1)$$

where $t_{AY}$ is the time of the direct shot, $t_{BX}$ is the time of the reverse shot, $t_{AB}$ is the reciprocal time between both profile ends, XY is the separation between the seismic traces, and $v_n$ is approximately the velocity of propagation beneath the refractor (see **Figure 1**). XY distance corrects the times of the upgoing signals of rays, shifting them to the same refracting point. The values of $t_{AY}$ and $t_{BX}$ depend on the observation position $x$ and the value of XY, whereas $t_{AB}$ is constant.

In the ideal case where the arrivals come from the same point of the refractor at depth, the time calculated is similar to that which would be obtained at zero offset in seismic reflection data, applying a correction for the inclination of the rays, depending on the ratio between the velocities of the lower medium and the average velocities of the upper medium. The two-way travel time in reflection seismology can be approximated by dividing $t_g$ by the cosine of the critical angle, if the refractor is subhorizontal. If the rays are close to vertical, this correction is small, so the reflection and GRM times could be considered close and directly comparable.

If the same observation point is taken for the calculations for the direct shot and the reverse shot in the simplest case, the information does not come from the same point of the refractor (see in **Figure 1A**). In this case, XY = 0 and is equivalent to Hagedoorn (1959) Plus-Minus method. The preferred approach is to select pairs of observation points whose rays come from the same point on the refractor. In order to do this, it is necessary to choose observation points with appropriate offset separation; this is the optimum XY value of the above **Equation 1**, defined by Palmer (1980), Palmer (1981) (see in **Figure 1C**). In a horizontal plane layers model, the optimum XY would be equivalent to the critical distance.

In the case of OBS data, the acquisition geometry is in common receiver gathers. Each pair of seismic traces come from two different sources, separated by the XY distance, and are recorded by a pair of OBS instruments. If XY = 0, the same shot is recorded by the pair of OBS.

All times, $t_{AY}$, $t_{BX,}$ and $t_{AB}$, cannot be read directly from the original OBS seismograms and should be corrected because the recording instruments are not located at the surface (a static correction). On the contrary, the sources can be considered to be at the surface. Therefore, it is necessary to apply a time correction to each OBS common receiver gather due to the time difference between the OBS and the corresponding shot at the sea surface, resulting in the sea surface as the reference level. If the ray segments Shot A to OBS A and Shot B to OBS B are considered near vertical, it is possible to add to the values of $t_{AY}$ and $t_{BX}$ the depth of each OBS divided by the sea water velocity.

In **Figure 1**, $t_{AB}$ is the full reciprocal time from Shot A to OBS A to PQ to OBS B and to Shot B, or reverse, depicted in green, i.e., the total travel time between the ends of the seismic profile. If the near surface ray portions Shot A to OBS A and Shot B to OBS B are considered again approximately vertical, $t_{AB}$ can be directly observed from the static corrected common receiver gathers.

In real data, and even in some theoretical situations, it is often difficult to estimate the optimal XY value (Leung, 1995, 2003; Sjögren, 2000; Whiteley and Eccleston, 2006). According to the GRM, it is necessary to select the $t_g$ function with the highest detail, not a simple task and depending on the interpreter. Therefore, it is usual to simplify and directly select XY = 0 or XY´s value close to the optimum through simple modeling. In any case, if the XY value is not optimal, the effect is to smooth out the details of the refractor, although its geometry remains recognizable (Palmer, 1980, Palmer, 1981).

When it is required to combine different pairs of direct and reverse shots, such as for stacking purposes, in general, for each pair, there is at least one different optimal XY value, which can even be laterally variable when the depth of the refractor and the seismic velocities above it are changing (Seisa, 2007). To avoid having to calculate many different XY values, with their corresponding different time corrections, it is possible to take the single value of XY = 0. The value of $t_g$ in **Equation 1** is thus simplified:

$$t_g(x) = t_{AY}(x) + t_{BX}(x) - t_{AB} \quad (2)$$

The original GRM is a scalar approach and takes into consideration only arrival times. Based on it, the refraction convolution section or convolutional seismic section considers the complete waveform, so amplitude information is included. The convolution operation on the direct and inverse shot records acts as the sum of phases of refracted waves, equivalent to the scalar sum of $t_{AY}$ and $t_{BX}$ in **Equations 1**, **2**:

$$s_g(x, t + t_{AB}) = s_{AY}(x, t) * s_{BX}(x, t) \quad (3)$$

where $s_g$ corresponds to the refraction convolution section traces, $s_{AY}$ is the seismic trace of the direct shot, $s_{BX}$ is the trace of the reverse shot, and $*$ indicates the signal convolution. The convolution of waves that are not refracted, such as the direct wave, does not have meaning; only arrivals from the same refractor must be correlated to comply with **Equation 3**. de Franco (2005) showed that only those parts of the record sections for which the correct refractor range have been selected contribute constructively to the stack for each refractor. Other arrivals only introduce noise into the image. Palmer (2001a) showed that it is possible to apply f-k filtering to eliminate undesired waves. Another possibility is to apply surgical mute to the seismic sections before convolution.

A simple time correction can be directly applied for the subtraction of the reciprocal time $t_{AB}$ (Palmer, 2001b) by averaging the observations of the reciprocal times measured

on the direct and inverse gathers, with the static correction previously mentioned, as shown in **Equation 3**. Another alternative is to use the phase subtraction properties of the cross-correlation function. If one of the traces recorded at the position of one of the sources is selected, its time is reversed, and the cross-correlation is calculated with each of the traces resulting from the previous convolution, the effect is the correction for the reciprocal time. While the convolution operation is commutative, the cross-correlation is not, so it is necessary to apply the cross-correlation after convolution to preserve the correct sign for events in the time domain (de Franco, 2005):

$$s_g(x,t) = s_{AY}(x) * [s_{BX}(x,t) \otimes s_{AB}(x,-t)] \quad (4)$$

where $s_{AB}$ (x,-t) denotes a time-reversed seismic trace selected at one of the OBS locations, and ⊗ indicates cross-correlation. However, the time correction based on the reciprocal time $t_{AB}$ is the simplest approach if the signals are clear and the refraction arrivals are easy to pick, so it is the approach selected for the present work.

(Palmer, 2001b; Palmer 2001c) pointed out that the amplitudes of the refraction convolution section are proportional to the square of the head coefficient, which is proportional to the ratio of acoustic impedances across the refractor. Thus, the amplitudes are related to the acoustic impedance contrast.

## Velocity Analysis Convolution Section

The GRM also provides the velocity of the medium under the refractor. For this purpose, the velocity analysis function is calculated:

$$t_v(x) = \frac{1}{2}\left[t_{AY}\left(x + \frac{XY}{2}\right) - t_{BX}\left(x - \frac{XY}{2}\right) + t_{AB}\right] \quad (5)$$

It is observed that, unlike the time-depth function $t_g$ in **Equations 1**, **2**, there is now a subtraction between the travel times of the direct and inverse shots, $t_{AY}$ and $t_{BX}$. A modified version of the convolutional section can also be implemented here. To apply the subtraction instead of the addition, the inverse shot traces are reversed on the time axis before the convolution is performed. We call the resulting seismic section the velocity analysis convolutional section. For XY = 0:

$$s_v(x, t - t_{AB}) = \frac{1}{2}[s_{AY}(x,t) * s_{BX}(x,-t)] \quad (6)$$

where $s_{BX}$ (x,-t) are the time-reversed inverse shot traces $s_{BX}$ (x,t). Here, it is not strictly necessary to make the reciprocal time correction, as it appears in **Equation 3**, because $t_{AB}$ is a constant term, and what is needed for the velocity estimation is the slope of the $t_v$ function, whose variables are $t_{AY}$ and $t_{BX}$:

$$1/v(x) = dt_v/dx \quad (7)$$

To improve the visualization of the velocity analysis convolutional section $s_{v,}$ it is useful to apply a reduction velocity close to the expected velocity value. It is then possible to see more clearly small lateral variations in velocity, as $s_v$ is a function of x.

An alternate approach, using cross-correlation instead of convolution, was proposed by de Franco (2010).

## Ocean Bottom Seismometer and MCS Data

In 2002, as part of a deep exploration survey in the Gulf of California, an 881 km profile was acquired along the Alarcon Basin. The R/V Maurice Ewing towed a 7,860 $in^3$ (0.1288 $m^3$) tuned array of 20 air guns, shooting every 150 m. The R/V New Horizon deployed 53 OBS at 12.5 km intervals as recording instruments. The data were recorded in common receiver gathers, with a sampling rate of 125 Hz. For the purposes of the present work, we selected the recordings of 6 OBS, along 56 km, over a single basin: Tamayo Through (**Figure 2**).

In the same region where we applied the refraction convolution section method, Sutherland et al. (2012) interpreted reflection multichannel seismic (MCS) data, provided by the simultaneous recording of the same R/V Maurice Ewing shots, recorded by a towed 480-channel 6 km-long streamer with 12.5 m receiver groups. They interpreted the complete profile structure, including the Tamayo Trough Basin, observing there a semi-graben, with a maximum sedimentary thickness of 1.5 km and water depths up to 2 km. A much less detailed velocity model was previously proposed by Sutherland (2006) and Lizarralde et al. (2007), interpreting the same OBS data set that we used in the present paper by applying ray tracing and tomography methods.

## Tamayo Through Basin

The Tamayo Trough, located to the southeast of Alarcon Basin, in the southern Gulf of California, is an inactive basin, characterized by large subsidence without a clear basin-bounding fault. According to the interpretation of available seismic data, it developed over thinned continental crust before 11 Ma (Lizarralde et al., 2007). Based on potential field data, an alternative interpretation proposes that the basin is underlain by oceanic crust (Abera et al., 2016). At that time, the Tamayo Trough was aligned with the East Pacific Rise, and become abandoned as a failed rift basin (Lizarralde et al., 2007) or became magma starved and was abandoned, with a new ridge forming northwest (Abera et al., 2016). Extension in the Gulf of California started around this time. Seafloor spreading in Alarcon Rise was initiated later, after 3.7–3.5 Ma (Lizarralde et al., 2007).

MCS data (Sutherland et al., 2012) shows the presence of three main sedimentary units related to the subsidence history of the basin from terrestrial to shallow marine to a deep-marine environment. The lowest unit is mostly unreflective; the middle unit shows some layering with increased acoustic reflectivity upward; and the youngest unit consists of layered deep-marine sediments. Most of the faulting and basin subsidence have occurred preceding the deposition, as the sediments seem to be undeformed.

Under the sediments, a highly reflective layer is inferred to be volcaniclastic. The thickness of this layer appears to be thinner on the southeast margin of the basin. The thickness and widespread occurrence of this volcanic layer in other sections of the Alarcon Basin area suggest that it may be part of the 25–12 Ma prerift formation, known as Comondú Group (Umhoefer et al., 2001).

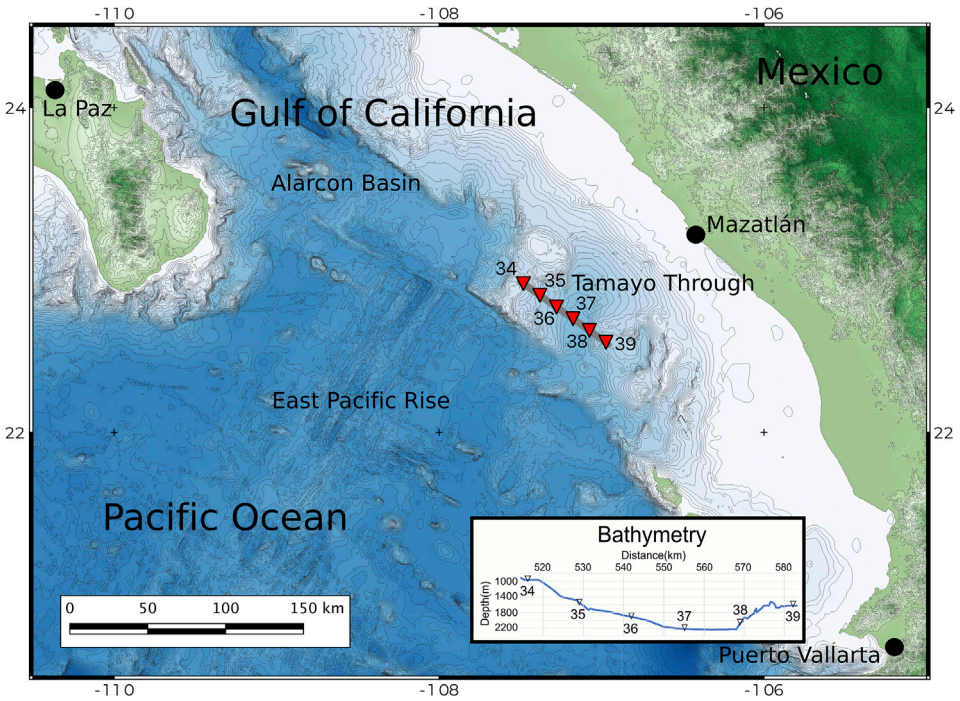


**FIGURE 2 |** Location of OBS (triangles) and shots (thick line). The study area corresponds to Tamayo Through in the southern Gulf of California, offshore Mexico. The inset shows the bathymetric profile with the location of the OBS.

Subduction-related calc-alkaline volcanic rocks of the Comondú Group were emplaced within the Gulf of California and along the eastern edge of what is now the Baja California peninsula, associated with the subduction of the Farallon plate beneath North America.

## DATA PROCESSING

### Refraction Convolution Section for a Single Forward-Reverse Pair

Initially, OBS data were processed with a 5–16 Hz minimum phase band-pass filter. The filter is based on the spectrum of the signals generated by the air guns. The procedure starts by identifying the range of offsets where a common refractor is observed between the different recordings. Particularly, for OBS data, the refractor best suited to apply the convolutional section method corresponds to the basement (commonly known as Pg). For each OBS record section in the zone to be studied, the corresponding range of offsets is selected (**Figure 3**). The representation of the data in reduced time helps in the correct identification of the refractor. The direct waves are thus excluded, because they can produce artifacts in the convolution process.

Once the traces are selected, a predictive deconvolution filter is applied to compress the source wavelet and reduce reverberations. This filter also attenuates a small amount of the multiple of the water layer. However, as the multiples have different paths than the primary waves, the filter´s effect is limited. To completely remove the multiples, a mute is applied. Mute also allows the arrivals corresponding to the remaining direct wave to be eliminated, which has a high amplitude and can interfere with the data´s interpretation (see **Figure 3D**). Afterward, the band-pass filter is re-applied to improve the signal-to-noise ratio, especially to reduce the high-frequency noise introduced by the deconvolution filter.

Before applying the convolution, a static time correction should be made to each OBS common receiver gather, to compensate for the receiver depth before calculating the reciprocal time. The depth of the OBS is divided by the water velocity (1,500 m/s in our case) and the result is added to the times of each trace. There is no need to correct for source depths because the shots were done at a constant depth close to the sea surface.

After the static correction, to compute the convolutional section (see in **Figure 4A**), the traces of all the pairs of the direct and inverse recordings for the same sources are selected, and the convolution is performed for each pair. According to **Equation 3**, after the convolution, another time correction is performed to eliminate the reciprocal time. Our estimation is based on the average of the reciprocal times observed in the direct and inverse static corrected common receiver gathers for the offsets to which the OBS are located (**Figure 3**).

If the selected XY value is not 0, the pairs of traces should be chosen accordingly. An additional time correction must also be added, according to **Equation 1**. In the latter case, it is necessary to have the value of the wave propagation velocity in the basement, which can be estimated from the slopes of the

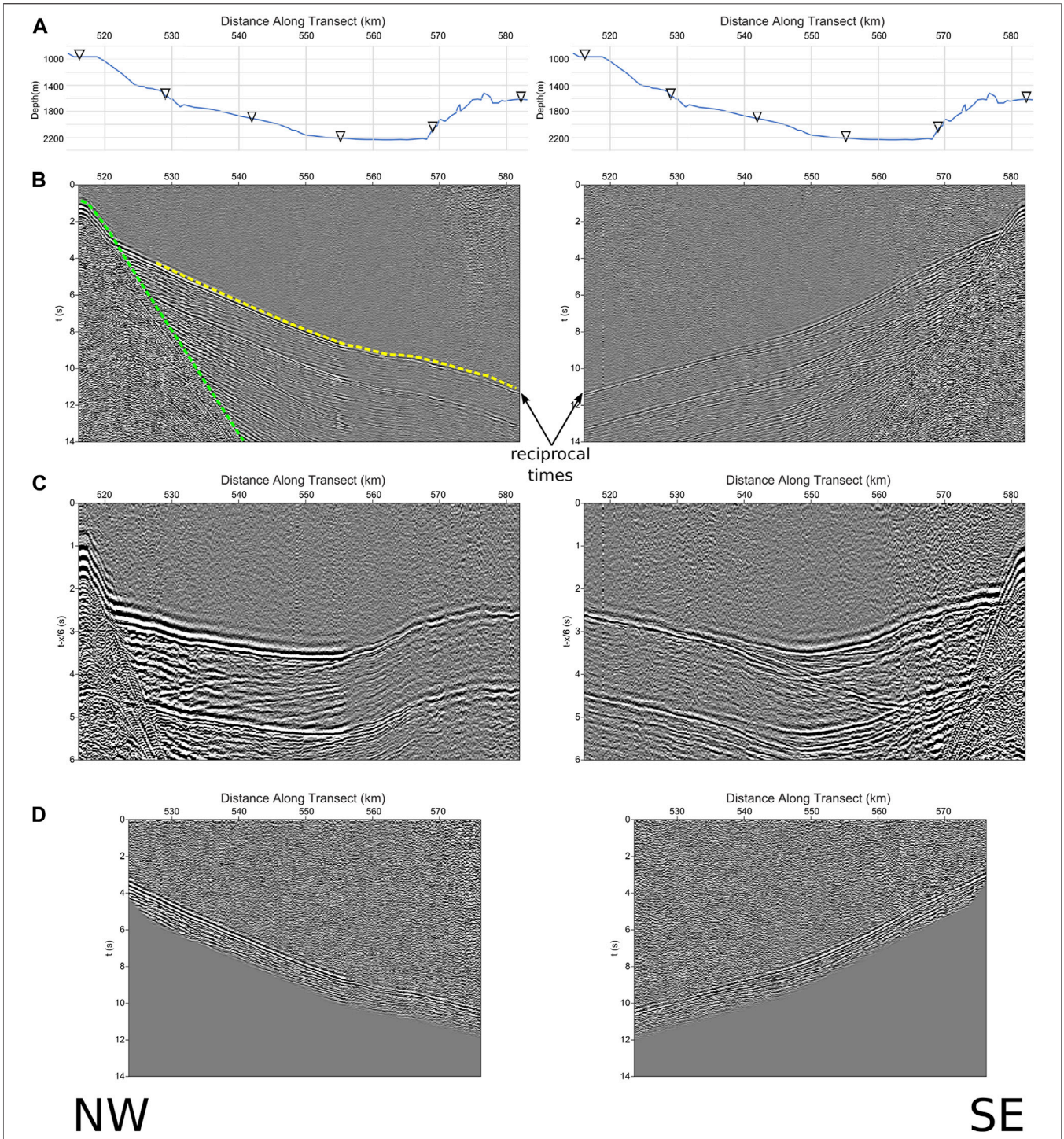


**FIGURE 3 |** Samples of OBS record seismic sections. **(A)** Bathymetry profile. **(B)** Direct (OBS 34) and inverse (OBS 39) shot gathers in record time; direct wave in green, refractions in yellow. **(C)** Same with reduction velocity tr = t-x/vr, where vr = 6 km/s. **(D)** Same in record time, basement only selected traces and muted to eliminate later arrivals corresponding to water multiples.

refracted wave or, for an improved value, from the velocity analysis convolutional section, as explained before.

If we assume the velocity profiles by Sutherland et al. (2012), the optimum XY values near the basin´s depocenter can be estimated by calculating the critical distance for a horizontally layered model. XY estimation resulted to be about 3.8–4.5 km, or about 25–30 shots. To show the possible improvement of the resulting image from XY = 0 to a value near the optimum, we

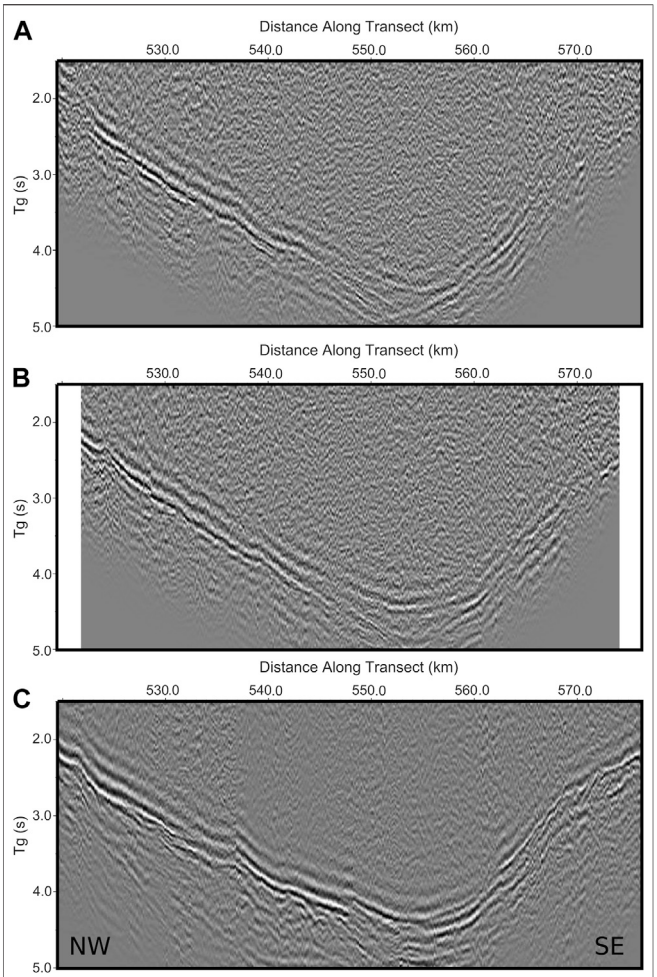


**FIGURE 4 | (A)** Refraction convolutional section for OBS pair 34–39 XY = 0; **(B)** same for XY = 30 shots; **(C)** stacked refraction convolutional section for all OBS pairs combinations, with XY = 0.

show in **Figure 4B** the same refraction convolutional section for XY = 30 and a velocity of 6.0 km/s. The improvement is small.

## Stacking of Refraction Convolution Sections

The stacked refraction convolution section is the sum of the convolved traces of all the possible pair combinations of direct and inverse recordings, located in the common shot positions:

$$s_{gs}(x, t + t_{AB}) = \Sigma\left[s_{AY}(x, t) * s_{BX}(x, y)\right] \quad (8)$$

where the signal sum, denoted by $\sum$, is performed on x for different A and B reversed shot configurations.

For the stacking process, since there is some uncertainty introduced by the estimation of the reciprocal times in each OBS pair and the calculation of the static corrections, and because the geometry is not strictly 2D, it may be necessary to apply a further time correction before stacking in order to ensure that the waves corresponding to the basement are in phase and are properly added. This can be done by taking as a reference the OBS pair for which the reciprocal time observations are most reliable and cover the largest area possible (34 and 39 in our case). The cross-correlation between each trace of the convolutional section of this reference OBS pair with the trace corresponding to the same distance in the profile in the other OBS pair is then calculated. The maximum values of the cross-correlation provide the time delays that offer the best fit between the convolutional sections. The mean value of these values was applied as time correction before stacking. Along the profiles, the delays are variable in terms of tenths of ms, probably due to velocity heterogeneities. As the variations are small, usually less than half a cycle of the dominant frequency, they should not adversely affect the stacking process. The result is a much-improved image, with a better signal to noise ratio, from a simple OBS pair (see in **Figure 4C**).

# RESULTS

If we compare Sutherland et al. (2012) multichannel reflection seismic section with our stacked refraction convolutional section (**Figure 5**), we notice a good agreement in the general shape. The stacked convolution section reproduces the outline of the basement in detail, with a depocenter at 556 km in the profile, in the form of a semi-graben and a gradual thinning towards the NW. The refractor with the largest amplitude is found at greater depth than most of the deeper reflections visible in the MCS section, especially in the NW part of the profile. The depocenter in the MCS section is apparently shifted 2 km to the SE.

Part of the differences in depth may be due to the correction factor indicated above (**Eq. 1**) or to the possible inaccuracies of the static correction. However, they are insufficient to explain the discrepancy completely. It is necessary to consider, in this case, the P-wave propagation velocity distribution model obtained by Sutherland et al. (2012) based on the velocity analysis of refractions in MCS supergathers (**Figure 6**). The basement beneath the interpreted volcanic layer in Sutherland et al. (2012), corresponding to velocities over 5 km/s, was directly extracted from Sutherland (2006) and Lizarralde et al. (2007) because the supergather refractions proceed only from shallow depths. In the northwestern part of the basin, there is a good agreement between the basement suggested by the stacked refraction convolutional section and the basement under the ropey and highly reflective layer of Sutherland et al. (2012) inferred to be volcaniclastic. In the southeastern margin, the acoustic basement in the MCS and the stacked refraction convolutional section nearly match. The Sutherland (2006) and Lizarralde et al. (2007) basement in the SE is close to the deeper refractions observed in the stacked refraction convolutional section.

Furthermore, Sutherland et al. (2012) had no velocity-depth profiles between 555 (near the depocenter) and 572 km to aid in interpreting the nature of the southeastern part of the basin. Velocities in between both distances were interpolated. The close match between the MCS reflections and the top of the stacked refraction convolutional section suggests that the only volcanic

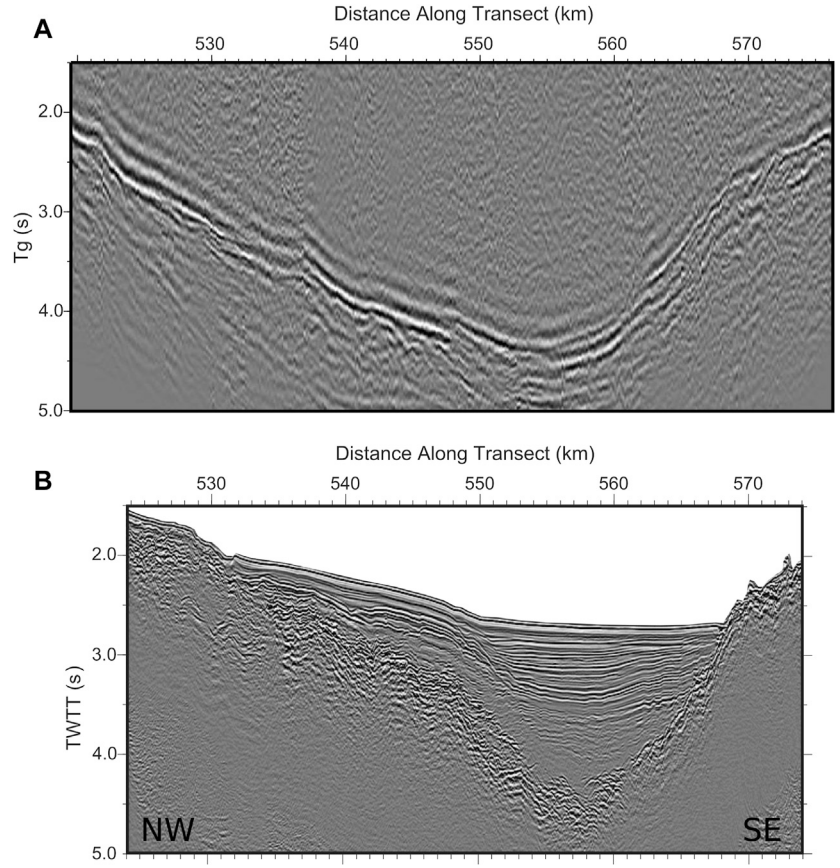


**FIGURE 5 |** Stacked refraction convolutional section **(A)** compared with migrated reflection multichannel seismic section **(B)** by Sutherland et al. (2012).

layers in the southeastern part of the basin are thin deposits around 570 km.

MCS and the refraction convolution section show different depocenters. MCS provides the deepest part of just the sedimentary layers, while the convolution section shows the depocenter for the sediments and the volcanic layer.

It is important to consider that the multichannel seismic section is illuminated from above, while the convolutional section receives the energy from below. Most of the multichannel section´s energy is reflected in the strong impedance contrast between the marine and volcanic sediments. In seismic refraction, most of the energy travels along the deeper basement and through the volcanic layer.

This example of applying the convolutional section to the seismic refraction interpretation shows how the proposed methodology complements the multichannel reflection seismic data, allowing a comparison between both seismic methods directly and visually.

**Figure 7** shows the velocity analysis convolutional section, corresponding to the OBS pair 35–39; **Equation 6** was used to convolve OBS 35 seismic traces and the inverted in time OBS 39 traces. No reciprocal time correction nor stacking was applied. As can be observed, the basement velocity is, on average, very close to 6.0 km/s, as the reduced time section is subhorizontal. Because $s_v$ in **Equation 6** depends on x, lateral velocity variations under the basement are possible. These variations are slight in our example but noticeable, especially between 550 and 565 km. Lower velocities, corresponding to upward slopes, are marked by orange dots, and higher velocities, with downward slopes, by magenta dots. The area with correlation around 550 km, marked in green, can be related to the presence of refractions shallower than the basement, with velocities lower than 6.0 km/s, possibly associated with the volcanic layer.

The velocities of 5.0–5.5 km/s reported by Sutherland et al. (2012) are found only in the shallower part of the basin. The deeper Sutherland (2006) and Lizarralde et al. (2007) velocity models proposed 6.0 km/s close to the depocenter of the basin. The velocity analysis convolutional section seems to confirm the higher velocity value of 6.0 km/s for most of the basement. The basement depth interpreted from the stacked convolutional section is similar to the one proposed in the model by Sutherland (2006) and Lizarralde et al. (2007) for the northwestern side of the basin. Still, it appears to be noticeably shallower for the southeast margin, considering the 6.0 km/s contour. Sutherland (2006), Lizarralde et al. (2007), and Sutherland et al. (2012) models were calculated using diving waves, while in the present work, we are assuming head waves. Furthermore, Sutherland (2006) showed that ray coverage was

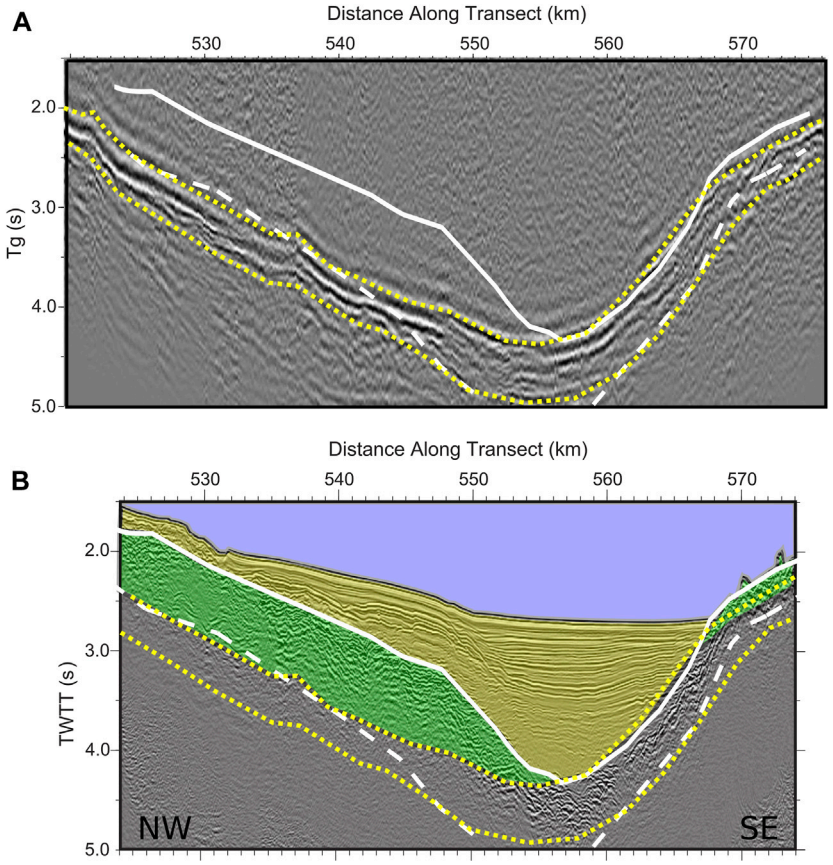


**FIGURE 6 |** Stacked refraction convolutional section **(A)** compared with migrated reflection multichannel seismic section **(B)**. In white lines, overlying velocity model by Sutherland et al. (2012). Above the solid white line: sediments; between the solid and dashed lines: volcanic layer; dashed line: basement. Between dotted yellow lines, area with the highest amplitudes of the stacked convolution section. Final geological interpretation in overlaid colors: water in blue, sediments in yellow, and volcanic layer in green.

poor for the shallow Tamayo area. Additionally, Abera et al. (2016) proposed a high density (2,900 kg/m$^3$) oceanic upper crust under the sedimentary and volcanic layers, consistent with our observed basement higher velocity.

## DISCUSSION

One of the GRM common criticisms is the assumption of a relatively homogeneous structure above the refractor, which is not always accurate. An advantage of seismic refraction recording at sea is the homogeneity in the most superficial layers. The water layer is extremely homogeneous; in the seismic refraction´s resolution ranges, it can be considered a constant velocity layer globally. The sedimentary layers, especially the shallower ones, are saturated with water, and their velocity distribution is smooth, with variations mainly in the vertical direction. This homogeneity simplifies the application of the GRM and similar methods in the marine environment, making it more reliable.

The main problem in stacking convolutional sections from different OBS pairs is the estimation of the reciprocal times. The needed static correction introduces some inaccuracy due to the assumption of vertical trajectories between the surface and the OBS, and the use of a particular value for the water velocity (1,500 m/s in our case). Furthermore, it is not a pure 2D problem, and the presence of subsurface heterogeneities, the reciprocal times observed in the forward and reverse shots do not precisely match. Therefore, uncertainty is introduced in the exact calculation of the $t_g$ times.

In combined marine reflection and refraction seismic surveys, the purpose of multichannel reflection seismic data is to provide high structural resolution, while refraction results in higher penetration. Although seismic refraction has lower resolution because of the lower frequencies used, since the rays travel longer distances, the refraction convolutional section method, with the use of full-wave information, not only allows a more direct comparison between reflection and refraction, but also permits the observation of differences between acoustic basements in both types of seismic data since the direction of illumination of the structures is practically opposite.

Regarding the low frequencies used in deep refraction studies, it is important to note that selecting the proper values for the optimum XY distances is not as critical as in near-surface surveys. For deep refractors and long wavelengths, the Fresnel zone radius

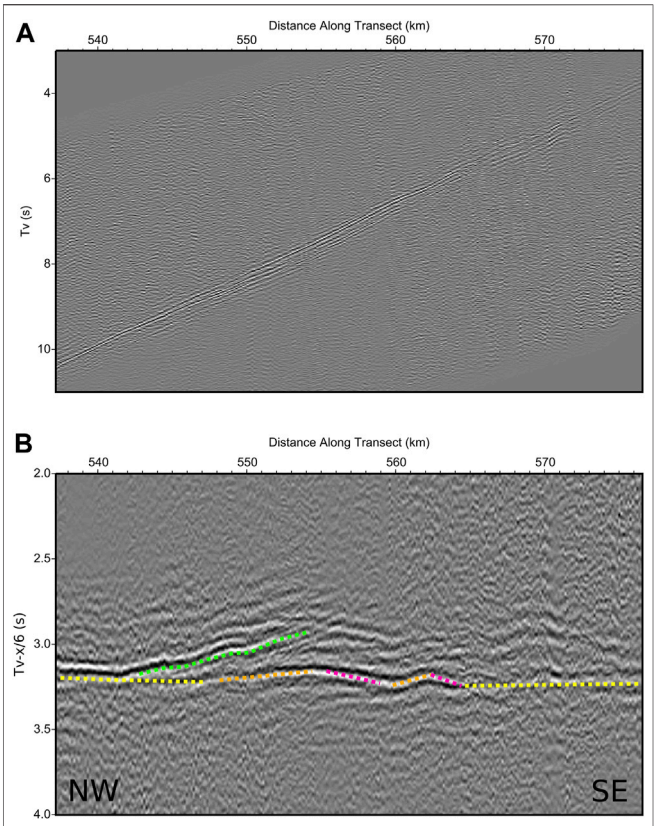


**FIGURE 7 |** Velocity analysis convolutional section for OBS pair 35–39, **(A)** original time, without reciprocal time correction, and **(B)** with 6 km/s reduction velocity. Note the lateral velocity variations, more clearly shown in **(B)**. In **(B)**, a downwards to the right slope indicates a velocity over 6 km/s and upwards a velocity lower than that. In yellow, areas of basement with velocities close to 6 km/s. In orange, lower velocities, in magenta, higher velocities. Note an area in green, low velocities possibly related to refractions above the basement, in the volcanic layer.

for head waves can be estimated in hundreds or even thousands of meters (Kvasnička and Červený, 1996; Jones and Drummond, 2001). A simple model-based estimation of the optimum XY, or the assumption of a plain XY = 0, can be both reasonable approaches for applying the refraction convolution section in deep surveys.

The major advantage of the refraction convolution section method over other refraction interpretation methodologies is that all the data can be convolved and stacked to maximize the signal-to-noise ratios, without the measurement of many travel times, just the reciprocal times are needed, reducing the time employed by the interpreter. Convolution and stacking are simple operations that involve small computational costs.

Can this methodology be applied to other deep seismic refractors? From a resolution and geometric point of view, the method is equally applicable to any refractor identified in the seismic sections. For deep refractors, such as the Moho refraction Pn in cortical-scale sections, the main difficulty is obtaining matching seismic arrivals in direct and inverse pairs, especially the reciprocal times, given the limited offset range of the energy generated by the air guns and recorded by the OBS. For the shallower sedimentary layers, the limitation is the distance between OBS, which prevents having pairs of OBS where direct and inverse shot information is received from the same point at the refractor. In all cases, care should be taken that the GRM methodology is based on sharp interfaces between constant velocity layers. Only critically reflected waves, or head waves, should be considered. Diving waves, from layers with vertical velocity gradients, should not be used.

## CONCLUSION

Different scalar interpretation methods of 2-dimensional refraction seismic data have been applied in the past, depending on the scale. On a crustal-scale, the traditional methods are based on ray tracing and synthetic seismogram calculation, and tomography methods. In near-surface refraction seismic interpretation, apart from tomography, delay time methods are frequently used. Among the delay time methods, one of the most popular is the Generalized Reciprocal Method. It is mostly assumed that the delay time methods are exclusive to shallow seismic exploration and have not been applied to deep problems. Based on interferometric imaging and migration, full-wave methods have been recently introduced for marine seismic refraction interpretation.

The stacked refraction convolution section provided a more detailed image of the basement in Tamayo Through Basin. Previous OBS-based velocity models offered low resolution. The MCS data, both the reflection migrated section or the supergather refractions model, lack deep enough penetration to image the basement properly. The interpretation of the stacked refraction convolution section confirms the presence of a constant thickness volcanic layer in the northwestern part of the basin. However, only thin volcanic deposits can be interpreted in the shallower part of the southeastern margin.

This paper has shown that the Generalized Reciprocal Method and its full-wave extension, the stacked refraction convolution section, are applicable for crustal-scale studies, with ocean bottom seismometers and air guns in marine sedimentary basins of several km of depth. The procedure is simpler than migration to implement. The main sources of uncertainty are the calculation of the reciprocal times, through the observation of the seismic records, and the evaluation of the static corrections needed because the OBS are located at depth. Furthermore, it is possible to calculate a velocity analysis convolutional section to analyze lateral variations of the basement seismic velocities. The main advantages of the stacked refraction convolutional section over traditional methods are: 1) it is not necessary to measure travel times for all records, just reciprocal times, reducing data processing times; 2) it is possible to compare the results with multichannel reflection seismic sections directly; 3) it is a simple methodology that involves small computational cost; 4) the results can be used in an initial OBS tomography model or to obtain further details of the basement in ray tracing.

## DATA AVAILABILITY STATEMENT

Publicly available datasets were analyzed in this study. This data can be found here: http://ds.iris.edu/mda/04-018/.

## AUTHOR CONTRIBUTIONS

The author confirms being the sole contributor of this work and has approved it for publication.

## FUNDING

Funding was provided by Centro de Investigación Científica y de Educación Superior de Ensenada (CICESE). Data were acquired as part of the projects Seismic and Geologic Study of Gulf of California Rifting and Magmatism, Sea of Cortez Continental Extension and Rifting, and The PESCADOR Seismic Experiment, and funding was provided by NSF grants OCE01-11738, OCE01-11983, OCE01-12058, OCE01-12149, and OCE01-12152.

## ACKNOWLEDGMENTS

I thank the three reviewers of this manuscript for their useful suggestions, which have raised the standard of this paper. Data processing was carried out with CWP/SU: Seismic Un*x open-source software developed by Center for Wave Phenomena, Colorado School of Mines, and currently maintained by John Stockwell.

## REFERENCES

Abera, R., van Wijk, J., and Axen, G. (2016). Formation of continental Fragments: The Tamayo Bank, Gulf of California, Mexico. *Geology*. 44 (8), 595–598. doi:10.1130/G38123.1

Červený, V., and Pšenčík, I. (1984). "SEIS83: Numerical Modeling of Seismic Wave fields in 2-D Laterally Varying Layered Structures by the ray Method," in *Documentation of Earthquake Algorithms, Report SE-35*. Editor E.R. Engdahl (Boulder, CO: World Data Center A for Solid Earth Geophysics), 36–40.

de Franco, R. (2005). Multi-Refractor Imaging with Stacked Refraction Convolution Section. *Geophys. Prospect.* 53 (3), 335–348. doi:10.1111/j.1365-2478.2005.00478.x

de Franco, R. (2010). Refractor Velocity Analysis: a Signal Processing Procedure. *Geophys. Prospecting.* 59, 432–454. doi:10.1111/j.1365-2478.2010.00931.x

Hagedoorn, J. G. (1959). The Plus-Minus Method of Interpreting Seismic Refraction Sections. *Geophys. Prospect.* 7, 158–182. doi:10.1111/j.1365-2478.1959.tb01460.x

Hobro, J. W. D., Singh, S. C., and Minshull, T. A. (2003). Three-Dimensional Tomographic Inversion of Combined Reflection and Refraction Seismic Traveltime Data. *Geophys. J. Int.* 152 (1), 79–93. doi:10.1046/j.1365-246X.2003.01822.x

Hobro, J. W. D. (1999). *Three-dimensional Tomographic Inversion of Combined Reflection and Refraction Seismic Travel-Time Data, Ph.D. Thesis, Department of Earth Sciences*. Cambridge, United Kingdom: University of Cambridge.

Hole, J. A. (1992). Nonlinear High-Resolution Three-Dimensional Seismic Travel Time Tomography. *J. Geophys. Res.* 97, 6553–6562. doi:10.1029/92JB00235

Jones, L. E. A., and Drummond, B. J. (2001). Effect of Smoothing Radius on Refraction Statics Corrections in Hard Rock Terrains. *ASEG Extended Abstr.* 2001, 1–4. doi:10.1071/ASEG2001ab065

Korenaga, J., Holbrook, W. S., Kent, G. M., Kelemen, P. B., Detrick, R. S., Larsen, H.-C., et al. (2000). Crustal Structure of the Southeast Greenland Margin From Joint Refraction and Reflection Seismic Tomography. *J. Geophys. Res.* 105, 21591–21614. doi:10.1029/2000JB900188

Kvasnička, M., and Červený, V. (1996). Analytical Expressions for Fresnel Volumes and Interface Fresnel Zones of Seismic Body Waves. Part 2: Transmitted and Converted Waves. Head Waves. *Studia Geophysica et Geodaetica.* 40, 381–397. doi:10.1007/BF02300766

Leung, T. M. (1995). Examination of the Optimum XY Value by ray Tracing. *Geophysics.* 60, 1151–1156. doi:10.1190/1.1443843

Leung, T. M. (2003). Controls of Traveltime Data and Problems of the Generalized Reciprocal Method. *Geophysics.* 68, 1626–1632. doi:10.1190/1.1620636

Lizarralde, D., Axen, G. J., Brown, H. E., Fletcher, J. M., González-Fernández, A., Harding, A. J., et al. (2007). Variation in Styles of Rifting in the Gulf of California. *Nature.* 448, 466–469. doi:10.1038/nature06035

Matsuoka, T., Taner, M. T., Hayashi, T., Ashida, Y., Watanabe, T., and Kusumi, H. (2000). *Imaging of Refracted Waves by Convolution70th SEG Meeting*. Calgary, Canada: Expanded Abstracts, 1187–1190. doi:10.1190/1.1815638

Meléndez, A., Korenaga, J., Sallarès, V., Miniussi, A., and Ranero, C. R. (2015). TOMO3D: 3-D Joint Refraction and Reflection Traveltime Tomography Parallel Code for Active-Source Seismic Data-Synthetic Test. *Geophys. J. Int.* 203 (1), 158–174. doi:10.1093/gji/ggv292

Palmer, D. (1980). *The Generalized Reciprocal Method of Seismic Refraction Interpretation*. Tulsa OK: Society of Exploration Geophysicists. doi:10.1190/1.9781560802426

Palmer, D. (1981). An Introduction to the Generalized Reciprocal Method of Seismic Refraction Interpretation. *Geophysics.* 46, 1508–1518. doi:10.1190/1.1441157

Palmer, D. (2001a). *Digital Processing of Shallow Seismic Refraction Data with the Refraction Convolution Section. Ph.D. Thesis*. Australia: University of New South Wales.

Palmer, D. (2001b). Imaging Refractors With the Convolution Section. *Geophysics.* 66, 1582–1589. doi:10.1190/1.1487103

Palmer, D. (2001c). A New Direction for Shallow Refraction Seismology: Integrating Amplitudes and Traveltimes With the Refraction Convolution Section. *Geophys. Prospecting.* 49, 657–673. doi:10.1046/j.1365-2478.2001.00293.x

Palmer, D., and Jones, L. (2005). A Simple Approach to Refraction Statics With the Generalized Reciprocal Method and the Refraction Convolution Section. *Exploration Geophys.* 36, 18–25. doi:10.1071/EG05018

Seisa, H. (2007). *Is the Optimum XY Spacing of the Generalized Reciprocal Method (GRM) Constant or Variable? 67th Annual Meeting of the German Geophysical Society (DGG)*. Editor E. V. Deutsche Geophysikalische Gesellschaft. Aachen, Germany. doi:10.4133/1.2924699

Sjögren, B. (2000). A Brief Study of Applications of the Generalized Reciprocal Method and of Some Limitations of the Method. *Geophys. Prospecting.* 48, 815–834. doi:10.1046/j.1365-2478.2000.00223.x

Sutherland, F. H. (2006). *Continental Rifting across the Southern Gulf of California. Ph.D. Thesis*. San Diego CA: University of California San Diego.

Sutherland, F. H., Kent, G. M., Harding, A. J., Umhoefer, P. J., Driscoll, N. W., Lizarralde, D., et al. (2012). Middle Miocene to Early Pliocene Oblique Extension in the Southern Gulf of California. *Geosphere.* 8 (4), 752–770. doi:10.1130/GES00770.1

Umhoefer, P. J., Dorsey, R. J., Willsey, S., Mayer, L., and Renne, P. (2001). Stratigraphy and Geochronology of the Comondú Group Near Loreto, Baja California sur, Mexico. *Sediment. Geology.* 144, 125–147. doi:10.1016/S0037-0738(01)00138-5

Verpahovskaya, A. O., Pilipenko, V. N., and Pylypenko, E. V. (2017). Formation Geological Depth Image According to Refraction and Reflection marine Seismic Data. *Geofizicheskiy Zhurnal.* 39 (6), 106–121. doi:10.24028/gzh.0203-3100.v39i6.2017.116375

Whiteley, R. J., and Eccleston, P. J. (2006). Comparison of Shallow Seismic Refraction Interpretation Methods for Regolith Mapping. *Exploration Geophys.* 37 (4), 340–347. doi:10.1071/EG06340

Yang, H., and Zhang, J. (2019). Reverse Time Migration of Refraction Waves in OBS Data. *Photon. Electromagnetics Res. Symp. Fall.* 1, 2812–2817. doi:10.1109/PIERS-Fall48861.2019.9021637

Zelt, C. A., and Barton, P. J. (1998). Three-Dimensional Seismic Refraction Tomography: A Comparison of Two Methods Applied to Data from the Faeroe Basin. *J. Geophys. Res.* 103, 7187–7210. doi:10.1029/97JB03536

Zelt, C. A., and Smith, R. B. (1992). Seismic Traveltime Inversion for 2-D Crustal Velocity Structure. *Geophys. J. Int.* 108, 16–34. doi:10.1111/j.1365-246X.1992.tb00836.x

Zhang, J., ten Brink, U. S., and Toksöz, M. N. (1998). Nonlinear Refraction and Reflection Travel Time Tomography. *J. Geophys. Res.* 103, 29743–29757. doi:10.1029/98JB01981

**Conflict of Interest:** The author declares that the research was conducted in the absence of any commercial or financial relationships that could be construed as a potential conflict of interest.

frontiers in Earth Science

ORIGINAL RESEARCH
published: 23 September 2021
doi: 10.3389/feart.2021.666272

# The Extended Continental Crust West of Islas Marías (Mexico)

*Diana Núñez[1*†], Jorge A. Acosta-Hernández[1†], Felipe de Jesús Escalona-Alcázar[1,2†], Simone Pilia[3†], Francisco Javier Núñez-Cornú[1†] and Diego Córdoba[4†]*

[1]Sismología y Volcanología de Occidente, CUCosta, Universidad de Guadalajara, Puerto Vallarta, Mexico, [2]Unidad Académica de Ciencias de la Tierra, Universidad Autónoma de Zacatecas, Zacatecas, Mexico, [3]Department of Earth Sciences-Bullard Labs, University of Cambridge, Cambridge, United Kingdom, [4]Departamento de Física de la Tierra y Astrofísica, Universidad Complutense de Madrid, Madrid, Spain

The crustal structure around the Islas Marías Archipelago has been debated for a long time. An important unresolved question is where the Rivera-North American plate subduction ends and the Tamayo fracture zone begins, from SE to NW. Results from the TsuJal project have shed light on the northwesternmost part of the Jalisco block structure. It is now clear that Sierra de Cleofas and the Islas Marías Escarpment comprise the northwestern continuation of the Middle America trench. However, other questions remain. In this paper, we present the structure of the shallow and deep crust and the upper mantle of the Islas Marías western region through the integration of multichannel seismic reflection, wide-angle seismic bathymetric and seismicity data, including records of an amphibious seismic network, OBS, and portable seismic stations, purposely deployed for this project, providing an onshore-offshore transect of 310 km length. Our findings disclose new evidence of the complex structure of the Rivera plate that dips 8°–9° underneath the NW Jalisco block as revealed by two seismic profiles parallel to the Islas Marías Escarpment. Moreover, we find five sedimentary basins and active normal faults at the edges of tectonic structures of the E-W oriented West Ranges and the N-S trending Sierra de Cleofas. Furthermore, the Sierra de Cleofas is the beginning of the active subduction of the Rivera plate beneath North America. The oceanic crust thickens and submerges towards the south while is coupled with the continental crust, from 6 km at the northern ends of the seismic profiles to 15 km in the contact region and 24 km at the coast and southern ends of them. The continental Moho was not fully characterized because of the geometry of the seismic transects, but a low-velocity layer associated with Rivera Plate subduction was observed beneath the Jalisco Block. Our results constrain the complexity of the area and reveal new structural features from the oceanic to continental crust and will be pivotal to assess geohazards in this area.

**Keywords: Islas Marías archipelago, crustal structure, basins, OBS, amphibious seismic network**

OPEN ACCESS

***Edited by:***
*Pier Paolo Bruno,*
*University of Naples Federico II, Italy*

***Reviewed by:***
*Takeshi Sato,*
*Japan Meteorological Agency, Japan*
*Drew Eddy,*
*BHP Billiton, Australia*

****Correspondence:***
*Diana Núñez*
*diana@sisvoc.mx*

*†ORCID:*
*Diana Núñez*
*orcid.org/0000-0003-0572-3905*
*Jorge A. Acosta-Hernández*
*orcid.org/0000-0002-6709-3577*
*Felipe de J. Escalona-Alcázar*
*orcid.org/0000-0002-4066-6160*
*Simone Pilia*
*orcid.org/0000-0002-3125-042X*
*Francisco J. Núñez-Cornú*
*orcid.org/0000-0003-1515-1349*
*Diego Córdoba*
*orcid.org/0000-0003-1106-3632*

***Specialty section:***
*This article was submitted to Solid Earth Geophysics, a section of the journal Frontiers in Earth Science*

***Received:*** *09 February 2021*
***Accepted:*** *27 August 2021*
***Published:*** *23 September 2021*

***Citation:***
*Núñez D, Acosta-Hernández JA, Escalona-Alcázar FdeJ, Pilia S, Núñez-Cornú FJ and Córdoba D (2021) The Extended Continental Crust West of Islas Marías (Mexico). Front. Earth Sci. 9:666272. doi: 10.3389/feart.2021.666272*

## INTRODUCTION

The study of active oceanic margins is the subject of numerous investigations globally, especially in regions whose boundaries are not well defined. Such is the case for the northern limit of the Rivera plate (RP). Traditionally, the northern limit has been defined as the Tamayo Fracture Zone (TFZ); however, the extent of this fracture zone and precisely where the North American plate (NOAM) begins along the region between Islas Marías and Bahía de Banderas (**Figure 1**) is not obvious. The Islas Marías Archipelago is located in the northern part of the RP and south of the Gulf of California mouth and includes San Juanito, María Madre, Magdalena, and Cleofas Islands (**Figure 1**). The origin of the islands is related to the opening of the Gulf of California (Lonsdale, 1989). This archipelago has a poorly-understood, complex tectonic history, with fragments of continental crust in several island's (San Juanito, María Madre and María Cleofas) (Pompa-Mera et al., 2013; Schaaf et al., 2015a), fragments of oceanic crust in María Magdalena (Schaaf et al., 2015b) and intraplate alkali basalts with mantle xenoliths (Isabel Island) (Ortega-Gutiérrez and González-González, 1980; Housh et al., 2010) (**Figure 1**).

The oceanic RP originated as a fragment of the Farallon plate with independent movement starting about 10 Ma (Atwater, 1970; Lonsdale, 1989). The RP, together with the Cocos plate (CP), interact with the NOAM through active subduction, whose morphotectonic expression is the Middle America Trench (MAT). Currently, the RP subducts beneath NOAM from the northern tip of the MAT to the south and forms new seafloor along its western boundary, the Pacific-Rivera rise (DeMets and Traylen, 2000). The southern boundary of the RP is shared with the CP and is currently defined by the transform Rivera Fault zone. Recent seismic studies of the southern boundary demonstrate that this limit is characterized by significant tectonic complexity (Núñez-Cornú et al., Submitted).

The tectonic complexity of the Islas Marías Archipelago is also evidenced by high seismicity that has generated earthquakes of moderate to large magnitudes, such as the M > 7.0, December 3, 1948 earthquake that occurred next to the Islas Marías Archipelago and caused significant damage to María Madre Island. Recent seismicity has been analyzed by Tinoco-Villa (2015) and constrained with the systematic recording by the Jalisco Seismic and Accelerometric Network (RESAJ in Spanish) (Núñez-Cornú et al., 2018). The historical seismicity of this region suggests that earthquakes of M > 7.5 have occurred. Some of the largest events occurred on June 3 and 18, 1932, with Ms 8.2 and 7.8, respectively, with an area of rupture from Bahía de Banderas to the Colima rift. In October 1995, a Ms 8.0 earthquake took place in the region, breaking only the southern half of the 1932 earthquake rupture area (Escobedo et al., 1998).

Recently, in the western Mexican margin, new geologic and marine geophysical research has been carried out to study the interaction between RP, CP, and NOAM (Núñez-Cornú et al., 2016; Dañobeitia et al., 2016; Núñez et al., 2019; Carrillo-de la Cruz et al., 2019, among others) and characterize the potentially tsunamigenic and seismogenic structures to assess geohazards and risks of this region. During the active acquisition stage of the TsuJal project, a combined off- and onshore experiment included two combined seismic methods, multichannel and wide-angle seismic, and multibeam bathymetry from Islas Marías (Nayarit

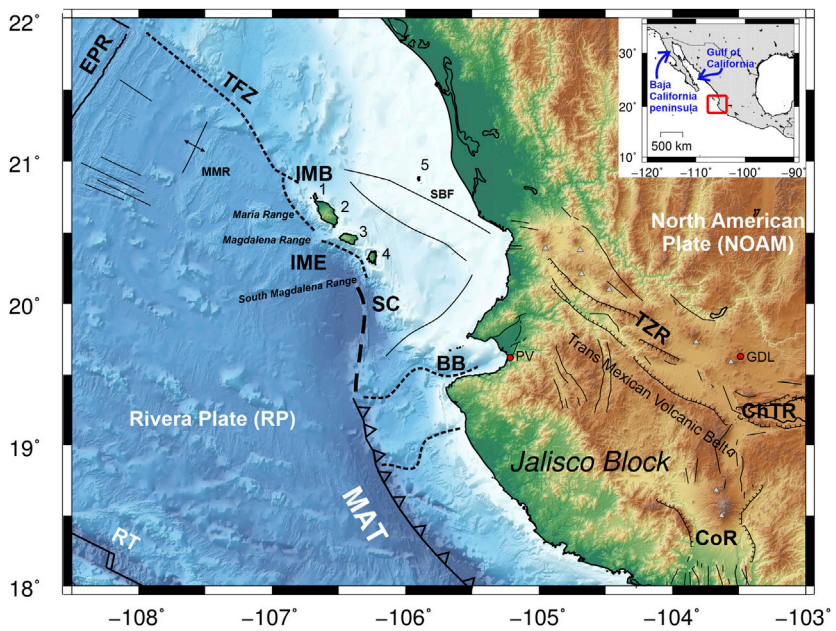


**FIGURE 1 |** Topographic map and tectonic setting of the western Mexican region. *Abbreviations*: *BB*, Bahía de Banderas; *CoR*, Colima rift; *ChTR*, Chapala-Tula rift; *EPR*, East Pacific Rise; *GDL*, Guadalajara; *IMB*, Islas Marías Block; *IME*, Islas Marías Escarpment; *MAT*, Middle America trench; *MMR*, María Magdalena Rise; *PV*, Puerto Vallarta; *RT*, Rivera Transform; *SBF*, San Blas fault; *SC*, Sierra de Cleofas; *TFZ*, Tamayo fault zone; *TZR*, Tepic–Zacoalco rift; *1*, San Juanito Island; *2*, María Madre Island; *3*, María Magdalena Island; *4,* María Cleofas Island; *5*, Isabel Island. (*Inset*) Location map of the study area within the North American continent.

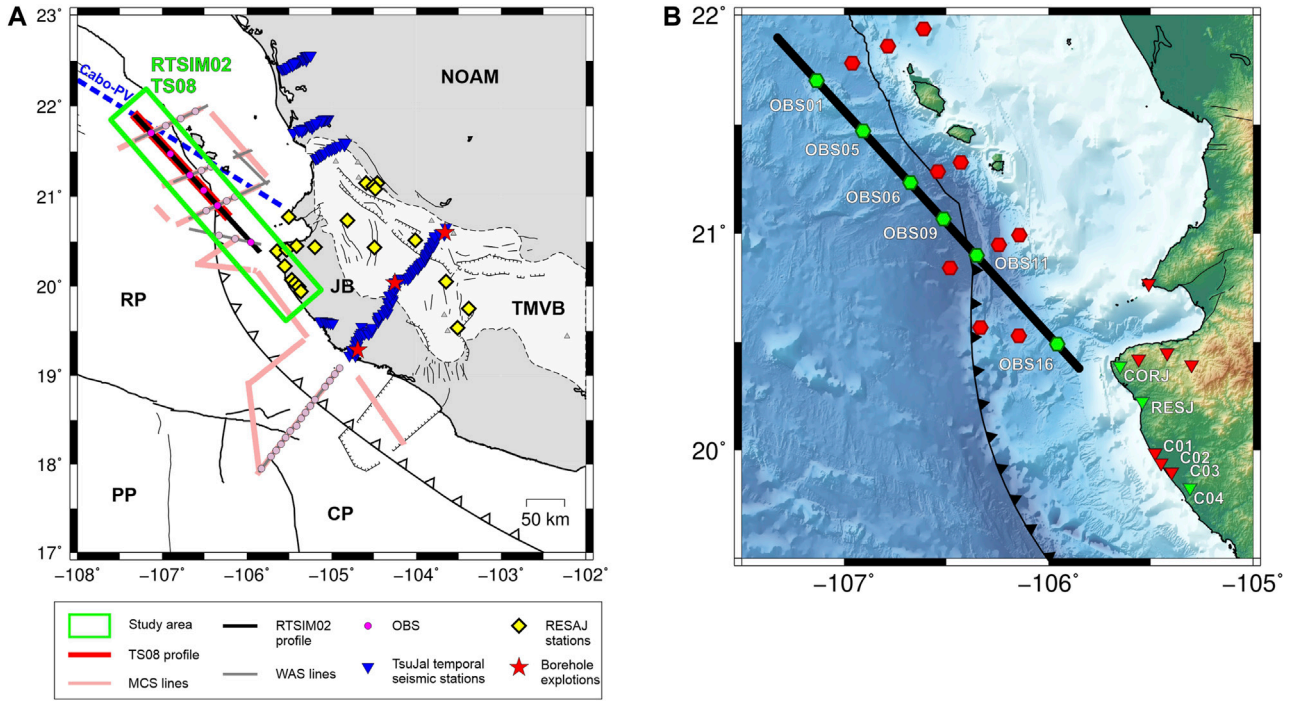


**FIGURE 2 | (A)** TsuJal experiment deployment map. Symbols are depicted in the legend below the Panel, and abbreviations are the same as in **Figure 1**. Dash blue line denotes Cabo-Puerto Vallarta segment studied by Lizarralde et al. (2007). Abbreviations: CP, Cocos plate; JB, Jalisco block; MCS, Multichannel Seismic; NOAM, North American plate; OBS, Ocean-bottom seismometer; PP, Pacific plate; RESAJ, Jalisco Seismic Accelerometric Telemetric Network stations; RP, Rivera plate; TMVB, Trans-Mexican volcanic belt; WAS, wide-angle seismic. **(B)** Deployment map in the study area with seismic stations used to generate the P-wave velocity model of RTSIM02 seismic transect (green symbols). Red polygons denote the seismic stations deployed but not used in this study.

state) to the south of Manzanillo (Colima state) (**Figure 2A**) (Dañobeitia et al., 2016; Núñez-Cornú et al., 2016). In this composite tectonic scenario, we focused on the crustal study of the western Islas Marías Archipelago. Here, we present the results by comparing a new P-wave velocity model from wide-angle seismic data with a multichannel seismic profile and hypsometric map of the northwestern boundary of the archipelago, which allow us to define the tectonic structures and interaction between RP and NOAM.

## REGIONAL TECTONIC SETTING

The interactions between RP-CP and RP-NOAM characterize the active western margin of Mexico (**Figure 1**). The tectonic processes include seafloor spreading, active subduction, transform faulting, and extensional zones (DeMets et al., 1994). Within the NOAM, the inland region is characterized by two relevant geologic and tectonic features, the Trans-Mexican Volcanic Belt (TMVB) and the Jalisco block (JB). The TMVB extends from Bahía de Banderas, Nayarit, to Los Tuxtlas volcano, Veracruz, with an E-W trend and an obliqueness of 16° from its central and eastern part to the Middle American Trench (MAT) (Ferrari, 2000). This volcanic arc presents variability in the style of volcanism, geochemical affinity, and width (Gómez-Tuena et al., 2018).

The other crucial tectonic feature of the NOAM is the JB. It is considered an independent tectonic unit of the NOAM, whose separation began in the Early Pliocene as a result of the Gulf of California rifting and subsequent extension (Luhr et al., 1985). The JB structural limit to the east is the Chapala-Tula rift with 100 km length and a width from 15 to 35 km (Luhr and Carmichael, 1990). The southeastern border of the JB is defined by the Colima rift, with a range of 190 km and a width of 20–65 km, whose seaward prolongation is the El Gordo-Manzanillo rift with an NNE-SSW trend extending from the coastline to few kilometers before the intersection with the MAT (Rutz-López and Núñez-Cornú, 2004). The northern border of the JB is the NW-SE oriented Tepic-Zacoalco rift (TZR) that is 250 km in length and has an average width of 50 km (Frey et al., 2007). The northwestern extension of the JB to the RP is considered to be the Tamayo fault zone (Bourgois and Michaud, 1991). Nevertheless, it is still not clearly defined and could also include the San Blas Fault or the Islas Marías Escarpment (IME) west of Islas Marías Archipelago.

In the offshore region, the southern and western JB boundaries correspond to the MAT. The RP is a young and small plate (Atwater, 1970), detached from the CP at about 5–10 Ma (DeMets and Traylen, 2000). Concerning the CP, NOAM, and JB, the relative movement of the RP has been the subject of study for a long time (Wilson and DeMets, 1998). The subduction of RP beneath JB is close to perpendicular to the MAT near Colima,

with a convergence rate of 5.0 cm/year to the NE (Bandy and Hilde, 2000). At the northwestern end, the convergence rate of RP beneath JB decreases to 2.0–3.0 cm/year and becomes oblique to the NNE (Kostoglodov and Bandy, 1995). Moreover, the dip angle of the subducting plate varies along the MAT. One of the first studies suggested an angle of 20° (Eissler and McNally, 1984); while Dañobeitia et al. (1997) argued that in the southern part, it is approximately 12° decreasing to the north to 7–8°. This almost-flat subduction angle has also been suggested by recent studies in this region (Gutiérrez-Peña et al., 2015; Núñez-Cornú et al., 2016; Núñez et al., 2019).

Detailed geologic and geophysical studies of the archipelago have been carried out only in recent years (e.g., Pompa-Mera et al., 2013; Schaaf et al., 2015a; Schaaf et al., 2015b; Ruiz-Martínez et al., 2016). In addition to the tectonic complexity of the poorly understood boundary between RP and NOAM, the structural and tectonic relationships between the continental and oceanic crust are vaguely understood in this region. Some seismic and tectonic studies around the archipelago provide new information about the structural characteristics to the north (Madrigal et al., 2021), west (Santibáñez-López, 2018), and south (Carrillo-de la Cruz et al., 2019). Further, the term "Islas Marías Block" (IMB) has been proposed as a tectonic unit bounded by the West Ranges, which are three linear morphological features controlled by NE-SW and NW-SE faults (Escalona-Alcázar et al., 2019).

In addition to the earthquakes caused by the subduction process between the RP and the NOAM, there are other tectonic structures in the north of the RP capable of producing seismic events of moderate magnitudes and significant seismic hazards (Marín-Mesa et al., 2019). In this region, the seismicity is principally concentrated around Sierra de Cleofas (SC) and Magdalena south fault, while in the north and east of the archipelago, seismic events are scarce (Tinoco-Villa, 2015; Núñez-Cornú et al., 2018; Escalona-Alcázar et al., 2019; Marín-Mesa et al., 2019). This scarcity could be due to the lack of seismic stations near the IMB, making it difficult to record and locate lower magnitude events or true quiescence. On December 4, 1948, an Mw 6.4 earthquake occurred at IME close to María Madre Island; the focal mechanism is consistent with high-angle reverse faults suggesting compression caused by oblique convergence in the accretionary prism (Jaramillo and Suárez, 2011). Other events occurred during January and February 2007 and September 2010 to the north and south of IMB, respectively, with Mw > 5.0. Additionally, Tinoco-Villa (2015) reported seismic swarms along the Sierra de Cleofas that could be grouped into families. The swarms occurred from October 2012 to February 2013 and were registered by the Jalisco Seismic Accelerometric Telemetric Network (RESAJ) (Núñez-Cornú et al., 2018).

# DATA AND METHODOLOGIES (MATERIALS AND METHODS)

The main tectonic structures from the western region of Islas Marías to the Jalisco coast were characterized using the seismic lines RTSIM02 and TS08 obtained during the active part of the TsuJal project (Núñez-Cornú et al., 2016). During February and March 2014, Spanish and Mexican researchers carried out the deployment and collection of multidisciplinary data offshore and onshore in western Mexico with the participation of the British oceanographic research vessel *RRS James Cook* during the cruise JC098. In a month of fieldwork, the RRS James Cook was tasked with providing the seismic source, deploying and collecting the ocean-bottom seismometers (OBSs), as well as acquiring multichannel seismic reflection (MCS), multibeam and high-resolution bathymetry, and potential fields (magnetism and gravity) data. The wide-angle seismic (WAS) data were recorded by the RESAJ stations, an on-land temporary seismic network, and the OBSs, particularly deployed for this project.

## Wide-Angle Seismic Data Acquisition and Seismic Phases

The RTSIM02 seismic transect was located west of the Islas Marías, parallel to the coastline, in a northwest-southeast orientation (**Figure 2A**). The shooting line had an approximate length of 230 km, where 749 shots were performed. The source design was adapted to this experiment to obtain the maximum possible energy concentrated in the lowest frequency range and the maximum possible offset distance. **Table 1** shows the seismic source parameters used for this transect. These shots were recorded by seismic stations located both on the continent and on the ocean bottom.

Throughout the RTSIM02 seismic profile, the WAS acquisition was recorded on six short-period OBSs (model LC2000SP with L28 three-component geophone sensors, natural frequency of 4.5 Hz), and a single HiTech HYI-90-U hydrophone deployed at OBS1, OBS5, OBS6, OBS9, OBS11, and OBS16 locations. On land, four Quanterra Q330S (Kinemetrics) instruments with LE-3D Lennartz sensor (1 Hz) were installed at C01, C02, C03, and C04 locations, as well as two permanent stations of the RESAJ network, were used (RESJ and CORJ) with the same type of sensors as the temporary land-based stations, making a total of 12 seismic instruments (**Figure 2B**). The WAS transect had a total length of 320 km.

The raw seismic data were processed, including band-pass filtering and merging with navigation data, corrections due to clock drift of instruments, and zero-phase band-pass filters (4–10 Hz). Traveltime corrections follow the methodology presented in Núñez et al. (2016). The P-wave phase interpretation was completed with the bathymetry and topography data (**Figures 3**, **4**).

P-wave refracted and reflected phases were correlated to determine the different discontinuities in the crust and the uppermost mantle along the RTSIM02 profile. The apparent velocities of refracted waves were determined for the generation of the initial velocity and depth distribution. We identified five refracted phases [two within the sediments ($P_{S1}$, $P_{S2}$), one within the crust ($P_g$), one in the lower crust ($P_{LC}$), and one within the uppermost mantle ($P_n$)], one reflected phase in the lower crust ($P_{LC}P$), one crust-mantle boundary reflection ($P_MP$),

**TABLE 1 |** Seismic source parameters used during the RTSIM02 wide-angle (WAS) and the TS08 multichannel seismic (MCS) data acquisition.

| Seismic source parameters | WAS | MCS |
|---|---|---|
| Source controller | Big Shot® | Big Shot® |
| Source type | Bolt® G.Guns 1500LL | Bolt® G.Guns 1500LL |
| Air pressure | 2,000 psi | 2,000 psi |
| Volume | 6,800 $in^3$ | 3,540 $in^3$ |
| Compressors | 4 × Hamworthy® $4^{TH}$ 565 W100 | 4 × Hamworthy® $4^{TH}$ 565 W100 |
| Number of air-guns and strings | 11 air-guns in 5 strings | 12 air-guns in 4 strings (3 air-gun/string) |
| Synchronization | ±0.1 ms | ±0.1 ms |
| Deployment depth | 15 m | 8 m |
| Trigger interval | 120 s | 50 m |

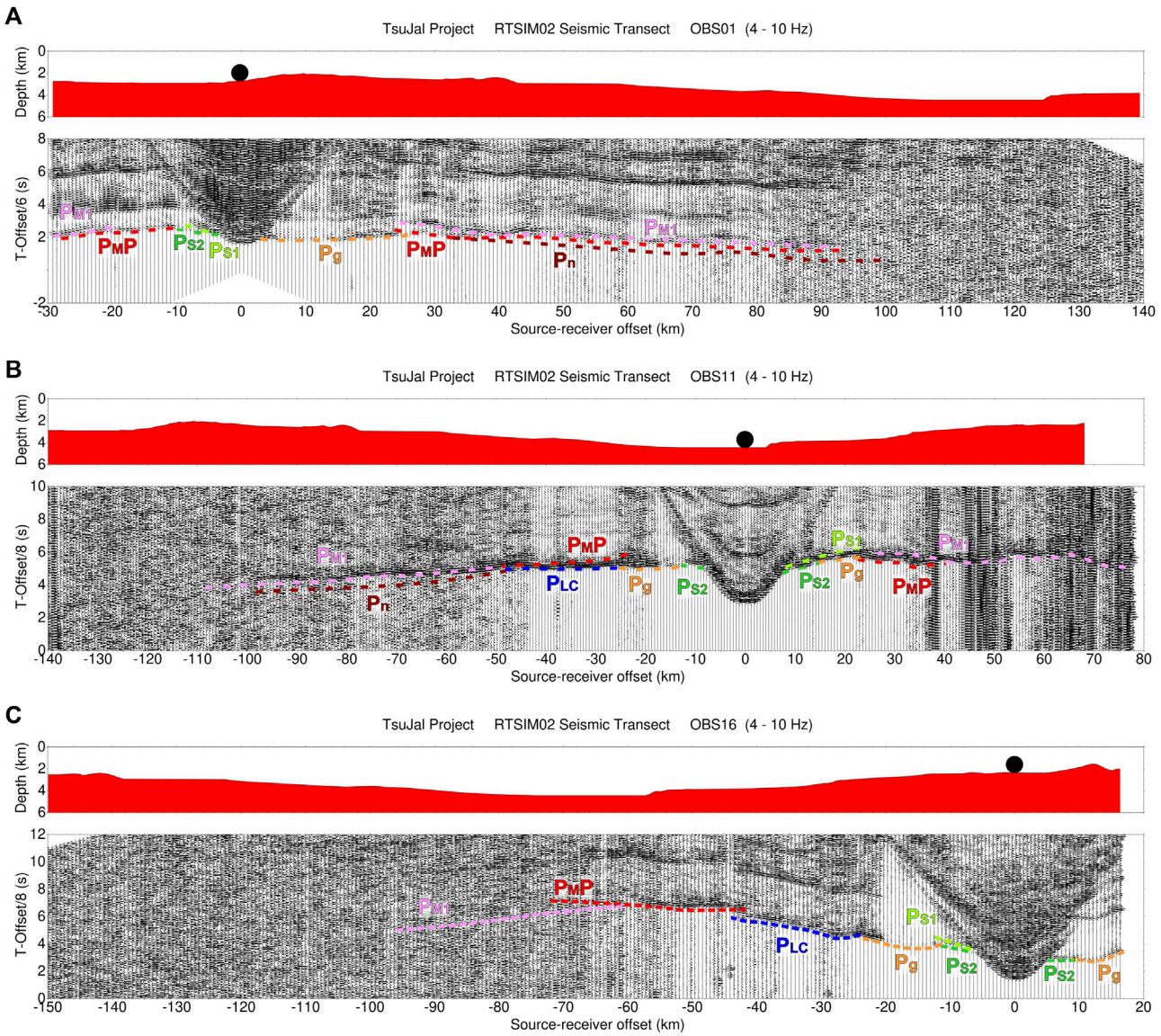


**FIGURE 3 |** Record sections of the marine seismic stations recording the RTSIM02 seismic transect. All of them have the bathymetry along with the RTSIM02 seismic profile in the upper panel. The lower panel shows the vertical component of the corresponding station with a reduced velocity of 6 km/s (OBS01) and 8 km/s (OBS11 and OBS16), 4–10 Hz band-pass filter applied, trace-normalized amplitudes, and interpreted reflected and refracted P-wave horizons indicated by different color dashed lines. **(A)** OBS01; **(B)** OBS11; **(C)** OBS16.

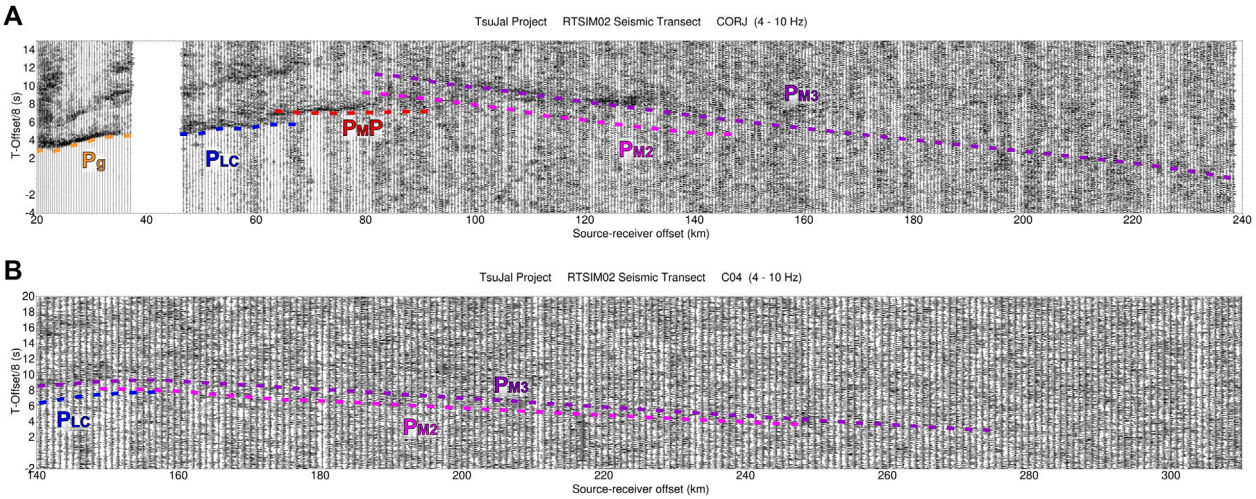


**FIGURE 4 |** Record sections of the terrestrial seismic stations recording the RTSIM02 seismic transect. Each panel shows the vertical component of the corresponding station with a reduced velocity of 8 km/s, 4–10 Hz band-pass filter applied, trace-normalized amplitudes, and interpreted reflected and refracted P-wave horizons indicated by different color dashed lines. **(A)** CORJ. **(B)** C04.

and three reflections in the first layers of the upper mantle $P_{M1}$, $P_{M2}$, and $P_{M3}$.

The OBS sections show phases traveling through the sediments, crust, and the most upper mantle discontinuity (**Figures 3A–C**), while the land station sections provide better insights into the most profound upper mantle boundaries (**Figures 4A,B**). A total of 5,402 first arrivals ($P_{S1}$, $P_{S2}$, $P_g$, $P_{LC}$, and $P_n$), $P_{LC}P$, $P_MP$, and reflections in the upper mantle were manually picked. A weighted average estimation for each phase picking error was calculated (**Supplementary Table S1**) following the methodology proposed by Núñez et al. (2016). The picking error estimation consisted in determining the individual uncertainties in arrival time picking of every seismic phase, adding the uncertainty due to the offset distance between the seismometer position and the shooting line. This factor was significant for seismic phases recorded by land stations. The two-dimensional (2-D) velocity and structure model was obtained after assembling the travel-time interpreted picks and using the Rayinvr software (Zelt and Smith, 1992) for forward modeling, while for travel-time inversion, we applied TOMO2D (Korenaga et al., 2000). Additional water depth and elevation values from bathymetry and navigation data provided by RRS James Cook and a regional digital elevation model were included. We established the origin of the model distance along this transect from a selected point located 30 km north of the OBS01 (**Figure 2**).

## Multichannel Seismic and Bathymetry Data

MCS data acquisition was carried out by a streamer of 5.85 km length (468 active channels, separated 12.5 m) deployed at 10 m depth. The common depth point (CDP) distance is 6.25 m, providing a CDP nominal fold of 58–59 traces. These data were sampled at 1 ms and recorded initially in SEG-D format. The technical parameters of the seismic source used in this study are shown in **Table 1**. The TS08 seismic line consisted of 3,445 shots with a total length of 172 km approximately.

The MCS data processing was carried out by Seismic Unix software (Cohen and Stockwell, 2013), applying the main stages and parameters shown in **Table 2**. Finally, we obtain our MCS images of the TS08 seismic profile.

The bathymetric data were acquired from a Kongsberg EM120 and Kongsberg EM710 multibeam echosounders mounted aboard the RRS James Cook. Using bathythermograph (XBT) probes, sound velocity profiles in the water column were obtained daily and included during processing.

The data recovered in the area of the RTSIM02 and TS08 seismic profiles were processed using CARIS HIPS and SIPS (Teledyne) software, including sound speed and tide corrections provided by CICESE (Centro de Investigación Científica y de Educación Superior de Ensenada). During this processing stage, vertical and horizontal data produced georeferenced data, including calculating the total propagated uncertainty for each sounding. Finally, regular grid and variable resolution surfaces with different filters and editors were applied to generate the final bathymetric surface with an 80 × 80 m resolution grid, which was interpolated and depicted using System for Automated Geoscientific Analyses (SAGA) and Geographic Information Systems (GIS) (Conrad et al., 2015).

# RESULTS

## MCS and Bathymetry Data

The bathymetric map shows the seafloor structures and their trends (**Figure 5**). The structural features of the continental borderland of the JB were described by Núñez-Cornú et al. (2016), Carrillo-de la Cruz et al. (2019). However, those of the RP near the JB are poorly known. During the TsuJal project, the

**TABLE 2 |** Processing flow applied to the TS08 multichannel seismic profile using Seismic Unix.

| Process | Parameters |
|---|---|
| Format change | SEG-D to SU |
| Trace and shot editing | Antialias and bad traces killed (252 and 260). Dummy events (486-495, 747-751, 811-821) |
| Bandpass filtering | 4-6-130-150 Hz |
| Predictive deconvolution | Maximum lag 200 ms, minimum lag 13.4 ms |
| Geometry specifications | CDP gathering |
| Bandpass filtering | 4-6-120-130 Hz |
| Velocity analysis | Semblance spectra, each 100 CDP |
| NMO correction | Velocity model |
| Stack | Velocity model |
| Second predictive deconvolution | Maximum lag 133 ms, minimum lag 5 ms |
| Migration | Phase-shift method |

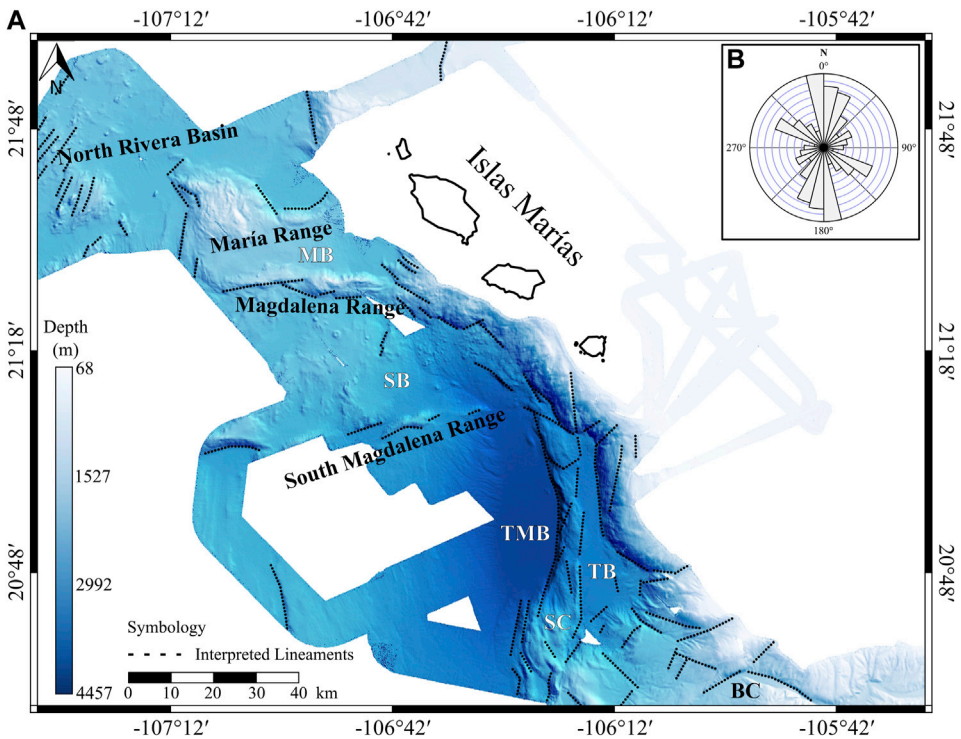


**FIGURE 5 |** Bathymetry map of the western Islas Marías region. **(A)** Hypsometric map with interpreted surface lineaments. **(B)** Bidirectional rose diagram of the structural features interpreted from bathymetry showing a N-S preferential tendency. Black dotted lines represent the interpreted lineaments observed. Data obtained with EM120 multibeam echosounder and processed with CARIS Hips and Sips (v.10.4). *Abbreviations*: *BC*, Banderas Canyon; *MB*, Magdalena basin; *SB*, Sisvoc basin; *SC*, Sierra de Cleofas; *TB*, TsuJal basin; *TMB*, Tres Marías basin.

new detailed bathymetry allowed us to generate a detailed seafloor map and combine it with the seismic reflectors. The seafloor patterns show that ranges and basins are structurally controlled. From NW to SE (**Figure 5A**), the Magdalena basin lies between the E-W oriented María and Magdalena ranges (Escalona-Alcázar et al., submitted). To the SE, the Sisvoc basin is limited by the ENE-WSW South Magdalena range (Escalona-Alcázar et al., submitted). To the south, this range is the northern limit of the larger Tres Marías basin (Núñez-Cornú et al., 2016) (**Figure 5A**). The continental borderland structures south of the Islas Marías Archipelago are mostly oriented N-S (**Figure 5B**) (Carrillo-de la Cruz et al., 2019). This structural trend changes to NW-SE along the IME, being oblique to the María, Magdalena, and South Magdalena ranges.

The TS08 seismic profile is oriented NW-SE, parallel to the Islas Marías Archipelago trend and the RP. This profile was made to characterize the shallow structure west of the archipelago. We divided the seismic section into three zones (I to III) according to the structures observed (**Figure 6**). Zone I is 90 km long, counting the CDPs 28,000 to 13,500. Normal faults define the morphology; the horsts are the María and Magdalena ranges (**Figure 6B**), while the grabens are the North Rivera, Magdalena, and Sisvoc basins.

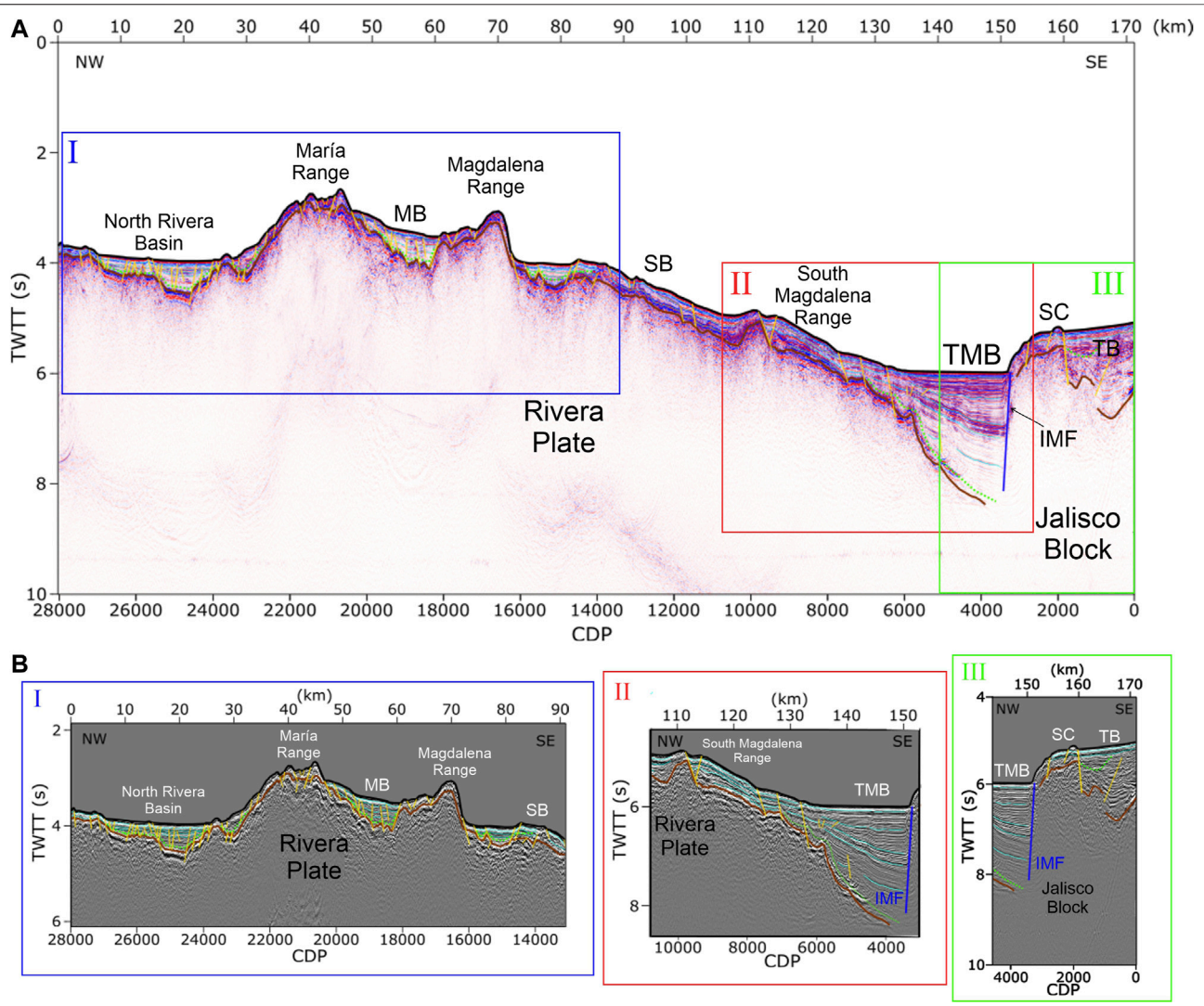


**FIGURE 6 |** TS08 Multichannel Seismic Profile. **(A)** Migrated seismic line with Zones I, II, and III indicated for a better interpretation. **(B)** Enlargements of Zones I, II, and III. *Abbreviations*: *CDP*, Common Depth Point; *IMF*, Islas Marías fault; *MB*, Magdalena basin; *SB*, Sisvoc basin; *SC*, Sierra de Cleofas; *TB*, TsuJal basin; *TMB*, Tres Marías basin; *TWTT*, two-way travel time.

The North Rivera basin has a buried horst in the middle; the two small basins show slightly tilted seismic reflectors to the SE, with a slim splayed array. The faults are no longer active since the uppermost reflector is subhorizontal in the whole basin. The maximum sedimentary depth is 0.6 s of TWTT. The structure of the Magdalena basin are normal faults, actually inactive, showing a synthetic array. The seismic reflectors are somewhat tilted to the SE. The Magdalena and South Magdalena ranges are the Sisvoc basin, showing subhorizontal seismic reflectors in its first 10 km. Advancing to the SE, zone II (**Figure 6B**) corresponds to the southern part of the Sisvoc Basin, the South Magdalena range, and the Tres Marías basin (TMB). The acoustic basement is faulted and composed of gabbroic intrusions and basalts overlayed by thin sedimentary layers of silt and clay according to the lithologies found at the DSDP site 473 (Yeats et al., 1981). The TMB has the maximum sedimentary thickness of the profile, equal to 2.5 s of TWTT. The main feature of this zone is the tilting to the SE and the splay array of the seismic reflectors towards the Islas Marías fault (IMF) (**Figure 6**). This array suggests that the IMF is currently active. Zone III is located in the southern part of the profile, with the IMF, SC, and TB as the main tectonic structures in this region (**Figure 6B**). The TB has 1.0 s of TTWT of sedimentary thickness, with its reflectors gently tilted to the NW.

## WAS Data

Modeling of the RTSIM02 data produced a P-wave velocity model that constrains sedimentary, crustal, and uppermost mantle structures of the western region of Islas Marías to a depth of 60 km. The model origin was placed at the northwesternmost shot location of the seismic line, 29.3 km from the OBS01 (**Figure 7**).

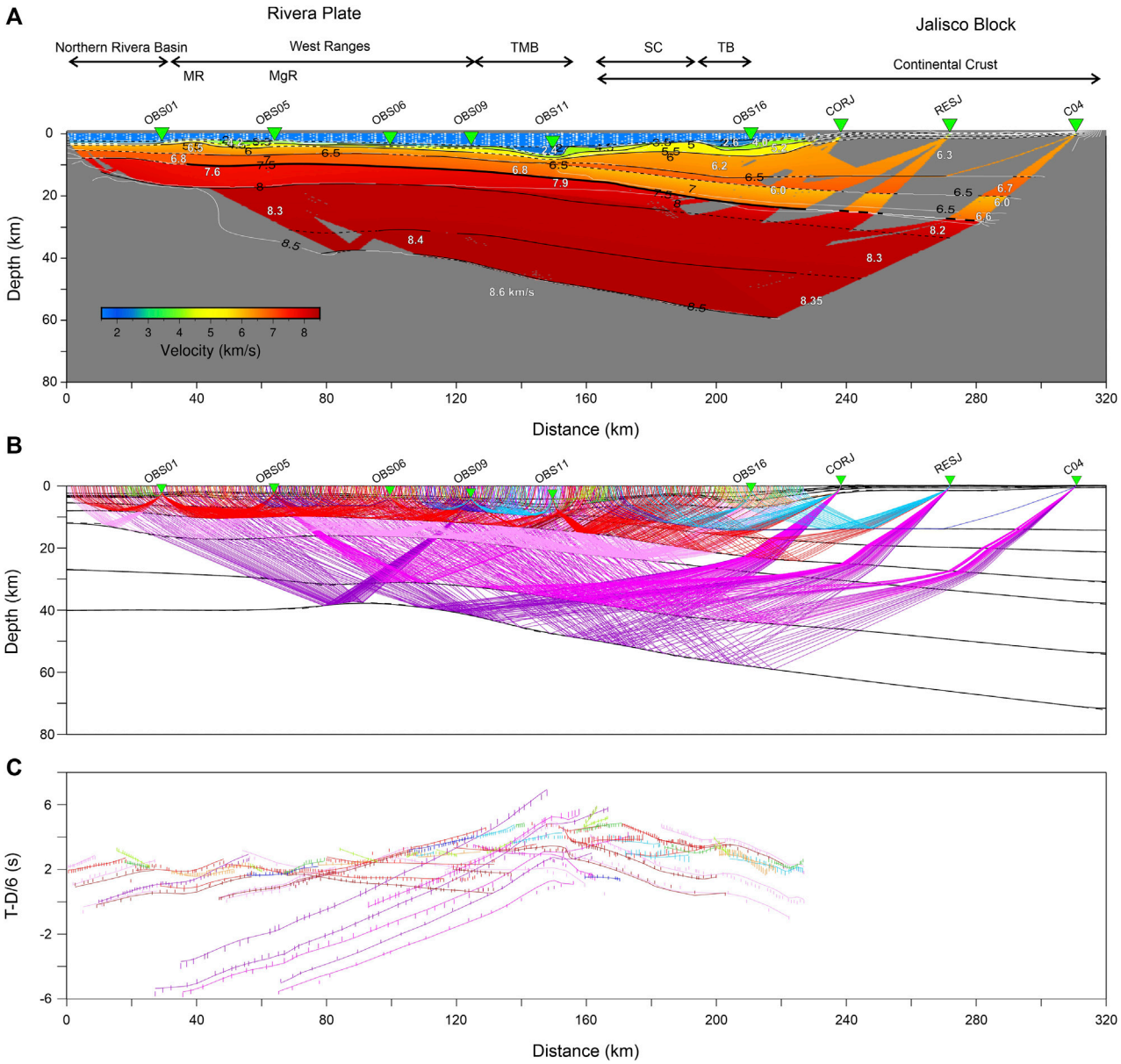


**FIGURE 7 | (A)** Final RTSIM02 P-wave velocity model across the western region of Islas Marías (Mexico). Black inverted triangles depict land stations of the TsuJal RTSIM02 seismic profile. Vertical and horizontal axes show depth below sea level and model position, respectively. The colored area is the region where ray tracing provides the velocity values. Black lines describe layer boundaries, and the thick ones mark positions where rays are reflected, showing the well-defined areas. The gray zone represents the area not crossed by rays. **(B)** Ray tracing and velocity model with average velocities in km/s. **(C)** Comparison between observed (vertical bars) and calculated (lines) travel times. In all panels, distances refer to the velocity model origin. *Abbreviations*: *MgR*, Magdalena range; *MR*, María range; *SC*, Sierra de Cleofas; *TB*, TsuJal basin; *TMB,* Tres Marías basin.

A 2 km-thick sedimentary sequence was imaged along the North Rivera Basin, composed of two layers whose velocity range varies from 2.5 km/s to 4.5 km/s top to bottom (**Figure 7A**). In the Magdalena basin, between the María and Magdalena ranges (40–50 km model distance), the sedimentary cover thickens from 2.0 to 4.6 km depth with similar velocities as the North Rivera Basin. From the Magdalena range, the Sisvoc basin throughout TMB, the seafloor deepens to ~2.0 and 4.1 km while the sediment layers are thickened 1.5–2.6 km. The TMB is characterized by a lateral velocity variation between 2.3 and 2.4 km/s at the top and 4.1–4.3 km/s at the bottom, being the first sedimentary layer ~3 km thick. To the southeast, the Sierra de Cleofas divides the TMB from TB. The TB presents two layers of sediments with P-wave velocities of 2.4-2-6 km/s and 4.0–4.2 km/s, and thicknesses of 2.1 and 1.2 km, respectively.

In the Rivera Plate region, a thin layer is located under the sedimentary cover with P-wave velocities between 5.1 and 5.3 km/s, and its lower limit would be associated with the

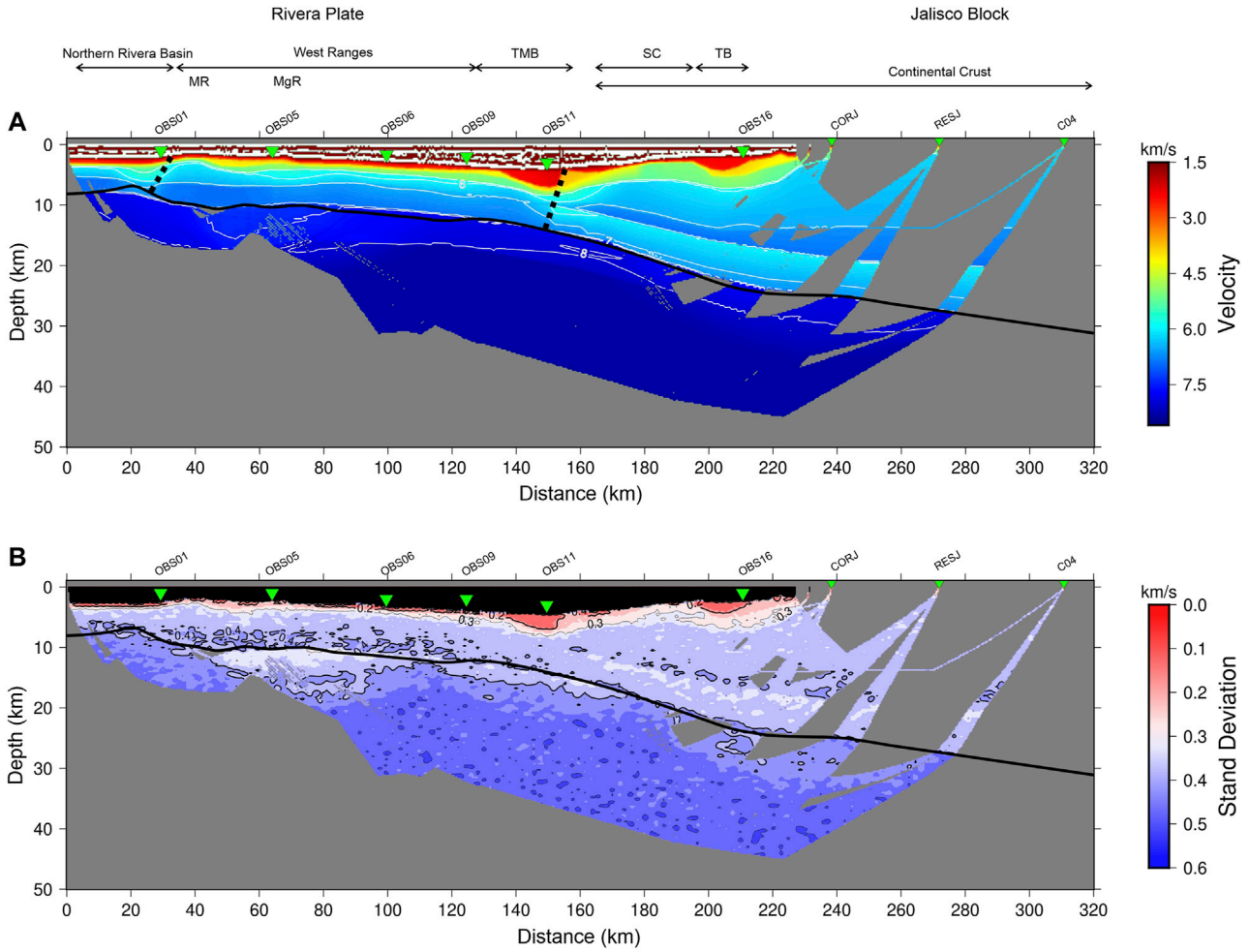


**FIGURE 8 | (A)** Final RTSIM02 seismic velocity model after inverting wide-angle refractions and reflections with TOMO2D. The black thick line shows the location of the Moho reflector and oblique dash black lines denote the region interpreted as extended and thinned continental crust. **(B)** Final standard deviation values for the P-wave velocity values resulted from the statistical uncertainty analysis.

acoustic basement observed in the TS08 profile. This layer has a maximum thickness of 0.5 km in the north Rivera basin region, approximately 1 km below the West Ranges (conjointly called the María, Magdalena, and South Magdalena ranges), increasing towards the TMB. In the Sierra de Cleofas and TB region up to the coastal zone, this layer appears thickened with values of 2–2.5 km, while in the continental region, the thickness decreases to values to less than 1 km.

The lower crust is characterized as thin in the oceanic region, showing a vertical gradient from 6.0–6.9 km/s with average thicknesses of 6 km and a cortical thickness between 7 and 9 km with a velocity contrast of 6.9–7.8 km/s. In the contact zone between RP and JB, the lower crust dips with an angle of 8°–9°, where the Moho is located deeper than 15 km, increasing in depth towards the coastal zone where it reaches 24 km. Due to the spatial arrangement of land seismic stations in the profile, it has not been possible to characterize continental Moho, but a low-velocity layer associated with RP subduction was observed under JB. Throughout the RTSIM02 seismic profile, we identified three seismic layers in the upper mantle with velocities increasing in depth, reaching maximum values of 8.6 km/s at 60 km depth.

Once adjusted for travel time and controlled by amplitudes through synthetic seismogram calculations, our model reproduces 5,246 of 5,402 (97%) of observed travel times throughout the entire length of the profile (320 km). We determined the arrival-time fit quality ($\chi^2_N$) for each interpreted phase with the following values for $P_{S1}$ (0.8), $P_{S2}$ (0.9), $P_g$ (1.0), $P_{LC}P$ (1.2), $P_{LC}$ (1.0), $P_MP$ (1.0), $P_n$ (0.9), and reflected P-phases observed in the mantle $P_{M1}$ (1.6), $P_{M2}$ (1.3), and $P_{M3}$ (1.2). Our final model is not far from the ideal case ($\chi^2_N = 1$) producing a $\chi^2_N$ of 1.2 (**Supplementary Table S1**).

## Tomography and Resolution

The seismic structure of the western Islas Marías Archipelago along RTSIM02 is constrained by the inversion of our wide-angle seismic travel time data for the previous 2D P-wave velocity model. We used a layer stripping strategy to find a seismic velocity model that fits our data by linear inversions. First, we

carried out an inversion of 897 first-arriving crustal phases ($P_{S1}$, $P_{S2}$, $P_g$, and $P_{LC}$) to create a smooth image of the seismic velocity structure with a root-mean-square misfit of 0.17 s. Secondly, we incorporated the $P_MP$ phases (1,087 travel-time picks) in our inversion with the initial Moho discontinuity reflector obtained from the previous forward 2D seismic velocity model. For the last inversion, $P_n$ phases (978 travel-time picks) and Moho reflector obtained from the previous inversion were included. Our simultaneous wide-angle refraction and reflection travel-times inversion constrains the boundary depths and velocities of the crust and upper mantle throughout our seismic profile (**Figure 8A**). We used a total of 2,962 travel-time picks.

The uncertainty of our velocity model was determined by calculating the standard deviation of successful inversions of random velocity models. The result of inverting 100 Monte Carlo realizations is shown in **Figure 8B**. From seafloor to basement, the standard deviation obtained is less than 0.3 km/s, which increases until 0.4 km/s close to Moho depth. Below Moho, maximum values of standard deviation are less than 0.6 km/s.

The P wave velocity distribution and their standard deviation shown in **Figure 8** clearly define the Moho. Its depth varies between 9–11 km until the OBS11, increasing up to 25 km at the OBS16 in the Tres Marías Fault.

## DISCUSSION

Other studies in Western Mexico have used a variety of seismic techniques to understand the tectonic relationship between the various tectonic plates and formation of their related structures (Dañobeitia et al., 1997; Fabriol et al., 1999; Aragón-Arreola et al., 2005; Lizarralde et al., 2007; Brothers et al., 2012; Núñez-Cornú et al., 2016; Núñez et al., 2019; Carrillo-de la Cruz et al., 2019; among others). The region of the Gulf of California and the tectonic processes involved have been addressed with different seismic techniques. The crustal structure at the mouth of the gulf region was defined by wide-angle seismic profiles that included OBS and land stations (Lizarralde et al., 2007).

Some experiments used multichannel and wide-angle seismic profiles, either with or without OBS and land stations, perpendicular to the main structural trend of the Gulf of California (e.g., Fabriol et al., 1999; Aragón-Arreola et al., 2005; Brothers et al., 2012; Macías-Iñiguez et al., 2019), finding that the end of the continental crust is a sharp zone along most of the eastern margin of Baja California. However, in the eastern margin of the gulf, there is an ocean-continent transition zone with extension and thinned continental crust. These studies suggest different rifting and basin evolution styles, some of them with related volcanism and others without, based on the thermal state of the mantle and the rigidity of the lower crust (Lizarralde et al., 2007).

In the region between Puerto Vallarta and Los Cabos and extending a bit further to the NW within the gulf, the geophysical, multichannel, and wide-angle seismic profiles were carried out with general NW-SE orientation, such that the trend of these profiles is perpendicular to the ridges in the Gulf of California and the East Pacific Rise (Lizarralde et al., 2007; Páramo et al., 2008; Sutherland et al., 2012; Abera et al., 2016). From the western Mexico coastline to the SW, the results obtained from the seismic and geophysical profiles have revealed different deformation styles and structures. Close to the western Mexican continental margin, the Tamayo Banks were defined as a microcontinent (Abera et al., 2016), bound to the SW by the Tamayo fracture zone, while to the NW is the Alarcón basin with oceanic crust. The SE limit is the Tamayo trough, an extended portion of continental crust with poor oceanic crust development (Lizarralde et al., 2007; Sutherland et al., 2012; Abera et al., 2016). Next to the SE is the San Blas basin, the largest in the region, built on continental crust, with a sedimentary thickness of 2 s of TWTT and slightly deformed (Sutherland et al., 2012).

Previous seismic profiles west of the Islas Marías Archipelago have different lengths and different levels of detail. Páramo et al. (2008) made multichannel seismic profiles from Los Cabos to the East Pacific Rise (EPR), 150 km west of the Islas Marías Archipelago. The horst and graben array found in the continental crust and the sharp ocean-continent transition are similar to those found along the western gulf coast. There is evidence of syndepositional deformation and post tectonic sedimentation (Páramo et al., 2008). Lizarralde et al. (2007) presented the wide-angle seismic profile from Los Cabos to Puerto Vallarta close to the RTSIM02 and TS08 profiles. From NW to SE, Lizarralde et al. (2007) showed the oceanic crust of the María Magdalena Rise, followed by a thinned continental crust with a thin sedimentary cover until it reaches the Sierra de Cleofas. The velocity model has a lower crust with velocities of 6 km/s, which were associated with granitic rocks, velocities of ~5 km/s were associated with volcanic and sedimentary rocks, and those of <3 km/s related to sediments (Lizarralde et al., 2007; Páramo et al., 2008). In our velocity model (**Figure 8A**), the thinned continental crust region is defined from the West Ranges to Tres Marías basin and Sierra de Cleofas, with small basins in between (Magdalena and Sisvoc basins). The area along the profile TS08/RTSIM02 is in the seaside west of the IMF, oriented NW-SE. Its location offers a unique opportunity to understand the nature of the crust immediately west of the Islas Marías Archipelago. Along our seismic profile (**Figure 8A**), around OBS05 to OBS11 (next of the IMF), we observe a thin and continuous layer of ~1 km thickness with velocities belonging to granitic and volcanic/sedimentary rocks. This cover is underlain by ~5 km thick lower crust. These crustal velocities are in agreement with those reported from 6.0 to 6.6 km/s for the average continental crust in this region (Chulick and Mooney, 2002); nonetheless, it is only ~6 km thick. Below it, the velocity increases to >7 km/s, typical values at the base of layer 3 for the oceanic crust (Christeson et al., 2019). The velocity distribution varies from ~3 to 6.6 km/s, except in the TMB, where it decreases to 2.4 km/s due to the sedimentary cover thickening. Our velocity model is similar to that from Lizarralde et al. (2007); however, ours is able to characterize the uppermost part of the crust.

We compare three 1-D velocity–depth profiles across our seismic transect with compilations made for young and old oceanic crust formed at slow-spreading centers (age <7.5 Ma,

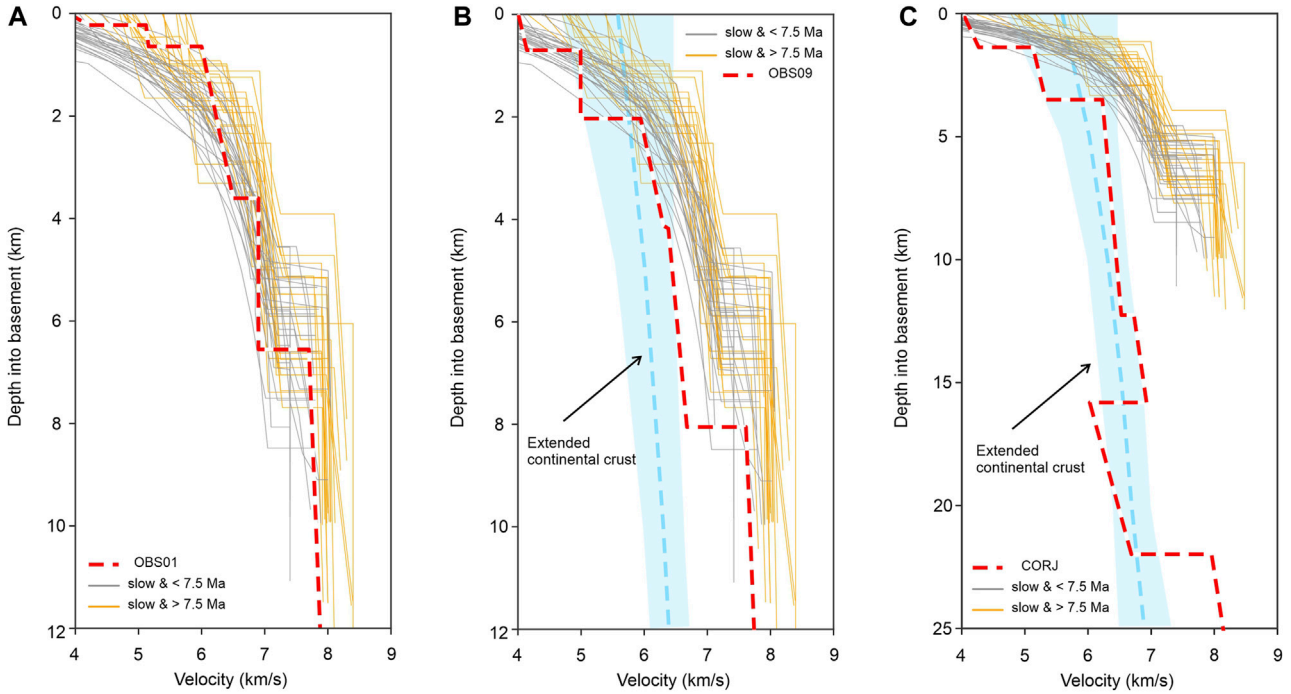


**FIGURE 9 |** 1-D velocity-depth profiles extracted from the final P-wave velocity model at distances corresponding to **(A)** OBS01 (30 km); **(B)** OBS09 (130 km), and **(C)** CORJ (210 km). We compare our velocity profiles with the range of typical velocity profiles for "young" and "old" oceanic crusts formed at slow-spreading centers (grey and orange 1-D profiles from Christeson et al. (2019) and extended continental crust (blue line, from Christensen and Mooney, 1995) with its uncertainty (light blue region).

> 7.5 Ma and 5–20 mm/yr half spreading rate, respectively, as defined by Christeson et al. (2019) as in Pilia et al. (2021). **Figure 9A** shows that our profile located at 30 km (OBS01) in the North Rivera Basin suggests velocities and thicknesses close to those reported for the young oceanic crust and according to RP age which is <7.5 Ma with possible remnants that could reach ca. 9 Ma (Lonsdale, 1989). However, in **Figure 9B**, our 1D velocity–depth profile at 130 km close to OBS09 (NE boundary of the Tres Marías Basin) is slower than the models of slow-spreading ridges (Christerson et al., 2019). This difference could be associated with the transition from oceanic to an extended and thinned continental crust, as proposed in the velocity model (**Figure 8A**), and could be related to gabbroic intrusions associated with the oceanic crust lithologic assemblage of María Magdalena Island (Schaaf et al., 2015b). **Figure 9C** also shows velocities slower than the young and old oceanic crust models characteristic of continental crust that is slightly extended in this region.

Our final velocity model in **Figure 8A** depicts a subparallel velocity distribution that gently becomes deeper and dips towards the SE. The velocities and thicknesses that characterize the crust have been considered as a continent-ocean transition (COT) in places like the Labrador Peninsula (Keen et al., 2018), the Flemish cap (Funck et al., 2003), or the South China Sea (Cameselle et al., 2015). In addition, due to the more detailed data, we were able to define the dip of the lower crust and the shallow structure of the NE edge of the Rivera plate. Based on our seismic reflection profile (**Figure 6**) and the velocity distribution (**Figure 8A**), the extended and thinned continental crust could vary from extended to extremely extended. From NW to SE the structural array is of horst (María, Magdalena and South Magdalena ranges) and grabens (Magdalena, Sisvoc and Tres Marías basins). In some parts, the extension could be large enough to break the continental crust and develop an oceanic one like the lithologic assemblage described in María Magdalena Island (Schaaf et al., 2015b). The lower crust gently dips to the SE until the Sierra de Cleofas with an angle of 8°–9° beneath the NW part of the Jalisco Block.

Our model integrated the bathymetric, multichannel, and wide-angle seismic data, together with the regional seismicity (see references in **Figure 10A**). Along with the TS08 multichannel seismic profile (**Figure 6**), the seismic reflectors are gently tilted to the SE and indicate post-depositional deformation in the North Rivera and Magdalena basins. In the northern part of the Sisvoc basin, the seismic reflectors are subhorizontal; then, they tilt to the SE until the northern fault bounding the South Magdalena range, where reflectors have a slight splay array towards this fault, suggesting that it is currently active. This observation is constrained by the seismicity around the region between the OBS9 and OBS11 (**Figure 9**). From the south of the Magdalena range, the seismic reflectors are faulted and tilted, following the slope direction. Although the sediments are faulted, these structures do not extend until the top of the sedimentary coverage; they are over-filled with thin post-rift sediments. At

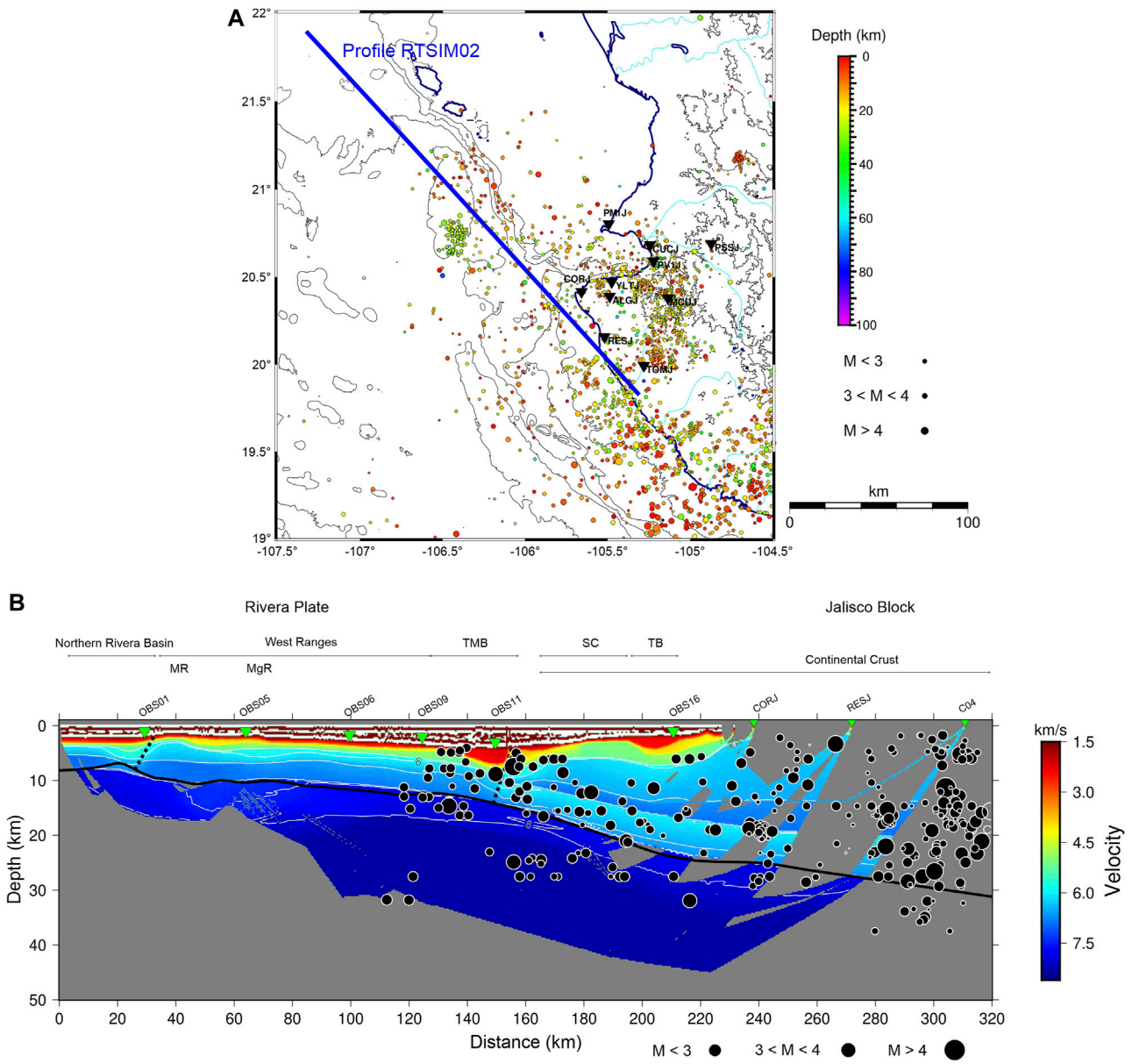


**FIGURE 10 | (A)** Seismicity map of western Mexico. Data sources obtained from Gutiérrez-Pena et al. (2015), Marín-Mesa et al. (2019), Núñez-Cornú et al. (2002), Núñez-Cornú et al. (2004), Núñez-Cornú et al. (2014), Núñez-Cornú et al. (2018), Núñez-Cornú et al. (2020), Rutz-López and Núñez-Cornú (2004), Rutz-López et al. (2013), Tinoco-Villa (2015). The blue line is the projection of seismicity throughout the RTSIM02 seismic profile with a width of 40 km. Black inverted triangles depict seismic stations which recorded these data. **(B)** RTSIM02 tomographic P-wave velocity model with the seismicity projected along the profile depicted in Panel **(A)** (40 km of total width). Abbreviations as for **Figure 7A**.

the change in slope, the reflectors dip, following it. Like in the Sisvoc basin, the lower sedimentary fill is faulted in the Tres Marías basins, while the uppermost layers are not. These faults are in an antithetic array with respect to Sierra de Cleofas (**Figure 6**). Covering the faults, the sedimentary layer is thin in the slope, but it thickens in the Tres Marías basin towards the SC, reaching a maximum sedimentary thickness of 1.7 s of TWTT with a splay array towards the fault (**Figure 6**).

**Figure 10A** shows the compilation of seismicity data in the study region carried out by the research group CA- SisVOc from different studies between 2002 and 2016 (Gutiérrez-Pena et al., 2015; Marín-Mesa et al., 2019; Núñez-Cornú et al., 2002; Núñez-Cornú et al., 2004; Núñez-Cornú et al., 2014; Núñez-Cornú et al., 2018; Núñez-Cornú et al., 2020; Rutz-López and Núñez-Cornú, 2004; Rutz-López et al., 2013; Tinoco-Villa, 2015). These data belong to different projects that SisVOc has been involved with, including RESAJ, MARS, and individual research projects. The hypocenters depicted were located using at least four P-phase and four S-phase readings. In some cases, P–Pn times were used to constrain hypocentral depths (Urías-Espinosa et al., 2016). The

criteria applied to select the better location were: root-mean-square (RMS) arrival time error <0.5 s, the epicentral and focal depth standard errors (ERH and ERZ, respectively) < 10.0 km. In the RP-JB contact region, the seismicity is mainly located above 40 km depth, which increases landward where the hypocenters reach maximum depths of 60 km at the coast. The hypocenter distribution shown in **Figure 10A** is in the uppermost part of the lithospheric mantle, the COT and the continental crust. These events are from the TMB towards the continent, being more abundant at the continental crust. The events distribution from TMB to TB could be related to the unbalanced stress and accommodation due to the NE movement of the Rivera Plate against the NW movement of the Jalisco Block. Both structural blocks could be coupled moving together, producing seismicity along the major faults. Previous studies in this region establish focal mechanisms of high-angle reverse faulting obtained from seismograms collected from regional and teleseismic stations (Jaramillo and Suárez, 2011), which could also be associated with the oblique convergence between RP and NAP. Additionally, the NW orientation of the MAT, whose end is bending towards the north, starts the N-S oriented Sierra de Cleofas (**Figure 1**), contributing to the unbalanced forces and the seismicity. Moreover, the splay array of the sedimentary reflectors in the TMB towards the IMF at the western edge of the Sierra de Cleofas suggests that the IMF is an active fault (**Figure 6B**).

**Figure 10B** shows the seismicity projected in a line of 320 km coincident with our RTSIM02 tomography velocity model (**Figure 8A**) with a total width of 40 km (20 km wide on each side of the line) to compare to the WAS and MCS results. The correlation between both data sets shows consistency with the structures we propose. Moreover, we observe that the seismicity data indicate the slab is subducting in this zone with a dip angle of 8° approximately, as previously was reported by Carrillo-de la Cruz et al. (2019) and less than reported by Núñez-Cornú et al. (2016).

The faults bounding the Sierra de Cleofas are active since the seismicity is widespread around it (**Figure 10**). Further research using the RESAJ network, as well as the records from the seismic stations installed in María Madre and María Cleofas islands, could improve the locations, depth, and azimuth coverage of the seismicity presents in the Islas Marías to determine the focal mechanisms and improve the tectonic evolution knowledge of the NW boundary of the Jalisco Block and its interaction with the Rivera Plate.

## CONCLUSION

The new multidisciplinary data acquired in the west of the Islas Marías Archipelago have allowed us to establish the cortical architecture of the transition between the oceanic crust of the Rivera Plate and the extended and thinned continental crust, where, from NW to SE, it is formed by the North Rivera basin, María range, Magdalena basin, Magdalena range, Sisvoc basin, South Magdalena range, and the Tres Marías basin. These new ranges and basins are defined along the RTSIM02 and TS08 profiles obtained by the new bathymetric and OBS–land stations combined wide-angle and multichannel seismic data.

The basins to the north of the South Magdalena range contain sedimentary cover that records the faulted syn-rift deposits covered by a thin post-rift sedimentary layer. The faults along the profile are active and inactive. Inactive faults cross-cut the lowermost sedimentary layers of the basins along with the profile. Simultaneously, active faults are located at the northern limit of the South Magdalena range and the Sierra de Cleofas, evidenced by the seismicity and the splay array of the sedimentary strata, where we establish the beginning of the northernmost active subduction between the Rivera and North American plates. In this region, the bottom of the crust dips from 8° to 9°.

This study contributes to the knowledge of the active tectonic structures in the Islas Marias Archipelago region, with potential implications on geohazard identification and associated risks in this area.

## DATA AVAILABILITY STATEMENT

The original contributions presented in the study are included in the article/**Supplementary Materials**, further inquiries can be directed to the corresponding author.

## AUTHOR CONTRIBUTIONS

DN: Conceptualization, methodology, investigation, data processing, data analysis, conclusions, and original draft writing. JA-H: Data processing, investigation. FE-A: Data analysis, methodology, investigation, original draft writing, and conclusions. SP: Data analysis, methodology, review and conclusions. FN-C: Conceptualization, funding acquisition, methodology, investigation, review, and editing. DC: Funding acquisition, review, and editing.

## FUNDING

This research was mainly funded by Consejo Nacional de Ciencia y Tecnología (CONACYT) –FOMIXJal (2012-08-189963) (Mexico), CGL (2011-29474-C02-01) (TsuJal Project) and RTI 2018-094827-B-C21 (KUK AHPAN Project) DGI Plan Nacional I + D + i (Spain); RESAJ network was funded by CONACYT–FOMIXJAL 2008–96538 (2009) (Mexico). JA-H was financially supported by a master fellowship from CONACyT with code 401435 and CVU 660422.

## ACKNOWLEDGMENTS

The authors gratefully acknowledge Wendy McCausland for her valuable comments and observations, including the English grammar revision that help to improve this article and Juan Luis Carrillo-de la Cruz for his help with bathymetric and 1-D velocity-depth profiles figures. The authors also truly appreciate

the colaboration during the TsuJal project of NOC Cruise JC098, RRS James Cook (United Kingdom); COIP/COPO/UNAM J-GAP2013 Cruise (BO El Puma); Unidad de Tecnología Marina (Spain); Secretaría de Marina (Mexico) ARM Holzinger; Secretaría de Defensa Nacional (Mexico); Unidad Municipal de Protección Civil y Bomberos (Jalisco State, Mexico); Unidad Municipal de Protección Civil y Bomberos (Puerto Vallarta, Mexico); Unidad Estatal de Protección Civil y Bomberos (Nayarit State, Mexico); Reserva de la Biosfera (Islas Marías) CONANP-SEMARNAT; Secretaría de Relaciones Exteriores (Mexico); and Órgano Desconcentrado de Prevención y Readaptación Social de la SEGOP. Some figures were generated using the Generic Mapping Tools (GMT-6; Wessel et al., 2019). SP acknowledges support from the European Union's Horizon 2020 research and innovation programme under Marie Skłodowska-Curie Grant Agreement 790203.

## SUPPLEMENTARY MATERIAL

The Supplementary Material for this article can be found online at: https://www.frontiersin.org/articles/10.3389/feart.2021.666272/full#supplementary-material

## REFERENCES

Abera, R., van Wijk, J., and Axen, G. (2016). Formation of continental Fragments: The Tamayo Bank, Gulf of California, Mexico. *Geology* 44, 595–598. doi:10.1130/G38123.1

Aragón-Arreola, M., Morandi, M., Martín-Barajas, A., Delgado-Argote, L., and González-Fernández, A. (2005). Structure of the Rift Basins in the central Gulf of California: Kinematic Implications for Oblique Rifting. *Tectonophysics* 409, 19–38. doi:10.1016/j.tecto.2005.08.002

Atwater, T. (1970). Implications of Plate Tectonics for the Cenozoic Tectonic Evolution of Western North America. *Geol. Soc. America Bull.* 81, 3513–3536. doi:10.1130/0016-7606(1970)81[3513:ioptft]2.0.co;2

Bandy, W. L., and Hilde, T. W. C. (2000). "Morphology and Recent History of the ridge Propagator System Located at 18° N, 106° W," in *Cenozoic Tectonics and Volcanism of Mexico. Geol. Soc. Am. Spec. Paper 334*. Editors H. Delgado-Granados, G. Aguirre-Díaz, and J. M. Stock (Boulder, Colorado, 29–40. doi:10.1130/0-8137-2334-5.29

Bourgois, J., and Michaud, F. (1991). Active Fragmentation of the North America Plate at the Mexican Triple junction Area off Manzanillo. *Geo-Marine Lett.* 11, 59–65. doi:10.1007/BF02431030

Brothers, D., Harding, A., González-Fernández, A., Holbrook, W. S., Kent, G., Driscoll, N., et al. (2012). Farallon Slab Detachment and Deformation of the Magdalena Shelf, Southern Baja California. *Geophys. Res. Lett.* 39, a–n. doi:10.1029/2011GL050828

Cameselle, A. L., Ranero, C. R., Franke, D., and Barckhausen, U. (2015). The Continent-Ocean Transition on the Northwestern South China Sea. *Basin Res.* 29, 73–95. doi:10.1111/bre.12137

Carrillo-de la Cruz, J. L., Núñez, D., Escalona-Alcázar, F. J., Núñez-Cornú, F. J., González-Fernández, A., Córdoba, D., et al. (2019). Tectonic Analysis of the Southern of María Cleofas Island from Bathymetric and Seismic Data. *Seismol. Res. Lett.* 90, 1748–1755.

Christensen, N. I., and Mooney, W. D. (1995). Seismic Velocity Structure and Composition of the continental Crust: A Global View. *J. Geophys. Res.* 100, 9761–9788. doi:10.1029/95jb00259

Christeson, G. L., Goff, J. A., and Reece, R. S. (2019). Synthesis of Oceanic Crustal Structure from Two-Dimensional Seismic Profiles. *Rev. Geophys.* 57 (2), 504–529. doi:10.1029/2019rg000641

Chulick, G. S., and Mooney, W. D. (2002). Seismic Structure of the Crust and Uppermost Mantle of North America and Adjacent Oceanic Basins: A Synthesis. *Bull. Seismological Soc. America* 92, 2478–2492. doi:10.1785/0120010188

Cohen, J. K., and Stockwell, J. W., Jr. (2013). *CWP/SU: Seismic Un*x Release No. 43R4: An Open Source Software Package for Seismic Research and Processing*. Center for Wave Phenomena, Colorado School of Mines.

Conrad, O., Bechtel, B., Bock, M., Dietrich, H., Fischer, E., Gerlitz, L., et al. (2015). System for Automated Geoscientific Analyses (SAGA) V. 2.1.4. *Geosci. Model. Dev.* 8, 1991–2007. doi:10.5194/gmd-8-1991-2015

Dañobeitia, J., Bartolomé, R., Prada, M., Nuñez-Cornú, F., Córdoba, D., Bandy, W. L., et al. (2016). Crustal Architecture at the Collision Zone between Rivera and North American Plates at the Jalisco Block: Tsujal projectGeodynamics of the Latin American Pacific Margin. *Pure Appl. Geophys.* 173, 3553–3573. doi:10.1007/978-3-319-51529-8_18

Dañobeitia, J. J., Córdoba, D., Delgado-Argote, L. A., Michaud, F., Bartolomé, R., Farrán, M., et al. CORTES-P96 Working Group (1997). Expedition Gathers New Data on Crust beneath Mexican West Coast. *Eos Trans. AGU* 78, 565–572. doi:10.1029/97eo00338

DeMets, C., Gordon, R. G., Argus, D. F., and Stein, S. (1994). Effect of Recent Revisions to the Geomagnetic Reversal Time Scale on Estimates of Current Plate Motions. *Geophys. Res. Lett.* 21, 2191–2194. doi:10.1029/94gl02118

DeMets, C., and Traylen, S. (2000). Motion of the Rivera Plate since 10 Ma Relative to the Pacific and North American Plates and the Mantle. *Tectonophysics* 318, 119–159. doi:10.1016/s0040-1951(99)00309-1

Eissler, H. K., and McNally, K. C. (1984). Seismicity and Tectonics of the Rivera Plate and Implications for the 1932 Jalisco, Mexico, Earthquake. *J. Geophys. Res.* 89, 4520–4530. doi:10.1029/jb089ib06p04520

Escalona-Alcázar, J. F., Núñez-Cornú, J. F., Núñez, D., and Córdoba-Barba, D. (2019). A Bathymetric and Structural Analysis of the Islas Marías Archipelago, Mexico, and Surroundings. *Submitted J. Struct. Geology.*, 90, 1748–1755. doi:10.1785/0220180398

Escobedo, D., Pacheco, J. F., and Suárez, G. (1998). Teleseismic Body-Wave Analysis of the 9 October, 1995 (Mw = 8.0), Colima-Jalisco, Mexico Earthquake, and its Largest Foreshock and Aftershock. *Geophys. Res. Lett.* 25, 547–550. doi:10.1029/98gl00061

Fabriol, H., Delgado-Argote, L. A., Dañobeitia, J. J., Córdoba, D., González, A., García-Abdeslem, J., et al. (1999). Backscattering and Geophysical Features of Volcanic Ridges Offshore Santa Rosalia, Baja California Sur, Gulf of California, Mexico. *J. Volcanology Geothermal Res.* 93, 75–92. doi:10.1016/S0377-0273(99)00084-0

Ferrari Pedraglio, L. (2000). Avances en el conocimiento de la Faja Volcánica Transmexicana durante la última década. *Bsgm* 53, 84–92. doi:10.18268/bsgm2000v53n1a5

Frey, H. M., Lange, R. A., Hall, C. M., Delgado-Granados, H., and Carmichael, I. S. E. (2007). A Pliocene Ignimbrite Flare-Up along the Tepic-Zacoalco Rift: Evidence for the Initial Stages of Rifting between the Jalisco Block (Mexico) and North America. *Geol. Soc. America Bull.* 119, 49–64. doi:10.1130/B25950.1

Funck, T., Hopper, J. R., Larsen, H. C., Louden, K. E., Tucholke, B. E., and Holbrook, W. S. (2003). Crustal Structure of the Ocean-Continent Transition at Flemish Cap: Seismic Refraction Results. *J. Geophys. Res.* 108, 2531. doi:10.1029/2003JB002434

Gómez-Tuena, A., Mori, L., and Straub, S. M. (2018). Geochemical and Petrological Insights into the Tectonic Origin of the Transmexican Volcanic Belt. *Earth-Science Rev.* 183, 153–181. doi:10.1016/j.earscirev.2016.12.006

Gutierrez, Q. J., Escudero, C. R., and Núñez-Cornú, F. J. (2015). Geometry of the Rivera-Cocos Subduction Zone Inferred from Local Seismicity. *Bull. Seismological Soc. America* 105 (6), 3104–3113. doi:10.1785/0120140358

Housh, T. B., Aranda-Gómez, J. J., and Luhr, J. F. (2010). Isla Isabel (Nayarit, México): Quaternary Alkalic Basalts with Mantle Xenoliths Erupted in the Mouth of the Gulf of California. *J. Volcanology Geothermal Res.* 197, 85–107. doi:10.1016/j.jvolgeores.2009.06.011

Jaramillo, S. H., and Suárez, G. (2011). The December 4, 1948, Islas Marías, Mexico Earthquake (Mw 6.4): Reverse Faulting beneath the Tres Marías Escarpment

and Implications for the Rivera-North American Relative Plate Motion. *Geofís. Int.* 50, 313–317. doi:10.22201/igeof.00167169p.2011.50.3.229

Keen, C. E., Dickie, K., and Dafoe, L. T. (2018). Structural Characteristics of the Ocean-Continent Transition along the Rifted continental Margin, Offshore central Labrador. *Mar. Pet. Geology.* 89, 443–463. doi:10.1016/j.marpetgeo.2017.10.012

Korenaga, J., Holbrook, W. S., Kent, G. M., Kelemen, P. B., Detrick, R. S., Larsen, H.-C., et al. (2000). Crustal Structure of the Southeast Greenland Margin from Joint Refraction and Reflection Seismic Tomography. *J. Geophys. Res.* 105 (B9), 21591–21614. doi:10.1029/2000JB900188

Kostoglodov, V., and Bandy, W. (1995). Seismotectonic Constraints on the Convergence Rate between the Rivera and North American Plates. *J. Geophys. Res.* 100, 17977–17989. doi:10.1029/95JB01484

Lizarralde, D., Axen, G. J., Brown, H. E., Fletcher, J. M., González-Fernández, A., Harding, A. J., et al. (2007). Variation in Styles of Rifting in the Gulf of California. *Nature* 448, 466–469. doi:10.1038/nature06035

Lonsdale, P. (1989). "Geology and Tectonic History of the Gulf of California," in *The Eastern Pacific Ocean and Hawaii. Geol. Soc. Am.* Editors E. L. Winterer, D. M. Hussong, and R. W. Decker (Boulder, Colorado. N: The Geology of North America), 499–521.

Luhr, J. F., and Carmichael, I. S. E. (1990). *Geology of the Volcán de Colima*, 107. Mexico City: Universidad Nacional Autónoma de México, Instituto de Geología, Boletín, 101.

Luhr, J. F., Nelson, S. A., Allan, J. F., and Carmichael, I. S. E. (1985). Active Rifting in Southwestern Mexico: Manifestations of an Incipient Eastward Spreading-ridge Jump. *Geol* 13, 54–57. doi:10.1130/0091-7613(1985)13<54:arismm>2.0.co;2

Macias-Iñiguez, I., Yarbuh, I., Spelz-Madero, R., González-Fernández, A., Fletcher, J. M., Contreras, J., et al. (2019). Modo de extension de la corteza y formacion del Sistema Extensional de Cerralvo, sur del Golfo de California, a partir de datos de reflexion sismica en 2D. *revmexcg* 36, 334–347. doi:10.22201/cgeo.20072902e.2019.3.1352

Madrigal, L. A., Núñez, D., Escalona-Alcázar, F. d. J., and Núñez-Cornú, F. J. (2021). Crustal Structure across the Northern Region of the Islas Marías Archipelago. *Front. Earth Sci.* 9. doi:10.3389/feart.2021.682206

Marín-Mesa, T., Núñez-Cornú, F. J., and Suárez-Plascencia, C. (2019). Analysis of the Seismicity in the Jalisco Block from June to December 2015. *Seism. Res. Lett.* 90, 1767–1778. doi:10.1785/0220190107

Núñez-Cornú, F. J., Gutiérrez-Peña, Q. J., Escudero, C. R., and Córdoba, D. (2014). Imaging the Rivera and Cocos Plates below Jalisco and Michocan Blocks from Seismicity Data. AGU Fall Meeting, San Francisco, California, 15–19 December 2014, Abstract T11C–4567.

Núñez, D., Córdoba, D., Cotilla, M. O., and Pazos, A. (2016). Modeling the Crust and Upper Mantle in Northern Beata ridge (CARIBE NORTE Project). *Pure Appl. Geophys.* 173, 1639–1661. doi:10.1007/s00024-015-1180-0

Núñez, D., Núñez-Cornú, F. J., Escalona-Alcázar, F. d. J., Córdoba, D., López Ortiz, J. Y., Carrillo de la Cruz, J. L., et al. (2019). Seismic Structure of the Southern Rivera Plate and Jalisco Block Subduction Zone. *Seismol. Res. Lett.* 90, 1756–1766. doi:10.1785/0220180399

Núñez-Cornú, F. J., Córdoba, D., Dañobeitia, J. J., Bandy, W. L., Figueroa, M. O., Bartolomé, R., et al. TsuJal Working Group (2016). Geophysical Studies across Rivera Plate and Jalisco Block, Mexico: TsuJal Project. *Seismological Res. Lett.* 87, 59–72. doi:10.1785/0220150144

Núñez-Cornú, F. J., Sandoval, J. M., Alarcón, E., Gómez, A., Suárez-Plascencia, C., Núñez, D., et al. (2018). The Jalisco Seismic Accelerometric Telemetric Network (RESAJ). *Seismol. Res. Lett.* 89, 363–372. doi:10.1785/0220170157

Núñez-Cornú, F. J., Escalona-Alcázar, F. d. J., Núñez, D., Trejo-Gómez, E., Suárez-Plascencia, C., and Rodríguez-Ayala, N. (2020). Study of Seismic Activity at Ceboruco Volcano (Nayarit, Mexico) in the Period 2012 to 2014. *J. South Am. Earth Sci.* 98, 102473. doi:10.1016/j.jsames.2019.102473

Núñez-Cornú, F. J., Marta, R. L., Nava P, F. A., Reyes-Dávila, G., and Suárez-Plascencia, C. (2002). Characteristics of Seismicity in the Coast and north of Jalisco Block, Mexico. *Phys. Earth Planet. Interiors* 132, 141–155. doi:10.1016/s0031-9201(02)00049-3

Núñez-Cornú, F. J., Reyes-Dávila, G. A., Lopez, M. R., Gomez, E. T., Camarena-García, M. A., and Ramírez-Vázquez, C. A. (2004). The 2003 Armeria, Mexico Earthquake (Mw 7.4): Mainshock and Early Aftershocks. *Seismological Res. Lett.* 75, 734–743. doi:10.1785/gssrl.75.6.734

Ortega-Gutiérrez, F., and González-González, R. (1980). Nódulos de peridotita en la Isla Isabel, Nayarit. *Rev. Mex. Cienc. Geol.* 4, 82–83.

Páramo, P., Holbrook, W. S., Brown, H. E., Lizarralde, D., Fletcher, J., Umhoefer, P., et al. (2008). Seismic Structure of the Southern Gulf of California from Los Cabos Block to the East Pacific Rise. *J. Geophys. Res.* 113, B03307. doi:10.1029/2007JB005113

Pilia, S., Ali, M. Y., Searle, M. P., Watts, A. B., Lü, C., and Thompson, D. A. (2021). Crustal Structure of the UAE-Oman Mountain Range and Arabian Rifted Passive Margin: New Constraints from Active and Passive Seismic Methods. *J. Geophys. Res. Solid Earth* 126 (4), e2020JB021374. doi:10.1029/2020jb021374

Pompa-Mera, V., Schaaf, P., Hernández-Treviño, T., Weber, B., Solís-Pichardo, G., Villanueva-Lascuraín, D., et al. (2013). Geology, Geochronology, and Geochemistry of Isla María Madre, Nayarit, Mexico. *Rev. Mex. Cienc. Geol.* 30, 1–23.

Ruiz-Martínez, V. C., Badillo-Cruz, E. R., Escalona-Alcázar, F. J., Núñez-Cornú, F. J., and Córdoba-Barba, D. (2016). Registro magnético de la paleotectónica de los plutones de María Madre y Puerto Vallarta (Cretácico Superior, México). *Geo-Temas* 16, 885–888.

Rutz López, M., Núñez Cornú, F. J., and Suárez Plascencia, C. (2013). Study of Seismic Clusters at Bahía de Banderas Region, Mexico. *Geofísica Internacional* 52, 59–72. doi:10.1016/s0016-7169(13)71462-4

Rutz-López, M., and Núñez-Cornú, F. J. (2004). Sismotectónica del norte y oeste del bloque de Jalisco usando datos sísmicos regionales. *GEOS* 24, 2–13.

Santibáñez-López, H. F. (2018). Imágenes Sísmicas en la Región Central de las Islas Marías. Maestría en Ciencias en Geofísica. M.Sc. Thesis Mexico: Universidad de Guadalajara, Puerto Vallarta, 105. ((In Spanish).

Schaaf, P., Böhnel, H., Weber, B., Hernández-Treviño, T., Solís-Pichardo, G., Pompa-Mera, V., et al. (2015a). Magmatic Activity at Islas Marías Archipelago: Key Events for Understanding Gulf of California Tectonics. 26th IUGG General Assembly. Prague, Czech. Czech Republic: Republic, VS-24. IAVCEI. IUGG-5302.

Schaaf, P. E. G., Solis-Pichardo, G., Hernandez-Trevino, T., Villanueva, D., Arrieta, G. F., Rochin, H., et al. (2015b). Magmatic Activity at Islas Marias Archipelago, Gulf of California: Oceanic Lithosphere with Gabbroic Sills versus Jurassic-Cretaceous Arc Components. Fall Meeting 2015. San Francisco (CA, USA). American Geophysical Union. Abstract Id V43B-3119.

Sutherland, F. H., Kent, G. M., Harding, A. J., Umhoefer, P. J., Driscoll, N. W., Lizarralde, D., et al. (2012). Middle Miocene to Early Pliocene Oblique Extension in the Southern Gulf of California. 8, 752–770. doi:10.1130/GES00770.1

Tinoco-Villa, M. E. (2015). Detección y Análisis de Enjambres Sísmicos en la Corteza Oceánica al Sur de las Islas Marías Maestría en Ciencias en Geofísica. M.Sc. Thesis Mexico: Universidad de Guadalajara, Puerto Vallarta, 69. ((in Spanish).

Urías Espinosa, J., Bandy, W. L., Mortera Gutiérrez, C. A., Núñez Cornú, F. J., and Mitchell, N. C. (2016). Multibeam Bathymetric Survey of the Ipala Submarine Canyon, Jalisco, Mexico (20°N): The Southern Boundary of the Banderas Forearc Block? *Tectonophysics* 671, 249–263. doi:10.1016/j.tecto.2015.12.029

Wessel, P., Luis, J. F., Uieda, L., Scharroo, R., Wobbe, F., Smith, W. H. F., et al. (2019). The Generic Mapping Tools Version 6. *Geochem. Geophys. Geosyst.* 20, 5556–5564. doi:10.1029/2019GC008515

Wilson, D. S., and DeMets, C. (1998). Reply [to "Comment on "Relative Motions of the Pacific, Rivera, North American, and Cocos Plates since 0.78 Ma" by Charles DeMets and Douglas S. Wilson"]. *J. Geophys. Res.* 103, 24251–24256. doi:10.1029/98JB02127

Yeats, R. S., Haq, B. U., Barron, J. A., Bukry, D., Crouch, J. K., Denham, C., et al. (1981). Initial Reports of the Deep Sea Drilling Project. *Initial Reports of the Deep Sea Drilling Project*, 63, 377–412. doi:10.2973/dsdp.proc.63.1981

Zelt, C. A., and Smith, R. B. (1992). Seismic Traveltime Inversion for 2-D Crustal Velocity Structure. *Geophys. J. Int.* 108, 16–34. doi:10.1111/j.1365-246x.1992.tb00836.x

**Conflict of Interest:** The authors declare that the research was conducted in the absence of any commercial or financial relationships that could be construed as a potential conflict of interest.

**Publisher's Note:** All claims expressed in this article are solely those of the authors and do not necessarily represent those of their affiliated organizations, or those of the publisher, the editors and the reviewers. Any product that may be evaluated in this article, or claim that may be made by its manufacturer, is not guaranteed or endorsed by the publisher.

frontiers in Earth Science

ORIGINAL RESEARCH
published: 02 November 2021
doi: 10.3389/feart.2021.738515

# The TsuJal Amphibious Seismic Network: A Passive-Source Seismic Experiment in Western Mexico

*Francisco Javier Núñez-Cornú[1]*, Diego Córdoba Barba[2], William Bandy[3], Juan José Dañobeitia[4,5], José Edgar Alarcón Salazar[1], Diana Núñez[1] and Carlos Suárez Plascencia[1]*

[1]C.A. Sismología y Volcanología de Occidente (SisVOc), CUC, CUCSH, Universidad de Guadalajara, Puerto Vallarta, Mexico, [2]Fac. CC. Físicas, Universidad Complutense de Madrid, Madrid, Spain, [3]Instituto de Geofísica, Universidad Nacional Autónoma de México, Mexico, Mexico, [4]EMSO ERIC, Rome, Italy, [5]Marine Technology Unit-CSIC, Barcelona, Spain

The geodynamic complexity in the western Mexican margin is controlled by the multiple interactions between the Rivera, Pacific, Cocos, and North American plates, as evidenced by a high seismicity rate, most of whose hypocenters are poorly located. To mitigate this uncertainty with the aim of improving these hypocentral locations, we undertook the TsuJal Project, a passive seafloor seismic project conducted from April to November 2016. In addition to the Jalisco Seismic Network, 10 LCHEAPO 2000 Ocean Bottom Seismometers (OBSs) were deployed by the BO El Puma in a seafloor array from the Islas Marías Archipelago (Nayarit) to the offshore contact between the states of Colima and Michoacan. We located 445 earthquakes in four or more OBSs within the deployed array. Most of these earthquakes occurred in the contact region of the Rivera, Pacific, and Cocos plates, and a first analysis suggests the existence of three seismogenic zones (West, Center, and East) along the Rivera Transform fault that can be correlated with its morphological expression throughout the three seismogenic zones. The seismicity estimates that the Moho discontinuity is located at 10 km depth and supports earlier works regarding the West zone earthquake distribution. Subcrustal seismicity in the Central zone suggests that the Intra-Transform Spreading Basin domain is an ultra-low spreading ridge. A seismic swarm occurred during May and June 2016 between the eastern tip of the Paleo-Rivera Transform fault and the northern tip of the East Pacific Rise-Pacific Cocos Segment, illuminating some unidentified tectonic feature.

**Keywords: OBS, Rivera transform, Rivera plate, Cocos plate, Jalisco block, amphibious seismic network**

OPEN ACCESS

***Edited by:***
*Nibir Mandal,*
*Jadavpur University, India*

***Reviewed by:***
*Shyam Rai,*
*Indian Institute of Science Education and Research, Pune, India*
*Helen Anne Janiszewski,*
*University of Hawaii at Manoa, United States*

****Correspondence:***
*Francisco Javier Núñez-Cornú*
*pacornu77@gmail.com*

***Specialty section:***
*This article was submitted to Solid Earth Geophysics, a section of the journal Frontiers in Earth Science*

***Received:*** *08 July 2021*
***Accepted:*** *14 October 2021*
***Published:*** *02 November 2021*

***Citation:***
*Núñez-Cornú FJ, Córdoba Barba D, Bandy W, Dañobeitia JJ, Alarcón Salazar JE, Núñez D and Suárez Plascencia C (2021) The TsuJal Amphibious Seismic Network: A Passive-Source Seismic Experiment in Western Mexico. Front. Earth Sci. 9:738515. doi: 10.3389/feart.2021.738515*

## INTRODUCTION

The Nayarit, Jalisco, and Colima coasts in the Pacific margin of Mexico are one of the most seismically active areas in North America, in which destructive earthquakes of great magnitude have occurred, generating small local tsunamis. There is also an important seismic gap (Vallarta Gap) on the northern coast of Jalisco (**Figure 1**). The TsuJal Project (Núñez-Cornú et al., 2016) had the objective of studying the seismic and tsunamigenic hazards associated with the interaction of the Rivera plate, Jalisco Block, and the North American plate. This project was conducted in two phases: 1) onshore and offshore active seismic experiments and geophysical surveys, and 2) passive observations of natural seismicity. The

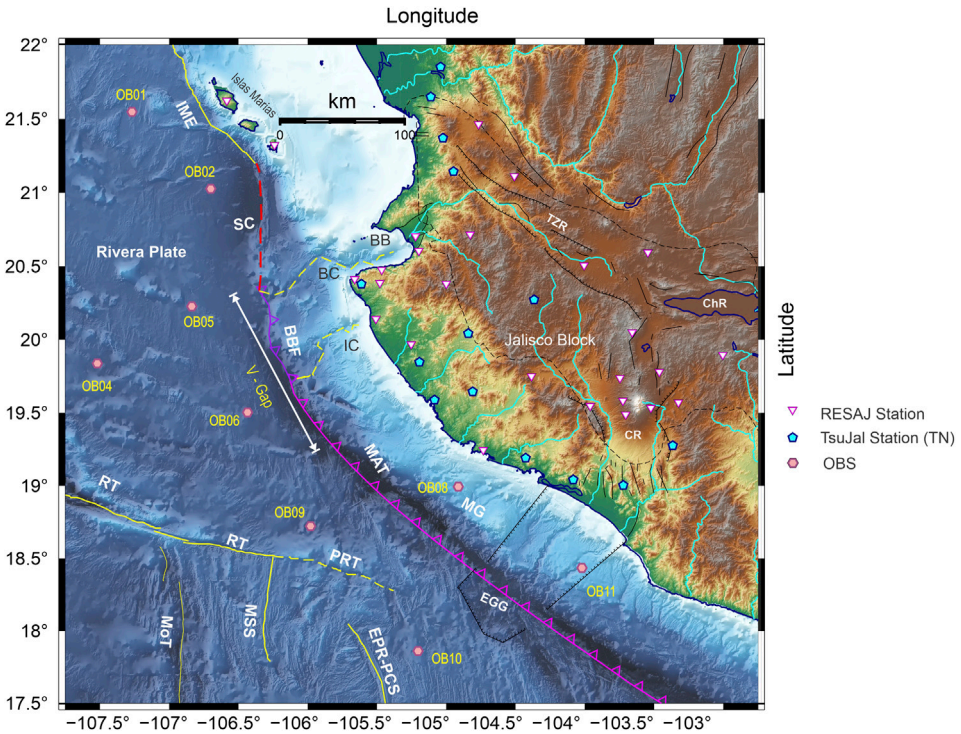


**FIGURE 1 |** Tectonic frame of the Pacific Mexican region. Abbreviations: BB, Bahía de Banderas; BBF, Bahía de Banderas fore-arc block (purple line); BC, Banderas Canyon (yellow dashed line); ChR, Chapala Rift zone; CR, Colima rift zone; EGG, El Gordo Graben; EPR-PCS, East Pacific Rise Pacific-Cocos Segment (yellow line); IC, Ipala Canyon (yellow dashed line); IME, Islas Marias Escarpment (yellow light line); MAT, Middle America Trench (red line); MG, Manzanillo Graben; MoT, Moctezuma Trough; MSS, Moctezuma Spreading Segment; PRT, Paleo Rivera Transform fault (yellow dashed line) [after Pelaéz-Gaviria et al. (2013); Núñez-Cornú et al. (2018)]; RT, Rivera Transform (yellow line); SC, Sierra de Cleofas (pink dashed line); TZR, Tepic-Zacoalco Rift zone; V-Gap, Vallarta Seismic Gap. Seismic networks used in this study: white inverted triangles correspond to RESAJ permanent stations; Cyan pentagons denote TsuJal temporary seismic stations (TN) and pink hexagons are Ocean Bottom Seismometers (OBS).

second phase sought to characterize the seismicity of the area between the Islas Marías, Bahía de Banderas, and along the Middle America Trench (MAT). We present here the first results for seismicity recorded during the second phase of the TsuJal Project.

In addition to the Jalisco Telemetric Seismic Network (RESAJ) (Núñez-Cornú et al., 2018), from April to November 2016, a temporary seismic network (TN) with 25 stations with sensor Le-3D MkIII was deployed from the northern part of the Nayarit to the south of Colima, including the Islas Marías Archipelago (from April 2016 to January 2017), providing a total of 50 seismic land stations. Offshore, a network of ten Ocean Bottom Seismometers (OBS) with four channels (3 short-period sensors and hydrophone) type LCHEAPO 2000 was deployed from the Islas Marías to offshore contact between Colima and Michoacan states. The OBSs were deployed and recovered by the research vessel BO El Puma (Universidad Nacional Autonoma de Mexico); nine of them worked well. Sensors recorded data from early April (**Figure 1**) through October 17. In this period, the USGS reported six earthquakes occurred in this region with magnitudes M > 5.0. Those were (1) May 7, 00:18 $M_W$ = 5.6; (2) May 7, 01:05, $M_W$ = 5.0; (3) June 1, 08:30, $M_W$ = 5.4; (4) Jun 2, 02:23, $M_W$ = 5.4; (5) June 7, 10:31, $M_W$ = 6.3; and (6) June 7, 10:51, $M_W$ = 5.5.

Previous seismicity studies in the East Pacific Rise and Rivera Fracture Zone using OBS were carried out between March and April 1974 using three OBS in small arrays (Prothero et al., 1976; Reid and Prothero, 1981). The areas studied were the Rivera Fracture zone, the junction of the ridge crest and the Rivera fracture zone, and the Rivera–Tamayo fracture zone.

## TECTONIC SETTING

The North American (NOAM), Pacific, Cocos, and Rivera (RP) lithospheric plates interact in the western margin of Mexico (**Figure 1**), but the seismotectonic processes are still not fully understood. In this region, a tectonic unit exists, known as the Jalisco Block (JB) (DeMets and Stein, 1990; Michaud et al., 1990; Allan et al., 1991; DeMets and Wilson, 1997). The JB (**Figure 1**) is limited to the east by the Colima rift zone, which extends northward from the Pacific coast and connects at its northern end with two other major extensional structures: The Tepic-Zacoalco rift zone (trending roughly NW-SE), defined as the northern boundary of the JB, and the Chapala rift zone (trending roughly E-W). The connection between the north-western border of the JB and the continent is not well defined.

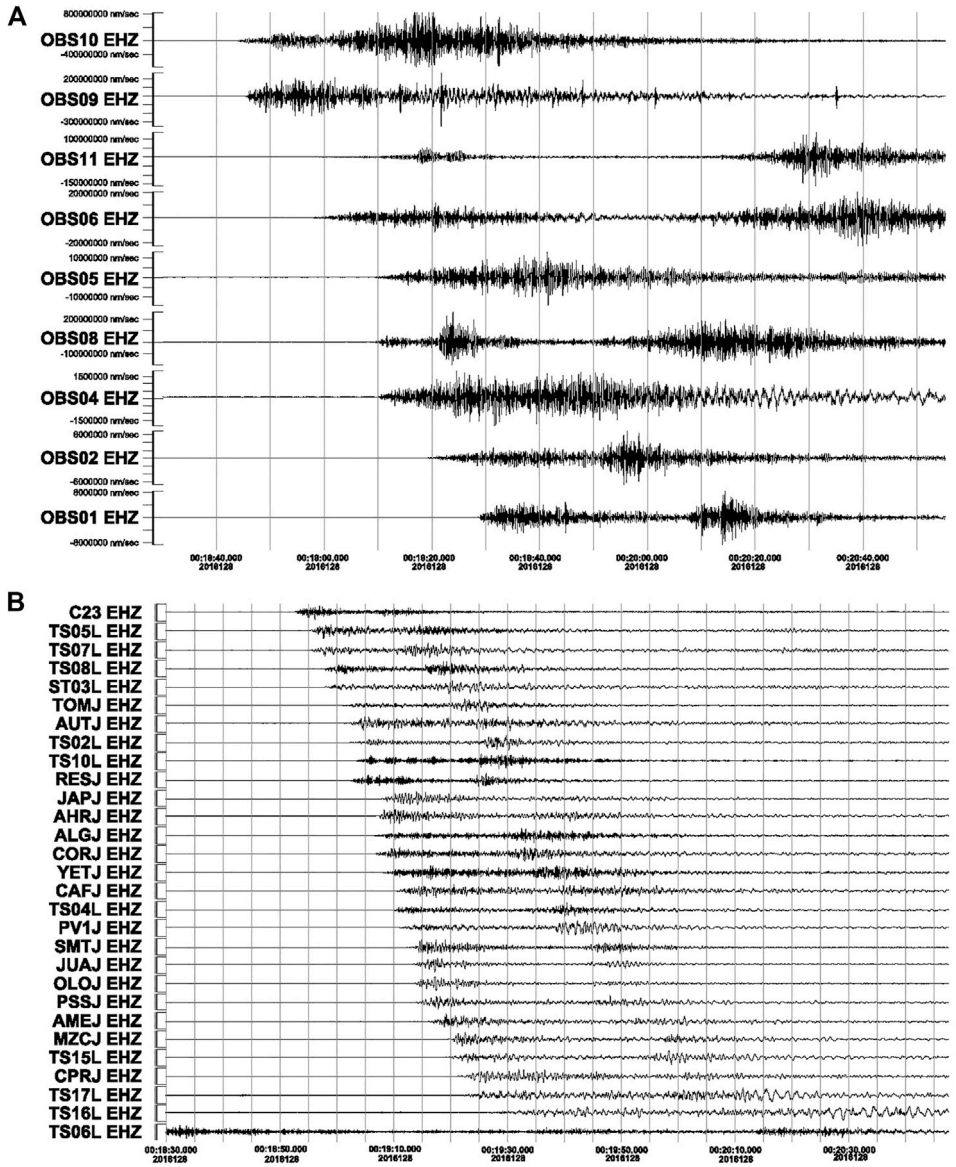


**FIGURE 2 |** Seismic traces corresponding to May 7, 2016, earthquake at 00:18 recorded by **(A)** Ocean Bottom Seismometers (OBS) and **(B)** Temporary seismic (TN) and RESAJ networks. Stations ordered from nearest (OBS10) to the furthest (TS06L) to the earthquake.

Recent studies (Dañobeitia et al., 2016; Núñez-Cornú et al., 2016; Madrigal et al., 2021) indicate that north of Islas Marías (from north to south: Maria Madre, Maria Magdalena, and Maria Cleofas), there is no evidence of an active subduction zone; instead, faulting at west flank of the Islas Marías is observed, while southwards between Maria Magdalena and Maria Cleofas islands the subducted slab of the RP is delineated by regional seismicity. These studies show the existence of a tectonic feature south of Maria Cleofas Island, the Sierra de Cleofas. This 100 km long structure is oriented N-S and marks the boundary of RP and JB, possibly arising from compression by RP against the JB. It establishes where the present-day subduction zone could begin and its presence is also supported by associated seismic activity. Núñez-Cornú et al. (2016) also suggest that Banderas Canyon may reflect the eastern extension, which seems to continue to the east through the Pitillal river's valley. Continental stresses control the morphology of Banderas Canyon. Núñez-Cornú et al. (2016) show that the Bahía de Banderas area is undergoing strong crustal stress *via* the convergence of RP (**Figure 1**). Urías Espinosa et al. (2016) suggest that the existence of Ipala Canyon is related to the extension produced by the sharp change in the RP convergence, and Ipala Canyon may lie along the southeast boundary of a major forearc block (**Figure 1**), termed Banderas Forearc Block.

The atypical Rivera-Pacific-Cocos plate boundary is considered to be a transform fault with a complex stress pattern, which many authors have studied (e.g., Larson, 1972;

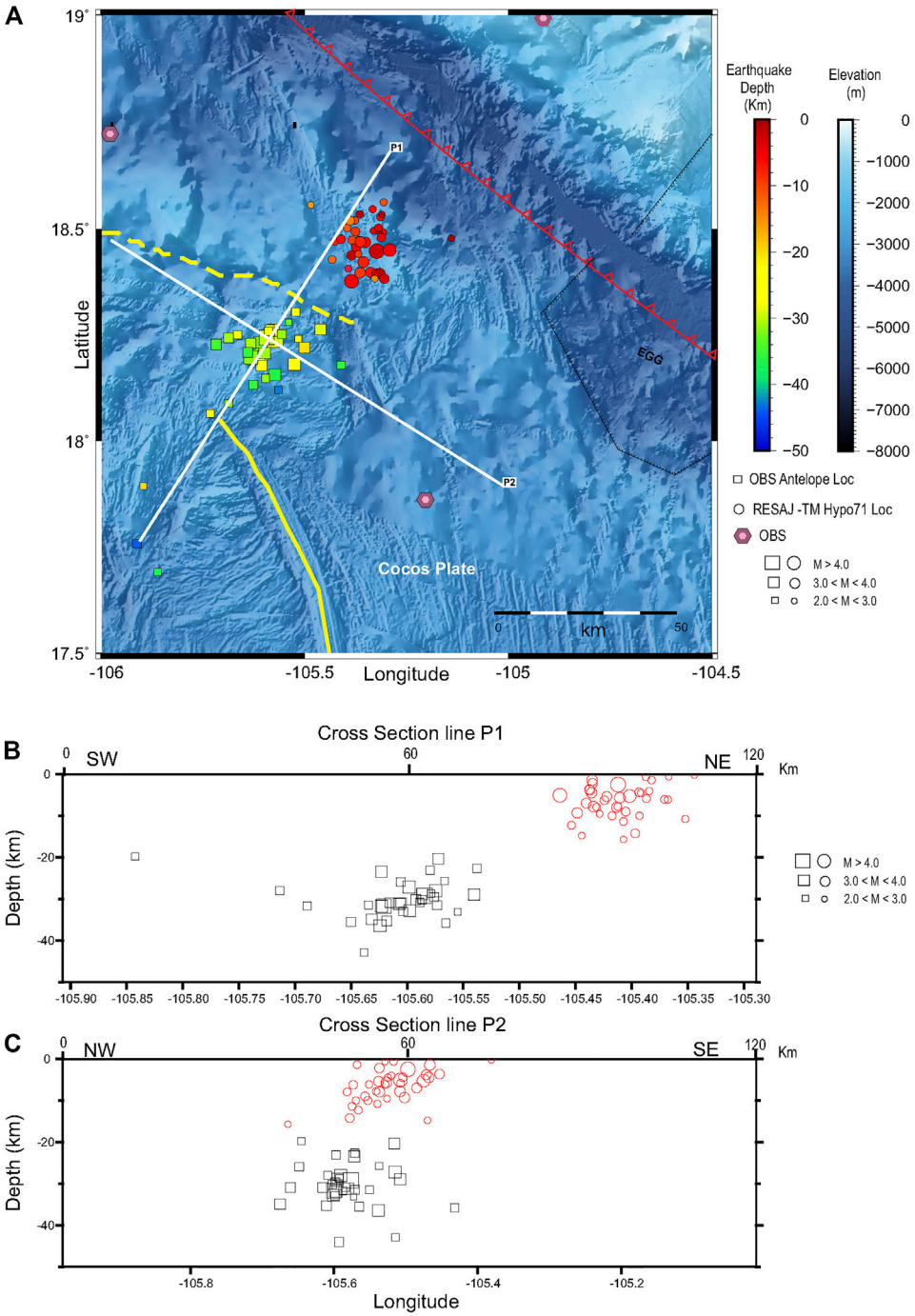


**FIGURE 3 |** Locations of the seismic sequence occurred on May 7–10, 2016 (86 earthquakes) with Antelope and Hypo-71. **(A)** Epicentral map (fill color proportional to depth), where square symbols denote earthquakes located with OBS data located using Antelope system and velocity model iasp91. In contrast, circles represent the RESAJ and TN data locations using Hypo-71 and P-wave velocity model VJB01 (Núñez-Cornú et al., 2002). **(B)** Cross-section along line P1. **(C)** Cross-section along P2 line. Pink hexagons depict OBS locations.

Reid, 1976; Mammerickx, 1980; Bourgois and Michaud, 1991; Michaud et al., 1997; DeMets and Traylen, 2000; Michaud et al., 2000; Peláez-Gaviria et al., 2013). Initially, the Rivera Transform (RT) was proposed to consist of two domains (Larson, 1972; Reid, 1976; Mammerickx, 1980) divided at 107.5°W. The west domain of the RT is an NW-SW elongate basin containing an intra-transform spreading center, known as the Mid-Rivera Transform Discordance. The presence of an intra-transform spreading center at 108.25°W was first proposed based on local seismicity studies conducted in the 1970s (Prothero et al.,

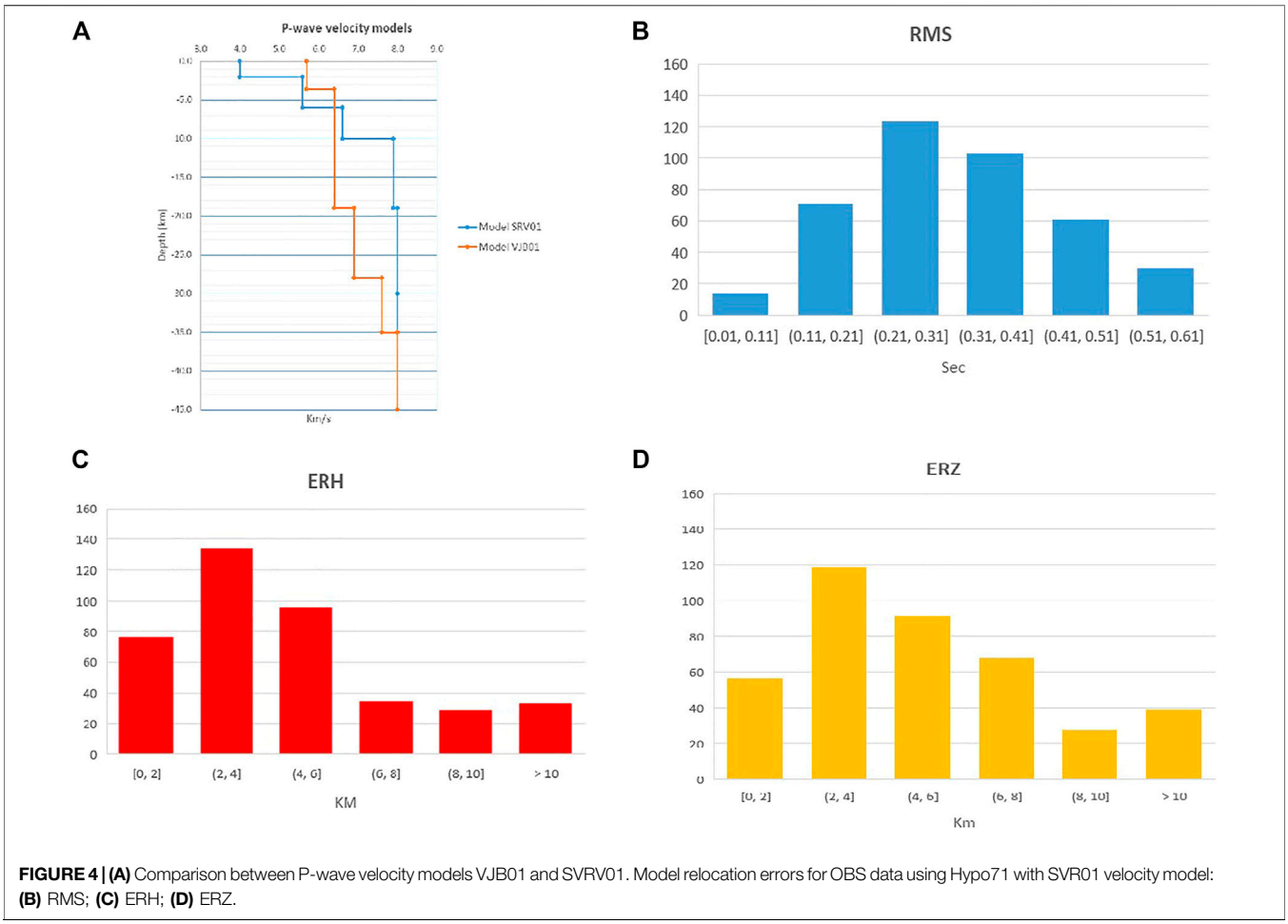


**FIGURE 4 | (A)** Comparison between P-wave velocity models VJB01 and SVRV01. Model relocation errors for OBS data using Hypo71 with SVR01 velocity model: **(B)** RMS; **(C)** ERH; **(D)** ERZ.

1976; Reid, 1976; Prothero and Reid, 1982). In contrast, within the east domain, the basin disappears and the transform fault was originally mapped as a series of discontinuous ridges. Bandy et al. (2011) proposed that the west domain of RT is divided into two very different domains. The first, named "Intra-Transform Spreading Basin," is about 115 km long, extending from 107.30 to 108.42°W in the NW-SE direction. The second, named "Leaky Transform Basin," is an NW-SE elongated structure, roughly 100 km long, extending from 108.42 to 109.21°W.

From bathymetry, Peláez-Gaviria et al. (2013) suggest that this region can be divided into several morphotectonic zones, some of which are described in previous studies. These include 1) zones related to the East Pacific Rise–Pacific Cocos Segment (EPR-PCS) propagation and Moctezuma Spreading Segment (Mammerickx, 1984; Bandy et al., 2008); 2) zones west of Moctezuma Trough (MoT) (**Figure 1**) that are the older crust created at the Mathematician Ridge through which the EPR propagated; 3) zones formed by the older crust at the Rivera Rise which is bent westward as it approaches the RT, due to shearing during the initial formation of the RT (Lonsdale, 1995); 4) zones related to the EPR-PCS propagation to the north of the Paleo Rivera Transform Fault (PRT), dated as 1.4 Ma; 5) the area of MAT, which could be subdivided into three domains; 6) zones located at NW of the El Gordo Graben, whose crust was formed at the EPR-PCS before 1.5 Ma; and 7) the Continental Shelf.

## DATA PROCESSING AND SEISMIC ANALYSIS

During the study period, the Jalisco Telemetric Seismic Network (RESAJ) operated 20 seismic stations in the region, using the Antelope system to acquire, process and store data in real-time. This system also provided automatic preliminary locations, using the iasp91 P-wave velocity model, in real-time. Afterward, a seismologist reviewed P and S pickings. However, the depths of the earthquakes were deeper than expected because the iasp91 model is not suitable for this complex tectonic setting. The earthquakes were relocated using Hypo71 and a suitable velocity model; locations and readings (P and S) were integrated into a database.

Data recorded by the TN network were downloaded directly and included in the Antelope system monthly, integrating with those obtained from RESAJ network. At the end of the

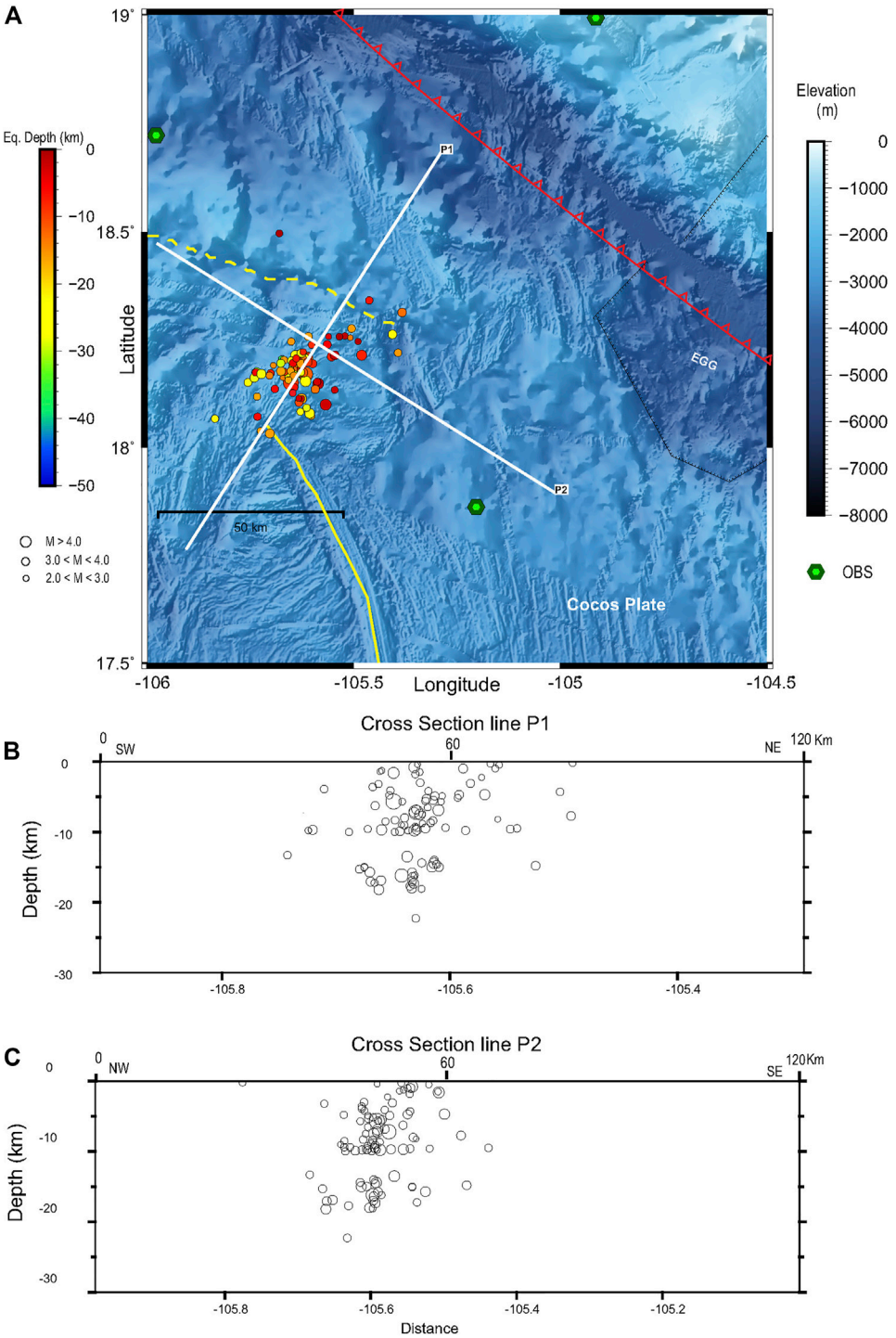


**FIGURE 5 | (A)** Epicentral map showing the May 7–10, 2016 swarm (86 earthquakes) located with Hypo-71 using OBS data and P-wave velocity model SVR01. The white lines are the projection of seismicity throughout P1 and P2 transects with a width of 20 km; **(B)** Cross-section along P1 line; **(C)** Cross-section along P2 line. Abbreviations as for **Figure 1**.

experiment, a database (Land) was generated with the records of both networks. The OBS data required a post-processing stage that took more time to be integrated into a database in the Antelope system. Our seismic databases (Land and OBS) include the seismicity from May 1 to October 17, 2016. For this first analysis, we follow the same methodology used by RESAJ in on-land recent studies (Gutiérrez et al., 2015; Tinoco Villa, 2015; Marín-Mesa et al., 2019) to establish a reference frame

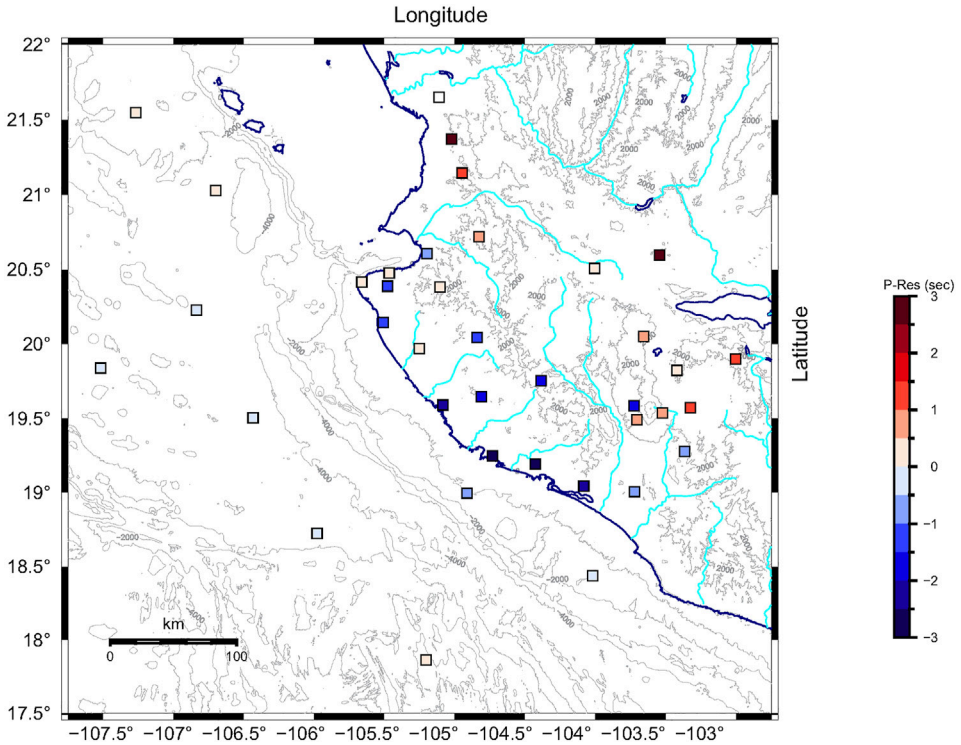


**FIGURE 6 |** P-wave residuals for the OBS, RESAJ, and TN stations from Hypo71 locations using OBS data and model SVR01.

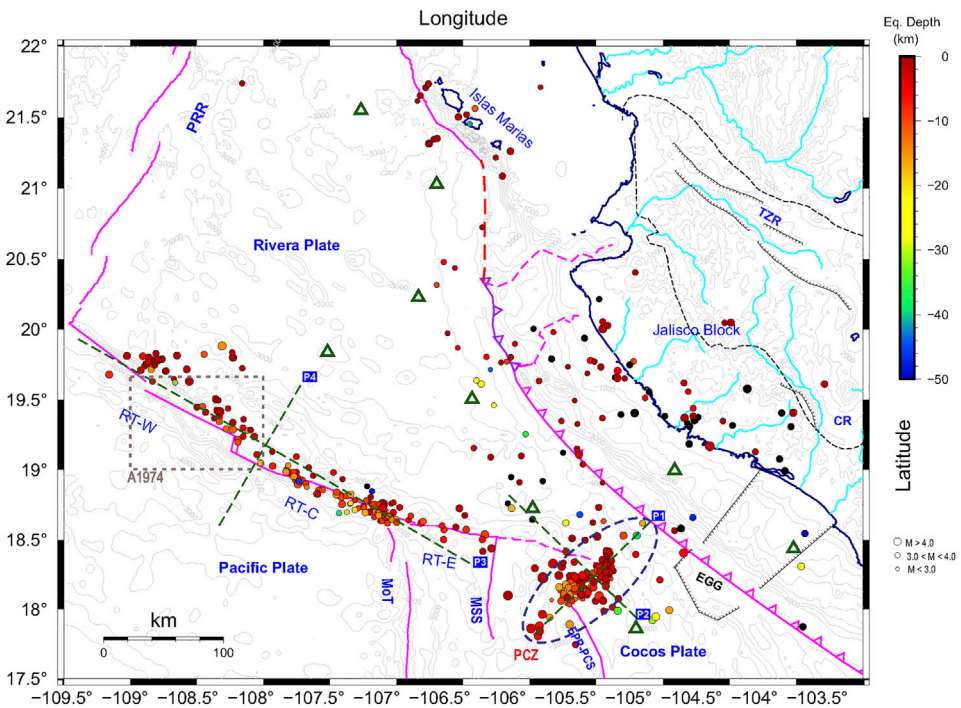


**FIGURE 7 |** Hypocentral map of the seismicity recorded from May 1 to October 17, 2016, using OBS (green triangles) database and relocated with Hypo-71 and SVR01 P-wave velocity model. The A1974 gray rectangle denotes the position of the study area (a) reported for Prothero and Reid (1982). The blue dashed ellipse shows the Pacific-Cocos zone (PCZ). Green dashed lines correspond to the projection of seismicity along P1, P2, P3, and P4 lines (see **Figure 8**). Abbreviations as for **Figure 1**. RT-W, RT-C, and RT-E represent the three active segments of Rivera Transform from west to east. PRR, Pacific-Rivera rise. exhibits three active segments, or seismogenic zones, from east to west.

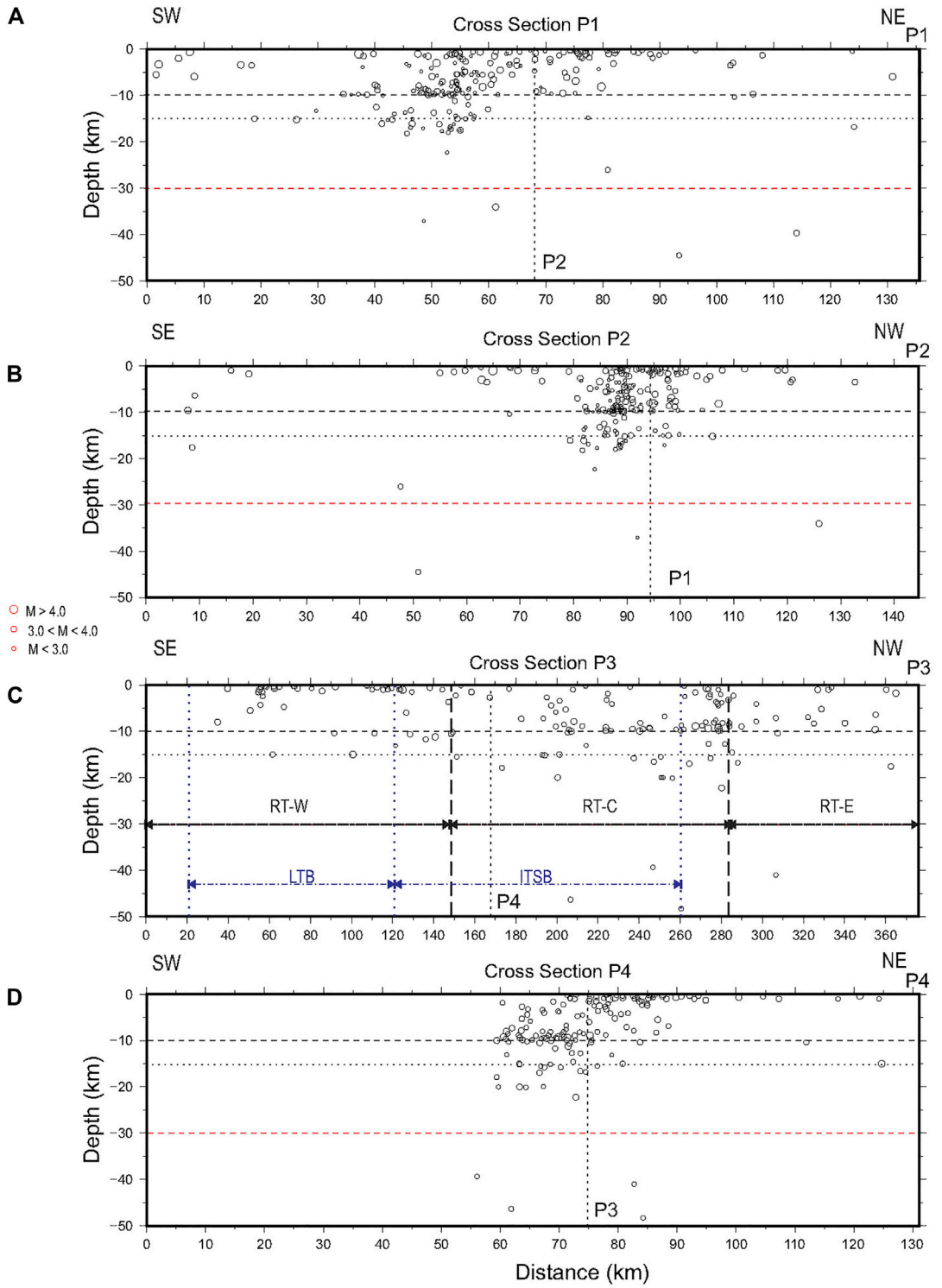


**FIGURE 8 |** Seismicity projections along P1, P2, P3, and P4 transects, whose locations are shown in **Figure 7**. **(A)** Hypocentral cross-section along line P1; **(B)** Hypocentral cross-section along line P2; **(C)** Hypocentral cross-section along line P3, ITSB: Intra-Transform Spreading Basin. LTB: Leaky Transform Basin (Bandy et al., 2011); **(D)** Hypocentral cross-section along line P4. Dashed horizontal lines at 10, 15, and 30 km used as reference.

and compare the locations with and without OBS data, allowing us to improve the methodology to locate oceanic seismicity.

Earthquakes registered by the OBS array were identified using the Antelope system (Lindquist et al., 2007) through a short-term average/long-term average signal energy algorithm with a STA

window of 1.0 s and LTA window of 60.0 s, with detections in at least four stations. Manual picking of P (vertical component) and S (horizontal components) wave arrivals was done. Some time readings from OBS (**Figure 2**) were arduous due to significant background noise. At some stations, the signals were masked by other oceanic signals; different passband filters to enhance the signal according to the station and the epicentral distance, main filters used were: (0.1, 1.0), (0.1, 5.0), (0.5, 3.0), (0.5, 10.0), (1.0, 5.0), (1.0, 10.0), (1.0, 15.0), (6.0, 8.0), (8.0, 10.0), (10.0, 12.0), (15.0, 30.0) Hz. Antelope automatically generates a hypocentral map; locations are estimated using the iasp91 P-wave velocity model these locations are shown in **Supplementary Figure S0**. Our initial analysis made it possible to locate 550 earthquakes using four or more OBS for the entire period. Some occurred outside of the study area, so location quality for those was poor and not considered.

The preliminary results using the Antelope OBS locations establish two main seismogenic areas. The first one corresponds to a longitudinal area where the seismicity is distributed along the RT, slightly shifted NW of the tectonic feature. In contrast, the second seismogenic region corresponds with an area between the eastern tip of the PRT and the northern tip of the EPR-PCS, defined as the Pacific-Cocos zone (PCZ), where epicenters are aligned in a SE–NW direction. Some events are observed on the west side and parallel to MAT. Scarce seismicity was identified in the Islas Marías area; those identified show hypocenter depths between 25 and 50 km or deeper. These values are questionable for the oceanic crust, and therefore the mismatch in the depths may be due to the P-wave velocity model (iasp91) used by Antelope, combined with the network distribution. We decided not to use Antelope locations for the analysis.

To analyze the quality of the earthquake locations, we studied the seismic sequence that occurred between May 7 and May 10 in the PCZ using both databases (Land and OBS). This seismic sequence is in an area in the vicinity of four OBSs. On May 7, at 00:18, an earthquake Mw = 5.5 occurred, followed by a second earthquake Mw = 5.2 occurred at 01:06. We located this swarm using Land database as routinely RESAJ does with Hypo 71, using the P-wave velocity model VJB01 (**Figure 4A**) (Núñez-Cornú et al., 2002) and comparing with OBS Antelope locations (**Figure 3A**). For this seismic swarm, 86 earthquakes were located. Different hypocentral determinations were observed; Antelope epicentral location depths are still greater than 20 km Hypo71 location depths agree with characteristic values of an oceanic crust, but the epicentral area is 50 km in NE away from Antelope epicentral area (**Figures 3B,C**).

To improve OBS locations, we adjust a 1D P-wave velocity model using the Rivera crustal velocity models proposed by Núñez-Cornú et al. (2016), Dañobeitia et al. (2016), and Núñez et al. (2019) to relocate through Hypo71. As a test group, we selected 30 earthquakes recorded by most of the OBSs (at least eight OBS with clear P and S waves) to adjust the SVRV01 model (**Figure 4A**) for which P and S residuals were minimum. To obtain the best solutions using Hypo71, eight different starting depths were used as the initial solution. The 86 earthquakes of this period were relocated using Hypo71 and SVR01 P-wave velocity model (**Figures 5A–C**), yielding a Root Mean Square (RMS) error with a

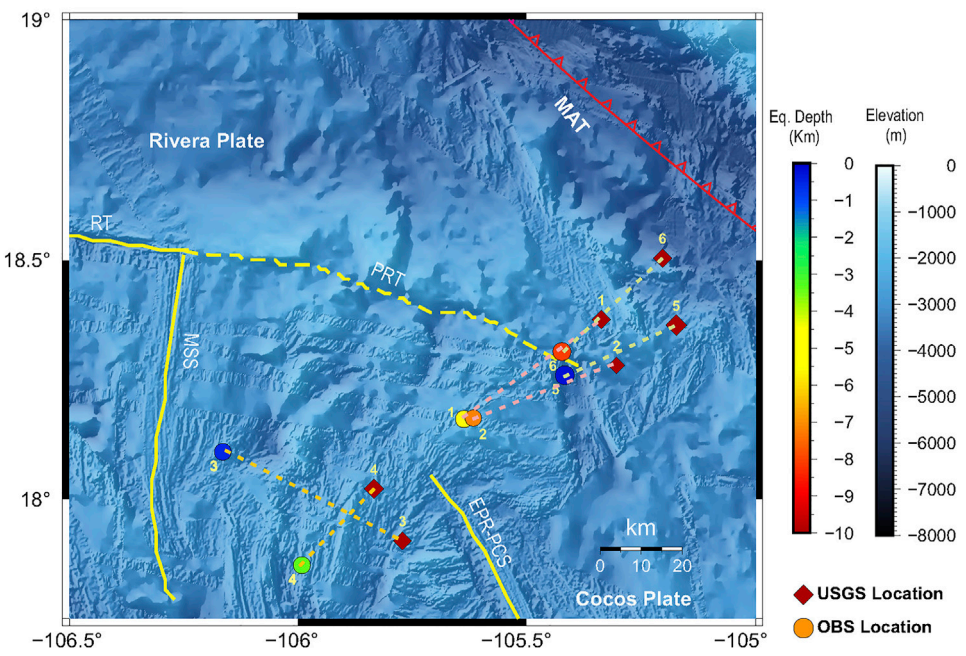


**FIGURE 9 |** Comparison between earthquake locations reported by the USGS and those obtained with the OBS network for our study period. (1) May 7, 00:18 $M_W$ = 5.6; (2) May 7, 01:05, $M_W$ = 5.0; (3) June 1, 08:30, $M_W$ = 5.4; (4) Jun 2, 02:23, $M_W$ = 5.4; (5) June 7, 10:31, $M_W$ = 6.3; and (6) June 7, 10:51, $M_W$ = 5.5.

mean value of 0.31 s. The standard mean error of the epicenter (ERH) and the standard mean value error of the focal depth (ERZ) present values of 2.8 and 2.6 km, respectively. The local magnitude (Lay and Wallace, 1995) relation was used in this study.

Localization tests were made with Hypo71 joining both databases (OBS and Land) and using both velocity models. The results were unsatisfactory, the solutions did not always converge, and the residuals were very high. To evaluate the use of Land data at this stage of the process, we used as master events this earthquake swarm (86 Eq.) located with OBS data using Hypo71 and SVR01 velocity model, eliminating solution weight for the Land stations. In this case, we observed that the stations in the range of 140–240 km from the epicentral zone had residuals of the P wave arrival times less than −1.0 s; distances greater than 330 km yielded residuals greater than 1.0 s (**Figure 6**). These differences result from the seismic wave pathways that traverse strong lateral velocity variations in the continental crust. This indicates that additional corrections should be applied for each seismogenic area to use on-land data. In the case of OB08 and OB11, located on the North American plate near the trench, the average residuals of the P-wave are −0.51 and −0.32 s, respectively, indicating that structure imposes a little significant effect on these OBSs (**Figure 6**).

The OBS dataset was relocated using Hypo71 and model SVR01, obtaining a total of 445 relocated earthquakes (**Figure 7**). The event distribution is similar to that obtained with Antelope, but epicenters now correlate more closely with known tectonic features. Not all the seismogenic areas have the same station coverage, so each will exhibit its uncertainty challenges and should be processed separately. However, this study processed all similarly, and the RMS, ERH, and ERZ errors for the region were within our chosen tolerances (**Figures 4B–D**). **Figure 8** shows the cross-sections at RT and PCZ, where important changes are observed in in-depth distribution for both areas. Most hypocenters were located between 0 and 10 km depth, agreeing with depths expected within the oceanic crust. Nevertheless, a second group is observed at depths between 15 and 25 km, suggesting activity in the lithospheric mantle.

## RESULTS AND DISCUSSION

More than 400 earthquakes were located in the study region from May 1 to October 17, 2016. The seismic data obtained with the nine OBS temporary array will provide new and valuable information on the tectonics of the Rivera plate and its interaction with the Jalisco block, Pacific and Cocos plates. Our work analyzed regions exhibiting the most seismic activity during the study period, corresponding to the Rivera Transform (RT) and the Pacific-Cocos zone (PCZ).

Despite the tectonic complexity of our study region, it is possible to deem the Rivera plate as a quasi-homogeneous structure. Considering that all the stations, except OB08 and OB11, were in the interior of this plate and seismicity is also located within it or at its edges, we use the SVR01 P-wave velocity model for event location at this processing and analysis stage.

The temporary network array design sought to record seismicity along the Islas Marías Archipelago, Bahía de Banderas, and the Middle America Trench, but events were scarce in those regions. The seismicity recorded in RT is mainly outside the network, resulting in a wide azimuthal station gap, so we must consider a thorough investigation to understand better the different seismogenic zones identified. The distribution of stations is oblique to the RT; however, it intersects this structure, providing reasonable control of earthquake locations along the tectonic edge. Also, S-wave readings for those events help constrain the depths, and their location uncertainty is reduced by the position of OB04 (**Figure 1**).

The relocation of the May swarm (**Figures 3**, **5**) indicates that estimated locations of Rivera plate seismicity using on-land stations are shifted ~50 km to the northwest. In **Figure 9**, we compare the locations of the six earthquakes reported by the USGS for this period with the OBS data locations. These events are also shifted between 30 and 50 km in the northwest direction, except for the earthquake (3), which is 50 km to the southeast.

We can observe some general features from this location study (**Figure 7**). The RT exhibits three active segments, or seismogenic zones, from east to west 1) the RT-E between the Moctezuma Spreading Segment and Moctezuma Trough; 2) The RT-C from Moctezuma Trough to −108.25°; and 3) The RT-W from −108.25 to −109.10°. The most active area is the intersection of Moctezuma Trough with RT. Another seismogenic zone is the PCZ, where the epicentral distribution is more compact and aligned to the SE-NW. Seismicity parallel and west of MAT is also observed. Near the Islas Marías, two alignments perpendicular to Islas Marías Escarpment, NW, and SE of Maria Madre Island are identified.

Hypocentral depths (**Figure 8**) range primarily from 0 to 10 km depth, suggesting crustal thickness of 10 km in both areas, PCZ and RT. An additional hypocentral distribution between 14 and 18 km is observed in PCZ (**Figures 8A,B**). The three sections along the RT (RT-W, RT-C, RT-E) are distinct (**Figure 8C**). At the RT-E section (**Figure 8C**), most depths range from 0 to 10 km. In the RT-C section, most of the events are located shallower than 10 km, but hypocenters greater than 15 km depth are observed. In the RT-W section, we observe very shallow seismicity. **Figure 8D** shows the subcrustal seismicity is SW of the RT, and the shallow seismicity is NE of the RT (see P3 mark as reference).

The seismogenic zones identified in this study correspond to three different domains that divide RT, determined from morphological studies (Bandy et al., 2011). From west to east are: the "*Leaky Transform Basin*" domain, the "*Intra-Transform Spreading Basin*" domain, and the East Domain (**Figure 8**), which correspond to RT-W, RT-C, and RT-E, respectively. Our observations suggest that the "*Intra-Transform Spreading Basin*" is an ultra-low spreading ridge, similar to an analogous feature exhibiting subcrustal seismicity as reported by Jokat et al. (2012) and Schlindwein and Schmid (2016).

Prothero et al. (1976) reported that all reliable earthquakes in this area were shallower than 10 km below the seafloor,

suggesting 10 km as a lower limit for the brittle zone thickness in this region. Our results agree with this value. Earthquake locations obtained in 1974 in the Rivera transform [zone (a)] were reported by Prothero and Reid (1982) (**Figure 5**), which are consistent with our results in the RT-W region (**Figure 7**, square A1974).

A monthly analysis allows us to study the seismicity that occurred in the region in more detail, identifying temporal patterns, swarms, mainshock-aftershock sequences, and possible migration activity. In May (**Supplementary Figure S1**), the most active area was the PCZ, where the May 5–7 mainshock-aftershock sequence with an alignment SW-NE was observed; this is also observed in **Supplementary Figures S2A,B**. The first earthquake 1) $M_W = 5.6$ was located 7.5 km deep, and the 2) $M_W = 5.2$ at 2.4 km. Along the RT, the most active area was the intersection of RT with Moctezuma Trough, which marks the limit between RT-E and RT-C; perpendicular alignments were also observed to Islas Marías Escarpment at María Madre Island.

On June 1 (**Supplementary Figures S3, S4**), a $M_W = 5.4$ earthquake 3) occurred at 0830 GMT, located at a depth of 1 km between the PCZ and the Moctezuma Spreading Segment. This event was followed by another earthquake 4) $M_W = 5.8$, which took place on June 2 at 0223 GMT and located SW of the May alignment, on the edge of the PCZ at 3.3 km depth. A new seismic sequence began on June 7 inside of the PCZ at the eastern tip of Paleo-Rivera Transform, with an earthquake 5) $M_W = 6.3$ occurred at 1051 GMT located 1 km deep, followed by another earthquake 6) at 1058 GMT in the same area, with a magnitude $M_W = 5.5$ and hypocenter depth of 8.1 km. The sequence consisted of 28 earthquakes for the period June 7–22 along a NS alignment. Moreover, we observed that seismicity is shallow along the RT-W area; meanwhile, at RT-C, it is deeper.

The seismicity observed in July is minimum in both areas (**Supplementary Figures S5, S6**). In August, the most active area is the intersection between RT and Moctezuma Trough (**Supplementary Figures S7, S8**); again, there is shallow seismicity at the RT-W area; meanwhile, the seismicity is deeper at RT-C and SE of RT. No seismicity was located at the PCZ in September (**Supplementary Figures S9, S10**). The most active area is the western tip of the RT-W, showing the same pattern of shallow seismicity at the RT-W and deeper seismicity at RT-C. The seismicity for October 1–17 periods is shown in **Supplementary Figures S11, S12**, where the most active area is located at the intersection of RT-C with Moctezuma Trough, which marks the border of RT-C with RT-E.

## CONCLUSION

The data analysis recorded during the TsuJal Project represents the first inspection at an onshore-offshore data acquisition and investigation in the region. Our catalog and waveform database will provide the opportunity to advance our knowledge moving forward significantly. This study supports previous findings of a 10 km deep Moho and confirms previously observed seismic patterns at the RT-E zone (Prothero et al., 1976; Prothero and Reid, 1982). Subcrustal seismicity seen at the RT-C zone suggests that the "Intra-Transform Spreading Basin" domain is an ultra-low spreading ridge. Seismic swarms occurred between May and June 2016 at the Pacific-Cocos zone, a previously unidentified tectonic feature. Temporal analysis of the seismicity for this period indicates that most of the seismicity in the region occurred by seismic swarms, as reported by other authors (Prothero et al., 1976; Tinoco Villa, 2015). We observed two mainshock-aftershocks sequences and aisled earthquakes $M_W > 5.0$. Locations from internationals and regional seismic networks are between 30 and 50 km shifted from OBS locations. Therefore, they cannot be used to characterize tectonic structures with a size smaller than 100 km.

Due to the tectonic complexity of the region, a more extensive and detailed study would be warranted. This study will improve the earthquake locations using more advanced methods, including 3D processes, and add land and island stations with appropriate station corrections and velocity models. The use of waveform analysis techniques (cross-correlations) will also improve and expand the catalog. Focal mechanism calculations will allow understanding the tectonic complexity of each identified seismogenic areas.

The study highlights the critical need for permanent OBS networks to monitor oceanic seismogenic regions adequately; this is particularly important in areas hosting potentially hazardous seismic activity, where significant crustal variability degrades confidence in seismic observations using land-based stations alone.

## DATA AVAILABILITY STATEMENT

All geophysical data collected by OBS, TN and RESAJ are in a database at the Research Group CA-UDG-276 SisVOc. The data may be available for collaborative research projects between CA-SisVOc and other interested institutions by specific agreements. For more information, please contact the corresponding author.

## AUTHOR CONTRIBUTIONS

FN-C: Conceptualization, methodology, investigation, conclusion, and original draft preparation. DC: Conceptualization, methodology, investigation. WB: Investigation, formal analysis, writing - original draft. JD: Conceptualization, methodology, investigation. EA: Software, Data processing. DN: Investigation, formal analysis, writing original draft, conclusion. CS: Investigation, formal analysis.

## FUNDING

This research was funded by: CONACYT–FOMIXJAL 2008–96567 (2009); CONACYT–FOMIXJAL 2008–96539 (2009); CONACYT–FOMIXJAL 2010–149245 (2011);

CONACyT-FOMIXJal (2012-08-189963) (MEXICO); CGL (2011-29474-C02-01) DGI Plan Nacional I + D + i (España). NOC Cruise JC098, RRS James Cook UK; B.O El Puma Campaigns, CABO-CIC-UNAM: JGAP2012, JGAP2013 Leg1 and Leg2; JGAP2016 Legs 1 and 2 Cruises.

## ACKNOWLEDGMENTS

The authors gratefully acknowledge Charlotte Rowe for her valuable suggestions, including the English grammar revision that notably improved this article and Claudia B. M. Quinteros Cartaya for her help with the Generic Mapping Tools figures. The authors thank Dr. Carlos Mortera, Cruise Chief, the Captain, and the crew of the B.O. El Puma (UNAM) for the support and facilities granted. Our special thanks to Francisco Ponce Núñez for technical support onboard B.O. El Puma. We gratefully appreciate the efforts to secure the ship-time to Dr. Arturo Iglesias Mendoza and Dr. William Lee Alardin for granting ship-time for JGAP2016-LEG2. Some figures were generated using the Generic Mapping Tools (GMT-6; Wessel et al., 2019).

## SUPPLEMENTARY MATERIAL

The Supplementary Material for this article can be found online at: https://www.frontiersin.org/articles/10.3389/feart.2021.738515/full#supplementary-material

## REFERENCES

Allan, J. F., Nelson, S. A., Luhr, J. F., Carmichael, I. S. E., Wopat, M., and Wallace, P. J. (1991). *Pliocene-recent Rifting in SW México and Associated Volcanism: An Exotic Terrane in the Making*, 47. Memoir: American Association of Petroleum Geologists, 425–445.

Bandy, W. L., Michaud, F., Mortera Gutiérrez, C. A., Dyment, J., Bourgois, J., Royer, J.-Y., et al. (2011). The Mid-rivera-transform Discordance: Morphology and Tectonic Development. *Pure Appl. Geophys.* 168, 1391–1413. doi:10.1007/s00024-010-0208-8

Bandy, W. L., Michaud, F., Dyment, F., Mortera-Gutiérrez, C. A., Bourgois, J., Calmus, T., et al. (2008). Multibeam Bathymetry and Sidescan Imaging of the Rivera Transform-Moctezuma Spreading Segment Junction, Northern East Pacific Rise: New Constraints on Rivera-Pacific Relative Plate Motion. *Tectonophysics* 454 (1-4), 70–85. doi:10.1016/j.tecto.2008.04.013

Bourgois, J., and Michaud, F. (1991). Active Fragmentation of the North America Plate at the Mexican Triple Junction Area off Manzanillo. *Geo-Marine Lett.* 11, 59–65. doi:10.1007/bf02431030

Dañobeitia, J., Bartolomé, R., Prada, M., Nuñez-Cornú, F., Córdoba, D., Bandy, W. L., et al. (2016). Crustal Architecture at the Collision Zone between Rivera and North American Plates at the Jalisco Block: Tsujal Project. *Pure Appl. Geophys.* 173 (10–11), 3553–3573. doi:10.1007/s00024-016-1388-7

DeMets, C., and Stein, S. (1990). Present-day Kinematics of the Rivera Plate and Implications for Tectonics in Southwestern Mexico. *J. Geophys. Res.* 95 (B1321), 21931. doi:10.1029/JB095iB13p21931

DeMets, C., and Traylen, S. (2000). Motion of the Rivera Plate since 10 Ma Relative to the Pacific and North American Plates and the Mantle. *Tectonophysics* 318, 119–159. doi:10.1016/s0040-1951(99)00309-1

DeMets, C., and Wilson, D. S. (1997). Relative Motions of the Pacific, Rivera, North American, and Cocos Plates since 0.78 Ma. *J. Geophys. Res.* 102, 2789–2806. doi:10.1029/96jb03170

Gutiérrez, Q. J., Escudero, C., and Núñez-Cornú, F. J. (2015). Geometry of the Rivera-Cocos Subduction Zone Inferred From Local Seismicity. *Bull. Seismol. Soc. Am.* 6, 3104–3133. doi:10.1785/0120140358

Jokat, W. J., Kollofrath, W. H., Geisslerand Jensen, L. (2012). Crustal Thickness and Earthquake Distribution South of the Logachev Seamount, Knipovich Ridge. *Geophys. Res. Lett.* 39, 1–6. doi:10.1029/2012GL051199

Larson, R. L. (1972). Bathymetry, Magnetic Anomalies, and Plate Tectonic History of the Mouth of the Gulf of California. *Geol. Soc. America Bull.* 83, 3345–3360. doi:10.1130/0016-7606(1972)83[3345:bmaapt]2.0.co;2

Lay, T., and Wallace, T. (1995). Modern Global Seismology. *Academic P mress*, 523.

Lindquist, K. G., Newman, R. L., and Vernon, F. L. (2007). The antelope Interface to PHP and Applications: Web-Based Real-Time Monitoring. *Seismological Res. Lett.* 78 (6), 663–670. doi:10.17885/gssrl.78.6.66310.1785/gssrl.78.6.663

Lonsdale, P. (1995). Segmentation and Disruption of the East Pacific Rise in the Mouth of the Gulf of California. *Mar. Geophys. Res.* 17, 323–359. doi:10.1007/bf01227039

Marín-Mesa, T., Núñez-Cornú, F. J., and Suárez-Plascencia (2019). Analysis of the seismicity in the Jalisco Block from June to December 2015. *Seism. Res. Lett.* 90 (5), 1767–1778. doi:10.1785/0220190107

Madrigal, L. A., Núñez, D., Escalona-Alcázar, F. d. J., and Núñez-Cornú, F. J. (2021). Crustal Structure across the Northern Region of the Islas Marías Archipelago. *Front. Earth Sci.* 9, 1–12. doi:10.3389/feart.2021.682206

Mammerickx, J. (1980). Neogene Reorganization of Spreading between the Tamayo and the Rivera Fracture Zone. *Mar. Geophys. Res.* 4, 305–318. doi:10.1007/bf00369105

Mammerickx, J. (1984). The Morphology of Propagating Spreading Centers: New and Old. *J. Geophys. Res.* 89, 1817–1828. doi:10.1029/jb089ib03p01817

Michaud, F., Bourgois, J., and Aubin, J. (19901990). "Active Fragmentation of the West Pacific Coast: The Jalisco Block a Future Unexpected Terrain," in *Tectonics of Circum-Pacific Continental Margins*. Editors J. Aubin and J. Bourgois (Netherlands: VSP-BV), 51–76.

Michaud, F., Dañobeitia, J. J., Carbonell, R., Bartolomé, R., Córdoba, D., Delgado, L., et al. (2000). New Insights into the Subducting Oceanic Crust in the Middle American Trench off Western Mexico (17-19°N). *Tectonophysics* 318, 187–200. doi:10.1016/s0040-1951(99)00311-x

Michaud, F., Royer, J.-y., Bourgois, J., de Lepinay, B. M., and Liaudon, G. P. (1997). The Rivera Fracture Zone Revisited. *Mar. Geology.* 137, 207–225. doi:10.1016/s0025-3227(96)00103-x

Núñez, D., Núñez-Cornú, F. J., Escalona-Alcázar, F. d. J., Córdoba, D., López Ortiz, J. Y., Carrillo de la Cruz, J. L., et al. (2019). Seismic Structure of the Southern Rivera Plate and Jalisco Block Subduction Zone. *Seismol. Res. Lett.* 90-5, 1756–1766. doi:10.1785/0220180399

Núñez-Cornú, F. J., Córdoba, D., Dañobeitia, J. J., Bandy, W. L., Figueroa, M. O., Bartolome, R., et al. (2016). Geophysical Studies across Rivera Plate and Jalisco Block, Mexico: TsuJal Project. *Seismological Res. Lett.* 87, 59–72. doi:10.1785/0220150144

Núñez-Cornú, F. J., Rutz-López, M., Nava, F. A., Reyes-Dávila, G., and Suárez-Plascencia, C. (2002). Characteristics of Seismicity in the Coast and north of Jalisco Block, Mexico. *Phys. Earth Plan. Ints.* 132 (1–3), 141–155. doi:10.1016/S0031-9201(02)00049-3

Núñez-Cornú, F. J., Sandoval, J. M., Alarcón, E., Gómez, A., Suárez-Plascencia, C., Núñez, D., et al. (2018). The Jalisco Seismic Accelerometric Telemetric Network (RESAJ). *Seismol. Res. Lett.* 89 (2A), 363–372. doi:10.1785/0220170157

Peláez Gaviria, J. R., Mortera Gutiérrez, C. A., Bandy, W. L., and Michaud, F. (2013). Morphology and Magnetic Survey of the Rivera-Cocos Plate Boundary of Colima, Mexico. *Geofísica Internacional* 52, 73–85. doi:10.1016/s0016-7169(13)71463-6

Prothero, W. A., and Reid, I. D. (1982). Microearthquakes on the East Pacific Rise at 21°N and the Rivera Fracture Zone. *J. Geophys. Res.* 87, 8509–8518. doi:10.1029/jb087ib10p08509

Prothero, W. A., Reid, I., Reichle, M. S. J. N., and Brune, J. N. (1976). Ocean Bottom Seismic Measurements on the East Pacific Rise and Rivera Fracture Zone. *Nature* 262, 121–124. doi:10.1038/262121a0

Reid, I., and Prothero, W. A. (1981). An Earthquake Sequence Studied with Ocean-Bottom Seismographs. *Geophys. J. Int.* 64, 381–391. doi:10.1111/j.1365-246x.1981.tb02673.x

Reid, I. (1976). The Rivera Plate: A Study in Seismology and Plate Tectonics. Ph.D. Thesis. La Jolla: University of California at San Diego, 280.

Schlindwein, V., and Schmid, F. (2016). Mid-ocean-ridge Seismicity Reveals Extreme Types of Ocean Lithosphere. *Nature* 535, 276–279. doi:10.1038/nature18277

Tinoco Villa, M. (2015). Detección y Análisis de Enjambres Sísmicos en la Corteza Oceánica al Sur de las Islas Marías. M.Sc. Thesis, Posgrado en Geofisica. Puerto Vallarta, Mexico: Universidad de Guadalajara, 67.

Urías Espinosa, J., Bandy, W. L., Mortera Gutiérrez, C. A., Núñez Cornú, F. J. J., and Mitchell, N. C. (2016). Multibeam Bathymetric Survey of the Ipala Submarine Canyon, Jalisco, Mexico (20°N): The Southern Boundary of the Banderas Forearc Block. *Tectonophysics* 671, 249–263. (ISSN 0040-1951). doi:10.1016/j.tecto.2015.12.029

Wessel, P., Luis, J. F., Uieda, L., Scharroo, R., Wobbe, F., Smith, W. H. F., et al. (2019). The Generic Mapping Tools Version 6. *Geochem. Geophys. Geosyst.* 20, 5556–5564. doi:10.1029/2019GC008515

**Conflict of Interest:** The authors declare that the research was conducted in the absence of any commercial or financial relationships that could be construed as a potential conflict of interest.

frontiers in Earth Science

REVIEW
published: 07 February 2022
doi: 10.3389/feart.2021.775544

# SMART Subsea Cables for Observing the Earth and Ocean, Mitigating Environmental Hazards, and Supporting the Blue Economy

*Bruce M. Howe[1]*, Michael Angove[2], Jérome Aucan[3], Christopher R. Barnes[4], José S. Barros[5], Nigel Bayliff[6], Nathan C. Becker[7], Fernando Carrilho[8], Matthew J. Fouch[9], Bill Fry[10], Anthony Jamelot[11], Helen Janiszewski[12], Laura S. L. Kong[13], Stephen Lentz[14], Douglas S. Luther[15], Giuditta Marinaro[16], Luís Manuel Matias[17], Charlotte A. Rowe[18], Andi E. Sakya[19,20], Amir Salaree[21], Torsten Thiele[22], Frederik J. Tilmann[23], Christa von Hillebrandt-Andrade[24], Laura Wallace[10,25], Stuart Weinstein[7] and William Wilcock[26]*

[1]Department of Ocean and Resources Engineering, University of Hawai'i at Mānoa, Honolulu, HI, United States, [2]NOAA National Weather Service Tsunami Program, Silver Spring, MD, United States, [3]Pacific Community Centre for Ocean Sciences, Nouméa, New Caledonia, [4]University of Victoria, Victoria, BC, Canada, [5]Autoridade Nacional de Comunicações (ANACOM), Lisbon, Portugal, [6]Aqua Comms, Dublin, Ireland, [7]NOAA Pacific Tsunami Warning Center, Honolulu, HI, United States, [8]Instituto Português Do Mar e da Atmosfera, Lisbon, Portugal, [9]Subsea Data Systems, Inc., Washington, DC, United States, [10]GNS Science, Lower Hutt, New Zealand, [11]Laboratoire de Géophysique de Pamatai, CEA, Papeete, French-Polynesia, [12]Department of Earth Sciences, University of Hawai'i at Mānoa, Honolulu, HI, United States, [13]UNESCO IOC—NOAA International Tsunami Information Center, Honolulu, HI, United States, [14]Ocean Specialists, Inc., McLean, VA, United States, [15]Department of Oceanography, University of Hawai'i at Mānoa, Honolulu, HI, United States, [16]Istituto Nazionale di Geofisica e Vulcanologia, Roma, Italy, [17]Instituto Dom Luiz, Faculdade de Ciências, Universidade de Lisboa, Lisboa, Portugal, [18]Los Alamos National Laboratory, Earth and Environmental Science, Los Alamos, NM, United States, [19]National Agency for Research and Innovation (BRIN), Jakarta, Indonesia, [20]Indonesia Institute of Technology (ITI), Tangerang, Indonesia, [21]Earth and Environmental Sciences, University of Michigan, Ann Arbor, MI, United States, [22]Institute for Advanced Sustainability Studies (IASS), Potsdam, Germany, [23]GFZ German Research Centre for Geosciences, Potsdam, Germany, [24]UNESCO IOC—NOAA International Tsunami Information Center, Caribbean Office, Mayagüez, PR, United States, [25]Institute for Geophysics, University of Texas at Austin, Austin, TX, United States, [26]School of Oceanography, University of Washington, Seattle, WA, United States

OPEN ACCESS

**Edited by:**
*Mourad Bezzeghoud, Universidade de Évora, Portugal*

**Reviewed by:**
*Ahmed Reda, Curtin University, Australia*
*Mairi M. R. Best, Consultant, Sudbury, ON, Canada*

***Correspondence:**
*Bruce M. Howe*
*bhowe@hawaii.edu*

**Specialty section:**
*This article was submitted to Solid Earth Geophysics, a section of the journal Frontiers in Earth Science*

**Received:** *14 September 2021*
**Accepted:** *30 December 2021*
**Published:** *07 February 2022*

**Citation:**
*Howe BM, Angove M, Aucan J, Barnes CR, Barros JS, Bayliff N, Becker NC, Carrilho F, Fouch MJ, Fry B, Jamelot A, Janiszewski H, Kong LSL, Lentz S, Luther DS, Marinaro G, Matias LM, Rowe CA, Sakya AE, Salaree A, Thiele T, Tilmann FJ, von Hillebrandt-Andrade C, Wallace L, Weinstein S and Wilcock W (2022) SMART Subsea Cables for Observing the Earth and Ocean, Mitigating Environmental Hazards, and Supporting the Blue Economy. Front. Earth Sci. 9:775544. doi: 10.3389/feart.2021.775544*

The Joint Task Force, Science Monitoring And Reliable Telecommunications (JTF SMART) Subsea Cables, is working to integrate environmental sensors for ocean bottom temperature, pressure, and seismic acceleration into submarine telecommunications cables. The purpose of SMART Cables is to support climate and ocean observation, sea level monitoring, observations of Earth structure, and tsunami and earthquake early warning and disaster risk reduction, including hazard quantification. Recent advances include regional SMART pilot systems that are the first steps to *trans*-ocean and global implementation. Examples of pilots include: InSEA wet demonstration project off Sicily at the European Multidisciplinary Seafloor and water column Observatory Western Ionian Facility; New Caledonia and Vanuatu; French Polynesia Natitua South system connecting Tahiti to Tubaui to the south; Indonesia starting with short pilot systems working toward systems for the Sumatra-Java megathrust zone; and the CAM-2 ring system connecting Lisbon, Azores, and Madeira. This paper describes observing system simulations for these and other regions. Funding reflects a blend of government, development bank, philanthropic foundation, and commercial contributions. In addition to notable scientific

and societal benefits, the telecommunications enterprise's mission of global connectivity will benefit directly, as environmental awareness improves both the integrity of individual cable systems as well as the resilience of the overall global communications network. SMART cables support the outcomes of a predicted, safe, and transparent ocean as envisioned by the UN Decade of Ocean Science for Sustainable Development and the Blue Economy. As a continuation of the OceanObs'19 conference and community white paper (Howe et al., 2019, doi: 10.3389/fmars.2019.00424), an overview of the SMART programme and a description of the status of ongoing projects are given.

**Keywords: SMART subsea cables, ocean observing, global geophysics, seismology, earthquake and tsunami early warning, environmental disaster risk reduction, submarine telecommunications cables, UN joint task force**

## 1 INTRODUCTION: THE SMART CABLES CONCEPT

The last two decades witnessed an astonishing advancement and confluence of priorities in scientific research, ocean sensor technologies, subsea telecommunication cables, and societal and political needs to meet major environmental threats and hazard mitigation. The potential for rapid acceptance and deployment of sophisticated subsea cable systems was articulated by Howe et al. (2019) and this present paper documents the significant advances over the last 2 years in both new deployments and subdisciplines in Earth and ocean sciences.

These developments come at a time when the telecommunications industry is managing a sharp increase in Internet traffic from multiple sources including high frequency stock market trading, video entertainment, 5G networks, the Internet of Things (IoT), remote classrooms and teleconferencing, and work-from-home employment spurred on by the COVID-19 pandemic. A decade or two ago there were only a few major *trans*-ocean cable installation companies, whereas now leading data companies (e.g., Google, Apple, Microsoft, Amazon, and Facebook) are themselves funding higher capacity cable systems and establishing new routes.

A recent workshop of the National Academies of Sciences, Engineering, and Medicine (National Academies of Sciences, Engineering, and Medicine, 2020, p. 1) noted that "Uninterrupted, multi-decadal observations of the ocean are critical to understanding the Earth system as a whole and managing the ocean's resources on which human lives and economies depend". Sustained and real-time ocean data are integral to the new Blue Economy (Spinrad, 2016; European Marine Board, 2019; Weller at al., 2019; World Ocean Initiative, 2020; Carney, 2021).

A complementary development in the last few years has been the international recognition for urgent and coordinated responses to environmental threats posed by climate change, sea level rise, and tsunamis, which imposed huge and unacceptable human tragedies, deaths, and financial losses. These were addressed in part by the Paris Climate Agreement, which was adopted by 191 national parties in 2015, with specified action targets to mid-century, and by the recent IPCC et al. (2021). Since 2000, over 250,000 deaths have been attributed to earthquakes and tsunamis worldwide with an associated damage cost of over $400 billion. Other relevant United Nations programs are discussed below. The net result is the alignment of scientific and technical advances, telecom and cable industries' expanding needs, and growing political and societal demands for environmental protection and hazard mitigation.

Deploying oceanographic sensors on new undersea telecommunication cables is a promising solution for obtaining the extensive, longitudinal, real-time data that are critical for understanding and managing these urgent environmental issues. Such sensors can provide important environmental data from sites in the deep ocean and continental margins that are otherwise difficult and expensive to obtain in real time, continuously, and over decadal time scales. Suitable sensors are already deployed on dedicated cabled ocean observatories, some of which are described below. With modest non-recurring engineering expenses, these sensors can be further integrated into future telecommunications cables to greatly increase spatial coverage and create a global network of **S**cience **M**onitoring **A**nd **R**eliable **T**elecommunication (SMART) cable systems (**Figure 1**).

The SMART cables concept originated decades ago and was demonstrated on a small scale by placing a few sensors at the end of disused cables, such as off the coast of Japan in the 1990s for detecting earthquakes and tsunamis. A major advancement came with using modern fiber-optic cables, capable of delivering power and high-bandwidth, as the backbone of dedicated sustained cabled observatories to obtain data on complex ocean systems well beyond what is available from conventional research vessels and fixed buoys (Favali et al., 2010, Favali et al., 2015; Lo Bue et al., 2021). The first such operational cabled observatories were the 2006 coastal VENUS system (Tunnicliffe et al., 2008) and the regional NEPTUNE observatory in 2009 (Barnes et al., 2015; Best et al., 2015), both now within Ocean Networks Canada (ONC). Similar observatories, tailored to national, scientific, and geographical needs, have included: Japan—DONET and S-net (Kawaguchi et al., 2015; Kanazawa et al., 2016; Aoi et al., 2020); USA—Ocean Observatories Initiative (OOI) and others (Massion and Raybould, 2006; Kelley et al., 2014; Howe et al., 2015); China (Lu et al., 2015); and Europe (Best et al., 2014; Person et al., 2015; Dañobeitia et al., 2020). These developments have in turn fostered the evolution of progressively smaller, more precise, and reliable sensors (Schaad, 2009; Paros et al., 2012; RBR,

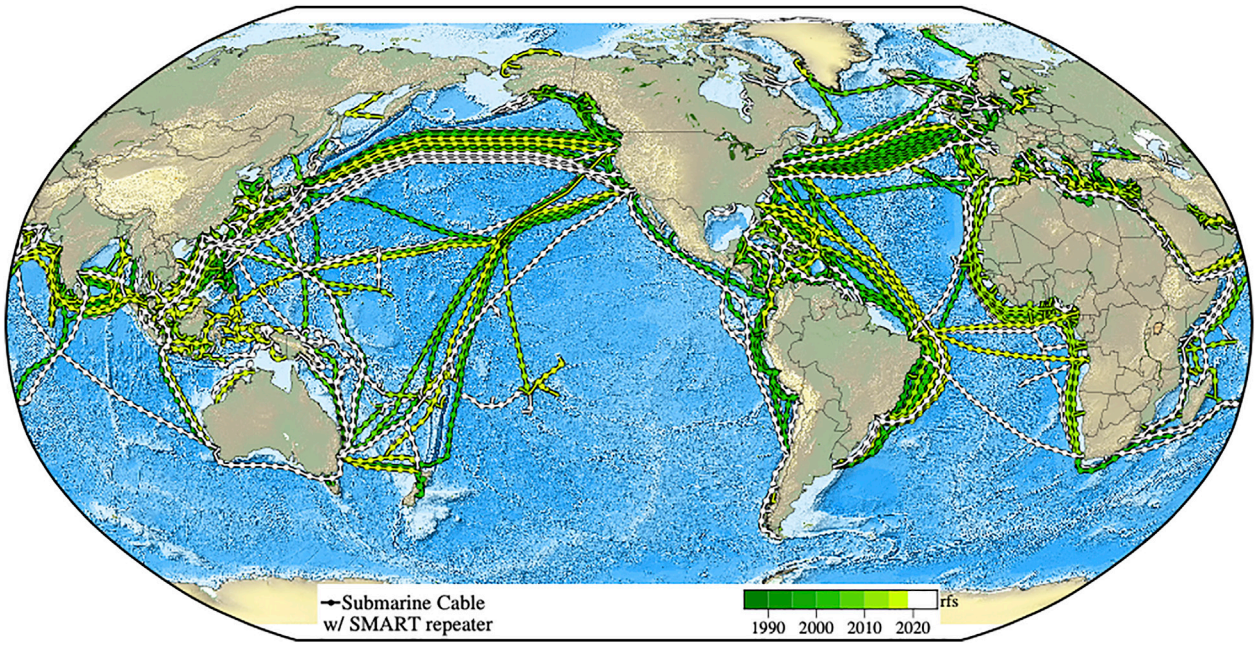


**FIGURE 1 |** Current and planned cables span the oceans, enabling the Internet and our modern society. As they are replaced and expanded over their 10–25-years refresh cycle, environmental sensors (pressure, temperature, acceleration) can be added to the cable repeaters every ~100 km, gradually obtaining real time global coverage (for clarity, repeaters are shown only every 300 km; rfs = year ready for service). Cable data: TeleGeography's Telecom Resources licensed under Creative Commons ShareAlike. Permission obtained for use of figure.

2017; Delory and Pearlman, 2018; Lin and Yang, 2020). Such developments have direct applications to programs (e.g., NASA) for extraterrestrial ocean exploration (Aguzzi et al., 2020), with reciprocal benefits as well.

Advocacy for the SMART cables concept began with a paper by You (2010). In 2012, following workshops in Rome (2011) and Paris (2012), three UN agencies (International Telecommunication Union (ITU), World Meteorological Organization (WMO), and the Intergovernmental Oceanographic Commission of the United Nations Educational, Scientific and Cultural Organization (UNESCO/IOC)) established the Joint Task Force (JTF) to facilitate development of the concept (Butler, et al., 2014). The initial period of development of JTF was described by Barnes (2018) and details of workshops and publications are provided on the JTF web site: https://www.itu.int/en/ITU-T/climatechange/task-force-sc.

SMART cables represent a potential major new element in the Global Ocean Observing System (GOOS Steering Committee, 2019). The JTF is engaging with the GOOS Framework for Ocean Observing (FOO) as it develops SMART cables (http://www.oceanobs09.net/foo/; Lindstrom et al., 2014). A core concept of the GOOS FOO is "Essential Ocean Variables" (EOV): high-impact, discrete, feasibly monitored observable attributes of the global oceans. SMART cables, by their nature as extensive, deep-ocean, high-data-rate observatories, directly address several of the GOOS EOVs. For example, Ocean Bottom Pressure (OBP) was recently accepted as an emerging EOV and SMART cables are potentially the most extensive and cost-effective source for such measurements. SMART cables also measure Subsurface Temperature EOV and the OBP capabilities of SMART cables would address one aspect of the Sea Surface Height EOV. GOOS prescribes a phased approach for new ocean observing technologies, from concept to regional pilots through global implementation. The JTF is following this approach to ensure that SMART cables and data derived from them can be seamlessly incorporated into GOOS within a comprehensive Deep Ocean Observing Strategy (DOOS; Levin et al., 2019).

A central feature of the SMART cables concept is combining two key themes of the 21st century: the increasing pressure for global connectivity and urgent need for coherent, concerted global effort on climate change and ocean management. The market-driven investment in information infrastructure can be harnessed to achieve tangible, social benefits in climate and ocean science. The relatively modest suite of proposed instruments will help address many of the applied science and societal needs and facilitate monitoring the physical integrity of the cable itself. The importance of such synergy is reflected in the themes of OceanObs'19 (e.g., the "Blue Economy" and "Ocean Discovery", particularly in the deep oceans) and the UN's Sustainable Development Goals (SDG 13—Climate and SDG 14—Oceans). With respect to the latter, the JTF has been endorsed as a project of the UN Decade of Ocean Science for Sustainable Development.

The JTF and its industry partners recognize the need for funding sources to contribute to the development costs of integrating sensors into existing submarine cable components and toward the incremental capital expenditures associated with

adding SMART capabilities to telecommunications cable systems. The first step underway is a wet demonstration/pilot project in which sensor packages are included on a relatively short submarine cable using standard industry practices, with real-time data retrieved over a minimum of 1 year. Multiple suitable cable projects are in the planning stages in the South Pacific, northeastern Atlantic, and Mediterranean where the JTF can validate not only the technical elements, but also the data management, regulatory clearances, and funding mechanisms (e.g., multilateral development banks).

We call out two specific positive developments. First, Alcatel Submarine Networks in a press release stated: "Global warming presents real and measurable risks for our society. ASN is launching a number of initiatives to help address climate change" and "Our entire portfolio will benefit from this new "CC" (Climate Change) philosophy to propose dedicated applications such as TEWS (tsunami early warning system), monitoring of underwater seismic activity, global warming, and water temperature and level" (Alcatel Submarine Networks, 2020). Second, The Portuguese government announced that it would finance and build the CAM-2 system connecting Lisbon, Azores, and Madeira in a ring system, including "provision of services, namely seismic detection, for the production of alerts, environmental measurements... and data transmission of scientific projects" (Government of Portugal, 2020). These two announcements indicate that suppliers acknowledge the societal demand for SMART systems and expect to provide them. More importantly, these developments demonstrate that there are governments investing in the same, recognizing the need to share the submarine critical infrastructure between telecom and science and early warning.

This paper is an update to *SMART Cables for Observing the Global Ocean: Science and Implementation* (Howe et al., 2019), with a scientific emphasis on geophysics and hazard early warning. The paper first explains how SMART cables can improve our understanding of myriad geophysical and ocean processes, including global seismology, tsunami modeling, ocean temperature and circulation, sea level rise, tides, and wind waves (**Section 2**). It then details practical aspects of creating such a network: what sensors with what requirements will SMART repeaters use and how will they integrate into subsea telecommunications cable systems (**Section 3**); and the presently planned and proposed systems (**Section 4**). In Other Developments, we discuss data management, legal, permitting and security, costs and financing, and relationship to other organizations (**Section 5**). Concluding remarks are given in **Section 6**.

# 2 IMPROVEMENTS IN EARTH AND OCEAN OBSERVING

The data collected by the SMART cables will greatly enhance and complement the observation networks already in place today. The variables measured by the SMART cable repeaters are ocean bottom temperature, pressure, and seismic acceleration. Importantly, as discussed in the Introduction, the direct measurements and their derivatives respond directly to the GOOS need for greater attention to EOVs and the UN imperative to contribute to the SDGs and the Decade of Ocean Science. More broadly and in the future, the SMART cable infrastructure will provide a general interface into the deep ocean.

## 2.1 Geophysics and Seismology

The inclusion of high-sensitivity accelerometers and pressure sensors on SMART cables holds great potential for significant advances for the field of seismology by improving our capacity to detect and locate small earthquakes below the ocean floor, improving our ability to determine the rupture type and dynamics for larger offshore earthquakes, and enhancing our ability to image the interior of the Earth, both locally and globally, from earthquakes occurring all around the globe.

One intriguing opportunity for leveraging the seismic sensors is the global characterization of seafloor seismic noise. Noise sources range from the primary and secondary oceanic microseisms to seafloor currents, anthropogenic sources such as shipping traffic and marine surveys, as well as narrow directional contributions from bathymetric anomalies. The deployment of permanent seismic sensors along widely distributed telecommunications cables offers an unprecedented opportunity to observe, characterize and attribute geographically extensive and dynamically changing seafloor seismic noise, whose features have only been sparsely sampled to date through isolated and usually time-limited ocean bottom seismometer (OBS) experiments.

Another exciting opportunity that the presence of SMART seismic sensors could provide is the ability to exploit random sources of opportunity for basic structural imaging. Nearby marine seismic surveys are one obvious example, but recent observations of whale song on seafloor sensors (Kuna and Nábělek. 2021) or well-established techniques based on the analysis of noise recordings (Crawford and Singh, 2008) suggest a similar leveraging for shallow geologic imaging along the lengths of any observing SMART cables.

Ranasinghe et al. (2018) used forward modeling to compare the potential improvement in ray coverage for global tomographic models, when notional SMART Cables are added to existing (or previous) observational capability. The naturally heterogeneous distribution of earthquake sources (**Figure 2**), along with predominantly land-based sensors (**Figure 2**), result in significant regions of the globe poorly or completely unsampled by propagating seismic waves.

Ranasinghe et al. (2018) demonstrated as much as 300% improvement in some oceanic areas (**Figures 3A,B**) by including notional SMART cables. **Figures 3C,D** illustrate a mantle cross-section comparing existing ray sampling vs. that achievable by the addition of SMART Cables. Ongoing research includes comparisons of global tomographic model resolution, which is critical to understanding the improved confidence in propagation times and, for properly calibrated sensors, path-dependent attenuation.

In addition to utility in tsunami warning (below), OBP sensors have also shown great promise for seafloor geodetic applications,

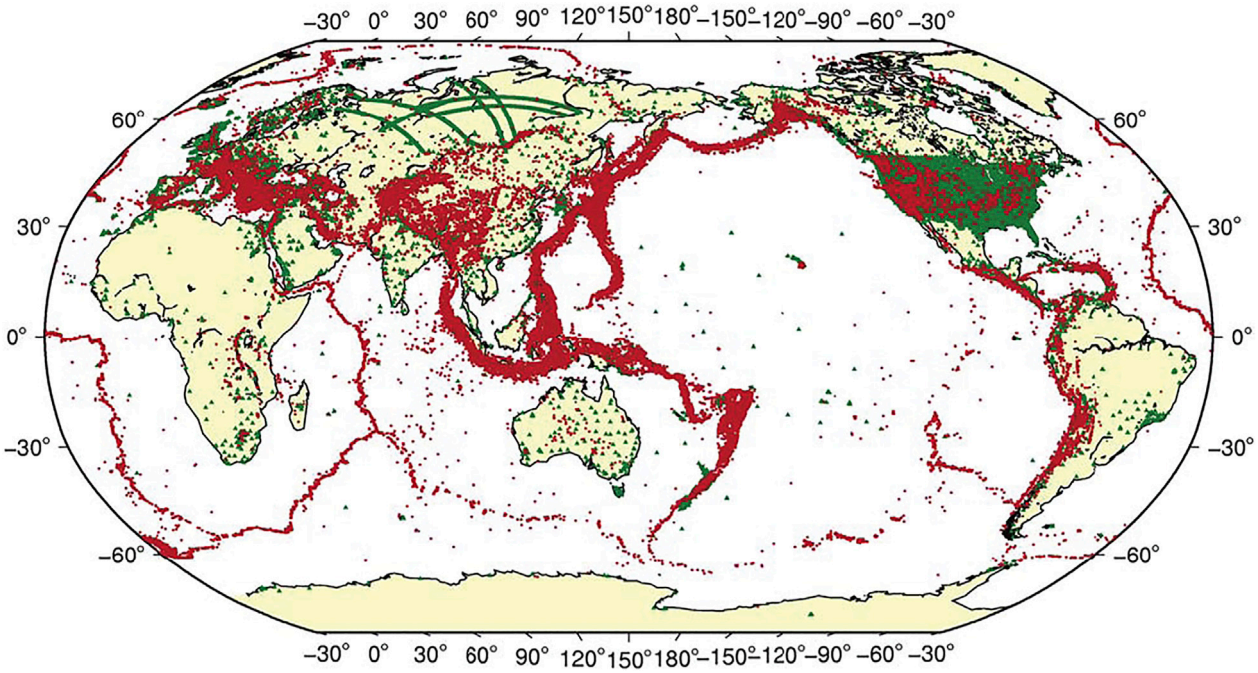


**FIGURE 2 |** Global seismic sources (red) and existing or previously existing seismic stations (green) showing heterogeneity of coverage, with particular absence of sources and receivers in the ocean basins.

specifically for identification of cm-level vertical tectonic deformation during earthquakes and slow slip events at subduction zones, and volcanic events (e.g., Chadwick et al., 2006; Iinuma et al., 2012; Ito et al., 2013; Wallace et al., 2016). Having OBP sensing capability on cables spanning regions that could host such events will add greatly to global seafloor geodetic sensing capability and enhance our ability to monitor a range of seafloor deformation processes at offshore tectonic plate boundaries.

## 2.2 Seismic and Tsunami Monitoring and Warning

In our previous paper, we presented a full discussion on how SMART cables can benefit tsunami warning capabilities (Howe et al., 2019). Angove et al. (2019) give more information on the tsunami warning problem. In this section we present a summary on how and why SMART cables can benefit tsunami warning systems. In tsunami early warning, there is generally a clear distinction between the near field, i.e., the coastline directly adjacent to the triggering earthquake or other tsunamigenic event where potential warning times are typically tens of minutes to maybe an hour, and the far field, where tsunami waves travel.

Prior to the 21st century several unnecessary evacuations occurred on Pacific coastlines especially for far field regions. Not because a tsunami was not generated but because the tsunami was not as destructive as predicted. Tsunami Warning Center (TWC) duty scientists only had knowledge of basic earthquake parameters, hypocenter and magnitude, and, mostly of potential use for far field warnings, readings from coastal sea-level stations. In the 21st Century, tsunami forecasting has been significantly improved by the investment of several Pacific countries into more instrumentation and real-time data sharing, such as the deep-ocean pressure sensors (DART buoys), coupled to richer information available on earthquakes through new methodology faster focal mechanism solutions and estimates of rupture area (Kanamori and Rivera, 2008; Duputel et al., 2011). But trying to assess the destructive potential of tsunamis on coastlines, even using the increased coastal sea-level network and DART buoys, in addition to the seismic information, is still fraught with uncertainty. The strength of the tsunami will strongly depend on the amount of vertical deformation of the seafloor and, importantly, at what depth beneath the seafloor and under what water depth this perturbation is occurring, with deeper water leading to greater tsunamis. Furthermore, the conversion of earthquake magnitude into a prediction of the seafloor displacement is strongly dependent on the elastic properties in the volume of material surrounding the fault rupture. The gradients in both seafloor topography and elastic properties are high in subduction zones (the source region of the most catastrophic tsunamis), meaning that typical uncertainties in earthquake location and the size of the rupture zone translate into very large uncertainties in the predicted size of the tsunami. This is an obvious problem for near-field warnings, which are currently usually based on seismic information alone; several pilot systems incorporate geodetic data (GNSS displacements), which reduces uncertainties, provides very fast complex moment tensor (CMT) solutions, and allows the estimation of rupture extent. Uncertainties remain significant,

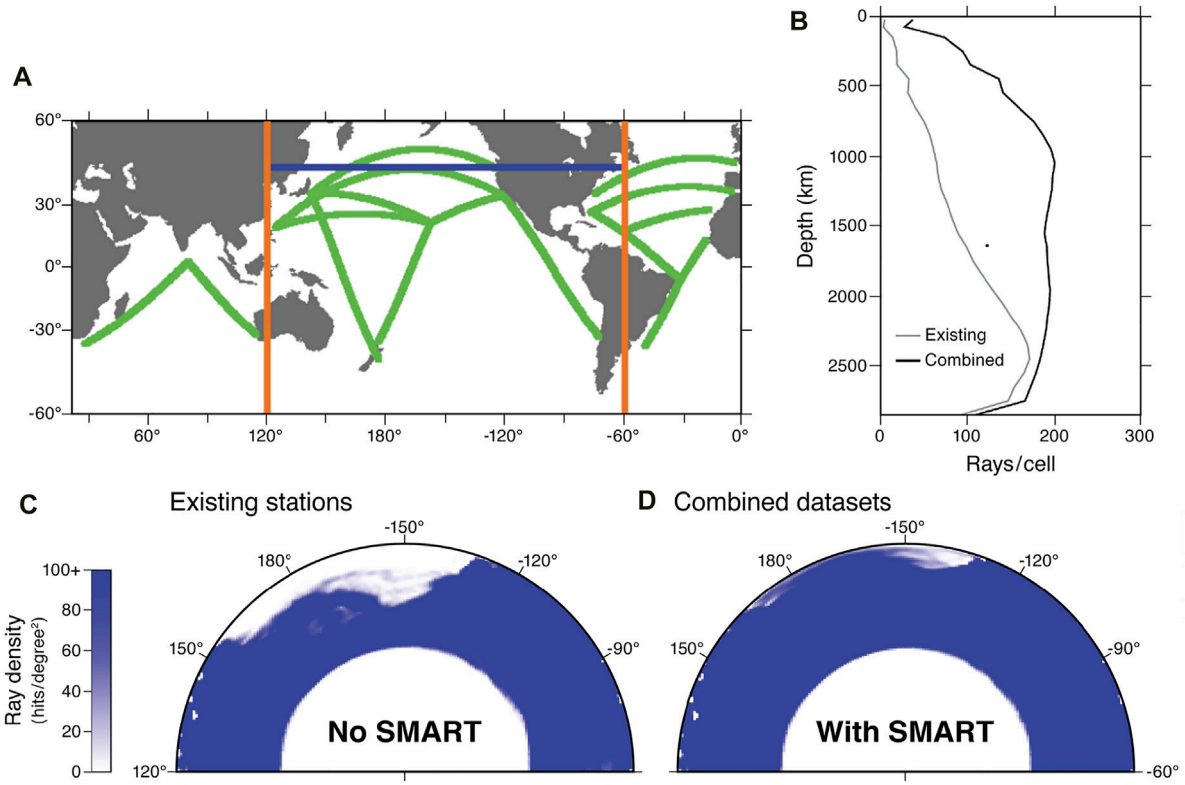


**FIGURE 3 | (A)** Notional SMART cable routes. **(B)** Comparison of coverage for seismic paths sampled beneath the northern Pacific Ocean, for existing stations (gray line) versus addition of notional SMART Cables (black). The curves represent the material volume in which each 1° × 1° x 100 km depth element is sampled by more than 100 rays. Horizontal axis represents units of $10^5$ cubic kilometers (Ranasinghe et al., 2018). **(C,D)** Example of ray path coverage (hit counts) for 1 × 1 degree x 100 km depth volumes in north-central Pacific, for **(C)** existing station coverage vs. **(D)** combined existing stations and SMART cables for the section indicated with a blue line in **(A)**. This modeling was undertaken using the global ak135 Earth model. Color scale saturates at 100 rays per volume element.

particularly for the highly tsunamigenic earthquakes with slip near a subduction zone's trench.

Coastal sea-level stations provide data on the local impact and are helpful for fast assessment of the most strongly influenced areas. However, tsunamis and the effects they have on coastal areas can be strongly affected by near shore bathymetry and shape of the coastline. The modification of the tsunami by shoaling and/or resonance make it difficult to assess a tsunami's impact on every shore far from the tsunami source, particularly as their numerical simulation is computationally very expensive because it requires very high-resolution bathymetry data. In contrast, propagation in deep water is well understood and described by the shallow water wave equation. Measurements of the tsunami in deep water (wavelength and amplitude) along the wave propagation are thus extremely useful for validating and augmenting tsunami forecasts and improving the precision with which the tsunami threat can be determined in the far field. It is precisely this kind of information that SMART cables can provide and at potentially much higher resolution than the existing sparse DART stations.

SMART cables parallel to offshore seismic zones can also be beneficial for issuing tsunami warnings in the near field. SMART cables will have pressure sensors as well as seismic instrumentation, accelerometers that will provide useful information regarding earthquakes. The additional seismic information will aid in detecting earthquakes (alerting TWC duty scientists) and determining the hypocenter, earthquake magnitude, finite fault slip pattern, and its CMT with less lag and lower uncertainties in comparison to relying on land-based measurements alone.

Tsunami forecasts can be based on the CMT (Wang and Becker, 2012), which provides the geometry of the fault, direction of faulting, and an authoritative estimate of the earthquake magnitude. This information allows the surface displacement to be calculated which in turn is used to force a tsunami propagation model, generating a tsunami wave-height forecast.

Unfortunately, the CMT has limitations when it comes to generating tsunami forecasts. For example, real-time CMT analysis is insufficient for resolving complex events such as the recent August 12, 2021 South Sandwich Islands earthquake sequence. In addition, the tsunami excitation can be further exacerbated by displacement along splay faults and earthquake-triggered submarine landslides (e.g., Carter et al., 2014), which are very difficult to detect by seismology alone. A recent example is the strike-slip Alaska earthquake of October

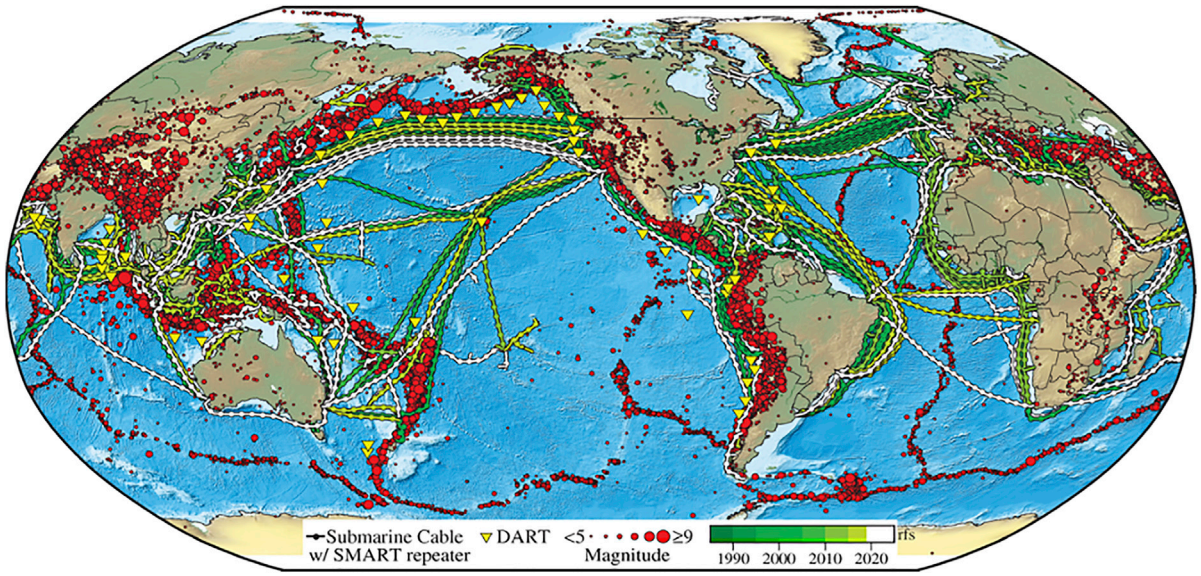


**FIGURE 4 |** Global map of ~1 million km of operational submarine telecommunications cables (green present, white in progress/planned; SMART repeaters shown every 300 km; rfs—year ready for service), historical earthquakes (red), and DART tsunami buoys (yellow triangles). Cable data: TeleGeography's Telecom Resources licensed under Creative Commons ShareAlike; DART Buoy locations: NOAA National Data Buoy Center; Seismic data: USGS Earthquake Catalog. Permission obtained for use of figure.

19, 2020 (Herman and Furlong, 2021). The tsunami recorded on nearby DART buoys was much greater than expected given the Pacific Tsunami Warning Center's (PTWC's) forecast based on the CMT. Another example of a tsunami generated or augmented by a submarine landslide is the tsunamis generated by 1998 Papua New Guinea M7.0 earthquake (Heidarzadeh and Satake, 2015). Subaerial landslides also pose a tsunami risk. For example, the Lituya Bay, Alaska, megatsunami (1958) was the result of a subaerial landslide triggered by an M7.8 strike-slip earthquake (Fritz and Hagar, 2001). Of particular concern in the United States is the potential for a great tsunamigenic subaerial landslide in Barry Arm Alaska (Dai et al., 2020). Although the standard repeater spacing in SMART cables would, in most cases, not be sufficient to have much of an impact on near field warnings from landslide events based on pressure recordings, governments could decide to decrease the spacing or optimize cable routes near coastal areas assessed to be at risk for such an event. For the seismic detection of submarine slides by accelerometers and pressure sensors even a standard SMART cable might be sufficient; however, too little is known about the seismic signature of submarine slides to be able to judge the feasibility of this approach.

Today there are only some 70 or so ocean bottom pressure sensors (e.g., on DARTs buoys, and installed on DONET, S-net, ONC and OOI cabled observatories) in the deep ocean, whose data are (openly) available in real-time to tsunami warning centers. The vast majority of these are in the Pacific Basin. SMART cables can increase that number by orders of magnitude, well into the thousands (**Figure 4**). Such an abundance of near-real-time information can be used to validate and/or revise forecasts making tsunami warnings for areas >1,000 km from an earthquake more precise and conversely greatly reducing the potential of unnecessary warnings and evacuations.

The previous paper (Howe et al., 2019) presented preliminary calculations performed at the PTWC as to how SMART cables can improve the tsunami warning system. In that study the calculations were based on five hypothetical cables spanning the Pacific basin containing ocean bottom pressure (OBP) sensor/seismometer packages. In this paper, PTWC added another hypothetical SMART cable that follows the coastline extending from central Mexico south along the west coast of South America. This cable roughly follows the outer rise of the subduction zone along this section of coastline. These routes are not specifically based on any existing telecommunication cable route. However, coast parallel telecommunication routes do currently exist. For instance, the recently installed Curie cable from Los Angeles, United States to Valparaiso, Chile, is roughly 300 km offshore.

**Figure 5** shows the routes of hypothetical SMART cables that contain OBP sensor/seismometer packages and the Pacific basin subduction zones with potential epicenters of great earthquakes. The SMART cable repeaters containing these instrument packages are spaced 100 km apart and the calculations assume 905 synthetic earthquake sources located every 50 km along the Pacific Basin subduction zones.

The estimation of the potential impact of SMART cables on the speed with which an earthquake hypocenter might be determined is based on two criteria. Five stations must detect the compressional primary P-wave and the largest azimuth gap between any two (azimuthally) neighboring stations with respect to the hypocenter must be less than 180°. The calculation assumes

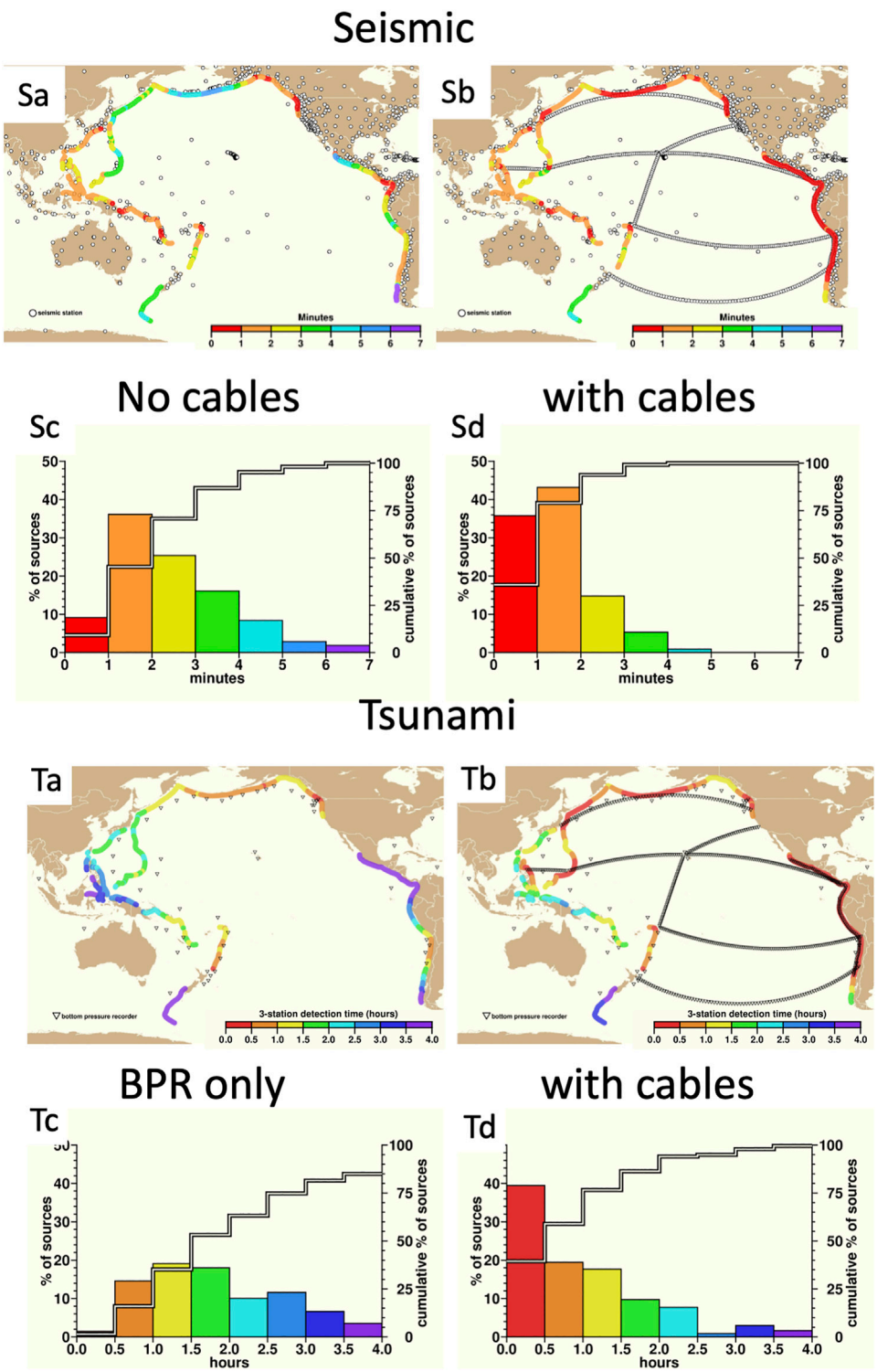


**FIGURE 5 |** Maps Sa and Sb (top) show existing seismic stations alone (Sa, gray circles) and then with six simulated SMART cables (Sb, repeaters gray circles), respectively. Colored dots represent simulated megathrust subduction earthquake epicenters, and the color bars the time to detection (0–7 min). Maps Ta and Tb show existing DART bottom pressure recorder (BPR) stations (triangles) and then with six simulated SMART cables (repeaters gray circles), respectively. The color bars denote the time to detection (0–4 h). Again, dots in both cases represent simulated potential megathrust subduction earthquake epicenters and the color bars the time to detection (red represents shorter time). The lower histograms are used to obtain statistics as discussed in the text.

an earthquake at each epicenter and then computes the minimum time required to meet the five station and azimuth gap requirement. The calculations are performed based on the seismic station distribution available to PTWC (as of early 2021) without and with the SMART cables in **Figure 5** Sa and Sb, respectively. The resulting distribution of time-to-detection is shown in **Figure 5** Sc and Sd. The inclusion of these six notional SMART cables would have the potential to speed up Pacific-wide earthquake epicenter determinations by an average of ~42%.

Similarly, we calculated the reduction in latency in tsunami detection that is achievable with cabled OBP sensors, following a tsunamigenic earthquake. Using the 905 epicenters in **Figure 5**, tsunami travel times are computed from each epicenter to the set of operational (56 as of September 2021) OBP sensors received by PTWC with and without the OBP sensors associated with the SMART cables. With SMART cables in place, the time required to observe the tsunami arrival at three or more OBP sensors is reduced by ~57%.

Specifically, the four histogram charts in **Figure 5** compare detection time for earthquakes (left) and tsunamis (right), first using only those sensors available in 2021 (Sc and Tc), and then using existing sensors augmented with simulated data from future SMART cable sensors (Sd and Td). Detection of an earthquake—meaning reception on ≥ 5 seismic instruments—is reduced from 2.44 to 1.42 min, or from an average of 2 min 26 s down to 1 min 25 s, which is a 42% reduction. Sixty seconds is an eternity in earthquake detection and warning for a duty scientist at a tsunami warning center.

Tsunami detection at ≥ 3 pressure sensors showed a similar percentage improvement, dropping from 2.4 to 1.0 h, for a 57% improvement. Although wide area tsunami warnings are already helping to save lives, unnecessary or overly broad warnings and evacuation orders have significant financial and safety costs. The reduction in detection time coupled with a better description of the wave field will help better characterize the source, improve forecasts in both the near and far field, and potentially reduce false alarms. Thus, SMART cable augmented tsunami detection will help reduce the direct and indirect costs associated with tsunami warning and evacuation programs, as well as likely improve confidence in the warning system and compliance in the event of a necessary evacuation.

The statistics presented here could be further improved if SMART-enabled repeaters were deployed more densely and/or nearer the coast or seismically active regions.

## 2.3 Oceanography

Oceans are currently predominantly monitored by surface *in-situ* (ships, buoys, moorings, or floats) and remote sensing (satellite) techniques. Each of these techniques covers specific time and space scales (daily, global but only surface measurement from satellites, real-time but only discrete location for moorings, global but limited to 2000 m depth for floats, etc.). The deep ocean and the important processes occurring there remain extremely undersampled and unobserved. Data from SMART cables would fill critical gaps in our existing monitoring systems, complement existing observations, increase our current level of understanding of the ocean, and improve our capability to predict its future evolution (Howe et al., 2019).

### 2.3.1 Ocean Temperature

The Antarctic Bottom Water, which fills much of the deep oceans (Johnson, 2008), is warming, absorbing substantial amounts of heat, and contributing to sea level rise (**Figure 6**; Purkey and Johnson, 2010). Oceanographers currently rely primarily on Global Ocean Ship (GO-SHIP) repeated transoceanic hydrographic sections (Talley et al., 2016) to monitor the deep ocean water properties, along with a few time series stations (Lukas et al., 2001) and deep instruments on moorings (McKee et al., 2011; Send and Lankhorst, 2011). Deep Argo floats operational to a depth of 6,000 m are being developed, with a few regional pilot arrays already deployed or planned (Jayne et al., 2017; Johnson et al., 2019), and a global network envisioned (Johnson et al., 2015). Changes in the deep ocean, however, remain undersampled (Johnson et al., 2015). SMART cables, with transoceanic sampling of temperature in the bottom boundary layer at roughly 50 km resolution, would complement other data sets and facilitate investigation into water temperature variability, trends, and circulation.

### 2.3.2 Ocean Circulation

The Atlantic meridional overturning circulation (AMOC), which redistributes heat in the Atlantic Ocean, is changing (Smeed et al., 2018). The changes are associated with variations in ocean temperature, air–sea heat flux, and sea level. Since 2004, the RAPID/MOCHA array has been providing estimates of the AMOC by estimating the pressure gradient between the western and eastern continental slopes at 26°N (McCarthy et al., 2015). From the AMOC strength, the climate-relevant meridional heat transport and its variation can also be inferred (Johns et al., 2011). SMART cables would complement and extend the existing AMOC estimates in two ways. First, OBP measurements on cables spanning an entire ocean basin could measure the pressure differences at many depths (for instance, over the Mid-Atlantic Ridge) between the western and eastern boundaries of the basin (Hughes et al., 2018). The pressure differences are directly related to the transports at those depths. Second, multiple cross-basin transects by SMART cables at different latitudes would allow a division of major ocean basins into boxes. This could also provide longitudinal resolution, for instance with the CAM-2 system between Portugal and the Azores (**Section 4.3**). Geostrophic transports across box boundaries could then be estimated from OBP observations as just described, allowing the mass balance of individual boxes to be calculated. These box models would finally allow a quantification of the long-term mass evolution in an ocean basin, based on unaliased measurements.

### 2.3.3 Sea Level Rise and Mass Distribution

Global warming has caused global mean sea level to rise at a rate of 3.0 ± 0.4 mm/year since 1992 (**Figure 7**), with an estimated current acceleration of 0.084 ± 0.025 mm/year$^2$ (Nerem et al., 2018). Depending on the emissions scenarios, the mean sea level

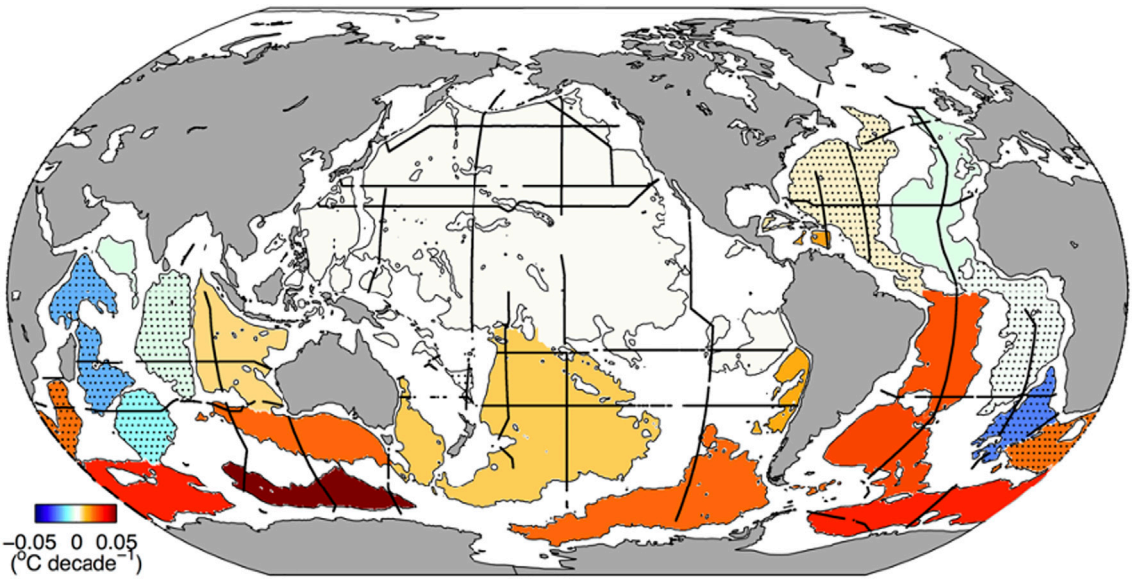


**FIGURE 6 |** Deep basin (thin solid lines) average warming rates below 4,000 m from the 1990s to the 2000s (°C decade$^{-1}$, colorbar) based on data from Purkey and Johnson (2010). Estimates are based on data from decadal repeats of hydrographic sections (thick solid lines) first occupied during the World Ocean Circulation Experiment (WOCE) (King et al., 2001) and subsequently by GO-SHIP (Talley et al., 2016). Stippled basins have average warming rates that are not statistically significantly different from zero at 95% confidence. Permission obtained for use of figure.

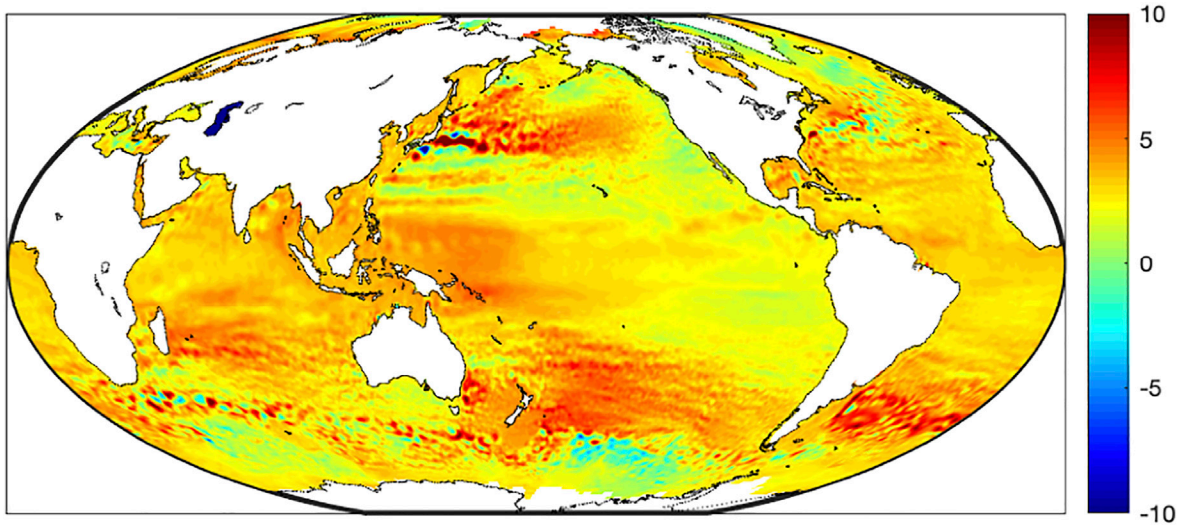


**FIGURE 7 |** Mean sea level trend (mm/y; January 1993–October 2019) from multi-mission satellite altimetry (data source: AVISO).

will rise between 41 cm (for the lowest emissions scenario) and 82 cm (for the highest emissions scenario) by 2100 (IPCC AR6).

Individual contributions to sea level change, such as barystatic (mass changes, e.g., due to melting land ice) and steric (expansion of water, e.g., due to warming) effects in the ocean, as well as Earth-produced eustatic (changes in ocean volume due to geometric changes in the seafloor boundary) and isostatic (changes in height of land) effects vary considerably across the ocean basins. Sea level rise is not homogeneous and sea level variability patterns can be determined directly by various measurement techniques and sensors (e.g., radar altimetry or gravity measurements from satellites and land-based tide gauges). The identification of individual contributing effects, however, requires complementary observation methods. OBP observations provide the amount of local barystatic sea level change, which is the change due to added water mass from melting land ice. SMART cables would provide a network of long-lasting, temporally unaliased OBP sensors that could be quite dense in

some basins and unaliased along the cables. The difference between total sea surface height (SSH) from satellite altimetry and OBP from the pressure sensors gives the steric component of SSH, e.g., due to density changes/thermal expansion of sea water. The OBP measurements reflecting added mass would enable separation of the steric and barystatic contributions to sea level change at a particular location, whose differentiation is required to understand the causes of sea level rise and thus for reliable sea level projections.

As there is drift in the currently used pressure sensors, the latter can effectively be calibrated by using GRACE satellite gravity data providing coarse estimates (300 km scales) of OBP (Worthington et al., 2019) or by measuring the steric component by occasional Argo float profiles, shipboard conductivity, temperature, depth (CTD) profiles, or inverted echosounders (Baker-Yeboah and Watts, 2009; Hughes et al., 2013). This should be adequate for determining signals with periods less than half the record length. See **Section 3.3** for more discussion of the pressure sensors.

### 2.3.4 Ocean Surface (Barotropic) Tides

SMART cable measurements of OBP would allow unique, basin-scale quantification of barotropic tidal variability over a wide range of timescales, necessary as a forcing term in ocean modeling, but also provide ground truth for secular and seasonal changes to tidal correction models used in altimetry and gravimetry.

Simulation of the gravitationally forced surface (barotropic) tides has now become quite accurate even without assimilation of satellite altimetry data. Forward tide models now routinely capture 90% or more of tidal sea surface height variance (Arbic et al., 2004; Egbert et al., 2004).

However, there are still tidal phenomena that are poorly described or understood such as the lesser tidal constituents, seasonal variability of all constituents, non-linear constituents, rapid variation of constituent structure in shallow water, and shifting sinks of energy as the global environment changes. Although these factors exhibit small amplitudes, their global distributions are sought due to their impacts on phenomena such as internal tide generation, deep ocean mixing, paleotide descriptions, and Earth structure. They also have utility in defining the tidal "correction" that must be applied to satellite altimetry and gravity data to extract the sub-diurnal variability of ocean circulation features as well as sea level rise over long periods. Ocean bottom pressure observations provide one of the better tools for exploring the finer details and changes of the barotropic tides, because the non-tidal "geophysical noise" (internal waves, mixed-layer currents, and coastal-trapped edge wave, etc.) in which the tides are embedded is much weaker at the seafloor far from the coast than at the sea surface or near the coast (Ray, 2013).

### 2.3.5 Microseisms and Infragravity Waves

Observations of the ambient noise in the ocean can improve our understanding of both the structure of the oceanic lithosphere and waves at the ocean surface. Wind waves breaking and interacting in the shallow waters of the continental shelves, as well as in the open ocean, generate seismic noise in the period band of the wind-driven surficial waves and at shorter periods (2–20 s). This noise, termed microseisms, constitutes the principal seismic noise source on Earth. The ambient noise spectrum in the deep ocean, and on land, is dominated by the so-called secondary microseisms with a peak period of ~6 s (Longuet-Higgins, 1950). They are generated from the interaction of opposing trains of ocean waves that impose a (non-linear) pressure signal at the seafloor with half the period of the interacting waves. This pressure signal, as measured with SMART pressure sensors, couples to the solid Earth and excites seismic Rayleigh waves measured on the accelerometers. With few exceptions, the occurrence of opposing wavetrains is limited to near shore regions due to wave reflection at the coast or shallows. Nevertheless, the excited Rayleigh waves have a long range and can be observed even at the farthest reaches from the oceans in central Asia (Bromirski et al., 2005; Ardhuin et al., 2011; Chen et al., 2015; Butler and Aucan, 2018) as well as in the centers of large ocean basins (Dahm et al., 2006).

Infragravity (IG) waves are surface waves with periods ranging from minutes to hours. Nonlinear interactions between wind waves in the open ocean and at the coasts generate IG waves at periods from 0.5 min to many tens of minutes. IG waves appear as either "free" or "bound" waves (Herbers and Guza, 1994; Herbers et al., 1995), where the bound waves are tied to underlying groups of wind waves and become free at the shoreline where the short wind waves break (Bertin et al., 2018). A small fraction of the resultant free IG energy leaks into the open ocean where it can spread for thousands of kilometers, with horizontal wavelengths of up to 10 s of kilometers and heights of up to 10 s of centimeters with significant seasonal variability (Aucan and Ardhuin, 2013). IG waves at longer periods up to hours have also been identified and appear to be forced by the surface barotropic tides and solar modes of oscillation (Chave et al., 2019). Given the size and wavelength of these IG waves, they are a source of aliasing noise in satellite measurements of sea surface elevation. Thus, a better understanding and modeling of the temporal and spatial variations of the IG waves as measured with the SMART pressure sensors could improve the processing of satellite altimetry data (Ardhuin et al., 2014).

# 3 TECHNICAL APPROACH

## 3.1 SMART Cable Concept Requirements

The defining characteristic of SMART cables is the integration of environmental sensors into commercial subsea telecommunications cables. The crucial objectives are: 1) to measure ocean bottom temperature and pressure, both of which are essential ocean variables, together with acceleration in three axes; 2) to have little or no impact on the operation of the telecommunications system that hosts the sensors; 3) to require no special handling or deployment methods; and 4) to be sufficiently reliable that 95% of all sensors operate for a minimum of 10 years. SMART cables will provide data that is unavailable or sparsely represented in current data sets. As a tsunami warning system, SMART cables can provide broader

coverage and greater reliability than the existing network of moored/buoy-based detection systems. Long term measurement at fixed locations will allow new insights into environmental processes. A world-spanning network of fiber optic cables is operated, maintained, and periodically renewed by the telecommunications industry. The technical aspects are reviewed by Chesnoy (2016). Present estimates (2021) indicate that over 1.3 million km of cable and more than 426 independent subsea cable systems are in service (Telegeography, 2021). On many of the more active (lucrative) transocean routes, new cables are installed to replace or supplement existing systems at intervals ranging from three to 10 years; each new deployment provides an opportunity to include sensor capabilities. On less active routes, cables can be left in service for their engineering design life of 25 years.

## 3.2 From Single-Purpose Cables to SMART Cables

Subsea telecommunications cables incorporate "repeaters"—cylindrical housings containing Erbium Doped Fiber Amplifiers (EDFAs)—at regular intervals along the cable. To create a SMART cable, sensor functions must be incorporated into the repeater. Necessary functional elements include the sensors, digital signal processing, optical transceivers, and associated power supply circuits. Data may be transmitted to shore over fibers added for that purpose or as an out-of-band channel on the main fibers.

Adding these elements requires substantial modifications to the repeater leading to several engineering challenges that must be addressed (Lentz and Howe, 2018). Accelerometers can be mounted inside the repeater housing. Temperature and pressure sensors must be placed outside the repeater housing, in contact with the environment, necessitating a penetration of the housing to connect these sensors to the internal circuitry. The sensors must be isolated from high voltages present within the repeater and fail-safe so that the normal operation of the repeater cannot be impacted by faults in the external sensors. All of this must be done in a manner that is consistent with the 25-year expected operating life and 8,000 m deployment depth of a commercial repeater.

The earliest example of a submarine cable observatory is the Geophysical and Oceanographysical-Trans Ocean Cable (GeO-TOC), which was installed in 1997 midway between Guam and Japan using the retired TPC-1 communications cable (Kasahara et al., 1998). The GeO-TOC system anticipated the development of SMART cables by almost two decades yet included all essential SMART cable features: a three-axis accelerometer; pressure sensor; and precision thermometer. These were incorporated into an in-line repeater housing that was deployed from a cable ship in a conventional manner.

In the first decade of the 2000 s, attention shifted to regional-scale observatories such as NEPTUNE (ONC), OOI RCA, and DONET (Barnes et al., 2007; Best et al., 2007; Hazell et al., 2007; Kawaguchi et al., 2008; Consortium for Ocean Leadership 2010). Each of these employed telecommunication cable and repeaters; bespoke housings (i.e., nodes) were developed for interconnection, power delivery, and communications. Sensors were installed on separate platforms outside the main pressure housings. These projects demonstrated the usefulness of commercial telecommunications technology in the realm of ocean observing but did not incorporate the close integration needed to create a true SMART cable.

Following the Tōhoku earthquake and tsunami of 2011, Japan undertook rapid development of a large-scale network of subsea seismic and pressure sensors (Aoi et al., 2020). The resulting S-net system incorporates many of the functions essential to a SMART cable. The overall deployment comprises 150 observation nodes along 5,700 km of cable divided into six independent subsystems (five running up and down the slope and one offshore of the trench), with average spacing between nodes of ~50 km. Each observation node consists of an underwater housing containing seismometers and pressure sensors connected in-line with a telecommunications cable. The result closely resembles a telecommunications repeater, however, with housings having a length of 2,260 mm, these require modification of conventional cable laying equipment.

Another in-line ocean bottom seismometer was developed by the University of Tokyo (Shinohara et al., 2014). This design is more compact than the S-Net observatory at 50 cm long and 13 cm in diameter. A total of four units and 25 km of cable were deployed off the west coast of Awashima in 2012 using conventional cable laying equipment. This system uses ethernet switches and optical transceivers are employed, an approach which could also be applied to SMART cables. In 2015, this was commercialized using an industry standard repeater housing and deployed off Sanriku with three nodes and a length of 105 km. The deepest node had an underwater mateable connector providing power over ethernet (PoE) to a pressure sensor (Shinohara et al., 2021).

The S-Net and Sanriku system designs demonstrate the technical feasibility of developing a SMART cable system but stop short of integrating sensor functions into a system built primarily for telecommunications. Further effort is needed to develop a SMART cable system that satisfies the needs of both science and commercial telecoms operators.

## 3.3 Sensors

The SMART cable sensor suite comprises sensors for temperature, pressure, and acceleration, chosen based on scientific merit and for engineering simplicity. Sensor performance parameters are based on well proven sensors, long used in oceanography, cabled observatories, and early warning systems. Temperature is a local measurement while pressure and acceleration provide remote sensing of the entire water column, remote events, and the intervening media. Detailed requirements for the SMART sensors are given in the several white papers (Lentz and Phibbs 2012; JTF Engineering Team, 2021).

Temperature sensors can meet the required initial accuracy of 1 mK and stability of 2 mK/year. They need to be mounted some distance from the repeater, a "heat island" dissipating ~50 W. This can be done in a sheath several meters from the repeater and, possibly, with several sensors azimuthally distributed around the cable to assure one is exposed to open water. Data from buried

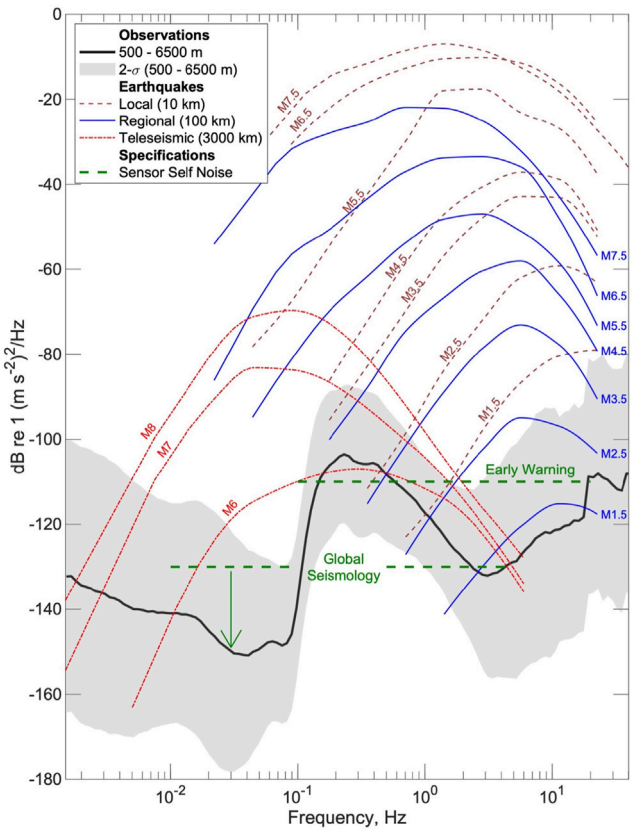


**FIGURE 8 |** Vertical acceleration spectra showing seafloor noise levels, typical earthquakes of various magnitudes at local (10 km), regional (100 km) and teleseismic (3,000 km) distances, and illustrative accelerometer self-noise specifications for earthquake and tsunami early warning and global seismology. The arrow illustrates the potential benefit for global seismology applications of sensors with very low self-noise at lower frequencies. Seafloor noise levels are from a compilation of over a decade of US ocean bottom seismometer experiments (Janiszewski et al., 2020) and show average noise levels and two standard deviation variations at depths greater than 500 m. The acceleration spectra of typical earthquakes are from Clinton and Heaton (2002) and have been converted from octave wide bandpass acceleration to power spectral density following Cauzzi and Clinton (2013).

temperature sensors will have to be evaluated on a case-by case basis to determine usefulness.

Pressure sensors also need to reside external to the repeater housing with access to local ambient pressure. Typically, there is a dedicated temperature sensor immediately next to the pressure sensing element to account for temperature dependence of the pressure measurements. The main requirement is a depth rating to 7,000 m with an overpressure tolerance to 8,000 m, the standard telecom rating. Nano-resolution Absolute Pressure Gauges (APG) manufactured by Paroscientific Inc. provide the resolution needed for tsunami detection, oceanographic observations, and other applications. Such APGs have initial sensor drift equivalent to several tens of centimeters per year. Further, as Wallace et al. (2016) point out, "The drift is composed of an initial exponential drift in the month or two following the deployment" that could include an initial settling signal.

Calibration methods to account for this are described in **Section 2.3.3**. The longest period signal that could be observed would be half the record length, so with the cabled sensors this could be a decade or so. Methods to overcome this with *in-situ* calibration are in development (Sasagawa and Zumberge, 2013; Wilcock et al., 2021). Shinohara et al. (2021) conclude that "Through the evaluation of records of tides and a tsunami, it is estimated that the buried pressure gauge records data with the same quality and amplitude as the pressure gauge on the seafloor."

Three-axis accelerometers, also called strong motion sensors, can reside inside the repeater housings; indeed, simple accelerometers are already included in one supplier's repeaters for engineering purposes (Xtera, 2016). Shinohara et al. (2021) state: "Rotation of the cylindrical pressure vessel around a longitudinal axis may occur due to its shape. Using long-term data from the accelerometers, rotation around the longitudinal axis was estimated. No large rotation of the cylindrical vessel was observed during the observation period." And further, "The [node] buried below the seafloor has a lower noise environment than the [node] on the seafloor," as is commonly found with seafloor seismic instrumentation (Duennebier and Sutton, 2007).

We note that the wet demonstration off Sicily will add to information on the effective transfer functions of all three sensors; see **Section 4.1**.

As discussed in **Section 2**, there are many potential applications of seismic observations on SMART cables, each of which may guide accelerometer specifications. Generally, the three most important applications are: 1) the early detection and characterization of great subduction zone earthquakes for earthquake and tsunami early warning; 2) filling ocean gaps in the global seismic networks to improve earthquake catalogs and seismic images of the Earth's deep interior; and 3) providing additional monitoring capability for local earthquakes in the offshore regions of active margins. The sensor specification for these goals can be broadly understood by comparing spectra of seafloor seismic noise levels with the typical amplitudes expected for earthquakes at teleseismic, regional and local distances (**Figure 8**).

For earthquake and tsunami early warning on and near subduction zones, it is essential that the seismic sensors deployed do not go off scale for the largest earthquakes. This mandates the use of strong motion accelerometers with a full-scale range of several *g*. For example, peak accelerations recorded for the 2011 Tōhoku-Oki earthquake reached nearly ±3 *g* (Goto and Morikawa, 2012). Because the orientation of the repeater housing may vary, the accelerometer should measure accelerations in three-orthogonal directions in all physical orientations. The ShakeAlert earthquake early warning system on the US west coast utilizes vertical accelerometer data that is high pass filtered with a 0.075 Hz cutoff (Kohler et al., 2020); at longer periods the acceleration records cannot be reliably integrated to yield ground displacements. No high frequency cutoff is applied in the ShakeAlert system although most of the spectral power will be at frequencies of <10–20 Hz. The self-noise requirements of a sensor for earthquake early warning are not

very onerous because the goal is to warn for large earthquakes with a system that has been verified by successfully detecting moderate earthquakes. The ShakeAlert system is designed for earthquakes down to magnitude 3.0 (Kohler et al., 2020), which, considering the high noise levels in the secondary microseism band from 0.15 to 0.5 Hz, can be accomplished by an accelerometer with a noise floor of −110 dB re 1 $(m\ s^{-2})^2\ Hz^{-1}$ from 0.1 to 20 Hz (**Figure 8**).

For studies of teleseismic earthquakes with seismic sensors deployed in deep waters, only the very largest earthquakes (magnitude ≥ ~6.5 at 3,000 km in **Figure 8**) will have amplitudes that exceed secondary microseism noise levels. For smaller earthquakes, there are two key frequency bands (Webb, 1998). The first is the low noise notch between ~0.03 and 0.1 Hz that lies below the secondary microseism band but above the frequencies at which long period ocean waves (infragravity waves) are felt on the deep seafloor. In this band, the surface waves and long period body waves from even quite small earthquakes can be detected. **Figure 8** shows that a noise floor of −130 dB re 1 $(m\ s^{-2})^2\ Hz^{-1}$ is sufficient to record a magnitude six earthquake at 3,000 km even at noisy sites, while lowering the sensor noise floor to −150 dB re 1 $(m\ s^{-2})^2\ Hz^{-1}$ would facilitate studies of earthquakes of magnitude five at sites where the seafloor noise levels are sufficiently low. Extending this frequency band down to ~0.01 Hz would facilitate the recording of longer period surface waves for large earthquakes. The second frequency band of interest extends from ~0.5–5 Hz. Here a sensor noise floor of about −130 dB re 1 $(m\ s^{-2})^2\ Hz^{-1}$ is sufficient to record high frequency teleseismic P waves when their amplitudes exceed seafloor noise levels (**Figure 8**). We note that leveraging array techniques and azimuth/slowness stacking of adjacent sensor packets can lower the effective detection threshold for regional and teleseismic earthquakes. However, it is also important to recognize that the cable attached to the repeater may impact the coupling of the repeater housing to the seafloor and lead to enhanced susceptibility to water current noise, thus potentially limiting the fidelity of recorded ground motions, particularly at the shorter periods. Here, analysis of the data from initial demonstrator deployments is needed to obtain robust data on coupling and wave-induced noise for sensors in repeater housings.

The combined specifications for these two objectives suggest a sensor noise floor of −110 dB re 1 $(m\ s^{-2})^2\ Hz^{-1}$ from 0.1 to 20 Hz decreasing to −130 dB re 1 $(m\ s^{-2})^2\ Hz^{-1}$ at 0.5–53 Hz and at least as low as -130 dB re 1 $(m\ s^{-2})^2\ Hz^{-1}$ at ~0.01 and 0.1 Hz, and ideally lower within this band (**Figure 8**). Note that a high-resolution low-noise broadband pressure gauge provides a complementary means to record earthquakes (Webb, 1998) and so the needs of seismology should also contribute to the pressure sensor specifications.

Existing commercial sensors meeting these requirements will be used for the first SMART systems. Improvements in size, reliability, and ease of use would facilitate wider adoption in cable systems and an evolution towards sensor designs developed specifically for SMART cables could set off a virtuous circle of easier implementation of SMART cables driving demand and further development of sensor designs optimized for the SMART environment.

The addition of other sensor types, including hydrophones, conductivity sensors, inverted echosounders, as well as acoustic or optical modems capable of relaying data from free swimming sensors, has been considered. A new *in-situ* calibration method called ambient-zero/internal pressure case-ambient (A-0-A; Wilcock et al., 2021) would approach accuracies required for detecting longer-term (secular) vertical deformation signals, seafloor geodesy, and absolute sea level rise. Given that the SMART repeater will provide a general interface, in principle it should be possible to add these and others once the initial concept has been successfully demonstrated. However, it is very important to keep the initial systems as simple as possible to minimize their impact on the telecommunications functions of the system.

There is a new distributed sensing technology based on using optical fibers themselves as sensors. Any strain (stretch) in the fibers can be detected by Brillouin optical correlation domain reflectometry (BOCDR; presently to 50 km; Galindez-Jamioy and López-Higuera, 2012), Rayleigh backscatter interferometry (Lindsey et al., 2017), or a combination of bi-directional transmission optical interferometry and absolute time measurement (Marra et al., 2018). A more recent development correlates changes in the polarization states of the optical signals carrying telecommunications traffic with localized stress on the fiber and has been used to detect seismic events along the west coasts of North and South America (Kamalov and Cantono, 2020; Zhan et al., 2021). These two methods open the possibility of passively using both existing and future *trans*-ocean fibers as continuously distributed seismic sensors. It is important to note that both these are distributed methods and do not provide the same resolution or precision as the point sensors, which will be used in SMART cables. For the benefit of the telecom mission, they can provide measurements directly related to cable integrity, e.g., cable movement due to external aggression (fishing and bottom trawling, anchors, submarine landslides, etc.). SMART cables with *in-situ* sensors and distributed "remote" sensing are complementary and both should be implemented in parallel.

## 3.4 Design and Development

The design and development of SMART cables will require an unprecedented level of cooperation between scientific organizations, cable system suppliers, and cable system operators. Achieving integration with telecommunications systems will require further refinement of the sensors, design and development of the signal processing and data transmission circuits, and mechanical integration into the repeaters. A full set of technical requirements is proposed in (Joint Task Force, 2015a).

Integration of the SMART functions into cable systems requires a substantial investment on the part of the cable system suppliers. Despite similarities in function, each supplier has different mechanical arrangements and manufacturing processes. Development of a reference design for the sensors, signal processing boards, and data communications should be pursued to reduce the burden on each potential supplier and to

ensure consistent results from the first generation of systems. Such a reference design would incorporate, at a minimum, circuit diagrams and functional code; one or more working benchtop prototypes would be assembled. Individual suppliers could then utilize this to create a functional design that is compatible with their repeater design.

Reliability is a significant concern for telecommunications cables. A rate of no more than one repair due to intrinsic failures in 25 years for 5,000 km of cable is a typical objective. As a matter of principle, the sensor functions must not impinge on the reliability of the telecommunications system. The sensor functions are unlikely to achieve this same level of reliability and must be designed to "fail safe" so that the telecommunications capabilities continue to function. A 10-year operating life is the initial goal (95 percent of sensors working at the end of 10 years), as this represents the timeframe in which a newer cable can be expected to be installed along the same route. Preliminary simulations indicate this is achievable but will require some level of redundancy, particularly in the optical transceiver functions.

Moving beyond the system suppliers, commercial cable system owners and operators must be persuaded to support SMART cables. Submarine cable systems represent a significant investment and a critical piece of strategic network infrastructure. Any interruption in operations has the potential to cause major disruptions. For this reason, system owners are reluctant to accept new or unproven modifications to existing designs without some substantial benefit in exchange. Smaller projects, particularly those serving island nations that are most at risk from climate change and tsunamis, are expected to be more amenable to SMART cables. Regional systems are also more likely to have unallocated fiber pairs and sufficient overhead margin in the electrical power budget, thus eliminating the objection that adding SMART functions reduces the cable's overall capacity. Addressing the concerns of the telecommunications industry will require a series of projects that demonstrate that all technical issues have been fully addressed.

# 4 PROJECTS UNDERWAY OR PLANNED

Here we describe five SMART projects at various stages of planning and implementation. The first, the InSEA Wet Demonstration, will show that sensors in a cable repeater mechanical configuration can return good science data. The second, Vanuatu-New Caledonia, is still in the planning stage, although some funding is already allocated. The Natitua South system connecting French Polynesia Tahiti to Tubaui to the south is in the RFP process at the time of this writing. Indonesia is developing in-country capability because SMART cables are seen as the basis of "cable-based tsunami" warning, which, in turn, will be the basis of the entire *in situ* tsunami warning system. Lastly, the most advanced SMART system is the CAM-2 project, linking Lisbon, the Azores, Madeira Islands together in a ring. This approved project is funded by the Portuguese government and should be ready for service in 2025.

## 4.1 InSEA Wet Demo

The Western Ionian Sea hosts one of the European Multidisciplinary Seafloor and water column Observatory (EMSO) Regional Facilities, about 25 km off the Eastern Sicily coast at 2,100 m water depth. An underwater electro-optical cable runs on the seafloor from Catania harbor and splits into two branches that host geophysical, environmental, and oceanographic seafloor platforms. It is managed by Istituto Nazionale di Geofisica e Vulcanologia (INGV) and Istituto Nazionale di Fisica Nucleare (INFN).

The observation area is prone to numerous natural hazards due to the high seismicity and nearby Mount Etna. A major earthquake/tsunami in this area in 1693 caused 60,000 casualties in and around Catania (Tonini et al., 2011), and another event in 1908 in nearby Messina killed about 75,000 people (Mildon and Meschis, 2019).

In 2019 the project InSEA, funded by the Italian Ministry of Research, began enhancements to the Western Ionian Sea infrastructure capabilities. One of the main goals of InSEA is to realize the SMART wet demonstrator (Joint Task Force, 2015b; Joint Task Force, 2016). A map of the areas with the cables and detail of the wet demo portion is shown in **Figure 9**.

The wet demo is designed to establish the effectiveness of seismometers and environmental monitoring components installed in and around the repeater housings of a traditional communications cable. The key objectives are to demonstrate that the cable can be deployed using an unmodified cable laying system and ensure that the acquired data are robust, valid, and scientifically useful.

The contract for the wet demonstrator was awarded to Guralp Systems Ltd. (GSL) by INGV in 2020. The wet demo project will consist of a 17 mm LW cable of 19 km length with sensors integrated into the housing of three industry standard repeaters. The housings will be installed 6 km from one another (**Figure 9**). Each housing will include a temperature sensor (SBE 39plus), absolute pressure gauge (APG, Paroscientific 8,000 series, 3,000 m version), GSL force balance accelerometer (FBA), and GSL broadband seismometer.

The GSL accelerometer has selectable gain between 0.5 and 4 g and a frequency response between DC and 200 Hz, with a noise floor of 10.2 ng $Hz^{-1/2}$ at 20 Hz. The GSL broadband seismometer has a velocity frequency response flat between 120 s and 100 Hz, with a noise floor of −173 dB at 0.1 Hz.

With a broadband seismometer, a force-feedback accelerometer and a MEMs accelerometer in the same enclosure, the system will provide a range of seismic data acquisition characteristics. After appropriate comparative analysis and evaluation, this data will provide input to the design decisions of future SMART cable installations.

Significant design work is underway to repackage existing Guralp instruments so they can be accommodated within a reclaimed repeater housing, while the temperature sensor and the APG will be housed in sensor pods connected to each repeater by external cables.

The wet demo will be deployed mid-2022 and connected to the Western Ionian Sea Junction Box that will provide power to the SMART cable demonstrator and data transmission to the shore

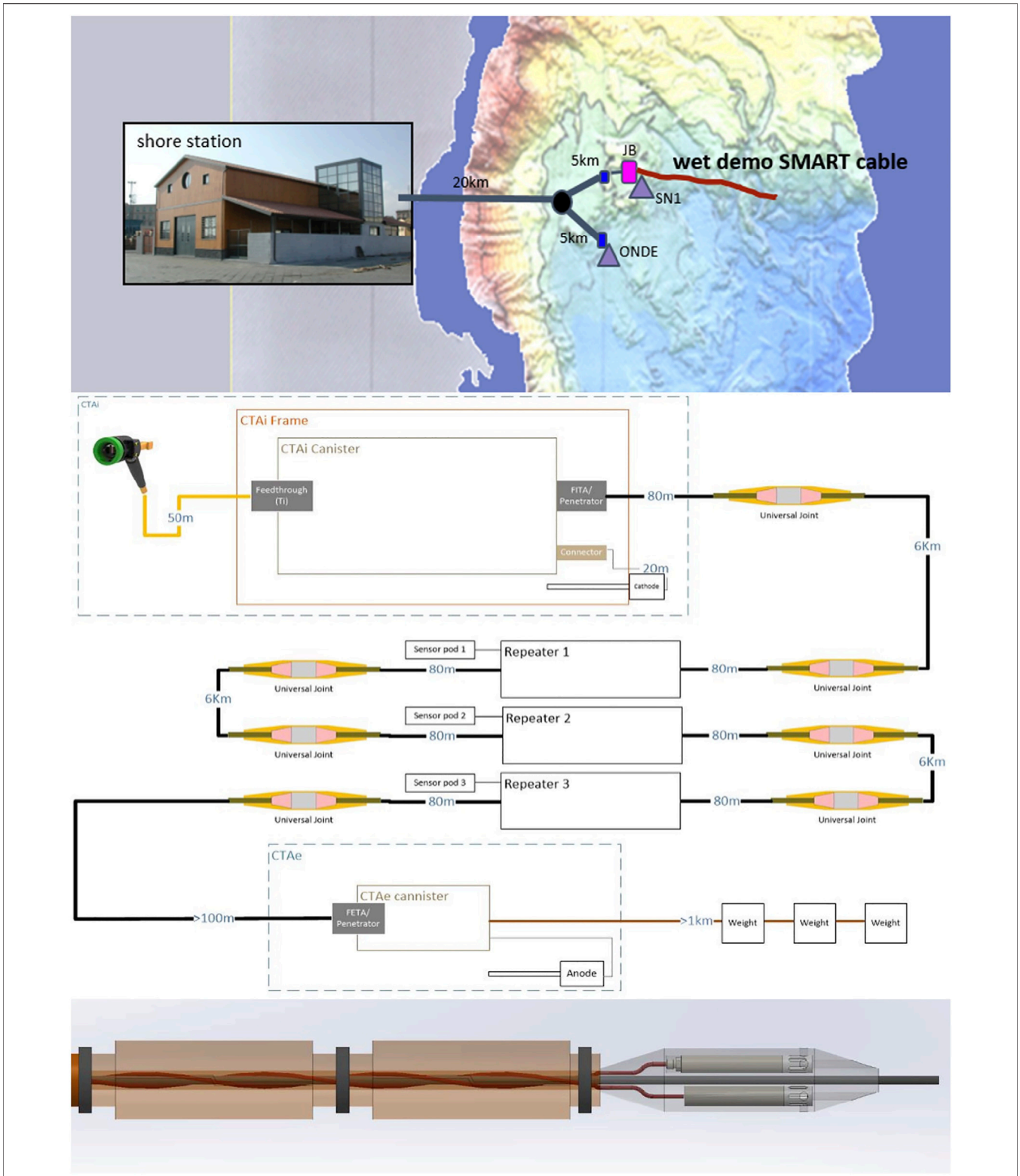


**FIGURE 9 |** (top) The EMSO Western Ionian Sea Facility where the InSEA wet demo SMART cable will be laid in 2022. (middle) The complete system diagram (bottom) Sensor pod containing pressure and temperature sensors.

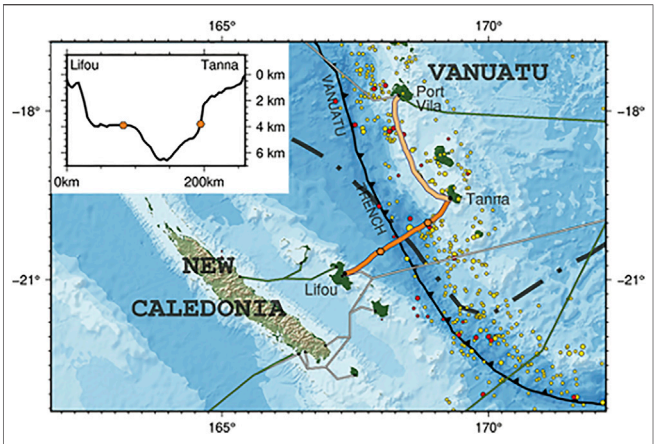


**FIGURE 10 |** Proposed SMART cable connecting Vanuatu and New Caledonia, with a SMART repeater on each side of the Vanuatu/New Hebrides Trench.

station in Catania harbor (**Figure 9**). All acquired data will be fully available to JTF for validation of the wet demo and the data will be open to the scientific community following JTF analysis and quality checking.

## 4.2 Vanuatu—New Caledonia

The archipelagic countries of Vanuatu and New Caledonia are in the South-West Pacific on either side of the New Hebrides/ Vanuatu trench. This trench is a very active, geologically young, subduction zone that regularly generates local to regional tsunamis (cf. Roger et al., 2019).

Vanuatu is the world's most at-risk country for natural disasters (United Nations World Risk Report, 2016). Due to its location near the seismically active Pacific Rim of high rate, active plate subduction, Vanuatu frequently experiences tsunamigenic earthquakes. Although Vanuatu and New Caledonia themselves have not experienced high death tolls from tsunamis or earthquakes, their tsunamis have historically caused devastation in the region and beyond. Vanuatu and New Caledonia recognize that better earthquake and tsunami monitoring is necessary. Sea level rise also continues to threaten the coastal communities of all Pacific Island nations, including Vanuatu. Higher sea levels will increase both the frequency of coastal damage and typhoon and tsunami inundation areas. Better data on ocean circulation and warming are critical for projecting the specific impacts of these threats to the local ecosystem and economy, and to guide mitigation strategies.

Planning is underway for a cable crossing the trench/ subduction zone to improve the international connectivity of Vanuatu and New Caledonia; provide valuable early warning tsunami capabilities for both countries and the region; and better understand geophysics of this subduction zone (**Figure 10**). The tentative installation date is 2025.

## 4.3 French Polynesia

In French Polynesia at the start of 2021 there were ~2,700 km of submarine optical fiber telecommunications cable across this oceanic territory, which is as large as Europe and comprised of 118 islands. Natitua is the name of the domestic submarine optical fiber telecommunication network handled by the Postal and Telecommunication Office (OPT) of French Polynesia (PF). Begun in 2017, this network interconnects the Society Islands to the Marquesas Islands and the Tuamotu archipelago. Since 2017 OPT has included SMART cables as an option in their Requests for Proposals (RFPs).

In November 2020 a Natitua extension called "Natitua South Cable" was funded to interconnect Tahiti to Rurutu and Tubuai islands in the Austral archipelago in the southern region of French Polynesia. This project would have an estimated 820 km cable divided in two segments: one of 765 km and another one of 55 km (**Figure 11**). At the time of this writing, the OPT is evaluating responses to an RFP that included the SMART option.

SMART capability in this region will provide many science and societal benefits. The seismic sensor will contribute to a long-term and potentially dynamic tomography investigation on the South Pacific superplume as well as an improved understanding of the regional upper mantle and French Polynesia hotspot properties (Barruol et al., 2009; Obayashi et al., 2016). Two major campaigns of ocean bottom sensors (seismic, pressure and electromagnetic) were conducted between 2003 and 2005 (Suetsugu et al., 2005), and then between 2009 and 2010 (Suetsugu et al., 2012) to illuminate the superplume beneath French-Polynesia. Analysis of the data from the campaigns demonstrated the detection of seismic events that could not be seen by the land seismic network, whose sensitivity is compromised by ocean (microseism) and anthropogenic noise. A SMART cable will consequently improve the regional seismic detection capability handled by the Geophysical Laboratory of Tahiti, French Alternative Energies and Atomic Energy Commission (CEA/LDG). Although French Polynesia is considered essentially aseismic, the 2018–2019 unexpected submarine eruption near Mayotte Island and presence of active volcanism in French Polynesia offer a reminder that appropriate seismic monitoring to establish baselines is prudent.

Currently, tsunamis (>5 cm) can be detected by the French Polynesian coastal tide gage network handled by the University of French Polynesia (Barriot et al., 2012) in addition to the University of Hawaii Sea Level Center (UHSLC) tide gage (Caldwell et al., 2015). The SMART pressure gages will be able to record with sub-millimeter resolution tsunami waves transiting the French Polynesia region. This data will enhance understanding of the tsunami behavior (amplification, reflection, and diffraction) for the three archipelagos (Austral, Society, and Tuamotu). This will drive further research to improve tsunami modeling and thus improve the tsunami forecasts for characterizing alert parameters for more distant impacted regions.

The temperature sensor allows the monitoring of the evolution of the long-term deep ocean temperature over a north-south profile. Such sensors networked along 8° of latitude will enhance our understanding of the potential bottom oceanic circulation and the long-term oceanic climate cycles at 1,000 m and 5,000 m depth (**Figure 11**) and link it to

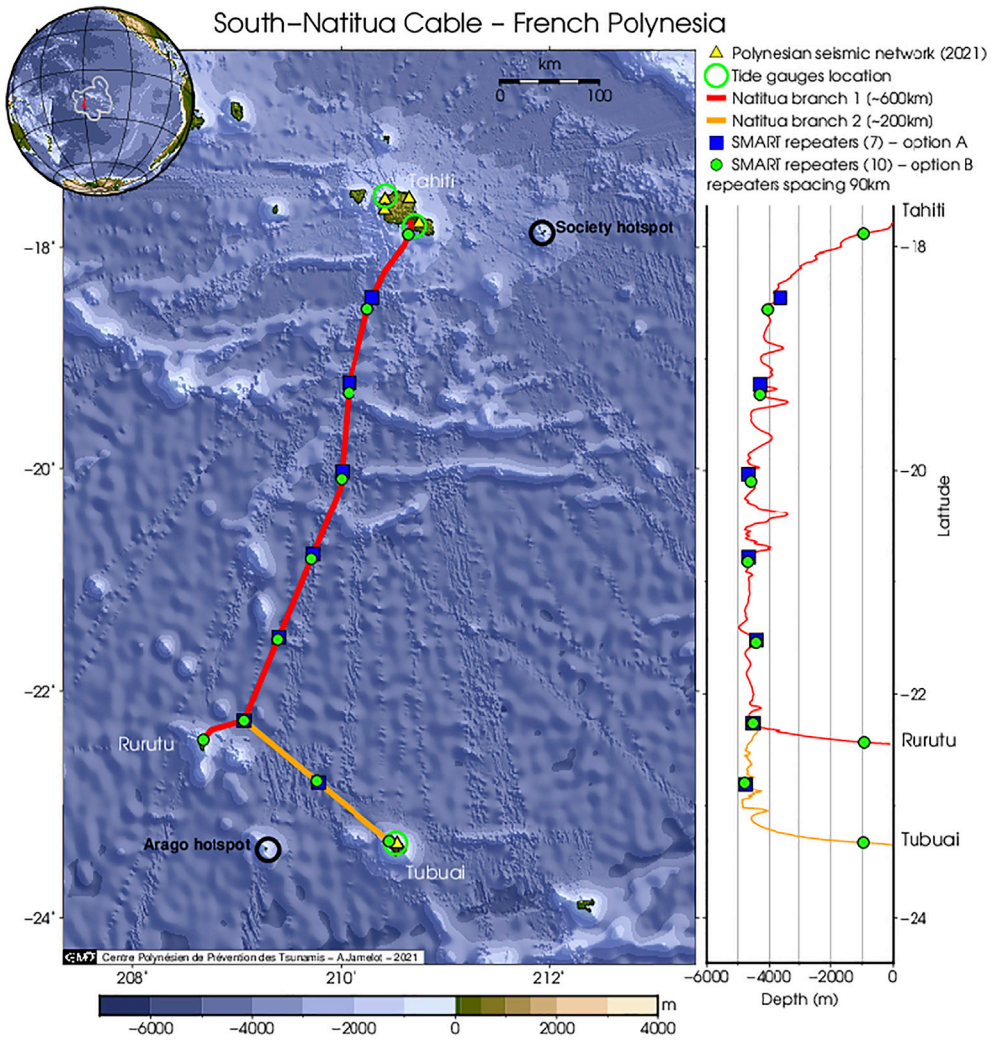


**FIGURE 11 |** The Natitua Cable two branch path configuration with a repeater spacing of 90 km along the cable (blue squares). Solid green markers represent a proposed dense deployment of instrumented repeaters. On the right are the projected depth profiles along each cable path with repeater locations. Most repeaters are at 5,000 m depth so three have been added at 1,000 m depth near each island. The perimeter of the hotspot is marked by a black circle. Open green circles represent tide gauge locations and yellow triangles mark existing onshore seismic stations.

near surface studies (Rougerie and Rancher, 1994; Martinez et al., 2009; Leichter et al., 2012).

## 4.4 Indonesia

Indonesia is one of the most active earthquake regions in the world and resides above three converging continental tectonic plates, namely: Indo-Australia to the west and south; Eurasia from the north; and the Philippines plate from the east. Indonesia is therefore highly vulnerable to tectonic earthquakes, volcanic eruptions, and underwater landslides that could trigger both normal tectonic or atypical tsunamis, and is threatened by far- and near-field tsunamis.

The importance of landslide-generated tsunamis is becoming more apparent (Salaree and Okal, 2018). Here we show an example of the estimated cumulative tsunami height due to seismically triggered submarine landslide scenarios (**Figure 12**). Considering the highly complex triggering mechanism, a cumulative field of peak ground acceleration (PGA) from CMT sources with depth shallower than 40 km was calculated. Fifty-eight dipole source scenarios were designed based on PGA and the underwater slope field. The results not only compel the need for more study of seismically triggered submarine landslides in Indonesia (Salaree et al., 2021) but also highlight the importance of a SMART cable system in detection of this underappreciated threat.

The Indonesia Tsunami Early Warning System (InaTEWS) was established following Aceh's tsunami in 2004. InaTEWS consists of three sub-systems. The upstream part includes observational equipment to monitor seismic vibrations and ocean tsunami wave heights. The acquired data are directly transmitted to the BMKG (Agency for Meteorology Climatology and Geophysics) processing center, which

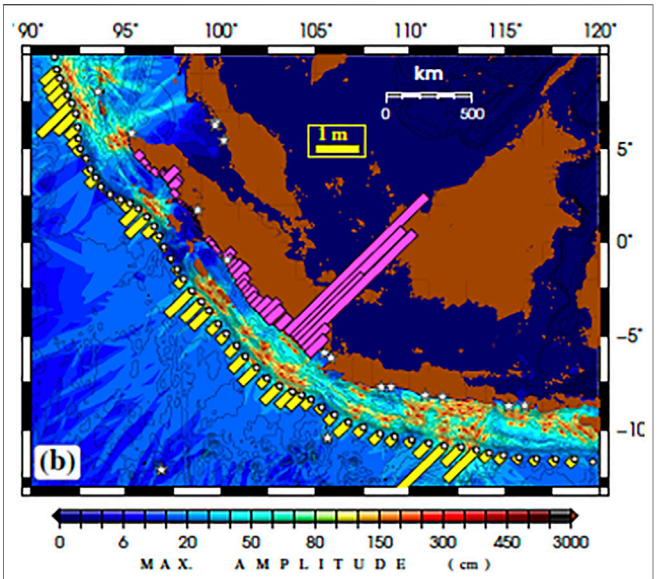


**FIGURE 12 |** For a possible SMART cable (yellow dots) scenario, tsunami wave heights are calculated from 52 landslide scenarios designed for peak ground acceleration >0.3 g based on the bottom slope. Yellow bars show predicted tsunami height at each SMART sensor. Pink bars give tsunami height near the shore (~60 m water depth). White stars represent existing tide gauges.

produces information on epicenter location, depth, origin time, magnitude of the earthquake, and its tsunamigenic potential. The resulting early warning information is directly disseminated to potentially affected communities through interface institutions or authorities.

Recently, the BPPT (Agency for the Assessment and Application of Technology) embarked on the development of the SMART-CBT (cable-based tsunami) or Advanced CBT system. The design, which began in early 2020, will accommodate both tsunami sensors as well as data communication. Early single-ended test systems are planned for Labuhan Bajo and Rokatenda, evolving to a double-ended system to be deployed across Makassar Strait connecting East Kalimantan and Mamuju in West Sulawesi (**Figure 13**). The COVID-19 pandemic, however, is delaying development.

Despite the COVID constraint, BPPT in collaboration with the University of Pittsburgh, United States, Woods Hole Oceanographic Institute, Bandung Institute of Technology (ITB), and Andalas University installed a hybrid cable-based tsunameter in July 2020 in Siberut. The objective is to detect events on the Mentawai-Siberut Megathrust segment. This hybrid system is a combination of optical cable, acoustic wireless links, and several autonomous ocean bottom pressure sensors (tsunameters). An acoustic modem on the end of a short electro-optical shore cable acts as a base transceiver station talking to several tsunameters nearby and in deeper water. The acoustic communications are facilitated by the bottom slope and the thermocline structure. With this configuration, information is quickly sent from instruments 20–30 km away to the mainland.

## 4.5 Portugal–CAM-2

Continent/Azores/Madeira (CAM) is the submarine telecommunication fiber optic cable system that interconnects the Portuguese mainland with the Azores and Madeira archipelagos in a triangle/ring. The current three cables will be obsolete between 2024 and 2028, the CA cable first and the MA last. The RFP for the new CAM-2 is estimated to be presented in

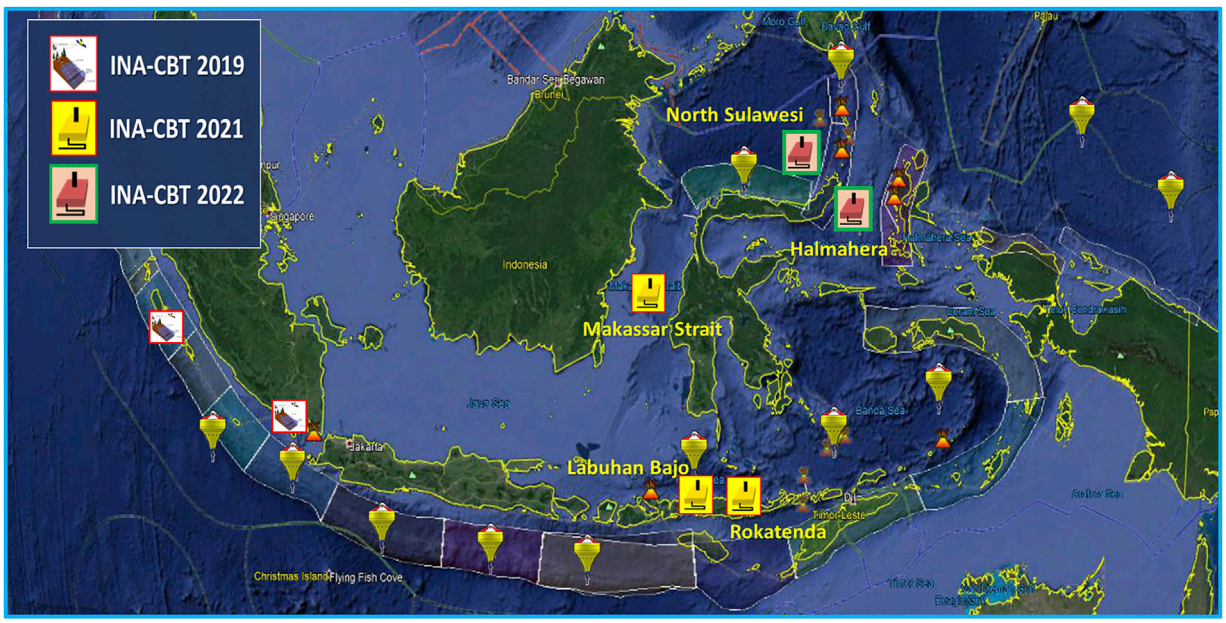


**FIGURE 13 |** Locations of Ina-CBT activities in Indonesia. The rectangle symbols show earlier (white), on-going (yellow), and future (beige) CBT cable systems.

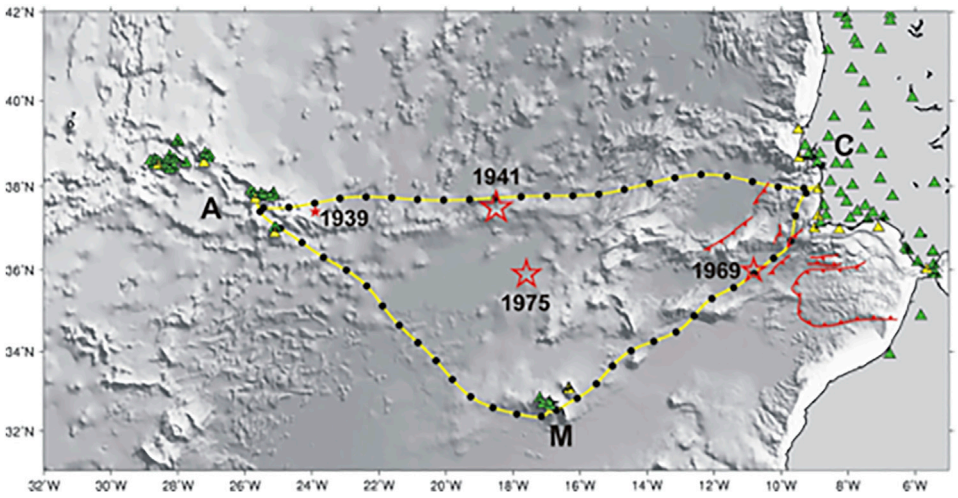


**FIGURE 14 |** Nominal route for the new CAM submarine cable with SMART repeaters (black dots), spaced ~70 km. The cables are identified by the landing points on both ends, C for the Portuguese mainland, M and A for the Madeira and Azores Archipelagos, respectively. The green triangles denote seismic stations currently monitored by the Instituto Português do Mar e da Atmosfera (IPMA). The yellow triangles show the location of coastal tide-gauges monitored by IPMA. The red stars show the location of 3 M > 7.7 large tsunamigenic earthquakes that occurred in the 20th century. The location of the November 1, 1755 earthquake is uncertain, and the faults shown (red lines) have been proposed as its source.

quarter 2, 2022, and follows a clear governmental requirement that the new cables must have seismic and environmental monitoring functionalities (Government of Portugal, 2020).

The CAM cables extend along the plate boundary between Eurasia and Nubia, an offshore domain prone to destructive earthquakes and tsunamis (**Figure 14**). This area was the source of the largest earthquake in Europe since 1000 (Stucchi et al., 2012), i.e., the November 1, 1755 (Mw 8.5) event, and the largest earthquake in Europe since 1900 causing casualties and destruction, i.e., the February 28, 1969 Mw 7.8 event (Grünthal and Wahlström, 2012). Three other significant earthquakes with M > 7 also occurred on this plate boundary in the 20th century (M7.1, 1939; M8.0, 1941; and Mw 7.9 1975), causing small tsunamis, less than 1 m high (Baptista and Miranda, 2009), as shown in **Figure 14**.

Mitigation of the hazards generated by offshore tectonic sources requires effective early warning systems for earthquakes and tsunamis. The response of these detection systems must rely on the first seismic and sea level data arriving to the monitoring networks. These are currently seismic land stations and coastal tide gauges (**Figure 14**). For the likeliest tsunami sources that may affect the Portugal mainland, Omira et al. (2009) showed the need for offshore sea level measurements to ensure at least 10 min advance warning time before the first tsunami arrives at any Portuguese coastal area.

To demonstrate the capability for earthquake and tsunami monitoring of the new SMART CAM cables, we use the tsunami source database in place at Instituto Português do Mar e da Atmosfera (IPMA) as shown on **Figure 14**. The new CAM layout is notional with sensors every 70 km along the cable track and the first repeater 30 km from the shore (**Figure 14**).

We computed the estimated tsunami arrival time (ETA) to each of the coastal tide gauges monitored by IPMA and compared these to the ETA computed for the new SMART CAM sensors. The difference reflects improvement in warning time that can be obtained by the instrumented submarine cables, as shown in **Figure 15A**. The usefulness of each sensor is roughly estimated by the number of tsunami sources reaching it first, as shown by the size of the symbols in **Figure 15A**.

At IPMA, following standard operating procedures, a hypocentral location must be provided within 5 min of an event based on the first ten waveforms received. This information and the corresponding tsunami threat level are provided to civil protection and national authorities. The quality of this first computation is critically dependent on the geometry of the ten stations used. We evaluated the contribution of the new SMART CAM network to the improvement of two geometric properties: 1) the maximum azimuthal gap between epicenter and stations; and 2) the network quality metric defined by Bondár and McLaughlin (2009) that also assesses the distribution of the epicenter to station azimuths (0 is the best and 1 means that all stations have the same azimuth). The gain obtained for azimuthal gap and the network quality metric by the new SMART CAM network are shown in **Figures 15B,C**, respectively. The relevance of each sensor is roughly estimated by the number of earthquake sources each sensor is contributing.

IPMA is testing an Earthquake Early Warning System (EEW) based on the amplitude of seismic waves recorded on the first five stations. With land stations only, the southern Portugal mainland cannot benefit from such a system, as the warning time to the Lisbon area is very short (~30 s or less). This performance can be greatly improved using the SMART new CAM network of sensors, as shown on **Figure 15D**. Again, the relevance of

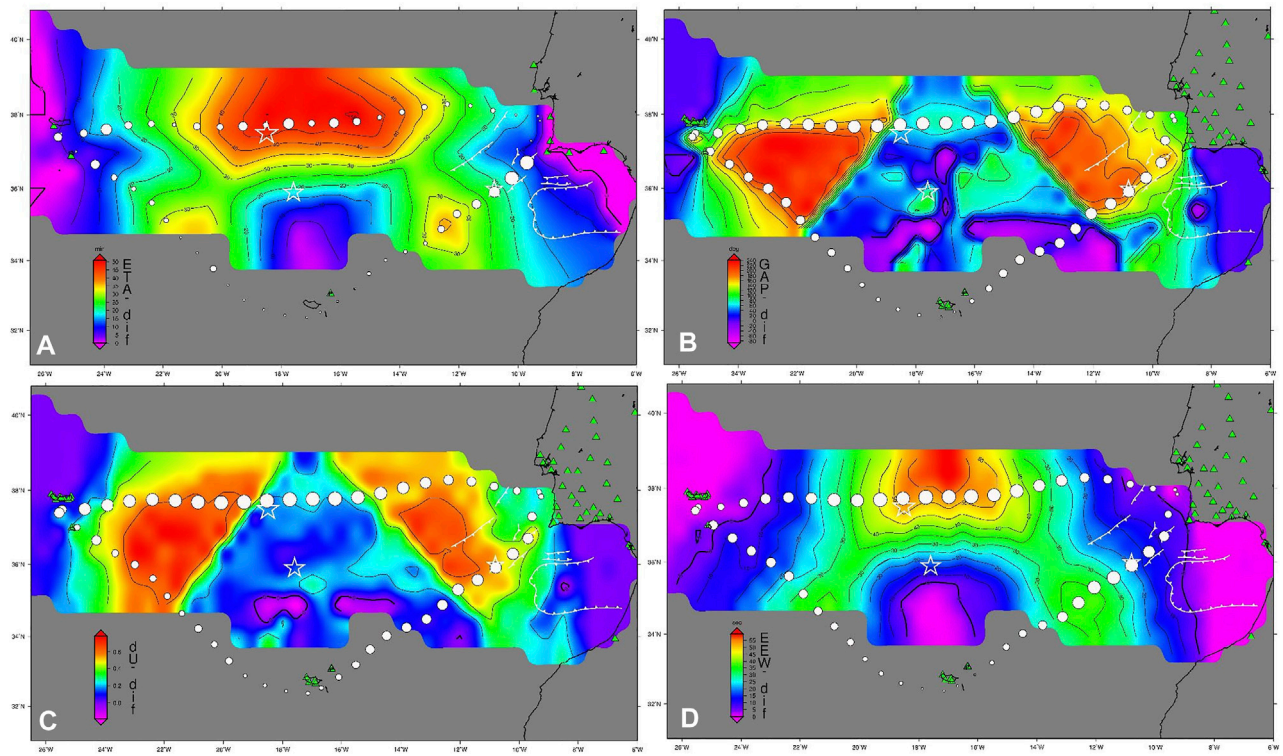


**FIGURE 15 | (A)** Reduction in tsunami arrival time (minutes) obtained by the CAM-2 set of sensors (white circles) when compared to the coastal tide gauge network monitored by IPMA (green triangles). **(B)** Comparative reduction in azimuthal gap (degrees). **(C)** Improvement in the network quality metric. **(D)** Reduction in earthquake early warning time (EEW in seconds) obtained by the CAM-2 set of sensors when compared to the seismic land network monitored by IPMA. The size of the cable sensor symbols is proportional to the number of events used. Purple area defines where the CAM-2 sensors did not improve the result. White stars show the location of 3 M > 7.7 20th century earthquakes that caused small tsunamis. The location of the November 1, 1755 earthquake is uncertain, and we show the tectonic faults (white lines) that are suggested to be at the source of that event by several authors.

each sensor is roughly estimated by the number of earthquake sources to which location each sensor is contributing.

All the examples presented show that the new SMART CAM network can contribute to earthquake and tsunami hazard mitigation for the Portugal mainland, as well as the Azores and Madeira. Using the source areas of historic large earthquakes and tsunamis, modeling using proposed SMART sensor locations indicates a significant improvement in tsunami early warning, earthquake fast location, and strong motion early warning.

## 4.6 Other Projects

There are several other systems presently in discussion and planning stages worthy of note. The first two are largely government driven, with telecom serving small communities in areas of science and early warning importance.

First, the New Zealand government has recognized that a need exists for improved telecommunications connectivity to the Chatham Islands, a remote island community ~800 km east of the New Zealand mainland. By adding scientific sensing capability, such a cable could also be leveraged to improve geohazards monitoring in the region (including tsunami and earthquake early warning) and enhance scientific understanding of a large range of geophysical and oceanographic processes. To address this, a workshop was convened in February 2021 to consider how to satisfy these needs. The report (Wallace et al., 2021) summarized the main findings and conclusions of the workshop and background information necessary for considering the development of permanent, offshore observing capability in New Zealand. A primary conclusion of the workshop, and a recommendation of the report, is "that a hybrid cable design incorporating both "in-line" sensors and external sensors connected to branching units, plus fiber strands usable for distributed acoustic sensing (DAS) would provide the best balance between the oceanographic, geophysical, and geohazards monitoring benefits of offshore scientific infrastructure. This approach to the cable design would future-proof the cable and its sensor payloads, maximizing the return on investment as technology improves in decades to come, while ensuring that the scientific components did not compromise the cable's primary mission." Discussions and planning regarding this possible cable system (and addition of scientific sensing capability) are currently ongoing.

Second, the US National Science Foundation is interested in a submarine fiber optic telecommunications cable from New Zealand to McMurdo Station in Antarctica, with terabit-scale networking capability that could eliminate current bandwidth constraints faced by researchers, educators, and support functions in the Antarctic, while also reducing the latency of current satellite-based communication. The cable

infrastructure can also serve as a scientific platform using SMART Cables with capability to monitor ocean conditions and seismic activity. To document the benefits of such a cable, a workshop (https://www.pgc.umn.edu/workshops/antarctic-cable/) was held 29 June–1 July 2021. The following insights are obtained from the workshop report (Neff et al., 2021). Observations of temperature and pressure on a new SMART cable to McMurdo will immediately provide important climate change metrics in the Southern Ocean, including Antarctic Bottom Water temperature and volume, Antarctic Circumpolar Current transport, and regional sea level rise. The cable's enabling characteristics would be real time, high frequency sampling, 24/7/365 acquisition, good spatial resolution (~50 km), the spanning of a major inter-ocean chokepoint, and rare observations below 2000 m. These measurements are invaluable for understanding the progression and causes of climate change and predicting global climate conditions into the future. SMART seismic accelerometers along such a cable would fill a large data gap in the southern oceans that limits the resolution of global seismic Earth models. SMART seismic acceleration data, augmented with inexpensive acoustic and optical fiber sensing, also enable the monitoring of grounded ice motion, ice shelf-breaking tsunamis, marine mammals, seismic ocean thermometry, and micro-earthquakes. The inclusion of additional branching nodes would open unprecedented opportunities in Southern Ocean biogeochemical, ecosystem, and water column sensing, AUV docking, acoustic communications and navigation. All these enhancements to the basic SMART cable would be neutral with respect to the fundamental communications mission of the cable and could enable the first step in a future Southern Ocean Observatory.

In the Atlantic, the GEANT research and education network is seeking ways to provide free fibers for scientific use along spurs of the EllaLink cable, which connects European and South American academic networks (https://www.geant.org/geolab). Different types of interrogators, e.g., Distributed Acoustic Sensing (DAS) or Distributed Temperature Sensing (DTS), could be attached by scientists to carry out distributed sensing along the fiber, although currently this technique is limited to a range of several tens of kilometers.

Lastly, Project Koete, connecting Perth-Darwin-Jakarta-Singapore-Malaysia, with additional branches to serve the Australian Northwest Territories, including offshore oil and gas, is largely commercially driven but will include a SMART component. Specifically, it will be designed to support earthquake and tsunami early warning, as well as monitor the ocean environment (Project Koete, 2021).

# 5 OTHER CONSIDERATIONS

## 5.1 Data Management

Data from SMART cables will transit through the cable fiber to land stations where they will be stored and distributed. Individual countries and cable operators can establish their own data policies, based on each system configuration. However, the JTF is advocating for the Findable, Accessible, Interoperable, Reusable (FAIR) data principles, especially for data critical to Early Warning Systems (seismic and pressure data).

The physical parameters measured by SMART cables are already measured by ocean and land-based systems. For example, an entire data ecosystem already exists for sea-level data though the Global Sea-Level Observing System (GLOSS, https://www.gloss-sealevel.org/), for seismic data through the Incorporated Research Institutions for Seismology (IRIS) Data Management Center (https://ds.iris.edu/ds/nodes/dmc/) or the federated European Integrated Data Archive (EIDA) (Strollo et al., 2021; http://www.orfeus-eu.org/data/eida/), and the US NOAA National Centers for Environmental Information (https://www.ncei.noaa.gov/). Real time data for the purposes of early warning and operational oceanography will make use of the WMO's Global Telecommunications System (GTS). High sampling rate data (accelerometer, pressure sensors) can also be supplied by established real time protocols already in use by seismic data and tsunami warning centers for land-based seismic sensors, for example seedlink (IRIS, 2021).

For SMART cables within a single country, in many cases national data centers will be the authoritative source of the data. As a specific example, for the CAM-2 system, the Instituto Português do Mar e da Atmosfera (IPMA) will handle the data.

## 5.2 Legal, Permitting, and Security Concerns

There are various concerns regarding marine science research and the legal and permitting status of the cables (Bressie, 2012). Our approach is, at this early stage, to deal only with domestic projects or between amicable countries and set precedents. If a planned cable route passes through a third party's waters and they object, the problem can be circumvented by simply not installing SMART in their waters. In the longer term we will work with IOC and WMO to develop a process to handle this. In the end, pragmatic advances may rely upon *a priori* arrangements with individual governments. The JTF is working with government regulators to encourage the adoption of incentives for SMART cables, such as expedited permitting, reduction in fees, and access.

Such a pragmatic approach also applies to cable integrity and security issues. Up to now, cables have largely been "deaf, dumb and blind" to their environment with damage detected only after a fault. SMART sensors and DAS can be used to improve cable protection, e.g., detect trawlers and dragging anchors before they hit the cable allowing for intervention before damage is done, as well as other external aggression with malign intent, for the benefit of the telecom mission. More generally, data from SMART cables can be used to improve routing of future cables to avoid, for instance, potential landslide areas, given recent experience off Taiwan (Carter et al., 2014) and the Congo River Canyon (Talling et al., 2020).

A concern often raised is that having the locations of sensors public, the cables may become easy targets for military or terrorist action. In fact, this information is already public. Cable route positions are not classified. Preliminary routes are open while final routes are merely business confidential. Cable ships use AIS (commercially and publicly available ship positions) and often

publish navigation screen images on social media so that a determined actor would generally be able to obtain cable positions. From inception, submarine cables have occasionally been military targets, when they are usually cut right at the very start of a conflict. A famous example is the British CS *Alert* cutting German submarine cables at the start of WWI (Winkler, 2008). SMART capability will not change this.

## 5.3 Costs and Financing

Typical submarine cable system costs range between US $20,000 and US $40,000 per kilometer. We estimate that the incremental cost of SMART capability is about 10% after the research and development costs are recouped by suppliers. During the first years, the cost will likely be higher. For example, a telecom cost of $30,000/km with a system length of 4,000 km and 15% incremental cost yields US $120M telecom + $18M SMART = US $138M total.

Several approaches can be considered to finance the additional cost of adding SMART sensing to telecommunications cables. Such funding can either be provided on a stand-alone basis to directly cover such cost or integrated into the overall financing structures of the cable project.

A variety of institutions may be motivated to provide grant funding for this effort. These include government agencies, international development institutions, and philanthropic foundations who might be interested in supporting early-warning systems for improved disaster resilience for Small Island Developing States (SIDS) and Least Developed Countries (LDCs), or who are seeking to build better real-time data infrastructures for science. Private companies aligned with the UN SDG goals who wish to be considered for Environment, Sustainability, and Governance (ESG) investment may likewise be interested to support such efforts, for instance, out of their Corporate Social Responsibility (CSR) budgets. This could also be the case for technology companies eager to get a foothold in the emerging ocean innovation space for blue infrastructure (Thiele et al., 2020).

A more complex but potentially larger and attractive financing perspective arises if the SMART infrastructure can become part of the overall finance package for the telecoms project (Thiele and Gerber, 2017). In practice, the use of such sensing adds additional beneficiaries to the cable infrastructure: the users of the SMART data. If such users, for instance a government research or operational body (e.g., tsunami early warning centers), are willing to enter into long-term capacity purchase agreements with the telecommunications operator, this additional source of cash flow could be attractive to the subsea cable operator and might be sufficient to cover the additional cost. Furthermore, by enlisting a client that is backed by a government with a solid credit rating, additional senior debt may be made available from international lenders, including potentially at concessional rates from multilateral development banks (Asian Development Bank, 2018).

Overall, a blended finance approach, with some upfront grant funding for project design and development, combined with longer term project debt could provide a solid base for rolling out SMART sensors on ocean cables at a low cost and as a key contribution to an innovative ocean data infrastructure for a sustainable future (Claudet et al., 2020).

## 5.4 Relationship to Other Programs and Organizations

The JTF is following several paths to encourage adoption by interacting with other entities and stakeholders. Within ITU (hosting the JTF Secretariat) several activities are advancing: a SMART Resolution before the World Technical Standards Assembly; amendments to existing climate and disaster risk reduction resolutions; SMART system recommendations being prepared by Study Group 15/Q8; and participation in the Global Symposium for Regulators. Via an ITU Circular, we are reaching out to all member states, suppliers, "over-the-top" (OTT) content providers (e.g., Google, Facebook), regulators, and development banks, as well as the UN hierarchy of climate, ocean, and disaster risk reduction for support.

Within the IOC, in June 2021, the General Assembly approved a Tsunami Programme explicitly including SMART, formulated by the Tsunami and other Sea Level Related Hazards Warning System (TOWS) Working Group, for the UN Decade of Ocean Science for Sustainable Development. JTF has been endorsed as a project of the UN Decade. All these activities are at a level involving the UN member states.

Within the framework of the UN Decade, we will interact with the Global Ocean Observing System (GOOS) to ensure that the measurements we provide will be assimilated properly into the System. SMART Cables are included as one component of the Deep Ocean Observing Strategy (Levin et al., 2019; https://deepoceanobserving.org/).

# 6 CONCLUDING REMARKS

SMART Cables follow an innovative implementation path outside the classical "oceanography box" with an unusual cast of stakeholders. The sum of combining cable and sensing technology will be greater than the parts. SMART cables can revolutionize access to the global deep ocean and enable unique ocean observations of major importance, while improving cable system performance and integrity. To achieve this, the ocean community and the telecom industry must work together in the context of the UN Decade of Ocean Science and the Blue Economy to produce a global telecom plus science network for societal benefit.

In this paper we show that SMART cables will fill scientific and societal needs via ocean monitoring of essential ocean variables (EOVs) and provide data critical to supporting disaster early warning services, directly and indirectly addressing multiple sustainable development goals. All cable system suppliers have said that SMART cable systems are technically achievable; Alcatel Submarine Networks has stated they will supply SMART capability. Systems are moving ahead without legal, permitting, or security issues, indicating that the establishment of SMART cable capability is tractable. Similarly, systems now underway demonstrate that SMART cable systems can be financially feasible, with the expectation that funding models will adapt to specific situations and change over time as the process matures.

We conclude with the recommendation from the OceanObs'19 conference:

Transition telecom + sensing SMART subsea cable systems from present pilots to *trans*-ocean and global implementation, to support climate, ocean circulation, sea level monitoring, and tsunami and earthquake early warning and disaster risk reduction.

## AUTHOR CONTRIBUTIONS

BH provided the overall guidance and editing for the paper. CB wrote the introduction. The following authors contributed to the science sections: CR, seismology; SW, NB, and BF, tsunamis; JA and DL, oceanography. SL wrote the technical approach section with WW contributing the part on seismic and pressure sensor specifications. HJ supplied the ocean seismic noise data. GM contributed the InSea Wet Demo section. JA contributed the Vanuatu-New Caledonia section. AS and AES contributed the Indonesia section. AJ contributed the French Polynesia section. LM and JB contributed the Portugal CAM2 section. TT and BH wrote the cost and finance section. FT contributed to all aspects of the paper. Other authors all provided input and editing

## FUNDING

BH was supported by NASA (via JPL) NNN13D462T for the writing of this paper.

## ACKNOWLEDGMENTS

We gratefully acknowledge discussions and input from Diego Arcas (NOAA, United States), Michael Begnaud (LANL, United States), John Balmer (Guralp Systems, United Kingdom), Laura Beranzoli (INGV, Italy), Esline Garaebiti Bule (Ministry of Climate and Disaster Risk Reduction, Vanuatu), Christopher Hughes (NOC, United Kingdom), David T. Meldrum (SAMS, United Kingdom), Yuelong Miao (BoM, Australia), Manfred Niehus (Instituto de Telecomunicações, Portugal), Yasser Omar (Instituto de Telecomunicações, Portugal), Sasono Rahardjo (BPPT, Indonesia), Mary Rengifo (Tsunami Warning Center, Colombia), Nelly Florida Riama (BMKG, Indonesia), Vasco Sá (Instituto de Telecomunicações, Portugal), Masanao Shinohara (University of Tokyo, Japan), Y. Tony Song (JPL/Caltech, United States), Udrekh (BNTP, Indonesia), and Carlos Zuniga (Servicio Hidrografco y Oceanografco de la Armada, Chile). J. You is acknowledged for providing the initial vision for the SMART cables concept. B. Bay worked on illustrations and M. Izumi and I. Ying on technical editing. Maps in **Figures 1**, **4** were provided by M. Chandler using GMT. Authors' and contributors' individual contributions and the support of their respective institutions are gratefully acknowledged. This is University of Hawai'i at Mānoa SOEST Contribution Number 11451. Los Alamos National Laboratory Publication LA-UR-21-29030.

## REFERENCES

Aguzzi, J., Flexas, M. M., Flögel, S., Lo Iacono, C., Tangherlini, M., Costa, C., et al. (2020). Exo-Ocean Exploration with Deep-Sea Sensor and Platform Technologies. *Astrobiology.* 20, 897–915. doi:10.1089/ast.2019.2129

Alcatel Submarine Networks (2020). *Climate Change*. Paris, France: Press release. Available at: https://web.asn.com/en/press-release/climate-change.html (Accessed September 29, 2020).

Angove, M., Arcas, D., Bailey, R., Carrasco, P., Coetzee, D., Fry, B., et al. (2019). Ocean Observations Required to Minimize Uncertainty in Global Tsunami Forecasts, Warnings, and Emergency Response. *Front. Mar. Sci.* 6, 350. doi:10.3389/fmars.2019.00350

Aoi, S., Asano, Y., Kunugi, T., Kimura, T., Uehira, K., Takahashi, N., et al. (2020). MOWLAS: NIED Observation Network for Earthquake, Tsunami and Volcano. *Earth Planets Space.* 72, 126. doi:10.1186/s40623-020-01250-x

Arbic, B. K., Garner, S. T., Hallberg, R. W., and Simmons, H. L. (2004). The Accuracy of Surface Elevations in Forward Global Barotropic and Baroclinic Tide Models. *Deep Sea Res.* 51 (25-26), 3069–3101. doi:10.1016/j.dsr2.2004.09.014

Ardhuin, F., Rawat, A., and Aucan, J. (2014). A Numerical Model for Free Infragravity Waves: Definition and Validation at Regional and Global Scalesfinition and Validation at Regional and Global Scales. *Ocean Model.* 77, 20–32. doi:10.1016/j.ocemod.2014.02.006

Ardhuin, F., Stutzmann, E., Schimmel, M., and Mangeney, A. (2011). Ocean Wave Sources of Seismic Noise. *J. Geophys. Res.* 116 (C9), C09004. doi:10.1029/2011JC006952

Asian Development Bank (2018). *Multilateral Banks Reaffirm Pledge to Support Resilient, Sustainable Infrastructure.* News Release, 13 October 2018. Available at https://www.adb.org/news/multilateral-banks-reaffirm-pledge-support-resilient-sustainable-infrastructure [Last accessed. January, 5 2022]

Aucan, J., and Ardhuin, F. (2013). Infragravity Waves in the Deep Ocean: An Upward Revision. *Geophys. Res. Lett.* 40, 3435–3439. doi:10.1002/grl.50321

Baker-Yeboah, S., Watts, D. R., and Byrne, D. A. (2009). Measurements of Sea Surface Height Variability in the Eastern South Atlantic from Pressure Sensor-Equipped Inverted echo Sounders: Baroclinic and Barotropic Components. *J. Atmos. Ocean. Techn.* 26 (12), 2593–2609. doi:10.1175/2009JTECHO659.1

Baptista, M. A., and Miranda, J. M. (2009). Revision of the Portuguese Catalog of Tsunamis. *Nat. Hazards Earth Syst. Sci.* 9 (1), 25–42. doi:10.5194/nhess-9-25-2009

Barnes, C. R., Best, M. M. R., Bornhold, B. D., Juniper, S. K., Pirenne, B., and Phibbs, P. (2007). *The NEPTUNE Project—A Cabled Ocean Observatory in the NE Pacific: Overview, Challenges and Scientific Objectives for the Installation and Operation of Stage I in Canadian Waters*. Tokyo: Fifth Underwater Technology Symposium, 7p.

Barnes, C. R., Best, M. M. R., Johnson, F. R., and Pirenne, B. (2015). "NEPTUNE Canada: Installation and Initial Operation of the World's First Regional Cabled Ocean Observatory," in *Seafloor Observatories: A New Vision from the Abyss* (Heidelberg: Springer Praxis Books), 415–438. doi:10.1007/978-3-642-11374-1_16

Barnes, C. R. (2018). "Quantum Leap in Platforms of Opportunity: Telecommunication Cables," in Challenges and Innovations in Ocean In-situ Sensors—Measuring Inner Ocean Processes and Health in the Digital Age (Elsevier), 205–216.

Barriot, J. P., Serafini, J., Sichoix, L., Reymond, D., and Hyvernaud, O. (2012). The Tsunami of March 11, 2011 as Observed by the Network of Tide Gauges of French Polynesia. *J. Mar. Sci. Tech.* 20 (6), 639–646. doi:10.6119/JMST-012-0430-1

Barruol, G., Suetsugu, D., Shiobara, H., Sugioka, H., Tanaka, S., Bokelmann, G. H. R., et al. (2009). Mapping Upper Mantle Flow beneath French Polynesia from Broadband Ocean Bottom Seismic Observations. *Geophys. Res. Lett.* 36, L14301. doi:10.1029/2009GL038139

Bertin, X., de Bakker, A., van Dongeren, A., Coco, G., André, G., Ardhuin, F., et al. (2018). Infragravity Waves: From Driving Mechanisms to Impacts. *Earth-Science Rev.* 177, 774–799. doi:10.1016/j.earscirev.2018.01.002

Best, M., Favali, P., Beranzoli, L., Cannat, M., Çağatay, M. N., Dañobeitia, J. J., et al. (2014). EMSO: A Distributed Infrastructure for Addressing Geohazards and Global Ocean Change. *oceanog.* 27 (2), 167–169. doi:10.5670/oceanog.2014.52

Best, M. M. R., Barnes, C., Bornhold, B., and Juniper, K. (2015). "Integrating Continuous Observatory Data from the Coast to the Abyss: A Multidisciplinary View of the Ocean in Four Dimensions," in *Seafloor Observatories: A New Vision of the Earth from the Abyss*. Editors P. Favali, A. de Santis, and L. Beranzoli (Berlin, Heidelberg: Springer Berlin Heidelberg).

Best, M. M. R., Bornhold, B. D., Juniper, S. K., and Barnes, C. R. (2007). "NEPTUNE Regional Cabled Observatory: Science Plan," in OCEANS 2007 International Meeting of the Marine Technology Society and Institute of Electrical and Electronics Engineers (Vancouver, B.C.: Canada).

Bondár, I., and McLaughlin, K. L. (2009). A New Ground Truth Data Set for Seismic Studies. *Seismological Res. Lett.* 80 (3), 465–472. doi:10.1785/gssrl.80.3.465

Bressie, K. (2012). Using Submarine Cables for Climate Monitoring and Disaster Warning: Opportunities and Legal Challenges. *International Telecommunication Union*, 36. Available at https://www.itu.int/dms_pub/itu-t/oth/4B/04/T4B040000160001PDFE.pdf.

Bromirski, P. D., Duennebier, F. K., and Stephen, R. A. (2005). Mid-Ocean Microseisms. *Geochem. Geophys. Geosyst.* 6 (4), a–n. doi:10.1029/2004GC000768

Butler, R., and Aucan, J. (2018). Multisensor, Microseismic Observations of a hurricane Transit Near the ALOHA Cabled Observatory. *J. Geophys. Res. Solid Earth.* 123 (4), 3027–3046. doi:10.1002/2017JB014885

Butler, R., Cochran, E., Collins, J., Eblé, M., Evans, J., Favali, P., et al. (2014). The Scientific and Societal Case for the Integration of Environmental Sensors into New Submarine Telecommunication Cables. *Joint Task Force on Green Cables*. Geneva, Switzerland: International Telecommunication Union. Available at https://www.itu.int/dms_pub/itu-t/opb/tut/T-TUT-ICT-2014-03-PDF-E.pdf.

Caldwell, P. C., Merrifield, M. A., and Thompson, P. R. (2015). "Sea Level Measured by Tide Gauges from Global Oceans," in *Joint Archive for Sea Level Holdings (NCEI Accession 0019568), Version 5.5* (NOAA National Centers for Environmental Information, Dataset). doi:10.7289/V5V40S7W

Carney, M. (2021). Clean and Green Finance. *International Monetary Fund* . Available at https://www.imf.org/external/pubs/ft/fandd/2021/09/pdf/mark-carney-net-zero-climate-change.pdf [Last accessed. January 6, 2022]

Carter, L., Gavey, R., Talling, P., and Liu, J. (2014). Insights Into Submarine Geohazards from Breaks in Subsea Telecommunication Cables. *oceanog.* 27 (2), 58–67. doi:10.5670/oceanog.2014.40

Cauzzi, C., and Clinton, J. (2013). A High- and Low-Noise Model for High-Quality Strong-Motion Accelerometer Stations. *Earthquake Spectra.* 29 (1), 85–102. doi:10.1193/1.4000107

Chadwick, W. W., Nooner, S. L., Zumberge, M. A., Embley, R. W., and Fox, C. G. (2006). Vertical Deformation Monitoring at Axial Seamount since its 1998 Eruption Using Deep-Sea Pressure Sensors. *J. Volcanology Geothermal Res.* 150, 313–327. doi:10.1016/j.jvolgeores.2005.07.006

Chave, A. D., Luther, D. S., and Thomson, D. J. (2019). High- Q Spectral Peaks and Nonstationarity in the Deep Ocean Infragravity Wave Band: Tidal Harmonics and Solar Normal Modes. *J. Geophys. Res. Oceans.* 124, 2072–2087. doi:10.1029/2018JC014586

Chen, B.-R., Feng, X.-T., Li, Q.-P., Luo, R.-Z., and Li, S. (2015). Rock Burst Intensity Classification Based on the Radiated Energy with Damage Intensity at Jinping II Hydropower Station, China. *Rock Mech. Rock Eng.* 48, 289–303. doi:10.1007/s00603-013-0524-2

Chesnoy, J. (2016). *Undersea Fiber Communication Systems*. 2nd Edition. Amsterdam: Elsevier.

Claudet, J., Bopp, L., Cheung, W. W. L., Devillers, R., Escobar-Briones, E., Haugan, P., et al. (2020). A Roadmap for Using the UN Decade of Ocean Science for Sustainable Development in Support of Science, Policy, and Action. *One Earth.* 2 (1), 34–42. ISSN 2590-3322. doi:10.1016/j.oneear.2019.10.012

Clinton, J. F., and Heaton, T. H. (2002). Potential Advantages of a Strong-Motion Velocity Meter Over a Strong-Motion Accelerometer. *Seismological Res. Lett.* 73 (3), 332–342. doi:10.1785/gssrl.73.3.332

Consortium for Ocean Leadership (2010). Ocean Observatories Initiative Final Network Design. Version 2-06-P, Document Control Number 1101-00000, 2010-04-22. Available at: http://www.oceanobservatories.org/wp-content/uploads/2012/04/1101-00000_FND_OOI_ver_2-06_Pub.pdf

Crawford, W. C., and Singh, S. C. (2008). Sediment Shear Properties from Seafloor Compliance Measurements: Faroes-Shetland basin Case Study. *Geophys. Prospect.* 56, 313–325. doi:10.1111/j.1365-2478.2007.00672.x

Dai, M., Higman, B., Lynett, P. J., Jacquemart, M., Howat, I. M., and Liljedahl, A. K. (2020). Detection and Assessment of a Large and Potentially Tsunamigenic Periglacial Landslide in Barry Arm, Alaska. *Geophy. Res. Lett.* 47, e2020GL089800. doi:10.1029/2020GL089800

Dahm, T., Tilmann, F., and Morgan, J.-P. (2006). Seismic Broadband Ocean-Bottom Data and Noise Observed with Free-Fall Stations: Experiences from Long-Term Deployments in the North Atlantic and the Tyrrhenian Sea. *Bull. Seismological Soc. America.* 96, 647–664. doi:10.1785/0120040064

Dañobeitia, J. J., Pouliquen, S., Johannessen, T., Basset, A., Cannat, M., Pfeil, B. G., et al. (2020). Toward a Comprehensive and Integrated Strategy of the European marine Research Infrastructures for Ocean Observations. *Front. Mar. Sci.* 7, 180. doi:10.3389/fmars.2020.00180

Delory, E., and Pearlman, J. (2018). *Challenges and Innovations in Ocean In-Situ Sensors—Measuring Inner Ocean Processes and Health in the Digital Age*. Cambridge, MA: Elsevier, Inc.

Duennebier, F. K., and Sutton, G. H. (2007). Why Bury Ocean Bottom Seismometers? *Geochem. Geophys. Geosyst.* 8 (2), a–n. doi:10.1029/2006GC001428

Duputel, Z., Rivera, L., Kanamori, H., et al. (2011). Real-time W Phase Inversion during the 2011 off the Pacific Coast of Tohoku Earthquake. *Earth PlanetSpace.* 63, 5. doi:10.5047/eps.2011.05.032

Egbert, G. D., Ray, R. D., and Bills, B. G. (2004). Numerical Modeling of the Global Semidiurnal Tide in the Present Day and in the Last Glacial Maximum. *J. Geophys. Res.* 109, C03003. doi:10.1029/2003JC001973

European Marine Board (2019). *Navigating the Future V: Marine Science for a Sustainable Future*. Ostend, Belgium: Position Paper 24 of the European Marine Board. 97894920437570167-9309. doi:10.5281/zenodo.2809392

Favali, P., Beranzoli, L., Best, M. M. R., Delaney, J. R., De Santis, A., Edwards, A. W., et al. (2015). "Concluding Remarks: Perspectives and Long-Term Vision," in *Seafloor Observatories: A New Vision of the Earth from the Abyss*. Editors P. Favali, A. de Santis, and L. Beranzoli (Springer Praxis Books), 663–666. doi:10.1007/978-3-642-11374-1_26

Favali, P., Person, R., Barnes, C. R., Kaneda, Y., Delaney, J. R., and Hsu, S-K. (2010). "Seafloor Observatory Science," in OceanObs'09: Sustained Ocean Observations and Information for Society, Venice Italy, September 21-25. Proceedings. Editors J. Hall and D. E. Harrison (D. Stammer). doi:10.5270/oceanobs09.cwp.28

Fritz, H. M., and Hager, W. H. (2001). Lituya Bay Case: Rockslide Impact and Wave Run-Up. *Sci. Tsunami Haz.* 19 (1), 3–19. Available at https://library.lanl.gov/tsunami/.

Galindez-Jamioy, C. A., and López-Higuera, J. M. (2012). Brillouin Distributed Fiber Sensors: an Overview and Applications. *J. Sensors.* 2012, 1–17. doi:10.1155/2012/204121

GOOS Steering Committee (2019). *The Global Ocean Observing System 2030 Strategy*. *UNESCO Intergovernmental Oceanographic Commision (IOC), Paris*. GOOS Report No. 239.

Goto, H., and Morikawa, H. (2012). Ground Motion Characteristics during the 2011 off the Pacific Coast of Tohoku Earthquake. *Soils and Foundations.* 52 (5), 769–779. doi:10.1016/j.sandf.2012.11.002

Government of Portugal (2020). CAM-2 Announcement. Despacho n.o 9333/2020, Publicação: Diário da República n.o 191/2020, Série II de 2020-09-30. Available at: https://dre.pt/web/guest/pesquisa/-/search/144137764/details/normal?q=9333%2F2020

Grünthal, G., and Wahlström, R. (2012). The European-Mediterranean Earthquake Catalogue (EMEC) for the Last Millennium. *J. Seismol.* 16 (3), 535–570. doi:10.1007/s10950-012-9302-y

Hazell, N., Lécroart, A., and Marcerou, J.-F. (2007). "Regional cable Observatory Solutions," in Oceans 2007 International Meeting of the Marine Technology Society and Institute of Electrical and Electronics Engineers (Canada: Vancouver, B.C.). doi:10.1109/oceans.2007.4449231

Heidarzadeh, M., and Satake, K. (2015). Source Properties of the 1998 July 17 Papua New Guinea Tsunami Based on Tide Gauge Records. *Geophys. J. Int.* 202 (1), 361–369. doi:10.1093/gji/ggv145

Herbers, T. H. C., Elgar, S., and Guza, R. T. (1995). Generation and Propagation of Infragravity Waves. *J. Geophys. Res.* 100 (C1224), 863–24872. doi:10.1029/95jc02680

Herbers, T. H. C., and Guza, R. T. (1994). Nonlinear Wave Interactions and High-Frequency Seafloor Pressure. *J. Geophys. Res.* 99 (10), 10. doi:10.1029/94jc00054

Herman, M. W., and Furlong, K. P. (2021). Triggering an Unexpected Earthquake in an Uncoupled Subduction Zone. *Sci. Adv.* 7 (13), eabf7590. doi:10.1126/sciadv.abf7590

Howe, B. M., Arbic, B. K., Aucan, J., Barnes, C. R., Bayliff, N., Becker, N., et al. (2019). SMART Cables for Observing the Global Ocean: Science and Implementation. *Front. Mar. Sci.* 6, 424. doi:10.3389/fmars.2019.00424

Howe, B. M., Duennebier, F. K., and Lukas, R. (2015). "The ALOHA Cabled Observatory," in *Ocean Observatories: A New Vision of the Earth from the Abyss* (Heidelberg: Springer Praxis Books), 439–463. Part 3, Ch. 17. doi:10.1007/978-3-642-11374-1_17

Hughes, C. W., Elipot, S., Morales Maqueda, M. Á., and Loder, J. W. (2013). Test of a Method for Monitoring the Geostrophic Meridional Overturning Circulation Using Only Boundary Measurements. *J. Atmos. Ocean. Tech.* 30, 789–809. doi:10.1175/JTECH-D-12-00149.1

Hughes, C. W., Williams, J., Blaker, A., Coward, A., and Stepanov, V. (2018). A Window on the Deep Ocean: The Special Value of Ocean Bottom Pressure for Monitoring the Large-Scale, Deep-Ocean Circulation. *Prog. Oceanography.* 161, 19–46. doi:10.1016/j.pocean.2018.01.011

Iinuma, T., Hino, R., Kido, M., Inazu, D., Osada, Y., Ito, Y., et al. (2012). Coseismic Slip Distribution of the 2011 off the Pacific Coast of Tohoku Earthquake (M9.0) Refined by Means of Seafloor Geodetic Data. *J. Geophys. Res.* 117, a–n. doi:10.1029/2012JB009186

IPCC (2021). "Climate Change 2021: The Physical Science Basis," in Contribution of Working Group I to the Sixth Assessment Report of the Intergovernmental Panel on Climate Change. Editors V. Masson-Delmotte, P. Zhai, A. Pirani, S. L. Connors, C. Péan, S. Berger, et al. (Cambridge University Press).

IRIS (Incorporated Research Institutions for Seismology) (2021). Seedlink Web page. Available at: http://ds.iris.edu/ds/nodes/dmc/services/seedlink/(Accessed December 20, 2021)

Ito, Y., Hino, R., Kido, M., Fujimoto, H., Osada, Y., Inazu, D., et al. (2013). Episodic Slow Slip Events in the Japan Subduction Zone before the 2011 Tohoku-Oki Earthquake. *Tectonophysics.* 600, 14–26. doi:10.1016/j.tecto.2012.08.022

Janiszewski, H. A., Russel, J. B., Hawley, W. B., Tan, Y. J., Lynner, C., Gaherty, J. B., et al. (2020). *10+ Years of Ocean Bottom Seismometer Noise: Fresh Insights and Persistent Questions*. Abstract S059-01, 1-17. San Francisco, CA: AGU Fall Meeting, 2020.

Jayne, S., Roemmich, D., Roemmich, D., Zilberman, N., Riser, S., Johnson, K., et al. (2017). The Argo Program: Present and Future. *Oceanog.* 30, 18–28. doi:10.5670/oceanog.2017.213

Johns, W. E., Baringer, M. O., Beal, L. M., Cunningham, S. A., Kanzow, T., Bryden, H. L., et al. (2011). Continuous, Array-Based Estimates of Atlantic Ocean Heat Transport at 26.5°N. *J. Clim.* 24, 2429–2449. doi:10.1175/2010JCLI3997.1

Johnson, G. C., Lyman, J. M., and Purkey, S. G. (2015). Informing Deep Argo Array Design Using Argo and Full-Depth Hydrographic Section Data. *J. Atmos. Ocean. Tech.* 32, 2187–2198. doi:10.1175/jtech-d-15-0139.1

Johnson, G. C., Purkey, S. G., Zilberman, N. V., and Roemmich, D. (2019). Deep Argo Quantifies Bottom Water Warming Rates in the Southwest Pacific basin. *Geophys. Res. Lett.* 46, 2662–2669. doi:10.1029/2018GL081685

Johnson, G. C. (2008). Quantifying Antarctic Bottom Water and north Atlantic Deep Water Volumes. *J. Geophys. Res.* 113, C05027. doi:10.1029/2007JC004477

Joint Task Force Engineering Team (2021). General Requirements for Sensor Enabled and Reliable Telecommunications (SMART) Cable Systems. *JTF Engineering Team White Paper* (10). Available at https://www.itu.int/en/ITU-T/climatechange/task-force-sc/Documents/General-Requirements-of-a-SMART-Cable-Issue-1.0.pdf.

Joint Task Force (2015a). Functional Requirements of "green" Submarine cable Systems. ITU. Available at: https://www.itu.int/en/ITU-T/climatechange/task-force-sc/Documents/Functional-requirements-2015-05.pdf

Joint Task Force (2015b). Wet Demonstrator: Scope Document and Budgetary Cost Estimate. Available at: https://www.itu.int/en/ITU-T/climatechange/task-force-sc/Documents/Wet-demonstrator-requirements-2015-05.pdf

Joint Task Force (2016). Sensor Enabled Scientific Monitoring and Reliable Telecommunications (SMART) cable Systems: Wet Demonstrator Project Description. Issue 1.0. Available at: https://www.itu.int/en/ITU-T/climatechange/task-force-sc/Documents/Wet-Demonstrator-Design-Issue-1.0.pdf

Kamalov, V., and Cantono, M. (2020). What's Shaking? Earthquake Detection with Submarine Cables. Available at: https://cloud.google.com/blog/products/infrastructure/using-subsea-cables-to-detect-earthquakes

Kanamori, H., and Rivera, L. (2008). Source Inversion of W Phase: Speeding up Seismic Tsunami Warning. *Geophys. J. Int.* 175 (1), 228–238. doi:10.1111/j.1365-246x.2008.03887.x

Kanazawa, T., Uehira, K., Mochizuki, M., Takashi, S., Fujimoto, H., Noguchi, S. I., et al. (2016). *S-net Project: Cabled Observation Network for Earthquakes and Tsunamis*. San Francisco, CA: American Geophysical UnionH43B1840M. Fall Meeting, Abstract #NH43B-1840, Bibcode: 2016AGUFMN.

Kasahara, J., Utada, H., Sato, T., and Kinoshita, H. (1998). Submarine cable OBS Using a Retired Submarine Telecommunication cable: GeO-TOC Program. *Phys. Earth Planet. Interiors.* 108 (2), 113–127. doi:10.1016/s0031-9201(98)00090-9

Kawaguchi, K., Araki, E., Kaneko, S., and Kaneda, Y. (2008). *Design of Deep Ocean Submarine cable Observation Network for Earthquakes and Tsunamis*. OCEANS 2008-MTS/IEEE Kobe, 1–4.

Kawaguchi, K., Kaneko, S., Nishida, T., and Komine, T. (2015). "Construction of the DONET Real-Time Seafloor Observatory for Earthquakes and Tsunami Monitoring," in *Ocean Observatories: A New Vision of the Earth from the Abyss*. Editors P. Favali and A. Santis (Heidelberg: Springer Praxis Books), 212–228. Part 2, Ch. 10. doi:10.1007/978-3-642-11374-1_10

Kelley, D. S., Delaney, J. R., and Juniper, S. K. (2014). Establishing a new era of Submarine Volcanic Observatories: Cabling Axial Seamount and the Endeavour Segment of the Juan de Fuca Ridge. *Mar. Geology.* 352, 426–450. doi:10.1016/j.margeo.2014.03.010

King, B. A., Firing, E., and M.Joyce, T. (2001). Chapter 3.1 Shipboard Observations During WOCE. *Int. Geophys.* 77, 99–122. doi:10.1016/s0074-6142(01)80114-5

Kohler, M. D., Smith, D. E., Andrews, J., Chung, A. I., Hartog, R., Henson, I., et al. (2020). Earthquake Early Warning ShakeAlert 2.0: Public Rollout. *Seismol. Res. Lett.* 91, 1763–1775. doi:10.1785/0220190245

Kuna, V. M., and Nábělek, J. L. (2021). Seismic Crustal Imaging Using Fin Whale Songs. *Science.* 371 (6530), 731–735. doi:10.1126/science.abf3962

Leichter, J. J., Stokes, M. D., Hench, J. L., Witting, J., and Washburn, L. (2012). The Island-Scale Internal Wave Climate of Moorea, French Polynesia. *J. Geophys. Res.* 117, a–n. doi:10.1029/2012JC007949

Lentz, S., and Howe, B. (2018). *Scientific Monitoring and Reliable Telecommunications (SMART) Cable Systems: Integration of Sensors into Telecommunications Repeaters*. Kobe, Japan: OCEANS'18 MTS/IEEE Kobe/Techno-Ocean.

Lentz, S., and Phibbs, P. (2012). *Engineering Feasibility Study: Using Submarine Cables for Climate Monitoring and Disaster Warning*. Geneva, Switzerland: Joint Task Force.

Levin, L. A., Bett, B. J., Gates, A. R., Heimbach, P., Howe, B. M., Janssen, F., et al. (2019). Global Observing Needs in the Deep Ocean. *Front. Mar. Sci.* 6, 241. doi:10.3389/fmars.2019.00241

Lin, M., and Yang, C. (2020). Ocean Observation Technologies: a Review. *Chin. J. Mech. Eng.* 33, 32. doi:10.1186/s10033-020-00449-z

Lindsey, N. J., Martin, E. R., Dreger, D. S., Freifeld, B., Cole, S., James, S. R., et al. (2017). Fiber-Optic Network Observations of Earthquake Wavefields. *Geophys. Res. Lett.* 4411 (23), 792799–792811. doi:10.1002/2017GL075722

Lindstrom, E., Gunn, J., Fischer, A., McCurdy, A., Glover, L. K., and Members, T. T. (2014). A Framework for Ocean Observing. UNESCO 2012 (revised in 2017). IOC/INF-1284 rev. 2. Available at: https://unesdoc.unesco.org/ark:/48223/pf0000211260

Lo Bue, N., Best, M. M. R., Embriaco, D., Abeysirigunawardena, D., Beranzoli, L., Dewey, R. K., et al. (2021). The Importance of marine Research Infrastructures in Capturing Processes and Impacts of Extreme Events. *Front. Mar. Sci.* 8, 626668. doi:10.3389/fmars.2021.626668

Longuet-Higgins, M. S. (1950). A Theory of the Origin of Microseisms. *Phil. Trans. R. Soc. Lond. A.* 243, 1–35. doi:10.1098/rsta.1950.0012

Lu, F., Zhou, H., Peng, X., Yue, J., and Wang, P. (2015). "Technical Preparation and Prototype Development for Long-Term Cabled Seafloor Observatories in Chinese Marginal Seas," in *Ocean Observatories: A New Vision of the Earth from the Abyss* (Heidelberg: Springer Praxis Books), 503–529. Part 3, Ch. 19. doi:10.1007/978-3-642-11374-1_19

Lukas, R., Santiago-Mandujano, F., Bingham, F., and Mantyla, A. (2001). Cold Bottom Water Events Observed in the Hawaii Ocean Time-Series: Implications for Vertical Mixing. *Deep Sea Res. Oceanographic Res. Pap.* 48, 995–1021. doi:10.1016/s0967-0637(00)00078-9

Marra, G., Clivati, C., Luckett, R., Tampellini, A., Kronjäger, J., Wright, L., et al. (2018). Ultrastable Laser Interferometry for Earthquake Detection with Terrestrial and Submarine Cables. *Science.* 361, 486–490. doi:10.1126/science.aat4458

Martinez, E., Ganachaud, A., Lefevre, J., and Maamaatuaiahutapu, K. (2009). Central South Pacific Thermocline Water Circulation from a High-Resolution Ocean Model Validated against Satellite Data: Seasonal Variability and El Niño 1997-1998 Influence. *J. Geophys. Res.* 114, C05012. doi:10.1029/2008JC004824

Massion, G., and Raybould, K. (2006). MARS: The Monterey Accelerated Research System. *Sea Technol.* 47, 39–42.

McCarthy, G. D., Smeed, D. A., Johns, W. E., Frajka-Williams, E., Moat, B. I., Rayner, D., et al. (2015). Measuring the Atlantic Meridional Overturning Circulation at 26°N. *Prog. Oceanography.* 130, 91–111. doi:10.1016/j.pocean.2014.10.006

McKee, D. C., Yuan, X. J., Gordon, A. L., Huber, B. A., and Dong, Z. Q. (2011). Climate Impact on Interannual Variability of Weddell Sea Bottom Water. *J. Geophys. Res.-Oceans.* 116, 17. doi:10.1029/2010jc006484

Mildon, Z., Meschis, M., and Meschis, M. (2019). Fault Responsible for the 1908 Messina Earthquake Identified. *Temblor.* doi:10.32858/temblor.028

National Academies of Sciences, Engineering, and Medicine (2020). *Sustaining Ocean Observations: Proceedings of a Workshop in Brief*. Washington, DC: The National Academies Press. doi:10.17226/25997

Neff, P. D., Andreasen, J. A., Roop, H. A., Pundsack, J., Howe, B., Jacobs, G., et al. (2021). *Antarctic Subsea Cable Workshop Report: High-Speed Connectivity Needs to Advance US Antarctic Science*. Saint Paul, MN: University of Minnesota. Available at https://drive.google.com/file/d/1Ao4Hz6-bBheFMpGSR4nMvSZJ9kHpjj0o/view.

Nerem, R. S., Beckley, B. D., Fasullo, J. T., Hamlington, B. D., Masters, D., and Mitchum, G. T. (2018). Climate-Change-Driven Accelerated Sea-Level Rise Detected in the Altimeter Era. *Proc. Natl. Acad. Sci. USA.* 115, 2022–2025. doi:10.1073/pnas.1717312115

Obayashi, M., Yoshimitsu, J., Sugioka, H., Ito, A., Isse, T., Shiobara, H., et al. (2016). Mantle Plumes beneath the South Pacific Superswell Revealed by Finite Frequency *P* Tomography Using Regional Seafloor and Island Data. *Geophys. Res. Lett.* 43 (11), 628634–628711. doi:10.1002/2016GL070793

Omira, R., Baptista, M. A., Matias, L., Miranda, J. M., Catita, C., Carrilho, F., et al. (2009). Design of a Sea-Level Tsunami Detection Network for the Gulf of Cadiz. *Nat. Hazards Earth Syst. Sci.* 9 (4), 1327–1338. doi:10.5194/nhess-9-1327-2009

Paros, J., Migliacio, P., and Schaad, T. (2012). "Nano-resolution Sensors for Disaster Warning Systems," in *Nano-Resolution Sensors for Disaster Warning Systems. 2012 Oceans-Yeosu*. doi:10.1109/OCEANS-YEOSU.2012.6263413

Person, R., Favali, P., Ruhl, H. A., Beranzoli, L., Rolin, J.-F., Waldmann, C., et al. (2015). "From ESONET Multidisciplinary Scientific Community to EMSO Novel European Research Infrastructure for Ocean Observation," in *Ocean Observatories: A New Vision of the Earth from the Abyss* (HeidelbergPart: Springer Praxis Books), 3, 531–563. doi:10.1007/978-3-642-11374-1_20

Project Koete (2021). Available at: https://www.fibreexpressway.com/index.html

Purkey, S. G., and Johnson, G. C. (2010). Warming of Global Abyssal and Deep Southern Ocean Waters between the 1990s and 2000s: Contributions to Global Heat and Sea Level Rise Budgets. *J. Clim.* 23, 6336–6351. doi:10.1175/2010jcli3682.1

Ranasinghe, N., Rowe, C., Syracuse, E., Larmat, C., and Begnaud, M. (2018). Enhanced Global Seismic Resolution Using Transoceanic SMART Cables. *Seismol. Res. Lett.* 89 (1), 77–85. doi:10.1785/0220170068

Ray, R. D. (2013). Precise Comparisons of Bottom-Pressure and Altimetric Ocean Tides. *J. Geophys. Res. Oceans.* 118, 4570–4584. doi:10.1002/jgrc.20336

RBR (2017). Introducing Generation$^3$. Available at: https://rbr-global.com/2017/introducing-generation%C2%B3

Roger, J., Pelletier, B., and Aucan, J. (2019). Update of the Tsunami Catalogue of New Caledonia Using a Decision Table Based on Seismic Data and Marigraphic Records. *Nat. Hazards Earth Syst. Sci.* 19 (7), 1471–1483. doi:10.5194/nhess-19-1471-2019

Rougerie, F., and Rancher, J. (1994). The Polynesian South Ocean: Features and Circulation. *Mar. Pollut. Bull.* 29, 14–25. doi:10.1016/0025-326X(94)90421-9

Salaree, A., Howe, B. M., Huang, Y., Weinstein, S., and Sakya, A. E. (2021). A Numerical Study of SMART Cables Potential in marine hazard Early Warning for the Sumatra and Java Regions. *Pure Appl. Geophys.* (submitted). doi:10.31223/X59K7Q

Salaree, A., and Okal, E. A. (2018). The "Tsunami Earthquake" of 13 April 1923 in Northern Kamchatka: Seismological and Hydrodynamic Investigations. *Pure Appl. Geophys.* 175 (4), 1257–1285. doi:10.1007/s00024-017-1721-9

Sasagawa, G., and Zumberge, M. A. (2013). A Self-Calibrating Pressure Recorder for Detecting Seafloor Height Change. *IEEE J. Oceanic Eng.* 38, 447–454. doi:10.1109/joe.2012.2233312

Schaad, T. (2009). Nano-Resolution: Oceanic, Atmospheric and Seismic Sensors with Parts-Per-Billion Resolution. Paroscientific, Inc. Technical Note Doc. No. G8218 Rev. F. Available at: http://paroscientific.com/pdf/G8218_Nano-Resolution.pdf

Send, U., and Lankhorst, M. (2011). The Global Component of the US Ocean Observatories Initiative and the Global OceanSITES Project. *OCEANS'11 MTS/IEEE Kona*. Red Hook, NY: Curran Associates. doi:10.23919/OCEANS.2011.6106959

Shinohara, M., Kanazawa, T., Yamada, T., Machida, Y., Shinbo, T., and Sakai, S. i. (2014). New Compact Ocean Bottom Cabled Seismometer System Deployed in the Japan Sea. *Mar. Geophys. Res.* 35, 231–242. doi:10.1007/s11001-013-9197-1

Shinohara, M., Yamada, T., Uehira, K., Sakai, S. i., Shiobara, H., and Kanazawa, T. (2021). Development and Operation of an Ocean Bottom Cable Seismic and Tsunami (OBCST) Observation System in the Source Region of the Tohoku-oki Earthquake. *Earth Space Sci.* 8, e2020EA001359. doi:10.1029/2020EA001359

Smeed, D. A., Josey, S. A., Beaulieu, C., Johns, W. E., Moat, B. I., Frajka-Williams, E., et al. (2018). The north Atlantic Ocean Is in a State of Reduced Overturning. *Geophys. Res. Lett.* 45, 1527–1533. doi:10.1002/2017gl076350

Spinrad, R. (2016). The New Blue Economy: a Vast Oceanic Frontier. *EOS Trans. Am. Geophys. Union.* 97, 1. doi:10.1029/2016EO053793

Strollo, A., Cambaz, D., Clinton, J., Danecek, P., Evangelidis, C. P., Marmureanu, A., et al. (2021). EIDA: The European Integrated Data Archive and Service Infrastructure Within ORFEUS. *Seismol. Res. Lett.* 92 (3), 1788–1795. doi:10.1785/0220200413

Suetsugu, D., Shiobara, H., Sugioka, H., Ito, A., Isse, T., Kasaya, T., et al. (2012). TIARES Project-Tomographic Investigation by Seafloor Array experiment for the Society Hotspot. *Earth Planet. Spspace.* 64, i–iv. doi:10.5047/eps.201.11.002

Suetsugu, D., Sugioka, H., Isse, T., Fukao, Y., Shiobara, H., Kanazawa, T., et al. (2005). Probing South Pacific Mantle Plumes with Ocean Bottom Seismographs. *Eos Trans. AGU.* 86, 429–435. doi:10.1029/2005eo440001

Talley, L. D., Feely, R. A., Sloyan, B. M., Wanninkhof, R., Baringer, M. O., Bullister, J. L., et al. (2016). Changes in Ocean Heat, Carbon Content, and Ventilation: a Review of the First Decade of GO-SHIP Global Repeat Hydrography. *Annu. Rev. Mar. Sci.* 8, 185–215. doi:10.1146/annurev-marine-052915-100829

Talling, P., de Silva Jacinto, R., Baker, M., Pope, E., Heijnen, M., Hage, S., et al. (2020). First Direct Monitoring and Time-Lapse Mapping Starts to Reveal How a Large Submarine Fan Works. *EGU Gen. Assembly.* 2020, EGU2020–2407. doi:10.5194/egusphere-egu2020-2407

Tappin, D. R., Grilli, S. T., Harris, J. C., Geller, R. J., Masterlark, T., Kirby, J. T., et al. (2014). Did a Submarine Landslide Contribute to the 2011 Tohoku Tsunami? *Mar. Geology.* 357, 344–361. doi:10.1016/j.margeo.2014.09.043

Telegeography (2021). Available at: https://www2.telegeography.com/submarine-cable-faqs-frequently-asked-questions

Thiele, T., Alleng, G., Biermann, A., Corwin, E., Crooks, S., Fieldhouse, P., et al. (2020). *Blue Infrastructure Finance: A New Approach, Integrating Nature-Based Solutions for Coastal Resilience*. Gland, Switzerland: IUCN

Thiele, T., and Gerber, L. R. (2017). Innovative Financing for the High Seas. *Aquat. Conserv: Mar. Freshw. Ecosyst.* 27 (S1), 89–99. doi:10.1002/aqc.2794

Tonini, R., Armigliato, A., Pagnoni, G., Zaniboni, F., and Tinti, S. (2011). Tsunami Hazard for the City of Catania, Eastern Sicily, Italy, Assessed by Means of Worst-Case Credible Tsunami Scenario Analysis (WCTSA). *Nat. Hazards Earth Syst. Sci.* 11 (5), 1217–1232. doi:10.5194/nhess-11-1217-2011

Tunnicliffe, V. J., Barnes, C. R., and Dewey, R. (2008). *Major Advances in Cabled Ocean Observatories (VENUS and NEPTUNE Canada) in Shallow and Deep Sea*

*Settings. US/EU-Baltic International Symposium*. Tallinn: IEEE/OES. *Estonia*. 7p

United Nations World Risk Report (2016). Available at: http://collections.unu.edu/view/UNU:5763#viewAttachments.

Wallace, L. M., Townend, J., Stevens, C., Kellett, R. L., De Spuza, J., Giorli, G., et al. (2021). Chatham Islands Cabled Observatory Science Opportunities: Workshop 23-24 February 2021, Summary Report. Lower Hutt (NZ). *GNS Sci.*, 70. doi:10.21420/K1BM-RP28

Wallace, L. M., Webb, S. C., Ito, Y., Mochizuki, K., Hino, R., Henrys, S., et al. (2016). Slow Slip Near the Trench at the Hikurangi Subduction Zone, New Zealand. *Science.* 352, 701–704. doi:10.1126/science.aaf2349

Wang, D., Becker, N. C., Walsh, D., Fryer, G. J., Weinstein, S. A., McCreery, C. S., et al. (2012). Real-time Forecasting of the April 11, 2012 Sumatra Tsunami. *Geophys. Res. Lett.* 39, a–n. doi:10.1029/2012GL053081

Webb, S. C. (1998). Broadband Seismology and Noise under the Ocean. *Rev. Geophys.* 36 (1), 105–142. doi:10.1029/97RG02287

Webb, S. C. (2008). The Earth's Hum: the Excitation of Earth normal Modes by Ocean Waves. *Geophys. J. Int.* 174 (2), 542–566. doi:10.1111/j.1365-246X.2008.03801.x

Weller, R. A., Baker, D. J., Glackin, M. M., Roberts, S. J., Schmitt, R. W., Twigg, E. S., et al. (2019). The Challenge of Sustaining Ocean Observations. *Front. Mar. Sci.* 6, 105. doi:10.3389/fmars.2019.00105

Wilcock, W. S. D., Manalang, D. A., Fredrickson, E. K., Harrington, M. J., Cram, G., Tilley, J., et al. (2021). A Thirty-Month Seafloor Test of the A-0-A Method for Calibrating Pressure Gauges. *Front. Earth Sci.* 8 (653), 600671. doi:10.3389/feart.2020.600671

Winkler, J. R. (2008). *Nexus: Strategic Communications and American Security in World War I*. Cambridge, MA: Harvard University Press. ISBN 0-674-02839-2.

World Ocean Initiative (2020). *A Sustainable Ocean Economy in 2030: Opportunities and Challenges*. The Economist Group Limited. Available at: http://www.woi.economist.com/sustainable-ocean-economy-2030

Worthington, E. L., Frajka-Williams, E., and McCarthy, G. D. (2019). Estimating the Deep Overturning Transport Variability at 26°N Using Bottom Pressure Recorders. *J. Geophys. Res. Oceans*. 124, 335–348. doi:10.1029/2018JC014221

Xtera (2016). Line Monitoring and Control in Subsea Networks. Available at: https://xtera.com/wp-content/uploads/2017/05/White-Paper-Line-Monitoring-and-Control-in-Subsea-Networks-Xtera-August-2016.pdf

You, Y. (2010). Harnessing Telecoms Cables for Science. *Nature.* 466, 690–691. doi:10.1038/466690a

Zhan, Z., Cantono, M., Kamalov, V., Mecozzi, A., Müller, R., Yin, S., et al. (2021). Optical Polarization-Based Seismic and Water Wave Sensing on Transoceanic Cables. *Science.* 26 (6532), 371931–371936. doi:10.1126/science.abe6648

**Conflict of Interest:** NB is employed by Aqua Comms. SL is employed by Ocean Specialists, Inc. MF is employed by Subsea Data Systems, Inc.

The remaining authors declare that the research was conducted in the absence of any commercial or financial relationships that could be construed as a potential conflict of interest.

**Publisher's Note:** All claims expressed in this article are solely those of the authors and do not necessarily represent those of their affiliated organizations, or those of the publisher, the editors and the reviewers. Any product that may be evaluated in this article, or claim that may be made by its manufacturer, is not guaranteed or endorsed by the publisher.

# Frontiers in Earth Science

**Investigates the processes operating within the major spheres of our planet**

Advances our understanding across the earth sciences, providing a theoretical background for better use of our planet's resources and equipping us to face major environmental challenges.

---

## Discover the latest Research Topics

See more →


**Frontiers**

Avenue du Tribunal-Fédéral 34
1005 Lausanne, Switzerland
frontiersin.org

**Contact us**

+41 (0)21 510 17 00
frontiersin.org/about/contact